



*metals*

Special Issue Reprint

---

# Machinability and Tribological Performance of Advanced Alloys

---

Edited by  
George A. Pantazopoulos

[www.mdpi.com/journal/metals](http://www.mdpi.com/journal/metals)



# **Machinability and Tribological Performance of Advanced Alloys**



# Machinability and Tribological Performance of Advanced Alloys

Editor

**George A. Pantazopoulos**

MDPI • Basel • Beijing • Wuhan • Barcelona • Belgrade • Manchester • Tokyo • Cluj • Tianjin



*Editor*

George A. Pantazopoulos  
ELKEME Hellenic Research  
Centre for Metals S.A  
Oinofyta Viotias, Greece

*Editorial Office*

MDPI  
St. Alban-Anlage 66  
4052 Basel, Switzerland

This is a reprint of articles from the Special Issue published online in the open access journal *Metals* (ISSN 2075-4701) (available at: [https://www.mdpi.com/journal/metals/special\\_issues/Machin\\_Tribo\\_Perf](https://www.mdpi.com/journal/metals/special_issues/Machin_Tribo_Perf)).

For citation purposes, cite each article independently as indicated on the article page online and as indicated below:

LastName, A.A.; LastName, B.B.; LastName, C.C. Article Title. <i>Journal Name</i> <b>Year</b> , <i>Volume Number</i> , Page Range.
--

**ISBN 978-3-0365-8280-1 (Hbk)**

**ISBN 978-3-0365-8281-8 (PDF)**

© 2023 by the authors. Articles in this book are Open Access and distributed under the Creative Commons Attribution (CC BY) license, which allows users to download, copy and build upon published articles, as long as the author and publisher are properly credited, which ensures maximum dissemination and a wider impact of our publications.

The book as a whole is distributed by MDPI under the terms and conditions of the Creative Commons license CC BY-NC-ND.

# Contents

<b>About the Editor</b> . . . . .	<b>vii</b>
<b>George A. Pantazopoulos</b> Machinability and Tribological Performance of Advanced Alloys Reprinted from: <i>Metals</i> <b>2023</b> , <i>13</i> , 1190, doi:10.3390/met13071190 . . . . .	<b>1</b>
<b>Yong Duan, Shengguan Qu, Siyu Jia and Xiaoqiang Li</b> Evolution of the Fretting Wear Damage of a Complex Phase Compound Layer for a Nitrided High-Carbon High-Chromium Steel Reprinted from: <i>Metals</i> <b>2020</b> , <i>10</i> , 1391, doi:10.3390/met10101391 . . . . .	<b>7</b>
<b>Zhihao Du, Guofeng Wang and Hailun Wang</b> The Process Design and Rapid Superplastic Forming of Industrial AA5083 for a Fender with a Negative Angle in a Small Batch Reprinted from: <i>Metals</i> <b>2021</b> , <i>11</i> , 497, doi:10.3390/met11030497 . . . . .	<b>19</b>
<b>Sarmad Ali Khan, Mudassar Rehman, Muhammad Umar Farooq, Muhammad Asad Ali, Rakhshanda Naveed, Catalin I. Pruncu and Waheed Ahmad</b> A Detailed Machinability Assessment of DC53 Steel for Die and Mold Industry through Wire Electric Discharge Machining Reprinted from: <i>Metals</i> <b>2021</b> , <i>11</i> , 816, doi:10.3390/met11050816 . . . . .	<b>33</b>
<b>Konstantinos Tserpes, Panagiotis Bazios, Spiros G. Pantelakis, Maria Pappa and Nikolaos Michailidis</b> Mechanical Characterization of Nanocrystalline Materials via a Finite Element Nanoindentation Model Reprinted from: <i>Metals</i> <b>2021</b> , <i>11</i> , 1827, doi:10.3390/met11111827 . . . . .	<b>51</b>
<b>Paul Stavroulakis, Anagnostis I. Toulfatzis, George A. Pantazopoulos and Alkiviadis S. Paipetis</b> Machinable Leaded and Eco-Friendly Brass Alloys for High Performance Manufacturing Processes: A Critical Review Reprinted from: <i>Metals</i> <b>2022</b> , <i>12</i> , 246, doi:10.3390/met12020246 . . . . .	<b>69</b>
<b>Guan Zhang, Wenlei Sun, Lei Xie, Chengwu Zhang, Jie Tan, Xuan Peng, et al.</b> Multicomponent Fe-Based Bulk Metallic Glasses with Excellent Corrosion and Wear Resistances Reprinted from: <i>Metals</i> <b>2022</b> , <i>12</i> , 564, doi:10.3390/met12040564 . . . . .	<b>101</b>
<b>Athanasios Vazdirvanidis, Andreas Rikos, Anagnostis I. Toulfatzis and George A. Pantazopoulos</b> Electron Backscatter Diffraction (EBSD) Analysis of Machinable Lead-Free Brass Alloys: Connecting Texture with Fracture Reprinted from: <i>Metals</i> <b>2022</b> , <i>12</i> , 569, doi:10.3390/met12040569 . . . . .	<b>113</b>
<b>Shih-Kang Kuo, Yi-Liang Ou and Dung-An Wang</b> An Analytical Model for Stress and Curvature Prediction of a Strip Leveling Process Reprinted from: <i>Metals</i> <b>2022</b> , <i>12</i> , 757, doi:10.3390/met12050757 . . . . .	<b>129</b>
<b>Monika Vargova, Miroslava Tavodova, Katarina Monkova and Miroslav Džupon</b> Research of Resistance of Selected Materials to Abrasive Wear to Increase the Ploughshare Lifetime Reprinted from: <i>Metals</i> <b>2022</b> , <i>12</i> , 940, doi:10.3390/met12060940 . . . . .	<b>147</b>

<b>Peter Pavol Monka, Katarina Monkova, Martin Vasina, Milena Kubisova, Martin Korol and Adriana Sekerakova</b> Effect of Machining Conditions on Temperature and Vickers Microhardness of Chips during Planing Reprinted from: <i>Metals</i> <b>2022</b> , <i>12</i> , 1605, doi:10.3390/met12101605 . . . . .	163
<b>Ye Yang, Hao Luan, Songshan Guo, Fengbin Liu, Yuanjing Dai, Chenhui Zhang, et al.</b> Tribological Behaviors of Inconel 718–Tungsten Carbide Friction Pair with Sulfur Additive Lubrication Reprinted from: <i>Metals</i> <b>2022</b> , <i>12</i> , 1841, doi:10.3390/met12111841 . . . . .	181
<b>Thi-Bich Mac, The-Thanh Luyen and Duc-Toan Nguyen</b> Assessment of the Effect of Thermal-Assisted Machining on the Machinability of SKD11 Alloy Steel Reprinted from: <i>Metals</i> <b>2023</b> , <i>13</i> , 699, doi:10.3390/met13040699 . . . . .	195
<b>Peter Pavol Monka, Katarina Monkova, George A. Pantazopoulos and Anagnostis I. Toulfatzis</b> Effect of Wear on Vibration Amplitude and Chip Shape Characteristics during Machining of Eco-Friendly and Leaded Brass Alloys Reprinted from: <i>Metals</i> <b>2023</b> , <i>13</i> , 828, doi:10.3390/met13050828 . . . . .	211
<b>Anna D. Zervaki, Samuel G. Lambrakos, Athanasios G. Mourlas, Ioannis G. Papantoniou, José Rodríguez and Pandora P. Psyllaki</b> Inverse Thermal Analysis as a Tool for Optimizing Concentrated Solar Energy Elaboration of Wear Resistant Surface Layers Reprinted from: <i>Metals</i> <b>2023</b> , <i>13</i> , 942, doi:10.3390/met13050942 . . . . .	233
<b>Kashif Ishfaq, Muhammad Sana, Muhammad Arif Mahmood, Saqib Anwar and Muhammad Umair Waseem</b> Evaluating Surface Quality of Inconel 617 by Employing Deep Cryogenically Treated Electrodes in Surfactant-Added Dielectrics of Transformer Oil Reprinted from: <i>Metals</i> <b>2023</b> , <i>13</i> , 1092, doi:10.3390/met13061092 . . . . .	249

## About the Editor

### **George A. Pantazopoulos**

George A. Pantazopoulos graduated from the Chemical Engineering Department of the National Technical University of Athens (NTUA) in 1992 (order of graduation considered equivalent to “summa cum laude”) with specialization in Materials Science. He received his Ph.D. from the Mechanical Engineering Department of NTUA in the field of Manufacturing Technology and Processing of Advanced Materials in 1999. He has served in the metals industry for more than 23 years as a quality control engineer, as a senior R&D project leader, and more recently, as a quality and technology manager. His principal scientific research interests are focused on the field of failure and fracture analysis, materials processing, manufacturing process technology, mechanical testing, and tribology. He is the author or co-author of more than 160 papers in the above areas, presented at international journals and conferences, as well as two books and various monographs/book chapters. He was an invited speaker at various conferences and academic institutions. He serves as a subject editor/editorial board member and reviewer for journals in the field of materials science and failure analysis. He has been the recipient of various awards and distinctions, including a best paper prize and a dissertation thesis prize. He was also included among the top-cited scientist career-long list, based on a statistical analysis of bibliometric indicators from the Scopus database (based on calculations using all Scopus author profiles as of 1 September 2022).





Editorial

# Machinability and Tribological Performance of Advanced Alloys

George A. Pantazopoulos

ELKEME Hellenic Research Centre for Metals S.A., 61st km Athens—Lamia National Road, 32011 Oinofyta, Viotias, Greece; gpantaz@elkeme.vionet.gr; Tel.: +30-2262-60-4463

## 1. Introduction and Scope

Machining is specially utilized to manufacture special, precision parts and difficult-to-form materials. The most challenging aspects of this topic are the continuously evolving quality and productivity requirements in modern industries and creating new and smart materials that meet energy and environmental (green/clean) regulations. In general, among the conventional machining operations, high-end, modern material removal processes are addressed in this Special Issue (e.g., using high-energy beams, such as laser machining).

The tribological performance of alloys plays an important role in the production or service environment. Because it is closely related to their materials and manufacturing characteristics, it is considered to be a combined topic in the frame of this Special Issue. The study of tribological behaviour suitably addresses the surface engineering aspects of modern and conventional alloys, either in bulk or in coating form, and receives special attention in the generic context of industrial component production and/or service in aggressive working environments.

The core subject of this Special Issue is the elaboration and presentation of studies on alloy design, manufacturing, testing and characterization in order to provide a clear insight into their machinability and/or tribological behaviour. The improvement of these properties has led to the development of new alloy chemistries, novel engineered microstructures and the application of coatings that produce better machinability and/or tribological endurance properties under poor service conditions. Environmental and health and safety regulations demand the use of ecofriendly components. The manufacture of anti-microbial copper alloys in healthcare facilities and the elimination of lead in brass components for drinking water applications constitute examples of this modern industrial trend.

Altering the manufacturing and service conditions is also essential for achieving the optimization of their machinability and tribological performance. The application of surface processes to enhance the tribological performance of alloys is addressed in this Special Issue.

Briefly, the main machinability parameters and outcomes are schematically depicted in Figure 1.

**Citation:** Pantazopoulos, G.A. Machinability and Tribological Performance of Advanced Alloys. *Metals* **2023**, *13*, 1190. <https://doi.org/10.3390/met13071190>

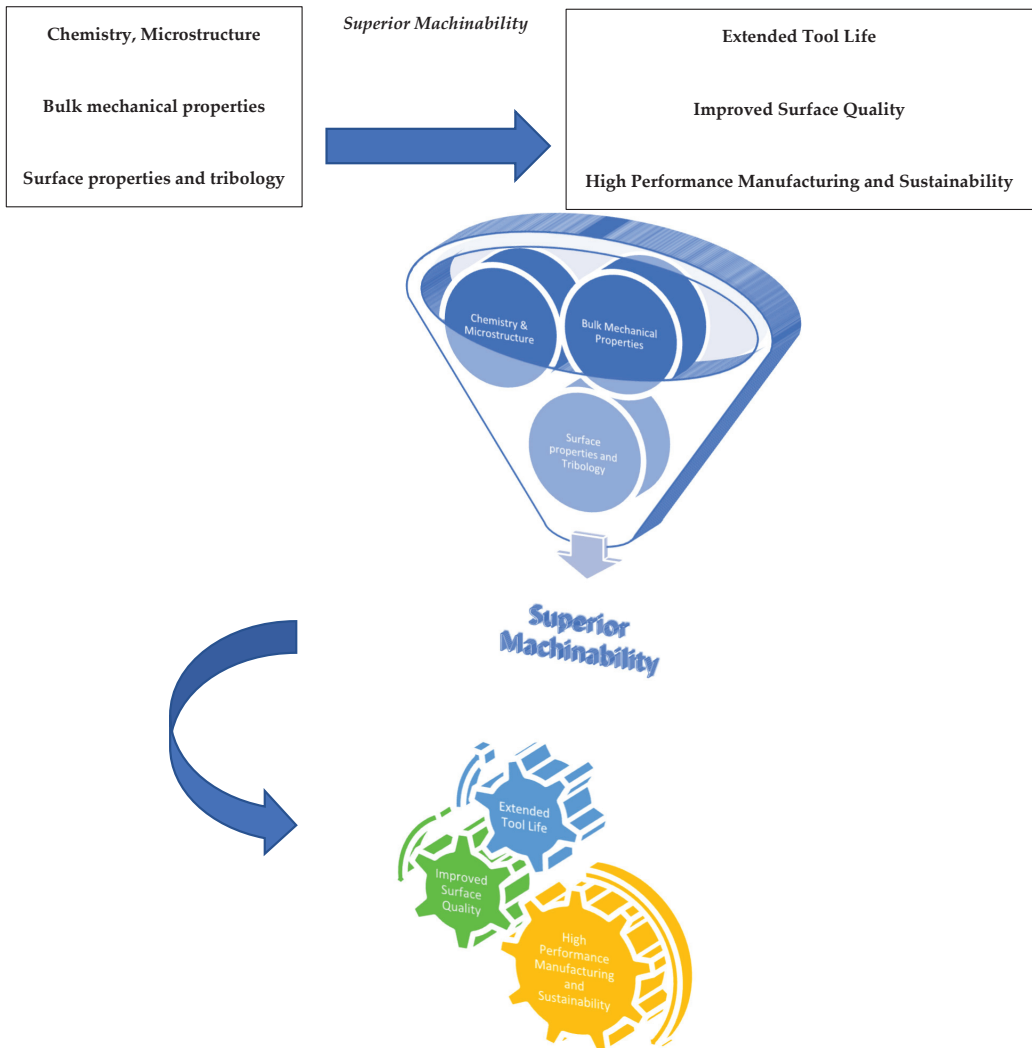
Received: 9 June 2023

Accepted: 26 June 2023

Published: 27 June 2023



**Copyright:** © 2023 by the author. Licensee MDPI, Basel, Switzerland. This article is an open access article distributed under the terms and conditions of the Creative Commons Attribution (CC BY) license (<https://creativecommons.org/licenses/by/4.0/>).



**Figure 1.** Schematic diagram illustrating that the special design of basic and generic material parameters could control level of the machinability and the major outcomes.

## 2. Contributions

The Special Issue “Machinability and Tribological Performance of Advanced Alloys” contains fifteen research articles [1–15], including one review paper [5]. The contents of this collection cover a wide spectrum of cross-disciplinary fields related to the machinability and tribological behaviour of materials with a variety of industrial applications. In addition, there are a few papers that, although they are not directly relevant to the core-subject area, provide valuable insight into the broader area of manufacturing technology [2,8] and the advanced characterization methodology of W-Cu nanocrystalline materials using FEM nanoindentation [4].

The main papers take a materials-focus perspective utilizing various manufacturing processes, such as turning [5,13], planing [10] and electric discharge machining [3,15]. A review paper reported on the basic categories of leaded and lead-free machinable brass alloys [5], while a specialized crystallographic investigation using Electron Backscatter

Diffraction (EBSD) analysis revealed the texture and fracture behaviour relationships of lead-free machinable brass alloys (such as CW511L and CW510L) [7]. Texture and phase analyses were performed before and after a heat treatment, which was applied for machinability improvement [7]. The combination of LAGBs and  $\Sigma 3$  boundaries together with  $\beta$ -phase content play a significant role in energy absorption and fracture resistance development [7]. The influence of induction heating on the machining of an SDK11 (high C, Cr-Mo) alloy steel is presented [12]. According to this study, the steel microstructure was not changed after heating it at a temperature between 200 and 400 °C, while a significant cutting force reduction was observed [12]. In [13], a comparative study on vibration monitoring among three brass alloys, two lead-free ones (CW510L and CW724R) and one leaded one (CW614N) was performed. According to this research, on average, CW510L and CW614N brass alloys demonstrated three times lower vibration damping values compared to that of CW724R brass alloy. In [15], the surface quality of an EDM-treated nickel based superalloy (Inconel 617) using cryogenically and non-cryogenically treated electrodes and various modified dielectrics of transformer oil was investigated.

Tribological behaviour research that aimed to improve the lifetime of materials/components by increasing the wear and/or corrosion resistance was undertaken in [1,6,9]. A comparative study concerning the abrasive wear resistance of different plughshare steels is presented in [9]. Furthermore, a study on the lubrication efficiency of Inconel 718 and the WC tribo-system is presented in [11]. The sulfurized fatty acid ester results in excellent anti-wear and anti-friction properties [11]. According to [14], a reverse thermal model and parametric modelling were applied to predict the temperature history of surface clads (carbide/steel systems) produced via a Concentrated Solar Energy surface treatment (CSE). This could result in the correlation between CSE processing parameters and the performance of created surface layers.

The content of the Special Issue is also presented to facilitate the readership and for taxonomy purposes (Table 1).

**Table 1.** List of topics and materials elaborated in the contents of the current S.I.

Reference Number	Relevant Topic			Materials
	Machinability	Tribology/Surface Properties	Miscellaneous	
[1]				X210CrW12 steel
[2]				AA5083 Al-alloy
[3]				DC53 steel
[4]				W-Cu (nanocrystalline)
[5]				Copper alloys (brasses)
[6]				Fe-Bulk metallic glasses
[7]				Copper alloys (brasses)
[8]				Mild steel
[9]				Steels (mainly S355J2G3, 37MnSi5, Hardox 450, UTP 690, OK 84.58)
[10]				EN C45 carbon steel
[11]				Inconel 718/WC
[12]				SKD11 Alloy Steel
[13]				Brass alloys (CW510L, CW614N, CW724R)
[14]				TiC/carbon steel, Cr <sub>3</sub> C <sub>2</sub> /carbon steel
[15]				Inconel 617

### 3. Conclusions and Outlook

The current Special Issue aims to place emphasis on this critical area of manufacturing, shedding light onto relationships governing the mutually influenced and interrelated properties of the machinability and tribological behaviour of metallic materials.

Since the industry demands more sustainable, energy efficient- and environmental-/ health and safety (E&HS)-friendly solutions, more research will be conducted on innovative and “green” materials (such as eco-friendly or lead-free copper alloys, environmentally friendly coatings and lubricants) and cost-efficient manufacturing processes. Industrial digitalization and modernization (in the frame of Industry 4.0) may further contribute to high-performance lean production, leading to the highest quality products and components, displaying minimum variation in their quality characteristics.

**Funding:** This research received no external funding.

**Acknowledgments:** The Guest Editor expresses his deep gratitude to the contributing authors who shared their valuable research works in this collection of papers, sharing research in the field of Machinability and Tribological Behaviour of Materials and shedding light on significant industrial applications and challenges. Moreover, we acknowledge the voluntary contributions of peer reviewers, together with the assistance and support provided generously by the MDPI *Metals* Editorial Team. Finally, the continuous support of ELKEME colleagues and management team is highly appreciated.

**Conflicts of Interest:** The author declares no conflict of interest.

**Profound Appreciation and Dedication :** The launch of the current Special Issue occurred almost three years ago and coincided with the outbreak of COVID-19, which was an unprecedented, dystopic period during which millions of lives were lost, people were fearful, strict measures were applied, including social distancing and the abrupt interruption of communication. At that time, Stoic philosophical/thinking principles provided me with outstanding mental support, courage, discipline and the vision to try to do the best I could within my power and my control. During this sorrowful and “dark” period, I received plentifully special and dedicated support from “close and skillful contributors and friends” who gave me courage and strength to continue and keep persisting towards my targets and goals. Because I feel sincerely indebted to them, I would like to express my deepest gratitude to these talented and Amazing Supporters (abbreviated as A.S.) who showed the path to find joy and the flowers of life. A.S. contributed to building an “inner citadel”, which together with the catalytic influence and wise insight amply offered to me, will remain unforgettable.

## References

- Duan, Y.; Qu, S.; Jia, S.; Li, X. Evolution of the Fretting Wear Damage of a Complex Phase Compound Layer for a Nitrided High-Carbon High-Chromium Steel. *Metals* **2020**, *10*, 1391. [[CrossRef](#)]
- Du, Z.; Wang, G.; Wang, H. The Process Design and Rapid Superplastic Forming of Industrial AA5083 for a Fender with a Negative Angle in a Small Batch. *Metals* **2021**, *11*, 497. [[CrossRef](#)]
- Khan, S.A.; Rehman, M.; Farooq, M.U.; Ali, M.A.; Naveed, R.; Pruncu, C.I.; Ahmad, W. A Detailed Machinability Assessment of DC53 Steel for Die and Mold Industry through Wire Electric Discharge Machining. *Metals* **2021**, *11*, 816. [[CrossRef](#)]
- Tserpes, K.; Bazios, P.; Pantelakis, S.G.; Pappa, M.; Michailidis, N. Mechanical Characterization of Nanocrystalline Materials via a Finite Element Nanoindentation Model. *Metals* **2021**, *11*, 1827. [[CrossRef](#)]
- Stavroulakis, P.; Toulfatzis, A.I.; Pantazopoulos, G.A.; Paipetis, A.S. Machinable Leaded and Eco-Friendly Brass Alloys for High Performance Manufacturing Processes: A Critical Review. *Metals* **2022**, *12*, 246. [[CrossRef](#)]
- Zhang, G.; Sun, W.; Xie, L.; Zhang, C.; Tan, J.; Peng, X.; Li, Q.; Ma, X.; Zhao, D.; Yu, J. Multicomponent Fe-Based Bulk Metallic Glasses with Excellent Corrosion and Wear Resistances. *Metals* **2022**, *12*, 564. [[CrossRef](#)]
- Vazdirvanidis, A.; Rikos, A.; Toulfatzis, A.I.; Pantazopoulos, G.A. Electron Backscatter Diffraction (EBSD) Analysis of Machinable Lead-Free Brass Alloys: Connecting Texture with Fracture. *Metals* **2022**, *12*, 569. [[CrossRef](#)]
- Kuo, S.-K.; Ou, Y.-L.; Wang, D.-A. An Analytical Model for Stress and Curvature Prediction of a Strip Leveling Process. *Metals* **2022**, *12*, 757. [[CrossRef](#)]
- Vargova, M.; Tavodova, M.; Monkova, K.; Dzupon, M. Research of Resistance of Selected Materials to Abrasive Wear to Increase the Ploughshare Lifetime. *Metals* **2022**, *12*, 940. [[CrossRef](#)]
- Monka, P.P.; Monkova, K.; Vasina, M.; Kubisova, M.; Korol, M.; Sekerakova, A. Effect of Machining Conditions on Temperature and Vickers Microhardness of Chips during Planing. *Metals* **2022**, *12*, 1605. [[CrossRef](#)]
- Yang, Y.; Luan, H.; Guo, S.; Liu, F.; Dai, Y.; Zhang, C.; Zhang, D.; Zhou, G. Tribological Behaviors of Inconel 718–Tungsten Carbide Friction Pair with Sulfur Additive Lubrication. *Metals* **2022**, *12*, 1841. [[CrossRef](#)]
- Mac, T.-B.; Luyen, T.-T.; Nguyen, D.-T. Assessment of the Effect of Thermal-Assisted Machining on the Machinability of SKD11 Alloy Steel. *Metals* **2023**, *13*, 699. [[CrossRef](#)]
- Monka, P.P.; Monkova, K.; Pantazopoulos, G.A.; Toulfatzis, A.I. Effect of Wear on Vibration Amplitude and Chip Shape Characteristics during Machining of Eco-Friendly and Leaded Brass Alloys. *Metals* **2023**, *13*, 828. [[CrossRef](#)]

14. Zervaki, A.D.; Lambrakos, S.G.; Mourlas, A.G.; Papantoniou, I.G.; Rodríguez, J.; Psyllaki, P.P. Inverse Thermal Analysis as a Tool for Optimizing Concentrated Solar Energy Elaboration of Wear Resistant Surface Layers. *Metals* **2023**, *13*, 942. [[CrossRef](#)]
15. Ishfaq, K.; Sana, M.; Mahmood, M.A.; Anwar, S.; Waseem, M.U. Evaluating Surface Quality of Inconel 617 by Employing Deep Cryogenically Treated Electrodes in Surfactant-Added Dielectrics of Transformer Oil. *Metals* **2023**, *13*, 1092. [[CrossRef](#)]

**Disclaimer/Publisher’s Note:** The statements, opinions and data contained in all publications are solely those of the individual author(s) and contributor(s) and not of MDPI and/or the editor(s). MDPI and/or the editor(s) disclaim responsibility for any injury to people or property resulting from any ideas, methods, instructions or products referred to in the content.



Article

# Evolution of the Fretting Wear Damage of a Complex Phase Compound Layer for a Nitrided High-Carbon High-Chromium Steel

Yong Duan, Shenguan Qu \*, Siyu Jia and Xiaoqiang Li

School of Mechanical and Automotive Engineering, South China University of Technology, Guangzhou 510640, China; yong\_duan\_scut@outlook.com (Y.D.); J15635223374@163.com (S.J.); lixq@scut.edu.cn (X.L.)

\* Correspondence: qusg@scut.edu.cn

Received: 29 September 2020; Accepted: 14 October 2020; Published: 19 October 2020

**Abstract:** In this paper, the X210CrW12 steel was subjected to gas nitriding to obtain a complex phase compound layer with limited porosity. The nitrided layer was characterized by scanning electron microscopy (SEM), energy dispersive spectroscopy (EDS) and X-ray diffraction (XRD). The fretting wear behavior and the evolution of fretting wear damage of the compound layer were studied, and the worn surfaces were characterized by SEM/EDS and 3D optical profilometry. The results indicated that the compound layer showed superior fretting wear resistance and sufficient load-carrying capacity in the low loading case of 35 N, but the fracture of coarse nitrides (transformed primary carbides) was obviously detrimental to wear resistance. For the high loading case of 70 N, the low toughness of the compound layer led to the occurrence of brittle cracks, and the decrease in the thickness of the compound layer due to wear resulted in the cracking and spalling of the compound layer.

**Keywords:** compound layer; brittle delamination; oxidative mechanism; fretting wear

## 1. Introduction

Gas nitriding, as a typical thermo-chemical surface treatment, is one of the most efficient methods to enhance the surface properties, such as surface hardness, corrosion and wear resistance [1–8]. The typical nitrided layer consists of two different structures, known as the compound layer and diffusion layer. Generally, the compound layer is composed of  $\gamma'$ -Fe<sub>4</sub>N,  $\epsilon$ -Fe<sub>2-3</sub>N, or a mixed phase ( $\epsilon + \gamma'$ ). The diffusion layer brings about an improvement of the fatigue properties, whereas the improvement of wear and corrosion properties is ascribed to the compound layer [3].

There are three main types of compound layer. One type of layer consists of a predominant percentage of  $\epsilon$  phase. Such a layer is very porous and its wear resistance is worsened [9,10]. However, the  $\gamma'$  phase is more ductile than  $\epsilon$  phase, but the compound layer consisting of monophase  $\gamma'$  is usually thin and prone to spalling in heavy conditions due to the extremely hardness differences occurring between the compound layer and diffusion zone [11]. The next layer consists of  $\gamma' + \epsilon$  iron nitrides with a limited percentage of  $\epsilon$  phase. Investigations show that if the porosity in this type of compound layer can be well controlled, the compound layer with a relative reasonable thickness is very beneficial to the wear and corrosion resistance in many cases [12–15]. In practice, the complex phase compound layers (with limited porosity) are widely applied in non-impact conditions to improve the resistance to damage affecting the component life such as wear and corrosion. Further, the sliding wear characteristics of this type of compound layer have been extensively studied [4–7,11–13,16–18]. As reported by Rad et al. [17], the specimens with a good thickness compound layer had a lower wear rate, but the thin compound layer was broken in small sliding distance, resulting in a high wear rate. In the paper [18], the sliding wear test of the nitrided specimens was carried out on a ball-on-disc machine under loads of 100 and 300 N, and the GCr15 steel ball (with a hardness of 63–65 HRC) was



used as the counterbody material. The results showed that the compound layer consisting of  $\gamma' + \epsilon$  phases showed excellent wear resistance under the light load of 100 N, but poor wear properties at the heavy load of 300 N.

Fretting wear, which is caused by the vibration of the mechanical system or the variation in loads, is found to be different from the sliding wear [19] due to the small displacement amplitude, and the material loss caused by it is much less than that caused by sliding wear. However, fretting wear can produce a loss of fitting and degrade the functionality of the mechanical system. The degradation of the component surface caused by fretting wear is the result of several wear mechanisms, such as abrasion, adhesion, crack and oxidation [20]. Although many experimental works have been carried out to study the sliding wear behavior of the compound layer, there is a lack of knowledge relating to the fretting wear behavior. Identification of the evolution of fretting wear damage of the compound layer is crucial to ensure stable service of the nitrided components.

In this study, the X210CrW12 steel was selected as the experiment material. It is a very hard material with high wear-resistance and can be widely used in tribological applications [21]. The material was subjected to gas nitriding to obtain a complex phase compound layer with limited porosity, and the fretting wear behavior and the evolution of fretting wear damage of the compound layer were analyzed in detail.

## 2. Materials and Methods

### 2.1. Material Preparation and Nitriding Treatment

The chemical composition (wt.%) of X210CrW12 steel used in this study is shown in Table 1. The discs with a diameter of 40 mm and thickness of 11 mm were cut from a bar received in the annealed condition. Before nitriding, specimens were austenitized at 1080 °C for 30 min followed by oil quenching, then triple tempered at the temperature of 580 °C for 2 h, leading to a hardness of  $495 \pm 15$  HV<sub>0.2</sub>. After the heat treatment, the thickness of all specimens was machined to 8 mm to remove the decarburized layer. Prior to the gas nitriding process, all specimens were ground with SiC abrasive papers of 600, 1200, 1500 and 2000 grits followed by mirror polishing, and ultrasonically cleaned in acetone for 10 min. Then, all specimens were hung in a gas nitriding furnace. Gas nitriding was performed using an industrial unit at 500 °C for nearly 70 h, and the high-purity NH<sub>3</sub> gas was used as the nitriding medium.

**Table 1.** Compositions of X210CrW12 steel specimen (wt.%).

C	Si	Mn	P	Cr	V	W	Fe
2.16	0.2	0.26	0.27	12.2	0.12	0.81	Bal.

### 2.2. Fretting Wear Test and Microstructure Characterization

Fretting wear tests were performed on an Optimol SRV IV (DIN51834, SRV, Optimol, Munchen, Germany) reciprocating friction and wear test machine under the dry condition at a temperature of 25 °C. The ball-on-flat method was adopted to perform the test, as illustrated in Figure 1. The upper ball specimen (SiC ball with a hardness of about 2600 HV) with a diameter of 10 mm was mounted in a holder attached to an oscillating electro-mechanical drive, and pressed against the stationary lower specimen (nitrided specimen). In addition, load, frequency and amplitude conditions were chosen for best test stability. The fretting wear tests were carried out under the load of 35 N and 70 N, because the fretting wear behavior of the nitrided samples under these two load conditions was representative. In order to study the evolution of fretting wear damage, the fretting cycle ranged from  $24 \times 10^3$  to  $72 \times 10^3$ . Each test was repeated at least three times to check the repeatability. The main test parameters are listed in Table 2. After each fretting wear test, the specimens were ultrasonically cleaned for 15 min, thus leaving any debris that was more firmly adhered to the worn surface.

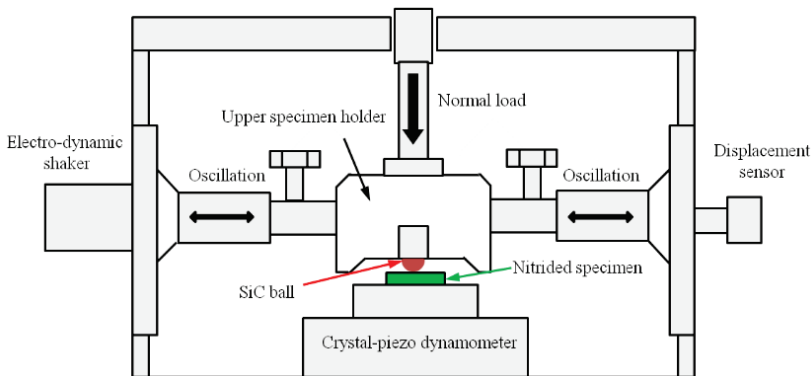


Figure 1. Schematic diagram of ball-on-disk fretting tribometer.

Table 2. Main test parameters.

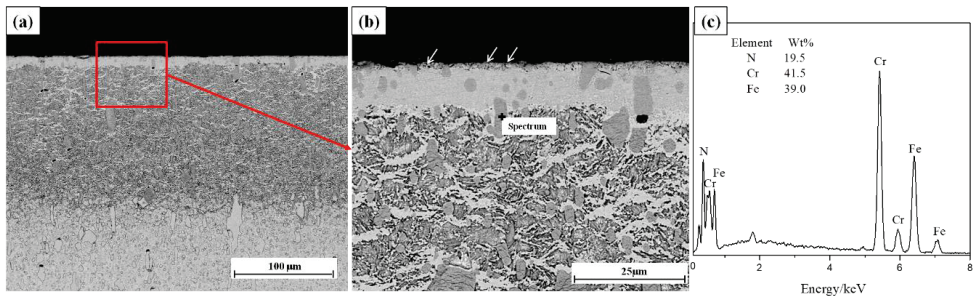
Load (N)	Frequency (Hz)	Stroke ( $\mu\text{m}$ )	Duration, N (Number of Cycles)
35, 70	20	200	$24 \times 10^3$ , $48 \times 10^3$ , $72 \times 10^3$

The cross-sectional microstructure of nitrided specimen and the fretting wear mechanism was studied by scanning electron microscopy using backscattered electron mode (SEM/BSE; Quanta 200 & Nova nanosem 430, FEI, Hillsboro, OR, USA). The microhardness of the nitrided specimen was measured using a Vickers microhardness tester (HDV-10002, SCTMC, Shanghai, China) with a load of 1.96 N and a holding time of 15 s. Phase composition of the un-nitrided and nitrided specimens was studied by X-ray diffraction (XRD; D8 Advance, Bruker-axs, Karlsruhe, Germany). The surface topography of wear scar was characterized by mean of a 3D optical profiler (America RTEC Up Dual-Mode), and the depth and volume of the wear scar were obtained by the instrument software.

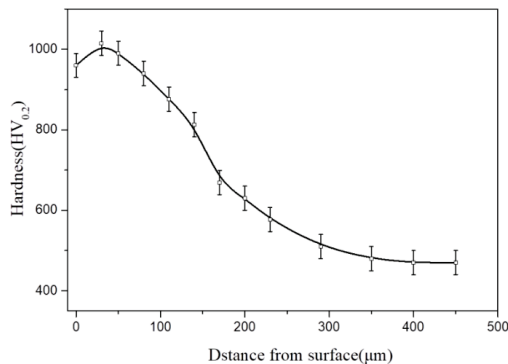
### 3. Results and Discussion

#### 3.1. Microstructural Characteristics

Figure 2 shows the cross-sectional microstructure of the nitrided layer. It can be found that the primary and secondary alloy carbides are dispersed throughout the base material. These phases represent the main microstructural characteristics of X210Crw12 steel. During nitriding, these initial carbides will be transformed into nitrides [22,23], as confirmed by the results of EDS analysis (Figure 2c), and the released carbon atoms will diffuse (i) toward the nitrogen diffusion front, forming the cementite precipitates along grain boundaries, and (ii) toward the outer surface, leading to decarburization of the surface adjacent region [23]. Figure 2b clearly shows that the compound layer is a compact layer, and the thickness of the compound layer was measured to be in the range of about 8–10  $\mu\text{m}$ . However, small pores formed on the top surface of the compound layer, as shown with arrows. Figure 3 shows the cross-sectional microhardness profile of the nitrided specimen. After nitriding, the surface hardness is  $960 \pm 30 \text{ HV}_{0.2}$ , which was measured after the removal of pores on the top surface of the compound layer. The decrease in the surface hardness may be caused by the occurrence of decarburization in the surface adjacent regions [23] or the long nitriding time [12,23].

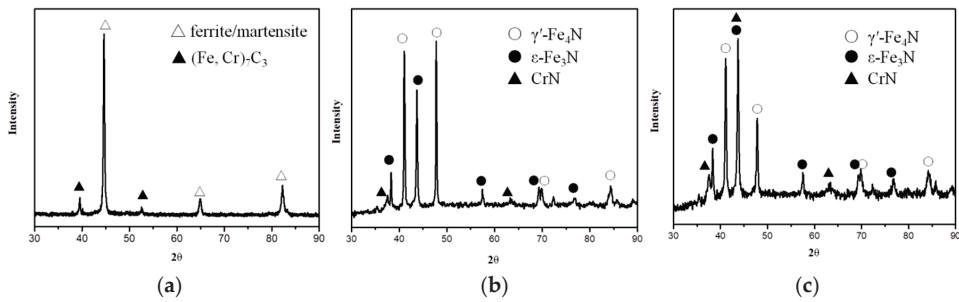


**Figure 2.** Cross-sectional microstructure of the nitrided layer: (a) overall features, (b) a close view of the rectangle in (a) and (c) energy dispersive spectroscopy (EDS) analysis of the point in (b).



**Figure 3.** Cross-sectional hardness–depth profile for the nitrided specimen.

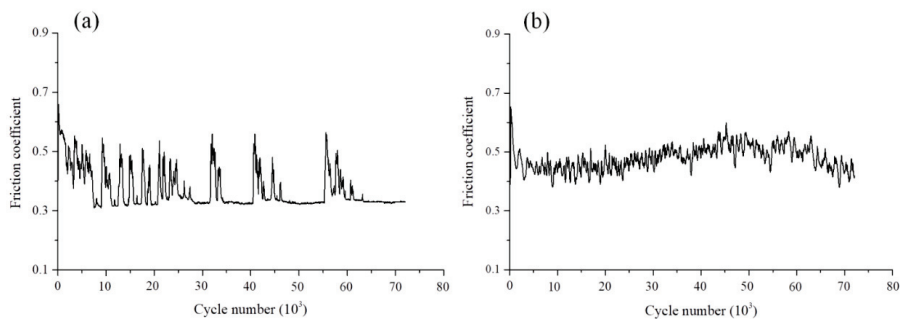
Figure 4 shows the X-ray diffraction patterns on the surface of the un-nitrided and nitrided specimens. Before nitriding, the substrate is characterized by ferrite (tempered martensite) and  $(Cr, M)_7C_3$  carbide diffraction patterns (Figure 4a). After nitriding, the presence of the  $\gamma'$  ( $Fe_4N$ ) and  $\epsilon$  ( $Fe_3N$ ) phases, together with the CrN phase can be identified (Figure 4b), confirming the formation of the compound layer constituted by these phases. Then, the nitrided specimen was polished to remove the pores on the top surface of the compound layer. Figure 4c shows the XRD phase analysis of the compound layer after polishing. It can be found that after polishing, the peak intensity of  $\epsilon$  phase becomes stronger, while the intensity of  $\gamma'$  phase peak becomes weak. Therefore, the existence of  $\epsilon$  phase should not be responsible for the formation of pores on the top surface of the compound layer. The reason for the formation of pores and the increase in the amount of  $\gamma'$  phase at the top surface of the compound layer may be due to the occurrence of decarburization in this region [24]. As estimated from the intensities of the respective diffraction lines (Figure 4c), the ratio of  $\epsilon/\gamma'$  for the compound layer is about 1.3, which provides high hardness for the compound layer and makes its porosity be well controlled.



**Figure 4.** X-ray diffraction from the surface of (a) un-nitrided specimen, (b) nitrided specimen before polishing and (c) nitrided specimen after polishing.

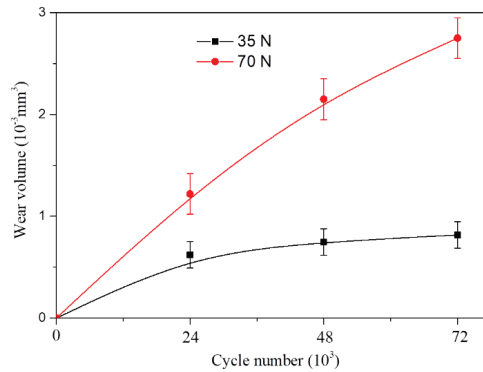
### 3.2. Fretting Wear Behavior

Figure 5 plots the evolution of the friction coefficient for  $72 \times 10^3$  fretting cycles under the two loading conditions. In the loading case of 35 N, the friction coefficient varies very much in the initial  $24 \times 10^3$  cycles, and then gets to a steady state with a small value of around 0.32. However, it is worth noting that the friction coefficient can increase rapidly at a certain time, and then decreases gradually to the stable value again. Under the normal load of 70 N, the frictional coefficient curve shows different characteristics from that in the loading case of 35 N. The friction coefficient varies very much throughout the whole wear process, and the average friction coefficient is 0.45, which is higher than that in the loading case of 35 N. This finding is in contrast with the results reported by many other investigators [25,26]. In their work, the friction coefficient decreased with increasing the normal load, which was proposed to be due to the fact that the surface contact was the elastic contact which resulted in the asperities interlock in the low loading case [26].



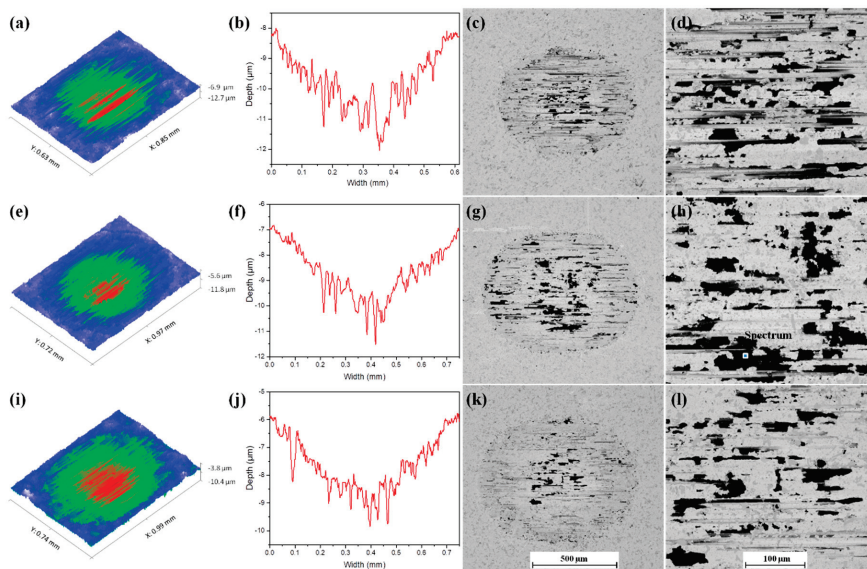
**Figure 5.** Evolution of friction coefficient under the load of (a) 35 N and (b) 70 N.

Figure 6 illustrates the wear volume of the nitrided specimens as a function of cycle number. For the two loading conditions, the wear volume increases with the number of cycles as expected. However, for the loading case of 35 N, it can be seen that the wear rate rapidly decreases to a very low value after the initial  $24 \times 10^3$  cycles. When the fretting cycle increases from  $24 \times 10^3$  to  $72 \times 10^3$  the wear volume increases slowly from  $0.62 \times 10^{-3} \text{ mm}^3$  to  $0.82 \times 10^{-3} \text{ mm}^3$ . Under the normal load of 70 N, the wear volume shows a different trend compared to that under the load of 35 N, it increases almost linearly with increasing the fretting cycle.

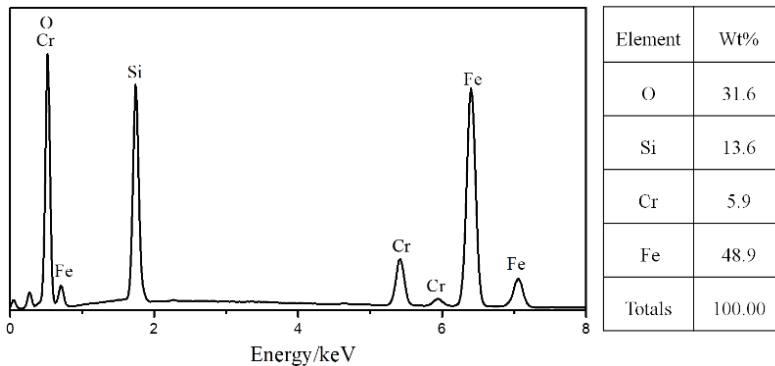


**Figure 6.** Wear volume of the nitrated specimens under the load of 35 N and 70 N.

Figure 7 shows the 3D surface morphologies and BSE images of the wear scars after different fretting cycles under the normal load of 35 N. The 3D surface morphologies show that the worn surfaces are dominated by the deep grooves parallel to the sliding direction, suggesting that the main wear mechanism is two-body abrasive wear. Furthermore, it can be seen that wear depth in the central region of the wear scars is maximum, which is proposed to be caused by the Hertzian contact pressure distribution. However, the wear area and depth increase slowly with the increasing number of cycles. From the SEM-BSE images of the wear scars, it can be seen that the worn surfaces for different cycle's tests show similar wear characteristics with some dark areas. EDS analysis of the dark area (point in Figure 7h) is shown in Figure 8, revealing that the dark area is oxidized wear debris consisting mainly of O, Fe and Si. These indicate that the abrasive particles generated from the wear of the nitrated specimens and SiC balls were oxidized, and material transfer from the balls to the worn surfaces occurred.

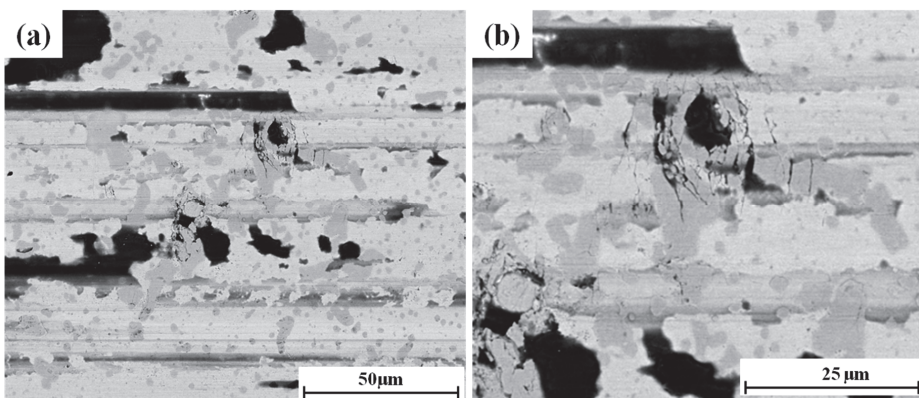


**Figure 7.** 3D surface morphologies, cross-sectional profiles and scanning electron microscopy using backscattered electron mode (SEM-BSE) images of the wear scars after fretting cycles of  $24 \times 10^3$  (a–d),  $48 \times 10^3$  (e–h) and  $72 \times 10^3$  (i–l) under the normal load of 35 N.



**Figure 8.** EDS analysis of the dark area (the point in Figure 7h).

Figure 9 shows the worn surface at the center of the wear scar after  $72 \times 10^3$  cycles. Some cracks can be observed on the worn surface, resulting from the fracture of coarse nitrides (transformed primary carbides) (Figure 9a). Under the high-frequency reciprocating sliding conditions, the cyclic stresses and local concentrated stresses were imposed, leading to the cracking of coarse nitrides due to their low toughness, and to their removal as fragments, leaving deep cavities on the worn surface (Figure 9a). Figure 9b clearly shows that cracks are observed around the broken coarse nitride, suggesting that the interfaces of the transformed primary carbides and matrix are the potential sites for the initiation as well as the propagation of cracks. It becomes clear that these transformed primary carbides are obviously detrimental to wear resistance in this situation. These observations are consistent with the work of Singh et al. [27] who studied the wear behavior of AISI D2 steel in two-body abrasive wear and stated that when the induced stress exceeded the fracture strength of primary carbides, the carbides fractured due to their low ductility, and the fracture and exfoliation of the primary carbides were the dominating factors affecting the wear resistance of the material. It can be observed that apart from the fracture of the coarse nitrides, brittle cracks or metallic ribbons ready to detach can be hardly observed in the matrix (Figure 9a), indicating that this type of compound layer shows good toughness and wear resistance in this loading case.



**Figure 9.** (a) Worn surface at the center of the wear scar after  $72 \times 10^3$  cycles under the normal load of 35 N. (b) Higher magnification BSE image of (a).

In all cases, the wear process itself can lead to a reduction of contact pressure due to the increased area of contact, subsequently resulting in the decrease in wear rate, as predicted by the literature [28]

which presented the macroscopic wear process using the finite element analysis (FEA). On the other hand, the oxide layer formed on the worn surfaces should be responsible for the very low wear rate in this loading case, because it acted as a lubricating film during the wear process [29,30], which favoured the wear resistance and decreased the wear rate and friction coefficient.

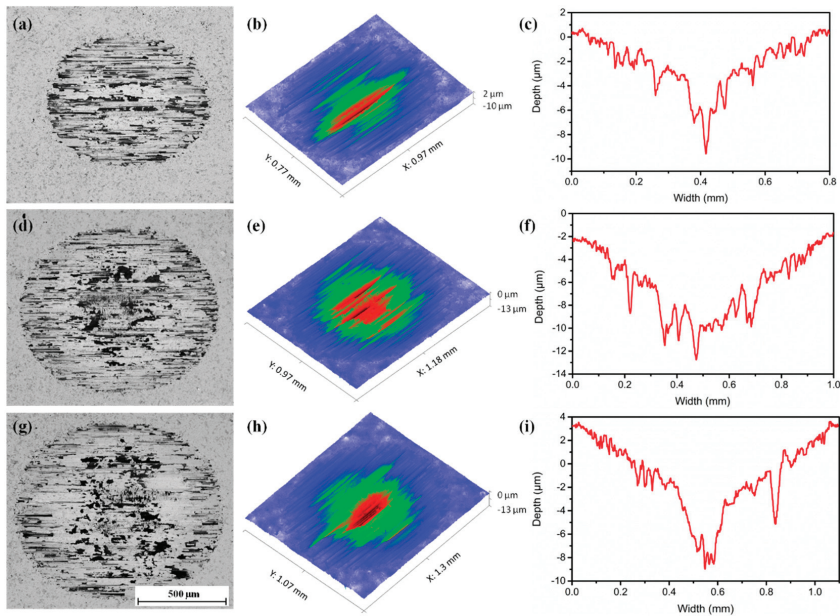
The friction coefficient shows that there are two main wear mechanisms involved in the wear of the nitrided specimens during the wear progress (Figure 5a). During the early fretting cycles of about  $24 \times 10^3$ , the friction coefficient varies very much. At this stage, the dominant wear mechanism is abrasive wear, accompanied by the rapid removal of material, which is confirmed by the deep grooves on the worn surface (Figure 7a) and the high wear rate (Figure 6). The oxidation mechanism is also active (confirmed by the oxide layer on the worn surface as shown in Figure 7c and d), but it is not the primary wear mechanism. Then, as the fretting cycle continues to increase, the friction coefficient decreases to a small value of around 0.32, but it is worth noting that the friction coefficient can increase rapidly at a certain time, and then decreases gradually to the stable value again. At this stage, the low friction coefficient suggests that oxidation becomes the primary wear mechanism, which explains the rapid decrease in the wear rate in this stage (Figure 6). It is reported that the changes in friction coefficient are controlled by the wear particles produced by microcutting and spalling, and the size of the wear particles at the contact surface plays a more important in raising friction, rather than the number of particles [31]. Therefore, it can be inferred that the rapid increase in the friction coefficient at the steady state should be caused by the large and hard particles resulted from the fracture of primary carbides. These particles were comminuted by repeated plastic deformation and fracture. Once they were reduced to a sufficiently small size, the friction coefficient was reduced to the stable value again. On the other hand, the accumulation and cohesion of the wear debris in the form of the fine oxide particles and their subsequent de-cohesion after reaching a critical size could also cause the appearance of peaks in the friction coefficient curve. Table 3 shows the wear mechanisms of nitrided specimens at different stages of testing.

**Table 3.** The wear mechanisms of nitrided specimens at different stages of testing under the load of 35 N.

Number of Cycles	Wear Mechanism	Coefficient of Friction	Wear Rate
$24 \times 10^3$	Abrasive wear * Oxidation mechanism	High	High
$48 \times 10^3$	Abrasive wear Oxidation mechanism *	Low	Low
$72 \times 10^3$	Abrasive wear Oxidation mechanism *	Low	Low

\* represents the main wear mechanism.

Figure 10 shows the SEM-BSE images of the wear scars and their corresponding 3D surface topographies and cross-sectional profiles under the normal load of 70 N. The cross-section profiles of the wear scars were measured vertical to the sliding direction, passing through the center of the wear scars. It can be seen that the worn surfaces exhibit similar characteristics to that from the tests conducted under the normal load of 35 N, showing many grooves parallel to the sliding direction and darker-coloured oxides. In contrast to the loading case of 35 N, the wear scar area and depth have an obvious increase with an increasing number of cycles. However, the average wear depth at the central region of the wear scar after the initial  $24 \times 10^3$  fretting cycles is about 6  $\mu\text{m}$ . When the fretting cycle continues to increase, the average wear depth at the central region gets to about 8  $\mu\text{m}$  at  $48 \times 10^3$  cycles and about 11  $\mu\text{m}$  at  $72 \times 10^3$  cycles. It is clear that the compound layer at the central region of the wear scar after the cycles of  $72 \times 10^3$  is worn through. On the other hand, a large number of cracks perpendicular to the sliding direction can be clearly observed in the central region of the wear scars following  $48 \times 10^3$  and  $72 \times 10^3$  cycles.



**Figure 10.** Plan view SEM-BSE images of the wear scars and their corresponding 3D surface morphologies and cross-sectional profiles under the normal load of 70 N after fretting cycles of  $24 \times 10^3$  (a–c),  $48 \times 10^3$  (d–f), and  $72 \times 10^3$  (g–i).

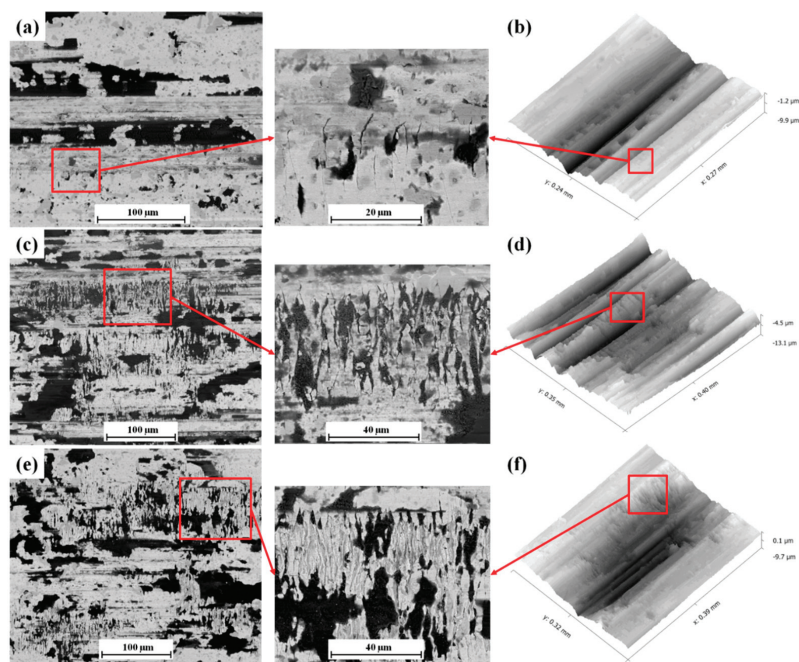
Figure 11 shows the SEM-BSE images of the central region of the wear scars and their corresponding 3D surface morphologies under the normal load of 70 N. It can be seen that there are few visible cracks that can be observed at the central region of the wear scar after the initial fretting cycles of  $24 \times 10^3$  (Figure 11a). However, the higher magnification image corresponding to the rectangular areas in Figure 11a and b clearly reveals that some brittle cracks perpendicular to the sliding direction do occur at the edge of the groove. Under the high normal load, the high contact pressure and shear stress can promote the rapid removal of the material and the generation of deep grooves, especially at the contact center (Figure 10). As shown in Figure 10b and c, the micro-cutting depth is quite deep in the early stage of wear, inducing great stresses around the grooves. Consequently, the brittle cracks emerged on the edge of the deep grooves due to the low toughness of the compound layer. It should be noted that the obvious brittle delamination of the compound layer cannot be observed on the worn surface, indicating that the compound layer still maintains a good load carrying capacity in this situation.

However, when the fretting cycle increases to  $48 \times 10^3$ , a large number of cracks perpendicular to the sliding direction can be clearly seen on the worn surface (Figure 11c), and the higher magnification image of rectangular areas in Figure 11c and d shows clear evidence that the propagation and interconnection of the cracks result in severe delamination type wear in the zone between two deep grooves. As the fretting cycle continues to increase to  $72 \times 10^3$ , there are only a few visible cracks in the contact center corresponding to the maximum depth, but large amounts of cracks are concentrated at the edge of the contact center, leading to severe delamination wear in these areas.

As predicted in the literature [28], the maximum contact pressure goes down with wear and the contact pressure becomes more uniform. Therefore, the high contact pressure should not be the main factor that leads to the severe brittle delamination of the compound layer at the central region of the wear scars. Studies have shown that the load-carrying capacity of the coated system increased with increasing substrate stiffness and coating thickness, and the very thin coatings were detrimental to the load-carrying capacity [17]. The brittle delamination mechanism for the compound layer in the central



region of the wear scar can be explained as follows. The rapid wear at the contact center reduced the thickness of the compound layer, which reduced the strength against the external stress resulting in the cracking or spalling of the compound layer. In general, the compound layer containing both  $\gamma'$  phase and  $\epsilon$  phase led to weak interface boundaries resulting in an increase in brittleness [16]. For the area between two grooves, highly concentrated stresses were imposed during abrasion, promoting the brittle fracture propagation, as shown in the higher magnification image of the rectangular areas in Figure 11c. The delaminated layer then turned into bulk and hard abrasive particles, promoting the wear in the contact region. Therefore, the primary wear mechanism throughout the wear process was abrasive wear, which led to the high friction coefficient and wear rate. The wear mechanisms of nitrided specimens at different stages of testing are shown in Table 4.



**Figure 11.** SEM-BSE images of the central region of the wear scars and their corresponding 3D surface morphologies under the normal load of 70 N after fretting cycles of  $24 \times 10^3$  (a,b),  $48 \times 10^3$  (c,d), and  $72 \times 10^3$  (e,f), and the higher magnification SEM-BSE image corresponding to the rectangular area.

**Table 4.** The wear mechanisms of nitrided specimens at different stages of testing under the load of 70 N.

Number of Cycles	Wear Mechanism	Coefficient of Friction	Wear Rate
$24 \times 10^3$	Abrasive wear * Oxidation mechanism	High	High
$48 \times 10^3$	Abrasive wear * Brittle delamination Oxidation mechanism	High	High
$72 \times 10^3$	Abrasive wear * Brittle delamination Oxidation mechanism	High	High

\* represents the main wear mechanism.

#### 4. Conclusions

In this paper, the X210CrW12 steel was selected and subjected to gas nitriding to obtain the complex phase compound layer. The fretting wear behavior and the evolution of fretting wear damage of the compound layer were studied in detail. Some conclusions were summarized as follows:

- (1) The obtained compound layer was a compact layer with limited porosity, and the ratio of  $\epsilon/\gamma'$  as estimated from XED peaks is about 1.3.
- (2) The compound layer showed superior fretting wear resistance and sufficient load-carrying capacity in a low loading case of 35 N, and provided a rigid substrate to support the oxide layer, leading to the oxidative mechanism.
- (3) In the low loading case of 35 N, the fracture of coarse nitrides (transformed primary carbides) was obviously detrimental to wear resistance, leading to crack initiation and propagation in the matrix, and the generated hard particles controlled the friction coefficient.
- (4) For the high loading case of 70 N, the compound layer still maintained good load carrying capacity and the brittle delamination of the compound layer was suppressed in the early stage of wear. However, some brittle cracks can be observed on the edge of the deep grooves due to the induced great stresses around the grooves and the low toughness of the compound layer.
- (5) Under the high loading case of 70 N, the rapid wear at the contact center reduced the thickness of the compound layer, which reduced the strength against the external stress resulting in the cracking and spalling of the compound layer.

**Author Contributions:** Conceptualization, Y.D.; methodology, Y.D. and S.Q.; software, Y.D. and S.J.; validation, X.L., Y.D. and S.J.; formal analysis, Y.D.; investigation, Y.D.; resources, S.Q.; data curation, X.L. and S.Q.; writing—original draft preparation, Y.D.; writing—review and editing, Y.D. and S.Q.; visualization, X.L.; supervision, S.Q.; project administration, S.Q.; funding acquisition, S.Q. All authors have read and agreed to the published version of the manuscript.

**Funding:** This research received no external funding.

**Conflicts of Interest:** The authors declare no conflict of interest.

#### References

1. Birol, Y. Analysis of wear of a gas nitrided H13 tool steel die in aluminium extrusion. *Eng. Fail. Anal.* **2012**, *26*, 203–210. [[CrossRef](#)]
2. Wang, B.; Sun, S.; Guo, M.; Jin, G.; Zhou, Z.; Fu, W. Study on pressurized gas nitriding characteristics for steel 38CrMoAlA. *Surf. Coat. Technol.* **2015**, *279*, 60–64. [[CrossRef](#)]
3. Akhtar, S.S.; Arif, A.F.M.; Yilbas, B. Evaluation of gas nitriding process with in-process variation of nitriding potential for AISI H13 tool steel. *Int. J. Adv. Manuf. Technol.* **2009**, *47*, 687–698. [[CrossRef](#)]
4. Yang, J.; Liu, Y.; Ye, Z.; Yang, D.; He, S. Microstructural and tribological characterization of plasma- and gas-nitrided 2Cr13 steel in vacuum. *Mater. Des.* **2011**, *32*, 808–814. [[CrossRef](#)]
5. Nolan, D.; Leskovsek, V.; Jenko, M. Estimation of fracture toughness of nitride compound layers on tool steel by application of the Vickers indentation method. *Surf. Coat. Technol.* **2006**, *201*, 182–188. [[CrossRef](#)]
6. Kundalkar, D.; Mavalankar, M.; Tewari, A. Effect of gas nitriding on the thermal fatigue behavior of martensitic chromium hot-work tool steel. *Mater. Sci. Eng. A* **2016**, *651*, 391–398. [[CrossRef](#)]
7. Yang, C.; Liu, J. Intermittent vacuum gas nitriding of TB8 titanium alloy. *Vacuum* **2019**, *163*, 52–58. [[CrossRef](#)]
8. Aghajani, H.; Torshizi, M.; Soltanieh, M. A new model for growth mechanism of nitride layers in plasma nitriding of AISI H11 hot work tool steel. *Vacuum* **2017**, *141*, 97–102. [[CrossRef](#)]
9. Schwarz, B.; Göhring, H.; Meka, S.; Schacherl, R.E.; Mittemeijer, E.J. Pore Formation Upon Nitriding Iron and Iron-Based Alloys: The Role of Alloying Elements and Grain Boundaries. *Met. Mater. Trans. A* **2014**, *45*, 6173–6186. [[CrossRef](#)]
10. Hernández, M.; Staia, M.; Cabrera, E.P. Evaluation of microstructure and mechanical properties of nitrided steels. *Surf. Coat. Technol.* **2008**, *202*, 1935–1943. [[CrossRef](#)]

11. Karamiş, M.; Gerçekcioğlu, E. Wear behaviour of plasma nitrided steels at ambient and elevated temperatures. *Wear* **2000**, *243*, 76–84. [[CrossRef](#)]
12. Karamis, M. An investigation of the properties and wear behaviour of plasma-nitrided hot-working steel (H13). *Wear* **1991**, *150*, 331–342. [[CrossRef](#)]
13. Xi, Y.-T.; Liu, D.-X.; Han, D. Improvement of corrosion and wear resistances of AISI 420 martensitic stainless steel using plasma nitriding at low temperature. *Surf. Coat. Technol.* **2008**, *202*, 2577–2583. [[CrossRef](#)]
14. Terčelj, M.; Smolej, A.; Fajfar, P.; Turk, R. Laboratory assessment of wear on nitrided surfaces of dies for hot extrusion of aluminium. *Tribol. Int.* **2007**, *40*, 374–384. [[CrossRef](#)]
15. Bombac, D.; Terčelj, M.; Peruš, I.; Fajfar, P. The progress of degradation on the bearing surfaces of nitrided dies for aluminium hot extrusion with two different relative lengths of bearing surface. *Wear* **2013**, *307*, 10–21. [[CrossRef](#)]
16. Castro, G.; Fernández-Vicente, A.; Cid, J. Influence of the nitriding time in the wear behaviour of an AISI H13 steel during a crankshaft forging process. *Wear* **2007**, *263*, 1375–1385. [[CrossRef](#)]
17. Rad, H.F.; Amadeh, A.; Moradi, H. Wear assessment of plasma nitrided AISI H11 steel. *Mater. Des.* **2011**, *32*, 2635–2643. [[CrossRef](#)]
18. Wang, B.; Zhao, X.; Li, W.; Qin, M.; Gu, J. Effect of nitrided-layer microstructure control on wear behavior of AISI H13 hot work die steel. *Appl. Surf. Sci.* **2018**, *431*, 39–43. [[CrossRef](#)]
19. Chen, G.; Zhou, Z. Study on transition between fretting and reciprocating sliding wear. *Wear* **2001**, *250*, 665–672. [[CrossRef](#)]
20. Varenberg, M.; Halperin, G.; Etsion, I. Different aspects of the role of wear debris in fretting wear. *Wear* **2002**, *252*, 902–910. [[CrossRef](#)]
21. Knauf, F.; Baadjou, R.; Hirt, G. Analysis of semi-solid extrusion products made of steel alloy X210CRW12. *Int. J. Mater. Form.* **2009**, *2*, 733–736. [[CrossRef](#)]
22. Jégou, S.; Barrallier, L.; Kübler, R. Phase transformations and induced volume changes in a nitrided ternary Fe–3%Cr–0.345%C alloy. *Acta Mater.* **2010**, *58*, 2666–2676. [[CrossRef](#)]
23. Van Wiggan, P.C.; Rozendaal, H.C.F.; Mittemeijer, E.J. The nitriding behaviour of iron-chromium-carbon alloys. *J. Mater. Sci.* **1985**, *20*, 4561–4582. [[CrossRef](#)]
24. Ruset, C.; Ciuca, S.; Grigore, E. The influence of the sputtering process on the constitution of the compound layers obtained by plasma nitriding. *Surf. Coat. Technol.* **2003**, *174*, 1201–1205. [[CrossRef](#)]
25. Shima, M.; Okado, J.; Mccoll, I.R. The influence of substrate material and hardness on the fretting behavior of TiN. *Wear* **1999**, *225*, 38–45. [[CrossRef](#)]
26. Zhang, D.K.; Ge, S.R.; Qiang, Y.H. Research on the fatigue and fracture behaviour due to the fretting wear of steel wire in hosting rope. *Wear* **2003**, *255*, 1233–1237. [[CrossRef](#)]
27. Singh, K.; Khatirkar, R.K.; Sapate, S.G. Microstructure evolution and abrasive wear behavior of D2 steel. *Wear* **2015**, 206–216. [[CrossRef](#)]
28. Ding, J.; Leen, S.B.; McColl, I. The effect of slip regime on fretting wear-induced stress evolution. *Int. J. Fatig.* **2004**, *26*, 521–531. [[CrossRef](#)]
29. Stott, F. The role of oxidation in the wear of alloys. *Tribol. Int.* **1998**, *31*, 61–71. [[CrossRef](#)]
30. So, H. The mechanism of oxidational wear. *Wear* **1995**, *184*, 161–167. [[CrossRef](#)]
31. Hwang, D.; Kim, D.; Lee, S. Influence of wear particle interaction in the sliding interface on friction of metals. *Wear* **1999**, *225*, 427–439. [[CrossRef](#)]

**Publisher’s Note:** MDPI stays neutral with regard to jurisdictional claims in published maps and institutional affiliations.



© 2020 by the authors. Licensee MDPI, Basel, Switzerland. This article is an open access article distributed under the terms and conditions of the Creative Commons Attribution (CC BY) license (<http://creativecommons.org/licenses/by/4.0/>).

Article

# The Process Design and Rapid Superplastic Forming of Industrial AA5083 for a Fender with a Negative Angle in a Small Batch

Zhihao Du <sup>1,\*</sup>, Guofeng Wang <sup>2</sup> and Hailun Wang <sup>2,3</sup><sup>1</sup> School of Mechanical and Electric Engineering, Nanyang Normal University, Nanyang 473061, China<sup>2</sup> School of Material Science and Engineering, Harbin Institute of Technology, Harbin 150001, China; gfwang@hit.edu.cn (G.W.); hlwyhzs@163.com (H.W.)<sup>3</sup> Capital Aerospace Machinery Corporation Limited, Beijing 100071, China

\* Correspondence: duzhihaoht@126.com; Tel.: +86-377-6351-3563

**Abstract:** A front automobile fender with a negative angle was trial produced via rapid superplastic forming (SPF) technology. The tensile test of industrial AA5083 was carried out at elevated temperatures, and the results showed that the maximum elongation was 242% at 480 °C/0.001 s<sup>-1</sup>. A rigid-plastic constitutive model of the SPF process was established. Initial dies of preforming and final forming were designed. The finite element method (FEM) was used to simulate the forming process and predict the thickness distribution of different areas. Furthermore, the dies were optimized to make the thickness distribution uniform. In the final structure, the maximum thinning ratio decreased from 83.2% to 63% due to the optimized design of the forming dies. The front automobile fender was then successfully fabricated by the preforming process and final forming process at 480 °C. A thickness measurement was carried out, and the minimum thickness of the preforming structure was 2.17 mm at the transverse tank, while that of the final structure was 2.49 mm near the edge of the lamp orifice. The average grain size grew from 20 to 35 μm. The grain growth led to the reduction of mechanical properties. Compared with the mechanical properties of the initial material, the maximum decrease in tensile strength for the material after superplastic forming was 5.78%, and that of elongation was 18.5%.

**Keywords:** AA5083; rapid SPF; FEM; mechanical property; microstructure evolution

**Citation:** Du, Z.; Wang, G.; Wang, H. The Process Design and Rapid Superplastic Forming of Industrial AA5083 for a Fender with a Negative Angle in a Small Batch. *Metals* **2021**, *11*, 497. <https://doi.org/10.3390/met11030497>

Academic Editors: Diego Celentano and Anders E. W. Jarfors

Received: 26 January 2021

Accepted: 14 March 2021

Published: 17 March 2021

**Publisher's Note:** MDPI stays neutral with regard to jurisdictional claims in published maps and institutional affiliations.



**Copyright:** © 2021 by the authors. Licensee MDPI, Basel, Switzerland. This article is an open access article distributed under the terms and conditions of the Creative Commons Attribution (CC BY) license (<https://creativecommons.org/licenses/by/4.0/>).

## 1. Introduction

Due to its high specific strength, high specific stiffness, excellent corrosion resistance, and mechanical properties, AA5083 has been in the spotlight of railway vehicles, shipbuilding, and other industries [1–4]. Many investigations have been conducted to determine the influencing factors such as superplasticity and the superplastic forming (SPF) of AA5083 [5–11]. The chemical composition optimization of AA5083 has been attempted to reduce cost [5], and the superplastic deformation behavior was analyzed [6]. The SPF of AA5083 has been widely used to fabricate automotive liftgates and declids [7], “high-end” automobiles [10], and components for aircraft applications [11].

The front fender is considered an essential part needed to protect nearby components and support other exteriors; however, it is the most challenging part to manufacture due to its complex shape and requirement for high machining accuracy [12–14]. The conventional forming process of a fender was the cold stamping of steel [15] and plastic injection molding [16]. Cold stamping has the disadvantages of spring-back and a high die cost, while injection molding has complex forming processes [17]. SPF has the advantages of low die costs, eliminating spring-back, and producing complex components [18]. Moreover, SPF is an effective forming process for lightweight alloys for automotive components [19]. Thus, SPF, in theory, could be used to fabricate the automotive fender of AA5083.

Jarrar et al. [20] investigated the superplastic forming of triangular channels with sharp radii, and the forming process was simulated. Zhang et al. [21] researched the controlling of the thickness distribution in superplastic forming. In comparison, a large thickness deviation existed in the produced part. As such, direct-reverse SPF was adopted to make the thickness more uniform [22–24]. Xing et al. [22] proposed a simple and efficient preform design method to improve the uniformity of wall thickness. Lan et al. [24] investigated the two-stage superplastic forming of a V-shaped aluminum sheet into a trough with a deep and irregular contour, and a superior thickness profile was provided. Another limitation of SPF was the slow forming rate, which made it inefficient. Thus, it was necessary to investigate the rapid direct-reverse SPF process for an automobile front fender with a negative angle.

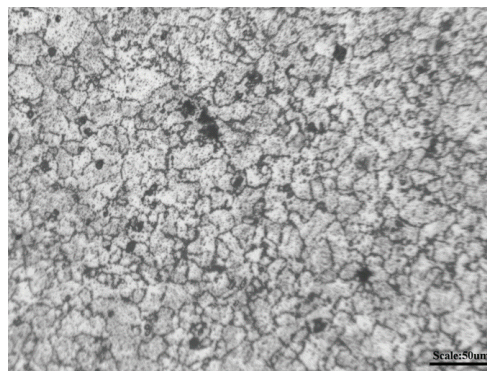
This manuscript aimed to fabricate a complex-shaped front automobile fender by the rapid direct-reverse SPF technology. The tensile test of an industrial AA5083 was carried out at elevated temperatures, and a constitutive equation in SPF was established. With the help of FEM, the forming process and the dies were established. The front automobile fender was then successfully manufactured by rapid SPF technology. A thickness measurement was made, and both the macroscopic and the microstructure behaviors were investigated.

## 2. Experimental

An industrial AA5083 sheet was used in this study, and the thickness of the sheet was 4 mm. The sheet was provided by the Northern Light Alloy Company Ltd. (Harbin, China), and the chemical composition is shown in Table 1. Figure 1 shows the initial microstructure of AA5083, and it can be seen that the grain size was about 20  $\mu\text{m}$ . The grain size of less than 10  $\mu\text{m}$  is typically one of the requirements for superplasticity [18], and this grain size was larger than that in other research papers investigating the superplasticity and SPF of AA5083 [25–28].

**Table 1.** Chemical composition of AA5083.

Elements	Si	Fe	Cu	Mn	Mg	Cr	Al
Content (wt %)	0.073	0.18	0.020	0.68	4.66	0.074	Bal.



**Figure 1.** Initial microstructure of AA5083.

Tensile test specimens were cut parallel to the rolling direction, and the gauge size was 15 mm  $\times$  5 mm  $\times$  4 mm. Tensile tests at elevated temperatures of 400–560  $^{\circ}\text{C}$  with an interval of 40  $^{\circ}\text{C}$  were carried out at the strain rate of  $5 \times 10^{-3} \text{ s}^{-1}$ – $5 \times 10^{-4} \text{ s}^{-1}$ , and the tests were conducted on an Instron 3343 testing machine (Instron Corporation, Norwood, MA, USA). The temperature diversity was less than 3  $^{\circ}\text{C}$  along the gauge length. The tensile tests at room temperature were conducted on the AG-X Plus testing machine, and

the tensile strain rate was  $1.67 \times 10^{-3} \text{ s}^{-1}$ . These specimens were cut from the initial sheet and the sheet after the forming process. To ensure the accuracy of tensile data, at least three tensile tests were performed for each condition, and the intermediate data at each condition were selected as the final result. The stress–strain data were captured at 10 Hz to guarantee the continuity of the data.

Rapid SPF of the fender was carried out on a 10,000 kN SPF machine. This rapid SPF process was divided into two stages: the preforming process and the final forming process. Each stage was composed of drawing and SPF, and the forming temperature was 480 °C. The target strain rate of the SPF process was  $1 \times 10^{-3} \text{ s}^{-1}$ .

The microstructural sample was cut into small pieces of 5 mm × 4 mm × T mm (where T is the thickness of different regions) by electron discharge wire cutting, then the plane of 5 mm × 4 mm was mechanically ground using SiC paper (from 400# to 2000#). Subsequently, the sample was electrolytically polished. The samples were corroded with Keller reagent for 60 s then cleaned with alcohol and distilled water. Scanning electron microscope (SEM) analysis of the microstructure of the as-received material, the preforming structure, and the final forming structure was performed on the Quanta 200 FEG-SEM machine (FEI company, Hillsboro, OR, USA).

### 3. Results and Discussion

#### 3.1. Flow Stress of AA5083 at Elevated Temperatures

The flow stress curves of AA5083 at the strain of  $5 \times 10^{-3}$ – $5 \times 10^{-4} \text{ s}^{-1}$  are shown in Figure 2. The flow stress was dependent on the temperature, strain rate, and true strain. The tensile strength decreased with increasing temperatures and decreasing strain rates, while the elongation increased firstly then reduced with the increasing temperature.

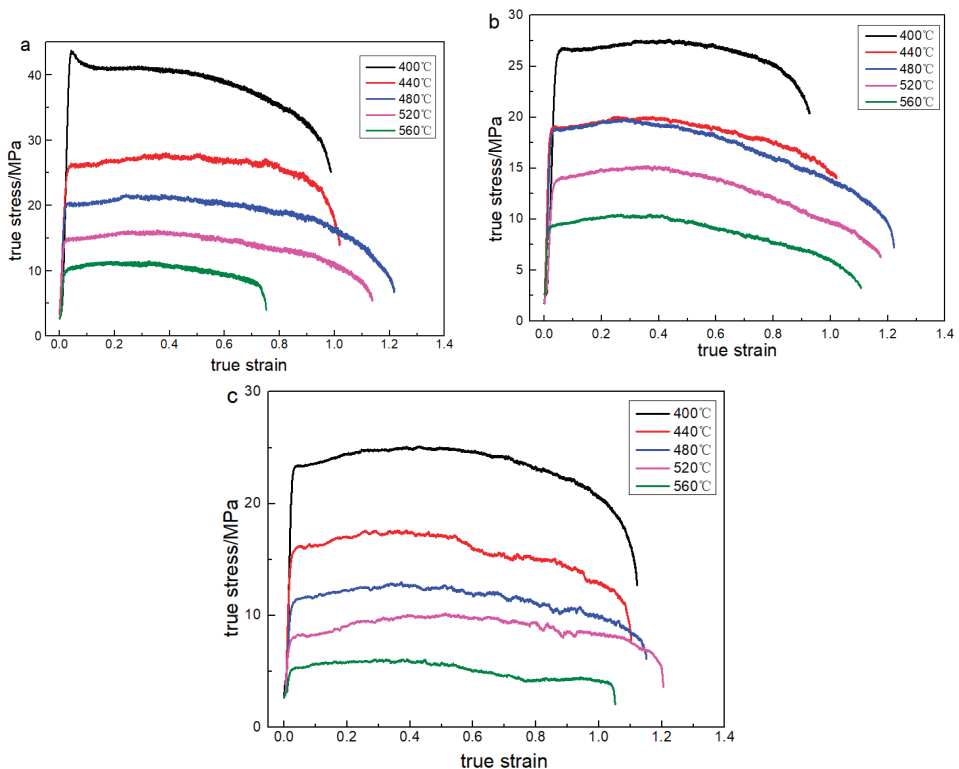


Figure 2. Flow stress curves of AA5083 at: (a)  $0.005 \text{ s}^{-1}$ ; (b)  $0.001 \text{ s}^{-1}$  (c)  $0.0005 \text{ s}^{-1}$ .

It can be seen that the elongation at some deformation parameters was more than 200% from Figure 2, and the maximum elongation obtained at 480 °C and  $1 \times 10^{-3} \text{ s}^{-1}$  was 242%. Thus, it can be concluded that the industrial AA5083 exhibited superplastic-like large elongation. This superplastic-like elongation of coarse-grained aluminum alloys with a grain size of more than 10  $\mu\text{m}$  has been reported in other investigations [29–31].

In the SPF process, the strain hardening was neglected. Thus, the constitutive model used to describe the SPF process was set as:

$$\sigma = K\dot{\epsilon}^m \quad (1)$$

where  $m$  is the strain rate sensitivity coefficient indicated the effect of strain rate on the flow stress.  $K$  is the material constant related to the deformation temperature and the microstructure. Equation (1) was taken for the logarithms, then it was expressed as:

$$\ln \sigma = \ln K + m \ln \dot{\epsilon} \quad (2)$$

For Equation (2), after being differential, the equation for  $m$  can be obtained as:

$$m = \frac{\partial \ln \sigma}{\partial \ln \dot{\epsilon}} \quad (3)$$

The value of  $m$  was then calculated to be about 0.35, and  $K$  was estimated to be 155 MPa·s on account of the flow stress curves at 480 °C with different strain rates. When the strain rate sensitivity exponent was 0.35, it was the value of the solute drag creep, which is different from the value indicating grain boundary sliding [32]. This value was lower than in the case of the fine-grained materials [33]. Furthermore, superplastic forming by solute drag creep has been reported by Honda Motor Co., Ltd. (Tokyo, Japan) and UACJ as high-temperature, high-speed blow forming. Thus, the material in this paper could be applied to the SPF process.

### 3.2. Structural Design and Process Optimization

The forming process of the fender is complex. Moreover, it is difficult to observe the deformation and the variation of thickness in the manufacturing process. Thus, the forming process was simulated by FEM, and the thickness distribution of the forming process was predicted, providing a theoretical reference for the final manufacturing process. The conventional SPF cannot achieve the final shape in one process due to the complex shape; thus the whole process included two steps. The first step was the preforming process, which comprised the drawing and the reverse superplastic bulging. The second step was the final process, consisting of the drawing and the direct superplastic bulging.

#### 3.2.1. Initial Design

The initial designs of the male die for the preforming process and the male die for the final forming process are shown in Figure 3. To ensure the thickness uniformity of the final product, appropriate material storage was prepared on the preformed male die. Storage tanks were mainly set in A, B and C parts, as shown in Figure 3a). The male die of the final forming shown in Figure 3b) was mainly used for further stretching and as supplementing material for the superplastic bulging of the final process.

The numerical simulation of the forming process was carried out by the MSC.MARC software (2010, MSC software Corporation, LA, USA). The initial model of the FEM analysis is shown in Figure 4. The color scales represent the plate thickness, and the units of the legend in each figure are millimeters. The dies were rigid, and the sheet was deformable in this model. The size of the sheet was 1900 mm  $\times$  2500 mm. The four-node shell element was selected to represent the sheet. The size of the shell element was 20 mm  $\times$  20 mm, and the number of the four-node shell element was 11,875. The thickness was set to be 3 mm. The friction coefficient between the die and the face sheet was set as 0.3, and the Coulomb friction model was selected to be the friction model.

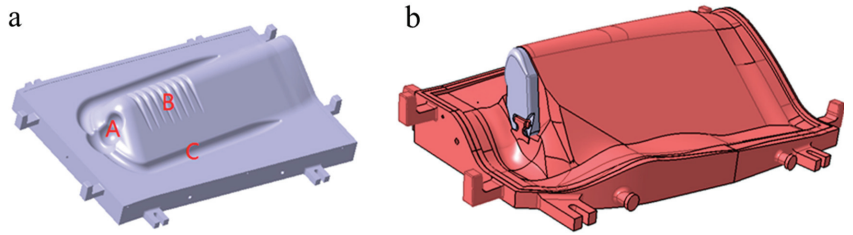


Figure 3. Male dies of (a) the preforming process; (b) final forming process.

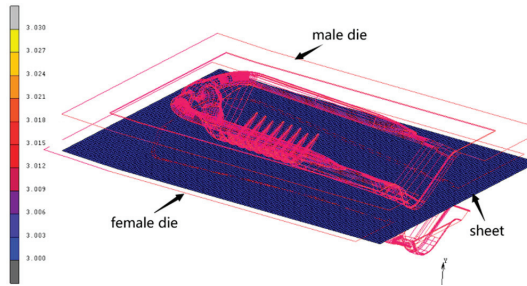


Figure 4. Initial FEM model.

(1) Drawing of the preforming process

The drawing depth was 250 mm. The thickness distribution of the drawing during the preforming process is shown in Figure 5. It can be seen that the minimum thickness at the lowest position of the drawing was 2.78 mm. The radial tensile stress of the material at this position was greater than the tangential compressive stress. Therefore, this resulted in thickness reduction, but the plate thickness reduction rate was only 7.33%.

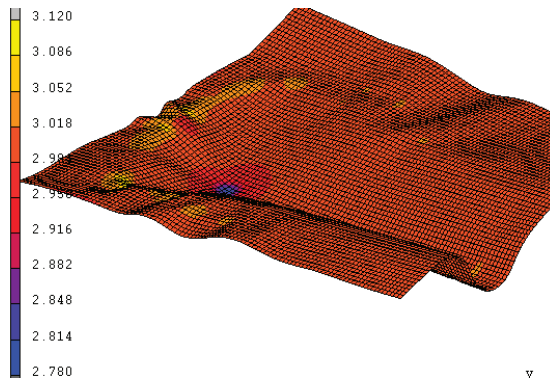


Figure 5. Thickness distribution of the drawing during the preforming process.

(2) Reverse superplastic bulging of the preforming process

The thickness distribution of the reverse superplastic bulging is shown in Figure 6. The minimum thickness was 1.631 mm at Region A, and the thinning ratio reached was 45.6%. The serious thickness reduction at this region resulted from the thickness reduction in the drawing of the preforming process and the further reduction in bulging.



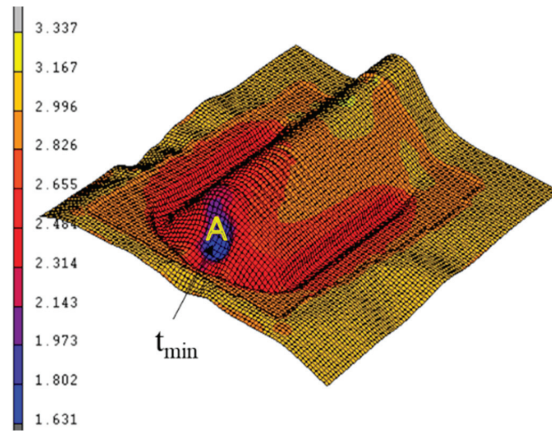


Figure 6. Thickness distribution of the drawing during the preforming process.

### (3) Drawing of the final forming process

A finite element analysis of the drawing was carried out, and the results are shown in Figure 7. The hot drawing depth of the final forming was 380 mm. The minimum thickness was reduced from 1.631 to 1.608 mm due to the stretching of the storage tank. In addition, the material of the storage tank at Region C in the preform process was provided to supply the drawing, and it decreased the thickness reduction. Hence, the thickness at the lowest point of the drawing was 2.106 mm.

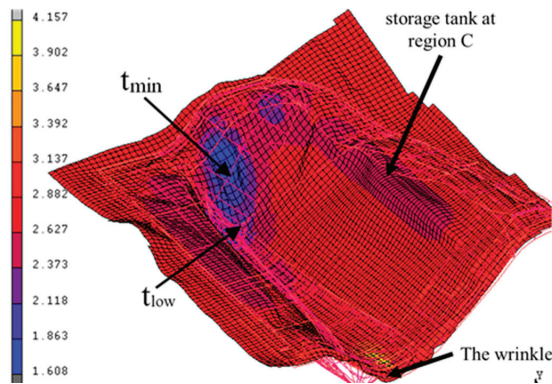
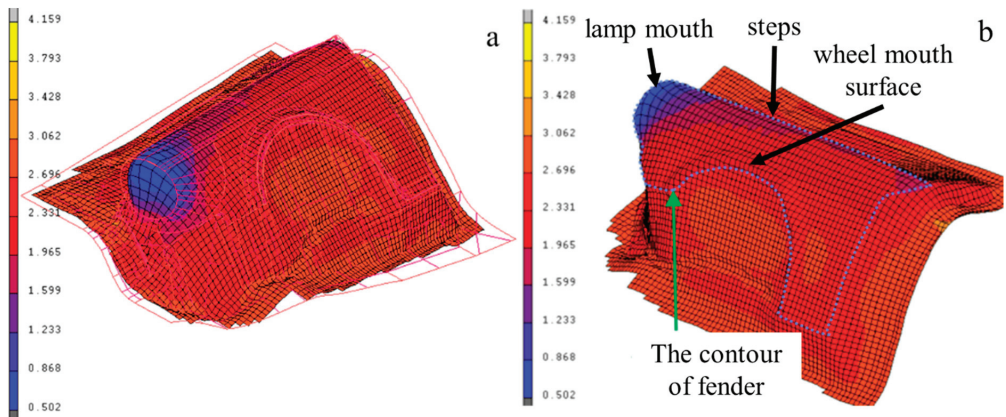


Figure 7. Thickness distribution of the drawing during the final forming process.

### (4) Superplastic bulging of the final forming process

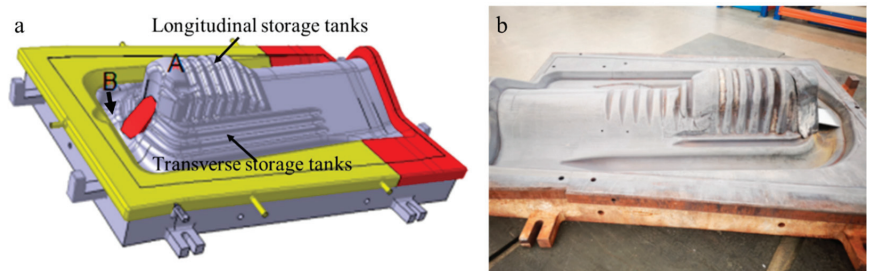
The thickness distribution of the SPF process and the contour of the fender are shown in Figure 8. It can be found that the complex surfaces such as the negative angle at the lamp mouth, the wheel mouth plane, and the steps were formed at the last stage. The minimum thickness occurred at the edge of the lamp mouth. The maximum thickness reduction ratio was 83.2%, and it was so severe that the material could not meet this requirement.



**Figure 8.** (a) Thickness distribution of the direct superplastic bulging; (b) contour of the fender.

### 3.2.2. Optimized Design

In order to optimize the process and make the thickness more uniform, the preformed die was redesigned. The stamping depth of the preformed die was increased, and the preformed material storage tanks were also added to provide sufficient material for the final product. The optimized preformed die is shown in Figure 9. The drawing depth was increased to 300 mm, material storage tanks near Region B were added, and the width of Region A was also increased.



**Figure 9.** Male die of the preforming process: (a) optimized model; (b) machined die.

#### (1) Drawing of the preforming process

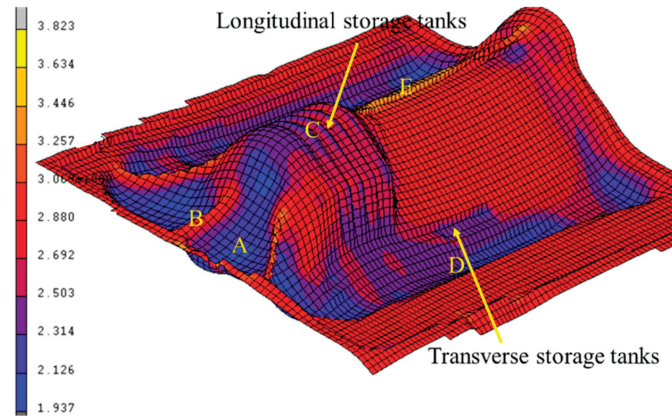
The thickness distribution resulting from the preforming process drawing after the optimized design is shown in Figure 10. During the stamping process, it was found that the minimum thickness was 2.736 mm, and it occurred at the lowest point of the drawing. The maximum thickness reduction ratio was 8.8%, and no cracks and other defects occurred. Simultaneously, a wrinkle was observed at Region A. Thus, the drawing rate needed to be controlled strictly to reduce wrinkle defects.



**Figure 10.** Thickness distribution of the drawing in the preforming process by the optimized design.

(2) Reverse bulging of the preforming process

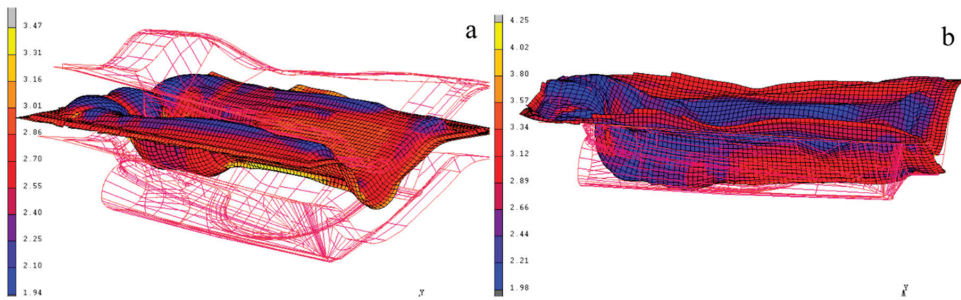
The thickness distribution after reverse bulging is shown in Figure 11. It can be seen that the thickness diversity increased due to the complex shape of the female die and the improved storage tanks. The minimum thickness was 1.937 mm in Region A, and the minimum thickness was 2.23 mm at the longitudinal storage tanks and 2.26 mm at the transverse storage tanks, respectively. Though the thickness at different regions was nonuniform, it was still greater than 1.9 mm. In addition, there are wrinkles at Regions B and E. The wrinkle at Region B could be flattened in the final forming process, while the deformation at Region E had little effect on the forming process.



**Figure 11.** Thickness distribution of reverse bulging during the preforming process.

(3) Drawing of the final forming process

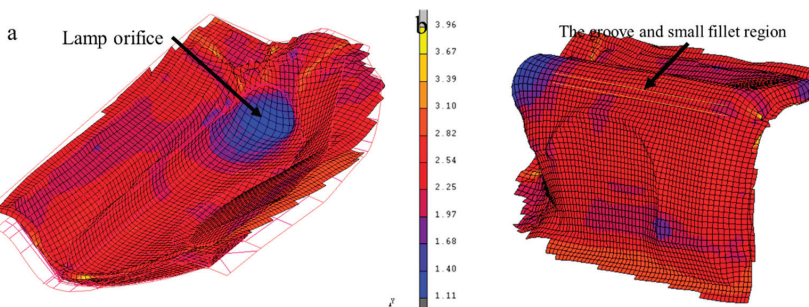
The maximum drawing depth of the final forming was 380 mm, and the minimum thickness at the initial stage of the drawing was 1.94 mm. The thickness distribution of the drawing at the beginning and at the end of the drawing is shown in Figure 12. The storage tanks expanded to supply more material for the next forming process, and the minimum thickness increased slightly to 1.98 mm. It can be seen in Figure 12b that the preformed storage tanks still retained a specific shape.



**Figure 12.** Thickness distribution of the drawing during the final forming process: (a) beginning; (b) end.

#### (4) SPF of the final forming process

SPF of the final forming process is shown in Figure 13. The wrinkled area at the end of the preformed structure had been flattened by the air bulging. When the fender was fully formed, the minimum thickness occurred at the lamp orifice, and the thickness reduction ratio was 63%. Compared to the thickness distribution of the initial design, the minimum thickness increased by 0.6 mm, indicating that the optimization of the preforming male die was effective. It was also observed that small fillet thickness was more than 2.25 mm, which could guarantee the uniformity of the thickness and part performance.



**Figure 13.** Thickness distribution of superplastic forming (SPF) during the final forming process. (a) interior perspective; (b) lateral perspective.

It was concluded that the optimized design could increase the minimum thickness of the final structure, and the optimized design had more feasibility than the original design in regards to fabricating the fender.

### 3.3. Rapid SPF of the Front Fender

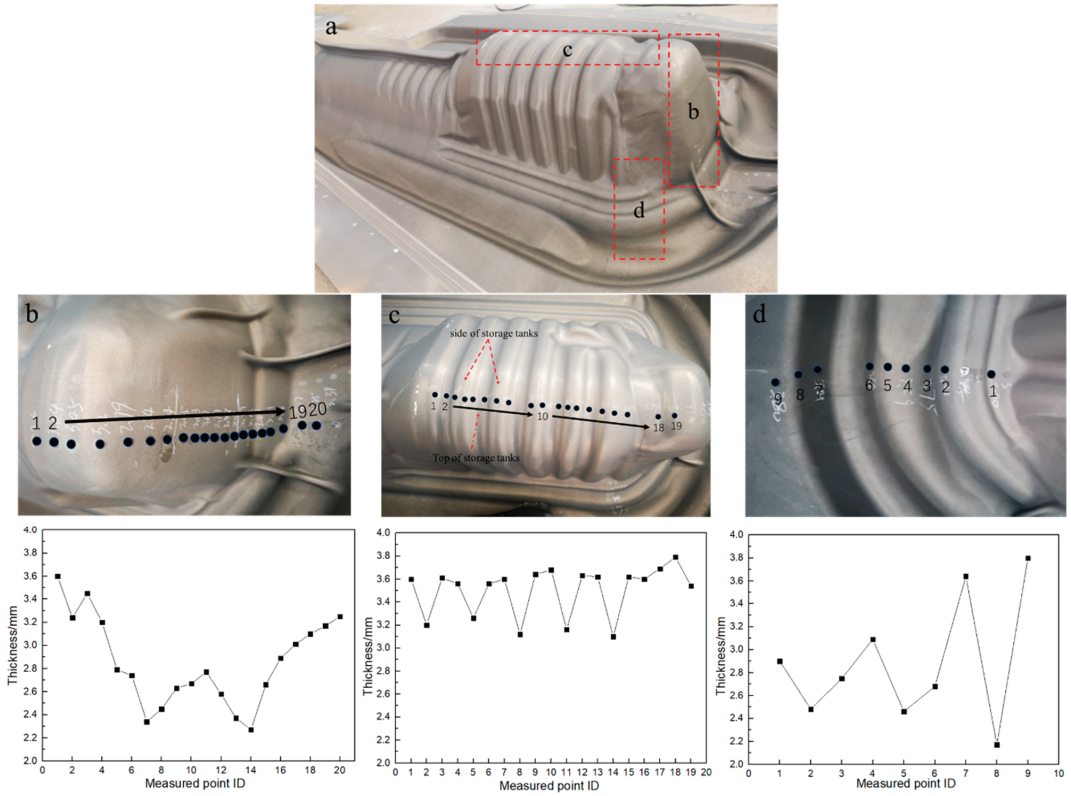
Based on the FEM results of the optimized design, the dies required to fabricate the fender were machined consistently with the dies of the optimized design. The front fender was then trial produced on the SPF machine, with the forming temperature set to be 480 °C.

#### 3.3.1. Thickness Distribution

##### (1) Preforming process

Figure 14 illustrates the measured points and the thickness distribution of the preforming structure. The structure after reverse superplastic bulging is shown in Figure 14a. Although wrinkles were observed, no crack appeared, indicating that superfluous material was supplied to some regions during the forming process. The thicknesses of three different areas were measured and are shown in Figure 14b–d. The results showed that the minimum thickness of the end was 2.34 mm, and the “W” shape of the thickness distribution was

presented. Furthermore, the thickness measurement of the storage tanks showed that the thickness was more than 3.0 mm at the longitudinal tanks, and the minimum thickness of the transverse tanks was 2.17 mm.



**Figure 14.** Measurement point ID and thickness: (a) preforming structure; (b) end; (c) longitudinal storage tanks; (d) transverse storage tanks.

## (2) Final forming process

Figure 15 illustrates the measured points of the structure obtained after the final forming and the thickness of each point. The thickness measurement showed that the thickness was almost more than 2.5 mm, and the thickness gradually reduced as the measured points approached the lamp orifice. The thickness reduction resulted from the large deformation at the lamp orifice, and the thickness distribution meets the demand for service. It can also be seen that the facet of the wheel opening contacted the female mold of the final forming process. Furthermore, the long groove and small fillet were formed completely.

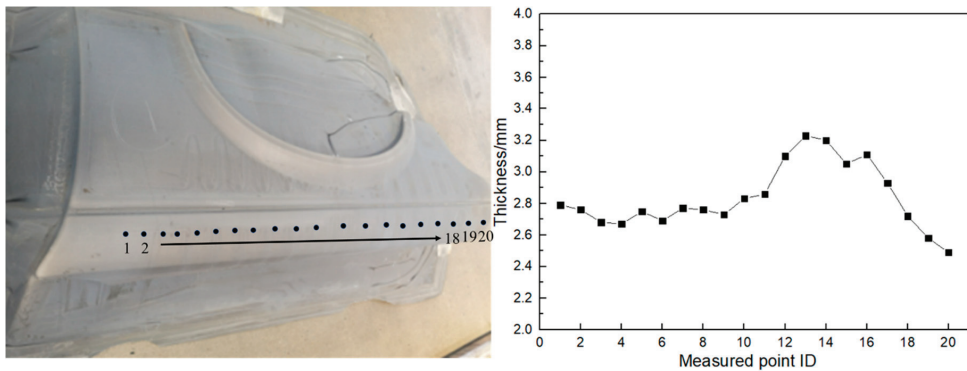


Figure 15. Final structure and thickness measurement points.

The final structure was wire cut and etched, as shown in Figure 16. The front automobile fender was successfully trial produced.

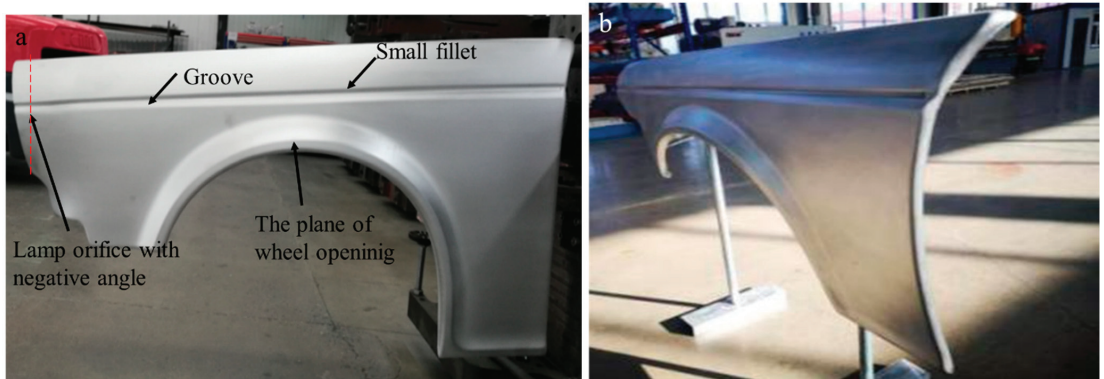


Figure 16. Front automobile fender: (a) elevation view; (b) side view.

### 3.3.2. Macro/Micro Performance of the Postmaterial

The elongation, tensile strength, and yield stress of the postforming material at different regions are shown in Figure 17. The result showed that the tensile strength of the original material was 294 MPa, the yield stress was 143 MPa, and the elongation was about 31%. The minimum tensile strength of the post-formed material was 277 MPa, and the minimum yield stress was 115 MPa at the transverse tank, while the minimum elongation was 24.9% at the lamp orifice. The measured tensile strength, yield stress, and elongation of the postformed material ranged between 270 and 284 MPa, 115 and 121 MPa, and 24.9 and 26.6%, respectively. The mechanical performance decreased after the rapid SPF process due to the grain growth resulted from the long exposure to elevated temperature and deformation.

The microstructures of the material at two stages are shown in Figure 18. The initial grain size was about 20  $\mu\text{m}$  in Figure 1. Hence, based on the comparison between Figures 1 and 18, it can be concluded that the grain size increased by 5  $\mu\text{m}$  after the pre-forming process and then further increased by 10  $\mu\text{m}$  after the final forming process. There is grain size growth resulting from the long time exposure at elevated temperature in the preforming process and the final forming process.

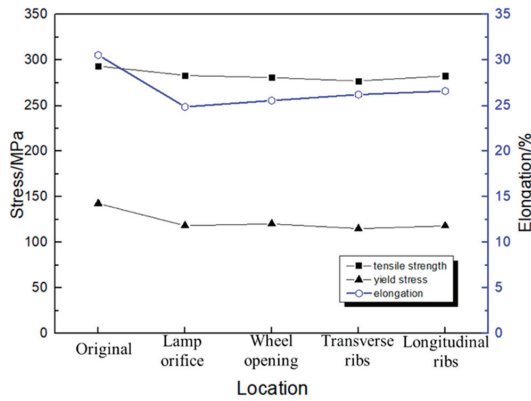


Figure 17. Mechanical properties of the material after the forming process.

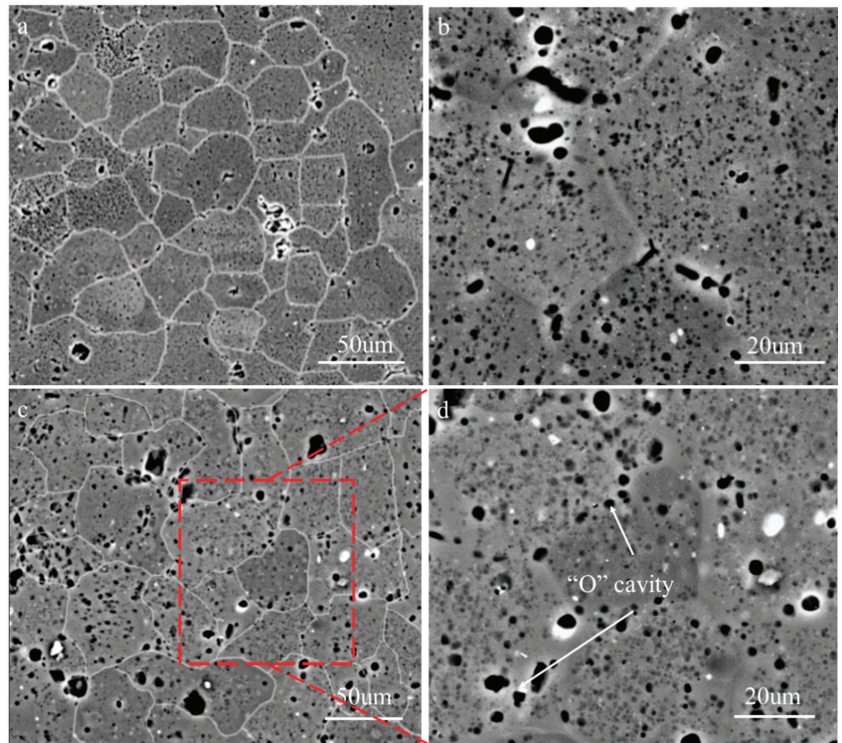


Figure 18. Microstructure of (a,b) the preforming structure; (c,d) final structure.

The cavity size grew with the increase of the deformation and holding time. It has been reported that most cavities nucleated at the interfaces between the particle and the matrix at both the grain boundary and the grain interior [34]. With the increase of deformation and insulation time, the size of the cavity increased gradually. As seen in Figure 18c,d, some cavities appeared at the grain boundary; however, these cavities were not interconnected. Therefore, the mechanical properties of the post-material decreased slightly.

#### 4. Conclusions

The mechanical properties of AA5083 were investigated at elevated temperatures, and the FEM established the structural design of the dies. Furthermore, the front fender was trial produced by a rapid SPF process. The following conclusions are drawn:

(1) Industrial AA5083 with the grain size of 20  $\mu\text{m}$  exhibited superplasticity at 480  $^{\circ}\text{C}/0.001\text{ s}^{-1}$ , and the maximum elongation was about 242% with the strain rate sensitivity value of 0.35.

(2) The optimized design of the forming dies and the forming process could fabricate the fender with a complex shape.

(3) The front fender was successfully trial produced by the rapid SPF process, and the minimum thickness was 2.49 mm at the edge of the lamp orifice.

(4) The grain size increased by 15  $\mu\text{m}$  after the forming process. The tensile strength reduced by 5.78%, and the elongation reduced by 18.5%. The inharmonious grain boundaries sliding resulted in the appearance of cavities at the grain boundaries.

**Author Contributions:** Z.D., data collection, writing; G.W., study design; H.W., data analysis, figures. All authors have read and agreed to the published version of the manuscript.

**Funding:** This research was funded by the Henan Provincial Department of Science and Technology Research Project (Grant No. 182102210468), and National Natural Science Foundation of China (Grant No. 51875122). And the APC was funded by the Henan Provincial Department of Science and Technology Research Project (Grant No. 182102210468).

**Institutional Review Board Statement:** Not applicable.

**Informed Consent Statement:** Not applicable.

**Data Availability Statement:** Data sharing not applicable.

**Acknowledgments:** This work was supported by the Henan Provincial Department of Science and Technology Research Project (Grant No. 182102210468), and National Natural Science Foundation of China (Grant No. 51875122).

**Conflicts of Interest:** The authors declare no conflict of interest.

#### References

- Ma, M.Y.; Wang, B.; Liu, H.Q.; Yi, D.Q.; Shen, F.H.; Zhai, T.G. Investigation of fatigue crack propagation behavior of 5083 aluminum alloy under various stress ratios: Role of grain boundary and schmid factor. *Mater. Sci. Eng. A* **2020**, *773*, 138871. [[CrossRef](#)]
- Holroyd, N.J.H.; Burnett, T.L.; Seifi, M.; Lewandowski, J.J. Improved understanding of environment-induced cracking (EIC) of sensitized 5XXX series aluminum alloys. *Mater. Sci. Eng. A* **2017**, *682*, 613–621. [[CrossRef](#)]
- Magee, A.C.; Ladani, L. Representation of a microstructure with bimodal grain size distribution through crystal plasticity and cohesive interface modeling. *Mech. Mater.* **2015**, *82*, 1–12. [[CrossRef](#)]
- Magee, A.; Ladani, L.; Topping, T.D.; Lavernia, E.J. Effects of tensile test parameters on the mechanical properties of a bimodal Al-Mg alloy. *Acta Mater.* **2012**, *60*, 5838–5849. [[CrossRef](#)]
- Jin, H. Optimization of aluminum alloy AA5083 for superplastic and quick plastic forming. *Metall. Mater. Trans. A* **2019**, *50*, 3868–3890. [[CrossRef](#)]
- Giuliano, G.; Samani, F. Comparison between superplastic and non-superplastic grade AA 5083. *J. Test. Eval.* **2016**, *44*, 2114–2119. [[CrossRef](#)]
- Krajewski, P.E.; Schroth, J.G. Overview of quick plastic forming technology. *Mater. Sci. Forum* **2007**, *551*, 3–12. [[CrossRef](#)]
- Liu, J.; Tan, M.J.; Lim, C.V.S.; Chua, B.W. Process optimization and microstructural development during superplastic-like forming of AA5083. *Int. J. Adv. Manuf. Technol.* **2013**, *69*, 2415–2422. [[CrossRef](#)]
- Liu, J.; Tan, M.J.; Aue-u-lan, Y.; Jarfors, A.E.W.; Fong, K.S.; Castagne, S. Superplastic-like forming of non-superplastic AA5083 combined with mechanical pre-forming. *Int. J. Adv. Manuf. Technol.* **2011**, *52*, 123–129. [[CrossRef](#)]
- Barnes, A.J.; Raman, H.; Lowerson, A.; Edwards, D. Recent application of superformed 5083 aluminum alloy in the aerospace industry. *Mater. Sci. Forum* **2012**, *735*, 361–371. [[CrossRef](#)]
- Hefli, L.D. Commercial airplane applications of superplastically formed AA5083 aluminum sheet. *J. Mater. Eng. Perform.* **2007**, *16*, 136–141. [[CrossRef](#)]
- Park, H.S.; Dang, X.P.; Roderburg, A.; Nau, B. Development of plastic front side panels for green cars. *CIRP J. Manuf. Sci. Technol.* **2013**, *6*, 44–52. [[CrossRef](#)]



13. Tao, W.; Liu, Z.; Zhu, P.; Zhu, C.; Chen, W. Multi-scale design of three dimensional woven composite automobile fender using modified particle swarm optimization algorithm. *Compos. Struct.* **2017**, *181*, 73–83. [[CrossRef](#)]
14. Hu, W.; Yao, L.G.; Hua, Z.Z. Optimization of sheet metal forming processes by adaptive response surface based on intelligent sampling method. *J. Mater. Process. Technol.* **2008**, *197*, 77–88. [[CrossRef](#)]
15. Fan, Z.J.; Gui, L.J.; Su, R.Y. Research and development of automotive lightweight technology. *J. Automot. Saf. Energy* **2014**, *5*, 1–16.
16. Park, H.S.; Nguyen, T.T. Optimization of injection molding process for car fender in consideration of energy efficiency and product quality. *J. Comput. Des. Eng.* **2014**, *1*, 256–265. [[CrossRef](#)]
17. Roth, R.; Clark, J.; Kelkar, A. Automobile bodies: Can aluminum be an economical alternative to steel? *JOM* **2001**, *53*, 28–32. [[CrossRef](#)]
18. Zhang, K.F.; Jiang, S.S. Superplastic forming. In *Comprehensive Materials Processing*, 1st ed.; Hashmi, S., Batalha, G.F., van Tyne, C.J., Yilbas, B., McGeough, J., Eds.; Elsevier: Amsterdam, The Netherlands, 2014; Volume 5, pp. 371–392.
19. Jafar, R.A.; Jarrar, F.S.; Al-Huniti, N.S. Two-stage approach for improving the thickness distribution in superplastic forming. *J. Mater. Sci. Res.* **2015**, *4*, 12–27. [[CrossRef](#)]
20. Jarrar, F.S.; Liewald, M.; Schmid, P.; Fortanier, A. Superplastic forming of triangular channels with sharp radii. *J. Mater. Eng. Perform.* **2014**, *23*, 1313–1320. [[CrossRef](#)]
21. Zhang, K.F.; Wang, G.F.; Wu, D.Z.; Wang, Z.R. Research on the controlling of the thickness distribution in superplastic forming. *J. Mater. Process. Technol.* **2004**, *151*, 54–57. [[CrossRef](#)]
22. Xing, H.L.; Zhang, K.F.; Wang, Z.R. A preform design method for sheet superplastic bulging with finite element modeling. *J. Mater. Process. Technol.* **2004**, *151*, 284–288. [[CrossRef](#)]
23. Jarrar, F.S.; Jr, L.G.H.; Khraisheh, M.K.; Bower, A.F. New approach to gas pressure profile prediction for high temperature AA5083 sheet forming. *J. Mater. Process. Technol.* **2010**, *210*, 825–834. [[CrossRef](#)]
24. Lan, H.C.; Fuh, Y.K.; Lee, S.; Chu, C.L.; Chang, T.C. Two-stage superplastic forming of a V-shaped aluminum sheet into a trough with deep and irregular contour. *J. Mater. Eng. Perform.* **2013**, *22*, 2241–2246. [[CrossRef](#)]
25. Xu, C.; Langdon, T.G.; Horita, Z.; Furukawa, M. Using equal-channel angular pressing for the production of superplastic aluminum and magnesium alloys. *J. Mater. Eng. Perform.* **2004**, *13*, 683–690. [[CrossRef](#)]
26. Hojjati, M.H.; Zoorabadi, M.; Hosseinipour, S.J. Optimization of superplastic hydroforming process of Aluminium alloy 5083. *J. Mater. Process. Technol.* **2008**, *205*, 482–488. [[CrossRef](#)]
27. Ko, Y.G.; Shin, D.H.; Park, K.T.; Lee, C.S. Superplastic deformation behavior of ultra-fine-grained 5083 Al alloy using load-relaxation tests. *Mater. Sci. Eng. A* **2007**, *449*, 756–760. [[CrossRef](#)]
28. Balasubramanian, M.; Stalin, B.; Ramanathan, K.; Ravichandran, M. Hot tensile test for determining the material constant on superplastic 5083Al alloy sheet. *Mater. Today Proc.* **2020**, *21*, 324–328. [[CrossRef](#)]
29. Taleff, E.M.; Wadsworth, L.J. Enhanced ductility in coarse-grained Al-Mg alloys. *Metall. Mater. Trans. A* **1996**, *27*, 343–352. [[CrossRef](#)]
30. Chezan, A.R.; de Hosson, J.T.M. Superplastic behavior of coarse-grained aluminum alloys. *Mater. Sci. Eng. A* **2005**, *410*, 120–123. [[CrossRef](#)]
31. Qiao, J.; Taleff, E.M. Superplasticity-like creep behavior of coarse grained ternary Al alloys. *Trans. Nonferrous Met. Soc. China* **2010**, *20*, 564–571. [[CrossRef](#)]
32. Sherby, O.D.; Taleff, E.M. Influence of grain size, solute atoms and second-phase particles on creep behavior of polycrystalline solids. *Mater. Sci. Eng. A* **2002**, *322*, 89–99. [[CrossRef](#)]
33. Bae, D.H.; Ghosh, A.K. Grain size and temperature dependence of superplastic deformation in an Al–Mg alloy under isostructural condition. *Acta Mater.* **2000**, *48*, 1207–1224. [[CrossRef](#)]
34. Iwasaki, H.; Mori, T.; Hosokawa, H.; Tagata, T.; Mabuchi, M.; Higashi, K. Cavitation behavior of coarse-grained Al-4.5Mg alloy exhibiting superplastic-like elongation. *Mrs Proc.* **1999**, *601*, 67–72. [[CrossRef](#)]

Article

# A Detailed Machinability Assessment of DC53 Steel for Die and Mold Industry through Wire Electric Discharge Machining

Sarmad Ali Khan<sup>1</sup>, Mudassar Rehman<sup>2</sup>, Muhammad Umar Farooq<sup>1,3,\*</sup>, Muhammad Asad Ali<sup>1,\*</sup>, Rakhshanda Naveed<sup>1</sup>, Catalin I. Pruncu<sup>4,5,\*</sup> and Waheed Ahmad<sup>1</sup>

<sup>1</sup> Department of Industrial and Manufacturing Engineering, University of Engineering and Technology Lahore, Lahore 54890, Pakistan; drsarmad@uet.edu.pk (S.A.K.); rakhshanda@uet.edu.pk (R.N.); 2012msime15@student.uet.edu.pk (W.A.)

<sup>2</sup> Department of Industrial Engineering, School of Mechanical Engineering, Northwestern Polytechnical University, Xi'an 710072, China; mudassar@mail.nwpu.edu.cn

<sup>3</sup> Department of Industrial and Systems Engineering, Korea Advanced Institute of Science and Technology, Daejeon 34141, Korea

<sup>4</sup> Department of Mechanical Engineering, Imperial College London, Exhibition Rd., London SW7 2AZ, UK

<sup>5</sup> Design, Manufacturing & Engineering Management, University of Strathclyde, Glasgow G1 1XJ, UK

\* Correspondence: umarmuf0@gmail.com (M.U.F.); asad.ali@uet.edu.pk (M.A.A.); c.pruncu@imperial.ac.uk or catalin.pruncu@strath.ac.uk (C.I.P.)

**Abstract:** Recently, DC53 die steel was introduced to the die and mold industry because of its excellent characteristics i.e., very good machinability and better engineering properties. DC53 demonstrates a strong capability to retain a near-net shape profile of the die, which is a very challenging process with materials. To produce complex and accurate die features, the use of the wire electric discharge machining (WEDM) process takes the lead in the manufacturing industry. However, the challenge is to understand the physical science of the process to improve surface features and service properties. In this study, a detailed yet systematic evaluation of process parameters investigation is made on the influence of a wire feed, pulse on duration, open voltage, and servo voltage on the productivity (material removal rate) and material quality (surface roughness, recast layer thickness, kerf width) against the requirements of mechanical-tooling industry. Based on parametric exploration, wire feed was found the most influential parameter on kerf width: KW (45.64%), pulse on time on surface roughness: SR (84.83%), open voltage on material removal rate: MRR (49.07%) and recast layer thickness: RLT (52.06%). Also, the optimized process parameters resulted in 1.710  $\mu\text{m}$  SR, 10.367  $\text{mm}^3/\text{min}$  MRR, 0.327 mm KW, and 10.443  $\mu\text{m}$  RLT. Moreover, the evolution of surface features and process complexities are thoroughly discussed based on the involved physical science. The recast layer, often considered as a process limitation, was explored with the aim of minimizing the layers' depth, as well as the recast layer and heat-affected zone. The research provides regression models based on thorough investigation to support machinists for achieving required features.

**Citation:** Khan, S.A.; Rehman, M.; Farooq, M.U.; Ali, M.A.; Naveed, R.; Pruncu, C.I.; Ahmad, W. A Detailed Machinability Assessment of DC53 Steel for Die and Mold Industry through Wire Electric Discharge Machining. *Metals* **2021**, *11*, 816. <https://doi.org/10.3390/met11050816>

Academic Editor: George A. Pantazopoulos

Received: 7 April 2021  
Accepted: 14 May 2021  
Published: 17 May 2021

**Publisher's Note:** MDPI stays neutral with regard to jurisdictional claims in published maps and institutional affiliations.

**Keywords:** WEDM; DC53 steel; recast layer thickness; material removal rate; Kerf



**Copyright:** © 2021 by the authors. Licensee MDPI, Basel, Switzerland. This article is an open access article distributed under the terms and conditions of the Creative Commons Attribution (CC BY) license (<https://creativecommons.org/licenses/by/4.0/>).

## 1. Introduction

Die-making industries employ a wide variety of engineering materials, such as variants of steel, for the fabrication of tools, dies, and molds based on their considerable application performance and increasing demand. Conventional steels involving D2 and D3 steel have been engaged for over a decade in the manufacturing of dies and molds. Among these steel families, DC53 steel is considered as an advancement over D2 and D3 steel in terms of its high hardness (64 HRC), better toughness, improved fatigue strength and wear resistance. Various engineering applications of DC53 steel involve the manufacturing of different rolling, forging, injection molding, extrusion, and stamping dies along with molds, cutting tools, along with a wide variety of high speed and wear resistant parts [1].

The processing of such materials also becomes challenging as a result of their improved properties. Therefore, advanced machining setups are employed to fulfil the requirements. These involve electrochemical machining, electric discharge machining, plasma arc cutting, ultrasonic machining and abrasive water jet machining. These setups are considered an improvement in machining hard materials and generating a variety of machining profiles. Processing of hard materials such as titanium alloys and various other hardened steel grades—for instance, DC53 steel—may be difficult in a conventional machining scenario because of their excessive tool wear during machining. Therefore, non-conventional machining processes may be employed to serve the same purpose with little/no tool wear. Wire electric discharge machining (WEDM) is one of the non-traditional machining processes in which spark-based discharge energy is produced among two electrodes (wire electrode and workpiece) and responsible for material erosion during machining with no mechanical stresses generated unlike traditional machining processes [2].

WEDM is employed to process D2, D3 and different tool and die steel materials. Several investigations are made on the performance attributes like kerf width, material removal rate, and surface morphology, including roughness and microstructural examination involving recast layer [3–5]. The aspects of DC53 steel machining have not been thoroughly explored, therefore, are mainly investigated herein. Thiagarajan et al. [6] reported the combined influence of machining variables like pulse on duration ( $P_{on}$ ), pulse off time ( $P_{off}$ ), wire feed (WF) and wire tension (WT) at the MRR and SR in electric discharge machining of AISI D3 steel. A detailed study as multi-objective optimization was made by Manajaiah et al. [7] for AISI D2 steel in WEDM and inferred that the MRR, SR and recast layer thickness (RLT) are found in direct proportion with  $P_{on}$ . Ikram et al. [8] carried an insight investigation in WEDM of AISI D2 steel. The study reports that  $P_{on}$  is influenced more on SR (52.14%), MRR (49.62%), and KW (47.06%). In the study, results proved that  $P_{on}$  is two times more significant for SR compared to open voltage (OV), the combined influence of (WT,  $P_{on}$  and OV) found significant for KW, and the combination of servo voltage (SV), OV and  $P_{on}$  found significant for MRR respectively.

The experimental investigation performed by Vaghela et al. [9] for AISI D3 steel in WEDM inferred that the set of process variables peak current,  $P_{on}$  and  $P_{off}$  to maximize MRR, minimize KW and SR, respectively. Zhang et al. [10] performed mathematical modelling using back-propagation neural-network integrated with genetic algorithm and response surface methodology (RSM) to obtain optimal values of MRR and SR in WEDM of SKD11(D2 steel). Rupajati et al. [11] determined the machining performance regarding SR and recast layer thickness (RLT) for AISI H13 tool steel in electric discharge machining using Taguchi methodology along with the fuzzy-logic technique.

Significant improvements were obtained in RLT (22.04% reduction) and SR (13.15% reduction) from design of experiments results. It was also inferred that the significant variables for SR and RLT included  $P_{on}$  (40.08%) and  $O_V$  (30.38%), respectively. Hasriadi et al. [12] machined two different tool steel grades in WEDM for the assessment of surface morphology in terms of SR, RLT, and density of microcracks and resulted in the previously stated response variables forming a direct linear relation with both  $P_{on}$  and the arc on duration. Castillo et al. [13] explored the parametric effects on AISI 304 stainless steel.

Saini et al. [14] achieved multi-objective optimization in WEDM of 16MnCr5 alloy steel. Obwald et al. [15] conducted an analysis of different pulses types generated in high-speed WEDM. A detailed study was made by Solomon et al. [16] to comprehend the effect of variation in process variables for obtaining optimized parameters in WEDM of the steel family. Multi-objective optimization performed by Shivade and Shinde [17] in WEDM of AISI D3 steel resulted that gap current, and MRR varied directly with  $P_{on}$  and peak current, and inversely with the machining time (tm). Azam et al. [18] optimized cutting speed (C.S) by the variation in  $P_{on}$ ,  $P_{off}$ , and pulse frequency in WEDM of HSLA steel. The machined surface characterization was conducted by Dhobe et al. [19] in the electric discharge of AISI D2 steel. It was reported that RLT is found directly proportional with both SR and fatigue life. Based upon scanning electron microscopy (SEM) and X-ray

diffraction results, it was reported that triple tempering (a heat treatment process) is better than single tempering as it improves the machined surface quality by reducing RLT and SR. Khanna and Singh [20] performed a comparative study in WEDM of cryogenic-treated and normal D3 tool steel for the cutting rate, MRR and SR. It was reported that the cryogenic treatment significantly influenced both the MRR (decreased 5.6%) and SR (surface finish increased 10.6%) compared to untreated D3 steel. Sharma et al. [21] endorsed similar findings on AISI D2 steel.

Ramaswamy et al. [22] predicted an optimal setting of machining parameters while performing optimization using a desirability function approach. Payla et al. [23] inferred that  $P_{on}$  directly influenced the MRR and power consumption during electric discharge machining of EN-31 die steel. It was also concluded that the MRR is reduced with an increase in SV because the energy density decreased as the spark gap expanded. Chen et al. [24] found that discharge capacitance has a direct and significant influence on MRR and the machining gap in microreciprocated WEDM of SKD11 (D2 steel). Singh et al. [25] supported the phenomenon for EN-31 tool steel. Abdulkareem et al. [26] worked to enhance the SR because of more adhesion of the debris particles and surface irregularities on the processed surface. Mouralova et al. [27] concluded that the frequency of discharge occurrence of the recast layer is highly influenced by cutting speed. Negrete [28] made a similar finding on AISI 01 tool steel. Kanlayasiri and Boonmung [1] investigated the influence of  $P_{on}$ ,  $P_{off}$ , peak current and WT on SR in WEDM of DC53 steel. Nawaz et al. [29] used molybdenum to machine steel with the aim of achieving higher material removal rate and lesser surface roughness. The study quantified the influence of process in enhancing the pulse discharge energy because of the deeper craters produced on the machined surface. Similarly, Rehman et al. [30] evaluated gamma wire and resulted the significant influence of  $P_{on}$  for C.S (80.21%), KW (48.25%), and MRR (45.21%) during WEDM of DC53 steel.

The literature review reveals that a significant amount of work has already been done on various tools and die steels, especially D2, and D3 steel, to improve machining accuracy and productivity in wire electric discharge machining. However, we have noted a lack of systematic evaluation for the main parameters affecting the output responses in the WEDM of DC53 steel (having superior mechanical properties and machining performance over D2 and D3 steel), which was the key objective of this research. Moreover, the supremacy of zinc-coated brass wire (as recommended by literature) is not thoroughly studied, which may provide superior results as compared to previous established methodologies. To resolve this problem and further improve the state of the art, the following issue are discussed in this research:

- Investigating the influence of machining parameters on recast layer thickness (process limitation), surface roughness and kerf width (quality), and material removal rate (productivity).
- Optimizing input parameters such as wire feed (WF), pulse on duration ( $P_{on}$ ), open voltage (OV), and servo voltage (SV) controlling process productivity and work quality of DC53 die steel processes with zinc-coated brass wire.
- Exploring the statistical significance of machining process science on physical changes on the material surface.
- Examining microstructural surface evolution using optical microscopy and scanning electron microscopy.

The results gathered in this work are of paramount importance for the forging industry (i.e., metal forming, flow forming, spinning) in order to create tools with higher integrity and superior surface characteristics.

## 2. Materials and Methods

DC53 steel has numerous applications in die- and mold-making industries and is the workpiece material for investigation. DC53 is a high chromium steel with high strength, good toughness, wear-resistance and excellent machinability over that of D2 and D3 steel. The composition details and other characteristics of DC53 are shown in Table 1. A DC53 steel flat bar was used with density of  $7.85 \times 10^3 \text{ kg/m}^3$ . Experimental trials were performed in deionized water dielectric medium using zinc-coated brass wire of 0.25-mm diameter as an electrode on a CNC wire EDM setup (G43S CHMER, KNB Technologies Sdn Bhd, Malaysia). The wire electrode is recommended for fast-roughing and fine-trimming with low SR features providing less frequent breakage. Wire breakage is limiting phenomena that minimizes the productivity and upsurges the tooling cost. A detailed demonstration to illustrate the machining setup and 3D CAD view of the machined specimen accompanied by its dimensions are presented in Figure 1.

The effects of four machining variables, namely wire feed (WF), pulse on duration ( $P_{on}$ ), open voltage (OV), and servo voltage (SV) have been carefully analyzed on the kerf width (KW), material removal rate (MRR), surface roughness (SR), and recast layer thickness (RLT). The choice of the said input parameters was made based on a comprehensive literature survey [1,15–17,19–25]. Additionally, preliminary experimentation (six trial experiments) was also performed before the mature experimentation to express the process parameter levels. In addition, the dielectric resistivity was carefully monitored and maintained at same level throughout the entire experimentation phase. Variables, in addition to the machining variables, were considered as the fixed factors. The particulars relating to the input variables and their ranges along with constant factors are reported in Table 2.

The use of full factorial design as an experimental process involves the consumption of time and cost [32] compared to the Taguchi experimental design. The Taguchi methodology is considered useful because of its precise and robust analysis by a reduction in experimental runs [30]. Consequently, Taguchi's fractional factorial design orthogonal array (OA) has been used for performing the experimentation. In total, 18 experiments under mature experimentation were successfully completed using  $L_{18}$  OA and were followed by the measurement of the established output responses.

**Table 1.** Key features of DC53 steel.

DC53 Chemical Specifications		DC53 Characteristics [29–31]		
Element	Wt (%)	Name	Unit	Value
Carbon (C)	1.10	Modulus of elasticity	GPa	150
Chromium (Cr)	8.50	Modulus of rigidity	GPa	58.5
Molybdenum (Mo)	2.00	Rockwell hardness	HRC	64
Silicon (Si)	0.90	Poisson's ratio	-	0.28
Vanadium (V)	0.30	Thermal conductivity (at room temperature)	W/m-K	23.86
Manganese (Mn)	0.35	Coefficient of thermal expansion	$1/^\circ\text{C}$	$13 \times 10^{-6}$
Phosphorous (P)	0.03	Density	$\text{kg/m}^3$	$7.85 \times 10^3$
Sulphur (S)	0.03	-	-	-
Iron (Fe)	BAL	-	-	-

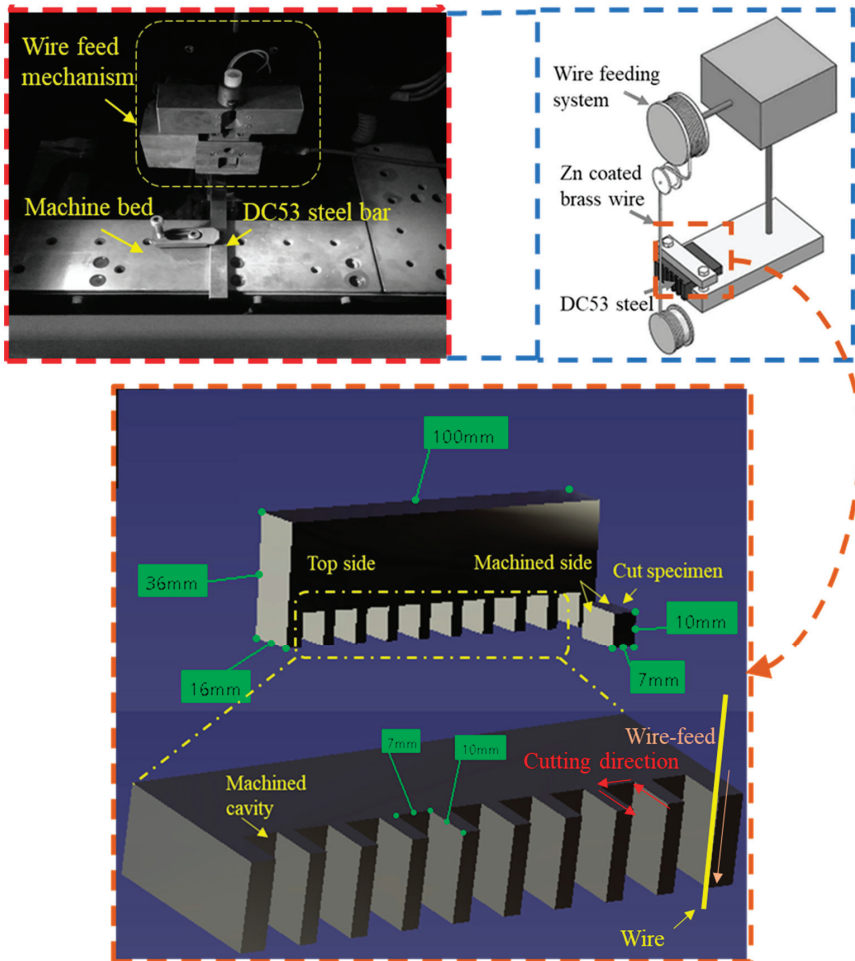


Figure 1. Illustration of experimental setup along with the workpiece.

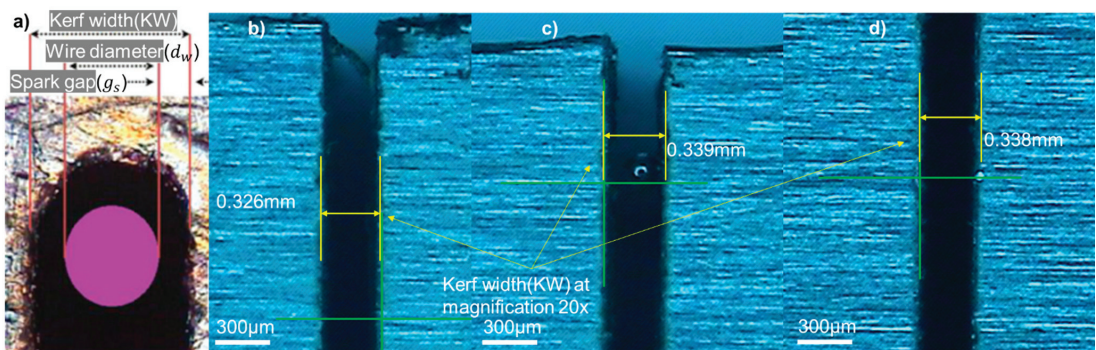
Table 2. Input machining variables levels along with response measures.

Process Variables	Symbol	Unit	Level			Output Responses	Symbol	Unit	Constant Parameters	Unit	Value
			1	2	3						
Wire feed	WF	mm/s	5	8		Kerf width	KW	$\mu\text{m}$	Pulse off-duration	$\mu\text{s}$	25
Pulse on-duration	$P_{on}$	$\mu\text{s}$	4	5	6	Surface roughness	SR	$\mu\text{m}$	Resistivity of dielectric	kg- $\Omega$ -cm	50–70
Open voltage	OV	volt	80	90	100	Material removal rate	MRR	$\text{mm}^3/\text{min}$	Wire tension	gms-f	1390
Servo voltage	SV	volt	40	50	60	Recast layer thickness	RLT	$\mu\text{m}$	Arc on time	$\mu\text{s}$	2

Kerf-width is the measurement of extra material removed from the processed surface of the workpiece during machining. KW was examined by measuring the cutting slot distance using a calibrated video probe of a coordinate-measuring-machine (CMM) (CE-450DV, Chien Wei Precise Technology Co., Ltd., Fengshan District, Taiwan), as illustrated in Figure 2. MRR calculation methodology is reported in Equation (1):

$$MRR = \left[ \frac{W_b - W_a}{t_m * \rho_w} \right] \tag{1}$$

where  $W_b$  and  $W_a$  denoted the weights of the workpiece before and after processing;  $t_m$  symbolized the machining time for each machining experiment, and  $\rho_w$  showed the workpiece density, respectively. The surface texture meter (Surtronic S128, Taylor Hobson Leicester, United Kingdom) measured the surface roughness SR of the machined surface. The SR measurements were performed at three different points on the machined work surface by calibrating at an evaluation length of 4 mm and a cut-off length of 0.8 mm. The averages of measurements were used for analytical purposes. A scanning electron microscope (Vega 3-TESCAN, TESCAN, Brno, Czechia) was employed for microstructural examination of machined surface of the workpiece and recast layer thickness was measured by using optical microscope (Olympus MM6C-PS2, Olympus Corporation, Tokyo, Japan).



**Figure 2.** Schematic and physical representation of (a) kerf width along with physical evidence of its measurement using CMM, (b) For Exp. 1 (WF 5 mm/s,  $P_{on}$  4  $\mu$ s, OV 80 volt, SV 40 volt), (c) For Exp. 10 (WF 8 mm/s,  $P_{on}$  4  $\mu$ s, OV 80 volt, SV 60 volt), and (d) Exp. 18 (WF 8 mm/s,  $P_{on}$  6  $\mu$ s, OV 100 volt, SV 50 volt).

To carry out the microscopic examination, samples were prepared by mounting, etching, grinding and polishing. SEM-based morphological analysis was used to explain the process science and physical phenomenon. The statistical analysis was completed by using Minitab 19 software (Minitab, LLC, State College, Pennsylvania, USA). Confirmatory experimentation was performed based on parametric settings for the validation of research results.

### 3. Results and Discussion

The experimentation on the DC53 steel work part was successfully performed according to Taguchi  $L_{18}$  to examine and investigate the behaviour of input process variables for output responses. The results of the examination are more profoundly observed and analysed using statistical analysis techniques, optical microscopy and the scanning electron microscopy. These analyses are conducted to enlighten the machining effects along with process physics involved on the microstructure of machined surface. The design of experiments (DOE) results revealed that minimum kerf width (KW) of 0.318 mm, least (average) surface roughness (SR) of 1.69  $\mu$ m, higher material removal rate (MRR) of 17.82 mm<sup>3</sup>/min, and a least average recast layer thickness (RLT) of 9.63  $\mu$ m were obtained. The obtained MRR results have shown maximum values as pulse on duration ( $P_{on}$ ) was increased. In addition to this, KW, SR, and RLT values were also decreased by reducing  $P_{on}$  because it influenced directly on the number of sparks produced resulting in adequate melting of the workpiece during machining. The facts explanation pertaining to the analysis are stated in the upcoming segments of discussion in variance and trend analyses.

#### 3.1. Parametric Significance Analysis

Variance analysis is considered a decisive tool to determine each process parameter's influence for a certain output response [8,30,33,34]. The insights of this analysis have been

reported in Table 3, containing the  $p$ -value and percent contribution (PCR). The  $p$ -value describes the significance in such a way that the process parameter with lower ( $<0.05$ ) value is considered highly influential for a specific output response compared to other control variables [35]. This is because variables with a  $p$ -value  $\leq 5\%$  in statistical output data, indicating a 95% confidence interval, were regarded as significant with respect to other input parameters [33]. Percentage contribution is another tool to determine the more detailed control of the machining parameters on responses. In this study, PCR was estimated to evaluate and prioritize their significance in accordance with output responses as described by formula reported in Equation (2).

$$\text{Percentage contribution (PCR)} = \left[ \frac{\text{Adj SS}}{\text{Total SS}} \times 100 \right] \% \quad (2)$$

where Adj SS = Adjusted sum of squares, and Total SS = Total sum of squares are used from analysis of variance to calculate the contribution. The detailed results of variance analysis from Table 3 inferred that WF (45.648%),  $P_{on}$  (41.56%), and SV (3.77%) are the significant factors for KW. However, the detailed influential variables for SR include  $P_{on}$  (84.83%), WF (8.32%), OV (2.10%), and SV (1.15%). Open voltage, pulse on duration, and wire feed with percentage-contribution of 49.07%, 32.81%, and 10.51%, respectively, influenced on material removal. Continually, the significant variables for recast layer thickness involved OV (52.06%) and  $P_{on}$  (40%). Thorough analysis of the statistical data reported in Table 3 resulted in the finding that the pulse on duration:  $P_{on}$  was the common and most influential input parameter for all defined output responses in this study.

**Table 3.** Summary of analysis of variance.

Sr No.	Output Responses	$p$ Value Variables				Percentage Contribution (PCR)				R-Sq (%)	R-Sq (Adj) (%)
		WF	$P_{on}$	OV	SV	WF	$P_{on}$	OV	SV		
1	Kerf width (KW)	<0.001	<0.001	0.08	0.02	45.64	41.56	1.95	3.77	92.95%	90.78%
2	Surface roughness (SR)	<0.001	<0.001	0.016	0.06	8.32	84.83	2.10	1.15	96.42%	95.31%
3	Material removal rate (MRR)	0.001	<0.001	<0.001	0.41	10.51	32.81	49.07	0.39	92.80%	90.58%
4	Recast layer thickness (RLT)	0.593	<0.001	<0.001	0.56	0.17	40.00	52.06	0.20	92.45%	90.13%

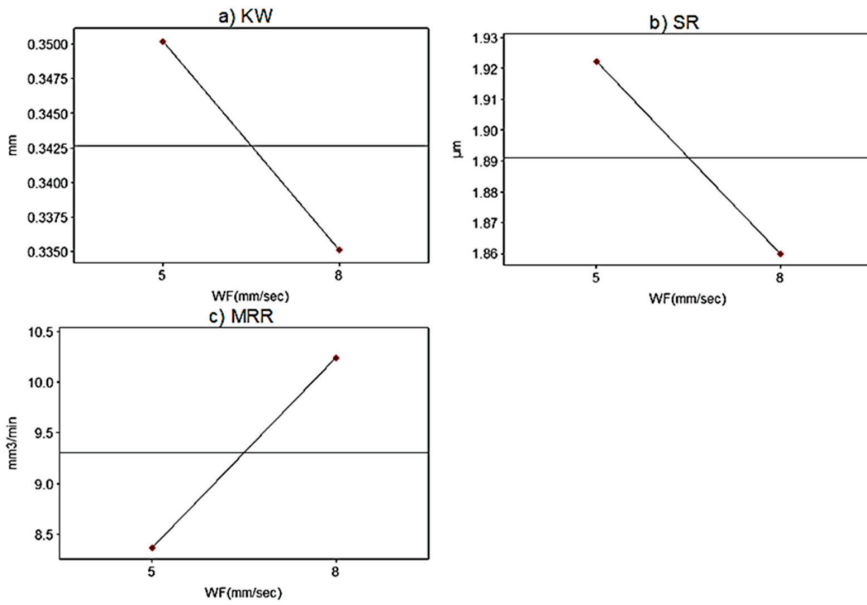
### 3.2. Process-Parametric Effect Analysis

The parametric-effect analysis was done to study the behaviour of process variables through graphical trends of output responses and the results based on statistical analysis. The analysis is shown in Figures 3–7.

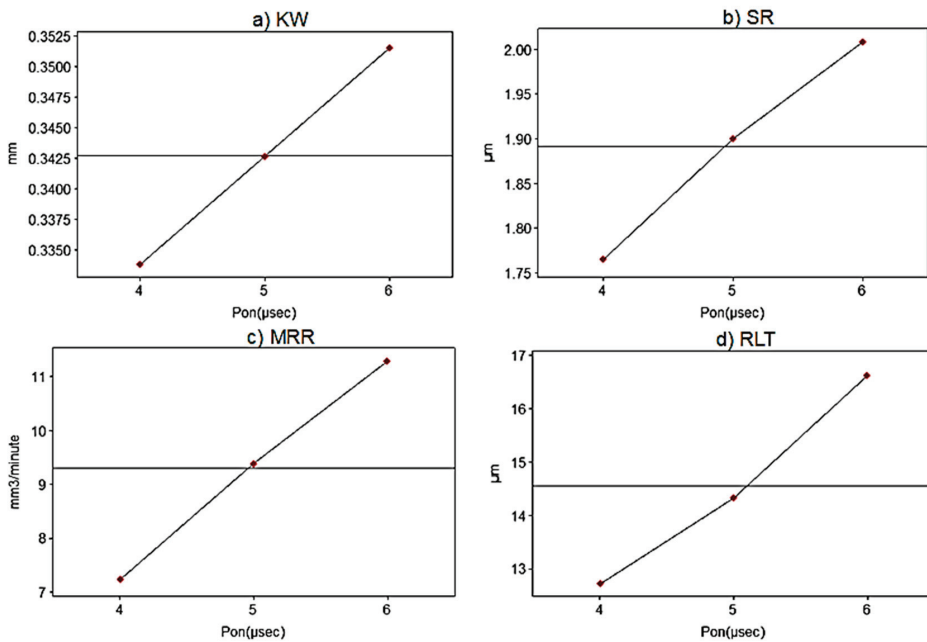
#### 3.2.1. Effects of the Wire Feed

The main effects result for WF, presented in Figure 3, has inferred that kerf width and surface roughness were decreased by increasing WF. The key reason behind this reduction is the rapid transport of wire, which resulted in less workpiece–wire electrode interaction, and produced a small heat-affected zone (HAZ). Moreover, it resulted in minor thermal damages, therefore, less molten material/debris was redeposited on the workpiece surface (will be revealed in Section 3.4). The machining efficiency of the wire electrode in WEDM was increased by increasing the WF. The effect was experienced irrespective of considering wire consumption because of a larger amount of the material removed in a shorter machining cycle was due to a rapid traverse of wire. Therefore, the material removal rate (MRR) increased with an increasing level of WF. Similar results on the wire feed were reported by Mussada et al. [36] and Negrete and Carmita [28]. It was confirmed that the increase in the WF assisted in the stable spark discharges produced and thus resulted in more melting and a redeposit of work material.





**Figure 3.** Parametric effects of wire feed (WF) for (a) kerf width (KW), (b) surface roughness (SR), and (c) material removal rate (MRR).



**Figure 4.** Parametric effects of pulse on duration ( $P_{on}$ ) for (a) kerf width (KW), (b) surface roughness (SR), (c) material removal rate (MRR), and (d) recast layer thickness (RLT).

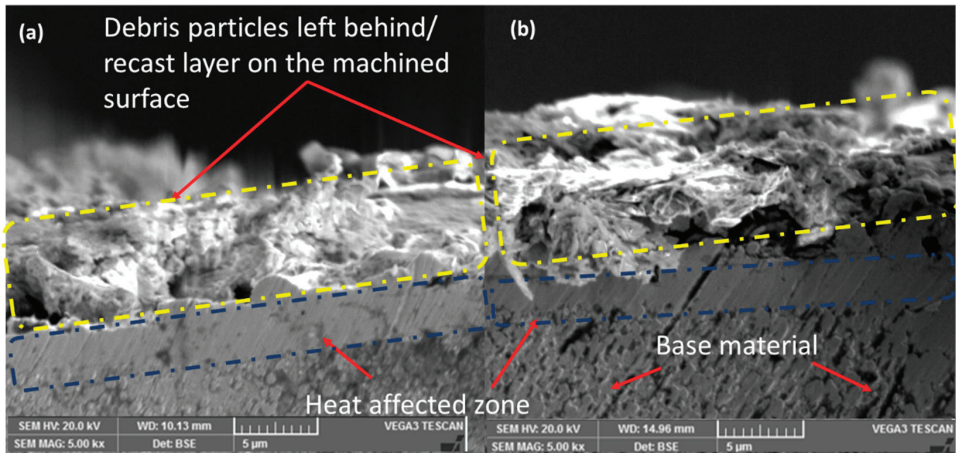


Figure 5. Representation of the recast layer formed on the machined work surface at random experimental settings (a)  $P_{on}$  4  $\mu$ sec (b)  $P_{on}$  5  $\mu$ sec.

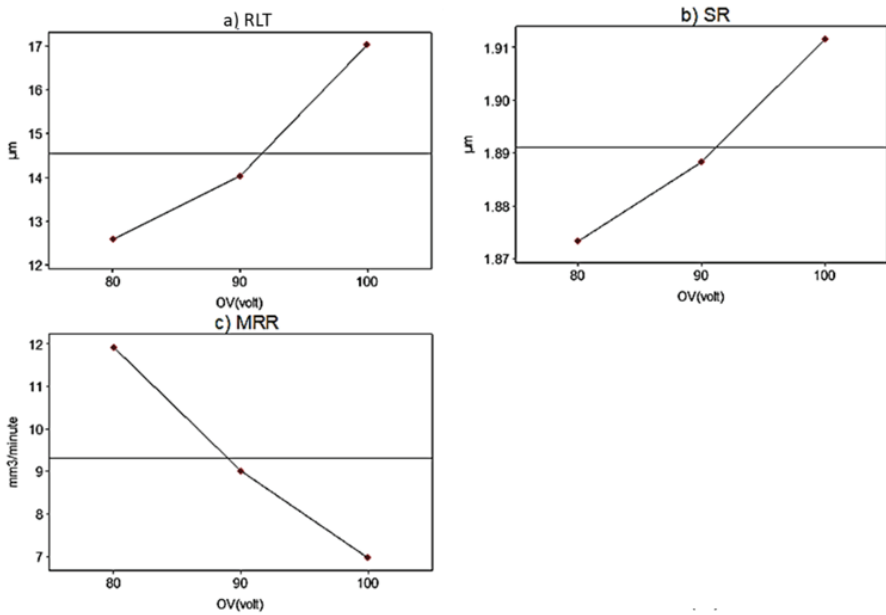


Figure 6. Parametric effects of open voltage (OV) for (a) recast layer thickness (RLT), (b) surface roughness (SR), (c) material removal rate (MRR).

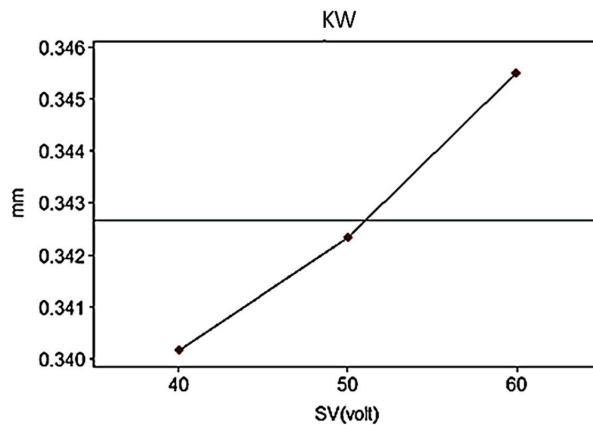


Figure 7. Parametric effects of servo voltage (SV) for kerf width (KW).

Kerf-width is defined as the measurement of excessive material removed during machining and its measurement demonstration is indicated in Figure 2. The analysis of means is shown as main effect plots in Figure 3a. It indicated an inverse relationship of WF with KW. The decreasing trend is observed for KW from 0.350 to 0.335 mm by increasing WF level from 5 to 8 mm/s. The rationale behind this effect lies in the minimal spark gap produced because of enhanced WF. The continual incoming fresh wire assisted in the minimizing the workpiece–wire electrode interaction time, and thus reduced the removal of excessive material from the work surface during machining.

However, the excessive increase in the WF produces irregularities on the machined surface, as reported by Somashekhar et al. [37]. The intensity of the current is enhanced because of consistent incoming fresh wire. This is because of the availability of increasingly present fresh ions and interacting surface. Furthermore, the wire breakage frequency may also be reduced because of adequate increase in WF. The decrease in KW happened at low  $P_{on}$  values. Hence, the kerf width is decreased by increasing the wire feed. Based on variance analysis from Table 3, the wire feed was also found to be top significant factor for kerf width (45.64%) compared to other process variables.

Surface roughness is the measurement of surface asperities on the machined surface [38]. The graphical trends of WF for SR from Figure 3b have resulted that the surface roughness was declined from 1.92 to 1.86  $\mu\text{m}$  because of increased levels of wire feed. This is because of less contact duration between the wire electrode and the workpiece. Therefore, a greater amount of debris is flushed away by the dielectric and less discrepancies occurred on the machined surface thus resulted in small SR. Similar findings were identified by Tilekar et al. [39] and it was also inferred that the incoming fresh wire in the machining zone assisted in reducing the heat energy (function of heat transfer and plasma generation) because of instability of discharges resulting from higher wire feed which produced less irregularities on the machined surface. In addition, increased wire feed decreases the spark stability time due to the speedy motion of the wire and increases the tooling cost (similar science is discussed by Farooq et al. [40]). ANOVA observations also indicated that WF was identified as the influential factor for SR (8.20%).

The material removal rate is the measurement of amount of material-removed in a particular machining time [38]. Higher MRR is usually desired to enhance the overall machining productivity of the machine and the process. The results data have indicated that the MRR increased from 8.5 to  $\sim 10.3 \text{ mm}^3/\text{min}$  by increasing the WF values (Figure 3c). The reason is the improved stability of thermal energy produced in the cutting zone with the help of constantly moving electrode wire. This has caused an increase in the sparks density in a shorter duration of machining cycle, which leads to enhance material melting and vaporization and thus resulted in more MRR. The comparison of the MRR trends was

made with the existing literature and similar findings were obtained [37]. Wire feed was found to be significant variable for MRR (10.51%) as viewed from the variance analysis in Table 3.

### 3.2.2. Effects of Pulse-On Duration

The analysis of the parametric effects of pulse-on duration on the selected output responses is indicated in Figure 4. It is generally said that  $P_{on}$  plays its key role in improving the machining performance/machinability of WEDM. The statistical data results have elaborated that all the response measures namely KW, SR, MRR and RLT were linearly boosted up by increasing  $P_{on}$ . The reason is that by increasing this variable leads to increase in the discharge energy among two electrodes and creates a plasma energy channel among the workpiece and wire electrode gap. This plasma channel consists of pool of electrons and ions melted material because of the generation of an adequate heat-affected zone on the machined surface. Therefore, it usually plays an important role in influencing on the machining quality. Similar insights were reported by Rehman et al. [30] and coherent results were obtained in their experimental investigation.

The graphical trend of  $P_{on}$  for KW is similar as of WF for MRR. The parametric plots from Figure 4a have shown the direct effect of pulse-on duration ( $P_{on}$ ) on KW, which means that kerf width is alleviated by varying the duration of pulses. This was because the number of sparks was amplified by increasing the time interval, resulting in the enhancement of the sparks energy and thus, a larger heat-affected zone was produced. The kerf width was increased by increasing the pulse duration. However, the analysis of trends also inferred that a small increase in KW was obtained when the pulse on duration was increased to one upper level from 4 to 5  $\mu$ s, whereas a sudden increase in the KW was observed as  $P_{on}$  was promoted from 5 to 6  $\mu$ s. However, 5  $\mu$ s is a threshold level of the pulse on duration, after which relatively more thermal energy is produced to melt the extra material from the sides of the workpiece because of consistently increasing sparks erosion. The variance analysis findings have also proved the most influential of  $P_{on}$  (41.56%) for KW.

The trend analysis of  $P_{on}$  is shown in Figure 4b,c for surface roughness (SR) and material removal rate (MRR), respectively. The melt material is highly depended on increased number of discharges and the discharge energy generates a large pool of electrons and ions. Thus, with the increase in the amount of material removed and surface asperities on the machined surface of the workpiece also increase. Pulse duration was found as the most remarkable parameter for SR (84.83%) and also influential variable for MRR (32.81%).

The white layer is produced during machining when the leftover melt material re-solidifies on the machined surface of the workpiece [41]. Therefore, the recast layer thickness plays a vital role in evaluating the surface integrity of the machined specimen. The number of leftover debris and unflushed material on the surface has increased linearly with the increase of spark on duration. The reason is thermally affected region due to enhanced thermal energy and stability of sparks because of more spark's duration. Therefore, the number of unflushed particles were increased as the  $P_{on}$  is increased from 4 to 6  $\mu$ s, resulting in a greater recast layer thickness, as shown in Figure 4d. A microscopic overview of the recast layer formation is shown in Figure 5. The craters produced are shallow and wider whereas the density of microcracks formation is also increased by increasing the  $P_{on}$ .

### 3.2.3. Effects of Open Voltage

The role of the open voltage is to perform a thermal breakdown to generate plasma channel [33]. SR was enhanced greatly by increasing OV as can be seen in Figure 6. SR possessed a direct relationship with OV similar to RLT. The thorough analysis of observations indicated that the increase in OV resulted in increasing SR, and RLT. The key reason involves discharge energy phenomenon because of thermal breakdown during machining.

The plasma channel width is increased because of the enhanced open voltage levels resulting in a larger thermal affected zone. The surface irregularities were increased at higher values of OV as shown in Figure 6a. The surface asperities are enhanced because of

increased discharge energy. This enlarged the width of the plasma channel, creating deeper craters. The volume of the material removed was decreased by increasing the OV from 80 to 100 V because of the instability of discharge energy (Figure 6b). The phenomenon involves inadequate melt generation due to a small amount of thermal energy and poor flushing conditions, resulting in the insufficient removal of melt. OV was found to have significant influence (49.07%) in controlling MRR.

The thickness of the recast layer increased linearly by enhancing the OV, as presented in Figure 6c. In this case, from OV from 80 to 100 V, a linearly increasing trend of RLT is observed similar to SR was obtained due to plasma energy channel. It was produced because the material was melted and redeposited in the surface. Therefore, discharge energy was enhanced by increasing OV leaving more material behind on the work surface. The open voltage was found as foremost significant variable (52.06%) compared to other variables affecting the recast layer thickness.

### 3.2.4. Effects of Servo Voltage

Servo voltage is usually responsible for the transfer of heat flux on the dedicated workpiece surface through controlling the workpiece and wire electrode gap. All the output responses possessed quadratic behaviour by increasing the SV. A detailed discussion of SV provided herein, and trends are shown in Figure 7.

Kerf width was increased gradually by increasing the SV from 40 to 50 V. The rationale of the gradual increase in KW at the first two levels of SV is the relatively small amount of erosion of the material from both edges of the workpiece. However, a relatively greater increase in KW with increased servo voltage levels from 50 to 60 V is due to increased spark gap between the wire and workpiece electrodes, which resulted in a wider kerf. The phenomenon behind the increasing trend of KW was endorsed by Rehman et al. [30].

### 3.3. Mathematical Modelling and Parametric Optimization

To determine the predictability of responses (productivity and quality), the general regression model is developed through converting variable parameters to continuous predictive variables [42]. The general algebraic expression of model is given as following.

$$y = b_0 + b_1x_1 + b_2x_2 + \dots + b_kx_k \tag{3}$$

In the general model,  $y$  represents the value of the response while  $b_0$  is the constant value and  $b_1, b_2, b_3, \dots, b_k$  represents the estimated variation in mean response for each unit change in the variable parameters. Experimental data was used to generate regression models using variable parameters as continuous predictors. The relationship of WEDM variable parameters on productivity quality measures using multiple regression analysis.

$$RLT = -14.03 - 0.070 WF + 1.947 Pon + 0.2222 OV - 0.0139 SV \tag{4}$$

$$W = 0.3007 - 0.005037 WF + 0.00883 Pon + 0.000192 OV + 0.000267 SV \tag{5}$$

$$SR = 1.3159 - 0.02074 WF + 0.12167 Pon + 0.001917 OV - 0.001417 SV \tag{6}$$

$$MRR = 18.53 + 0.624 WF + 2.027 Pon - 0.2478 OV - 0.0223 SV \tag{7}$$

Where “WF”, “P<sub>on</sub>”, “OV” and “SV” are representing wire feed (mm/s), pulse on time (µs), open voltage (V), and servo voltage (V), respectively.

Utilizing the experimental data, Minitab 19 was used to develop multiple regression models associated with recast layer thickness, kerf width, surface roughness and material removal rate presented in Equations (4)–(7), respectively. The output values of the response measures were predicted after obtaining the optimal parameters for each response, and the optimization results were validated by performing confirmatory experiments. The results of the experimentation (three experiments) as a result of this optimization produced a very minute standard deviation from the design of experiments results.

Moreover, the desirability function was employed to optimize process settings, such as the minimum, which was better for recast layer thickness, kerf width, surface roughness, and the maximum, which was better for the material removal rate. The results of the experimentation provided a major process improvement. The optimized parameters obtained are “WF 8 mm/s”, “P<sub>on</sub> 4 μs”, “OV 80 V” and “SV 56V”. In Table 4, the close agreement is shown between the predicted values and experimental trials on the optimized process settings ensures the adequacy of empirical models.

**Table 4.** Measured responses on optimized process parameters.

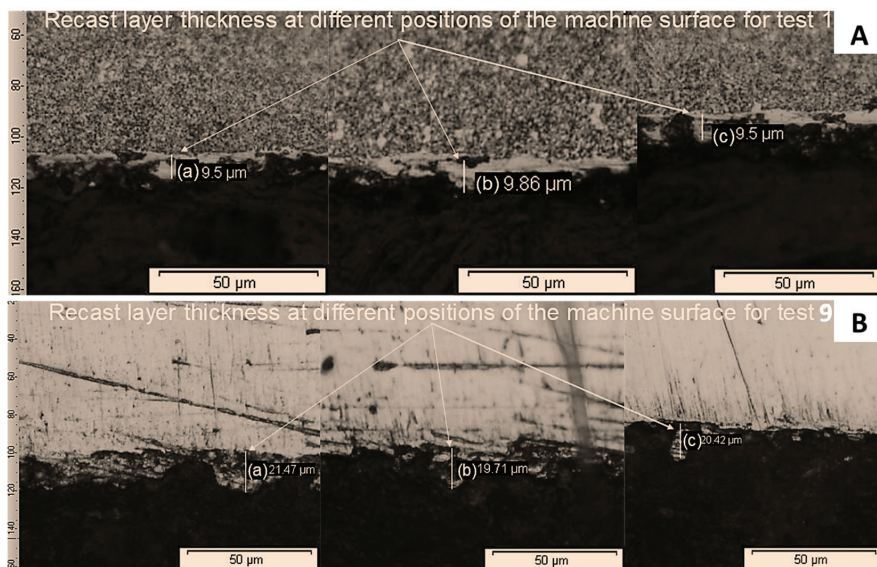
Sr. No.	Process Parameters				Response Indicators			
	WF (mm/s)	P <sub>on</sub> (μs)	OV (V)	SV (V)	SR (μm)	MRR (mm <sup>3</sup> /min)	KW (mm)	RLT (μm)
1	8	4	80	56	1.709	10.307	0.327	10.093
2	8	4	80	56	1.703	10.299	0.326	10.256
3	8	4	80	56	1.719	10.496	0.330	10.980
		Avg. experimental value			1.710	10.367	0.327	10.443
		Standard deviation			0.006	0.091	0.001	0.385
		Predicted value			1.711	10.554	0.326	10.191
		Error %			0.64	1.77	0.31	2.47

### 3.4. Recast Layer Measurement and Microstructural Evaluation

The microscopic analysis is usually performed to analyse the physical phenomena on the surface morphology of the workpiece. The optical and scanning electron microscopy-based analyses are explored herein.

#### 3.4.1. Optical-Based Microscopic Analysis

The detailed recast layer thickness analysis was carried out through optical microscope, (Figure 8A,B) to investigate the physics involved on the morphological alterations on the workpiece surface. The recast layer was measured at three distinct positions on the processed surface and average of the measurements was chosen for the analysis purpose.

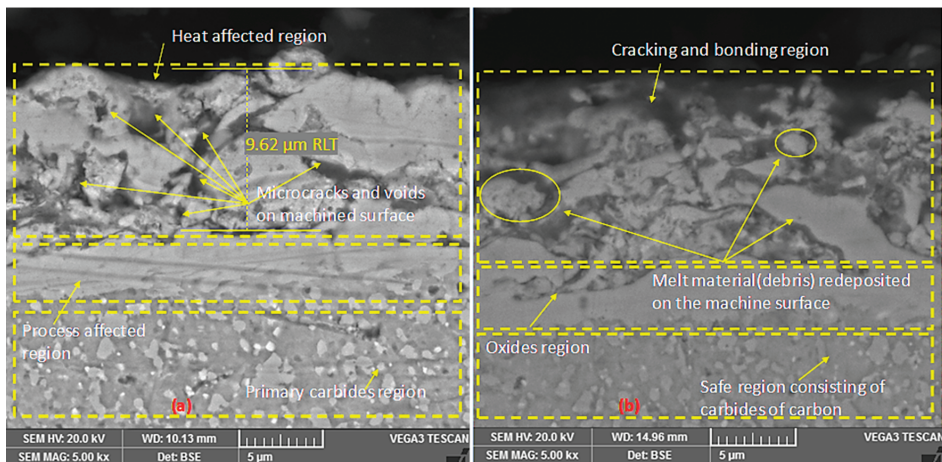


**Figure 8.** Optical microscopic examination (at three different points for one experiment) for recast layer measurement at different parametric settings for (A) WF 5 mm/s, Pon 4 μs, OV 80 V, and SV 40 V (B) WF 5 mm/s, Pon 6 μs, OV 100 V, and SV 40 V.

It can be extracted from Figure 8A,B that the significant thickness is deposited on the base metal layer. Its microstructure is different from the unaffected surface consisting of primary carbides. It was inferred that the maximum recast layer thickness of 19.52  $\mu\text{m}$  was obtained at the minimum WF (5 mm/s), high level of  $P_{\text{on}}$  (6  $\mu\text{s}$ ), higher value of OV (100 V), and the minimum SV (40 V). Similarly, the higher control is responsible for the thermal breakdown to improve the sparks' stability and smaller control level means that the sparks energy is focused on the specific region where material melting and redeposition occurred. Therefore, the recast layer thickness was increased at these parametric settings. Similarly, a minimum RLT was observed at WF 5 mm/s,  $P_{\text{on}}$  (4  $\mu\text{s}$ ), OV (80 V), and SV (40 V). The reason is that the debris redeposition is decreased as the sparks on duration is decreased because  $P_{\text{on}}$  is highly influential parameter for the recast layer thickness compared to other variables.

### 3.4.2. Scanning Electron Microscopic Analysis

The detailed investigation for the microstructure of the processed surface is demonstrated in Figure 9a,b. The evidence shows that microcracks appeared on the machined surface. Moreover, the properties of melt material redeposit on machined surface varied because of bonding and cracks generated in heat effected region. The recast layer properties are primarily different from the base metal because of heat treatment and quenching, as shown in Figure 9. The thermal energy generated between wire electrodes results in enlarged heat effected zone produced on the machined surface, providing opportunity to redeposit onto the machined layer.



**Figure 9.** Scanning electron microscopy results of machined specimens (a) WF1, Pon1, OV2, SV2, (b) WF1, Pon3, OV1, and SV2.

It can be seen from Figure 9 that the craters of different sizes and shapes, microcracks and thermally redeposit melt material/debris were evident on machined surface. The density of crack formation and the size of the craters increased by increasing the sparks-on duration (the discharge energy is linearly dependent on it). Likewise, the process is influenced by process variables on the microstructural evaluation, as evident from Table 3. Similarly, pulse on duration influenced its maximum on controlling the craters size, density of cracks formation, and size of debris globules formed on the processed surface. The measured RLT on the machined surface was found 9.62  $\mu\text{m}$ . The analysis of SEM images from Figure 9 inferred that an oxide layer formed just below the heat-affected layer. This process-affected region was generated because of large plasma channel width, resulting

in more irregularities on the machined surface. The layer below the process affected zone was considered as the safe region, consisting of primary carbides of carbon.

### 3.5. Comparison with Previous Studies

The tabular comparison of current output results was also compared with the published literature for DC53 steel in WEDM and summary is reported in Table 5. The research findings were found almost in good agreement with the existing results which also validated the experimental work. In addition, machinability of DC53 steel with zinc-coated wire produced superior results in comparison to established practices [29,30].

**Table 5.** Comparison of the obtained results with the existing literature.

Output Response	Unit	Current Work	Previous Work on Steel	References
SR	$\mu\text{m}$	1.71	1.72, 1.89, 1.68	[1,29,30]
MRR	$\text{mm}^3/\text{min}$	10.367	5.443, 10.205	[29,30]
KW	mm	0.327 (at 0.25 mm wire $\Phi$ )	0.220, 0.287 (at 0.20 mm wire $\Phi$ )	[29,30]
RLT	$\mu\text{m}$	10.443	-	-

## 4. Conclusions

This work was dedicated to providing experimental insight into the machining of DC53 die steel, and considering the most important process variables, namely wire feed-WF, pulse on duration- $P_{on}$ , open voltage-OV, and servo voltage-SV. The influence of these variables on kerf width-KW, surface roughness-SR, material removal rate-MRR, and recast layer thickness-RLT during wire electric discharge machining was studied. Through rigorous analysis based on physical phenomenon on surface morphology and material characteristics, the following conclusions are extracted:

- RLT was directly influenced by varying the  $P_{on}$  and it was observed that SEM examination revealed three surface regions; (i) thermally affected region consisting of debris particles of different sizes and shapes, cracks and craters, (ii) process-affected zone consisting of oxides, and (iii) safe region consisting of the primary carbides of carbon. Minimum average RLT of  $9.63 \mu\text{m}$  was measured and observed after the examination of machined surface morphology.
- The variance analysis results inferred that  $P_{on}$  was found to be the most significant machining variable for all output responses with higher contribution percentages such as SR (84.83%), KW (41.56%), RLT (40.00%), and MRR (32.81%), respectively. High  $P_{on}$  results in a high plasma channel consisting of the pool of electrons and ions melted material because of the generation of an adequate heat-affected zone on the machined surface.
- WF (45.64%),  $P_{on}$  (41.56%), and the SV (3.774%) are the significant factors for KW. However, the detailed influential variables for SR include  $P_{on}$  (84.83%), WF (8.320%), OV (2.10%), and SV (1.15%). The significant variables for recast layer thickness involved OV (52.06%) and  $P_{on}$  (40.00%). Open voltage, pulse on duration, and wire feed with percentage contributions of 49.07%, 32.81%, and 10.51%, respectively, are significant for MRR. The rapid transport of wire resulted in less workpiece-wire electrode interaction, and produced a smaller heat-affected zone because of minor thermal damages. Therefore, less molten material was redeposited on the workpiece surface.
- The experimental results reveal that WF influences prominently in reducing KW, SR, and RLT and increasing MRR. All response measures were directly increased by increasing  $P_{on}$  due to the amplified discharge energy of the sparks produced.
- The optimized parameters obtained are “WF 8 mm/s”, “ $P_{on}$  4  $\mu\text{s}$ ”, “OV 80 V” and “SV 56 V” resulting  $1.710 \mu\text{m}$  SR,  $10.367 \text{ mm}^3/\text{min}$  MRR, 0.327 mm KW, and  $10.443 \mu\text{m}$  RLT. The regression models (showing less than a 3% error from the physical experimentation) are developed based on a thorough investigation to support the machinists for achieving the required features.



Future work that could further improve the quality of dies tools should be focused on experimental investigation using other control variables like flushing pressure, wire tension, and corner accuracy (both top and bottom) in WEDM of DC53 steel using different wire electrodes.

**Author Contributions:** Conceptualization, S.A.K. and W.A.; Data curation, W.A.; Formal analysis, R.N. and M.R.; Funding acquisition, M.U.F., M.A.A. and C.I.P.; Investigation, W.A., M.R. and R.N.; Methodology, S.A.K. and M.R.; Resources, R.N.; Software, W.A. and M.R.; Supervision, S.A.K.; Validation, S.A.K., R.N. and C.I.P.; Visualization, M.U.F., M.A.A. and C.I.P.; Writing—original draft, M.U.F., M.R. and M.A.A.; Writing—review & editing, M.U.F., M.A.A., C.I.P. All authors have read and agreed to the published version of the manuscript.

**Funding:** This study did not receive any funding.

**Institutional Review Board Statement:** Not applicable.

**Informed Consent Statement:** Not applicable.

**Data Availability Statement:** The data is available as request from corresponding authors.

**Conflicts of Interest:** The authors declare no conflict of interest.

## Abbreviations

ANOVA	Analysis of variance
CMM	Coordinate measuring machine
DOE	Design of experiments
HAZ	Heat affected zone
KW	Kerf width ( $\mu\text{m}$ )
MRR	Material removal rate ( $\text{mm}^3/\text{min}$ )
OV	Open voltage (volt)
OA	Orthogonal array
$\rho$	Density ( $\text{kg/m}^3$ )
PCR	Percent contribution (%)
Pon	Pulse on duration ( $\mu\text{s}$ )
Poff	Pulse off time ( $\mu\text{s}$ )
RLT	Recast layer thickness ( $\mu\text{m}$ )
SR	Surface roughness ( $\mu\text{m}$ )
SV	Servo voltage (volt)
SEM	Scanning electron microscopy
WEDM	Wire electric discharge machining
WF	Wire feed ( $\text{mm/s}$ )
WT	Wire tension (gms-f)
$W_b$	Weight of the workpiece prior machining (g)
$W_a$	Weight of the workpiece prior after machining (g)

## References

1. Kanlayasiri, K.; Boonmung, S. Effects of wire-EDM machining variables on surface roughness of newly developed DC 53 die steel: Design of experiments and regression model. *J. Mater. Process. Technol.* **2007**, *192–193*, 459–464. [\[CrossRef\]](#)
2. Singh, V.; Bhandari, R.; Yadav, V.K. An experimental investigation on machining parameters of AISI D2 steel using WEDM. *Int. J. Adv. Manuf. Technol.* **2017**, *93*, 203–214. [\[CrossRef\]](#)
3. Durairaj, M.; Sudharsun, D.; Swamynathan, N. Analysis of process parameters in wire EDM with stainless steel using single objective Taguchi method and multi objective grey relational grade. *Procedia Eng.* **2013**, *64*, 868–877. [\[CrossRef\]](#)
4. Zhang, G.; Zhang, Z.; Guo, J.; Ming, W.; Li, M.; Huang, Y. Modeling and optimization of medium-speed WEDM process parameters for machining SKD11. *Mater. Manuf. Process.* **2013**, *28*, 1124–1132. [\[CrossRef\]](#)
5. Lodhi, B.K.; Agarwal, S. Optimization of machining parameters in WEDM of AISI D3 steel using taguchi technique. *Procedia CIRP* **2014**, *14*, 194–199. [\[CrossRef\]](#)
6. Thiagarajan, C.; Sararvanan, M.; Senthil, J. Performance Evaluation of Wire Electro Discharge Machining on D3-Tool Steel. *Int. J. Pure Appl. Math.* **2018**, *118*, 943–949.

7. Manjaiah, M.; Laubscher, R.F.; Kumar, A.; Basavarajappa, S. Parametric optimization of MRR and surface roughness in wire electro discharge machining (WEDM) of D2 steel using Taguchi-based utility approach. *Int. J. Mech. Mater. Eng.* **2016**, *11*, 7. [[CrossRef](#)]
8. Ikram, A.; Mufti, N.A.; Saleem, M.Q.; Khan, A.R. Parametric optimization for surface roughness, kerf and MRR in wire electrical discharge machining (WEDM) using Taguchi design of experiment. *J. Mech. Sci. Technol.* **2013**, *27*, 2133–2141. [[CrossRef](#)]
9. Vaghela, J.R.; Valaki, J.B.; Pandit, J.H. Parametric Optimization of Machining Parameters of AISI D3 Tool Steel Using Wire Cut Electric Discharge Machining—A Taguchi Based Approach. *Natl. Conf. Emerg. Res. Trends Eng.* **2016**. Available online: <https://www.researchgate.net/publication/300262070> (accessed on 22 March 2021).
10. Zhang, G.; Zhang, Z.; Guo, J.; Ming, W.; Li, M.; Huang, Y.; Shao, X. The multi-objective optimization of medium-speed WEDM process parameters for machining SKD11 steel by the hybrid method of RSM and NSGA-II. *Int. J. Adv. Manuf.* **2014**, *70*, 2097–2109. [[CrossRef](#)]
11. Rupajati, P.; Soepangkat, B.O.P.; Pramujati, B.; Agustin, H.C.K. Optimization of Recast Layer Thickness and Surface Roughness in the Wire EDM Process of AISI H13 Tool Steel Using Taguchi and Fuzzy Logic. *Appl. Mech. Mater.* **2014**, *493*, 529–534. [[CrossRef](#)]
12. Hasriadi, B.O.P.; Soepangkat, H.S. The Effects of Pulse on Time and Arc on Time on Surface Quality in Wire-EDM of ASSAB XW-42 and ASSAB 8407 2M Tool Steels. *Appl. Mech. Mater.* **2016**, *836*, 173–178. [[CrossRef](#)]
13. Hernández-Castillo, I.; Sánchez-López, O.; Lancho-Romero, G.A.; Castañeda-Roldán, C.H. An experimental study of surface roughness in electrical discharge machining of AISI 304 stainless steel. *Eng. Res.* **2018**, *38*, 90–96. [[CrossRef](#)]
14. Saini, T.; Goyal, K.; Bhandari, D. Multi-response optimization of WEDM parameters on machining 16MnCr5 alloy steel using Taguchi technique. *Multiscale Multidiscip. Model. Exp. Des.* **2018**. [[CrossRef](#)]
15. Oswald, K.; Lochmahr, I.; Schulze, H.P.; Kröning, O. Automated Analysis of Pulse Types in High Speed Wire EDM. *Procedia CIRP* **2018**, *68*, 796–801. [[CrossRef](#)]
16. Solomon, R.S.; Sevvell, P.; Jaiganesh, V.; Satheesh, C. An Investigational Review on Influence of Performance Parameters during Wire Electrical Discharge Machining of Various Grades of Steels. *J. Adv. Res. Dyn. Cont. Sys.* **2017**, *9*, 101–109.
17. Shivade, A.S.; Shinde, V.D. Multi-objective optimization in WEDM of D3 tool steel using integrated approach of Taguchi method & Grey relational analysis. *J. Ind. Eng. Int.* **2014**, *10*, 149–162. [[CrossRef](#)]
18. Azam, M.; Jahanzaib, M.; Abbasi, J.A.; Wasim, A. Modeling of cutting speed (CS) for HSLA steel in wire electrical discharge machining (WEDM) using moly wire. *J. Chin. Inst. Engr.* **2016**, *39*, 802–808. [[CrossRef](#)]
19. Dhobe, M.M.; Chopde, I.K.; Gogte, C.L. Investigations on Surface Characteristics of Heat Treated Tool Steel after Wire Electro-Discharge Machining Investigations on Surface Characteristics of Heat Treated Tool Steel after Wire Electro-Discharge Machining. *Mater. Manuf. Process.* **2013**, *28*, 1143–1146. [[CrossRef](#)]
20. Khanna, R.; Singh, H. Comparison of optimized settings for cryogenic-treated and normal D-3 steel on WEDM using grey relational theory. *Proc. Inst. Mech. Eng. Part L J. Mater. Des. Appl.* **2016**, *230*, 219–232. [[CrossRef](#)]
21. Sharma, S.; Kumar Vates, U.; Bansal, A. Parametric optimization in wire EDM of D2 tool steel using Taguchi method. *Mater. Today Proc* **2020**. [[CrossRef](#)]
22. Ramaswamy, A.; Perumal, A.V.; Jagadeesan, J.; Nagarajan, H.V. Optimization of WEDM process parameters for D3 die steel using RSM. *Mater. Today Proc.* **2020**, *37*, 2063–2069. [[CrossRef](#)]
23. Payla, A.; Chopra, K.; Mussada, E.K. Investigations on power consumption in WEDM of EN31 steel for sustainable production. *Mater. Manuf. Process.* **2019**, *34*, 1855–1865. [[CrossRef](#)]
24. Chen, X.; Wang, Z.; Wang, Y.; Chi, G. Investigation on MRR and Machining Gap of Micro Reciprocated Wire-EDM for SKD11. *Int. J. Precis. Eng. Manuf.* **2020**, *21*, 11–22. [[CrossRef](#)]
25. Singh, S.; Maheshwari, S.; Pandey, P.C. Some investigations into the electric discharge machining of hardened tool steel using different electrode materials. *J. Mater. Process. Technol.* **2004**, *149*, 272–277. [[CrossRef](#)]
26. Abdulkareem, S.; Khan, A.A.; Zain, Z.M. Experimental investigation of machining parameters on surface roughness in dry and wet wire-electrical discharge machining. *Adv. Mater. Res.* **2011**, *264–265*, 831–836. [[CrossRef](#)]
27. Mouralova, K.; Benes, L.; Bednar, J.; Zahradnicek, R.; Prokes, T.; Matousek, R.; Hrabec, P.; Fiserova, Z.; Otoupalik, J. Using a DoE for a comprehensive analysis of the surface quality and cutting speed in WED-machined hadfield steel. *J. Mech. Sci. Technol.* **2019**, *33*, 2371–2386. [[CrossRef](#)]
28. Camposeco-Negrete, C. Prediction and optimization of machining time and surface roughness of AISI O1 tool steel in wire-cut EDM using robust design and desirability approach. *Int. J. Adv. Manuf. Technol.* **2019**, *103*, 2411–2422. [[CrossRef](#)]
29. Nawaz, Y.; Maqsood, S.; Naeem, K.; Nawaz, R.; Omair, M.; Habib, T. Parametric optimization of material removal rate, surface roughness, and kerf width in high-speed wire electric discharge machining (HS-WEDM) of DC53 die steel. *Int. J. Adv. Manuf. Technol.* **2020**, *107*, 3231–3245. [[CrossRef](#)]
30. Rehman, M.; Khan, S.A.; Naveed, R. Parametric optimization in wire electric discharge machining of DC53 steel using gamma phase coated wire. *J. Mech. Sci Technol.* **2020**, *34*, 2767–2773. [[CrossRef](#)]
31. Çardaklı, İ.S. *Thin Section High Cooling Rate Solidification, Thermomechanical Processing and Characterization of AISI DC53 Cold Work Tool Steel*; Middle East Technical University: Ankara, Turkey, 2019; Available online: <https://open.metu.edu.tr/bitstream/handle/11511/45197/index.pdf> (accessed on 31 March 2021).
32. Ishfaq, K.; Anwar, S.; Ali, M.A.; Raza, M.H.; Farooq, M.U.; Ahmad, S.; Salah, B. Optimization of WEDM for precise machining of novel developed Al6061-7.5% SiC squeeze casted composite. *Int. J. Adv. Manuf. Technol.* **2020**. [[CrossRef](#)]

33. Mughal, M.P.; Farooq, M.U.; Mumtaz, J.; Mia, M.; Shareef, M.; Javed, M.; Pruncu, C.I. Surface modification for osseointegration of Ti6Al4V ELI using powder mixed sinking EDM. *J. Mech. Behav. Biomed. Mater.* **2020**, 104145. [[CrossRef](#)] [[PubMed](#)]
34. Umar Farooq, M.; Pervez Mughal, M.; Ahmed, N.; Ahmad Mufti, N.; Al-Ahmari, A.M.; He, Y. On the Investigation of Surface Integrity of Ti6Al4V ELI Using Si-Mixed Electric Discharge Machining. *Materials* **2020**, *13*, 1549. [[CrossRef](#)] [[PubMed](#)]
35. Tosun, N.; Cogun, C.; Tosun, G. A study on kerf and material removal rate in wire electrical discharge machining based on Taguchi method. *J. Mater. Process. Technol.* **2004**, *152*, 316–322. [[CrossRef](#)]
36. Mussada, E.K.; Hua, C.C. Rao AKP Surface hardenability studies of the die steel machined by WEDM. *Mater. Manuf. Process.* **2018**, *33*, 1745–1750. [[CrossRef](#)]
37. Somashekhar, K.P.; Ramachandran, N.; Mathew, J. Material removal characteristics of microslot (kerf) geometry in  $\mu$ -WEDM on aluminum. *Int. J. Adv. Manuf. Technol.* **2010**, *51*, 611–626. [[CrossRef](#)]
38. Groover, M. *Fundamentals of Modern Manufacturing: Materials, Processes, and Systems*, 4th ed.; John Wiley & Sons, Inc.: Hoboken, NJ, USA, 2013; ISBN 978-0470467008.
39. Tilekar, S.; Das, S.S.; Patowari, P.K. Process Parameter Optimization of Wire EDM on Aluminum and Mild Steel by Using Taguchi Method. *Procedia Mater. Sci.* **2014**, *5*, 2577–2584. [[CrossRef](#)]
40. Farooq, M.U.; Ali, M.A.; He, Y.; Khan, A.M.; Pruncu, C.I.; Kashif, M.; Asif, N. Curved profiles machining of Ti6Al4V alloy through WEDM: Investigations on geometrical errors. *J. Mater. Res. Technol.* **2020**, *9*, 16186–16201. [[CrossRef](#)]
41. Ishfaq, K.; Farooq, M.U.; Anwar, S.; Ali, M.A.; Ahmad, S.; El-Sherbeeney, A.M. A comprehensive investigation of geometrical accuracy errors during WEDM of Al6061-7. 5% SiC composite. *Mater. Manuf. Process.* **2020**, *36*, 362–372. [[CrossRef](#)]
42. Asad, A.M.; Kashif, I.; Raza, M.H.; Umar, F.M.; Mufti, N.A.; Pruncu, C.I. Mechanical characterization of aged AA2026-AA2026 overcast joints fabricated by squeeze casting. *Int. J. Adv. Manuf. Technol.* **2020**, *107*, 3277–3297.

Article

# Mechanical Characterization of Nanocrystalline Materials via a Finite Element Nanoindentation Model

Konstantinos Tserpes<sup>1,\*</sup>, Panagiotis Bazios<sup>1</sup>, Spiros G. Pantelakis<sup>1</sup>, Maria Pappa<sup>2</sup> and Nikolaos Michailidis<sup>2</sup>

- <sup>1</sup> Laboratory of Technology & Strength of Materials, Department of Mechanical Engineering & Aeronautics, University of Patras, 26500 Patras, Greece; pbazios@upatras.gr (P.B.); pantelak@mech.upatras.gr (S.G.P.)  
<sup>2</sup> Physical Metallurgy Laboratory, Mechanical Engineering Department, School of Engineering, Aristotle University of Thessaloniki, 54124 Thessaloniki, Greece; pappmari@auth.gr (M.P.); nmichail@auth.gr (N.M.)  
\* Correspondence: kiterpes@upatras.gr; Tel.: +30-261-096-9498

**Abstract:** The difficulty of producing sufficient quantities of nanocrystalline materials for test specimens has led to an effort to explore alternative means for the mechanical characterization of small material volumes. In the present work, a numerical model simulating a nanoindentation test was developed using Abaqus software. In order to implement the model, the principal material properties were used. The numerical nanoindentation results were converted to stress–strain curves through an inverse algorithm in order to obtain the macroscopic mechanical properties. For the validation of the developed model, nanoindentation tests were carried out in accordance with the ISO 14577. The composition of 75% wt. tungsten and 25% wt. copper was investigated by producing two batches of specimens with a coarse-grain microstructure with an average grain size of 150 nm and a nanocrystalline microstructure with a grain diameter of 100 nm, respectively. The porosity of both batches was derived to range between 9% and 10% based on X-ray diffraction analyses. The experimental nanoindentation results in terms of load–displacement curves show a good agreement with the numerical nanoindentation results. The proposed numerical technique combined with the inverse algorithm predicts the material properties of a fully dense, nanocrystalline material with very good accuracy, but it shows an appreciable deviation with the corresponding compression results, leading to the finding that the porosity effect is a crucial parameter which needs to be taken into account in the multiscale numerical methodology.

**Keywords:** nanocrystalline materials; finite element analysis; inverse algorithm

**Citation:** Tserpes, K.; Bazios, P.; Pantelakis, S.G.; Pappa, M.; Michailidis, N. Mechanical Characterization of Nanocrystalline Materials via a Finite Element Nanoindentation Model. *Metals* **2021**, *11*, 1827. <https://doi.org/10.3390/met11111827>

Academic Editor: George A. Pantazopoulos

Received: 11 October 2021  
Accepted: 10 November 2021  
Published: 13 November 2021

**Publisher's Note:** MDPI stays neutral with regard to jurisdictional claims in published maps and institutional affiliations.



**Copyright:** © 2021 by the authors. Licensee MDPI, Basel, Switzerland. This article is an open access article distributed under the terms and conditions of the Creative Commons Attribution (CC BY) license (<https://creativecommons.org/licenses/by/4.0/>).

## 1. Introduction

Notable attempts have been made, in recent years, at the production of materials with a nanocrystalline microstructure, due to their improved mechanical properties [1,2]. The enhancement in terms of strength by decreasing the grain size has been described by the Hall–Petch equation effect [3].

Various manufacturing methods are applied to obtain nanocrystalline alloys (i.e., a grain size less than 100 nm), including electrodeposition [1,4], powder metallurgy [5,6], magnetron sputtering [7–10], and inert gas condensation followed by the consolidation of powders [1] and severe plastic deformation (SPD) [11,12]. The vast majority of nanocrystalline materials are produced by the mechanical alloying method or electrodeposition technique. The electrodeposition technique has some inherent limitations in terms of the quality of the produced specimens because they show extensive porosity or impurities. On the other hand, the fabrication technique of mechanical alloying is able to produce materials with a nanocrystalline microstructure at a high manufacturing speed and with complete control of the fabrication parameters, so as to obtain defect-free bulk materials [13]. However, the main obstacle of the mechanical alloying method is the production of specimens without a uniform grain size, which in turn influences the macroscopic mechanical response of the materials, especially in a harsh environment. The material

microstructure changes rapidly at elevated temperatures. This is the commonly-known coarsening effect. The mechanical response of said materials is completely influenced by their different interphases into the microstructure. This kind of material is the so-called graded material [14,15].

Taking for granted said facts, all of the proposed production techniques are cost-effective, but the produced materials are influenced by several imperfections (like flaws and pores) which drive to the degradation of the material properties. With respect to limitations in the manufacturing methods of nano-crystalline materials, the mass production of fully dense, bulk forms with a nanocrystalline microstructure at sufficient quantities has hardly been achievable up to now, and it has not been industrialized.

With the aforementioned increasing interest in the production of innovative metallic materials, mechanical testing procedures using small material volumes are more than necessary nowadays. Moreover, the conventional testing techniques like tensile or compression testing become noticeably challenging with specimens of small volume. Furthermore, limited results are shown in journals concerning the correlation between the microstructure and the resulting material properties. Some of the desirable material properties in the frame of nanocrystalline materials are the yield stress, the ultimate strength at fracture, the enhanced wear resistance and the improved plasticity compared to that of their microcrystalline counterparts [16–20]. A more detailed and extensive mechanical characterization is needed so as to obtain more reliable results.

Based on the obstacles of the mechanical characterization utilizing conventional experimental tests, scientific progress has resulted in the extensive use of nanoindentation experiments [21–34]. Berkovich indenters allow precise measurements by varying the force of the nanoindentation ( $P$ ) in relation to the depth of penetration ( $h$ ). Observations through experimental nanoindentation tests were performed on many materials so as to determine material features such as residual stresses and hardness [23–25,29,33–37].

At the same time, a noticeable effort has been made to use analytical and numerical investigations in order to determine the deformation mechanisms and the contact mechanics of the nanoindentation effect. The main purpose is to define the mechanical response to the applied load of nanoindentation ( $P$ ) versus penetration depth ( $h$ ) diagrams acquired from instrumented nanoindentation [23,25,31,32,36–41]. More specifically, researchers [23,25] suggested analytical approaches in which the modulus of elasticity and hardness could be extracted from the  $P_{max}$  and the unloading incline at the starting stages. Additionally, Giannakopoulos and Suresh [40] proposed a procedure in which all of elastoplastic properties may be extracted through a  $P$ - $h$  diagram. Based on [40], Suresh and Giannakopoulos [42] developed an up-to-date methodology which was able to export the residual stresses. In terms of numerical methods, several numerical attempts were conducted on the case studies of thin-film systems [43–45].

To conclude, a methodology was developed by Hill et al. [46] for the case study of materials with power law plastic behavior under the indentation load of a spherical indenter. The calculations of a sharp indenter, such as a Berkovich indenter, for the case of elastoplastic materials were numerically extracted by Larsson et al. [47] and Giannakopoulos et al. [38]. Moreover, scale factors were carried out so as to investigate bulk materials [31,32,39] and coated material [45]. To this end, researchers [32] have developed a comprehensive analytical approach, and several investigations were conducted on the basis of the dimensional analysis of sharp indentation. The results from the aforementioned approach showed that Kick's Law is a constitutive factor of the dimensional analysis of sharp indentation.

The scope of the present paper is to develop an innovative multiscale finite element methodology simulating the nanoindentation test which accounts for the different material phases, as they are described in [48], in order to define the macroscopic mechanical response of nanocrystalline materials. Through the aforementioned model, the nanoindentation behavior of nanocrystalline materials was extracted, and the corresponding macroscopic mechanical behavior was evaluated via the implementation of an inverse analytical algo-

rithm. By utilizing a homogenized RVE for the last simulation in conjunction with the inverse algorithm, we are able to predict the macroscopic mechanical response.

## 2. Modelling

### 2.1. Analytical Approach

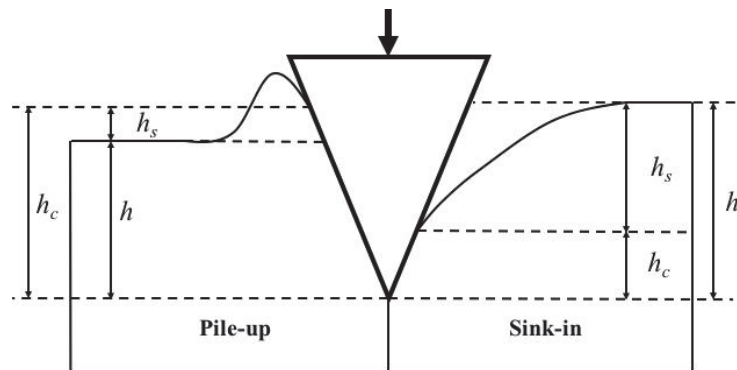
As referred to above, the nanoindentation method is a very attractive testing procedure to obtain the mechanical properties of such kinds of materials as nanocrystalline metals, which are difficult to produce in large quantities, leading to the need for the mechanical characterization of small-volume specimens. The uniqueness of the nanoindentation technique relies on the extracted results which come from the  $P$ - $h$  diagram. More specifically, the estimation of the contact pressure between the nano-indenter and the target material—and the resulting hardness—comes from the measurement of the contact area between said parts in terms of the indentation load and penetration depth. A continuous data acquisition in the loading phase of a typical indentation test is involved. In the following unloading part of the  $P$ - $h$  diagram, the Young's modulus and Poisson ratio of the indented material can be exported at the early stages of the unloading phase because of the strain relaxation within the material [49,50]. Furthermore, material features like residual stress [46,51], initial plasticity [51–53], creep [54], and hardening [55] are very important parameters for property extraction in the nanoindentation testing method. Additionally, the surface deformation around the plastic deformation induced by the nano-indenter creates sink-in and pile-up residual strains, which are very important for the mechanical characterization of the target material [56]. The aforementioned alteration of the surface plays an important role in determining the contact area, and is also an effective factor for the definition of material properties like the strain-hardening behavior [57,58].

According to the literature for the indentation testing method, a nanoindentation test is commonly known for the creation of a non-uniform stress field at the surface of the target material, which leads to the average calculation of induced stresses [59]. The mean value of stresses in terms of von Mises stress, according to Meyer's hardness [49,59], is defined utilizing the Tabor Relation [59–61]:

$$\sigma \approx \frac{H}{3}, \quad (1)$$

$$H = \frac{P}{A}, \quad (2)$$

where  $H$  is the resulting hardness,  $P$  is the applied force of the nano-indenter on the target material, and  $A$  is the contact area of the Berkovich nanoindenter. The indentation area is calculated taking into consideration the geometry of the nanoindenter's tip and the pile-up or sink-in that take place around the tip, as shown in Figure 1.



**Figure 1.** Indentation geometry showing the pile-up and sink-in.

The mathematical expressions followed for the calculation of the projected contact area of the nanoindenter are presented in Equation (3) for the case study of a Berkovich indenter’s tip [62], and in Equation (4) for the case study of the spherical indenter’s tip:

$$A = 24.5h_c^2 + Ch_c, \tag{3}$$

$$A = \pi(2Rh_c - h_c^2), \tag{4}$$

where  $h_c$  is the penetration depth of the indenter tip into the target specimen,  $C$  is a constant for the case of Berkovich indenters (150 nm) referring to the geometrical features of the specific indenter [62], and  $R$  refers to the curvature of the nanoindenter. The penetration depth of the indenter’s tip was calculated according to the contact mechanics’ analytical expressions (Figure 1) [49,59,63]:

$$h_c = h - h_s = h - \delta\left(\frac{P_{max}}{S}\right), \tag{5}$$

$$S = \frac{dP}{dh}, \tag{6}$$

where  $h$  is the overall displacement of the nanoindenter;  $\delta$  is a geometric constant parameter referring to the geometrical characteristics of the indenter’s tip, which is equal to 0.75 for Berkovich indenters; the variable  $h_s$  describes the displacement of the target material’s surface during the nanoindentation load, taking into account the pile-up and sink-in deformation mechanisms; and  $S$  is the stiffness at the unloading phase. At this point, it is of paramount importance to mention that the stiffness at the unloading step is defined by the incline of the  $P$ - $h$  diagram (an indicative plot is shown in Figure 2).

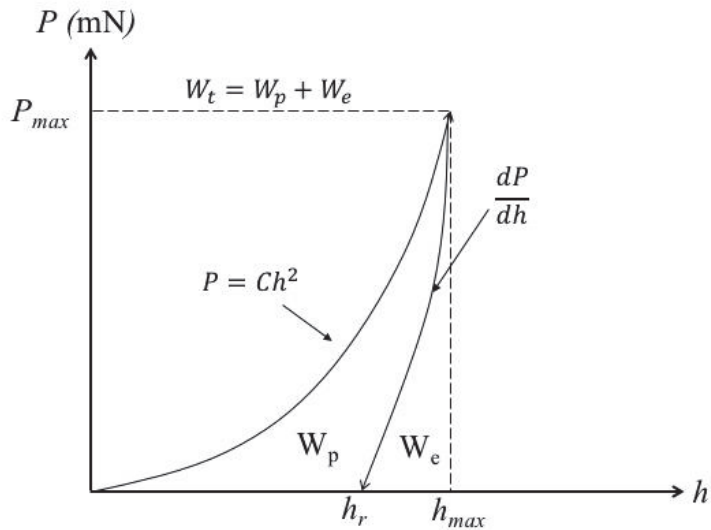


Figure 2. Indentation load–penetration depth curve from an indentation test.

It is noteworthy to mention that Equations (2)–(6) were from research papers in the frame of homogeneous materials. Based on this aspect, extensive work needs to be carried out so as to verify the effectiveness of the proposed mathematical procedure on heterogeneous materials like the nanocrystalline tungsten–copper materials produced and tested in the present paper. The selection of the tungsten–copper alloy was made in the frame of the European FET-Open project ICARUS [64] due to its inherent thermodynamic stability for aerospace applications. Moreover, the strain rate of the indentation at the

surface of the target material is also non-uniform, and it leads to the creation of the corresponding non-uniform stress field, as referred to above. It is of paramount importance to define the mean deformation rate as the rate of the complete penetration depth into the target material over the current total displacement of the indenter [60]:

$$\dot{\epsilon} = \frac{\dot{h}}{h} \quad (7)$$

## 2.2. Numerical Model

For the purpose of the nanoindentation simulation of a nanostructured material, a FE-based model was utilized. The recommended numerical methodology is utilized on RVEs with a nanocrystalline morphology. The numerical methodology is presented in the flowchart of Figure 3. The methodology begins with the computer tomograph YXLON FF35 CT (YXLON International GmbH, Hamburg, Germany) and X-ray diffraction images (Bruker D8 Discover, Bruker Corp., Billerica, MA, USA), and evolves with the image analysis and the multi-level simulation [48].

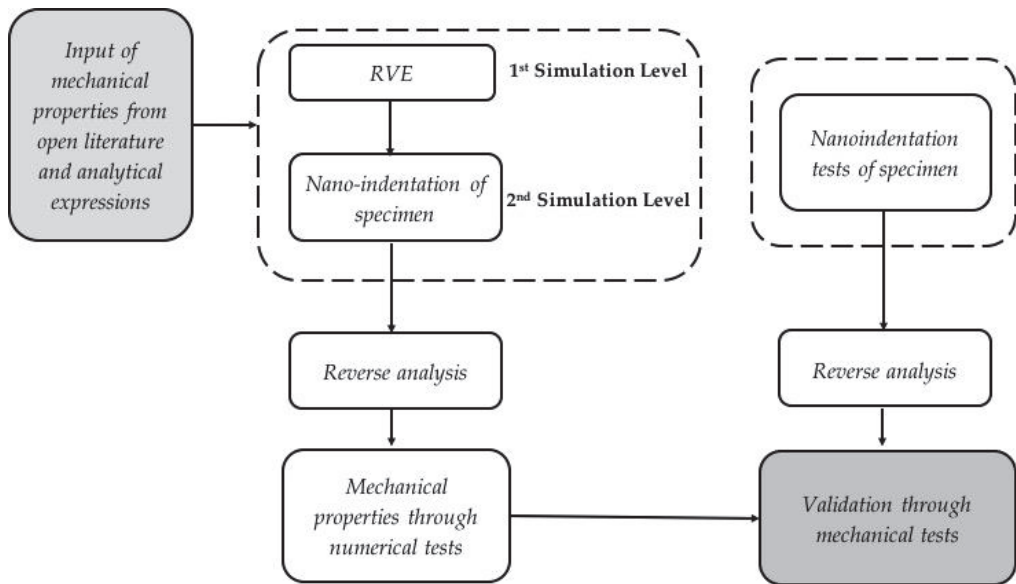
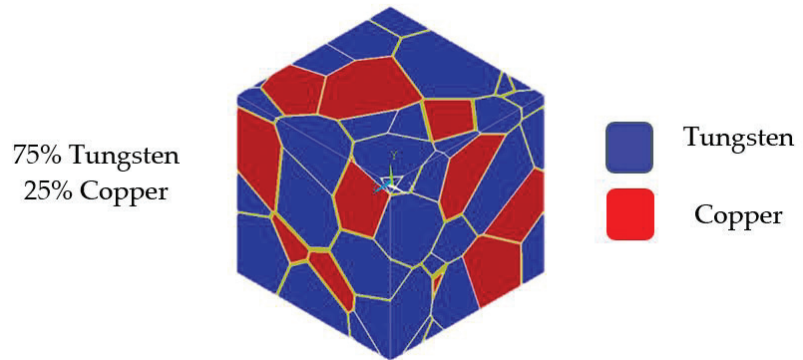


Figure 3. Flowchart of the methodology.

As it is commonly known, RVE is the smallest numerical volume for any material in which a macro-mechanical property can be defined through a multi-scale modelling approach. Due to the microscopic size of representative-volume elements, the detailed morphology of the materials' microstructural characteristics can be modelled. The analysis' objective is focused on the development of a numerical procedure via the parametric interaction representing the geometrical characteristics of nanostructured metals. The presumptions and the extensive numerical methodology used in the present work are described extensively in [48,65], on account of the completeness of the paper. The nanocrystalline materials are heterogeneous materials due to their discrete areas showing different physico-chemical and mechanical properties at the microscale level. Based on this paradox, the mechanical response, taken by the proposed numerical methodology shown in [48,65], is the homogenized average medium of the equivalent heterogeneous nanocrystalline material. More specifically, in [48,65], the presumptions were applied for the investigation of mechanical behavior of a fully dense, nanocrystalline material under uniaxial compressive

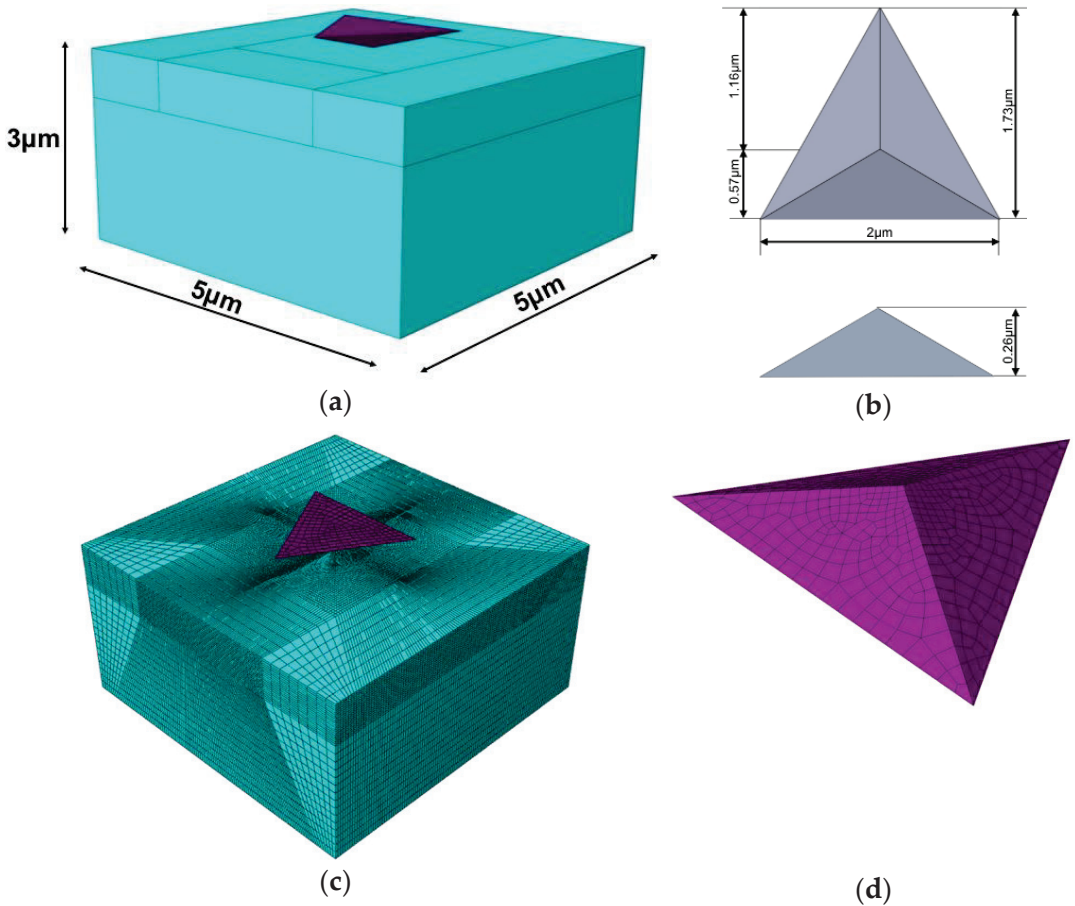


loading, so as to extract the stress–strain response of an equivalent homogenized material from the heterogenous RVE (see Figure 4) at the nanoscale level under compression loading. In the present publication, we follow strictly the above-said numerical methodology by extending it to the application of a nanoindentation testing method, so as to define the mechanical response of nanocrystalline metals at the microscale level.



**Figure 4.** The representative volume element of a tungsten–copper nanocrystalline alloy.

The finite element modeling of the nanoindentation test was developed utilizing Abaqus CAE (Computer Aided Engineering) (Dassault Systemes Simulia Corp., Providence, RI, USA). The model was developed in three dimensions consisting of 2 objects, a representative pyramidal-like indenter with the real dimensions of Berkovich indenter and a cube representing the specimen with dimensions of  $5\ \mu\text{m} \times 5\ \mu\text{m} \times 3\ \mu\text{m}$  (Figure 5). The indenter was modeled to be rigid. The definition of elastoplastic response of cubic specimen was achieved by using the innovative nanoscale numerical model which was described above [48]. The material properties applied to the cubic specimen were extracted from the RVE as the homogenized average medium. The aforementioned mechanical properties were achieved by applying a compressive loading on the RVE. Additionally, a surface-to-surface frictional contact with a coefficient of 0.1 was implemented for the indentation model. Several numerical investigations have shown that the frictional coefficient between the indenter and target material is an insignificant parameter regarding the experimental nanoindentation outcomes. In the present work, the influence of the frictional contact was taken into account in the numerical model in order to develop numerically the same experimental conditions, with the ultimate goal of the maximum similarity between the numerical model and the experiments. Regarding the numerical parameters, the target material was meshed with 62,000 hexahedral elements of type C3D8R (eight node), with a dense mesh at the area of the target material directly beneath Berkovich’s tip. Moreover, the indenter had a constant penetration speed of 5.5 nm/s until it reached the load of 15 mN, in the loading phase, which is a pre-defined setup parameter. After this step, the indenter was removed from the target material with a constant speed of 16 nm/s in the unloading phase. At this point, it is important to mention that the ratio of the cube’s height to the maximum penetration depth is approximately equal to 8 in the current model, so as to reduce computational time. From the scope of parametric study, higher ratios of 10 and 20 were also investigated, and the results presented an insignificant divergence in the resulting  $P$ - $h$  diagram compared to that of the ratio of 8.



**Figure 5.** Three-dimensional finite element model of the nanoindentation: (a) the dimensions of the target material, (b) the dimensions of the Berkovich indenter, (c) the meshed model and (d) the meshed Berkovich indenter.

The main advantage of the numerical nanoindentation models is that they are able to acquire the load-versus-depth curve of a specified reference point by continuous data acquisition throughout the duration of the simulation, just as during an experiment in situ. Furthermore, another important aspect that should be mentioned is that the proposed numerical methodology has taken into account the importance of the dimensional definition of the indented cube. In this way, the boundary effects are eliminated on the nanoindentation model, and the assumption of a continuous medium was validated. During the setup of the FE parameters, one of the most important boundary conditions applied in this model is the fixation of the target material's base so as to ensure an ideal indentation test. A second important boundary condition applied is the constraint of the nanoindenter in such a way that the nanoindenter is fixed to allow motion in the vertical direction.

### 2.3. Inverse Analysis Algorithm

A comprehensive analytical methodology for instrumented indentation was identified in this paper, which allows us to define the mechanical properties of materials by using a Berkovich nanoindenter. The current paper is focused on the development of an inverse analysis algorithm so as to obtain the material properties via nanoindentation tests and numerical nanoindentation models. Figure 2 shows the  $P$ - $h$  curve for a Berkovich indenter.

In the loading phase, it seems that the curve is in consistency with the relation  $P = Ch^2$ , where parameter  $C$  is responsible for the indentation curvature. This curvature represents the resistance of the target material to the indentation effect. Additionally, the calculated pressure of contact,  $p_{av} = P_{max}/A_{max}$ , could be determined with the hardness of the target material, where  $P_{max}$  is the maximum applied force for the indentation. The  $P_{max}$  provides the necessary energy to the nanoindenter to penetrate the target material by a depth of  $h_{max}$ , by that means creating the  $A_{max}$  (the maximum projected contact area on the surface of the target material). Elastoplastic FE models with a Berkovich indenter, conducted on the present paper utilizing computational analyses comparable with those presented in reference [38], also show that

$$\frac{h_r}{h_{max}} = 1 - d^*S, \quad (8)$$

where  $d^* = 4.678$  for the case of a Berkovich indenter. Equation (8) is in rational accordance with the experimental observations of Breval and MacMillan [66]. Taking into consideration the true contact area on three-dimensional numerical models and the strain hardening effects imposed on pile-up and sink-in strains, the subsequent mathematical expression, which correlates  $A_{max}$  with  $h_{max}$ , was obtained for the case study of elastic-plastic materials [30,38]:

$$\frac{A_{max}}{h_{max}^2} = 9.96 - 12.64 * (1 - S) + 105.42(1 - S)^2 - 229.57(1 - S)^3 + 157.67(1 - S)^4, \text{ with } S = \frac{p_{av}}{E^*} \quad (9)$$

The aforementioned mathematical expression is a polynomial regression to the calculated values of  $A_{max}/h_{max}^2$ . In Equation (9), the resulting Young's modulus of the Berkovich nanoindenter-target material system,  $E^*$ , is derived as:

$$E^* = \frac{1}{c^* \sqrt{A_{max}}} \left( \frac{dP}{dh} \right), \quad (10)$$

where  $dP/dh$  is the incline of the  $P$ - $h$  diagram at the unloading phase from  $P_{max}$ , while the  $c^*$  parameter is equal to 1.167 for the case study of the Berkovich nanoindenter. Furthermore, the ratio of the residual penetration depth  $h_r$  to the maximum depth of indentation,  $h_{max}$ , is typical of the magnitude of strain hardening and plastic deformation [41,67,68]:

$$\frac{\sigma_{0.29} - \sigma_y}{0.29E^*} = 1 - 0.142 \frac{h_r}{h_{max}} - 0.957 \left( \frac{h_r}{h_{max}} \right)^2 \quad (11)$$

In the aforementioned Equation,  $\sigma_y$  refers to the yield strength, while  $\sigma_{0.29}$  refers on the indicative plastic strain of 0.29 for the target material in uniaxial loading.

At this point, it is noteworthy to mention that the combination of Equations (8) and (9) gives an important relationship which correlates  $A_{max}$  with  $h_{max}$ . Using the aforementioned combined mathematical expression, we are able to extract the true contact area from the  $P$ - $h$  diagram without the need of any visual examination. Knowing that

$$P_{max} \approx Ch_{max}^2, \quad (12)$$

we can calculate the parameter  $C$  so as to use it into the following equation, which comes from 3D numerical simulations of elastic-plastic nanoindentation, in addition to the corresponding experiments [36,38,42,67,68]:

$$C = \frac{P}{h^2} = M_1 \sigma_{0.29} \left\{ 1 + \frac{\sigma_y}{\sigma_{0.29}} \right\} \left\{ M_2 + \ln \frac{E^*}{\sigma_y} \right\} \quad (13)$$

The constants in this mathematical expression are  $M_1$  and  $M_2$ , where  $M_1$  is equal to 6.618 and  $M_2$  is equal to  $-0.875$  for the case study of a Berkovich indenter [40].

With all of the values calculated using the above-said analytical expressions, the strain hardening exponent can be easily calculated by applying the subsequent equation:

$$n \approx \ln\{\sigma_{0.29} - \ln(\sigma_y)\} / 5 \quad (14)$$

### 3. Experimental

#### 3.1. Materials

To begin with, the tungsten–copper alloy system was selected for the present investigation. As mentioned above, the selection of the present alloying element combination was made in the frame of the European project ICARUS [64], which was focused on the investigation of coarsening-resistant alloys for aerospace applications. The alloy consisted of 75% tungsten and 25% copper in weight. For this material composition, two different types of tungsten–copper alloy were produced in terms of the resulting microstructure. Both types were manufactured using the same powders originating from the same powder batch.

The coarse-grained tungsten–copper specimens (cW-Cu) were fabricated through the simple mixture of the as-received commercial powders of tungsten and copper elements without any grain refinement process being involved. Additionally, the well-known manufacturing approach consisting of cold pressing, hot isostatic pressing (HIP) (University of Miskolc, Miskolc, Hungary) and heat treatment was implemented so as to obtain the consolidated specimens. The coarse-grained tungsten–copper specimen has an average grain size of 150 nm.

On the other hand, the high energy ball milling (HEBM) (MBN Nanomaterialia S.p.A., Treviso, Italy) method was utilized in order to mill tungsten and copper powders, achieving a nanocrystalline morphology with a grain diameter of 100 nm. The nanocrystalline tungsten–copper powders used for the production of the alloy will be referred in the following as W-Cu. Following the same consolidation technique of the cW-Cu specimens for the production of the corresponding W-Cu specimens, the fabrication method of cold pressing, hot isostatic pressing (HIP) and heat treatment was implemented here again. An extensive description of the produced materials' microstructures and their resulting imperfections (pores and impurities) can be found in [48]. The above-mentioned production of the two types of tungsten–copper alloys was performed by the company MBN Nanomaterialia.

#### 3.2. Nanoindentation Test

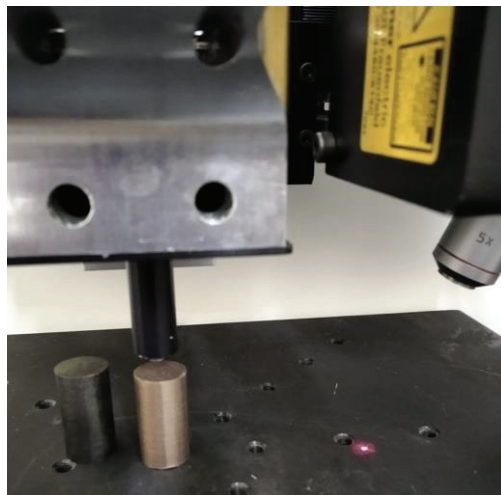
Nanoindentation refers to a variety of hardness tests which are applied on a small scale. Penetration is perhaps the most common way of checking the mechanical properties of materials facilitated by high-precision instrumentation in the nanometer scale. In 2008, the ISO/TR 29381 was published, allowing for the evaluation of the tensile properties of metallic materials by instrumented indentation [69].

A nanoindentation device was developed at the Physical Metallurgy Laboratory, and is presented in Figures 6 and 7. The device performs testing using a Berkovich, Vickers, or Knoop diamond, or 0.5–2 mm indenters. The travel distance of the workbench can reach 50 by 140 mm, guided by specially developed computer software. The height of the optics is measured by means of a laser distance meter coupled with a rotary encoder attached to the fine adjustment dial of the microscope. The accuracy of the device in the XY direction is in the order of 1  $\mu\text{m}$ . The applied load can vary from 1 to 1000 mN with a resolution of 0.1 mN, strictly following the ISO 14577 [70]. The measurement consists of two stages: the loading phase and the unloading phase. During the loading, force is applied gradually to the diamond indenter, and as it penetrates the test piece, the depth measurement is recorded. During the unloading, a residual depth remains due to the plastic deformation of the sample, which depends on the properties of the material, the size of the applied force, and the geometry of the indenter. The maximum indentation depth fluctuations measured on the same sample are mainly induced by different contact conditions between the indenter tip and the tested surface due to roughness [71]. The roughness effect can be confronted with the execution of an appreciable number of measurements to attain the stabilization of

the maximum indentation depth's mean value [71]. The proper preparation of the examined specimens is a meticulous and time-consuming process that ensures the repeatability and robustness of the results, while eliminating those parameters that could tamper with the outcome due to mishandling or human error. The mounted samples were gently, mechanically ground and polished in several sequential steps employing a BUEHLER Vanguard™ 2000 (Lake Bluff, IL, USA) automatic sample preparation system [72]. The mechanical grinding took place in several sequential steps, starting with coarse grinding discs (60 grit) and ending with finer ones (1600 grit). The polishing was obtained by employing an aqueous suspension of fine alumina powder with a particle size of 0.3  $\mu\text{m}$  applied on the respective polishing cloths. In this work, 50 nanoindentation tests were performed on each specimen to eliminate roughness effects.



**Figure 6.** Nanoindentation test of nanocrystalline specimens according to ISO 14577.



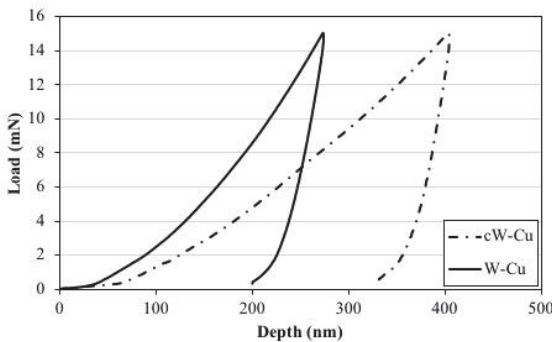
**Figure 7.** Specimen's fixation for the nanoindentation test.

The evolution of FEM-based algorithms in the evaluation of nanoindentation results offers advanced capabilities in the determination of the exact contact between the indenter and the test piece, thus allowing the accurate calculation of the material's hardness and the stress–strain curve. The FEM model simulating the nanoindentation procedure and the actual indenter tip geometry, introduced in [72], can be applied to calculate the contact geometry during the loading and the shape of the surface impression after unloading. The

“SSCUBONI” algorithm employed for the continuous simulation of the nanoindentation enables the extraction of materials’ stress–strain laws. FEM-supported methods offer advanced capabilities in the determination of mechanical properties, such as the Young’s modulus, yield and rupture strength. Stress–strain curves of various materials—such as cemented carbide, ceramics and hardened steels—determined by a FEM-based algorithm of nanoindentation can be applied in FEM-supported simulations of micro- and macro-scale indentation procedures to allow the capture of the material response at various scales [73].

#### 4. Results

The indentation force ( $P$ )–penetration depth ( $h$ ) curves obtained using a Berkovich indenter tip, after a set of 50 measurements that were statistically evaluated to present the averages for the cW-Cu and the W-Cu type of alloy are presented in Figure 8, as well as the scatter of the measurement at the maximum indentation depth. As shown in Figure 8, the coarse-grained tungsten–copper alloy (cW-Cu) exhibits a higher penetration of about 400nm depth at an indentation load of 15 mN [73,74] compared to that of nanocrystalline the tungsten–copper alloy (W-Cu), which presents a penetration depth of about 250 nm at the applied penetration load of 15 mN, correspondingly. The aforementioned outcomes are reasonable due to the fact that the Hall–Petch effect governs this type of material, and the yield stress is increased by decreasing the grain size. Thus, the nanocrystalline specimen shows a higher “resistance” to the indentation effect and to plastic deformation.



(a)

	cW-cu	W-cu
Min. Depth (nm)	352	224
Aver. Depth (nm)	407	258
Max. depth (nm)	522	284

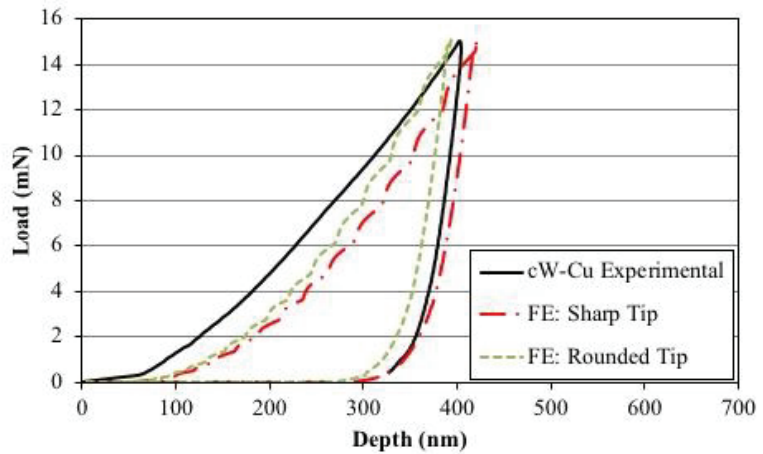
(b)

**Figure 8.** (a) The experimental results of cW-Cu and WCu specimens in accordance with ISO 14577, and (b) the scatter of the nanoindentation results.

##### 4.1. Validation of the Numerical Nanoindentation Model

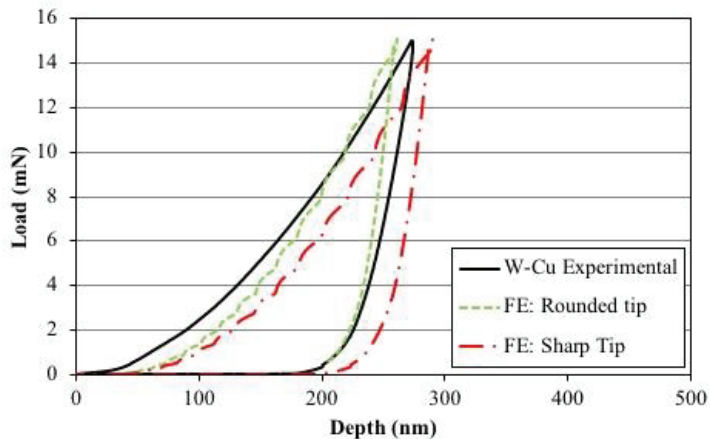
Using the numerical multiscale model, the homogenized nanoindentation response of the fully dense, indented material was calculated for the case of a coarse-grained W-Cu (cW-Cu) material, and is shown in Figure 9. In this Figure, the computed  $P$ - $h$  curves of a fully dense, nanocrystalline material using two Berkovich indenters—one with a sharp tip and one with a rounded tip with a roundness of 100 nm—are displayed and compared to the respective experimental curve. The geometrical features and the material properties applied on the cubic specimen are described extensively in [48]. The divergence of the numerical outcomes from the experimental result is negligible because the nanoindentation model does not take into account any defect (like pores) which might be located in the microstructure of the specimens. The aforementioned assumption of the absence of defects on the numerical model leads to the simulation of a fully dense, homogeneous-like material which may be different from that reality. On the other hand, the existing impurities or pores are mostly located at the lower layers of specimens, and as a result the nanoindenter cannot reach it through the nanoindentation test due to the very small indentation depth.

This phenomenon leads to the prediction of a nanoindentation response of a fully dense material without microstructure irregularities.



**Figure 9.** Comparison of the experimental result of the cW-Cu specimen with the numerical results utilizing sharp and rounded Berkovich indenters.

Taking for granted the above assumption, the only parameter which plays an important role on the definition of the nanoindentation response is the sharpness of the nanoindenter. In terms of the tip sharpness, both the tungsten–copper alloys and their corresponding numerical results (Figures 9 and 10) present the same tendency. More specifically, the numerical results of the sharp Berkovich indenter present the higher penetration depth of both materials. This phenomenon is reasonable due to the extensive stress concentration beneath the Berkovich tip. The sharper the tip, the higher the stress concentration factor is. On the other hand, the implementation of a rounded tip of the Berkovich indenter is a more realistic approach due to the unavoidable degeneration of the nanoindentation apparatus through its extensive usage. The above fact is logical, and the effect of the indenter’s sharpness on the mechanical response in nanoindentation experiment was reported in [75]. Taking this aspect for granted, the numerical results of the rounded Berkovich indenter tend to show the most reliable nanoindentation behavior.



**Figure 10.** Comparison of the experimental result of a W-Cu specimen with the numerical results of a fully dense model utilizing sharp and rounded Berkovich indenters.

To sum up, the experimental  $P$ - $h$  curve better reflects the nanoindentation behavior of a fully dense material than of a material with an extensive porosity like the examined specimens in this paper. The proposed numerical methodology shows a very good convergence with the nanoindentation test. On the other hand, utilizing the inverse algorithm as it is shown in Section 4.2, the macroscopic compression behavior obtained by the inverse algorithm of the numerical nanoindentation results will differ from the experimental compression tests examined in [48] because it does not take into account the inherent defects (impurities and pores) of the microstructure.

4.2. Comparison of Nanoindentation Experimental Results Utilizing the SSCUBONI Algorithm

Implementing the SSCUBONI algorithm, the resulting representative von Mises stress-strain curves of the cW-Cu and W-Cu specimens from the nanoindentation tests are shown in Figures 11 and 12, respectively. The aforementioned curves are compared to those of the compression tests for the same batches.

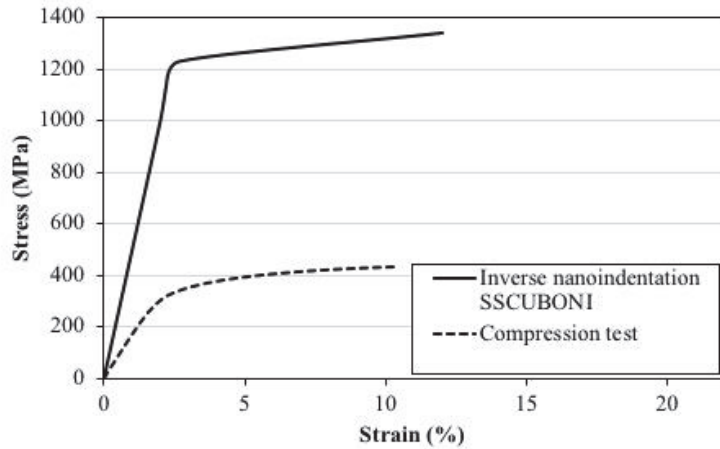


Figure 11. Comparison of the S-S curves of the experimental compression test with the corresponding inverse SSCUBONI-based experimental test for the cW-Cu specimens.

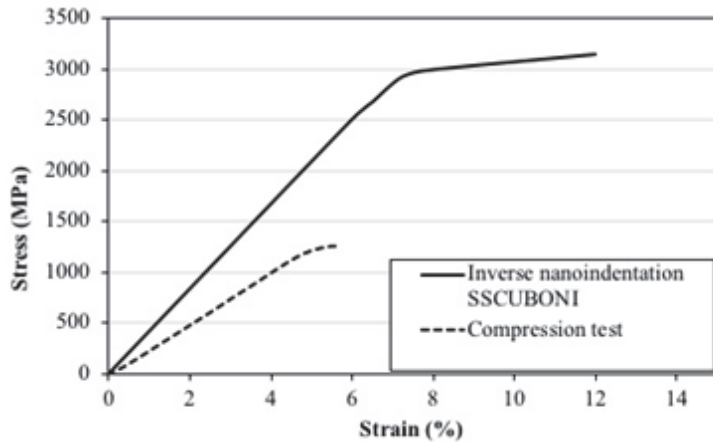


Figure 12. Comparison of the S-S curves of the experimental compression test with the corresponding inverse SSCUBONI-based experimental test for the W-Cu specimens.

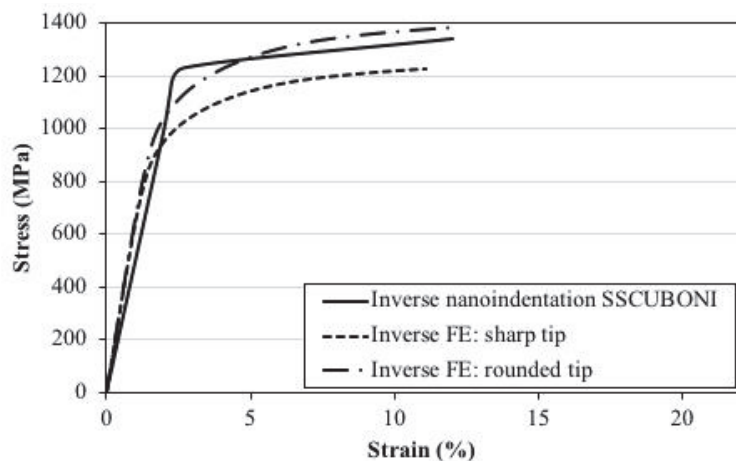


As can be seen from both Figures, the inverse experimental nanoindentation results present a remarkable deviation from the compression test of the cW-Cu and W-Cu counterparts. More specifically, in Figure 11, the inverse SSCUBONI nanoindentation curve exhibits a Young's modulus of 200 GPa and a yield stress of 1340 MPa, while the corresponding compression curve shows a Young's modulus of 180 GPa and a yield stress of 450 MPa. Moreover, in the case of W-Cu specimens (Figure 12), the inverse SSCUBONI curve from the experimental nanoindentation curve shows a Young's modulus of 250 GPa and a yield stress of 2.8 GPa, while the respective compression curve for the case of the W-Cu specimen exhibits a Young's modulus of 220 GPa and a yield stress of 1150 MPa.

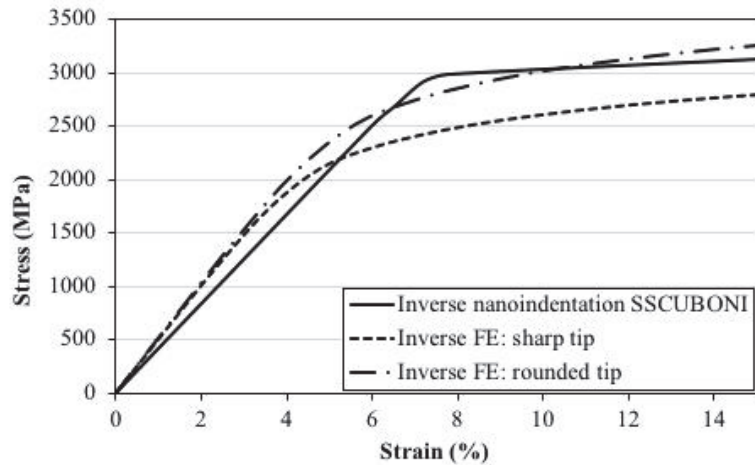
It is evident that the deviation of the inverse experimental nanoindentation outcomes from the experimental compression results is appreciable but reasonable. The porosity effect is the main characteristic which relies on the aforementioned deviation. As was already explained above, the nanoindenter penetrates the target material at a contact area of a few nanometers for an indentation depth of some nanometers. The contact area of the nanoindentation is extremely small compared to the volume of the specimen, and as a result the obtained experimental results reflect a nanoindentation behavior of a homogeneous-like material excluding all of the present heterogeneities into its microstructure by extracting a nanoindentation behavior of an ideal material. This procedure leads to unreliable results in the case of a material with several defects or impurities in its microstructure. The experimental test is not able to perceive the extensive presence of pores which are located in the lower layers. In our case, the experimental  $P$ - $h$  curve better reflects the nanoindentation behaviour of a fully dense material than that of a material with an extensive porosity like the examined specimens of the current project.

#### 4.3. Comparison of Numerical Nanoindentation Results Utilizing the Inverse Algorithm

In an effort to predict the macroscopic material properties via the nanoindentation testing method, an inverse algorithm was proposed and utilized in this paper. The macroscopic mechanical responses of the experimental results and the numerical outcomes of nanoindentation models were calculated for the case of a cW-Cu material and a W-Cu material, and they are shown in Figures 13 and 14, respectively. As can be seen, the experimental nanoindentation results obtained from the SSCUBONI algorithm show an appreciable convergence with the corresponding numerical nanoindentation results obtained by the proposed inverse algorithm.



**Figure 13.** Comparison of the S-S curves of the experimental compression test with the corresponding inverse numerical nanoindentation results and the inverse SSCUBONI-based experimental test for the cW-Cu specimens.



**Figure 14.** Comparison of the S-S curves of the experimental compression test with the corresponding inverse numerical nanoindentation results and the inverse SSCUBONI-based experimental test for the W-Cu specimens.

Both of the inverse analysis algorithms seem to be efficient in converting the penetration load–indentation depth curve to stress–strain curves, but the proposed multiscale nanoindentation model in conjunction with the inverse algorithm provides an advantage to the scientific community because it is able to predict the macroscopic mechanical response of any nanocrystalline material without executing any experimental test. However, it is noteworthy to mention at this point that the porosity effect is a crucial parameter for the mechanical behavior. For the aforementioned reason, the numerical multiscale nanoindentation methodology implementing the porosity effect for the case study of porous nanocrystalline alloys in combination with the proposed inverse analysis algorithm needs to be developed so as to predict the macroscopic mechanical response more efficiently.

## 5. Conclusions

Herein, a methodology was developed for the simulation of the nanoindentation testing of fully dense nanocrystalline materials utilizing a combination of numerical and analytical approaches. The numerical nanoindentation outcomes correlate very well with the experimental nanoindentation results, which validates the proposed methodology in terms of simulating the nanoindentation test. However, in the scope of the prediction of mechanical properties at the macroscale level, the proposed methodology shows an appreciable divergence with the experimental compression tests due to the porosity effect. For the aforementioned reason, it is of paramount importance that the proposed multiscale numerical methodology be modified so as to take into account the porosity effect. Additionally, a thorough investigation of the proposed methodology has to be carried out by applying different indentation loads, through numerical simulations and experimental tests, and by testing various specimens with different alloying elements, compositions and grain sizes so as to be validated for any alloy. Considering the above, it can be stated that the proposed numerical approach in conjunction with the inverse algorithm represents a preliminary contribution towards the development of a numerical nanoindentation model, and may serve as the basis for the development of large-scale models to be applied in the quality control of the mass production systems of the aforementioned promising materials in the near future.

**Author Contributions:** Conceptualization, S.G.P., K.T. and N.M.; methodology, S.G.P. and K.T.; software, P.B.; validation, P.B. and M.P.; formal analysis, P.B.; investigation, P.B.; data curation, P.B. and M.P.; writing—original draft preparation, P.B.; writing—review and editing, P.B. and M.P.; visualization, P.B.; supervision, S.G.P., K.T. and N.M.; project administration, S.G.P. All authors have read and agreed to the published version of the manuscript.

**Funding:** This research was funded by ICARUS, grant agreement No. 713514, of the European Union's Horizon 2020 research and innovation programme.

**Data Availability Statement:** Data sharing not applicable.

**Acknowledgments:** The work described in this paper received funding from the European Union's Horizon 2020-FETOPEN research and innovation programme under Grant Agreement no. 713514: ICARUS project (Innovative Coarsening-resistant Alloys with enhanced Radiation tolerance and Ultrafine-grained Structure for aerospace application). This paper originated from a presentation made in the frame of the sixth International Conference of Engineering Against Failure-ICEAF VI.

**Conflicts of Interest:** The authors declare no conflict of interest.

## References

1. Gleiter, H. Nanostructured materials: Basic concepts and microstructure. *Acta Mater.* **2000**, *48*, 1–29. [[CrossRef](#)]
2. Kumar, K.; Van Swygenhoven, H.; Suresh, S. Mechanical behavior of nanocrystalline metals and alloys The Golden Jubilee Issue—Selected topics in Materials Science and Engineering: Past, Present and Future, edited by S. Suresh. *Acta Mater.* **2003**, *51*, 5743–5774. [[CrossRef](#)]
3. Naik, S.; Walley, S. The Hall–Petch and inverse Hall–Petch relations and the hardness of nanocrystalline metals. *J. Mater. Sci.* **2019**, *55*, 2661–2681. [[CrossRef](#)]
4. Hibbard, G.; Erb, U.; Aust, K.; Klement, U.; Palumbo, G. Thermal Stability of Nanostructured Electrodeposits. *J. Metastable Nanocryst. Mater.* **2002**, *13*, 387–396. [[CrossRef](#)]
5. Suryanarayana, C. Nanocrystalline materials. *Int. Mater. Rev.* **1995**, *40*, 41–64. [[CrossRef](#)]
6. Groza, J. Nanostructured Materials. *Mater. Today* **2002**, *5*, 55.
7. Liao, W.; Lan, S.; Gao, L.; Zhang, H.; Xu, S.; Song, J.; Wang, X.; Lu, Y. Nanocrystalline high-entropy alloy (CoCrFeNiAl0.3) thin-film coating by magnetron sputtering. *Thin Solid Films* **2017**, *638*, 383–388. [[CrossRef](#)]
8. Liao, W.; Zhang, H.; Liu, Z.; Li, P.; Huang, J.; Yu, C.; Lu, Y. High Strength and Deformation Mechanisms of Al0.3CoCrFeNi High-Entropy Alloy Thin Films Fabricated by Magnetron Sputtering. *Entropy* **2019**, *21*, 146. [[CrossRef](#)] [[PubMed](#)]
9. Xing, Q.; Ma, J.; Zhang, Y. Phase thermal stability and mechanical properties analyses of (Cr,Fe,V)-(Ta,W) multiple-based elemental system using a compositional gradient film. *Int. J. Miner. Metall. Mater.* **2020**, *27*, 1379–1387. [[CrossRef](#)]
10. Xing, Q.; Ma, J.; Wang, C.; Zhang, Y. High-Throughput Screening Solar-Thermal Conversion Films in a Pseudobinary (Cr, Fe, V)-(Ta, W) System. *ACS Comb. Sci.* **2018**, *20*, 602–610. [[CrossRef](#)]
11. Lowe, T.; Valiev, R. Producing nanoscale microstructures through severe plastic deformation. *JOM* **2000**, *52*, 27–28. [[CrossRef](#)]
12. Valiev, R.; Islamgaliev, R.; Alexandrov, I. Bulk nanostructured materials from severe plastic deformation. *Prog. Mater. Sci.* **2000**, *45*, 103–189. [[CrossRef](#)]
13. Zhou, H.; Hu, L.; Sun, Y.; Zhang, H.; Duan, C.; Yu, H. Synthesis of nanocrystalline AZ31 magnesium alloy with titanium addition by mechanical milling. *Mater. Charact.* **2016**, *113*, 108–116. [[CrossRef](#)]
14. Suresh, S. Graded Materials for Resistance to Contact Deformation and Damage. *Science* **2001**, *292*, 2447–2451. [[CrossRef](#)]
15. Delfosse, D. Fundamentals of Functionally Graded Materials. *Mater. Today* **1998**, *1*, 18. [[CrossRef](#)]
16. Masumura, R.; Hazzledine, P.; Pande, C. Yield stress of fine grained materials. *Acta Mater.* **1998**, *46*, 4527–4534. [[CrossRef](#)]
17. Jeong, D.; Gonzalez, F.; Palumbo, G.; Aust, K.; Erb, U. The effect of grain size on the wear properties of electrodeposited nanocrystalline nickel coatings. *Scr. Mater.* **2001**, *44*, 493–499. [[CrossRef](#)]
18. Hayes, R.; Witkin, D.; Zhou, F.; Lavernia, E. Deformation and activation volumes of cryomilled ultrafine-grained aluminum. *Acta Mater.* **2004**, *52*, 4259–4271. [[CrossRef](#)]
19. Jia, D.; Ramesh, K.; Ma, E. Effects of nanocrystalline and ultrafine grain sizes on constitutive behavior and shear bands in iron. *Acta Mater.* **2003**, *51*, 3495–3509. [[CrossRef](#)]
20. Cavaliere, P. Strain Rate Sensitivity and Fatigue Properties of an Al-fe Nanocrystalline Alloy Produced by Cryogenic Ball Milling. *Multidiscip. Model. Mater. Struct.* **2007**, *3*, 225–234. [[CrossRef](#)]
21. Tabor, D. *The Hardness of Metals*; Oxford University Press: New York, NY, USA, 1951.
22. Tabor, D. The hardness of solids. *Rev. Phys. Technol.* **1970**, *1*, 145–179. [[CrossRef](#)]
23. Doerner, M.; Nix, W. A method for interpreting the data from depth-sensing indentation instruments. *J. Mater. Res.* **1986**, *1*, 601–609. [[CrossRef](#)]
24. Pharr, G.; Cook, R. Instrumentation of a conventional hardness tester for load-displacement measurement during indentation. *J. Mater. Res.* **1990**, *5*, 847–851. [[CrossRef](#)]

25. Oliver, W.; Pharr, G. An improved technique for determining hardness and elastic modulus using load and displacement sensing indentation experiments. *J. Mater. Res.* **1992**, *7*, 1564–1583. [[CrossRef](#)]
26. Field, J.; Swain, M. A simple predictive model for spherical indentation. *J. Mater. Res.* **1993**, *8*, 297–306. [[CrossRef](#)]
27. Field, J.; Swain, M. Determining the mechanical properties of small volumes of material from submicrometer spherical indentations. *J. Mater. Res.* **1995**, *10*, 101–112. [[CrossRef](#)]
28. Gerberich, W.; Nelson, J.; Lilleodden, E.; Anderson, P.; Wyrobek, J. Indentation induced dislocation nucleation: The initial yield point. *Acta Mater.* **1996**, *44*, 3585–3598. [[CrossRef](#)]
29. Bolshakov, A.; Oliver, W.; Pharr, G. Influences of stress on the measurement of mechanical properties using nanoindentation: Part II. Finite element simulations. *J. Mater. Res.* **1996**, *11*, 760–768. [[CrossRef](#)]
30. Alcalá, J.; Giannakopoulos, A.; Suresh, S. Continuous measurements of load-penetration curves with spherical microindenters and the estimation of mechanical properties. *J. Mater. Res.* **1998**, *13*, 1390–1400. [[CrossRef](#)]
31. Cheng, Y.; Cheng, C. Scaling approach to conical indentation in elastic-plastic solids with work hardening. *J. Appl. Phys.* **1998**, *84*, 1284–1291. [[CrossRef](#)]
32. Cheng, Y.; Cheng, C. Relationships between hardness, elastic modulus, and the work of indentation. *Appl. Phys. Lett.* **1998**, *73*, 614–616. [[CrossRef](#)]
33. Suresh, S.; Nieh, T.; Choi, B. Nano-indentation of copper thin films on silicon substrates. *Scr. Mater.* **1999**, *41*, 951–957. [[CrossRef](#)]
34. Gouldstone, A.; Koh, H.; Zeng, K.; Giannakopoulos, A.; Suresh, S. Discrete and continuous deformation during nanoindentation of thin films. *Acta Mater.* **2000**, *48*, 2277–2295. [[CrossRef](#)]
35. Johnson, K. The correlation of indentation experiments. *J. Mech. Phys. Solids* **1970**, *18*, 115–126. [[CrossRef](#)]
36. Suresh, S.; Alcalá, J.; Giannakopoulos, A. Depth Sensing Indentation and Methodology for Mechanical Property Measurements. U.S. Patent 6134954A, 19 June 2020.
37. Dao, M.; Chollacoop, N.; Van Vliet, K.; Venkatesh, T.; Suresh, S. Computational modeling of the forward and reverse problems in instrumented sharp indentation. *Acta Mater.* **2001**, *49*, 3899–3918. [[CrossRef](#)]
38. Giannakopoulos, A.; Larsson, P.; Vestergaard, R. Analysis of Vickers indentation. *Int. J. Solids Struct.* **1994**, *31*, 2679–2708. [[CrossRef](#)]
39. Cheng, Y.; Cheng, C. Can stress–strain relationships be obtained from indentation curves using conical and pyramidal indenters? *J. Mater. Res.* **1999**, *14*, 3493–3496. [[CrossRef](#)]
40. Giannakopoulos, A.; Suresh, S. Determination of elastoplastic properties by instrumented sharp indentation. *Scr. Mater.* **1999**, *40*, 1191–1198. [[CrossRef](#)]
41. Venkatesh, T. Determination of elasto-plastic properties by instrumented sharp indentation: Guidelines for property extraction. *Scr. Mater.* **2000**, *42*, 833–839. [[CrossRef](#)]
42. Suresh, S.; Giannakopoulos, A. A new method for estimating residual stresses by instrumented sharp indentation. *Acta Mater.* **1998**, *46*, 5755–5767. [[CrossRef](#)]
43. Bhattacharya, A.; Nix, W. Finite element simulation of indentation experiments. *Int. J. Solids Struct.* **1988**, *24*, 881–891. [[CrossRef](#)]
44. Laursen, T.; Simo, J. A study of the mechanics of microindentation using finite elements. *J. Mater. Res.* **1992**, *7*, 618–626. [[CrossRef](#)]
45. Tunvisut, K.; O’Dowd, N.; Busso, E. Use of scaling functions to determine mechanical properties of thin coatings from microindentation tests. *Int. J. Solids Struct.* **2001**, *38*, 335–351. [[CrossRef](#)]
46. Hill, R.; Storakers, B.; Zdunek, A. A theoretical study of the Brinell hardness test. *Proc. R. Soc. Lond. A Math. Phys. Sci.* **1989**, *423*, 301–330.
47. Larsson, P.; Giannakopoulos, A.; Söderlund, E.; Rowcliffe, D.; Vestergaard, R. Analysis of Berkovich indentation. *Int. J. Solids Struct.* **1996**, *33*, 221–248. [[CrossRef](#)]
48. Bazios, P.; Tserpes, K.; Pantelakis, S. Modelling and Experimental Validation of the Porosity Effect on the Behaviour of Nano-Crystalline Materials. *Metals* **2020**, *10*, 821. [[CrossRef](#)]
49. Oliver, W.; Pharr, G. Measurement of hardness and elastic modulus by instrumented indentation: Advances in understanding and refinements to methodology. *J. Mater. Res.* **2004**, *19*, 3–20. [[CrossRef](#)]
50. Chrobak, D.; Kim, K.; Kurzydowski, K.; Nowak, R. Nanoindentation experiments with different loading rate distinguish the mechanism of incipient plasticity. *Appl. Phys. Lett.* **2013**, *103*, 072101. [[CrossRef](#)]
51. Wang, Y.; Raabe, D.; Klüber, C.; Roters, F. Orientation dependence of nanoindentation pile-up patterns and of nanoindentation microtextures in copper single crystals. *Acta Mater.* **2004**, *52*, 2229–2238. [[CrossRef](#)]
52. Tadmor, E.; Miller, R.; Phillips, R.; Ortiz, M. Nanoindentation and incipient plasticity. *J. Mater. Res.* **1999**, *14*, 2233–2250. [[CrossRef](#)]
53. Zhang, J.; Zhang, J.; Wang, Z.; Hartmaier, A.; Yan, Y.; Sun, T. Interaction between phase transformations and dislocations at incipient plasticity of monocrystalline silicon under nanoindentation. *Comput. Mater. Sci.* **2017**, *131*, 55–61. [[CrossRef](#)]
54. Fischer-Cripps, A. A simple phenomenological approach to nanoindentation creep. *Mater. Sci. Eng. A* **2004**, *385*, 74–82. [[CrossRef](#)]
55. Elmustafa, A.; Stone, D. Nanoindentation and the indentation size effect: Kinetics of deformation and strain gradient plasticity. *J. Mech. Phys. Solids* **2003**, *51*, 357–381. [[CrossRef](#)]
56. Karthik, V.; Visweswaran, P.; Bhushan, A.; Pawaskar, D.; Kasiviswanathan, K.; Jayakumar, T.; Raj, B. Finite element analysis of spherical indentation to study pile-up/sink-in phenomena in steels and experimental validation. *Int. J. Mech. Sci.* **2012**, *54*, 74–83. [[CrossRef](#)]

57. Biener, M.; Biener, J.; Hodge, A.; Hamza, A. Dislocation nucleation in bcc Ta single crystals studied by nanoindentation. *Phys. Rev. B* **2007**, *76*, 165422. [[CrossRef](#)]
58. Morris, J.; Bei, H.; Pharr, G.; George, E. Size Effects and Stochastic Behavior of Nanoindentation Pop In. *Phys. Rev. Lett.* **2011**, *106*. [[CrossRef](#)]
59. Hasnine, M.; Mustafa, M.; Suhling, J.; Prorok, B.; Bozack, M.; Lall, P. Characterization of aging effects in lead free solder joints using nanoindentation. In Proceedings of the 2013 IEEE 63rd Electronic Components and Technology Conference, Las Vegas, NV, USA, 28–31 May 2013; pp. 166–178. [[CrossRef](#)]
60. Lucas, B.; Oliver, W. Indentation power-law creep of high-purity indium. *Metall. Mater. Trans. A* **1999**, *30*, 601–610. [[CrossRef](#)]
61. Zhang, P.; Li, S.; Zhang, Z. General relationship between strength and hardness. *Mater. Sci. Eng. A* **2011**, *529*, 62–73. [[CrossRef](#)]
62. Hay, J.; Agee, P.; Herbert, E. Continuous stiffness measurement during instrumented indentation testing. *Exp. Tech.* **2010**, *34*, 86–94. [[CrossRef](#)]
63. Chen, X.; Xiang, Y.; Vlassak, J. Novel technique for measuring the mechanical properties of porous materials by nanoindentation. *J. Mater. Res.* **2006**, *21*, 715–724. [[CrossRef](#)]
64. Innovative Coarsening-Resistant Alloys with Enhanced Radiation Tolerance and Ultrafine-Grained Structure for Aerospace Application | ICARUS. Available online: <http://icarus-alloys.eu> (accessed on 14 June 2020).
65. Bazios, P.; Tserpes, K.; Pantelakis, S. Numerical Computation of Material Properties of Nanocrystalline Materials Utilizing Three-Dimensional Voronoi Models. *Metals* **2019**, *9*, 202. [[CrossRef](#)]
66. Breval, E.; Macmillan, N. Elastic recovery at Vickers hardness impressions. *J. Mater. Sci. Lett.* **1985**, *4*, 741–742. [[CrossRef](#)]
67. Suresh, S.; Giannakopoulos, A.; Alcalá, J. Spherical indentation of compositionally graded materials: Theory and experiments. *Acta Mater.* **1997**, *45*, 1307–1321. [[CrossRef](#)]
68. Suresh, S.A.; Giannakopoulos, A. *Report Inst-2/98*; Massachusetts Institute of Technology: Cambridge, MA, USA, 1998.
69. ISO/TR 29381. *Metallic Materials—Measurement of Mechanical Properties by an Instrumented Indentation Test—Indentation Tensile Properties*; ISO: Geneva, Switzerland, 2008.
70. ISO 14577. *Metallic Materials—Instrumented Indentation Test for Hardness and Materials Parameters, Part 1: Test Method, 2002, Part 2: Verification and Calibration of Testing Machines, 2002, Part 3: Calibration of Reference Blocks, 2002, Part 4: Test Method for Metallic and Non-Metallic Coatings*; ISO: Geneva, Switzerland, 2007.
71. Bouzakis, K.; Michailidis, N.; Hadjiyiannis, S.; Skordaris, G.; Erkens, G. The effect of specimen roughness and indenter tip geometry on the determination accuracy of thin hard coatings stress–strain laws by nanoindentation. *Mater. Charact.* **2002**, *49*, 149–156. [[CrossRef](#)]
72. Available online: <http://www.horizonindia.in/buehler/grinders-polishers/3-BUEHLERVANGUARD.pdf> (accessed on 31 October 2021).
73. Michailidis, N.; Pappa, M. Application of strength properties determined by nanoindentations to describe the material response in micro- and macro-indentation. *CIRP Ann.* **2009**, *58*, 511–514. [[CrossRef](#)]
74. Michailidis, N.; Bouzakis, K.; Koenders, L.; Herrmann, K. *Nanoindentation, CIRP Encyclopedia of Production Engineering*; Springer: Berlin/Heidelberg, Germany, 2014; pp. 1–9.
75. Lichinchi, M.; Lenardi, C.; Haupt, J.; Vitali, R. Simulation of Berkovich nanoindentation experiments on thin films using finite element method. *Thin Solid Films* **1998**, *312*, 240–248. [[CrossRef](#)]

Review

# Machinable Leaded and Eco-Friendly Brass Alloys for High Performance Manufacturing Processes: A Critical Review

Paul Stavroulakis <sup>1</sup>, Anagnostis I. Toulfatzis <sup>2</sup>, George A. Pantazopoulos <sup>2,\*</sup> and Alkiviadis S. Paipetis <sup>3</sup>

<sup>1</sup> Sir Robert Hadfield Building, Department of Materials Science and Engineering, The University of Sheffield, Mappin St., Sheffield S1 3JD, UK; ppstavroulakis1@sheffield.ac.uk

<sup>2</sup> ELKEME Hellenic Research Centre for Metals S.A., 61st km Athens—Lamia National Road, 32011 Oinofyta, Greece; atoulfatzis@elkeme.vionet.gr

<sup>3</sup> Department of Materials Science and Engineering, University of Ioannina, 45110 Ioannina, Greece; paipetis@cc.uoi.gr

\* Correspondence: gpantaz@elkeme.vionet.gr; Tel.: +30-2262-60-4463

**Abstract:** The recent environmental/health and safety regulations placed restrictions of use of hazardous substances on critical manufacturing sectors and consumers' products. Brass alloys specifically face a challenging issue concerning the elimination of lead (Pb) which has been a critical element affecting both the machinability and overall quality and efficiency of their manufacturing process. The adaptation of novel materials and processing routes in the green economy constitutes a crucial decision for competitive business and industry growth as a worldwide perspective with substantial industrial and social impact. This paper aims to review the emergent innovative and sustainable material solutions in the manufacturing industry, in line with environmental regulations, by highlighting smart alloy design practices and promoting new and innovative approaches for material selection and manufacturing process optimisation. In this review we analyse the processing, structure and machinability aspects of leaded brasses and underline the major guidelines and research methodologies required to overcome this technical challenge and further improve the mechanical properties and machinability of lead-free brass alloys. Various alloying and processing strategies were reviewed together with the most important failure types, as they were extracted from the existing industrial and technological experience, covering more than 20 years of research in this field.

**Keywords:** leaded brasses; lead-free brasses; eco-friendly; machinability; brass failures; design-of-experiments

**Citation:** Stavroulakis, P.; Toulfatzis, A.I.; Pantazopoulos, G.A.; Paipetis, A.S. Machinable Leaded and Eco-Friendly Brass Alloys for High Performance Manufacturing Processes: A Critical Review. *Metals* **2022**, *12*, 246. <https://doi.org/10.3390/met12020246>

Academic Editor: Joao Paulo Davim

Received: 13 December 2021

Accepted: 24 January 2022

Published: 27 January 2022

**Publisher's Note:** MDPI stays neutral with regard to jurisdictional claims in published maps and institutional affiliations.



**Copyright:** © 2022 by the authors. Licensee MDPI, Basel, Switzerland. This article is an open access article distributed under the terms and conditions of the Creative Commons Attribution (CC BY) license (<https://creativecommons.org/licenses/by/4.0/>).

## 1. Introduction

Cu–Zn alloys (brasses) are widely used industrial materials because of their superior properties such as high corrosion resistance, low friction coefficient, non-magnetism, good plastic deformability (forgeability) and machinability [1–4]. Lead (Pb) has been commonly added to brass alloys to ensure pressure tightness and improve the machinability of the alloy, directly affecting cutting-tool life [5–7]. Owing to its low solidification temperature, lead acts as a filler for micropores that form during casting. Subsequently, these lead particles improve the machinability of brasses through their dual functionality as a lubricant and a stress concentration point, promoting the formation of small discontinuous chips and minimising tool wear [8]. As such, leaded brasses have seen use in a wide range of applications such as the base screw machine material for architectural hardware, cosmetics, musical instruments, screw machine parts, valves, fitting and general fasteners, while also being extensively used for plumbing applications [9]. Nevertheless, the health hazards associated with lead resulted in the implementation of stricter regulations for permissible lead content levels in brass products. More specifically, as leaded brasses have been extensively used for plumbing applications, particulate lead could be traced in drinking water due to the gradual corrosion of the brass components. Additionally, particles originating from

solders used in plumbing led to the further contamination of the potable water supply. The gradual intake of particulate lead would elevate the blood lead levels, eventually leading to poisoning with devastating effects to human health. These include slower cognitive development in children, hypertension and even renal failure [10–16]. Thus, the development of lead-free brasses became a focal research point to ensure compliance with the regulatory standards and improve quality of life [17,18].

From a purely manufacturing–economic standpoint, substitution of lead-containing brass with a lead-free alternative does not appear to be an economically viable option, but it is technically possible, satisfying the requirements of the enforced legislation [19]. As such, efforts were made into incorporating soft second phase particles (SPPs) in the microstructure of copper–base alloys to attain the positive effects of Pb. Soft SPPs reduce shear ductility allowing for the formation of small chips, resulting in lesser machining power demands and a temperature reduction in the cutting tool, extending tool life. Such particles also reduce the shear strength of the brass at the secondary shear zone through the provision of internal lubrication, improving surface finish and further reducing the forces applied on the cutting tool [20]. In turn, this challenge sparked significant interest for the development of brass systems that enable the formation of said particles through the incorporation of various alloying elements such as bismuth (Bi), graphite, magnesium (Mg) silicon (Si), tin (Sn) and titanium (Ti) [21–23]. C. Yang et al. proposed the development of novel brass compositions by including beta ( $\beta$ ) phase stabilisers and solid-solution strengtheners while simultaneously reducing the Zn content to enable the manifestation of high-strength and proper machinability [24]. The main drawback of these design routes however is the deviation from standardised compositions, requiring for additional approval requirements by International Organizations and Regulatory Authorities to be adopted in the supply chain. An alternative pathway towards improving the machinability of lead-free brasses through optimising the heat-treatment process of standardised compositions was proposed and investigated by Toulfatzis et al. [25]. This is achieved through a partial or complete suppression of the beta ( $\beta$ ) to alpha ( $\alpha$ ) phase transformation by water quenching post heat-treating, resulting in beta-dominant microstructures. This microstructural modification allows for a shift in the fracture mechanism enabling intergranular fracture, thus promoting easier chip breaking and lower power consumption [26]. However, although interesting in nature, both approaches to this technical challenge are still in their infancy and require further development before they meet industrial implementation. It is thus equally as important to investigate both novel alloy design approaches that yield suitable material properties and their viability for incorporation in an industrial manufacturing process.

The primary microstructural features of conventional and modern brass rods have been extensively highlighted and discussed in relation to behaviour during machining [27]. Factors such as the chip size, cutting tool type and wear, cutting force, surface roughness and testing methodology play an important role in the optimisation of cutting processes in terms of time and cost [28–30]. In this direction, optimisation algorithms have been applied to investigate the optimal number of passes and the corresponding parameters such as speed, feed rate and depth of cut in each pass for multi-pass and multi-criterion plain turning problems [31]. This optimisation could be achieved by fractional factorial designs, preventing any potential complications arising from the use of analysis of variance (ANOVA) even in small samples [32,33]. The machinability of various alloys can also be reviewed, evaluated, and optimised using neural networks; however, noise factors generated during the machining process are known to cause errors in such computational efforts [34,35]. Therefore, it becomes clear that a precise data extraction process needs to be facilitated, minimising the relevant noise factors to enable more advanced computational tools. As such, the introduction of automated image processing tools would be beneficial to aid the data acquisition process especially in cases where segmented chip formation is observed [36]. The methodology of Taguchi Design of Experiments (DOE) applied using orthogonal arrays is very efficient in statistics for small sampling rates, constituting an optimisation technique for improving reliability [37,38]. Fractional factorials in robust de-

sign methodology designs have been extensively reviewed by Arvidsson and Gremyr [39]. The fundamental principle of robust design is to improve the quality of a product through minimising the property variation causes without their exclusive elimination [40]. This can be achieved by a joint product-process optimisation to disassociate the end-properties from the various causes of variation. As reported by Manna and Bhattacharyya, these causes were affected due to the noise factors associated with parameter design [40]. In their work, the signal to noise factor was used as a measure of the quality, and orthogonal arrays were used to study many design parameters simultaneously. Various examples of similar scientific work based on the practical design of experiments (DOE) methodology have been published in recent years [41]. These investigations considered the size of the experiments, the applied design, the number of factors that influenced the response variable and the sector of application of the experimental design. Viles et al., presented a real case of design of experiments focusing on the preliminary stages of experimentation, e.g., how to choose the best response analysis, how to evaluate the crucial factors and what the data sample collection should be [42]. Engineers may encounter key barriers in their trial to use DOE methodologies, so an exhaustive literature review was performed to classify these barriers [43]. Numerous scientific articles have verified that there is a gap between theoretical development of DOE and its effective application in industry [44]. Therefore, a simple methodology was proposed to facilitate the implementation of DOE in companies, through a framework that follows the traditional DMAIC (Define–Measure–Analyse–Improve–Control) steps of ‘Six Sigma’ as a generic problem-solving methodology.

In this paper, a brief and concise review of conventional leaded (Pb-ed) as well as modern lead-free (Pb-free) brass alloys was realised, evaluating the alloys in terms of their microstructure, mechanical properties and machinability. The principles governing the manifestation of an optimal combination of properties in leaded brasses are laid out in detail to be used as a foundation for novel lead-free brass development, evaluation and optimisation. Furthermore, the state of the art concerning novel lead-free brass design is presented and summarised to facilitate the benefits and drawbacks associated with each material design approach. We believe that highlighting the efforts of various research groups around the globe concerning brass design, thermomechanical processing and machining is a crucial step for tackling this critical technical challenge. The introduction of innovative and sustainable material solutions in the manufacturing industry that are aligned with environmental/health and safety regulations. To the best of the authors’ knowledge, no such updated and comprehensive review focused on machinable brass alloys has been published so far. The authors’ team incorporate long term expertise in the field of research of copper and copper alloys processing and properties counting more than 20 years, where a considerable amount of papers have been published and reviewed in the current study.

## 2. Chemical Composition of Leaded and Lead-Free Brass Alloys

The elemental chemical analysis of the alloys presented within our work and the related references are listed in Tables A1–A9 (Appendix A).

## 3. Microstructure, Mechanical Properties and Processing Relationships

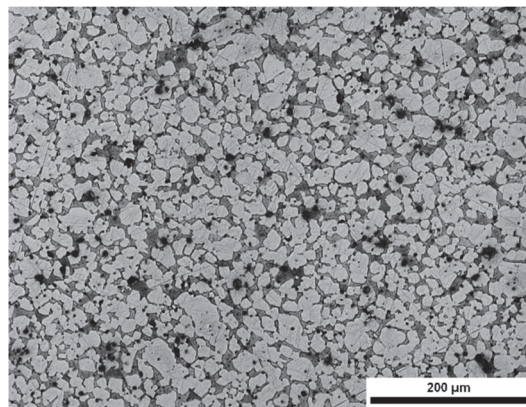
### 3.1. Leaded Brasses

#### 3.1.1. Microstructure

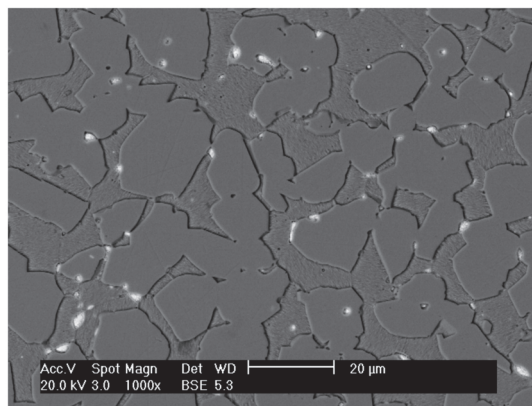
The phase structure of leaded (Pb) brass alloys is governed by a variety of mechanisms. As mentioned previously, Pb addition in conventional brass alloys serves to improve their machinability. Pb preferred accumulation sites are mainly the  $\alpha/\beta$  interphase boundaries (Figure 1). Depending upon the casting and thermomechanical process (TMP) parameters, Pb as a liquid phase during metal forming tends to reduce its surface energy by attaining a spherical shape [27]. To further minimize their interfacial energy, the Pb globules coalesce, forming coarse islands arranged at the  $\alpha/\beta$  interfaces. Pb coalescence increases mean particle size and reduces the Pb particle distribution density, with an adverse effect on



machinability [27]. On the contrary, fine and uniform lead distribution enables superior machining behaviour through better chip fracturing and minimises tool wear, while an increased volume fraction of Pb or a non-uniform particle distribution may cause surface cracking during hot working due to hot-shortness [45]. However, hot shortness can also be induced from the excess heat generated in the brass billet from the friction between the brass billet and the container during the extrusion process [25]. As mentioned, the  $\alpha/\beta$  interphase boundaries constitute high interfacial energy sites and thus potential Pb accumulation areas [27,46,47]. When machined, an  $(\alpha + \beta)$ -brass has better chip breaking properties than a pure  $\alpha$ -alloy. Further machinability improvements are attained by increasing the length of interphase boundaries, which in turn depends on the  $\beta$ -phase content and the size of the  $\alpha$ -phase crystals. Higher  $\beta$ -phase volume fraction and finer  $\alpha$ -crystals (for a constant  $\alpha$ -phase content) tend to create longer interphase boundaries acting as Pb concentration sites [27,48]. Therefore, lower temperatures would be used during an extrusion process to enable the formation of extended  $\alpha/\beta$  interfaces, an increase in strength and improve the machinability [47,48]. As Pb forms near the end of the solidification process, its particle size and distribution are primarily affected by the casting and solidification conditions, while the phase structure (volume fraction, grain size) is mainly influenced by the extrusion conditions (e.g., temperature, extrusion ratio, speed and cooling rate) [49].



(a)



(b)

**Figure 1.** (a) Optical micrograph and (b) SEM micrograph showing the typical microstructure of CuZn39Pb3 (CW614N) brass [50].

### 3.1.2. Thermomechanical Processing

The sawing performance of brass bars (CuZn39Pb3) and its relationship to Pb particle size, distribution and the phase structure was reported in a previous study [49]. In this work the presence of  $\beta$ -phase reduced the overall ductility of the alloy and therefore enhanced the segmentation of the machining chips. Holler et al. examined the influence of the extrusion parameters on the phase structure in CuZn40Pb2 [51]. They showed that the percentage of  $\beta$ -phase decreased with an increasing billet temperature and extrusion ratio, while the grain size decreased with decreasing billet temperature and increasing extrusion ratio. Both the grain size and  $\beta$ -phase fraction were less influenced by the extrusion speed. Nevertheless, a study by Loginov et al. concluded that brasses with compositions similar to those mentioned above could benefit greatly from increasing the extrusion temperature to 780–800 °C as the TMP would be taking place entirely within the beta single phase region ensuring better property uniformity [52]. Kunčická et al. further highlighted the importance of maintaining controlled manufacturing processes by studying the failure of CuZn40Pb2 brass fittings from a computational and experimental standpoint. They unveiled that an inhomogeneous temperature profile during the manufacturing process may produce residual stresses in the cooler regions and initiate undesired phase transformations which eventually lead to the manifestation of forming defects [53]. In another case, they investigated a hot-die forged component [53,54]. There, failure originated from a region characterised by plastic flow instability and inhomogeneous stress distribution deeming the area prone to the generation of defects. The cracked region was also characterised by a localised depletion of  $\beta$  phase in favour of the formation of the  $\alpha$  phase, thus decreasing the ductility. Sub-micron oxide particles were also present within the crack which were detrimental for the ductility and the cohesive toughness of the material [55].

According to Pantazopoulos and Vazdirvanidis, the beta ( $\beta$ ) phase formed in the CuZn39Pb3 alloy may exhibit a characteristic plate-like type morphology possessing different orientations among the various grains [27]. Such morphological characteristics may be considered beneficial for chip-breaking during the machining process. Chandra et al. investigated the intergranular and interphase cavitation in binary alpha/beta brass at 600 °C during superplastic deformation [56]. The process of cavitation was associated with grain boundary sliding. Cavity nucleation occurred at points of stress concentration and such as the sliding interfaces between  $\alpha$ - $\beta$  boundaries rather than on  $\alpha$ - $\alpha$  and  $\beta$ - $\beta$  interfaces [56]. Hentati et al. investigated an incidence of cracking of CuZn39Pb2 during hot forging [57]. The forgeability of the alloy was significantly affected by the work hardening capacity. A decrease in ductility was observed as a result of work hardening and  $\alpha$ -phase size reduction during a hot stamping process at 750 °C. Microhardness tests confirmed that stamping increased the brass hardness, while the size of  $\alpha$ -phase also decreased. The reduction in  $\alpha$ -crystal size and subsequent hardness increase degraded the ductility of the material, causing cracks during the forming process. Such cracks could have been caused from residual stresses generated during TMP. On the other hand, a heat treatment at 300 °C for 1 h had a positive contribution in both tackling the cracking problem and enabling an increase in elongation to fracture up from 22% to 28% [57]. Blaz et al. showed that the reduction in the flow stress during hot deformation of a CuZn39Pb3 alloy resulted from dynamic recovery and dynamic recrystallisation occurring during operation above ~677 °C [58]. Fine Pb particles did not fully inhibit the grain coarsening during dynamic recrystallisation at higher deformation temperatures. During hot deformation above ~727 °C,  $\alpha \rightarrow \beta$  phase transformation was found to overlap with the structural softening process, resulting in effective grain coarsening followed by effective flow stress reduction. All of the cases presented here further strengthen the fact that attaining a proper microstructure, appropriate mechanical properties and avoid in-process defects or failures heavily depends on the careful control of the TMP.

### 3.1.3. Mechanical Behaviour

Pantazopoulos and Toulfatzis studied the mechanical behaviour and fracture mechanisms of conventional leaded brasses [59]. A comparison between the CuZn39Pb3 and CuZn36Pb2As brasses showed that the former contained a significantly higher volume fraction of the  $\beta$ -phase than the latter. The beta ( $\beta$ )-phase (CuZn) is an ordered intermetallic phase possessing a body-centred cubic (BCC) crystal structure. This phase is characterised by a higher hardness but less ductility compared to the  $\alpha$ -phase which refers to a Cu-based solid solution with the face-centred cubic (FCC) crystal structure. Therefore, the CuZn39Pb3 brass which is a dual phase ( $\alpha + \beta$ ) brass containing ~35%  $\beta$ -phase exhibits higher strength, hardness and lower total elongation than the near single  $\alpha$ -phase CuZn36Pb2As brass. As expected, the CuZn39Pb3 brass had higher yield strength and tensile strength, but lower elongation compared to the CuZn36Pb2As brass [46]. Upon investigating the side views of the fractured specimens in tension, a ductile fracture mechanism was uncovered in both compositions. The reduction in area was also higher in the CuZn36Pb2As brass compared to CuZn39Pb3, indicating that post-uniform elongation was more pronounced for the CuZn36Pb2As brass [46]. This deviation between the two specimens was attributed to a more extended region of non-uniform elongation in the case of the CuZn36Pb2As brass and was indicative of pronounced post-necking deformation during tensile testing. As the microstructure of the aforementioned specimen consisted primarily of  $\alpha$ -phase grains with a uniform distribution of a small percentage of  $\beta$ -phase, it was found to be more resistant to micro-void growth and coalescence under tri-axial stress leading to substantially higher post-uniform elongation and higher reduction of area during necking [59]. Hardness measurements indicated a more homogeneous hardness profile (lower hardness gradient) to CuZn39Pb3 brass compared to the CuZn36Pb2As brass [46]. In this research, the CuZn39Pb3 alloy was characterized by higher hardness values (core ~136 to surface ~149 HV) as compared to CuZn36Pb2As (core ~104 to surface ~136 HV). The topographic features of tensile fracture surfaces of CuZn39Pb3 and CuZn36Pb2As alloys were studied using Scanning Electron Microscopy [59]. In this study, a mixed-mode fracture combining dimple formation and planar faceted fracture induced by a quasi-cleavage process was identified in the case of CuZn39Pb3 alloy. On the other hand, the CuZn36Pb2As alloy exhibited a typical ductile fracture consisting of fine equiaxed dimples. Pantazopoulos investigated the mechanical properties of the CuZn39Pb3 leaded brass [8]. Appreciable ductility was observed prior to fracture through the formation of a localised neck. The subsequent fracture was primarily ductile, and the resulting matched surfaces consisted of interconnected shear cracks. The final metal forming process, cold drawing, led to hardness inhomogeneities due to heterogeneous plastic deformation between the surface and core [8]. Tensile testing at higher temperatures during quasi-static and static loading revealed that the flow stress decreased proportionally to the testing temperature which was expected. The presence of brittle phases (such as  $\beta'$ ) together with their morphology is also related to better machinability [60]. Nevertheless, a significant decrease in the ductility between 200 and 400 °C was observed, owing to the partial or complete melting of Pb [46]. Moreover, the strain rate sensitivity index increased proportionally to the testing temperature without enabling relevant increases in ductility to take place due to the hot-shortness mechanism [61].

Generally, copper alloys tend to exhibit a reduction in ductility between 300 and 600 °C through a phenomenon called intermediate temperature embrittlement (ITE). This is due to a change in the involved fracture mechanism from transgranular to intergranular fracture as exposure to intermediate temperatures enables grain boundary voiding. Eventually, the ductility of the alloy is restored once the intermediate temperature range is exceeded, enabling dynamic recrystallisation and an operative grain boundary mobility. This effect is enhanced by the presence of alloying elements in the grain boundaries that reduce their structural integrity by encouraging void generation and growth along grain boundaries [62]. In the case of leaded brasses, however, this effect is further amplified due to the synergistic effect of liquid metal embrittlement (LME) where, as previously seen, the partial or complete

melting of lead may introduce a liquid phase between crack faces. As such, the local cohesion of the alloy is modified and the kinetics of dynamic embrittlement related to ITE are accelerated as the presence of the liquid phase promotes the rapid diffusion of impurities and void mobility within the grain boundaries [62,63].

The mechanical behaviour of CC763S brass during cyclic loading was investigated by Flegeau et al. under torsional stress. They pinpointed that the fracture mechanism consisted of both ductile and brittle characteristics, with crack growth taking place along  $\alpha/\beta$  grain boundaries where the concentration of intermetallic compounds and pores was the highest. Generally, a higher dislocation density was identified in the interphase  $\alpha/\beta$  boundaries, while  $\alpha$  grains remained relatively vacant of dislocations. Subsequently, the interphase boundaries were deemed as the crack nucleation points [64]. In their investigation, Johansson et al. also highlighted the interesting mechanical properties of the CW724R brass compared to the CW614N. The alloy was characterised by  $R_{p0.2}$  and  $R_m$  values of 441.4 MPa and 811.9 MPa, respectively, compared to 254.9 MPa and 561.5 MPa for the high-lead counterpart while retaining similar levels of ductility.

### 3.2. Eco-Friendly Brasses (Pb-Free)

#### 3.2.1. Novel Lead-Free Brasses

The absence of Pb and potentially other alloying elements directly affects the microstructure of Pb-free brasses. As such, the introduction of soft intermetallic phases that could imitate the effects caused by Pb particles in leaded brasses became a focal research point. The addition of iron (Fe) alongside silicon (Si) was investigated by Johansson et al. [65], attempting to formulate a low-Pb variant of the CW614N brass. Although, the  $Fe_4Si$  intermetallics were formulated, their intergranular precipitation points did not enable similar effects as in the case of Pb to come into play [65]. Atsumi et al. investigated a high-strength brass (Cu-40% Zn) alloy with magnesium (Mg) fabricated through a powder technology process to uncover the effect of the Mg addition on the microstructural properties of extruded  $\alpha$ - $\beta$  duplex brass alloys [23]. In this work, pre-mixed Cu-40% Zn alloy powder with 0.5–1.5 mass% pure Mg powder (Cu-40% Zn + Mg) was consolidated using spark plasma sintering (SPS). The SPSed Cu-40% Zn + Mg specimens consisted of  $\alpha$ - $\beta$  duplex microstructure containing  $Mg(Cu_{1-x}Zn_x)_2$  intermetallic compounds (IMCs) with a mean particle size of 10–30  $\mu m$ . Initially, Mg was completely dissolved in the  $\alpha$ - $\beta$  duplex phases through a heat-treatment at 700 °C for 15 min. Thus, to disperse fine IMCs on  $\alpha$ - $\beta$  duplex phase matrix, the SPSed Cu-40% Zn + Mg specimens were pre-heated to achieve a solid solution condition and were afterwards immediately extruded. They studied the tensile properties of the extruded Cu-40% Zn + 1.0% Mg brass and reported an average yield strength (YS) of 328 MPa, ultimate tensile strength (UTS) of 553 MPa and elongation of 25% [66]. The extruded Cu-40% Zn + 1.0% Mg alloy outperformed the conventional binary brass alloy, exhibiting 229 MPa yield strength (YS) and 464 MPa ultimate tensile strength (UTS). The strengthening mechanism of this wrought brass alloy was attributed to the grain refinement due to the pinning effect produced by the fine  $Mg(Cu_{1-x}Zn_x)_2$  precipitates forming at interphase boundaries. The extruded specimen exhibited fine  $\alpha$ - $\beta$  duplex phases containing very fine precipitates of the above  $Mg(Cu_{1-x}Zn_x)_2$  IMCs with 0.5–3.0  $\mu m$  in diameter [66]. The fracture surfaces of both extruded specimens consisted of fine dimples owing to the evident extremely fine  $\alpha$ - $\beta$  duplex phase structures. The hills and valleys of the extruded Cu-40% Zn fracture surface indicated that the crack paths preferentially followed the primary powder particle interface region. On the other hand, such hills and valleys were never observed in the extruded Cu-40% Zn + 1.5% Mg specimen; however, some fine particles were observed on the fracture surface [66]. Atsumi et al. also investigated the microstructural properties of the Cu-40Zn-0.5Ti ternary alloys having undergone a solid solution treatment [23]. The specimen was pre-heated at 700 °C for 15 min and subsequently extruded consisting of a fine and uniform  $\alpha$ - $\beta$  duplex phase structure with an average grain size of 2.14  $\mu m$ . Furthermore, fine Ti-based particles with a mean size of 0.5  $\mu m$  were densely dispersed in the matrix [23]. Atsumi et al. reported

that the extruded Cu-40%Zn-0.5 Ti alloy had a mean yield strength of 304 MPa, ultimate tensile strength of 543 MPa and elongation of 44% [23]. Cu-40%Zn-0.5Ti brasses revealed satisfactory strength and good ductility. The high strength of the wrought brass alloy was mainly due to the fine grain size of  $\alpha$  and  $\beta$  phases caused by the precipitation of fine Ti-based particles at the grain boundaries [23]. In a previous research Li et al. reported that remarkable grain-refinement and strengthening effects were achieved by the addition of Ti to 60/40 brass through a powder metallurgy process route [67]. However, Ti segregated to the powder particle interface at elevated temperatures, significantly deteriorating the mechanical properties of the BS40–1.0Ti. To inhibit this segregation behaviour of the Ti in the BS40–1.0Ti, the addition of Sn was investigated. Ti was incorporated in the formation of CuSn<sub>3</sub>Ti<sub>5</sub> particles at the grain boundaries, rather than segregating at the powder particle interface, leading to significant grain refinement and enabling strengthening effects on the BS40–0.6Sn1.0Ti brass. These results showed that the introduction of Sn via powder metallurgy to BS40–1.0Ti brass can effectively impede the segregation of Ti and stabilise the mechanical properties at high processing temperatures [67].

An investigation attempting to introduce both Ti and graphite (Gr) to the Cu-40Zn brass showed that the sole addition of Gr to the alloy would yield a better cutting performance alongside a progressive deterioration of the mechanical properties. Nevertheless, the combination of both additives should enable precipitation and dispersion strengthening mechanisms to manifest through the formation of nano Ti clusters and Cu<sub>2</sub>Ti<sub>4</sub>O particles, thus maintaining reasonable mechanical properties [68]. The concept of Gr globules incorporation as a microstructural constituent was previously studied by Zhuo et al. through the introduction of cementite (Fe<sub>3</sub>C) particles in the alloy and a subsequent heat treatment to enable the Fe<sub>3</sub>C to undergo a graphitisation process [69]. Si has also been extensively investigated as an alloying addition to replace Pb. It acts as a  $\beta$  and  $\beta'$  phase stabiliser and enables the formation of Widmanstätten-type  $\alpha$  phase nucleating from the  $\beta$  interface. Moreover, conducting a solution heat treatment followed by water quenching would further suppress the diffusional nature of the  $\beta \rightarrow \beta'$  transformation, resulting in a martensitic transformation instead. The ease of this process is directly related to the Si content. This concept was explored by Alirezaei and Doostmohammadi and used to design a high-hardness Cu30Zn-Si brass [70]. For the design of novel Pb-free brasses the Zn equivalent rule has been used extensively to predict the formulating phases in said alloys (Equation (1)) [24,71].

$$X(\%) = 100\% \frac{(C_{Zn} + \sum C_i \cdot K_i)}{(C_{Zn} + C_{Cu} + \sum C_i \cdot K_i)} \quad (1)$$

where  $X\%$  is the fictitious zinc equivalent,  $C_{Zn}$  and  $C_{Cu}$  the Zn and Cu contents in the specific alloy of interest and  $\sum C_i \cdot K_i$  the sum of the products of content  $C_i$  and the fictitious Zn equivalent  $K_i$  of each alloying element. As such, dual phase or single-phase brasses can be designed and compositionally fine-tuned to achieve an ideal combination of properties. Yang et al. used this approach to design an  $\alpha + \beta$  Cu-39Zn-Si-Al brass and manufacture it through low-pressure die casting (LPDC). By altering the processing parameters, they were able to significantly alter the average grain size of the  $\beta$  phase and the morphology of the  $\alpha$  phase. Their investigation led to the design of a microstructure consisting of fine  $\beta$  grains and a higher content of rod-like or granular  $\alpha$  phase allowing for the manifestation of superior mechanical properties, namely a YS of 359.8 MPa, UTS of 598.9 MPa and an elongation of 15%. Nevertheless, the present composition has not been evaluated in terms of machinability [72]. Expanding upon the concept of Al and Si-containing brasses, D. Suksongram et al. sought to create a high-hardness dual-phase  $\beta + \gamma$  CuZnSiAlSn brass through the addition of antimony (Sb). According to their research, increasing amounts of Sb up to 1.5 wt.% would enable the inter and intragranular formation of increased amounts of  $\gamma$  phase to the  $\beta$  phase resulting in a significant hardness increase. This could be attributed to an increased solid solution strengthening effect taking place due to the incorporation of Sb within the  $\gamma$  phase. Nonetheless, upon reaching 2.0 wt.% Sb content, a

high-Sb intermetallic phase would form, reducing the hardness of the investigated alloying system by roughly 17% [73].

Chandra et al. found that both the ductility as well as the flow stress of  $\alpha$ - $\beta$  brass is significantly affected by the addition of Cerium (Ce) [74]. Ce decreased the solubility of Zn in the  $\alpha$  (FCC) phase between 475 °C and 675 °C, consequently shifting the  $\alpha/(\alpha + \beta)$  region of the phase diagram towards lower Zn concentrations. More specifically, the addition of 0.07 wt.% of Ce decreased the  $\alpha/\beta$  ratio from 70:30 to 55:45, improving the ductility and decreasing the flow stress up to a factor of three, at the tested temperature range. Moreover, the hindering effect of Ce addition on Zn solubility indirectly contributed to an expected increase in stacking fault energy (SFE) of the  $\alpha$ -phase, improving dislocation mobility. Atsumi et al. investigated the mechanical properties of the high-strength, Pb-free machinable  $\alpha$ - $\beta$  duplex phase Cu-40Zn-Cr-Fe-Sn-Bi alloys [75]. The extruded Cu-40Zn-Cr-Fe-Sn-Bi alloys consisted of  $\alpha$ - $\beta$  phases containing the fine, uniform Cr-Fe IMCs and Bi particles. The average yield strength (YS) and ultimate tensile strength (UTS) of the extruded Cu-40Zn-Cr-Fe-Sn-Bi alloys were 288 MPa and 601 MPa, respectively. These alloys exhibited YS and UTS that were 29% and 40% higher than that of conventional machinable brass Cu-40Zn-Pb alloy. The extruded Cu-40Zn-Cr-Fe-Sn-Bi alloys also maintained 75% of the machinability of the Cu-40Zn-Pb alloy [23]. Fontaine and Keast, compared a lead-free Bi-containing brass (EnviroBrass C89520) to a conventional brass C84400 [5]. In this work, the large difference in grain size was attributed to the dependence of grain growth on alloy chemistry, while the excess concentration of Sn around the particles and at the grain boundaries was due to 'coring', a well-documented phenomenon. However, the presence of Sn prevented the segregation of Bi to the grain boundaries and inhibited hot-tearing phenomena during processing involving Bi segregation. It was not clear at this stage how the presence of Sn prevented the segregation of Bi. Either the wetting behaviour of Bi was different in a Cu-Sn alloy than in pure copper or an excess of Sn at the boundaries prevented the segregation of Bi. Scanning transmission electron microscopy (STEM) coupled with electron dispersive X-ray spectroscopy (EDS) did uncover traces of Bi segregation at the boundaries in the brass, even though Bi segregates strongly in pure copper alloys [5]. Further analysis regarding the Bi addition as a possible replacement for Pb was conducted by Thomson et al., who modified the C93700 to replace Pb with Bi. Bi was noted to accomplish a similar role as that of Pb in the present alloying system. Indeed, Bi proved to be a possible replacement, achieving similar mechanical properties as the Pb case. Increased amounts of Bi would be detrimental for the mechanical properties instead. Nevertheless, the morphological characteristics of Bi deem it inferior to Pb by comparison, specifically for bearing applications. The Pb-containing alloy also exhibited greater fatigue resistance compared to the Bi cases. Lastly, tribological testing showed that the Bi-containing compositions induced higher friction forces than those encountered in the Pb-containing alloy. However, the friction forces of the Bi-containing compositions showed less fluctuation compared to that encountered in the Pb-containing alloy [76].

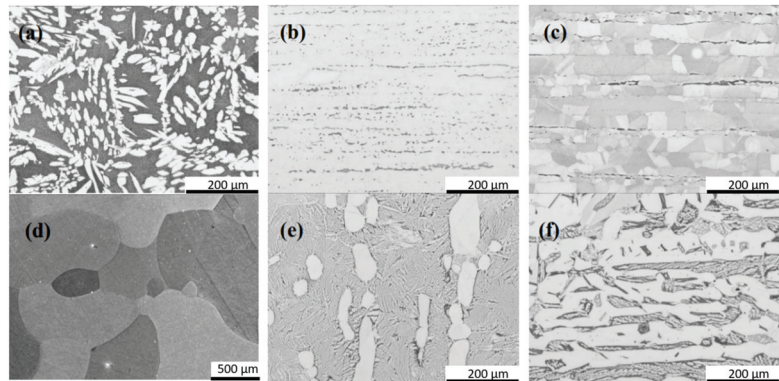
Basori et al. modified the Cu-29Zn brass through the addition of manganese (Mn). The progressive addition of Mn increased the volume fraction of the  $\beta$ -phase in the microstructure as Mn acts as a  $\beta$ -phase stabiliser. Furthermore, the increased Mn content had a minimal effect on twin formation during deformation, while dislocation motion through slip was inhibited due to the pronounced solid solution strengthening effect of Mn [77]. Quan Li et al. showed that the microstructure of the hot extruded Sb-Mg lead-free brass was composed of  $\alpha$ ,  $\beta$  phases and (Sb, Mg)-containing intermetallic compounds [78]. In this research, the developed Sb-Mg brass was compared to the HPb59-1 brass (CuZn40Pb2) in terms of its mechanical properties and was found to be a suitable replacement, reducing the cost and environment impact of the material. Basori et al. noted that in the Cu-29ZnMn system, the progressive addition of Mn was directly associated with an increase in hardness,  $R_{p0.2}$  and  $R_m$ . An unexpected trend was obtained regarding the maximum elongation of the samples where Mn additions over 3 wt.% would reduce negatively impact ductility.

Nevertheless, an addition of up to 3 wt.% Mn had a positive effect instead. This was attributed to the increased  $\beta$ -phase presence at higher Mn contents [77].

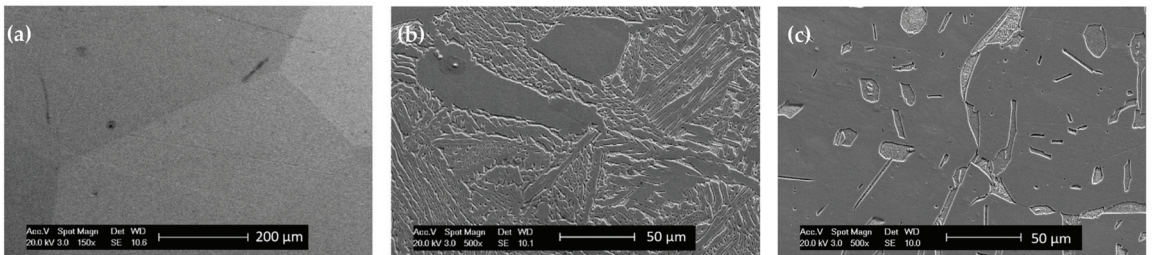
### 3.2.2. Conventional Lead-Free Brasses—Microstructure and Mechanical Properties Optimisation

Toufatzis et al. studied the fracture behaviour of lead-free brass alloys for machining applications [79]. In this work, the mechanical behaviour under static and dynamic loading of three lead-free brass alloys CuZn42 (CW510L), CuZn38As (CW511L) and CuZn36 (C27450) lead-free brass alloys in comparison to the conventional CuZn39Pb3 (CW614N) leaded brass alloy was studied. The fractographic evaluation was performed on impact tested brass samples to identify the involved fracture mechanisms and their relation to the alloy microstructure. The action of the dimpled fracture mechanism was evident to all the studied alloys; however, the dimple size and distribution exhibited a considerable variation signifying differences in the evolved plastic deformation prior to failure. The largest dimples were detected in the case of CW511L and C27450 alloys, which is consistent with their higher values of impact energy and fracture toughness. In this study, it was also shown that the CuZn42 (CW510L) lead-free brass alloy is a potential candidate in replacing the conventional CuZn39Pb3 (CW614N) leaded brass, combining high tensile strength and tolerable fracture toughness, due to the high presence of the  $\beta$ -phase in the alloy microstructure. The fracture toughness of CW510L and CW511L lead-free alloys, after post-processing heat treatment, was assessed via impact and Crack-Tip-Opening-Displacement (CTOD) testing and presented in Ref. [80]. Moderate improvement in impact energy and CTOD values were obtained for heat treated CW510L brass, showing a salient fracture mode, exhibiting a dominant intergranular crack propagation [80]. Similarly, Kozana et al. manufactured a CuZn39 alloy using various casting techniques. They observed significant differences in the hardness and  $R_m$  values of all samples while the only condition altered was the casting mould [81]. G. Jecks et al. carried out investment casting trials on the C35ZA and C30ZA alloys with the addition of aluminium (Al). Due to the segregation of the alloying elements, a finer microstructure was formed with greater hardness compared to other regions of the casting. A thinner cast component exhibited a fine  $\beta$ -phase Widmanstätten structure because of the higher cooling rate. The fineness of Widmanstätten structure is also directly affected by the Al content resulting in variations of hardness [82].

Microstructural evolution studies during severe plastic deformation (SPD) conditions are also important to discern the characteristics and evolution of the phases evident in dual phase brasses throughout the thermomechanical processing of the material [83]. Dhinwal et al. investigated the microstructural changes of a dual phase brass during severe plastic deformation (SPD). The  $\alpha$  phase formed mechanical twins with each successive pass resulting in a more random crystallographic texture. The  $\beta$ -phase grains formed an interconnected structure. The overall grain size of the material was also significantly reduced [84]. Kozana et al. attempted to manipulate the microstructural characteristics of the CW511L brass using different casting moulds. Due to the differences between the moulds in terms of the heat transfer coefficients, various microstructures were obtained, the point of variation being the average grain size of the constituent microstructural features [81]. Toufatzis et al. attempted to modify the microstructure of the CW510L, CW511L and C27450 brasses to improve their machinability by retaining an increased metastable  $\beta$ -phase fraction. This was accomplished by heat treating the alloys at temperatures between 700 and 850 °C for 60–120 min and then immediately subjecting the material to a water quench to suppress the  $\beta$  to  $\alpha$  phase transformation. In turn, the increased volume fraction of  $\beta$  phase allowed further strengthening of the alloy at the cost of ductility. Specifically, in the case of the CW510L the amount of  $\beta$  phase present in the microstructure increased from 60% to 100%, whilst reaching 35% and 20% from an initial 5% and 2% for the CW511L and C27450 brasses, respectively, under the ideal heat treatment conditions (Figures 2 and 3, see Ref. [25]). As previously encountered in research investigating similar para-equilibrium conditions, Widmanstätten  $\alpha$ -phase was present in the case of CW510L [85].



**Figure 2.** Optical micrographs of the (a) CuZn42, (b) CuZn38As, (c) CuZn36 alloys before heat-treating and (d) CuZn42, (e) CuZn38As, (f) CuZn36 alloys after the heat-treatment process [25].



**Figure 3.** SEM micrographs on longitudinal sections showing the microstructures of (a) CuZn42, (b) CuZn38As and (c) CuZn36, after the selected heat treatment condition [25].

### 3.3. Failure Types Encountered in Leaded and Lead-Free Brass Components

As a wider range of brasses becomes integrated into the production line, the matter of component failure and the underlying principles dictating the manifestation of such incidents need to be highlighted. Generally, different types of brasses are more susceptible to different modes of failure owing to their processing route or service life and are extensively analysed in the work by Pantazopoulos [86] and Gupta et al. [87]. However, failure modes that are particularly related to the chemical composition of brasses are further expanded below to provide a potential alloy design direction.

#### 3.3.1. In-Process Failure Modes

The failure of brasses during their thermomechanical processing can be attributed to factors owing mostly to the parameters involved in the casting, extrusion or cold-drawing process [86]. Nevertheless, there are also cases that are dependent exclusively on the alloy composition, with the most prominent one being hot-shortness.

#### Hot-Shortness

Hot-shortness occurs during the extrusion process in cases where the extrusion temperature is amplified due to the friction between the billet and the container. In turn, this causes SPPs with a low melting point such as Pb particles and regions exhibiting notable chemical segregation to partially melt or become hot short resulting in the possible formation of tears in close proximity to the metal surface [45,86,88]. In cases where novel brass compositions are designed, aiming to replace the Pb particles with a different type of SPPs, this failure mode becomes particularly important. This becomes apparent in cases where Pb has been replaced by Bi. As Bi migrates to the grain boundaries and has a low



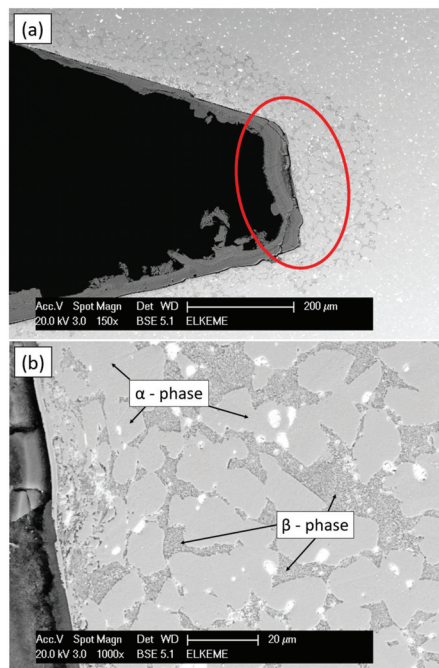
melting point overheating the brass component can yet again cause hot-shortness [89–92]. Therefore, a suitable SPP melting point needs to be one of the main points of alloy design to pre-emptively address hot-shortness. This can also be entirely circumvented through the complete elimination of SPPs in cases where the machinability of the brass would not be compromised.

### 3.3.2. In-Service Failure Modes

Brass components tend to fail during service mostly due to corrosion-related phenomena that are evident in most alloying systems. However, the increased Zn content of brasses can lead to the manifestation of mechanisms almost exclusive to brasses such as dezincification or enhance certain types of corrosion leading to failure such as stress corrosion cracking (SCC) [93,94].

#### Dezincification

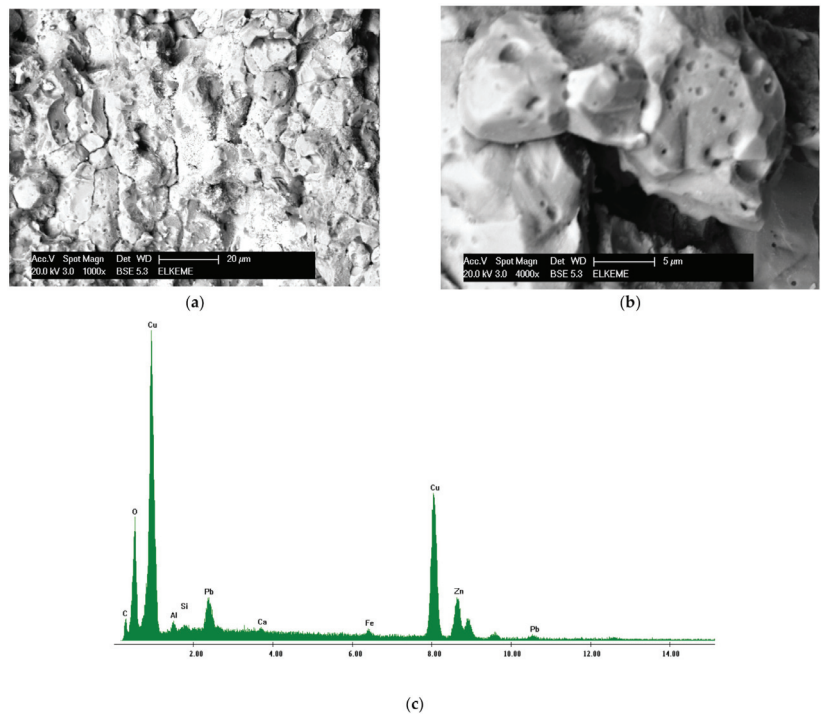
Dezincification may occur during the exposure of brass components to saline and water environments (Figure 4). The mechanism is based upon the selective leaching of Zn due to the electrochemical potential formulating through the interaction between Zn and Cu atoms. This process is facilitated either through the exclusive interaction of Zn with oxygen or chloride ions present in water or through the combined oxidation of both Cu and Zn leading to the eventual establishment of an equilibrium between Cu ions and metallic water and the subsequent deposition of metallic Cu on the brass surface. Therefore, the base material is depleted of Zn leading to the formation a porous Cu-rich layer in the form of red patches on the surface of the material. Dezincification has devastating effects on the mechanical properties of the brass component. This corrosive mechanism can be inhibited from an alloy design perspective through the introduction of tin and arsenic as alloying elements or by controlling the Zn content as this effect is most prominent in brasses containing between 15 and 30 wt.% Zn [86,87].



**Figure 4.** (a) BSE SEM Micrograph showing the dezincification area of a brass component. (b) Detail of (a) [93].

### Stress Corrosion Cracking (SCC)

Stress corrosion cracking consists of the formation of intergranular cracks propagating through a metallic material due to the combinatory effect of high residual stresses alongside exposure to a specific corrosive medium and alkalinity. SCC manifests through the selective corrosion of the base material along the more chemically active paths such as interphase and grain boundaries compromising the material integrity in said points. Upon exposure to additional external stresses, cracks form along the compromised regions leading to the formation of additional free surfaces where the corrosion products are deposited and further accelerate the process. SCC occurs mostly in dual-phase brasses with a Zn content around 20–40 wt.%. This failure mode can be avoided by subjecting the component to a low-temperature heat-treatment to erase residual stresses caused by the manufacturing process in the component. In addition, laser shock peening has been proven to improve the SCC resistance of the material by introducing compressive stresses. Furthermore, protective coatings can be employed to further enhance the corrosion resistance of the material. As the Zn content range where this effect occurs is extensive, there are limited alloy design strategies that can be employed as of yet to alleviate SCC in brasses [86,87,95,96]. The fracture caused by SCC usually follows an intergranular path with multiple branching patterns. Typical SCC fracture surfaces and the corresponding EDS spectrum of a machinable brass component are presented in Figure 5 [93].



**Figure 5.** (a,b) Backscattered Electron (BSE) micrographs showing the fracture surface of a brass component showing intergranular morphology, (c) EDS spectrum of the fracture surface showing the presence of oxides. See Reference [93].

## 4. Machinability Evaluation

### 4.1. Chip Formation and Tool Wear

#### 4.1.1. Leaded Brasses

Toufatzis et al. investigated the machinability of CuZn39Pb3 and CuZn36Pb2As brasses [46]. In this research, machinability was assessed qualitatively and quantitatively by evaluating the chip size and morphology, and the corresponding cutting tool wear land, employing a single point turning technique according to ISO 3685 [97]. Experimental results indicated that the most critical factors affecting the chip formation quality during brass bar machining were the type of copper alloy used (CuZn39Pb3 and CuZn36Pb2As alloys) and the cutting speed, while it was not found to be sensitive to depth of cut and feed rate variations [46]. It was evident that a significant variety of chip morphology was produced by changing the turning conditions. The single needle, feathery and continuous helical were representative forms that constituted a qualitative indicator of the machining process performance [46]. The formation of shorter chips resulted in better surface finish, lower tool wear and ease of operation, allowing higher cutting speeds, while chip fracturing and removal led to the reduction in tool–chip contact, minimising the risk of built-up edge formation [46].

Gane has shown that the addition of a small quantity of Pb to brass was very effective in reducing friction, both in cutting experiments and in simple sliding-friction experiments [98]. In addition, the ductility of brass was substantially reduced when Pb was present. Both these factors contributed to the considerable improvement in machining properties observed in lead-containing alloys. The reduced friction on the rake face of the tool decreased the specific cutting energy by a factor of about two. As a result, the tool temperature decreased and the tool life improved [98]. As the Pb particles became finer (less than 5  $\mu\text{m}$ ) and their distribution more homogeneous, chip-breaking during cutting became more pronounced, and, as a result, machinability improved. Chip fracture in short pieces allows for ease of machining operation; maximum productivity, lower cutting forces, better surface finish of the workpiece, closer tolerances of the final component and less tool wear, thus longer tool life [98]. Preliminary machinability tests were performed by Pantazopoulos in turning operation [8]. The turning speed was up to 395 rpm (the linear speed was up to 0.165 m/s) using a cemented tungsten carbide insert as a cutting tool. The chip size tended to increase by increasing the depth of cut, while no appreciable changes were recorded by changing the feed rate. The depth of cut was constant within the turning cycle (i.e., 0.4, 1.0, or 3.0 mm). The horizontal advancement of the tool per revolution was defined as a function of the feed rate (0.25 or 0.50 mm/rev) [8]. Morphological observations of the produced chips, using optical microscopy, indicated the absence of a flow-zone. Segmented chips with intense shear fractures were produced during turning as a result of the dual phase microstructure ( $\alpha$ – $\beta$ ) and the distribution of Pb particles at interphase boundaries. The presence of Pb decreased friction and temperature at the tool–workpiece interface, therefore increasing tool life [8]. Cutting tool wear was principally controlled mainly by the cutting speed and depth of cut used during machining experiments while it appeared to be less sensitive to feed rate or the type of copper alloy variations [46]. Adhesion and sticking of the workpiece debris on the flank face intensified at higher cutting speeds. Moreover, the flank zone revealed several typical wear features, such as abrasive marks and chipping (edge fracturing), of increasing severity as the cutting speed increased (from 2000 to 4000 rpm) [46].

As such, chipping caused the edge fracture of the machining tool, impairing cutting edge sharpness and leading to tool blunting. This type of tool failure increased cutting forces, resulting therefore in further degradation of the machining performance (longer chips, higher fluctuations and chattering, part distortion), causing serious defects on the machined surface quality. Severe damage phenomena such as thermal cracking or flaking were not observed in this study [46]. Toufatzis et al. determined the optimum cutting conditions using non-parametric design of experiments methods applied in turning processes of leaded brass bars (CuZn39Pb3 and CuZn36Pb2As) for industrial applications [46].

Non-linear fractional factorial designs for the nine-run, three-level, four-factor saturated orthogonal array ( $L_9 = 3^4$ ) were applied to collect sufficient data to investigate the multi-response optimisation of two main machinability quality characteristics such as the chip morphology and cutting tool wear. The study suggested that concurrent multi-response optimisation gave rise to no specific effect. These optimal settings of the cutting parameters for chip morphology could also be used for cutting tool wear optimization. Confirmation experiments seem to verify the conclusion of this work [46].

Hassan et al. evaluated the influence of cutting parameters such as cutting speed, feed rate and depth of cut in C34000 leaded brass using an analysis of variance (ANOVA) methodology [99]. The purpose of ANOVA was to identify the important parameters for predicting material removal rate. Feed rate was found to be the most significant factor and its contribution to material removal rate was 42.77% within a 95% confidence interval. As such, the feed rate was the most significant factor affecting the material removal rate. The interaction between cutting speed and feed rate was found to be significant with a contribution of 7.75%. The best results for optimal material removal rate were achieved when C34000 leaded brass was machined at a cutting speed of 55 m/min, using a depth of cut of 0.2 mm and a feed rate of 0.35 mm/rev. Johansson et al. investigated brasses with both higher and lower Pb content. It was observed that the machinability of the conventional leaded brass exceeded that of its lower Pb content counterparts by a significant margin. It was however mentioned that the machinability of the CW724R brass was tolerable compared to the original CW614N, while also exhibiting interesting mechanical properties [65]. Thus, the importance of Pb as an addition cannot be overlooked as it directly affects the machinability of the material to a significant extent.

#### 4.1.2. Eco-Friendly Brasses (Pb-Free)

The design criterion for the Pb-free brasses typically concerns the introduction of a soft intermetallic phase uniformly dispersed within the material. Upon contact with the cutting tool, the intermetallic particles should act as a stress concentration point, leading to the segmentation of the formulating chip. Li et al. studied the influence of Ti addition on lead-free brasses [67]. They showed that BS40-2.2Bi alloy exhibited an excellent machinability compared to the Cu40Zn3.2Pb conventional leaded brass. The average drilling time increased with increasing Ti content from 0.3 wt.% to 1.0 wt.%. BS40-2.2Bi with 1.0 wt.% Ti addition could not be penetrated by drilling for more than 180 sec. The different chip morphologies obtained during drilling operations were used to evaluate the machinability of the alloys produced. Compared with the chip shape of the conventional leaded brass (Cu40Zn3.2Pb), BS40-2.2Bi exhibited a different morphology due to the substantial brittleness of Bi affecting the fracture behaviour of the chip and the Ti addition to BS40-2.2Bi, affecting the chip geometry considerably, which transformed into a continuous spiral shape when the Ti content increased to 0.5 wt.% [67].

As the phase diagram indicates, both antimony (Sb) and magnesium can be dissolved partly in copper forming intermetallic compounds with copper [78]. If these intermetallic compounds were dispersedly distributed in the Cu-Zn system, such particles or strips would disturb the metallic matrix continuity and make the chips rupture easily. Thus, the cutting performance of the brass would be improved without the addition of Pb. Additionally, the particles in Sb-Mg brass are not expected to produce stress concentration during forming as they deformed plastically during extrusion, while improving the cutting performance and mechanical properties of the alloy [78].

Toufatzis et al. evaluated the machinability of the CuZn42, CuZn38As and CuZn36 lead-free brasses, comparing them to the conventional leaded CuZn39Pb3 brass [25]. Their results reinforced the perception that an increased volume fraction of  $\beta$ -phase would enable the generation of micro-cracks during the machining process owing to the formation of shear bands. Nevertheless, the chip segmentation process was predominantly controlled by the distribution of Pb particles. Expanding upon this concept, by subjecting the Pb-free alloys to a series of heat treatments (at 775 °C for 60 min for CuZn42 and at 850 °C for 2 h for

CuZn38As), a higher volume fraction of  $\beta$ -phase would be stabilised in room temperature as previously discussed. As such, a mild improvement in machinability was to be expected. Indeed, the alloys showed an improvement in machinability relevant to the increased volume fraction of the  $\beta$ -phase and, specifically in the case of the CuZn38As alloy, surpass the conventional leaded counterpart in terms of surface quality [20,21,25,35]. The chip morphologies of the heat-treated lead-free brass alloys compared to the as received ones are depicted in Figures 6 and 7, while the typical characteristic topographic patterns obtained by optical profilometry is presented in Figure 8.

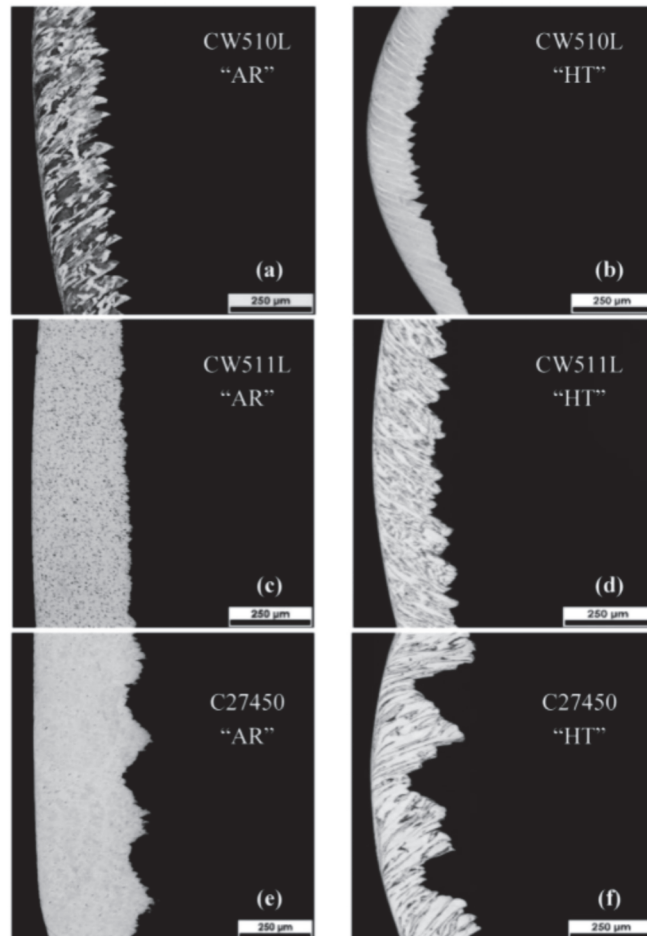


**Figure 6.** Chip morphology of the as-received (AR) and heat-treated (HT) CW510L-CuZn42 (a,b), CW511L-CuZn38As (c,d) and C27450-CuZn36 (e,f) brass alloys [25]. Note: the decrease in Class number denotes improvement in chip morphology [25].

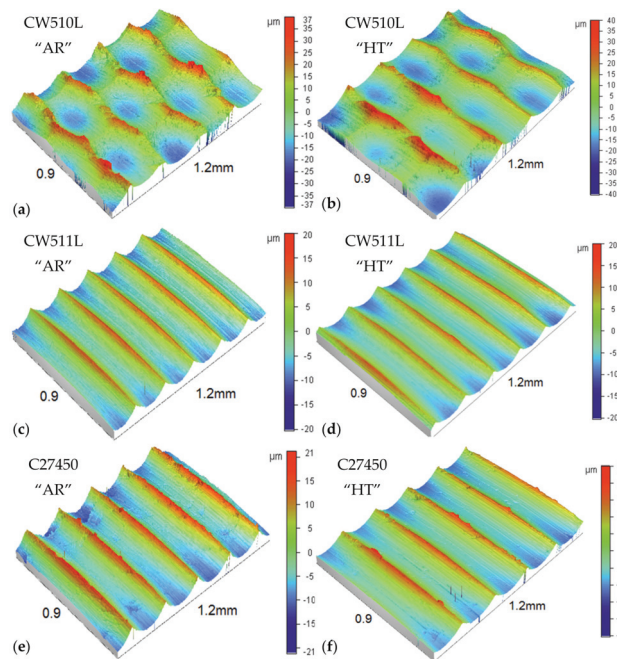
Nobel et al. also studied the machinability of various lead-free alloys, i.e., CW510L, CW511L and CW724R, correlating their machinability to the use of different cutting tool materials [100]. CW724R lead-free silicon brass, in comparison to other lead-free brasses, such as CuZn42 (CW510L) and CuZn38As (CW511L), showed improved machinability concerning chip formation. However, CW724R caused higher tool wear due to the abrasive nature of the Si-rich  $\kappa$ -phase when used alongside a TiAlN-coated carbide tool. In this study the CW510L machining performance using various cutting tools with different coatings (TiAlN, TiB<sub>2</sub>, DLC, CVD-diamond) was investigated. Adhesive and abrasive wear was reduced by using DLC-coating among the tested PVD-coated tool systems. An additional improvement of cutting performance was achieved using CVD-diamond coating which exhibited exceptional abrasive wear resistance, while adhesion on the rake and flank face was minimised. Polycrystalline diamond tools (PCD) provide another alternative with significant abrasive wear resistance and low adhesion properties. However, the production demand for long tubular chips restricts the use of PCD tools and poses the need for the manufacture of such tools with favourable chip breaking geometry.

Experiments and simulations were implemented by Laakso et al. in order to investigate the effects of different cutting parameters on chip morphology of a low-lead

brass [101]. This low-lead brass is not standardised but is compositionally close to the standard CuZn38As (CW511L) lead-free brass. Based on these simulations and experiments it was found that the use of a positive rake angle ( $+5^\circ$ ), high cutting speed (300 m/min) and low cutting feed rate (0.1 mm/rev) improved chip breakage from a continuous chip to a chip of an average length of 4 mm. High cutting speeds favour chip breakage by increasing chip brittleness due to the suppression of softening effects at high strain rate conditions. Minimisation of cutting force and friction force is achieved by using a positive rake angle (e.g.,  $+5^\circ$ ). Reduction in friction could be realised by decreasing of tool–chip contact area by decreasing feed rate and/or depth of cut. Finite Element Modelling (FEM) simulations agreed with the above results. Furthermore, in a very recent work, the influence of Zn equivalent on the evaluation of chip morphology and machining surface quality of free cutting silicon brasses were investigated by adding Pb replacers (Si and Al elements) [24].



**Figure 7.** Optical micrographs showing the morphology of chips generated during the machining process of (a) CuZn42, (c) CuZn38As, (e) CuZn36 alloys before heat-treating (AR) and (b) CuZn42, (d) CuZn38As, (f) CuZn36 alloys after the heat-treatment process, HT [25].



**Figure 8.** Surface topography derived from profilometric measurements: (a) CW510L, as received, (b) CW510L, heat-treated, (c) CW511L, as received, (d) CW511L, heat-treated, (e) C27450, as received and (f) C27450, heat-treated [25].

The introduction of additional alloying elements may also enable the stabilisation of various primary phases (i.e., the presence of  $\alpha$ ,  $\beta$  or  $\gamma$  phases in the Cu-Zn system) at equilibrium. This effect can be expanded further through TMP, directly affecting the fracture behaviour and consequently, the chip-breaking properties and machinability performance of novel compositions [102,103]. Taha et al. showed that, as the Si content increased from 0 wt.% to 1 wt.% in modern lead-free brasses (CuZn40), tool wear slightly increased as well [104]. This was attributed to the decreased volume fractions of the softer phase  $\alpha$  and the respective increase in the harder phase  $\beta$ . In Si-containing brass alloys, the detrimental effect of  $\beta$  phase on tool wear has been confirmed. The increase in Si content, from 1 wt.% to 4 wt.% Si, led to a moderate increase in tool wear due to the increased volume fraction of brittle  $\lambda$ ,  $\eta$ , and  $\chi$  intermetallic phases, albeit no significant effects of hardness and microstructure changes were observed. It was also seen that chip formation changed from continuous to discontinuous type with decreasing cutting speed [104]. However, decreasing the cutting speed is recommended as a method to achieve the desirable discontinuous chip type as it results in lower productivity. By adding 4 wt.% Si to the unleaded CuZn40 brass, the chip formation process changed from the undesirable continuous type to an acceptable long bevel and cylindrical long types. It was clearly shown that the chip type was affected by the formation of hard secondary  $\lambda$ -phase precipitates rather than the variation in mechanical properties [104]. Scientific research revealed the benefits of the recycled bismuth–tin (Bi-Sn) solder addition in the lead-free brass alloy Cu-38Zn-0.5Si by reducing the chip-size morphology [105]. The improvement of chip-breaking efficiency was attributed to the presence of the  $\kappa$ -phase in CuZn21Si3P, as opposed to the effect of the  $\alpha$ -phase in CuZn38As brass. Likewise, the high percentage of  $\beta$ -phase in the microstructure of CuZn41.5 resulted in the reduction in chip morphology. The influence of the coating type (TiN, TiAlN, TiB<sub>2</sub> and DLC on carbide tools) as well as the use of polycrystalline diamond (PCD) tools on chip formation and workpiece quality was analysed for the evaluation of machinability in three low-lead brass alloys (CuZn38As, CuZn42 and CuZn21Si3P). The

machining problems were diminished using a diamond-like carbon coating, especially through the reduction in the friction in the secondary shear zone [106]. A machinability comparison between leaded (CuZn39Pb3) and lead-free brass (CuZn21Si3P) alloys was implemented in a relevant work concerning tool wear during machining. Machining of the lead-free brass alloy (CuZn21Si3P) resulted in longer chip size and, eventually, higher tool-wear rates using cemented carbides. The use of coating on carbide tools, e.g., (Ti, V, Zr, Hf, Nb, Ta), was recommended as a possible solution for overcoming excessive tool-wear rates [107,108]. In terms of the chip morphology specifically, high-Si brasses are generally found to produce discontinuous chip types while a lower Si content is associated with better tool interaction and superior surface quality with the added benefit of greater mechanical properties. Nevertheless, the produced chip is of the discontinuous type for the low-Si brasses investigated in the present study [104].

#### 4.2. Cutting Force and Surface Roughness

Vilarinho et al. uncovered several relationships concerning the influence of the chemical composition and the hardness on the different components of cutting forces [109]. The suggested empirical relationships considered both the well-established effect of Pb on the machinability behaviour already shown by several authors and the effect of various alloying elements usually present in brass composition. Conventional alloys (CuZn36Pb3, CuZn39Pb3), with and without additional alloying elements, showed lower values of cutting forces ( $F_z$ ) than the modern brass alloys of the studied ternary systems, Cu-Sn-Zn, Cu-Al-Zn and Cu-Fe-Zn [109]. However, in some cases conventional alloys exhibited similar or higher values of feed and depth forces in relation to modern brasses. The cutting forces used for machining modern brass alloys of the ternary systems studied in this work were affected by the type and content of each alloying element. Comparing the development of residual stresses on the CuZn21Si3P and CuZn39Pb3 brasses showed the retainment of lower residual stresses in the Si-containing alloy and achieving better abrasion resistance, although higher cutting forces were required. This could also point towards better fatigue and stress-corrosion cracking resistance, but additional investigations are required [110]. When comparing the machinability conventional leaded brasses to their Pb-free counterparts, it becomes apparent that in both cases the depth of cut and feed rate are the most vital parameters influencing the resulting cutting force and surface roughness. The optimisation of said parameters enables the control of both machinability criteria and thus their investigation is of the utmost importance [111]. Scientific research revealed the benefits of the recycled Bi-Sn solder addition in lead-free brass alloy (Cu-38Zn-0.5Si) by reducing the required cutting forces in machining [105]. The influence of the coating type (TiN, TiAlN, TiB2 and DLC on carbide tools), as well as the use of polycrystalline diamond (PCD) tools on machining forces, was analysed to evaluate the machinability in three low-lead brass alloys (CuZn38As, CuZn42, and CuZn21Si3P). The machining problems were diminished using a diamond-like carbon coating, especially through the reduction in the friction in the secondary shear zone [106]. Machining the lead-free brass alloy (CuZn21Si3P) required higher cutting forces using cemented carbides. As such, the use of coating on carbide tools such as (Ti, V, Zr, Hf, Nb, Ta) N was recommended as a possible solution for reducing the cutting forces [107,108].

Concerning the alloys of the Cu-Sn-Zn system, the lowest values of cutting and feed forces were obtained for Sn contents that led to a dual-phase  $\beta$ - $\gamma$  microstructure. On the other hand, the presence of Al in alloys of the Cu-Al-Zn system had the opposite effect to that of Sn, rising the cutting force as its content increased [109]. In this ternary system, the highest values of cutting force  $F_z$  were always obtained for alloys with a  $\beta$ - $\gamma$  or pure  $\beta$  structures. Regarding Cu-Fe-Zn alloys, no relationship was found between the Fe content and the machinability parameters. Additionally, no significant correlations were made between the cutting forces and the chemical composition when expressed in terms of effective Cu content. However, a minor correlation between the feed force and the effective



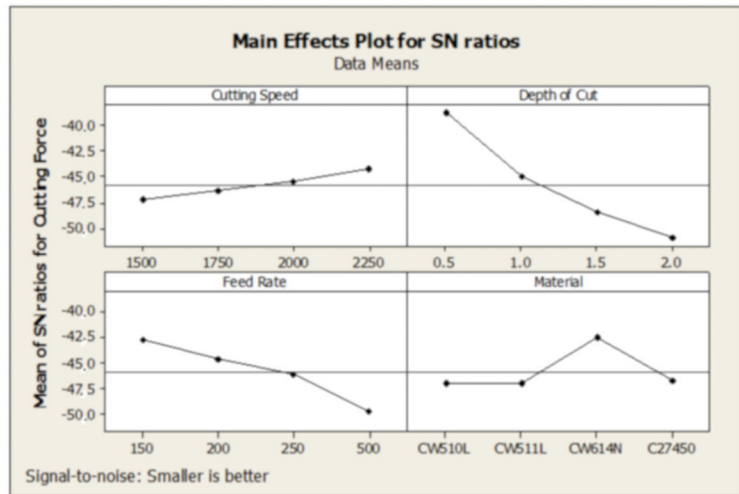
Cu content on conventional alloys was established, although the authors indicated that further studies would be needed to confirm this behaviour [109].

Gaitonde et al. employed Artificial Neural Networks (ANN) to study the effect of cutting speed, feed rate and the required amount of minimum quantity of lubrication (MQL) on two aspects of machinability, namely the specific cutting force and surface roughness in turning of CuZn39Pb3 brass using a K10 carbide tool [112]. In their study, a multilayer feed forward ANN was employed trained by EBPTA (Error-Back Propagation-Training Algorithm). The training patterns required for an input-output database generation were obtained through turning experiments conducted as per Full Factorial Design (FFD). 3D surface plots were generated to analyse the interaction effects of process parameters and the following conclusions were drawn from the present investigation. The minimum specific cutting force existed at high MQL (160–170 mL/h) with medium range of cutting speed (210–220 m/min). Additionally, the specific cutting force was found to be minimal at a higher feed rate (0.20 mm/rev) with a low MQL (100 mL/h). The specific cutting force was highly sensitive to feed rate variations for all values of MQL. The minimum surface roughness resulted in high MQL (160–180 mL/h) with low cutting speed values. Lastly, the surface roughness sharply increased with increasing feed rate irrespective of MQL [94]. They employed the Taguchi method to determine the optimal process parameters for simultaneously minimising the surface roughness and specific cutting force during turning of CuZn39Pb3 brass with a K10 carbide tool [111,112]. In this work, the optimum amount of MQL and the most appropriate cutting speed and feed rate were determined using Analysis of Means (ANOM) and the relative significance of the parameters was identified through ANOVA. The ANOM on multi-response S/N ratio indicated that an optimum MQL of 200 mL/h, cutting speed of 200 m/min and a feed rate of 0.05 mm/rev was necessary to simultaneously minimise surface roughness and specific cutting force. ANOVA illustrated that feed rate was the most dominant parameter followed by MQL and cutting speed in optimising the machinability characteristics. ANOVA also showed that the error contribution was 0.55%, which clearly indicated the absence of the interaction effects of process parameters on optimisation of multiple performance characteristics. Lastly, validation experiments confirmed that the additive model was adequate for determining the optimum quality characteristics at the 95% confidence interval. Utilising ANOVA as means of analysis and optimisation was also explored in the work of Toulfatzis et al. towards the improvement of machinability in CuZn42, CuZn38As and CuZn36 compared to a conventional CuZn39Pb3 brass. To reduce the volume of experiments required for the machinability trials, a DOE Taguchi method in conjunction with ANOVA was used. As such, their statistical analysis converged on the use of a standard  $L_{16}$  orthogonal array. Their work further demonstrated the efficiency of ANOVA in identifying the contributions of individual machining parameters towards the optimisation of the cutting force within 90% accuracy and, to a lesser extent, the surface roughness. Furthermore, the S/N response diagrams showed that the depth of cut would be considered the most significant factor in the machining process which was backed up through ANOVA [50]. Plots of S/N response and data means for cutting force and surface roughness are presented in Figures 9 and 10 [50]. As was confirmed by the ANOVA results, the depth of cut is the most influential factor for cutting force ( $P_p = 64.3992\%$ ) while feed rate is the most influential factor ( $P_p = 55.3085$ ) for surface roughness, see Tables 1 and 2 [50].

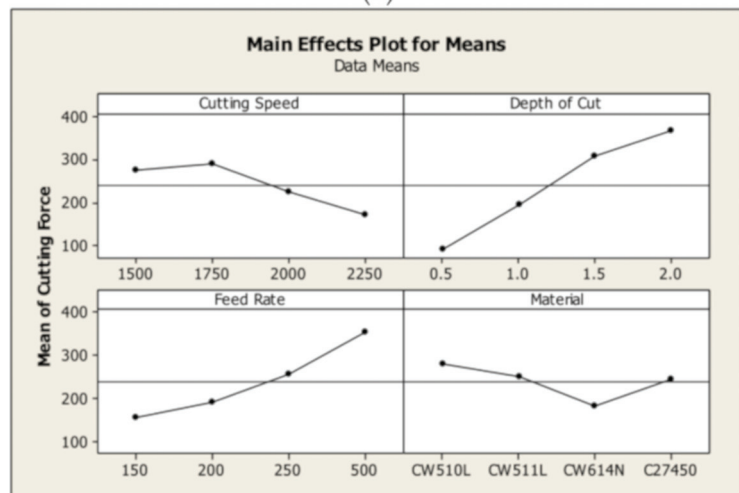
Taha et al. investigated the machinability based on surface quality and cutting forces in lead-free silicon brass alloys [104]. In this work, the ease of machinability was derived from the machined surface quality. This was evaluated by measuring the machined average surface roughness (Ra) at selected cutting conditions using H20 and H123 tools. Evidently, for all Si-containing brass alloys investigated, Ra was almost independent of depth of cut. Ra increased as the cutting feed increased and gradually decreased as speed increased. Minimum values of Ra were observed for leaded brass, followed by 1 wt.% Si and 2 wt.% Si Alloys, and finally the leaded brass C37700. Even higher Ra values were observed for 3 wt.% Si and 4 wt.% Si alloys [104]. The Ra was found to increase by 40% as the silicon

content increased from 1 wt.% to 4 wt.% Si. For all leaded and unleaded alloys, cutting forces were proportional to the depth of cut.

In both cases, the machining behaviour was attributed to increased resistance of chip formation as a result of the increase in the volume of the material removal. The cutting force increased with increasing cutting speed up to a maximum of 50 m/min. This was attributed to the increase in friction on the tool face caused by the chip flow. Further increase in speed led to the decrease in cutting force, which was attributed to the increase in the cutting temperature at high speeds, which in turn resulted in the decrease in the friction forces and shear strength of the material due to thermally induced softening. Moreover, leaded brass exhibited the lowest cutting force value due to the reduction in the coefficient of friction between the chip and the tool face caused by the lubricating effect of Pb. The maximum cutting force was measured for 1% Si and was attributed to the highest alloy strength [104].



(a)

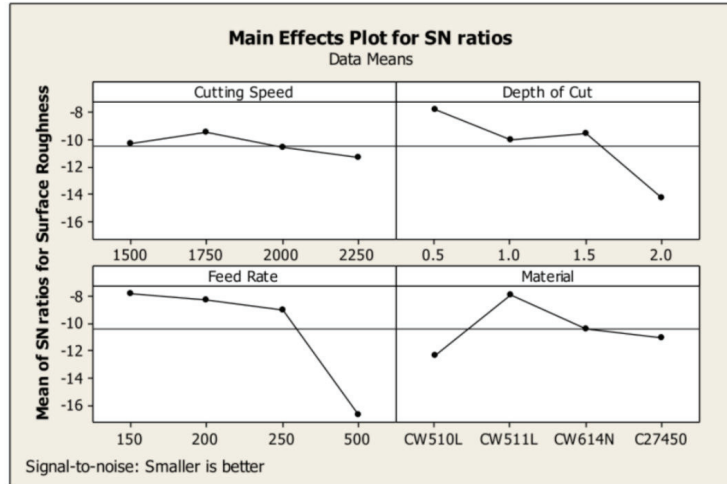


(b)

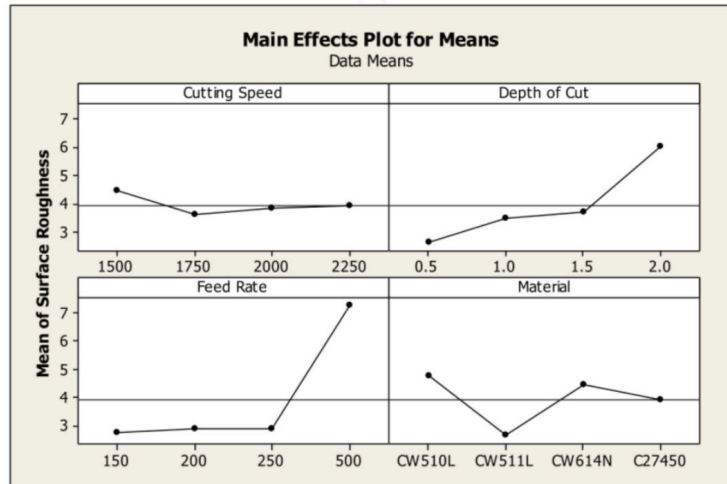
**Figure 9.** Diagrams showing the responses of (a) S/N ratios and (b) data means when evaluated against the cutting parameters which optimise the cutting force [50].

Table 1. Analysis of variance (ANOVA) for the cutting force [50].

Factor	Degrees of Freedom	Sum of Squares (SS)	Corrected Sum of Squares (SS')	Variance	Percent Contribution P <sub>p</sub> (%)	Rank
Cutting Speed	3	19.0425	18.8254	6.3475	3.5728	4
Depth of Cut	3	339.5408	339.3238	113.1803	64.3992	1
Feed Rate	3	108.0831	107.8660	36.0277	20.4715	2
Material	3	58.8660	58.6489	19.6220	11.1308	3
Error	19	1.3746	2.2428	0.0723	0.4257	
Total	31	526.9070	526.9070		100.0000	



(a)



(b)

Figure 10. Diagrams showing the responses of (a) S/N ratios and (b) data means when evaluated against the cutting parameters which optimise the surface roughness [50].

**Table 2.** Analysis of variance (ANOVA) for the surface roughness [50].

Factor	Degrees of Freedom	Sum of Square (SS)	Corrected Sum of Squares (SS')	Variance	Percent Contribution $P_p$ (%)	Rank
Cutting Speed	3	7.3498	3.5422	2.4499	0.9460	4
Depth of Cut	3	91.6606	87.8530	30.5535	23.4625	2
Feed Rate	3	210.9051	207.0974	70.3017	55.3085	1
Material	3	40.4101	36.6025	13.4700	9.7753	3
Error	19	24.1149	39.3453	1.2692	10.5078	
Total	31	374.4404	374.4404		100.0000	

#### 4.3. Employment of Vibrational Analysis towards Machinability Evaluation

An emerging trend towards achieving a proper surface finish alongside good economic performance concerns the use of vibrodiagnostics to evaluate the machined components integrity. The term vibrodiagnostics refers to the analysis of the vibrations generated during the machining process. As different materials are characterised by different mechanical and microstructural properties, these variations cause the manifestation of vibrational differences during the cutting process. Specifically, in cases where the workpiece contains for example hard intermetallic phases or inclusions, these irregularities may cause the formation of unwanted vibrations which, in turn can contribute towards an increased oscillation compared to that of a uniform material. Furthermore, tool wear can also be identified through vibrodiagnostics as the geometry of the cutting tool edge is altered during the machining process, generating vibrational differences compared to the initial ones. Thus, by analysing the vibrational characteristics of the cutting process both the workpiece and cutting tool characteristics can be optimised to enable more efficient machinability [113–115]. P. Monka et al. applied such methodologies to optimise the cutting parameters for novel milling tools. In this case study, an S-grade sintered carbide with an AlTiN physical vapor deposition (PVD) coating was used to machine a 16MnCr5 steel. Their analysis pointed at the potential for tool optimisation through modifying the tool geometry [116]. In another study, vibrodiagnostics were used to evaluate the tap failure during internal threads machining. Specifically tailored towards tool behaviour prediction, their analysis showed that cutting tool wear was not affected only by the cutting speed but the angle of the tap as well [117]. Similarly, vibrational studies can be used to unveil the tribological characteristics of the newly formed material surfaces [81].

## 5. Conclusions and Further Research

The development of eco-friendly brass alloys constitutes a critical research field with significant industrial and environmental impact going forward. Brasses are used in a wide range of applications ranging from plumbing fittings to architectural hardware and decorations. This is due to their superior machinability and corrosion resistance compared to most other industrial materials. The machinability of said alloys has been heavily dependent on the incorporation of Pb, which has traditionally been the key to their success. However, as Pb is currently a heavily regulated substance due to environmental and health concerns its substitution is of paramount importance. Through this review we explored the various ways research has progressed relating to the assessment and resolution of the aforementioned challenge. Two primary approaches for solving this problem were evaluated. The design of novel brass compositions and a compositionally invariant route dependent on a series of heat treatments. Compositional modification aims to replicate the beneficial effects of Pb through the incorporation of second phase particles, while the alternative route is intended to stabilise the  $\beta$ -phase. Overall, in terms of mechanical properties, novel compositions were shown to exhibit much improved mechanical properties compared to the conventional ones. The flexibility pertaining to the inclusion of a wide variety of alloying elements enables various strengthening mechanisms to manifest. Similarly, the  $\beta$ -stabilised heat treated Pb-free conventional compositions showed an increase in hardness and strength at the expense of ductility compared to conventional leaded compositions. Regardless, most of the novel compositions were characterised by mediocre

machinability compared to conventional leaded brasses, rarely combining both acceptable mechanical properties and machinability. On the contrary, the heat treated conventional Pb-free compositions showed a degree of machinability similar to the leaded compositions, while retaining a good combination of mechanical properties and fracture resistance. It has thus become clear that both approaches are characterised by complementary benefits. As such, we believe that the optimal way towards the next generation of lead-free brasses lies in the development of alloys that can utilise a combination of both aspects of design. Therefore, we recommend the following pathways for further applied research, aiming at the optimisation of the design and processing routes of lead-free copper alloys to surpass the properties and functionality of the conventional leaded brasses satisfying in parallel the requirements of environmental protection, human health and sustainable development:

- (a) The compositional and microstructural design of novel lead-free alloys through computational techniques such as ab initio calculations, CAPHAD (calculation of phase diagrams) approaches alongside general thermodynamic/kinetics and finite element modelling. Such approaches could assess novel compositions in terms of their thermodynamic stability, constituent phases, mechanical properties and corrosion resistance without the expense of physically manufacturing the alloys. Furthermore, these computational approaches could be used alongside experiments to validate and assist in optimization of the thermomechanical processing route of discovered compositions.
- (b) Simultaneous “multi-objective” optimisation of the major quality characteristics (chip morphology, power consumption, cutting force and surface roughness) utilising advanced statistical techniques, such as Desirability Functions (DFs) for the machinability of lead-free brass alloys. The optimisation and validation of the cutting conditions in industrial scale for the fabrication of exemplary final brass industrial component by using complex machining operations (such as CNC machining center).
- (c) Application of on-line monitoring techniques (e.g., vibration sensors/vibrodiagnostics) might be also employed to forecast the cutting tool durability and service lifetime. In addition, the incurred cutting mechanisms could be further predicted and quantified using appropriate numerical simulation by Finite Element Analysis/FEA software.
- (d) Comparative studies concerning the elemental leaching effects between novel lead-free brasses and conventional leaded brasses. This is especially crucial in cases where new alloying additions have been introduced and the resulting alloys have not been investigated in terms of their corrosion performance. This research must be carried out to conduct a risk assessment type study aiming to acknowledge and minimise any impact of these new compositions may have on human health and environment.

**Author Contributions:** Conceptualization, A.S.P., A.I.T., G.A.P.; methodology, A.I.T. and G.A.P.; literature review A.I.T., G.A.P., P.S.; writing—original draft preparation, A.I.T. and P.S.; writing—review and editing, A.I.T., G.A.P., P.S.; supervision, A.S.P., A.I.T. and G.A.P. All authors have read and agreed to the published version of the manuscript.

**Funding:** This research received no external funding.

**Institutional Review Board Statement:** Not applicable.

**Informed Consent Statement:** Not applicable.

**Data Availability Statement:** The data supporting the findings of this study are available on request from the corresponding author.

**Acknowledgments:** The encouragement and support of ELKEME management is highly appreciated.

**Conflicts of Interest:** The authors declare no conflict of interest.

## Appendix A. Chemical Composition of Machinable Brass Alloys

Table A1. Conventional leaded brass compositions.

Conventional Leaded Brasses	
Alloy Composition	Ref.
CuZn40Pb	[4,7]
CuZn39Pb3	[8,19,26,27,29,45–50,58,59,64,78,82,104–106]
CuZn40Pb2	[51–55]
CuZn40Pb3	[6,7]
CuZn40Pb4	[7]
CuZn39Pb2	[47,48,57,102]
CuZn36Pb2As	[46,50,59]

Table A2. Conventional lead-free (Pb-free) brass compositions.

Conventional Lead-Free Brasses	
Alloy Composition	Ref.
CuZn42	[25,30,79,80,91,104]
CuZn41.5	[31]
CuZn40	[7,23]
CuZn38	[25]
CuZn38As	[24,25,31,50,80–82,92,93,104]
CuZn38Sn	[81]
CuZn37	[108]
CuZn36	[25,50,79]
CuZn32	[64]
CuZn21Si3P	[19,30,65,100,106–109]

Table A3. Novel brass compositions with an increased aluminium (Al) content (alloying elements expressed in wt.%).

Novel Brass Compositions–High Aluminium (Al) Content								
Cu	Pb	Ni	Fe	Sn	Zn	Al	Si	Ref.
Bal.	-	-	-	-	37.6	3.68	-	[109]
Bal.	2.32	0.24	0.33	0.53	32.67	2.88	0.06	[109]
Bal.	-	-	0.028	-	30.2	1.66	-	[82]
Bal.	-	-	0.03	-	33.7	1.51	-	[82]
Bal.	-	-	0.033	-	34.2	1.49	-	[82]
Bal.	-	-	0.032	-	34.5	1.48	-	[82]

Al addition improves corrosion resistance, mechanical properties and in significant amounts can produce a lightweight effect. Al also affects the stability of  $\alpha/\beta/\gamma$  phases.

Table A4. Novel brass compositions with an increased lead (Pb) content (alloying elements expressed in wt.%).

Novel Brass Compositions–High Lead (Pb) Content								
Cu	Pb	Ni	Fe	Sn	Zn	Al	Si	Ref.
Bal.	4.23	0.24	0.33	1.08	32.28	1.57	0.06	[109]
Bal.	3.5	-	-	-	39.6	-	-	[61]
Bal.	3.04	0.02	0.17	0.06	37.96	0.02	-	[3]
Bal.	2.9	-	-	-	38.8	-	-	[85]
Bal.	2.6	-	0.2	0.2	39	0.02	-	[48]
Bal.	2.46	0.25	0.34	0.55	33.63	0.8	-	[109]
Bal.	2.43	0.24	0.33	0.54	33.15	2.01	0.06	[109]
Bal.	1.65	0.25	0.36	0.54	33.75	0.84	0.1	[109]
Bal.	1.46	-	0.114	0.096	35.02	0.503	-	[33]
Bal.	1.45	-	0.116	0.096	34.89	0.506	-	[33]
Bal.	0.95	-	0.07	-	38.77	1.01	-	[109]
Bal.	0.909	-	0.095	0.104	39.1	0.59	-	[33]
Bal.	0.894	-	0.095	0.104	38.97	0.594	-	[33]

**Table A5.** Novel brass compositions with an increased tin (Sn) content (alloying elements expressed in wt.%).

Novel Brass Compositions–High Tin (Sn) Content						
Cu	Pb	Fe	Sn	Zn	Ref.	
Bal.	0.02	0.03	17.37	27.49	[103]	
Bal.	0.01	0.04	13.89	26.74	[103]	
Bal.	-	0.06	11.36	26.72	[103]	
Bal.	0.02	0.04	8.02	28.16	[103]	
Bal.	0.02	0.05	5.43	28.63	[103]	
Bal.	-	-	5.3	39.33	[109]	
Bal.	-	-	1.0–4.0	38	[21]	
Bal.	-	-	3.84	39.61	[109]	
Bal.	-	0.04	3.16	28.57	[103]	
Bal.	-	-	1.78	31.53	[109]	
Bal.	-	-	1.39	31.9	[109]	
Bal.	-	0.03	1.2	28.8	[102]	
Bal.	-	-	0.95	34.22	[109]	
Bal.	-	-	0.85	32.11	[109]	
Bal.	-	-	0.78	39.93	[109]	
Bal.	-	-	0.76	38.2	[109]	

Sn addition may promote the formation of  $\beta'$  enhancing both the machinability and hardness.

**Table A6.** Novel brass compositions with an increased bismuth (Bi) content (alloying elements expressed in wt.%).

Novel Brass Compositions–High Bismuth (Bi) Content							
Cu	Fe	Sn	Zn	Bi	Si	Cr	Ref.
Bal.	0.22	0.58	40.83	2.85	-	0.22	[75]
Bal.	-	-	40.19	2.20	-	-	[17]
Bal.	0.23	0.6	40.64	2.02	-	0.26	[75]
Bal.	-	2	38	2.00	0.5	-	[105]
Bal.	-	1.5	38	1.50	0.5	-	[105]
Bal.	-	1	38	1.00	0.5	-	[105]
Bal.	0.23	0.60	40.81	0.99	-	0.26	[75]
Bal.	-	0.7	38	0.80	0.5	-	[105]
Bal.	-	0.3	38	0.40	0.5	-	[105]
Bal.	-	-	29.2	0.27	-	-	[77]

Bi addition operates similarly to the Pb addition, improving the machinability through chip segmentation and providing cutting tool lubrication.

**Table A7.** Novel brass compositions with an increased titanium (Ti) content (alloying elements expressed in wt.%).

Novel Brass Compositions–High Titanium (Ti) Content							
Cu	Pb	Fe	Sn	Zn	Si	Ti	Ref.
Bal.	0.02	0.09	0.03	39.6	-	1.03	[65]
Bal.	-	-	0.65	40.1	-	1.03	[67]
Bal.	-	-	-	41.2	-	0.99	[67]
Bal.	0.16	0.58	0.41	38.9	0.13	0.71	[65]
Bal.	-	-	-	39.0	-	0.50	[23]

Ti addition induces  $\text{Cu}_x\text{Ti}_y$  type particle precipitation, thus increasing the mechanical properties through precipitation hardening and acting as a grain refiner.

**Table A8.** Novel brass compositions with an increased silicon (Si) content (alloying elements expressed in wt.%).

Novel Brass Compositions—High Silicon (Si) Content								
Cu	Pb	Ni	Fe	Sn	Zn	Al	Si	Ref.
Bal.	-	-	-	1.04	34.78	-	3.68	[109]
Bal.	-	-	-	-	31.91	3.37	3.37	[109]
Bal.	2.27	0.25	0.4	0.53	31.77	0.8	2.34	[109]
Bal.	0.01	-	0.01	-	31	-	2.2	[73]
Bal.	-	-	-	-	39.77	-	1.73	[108]
Bal.	0.01	-	0.04	-	29	-	1.65	[73]
Bal.	-	-	-	-	35.98	1.6	1.6	[109]
Bal.	-	-	-	-	40.55	-	1.21	[109]
Bal.	-	-	-	-	39.49	1	1.11	[24]
Bal.	-	-	-	-	39.73	0.7	1.1	[71]
Bal.	-	-	-	-	38.42	0.68	1.1	[24]
Bal.	-	-	-	-	38.44	1.09	1.09	[109]
Bal.	-	-	-	0.5	42	0.5	1	[73]
Bal.	-	-	-	-	38.37	0.34	0.95	[71]
Bal.	-	-	-	-	39.37	0.18	0.95	[24]
Bal.	0.01	-	0.04	-	30	-	0.93	[70]
Bal.	-	-	-	-	40.43	0.38	0.87	[71]
Bal.	-	-	-	-	38.75	0.9	0.85	[24]
Bal.	-	-	-	-	40.9	-	0.83	[102]
Bal.	-	-	-	-	39.13	0.69	0.78	[24]
Bal.	-	-	-	-	38.64	0.51	0.78	[72]
Bal.	-	-	-	-	36.92	0.27	0.78	[71]
Bal.	-	-	-	-	33.68	0.2	0.73	[71]
Bal.	-	-	-	-	38.91	0.5	0.69	[24]
Bal.	-	-	-	-	39.29	0.54	0.54	[109]
Bal.	-	-	-	-	38	-	0.5	[105]
Bal.	-	-	-	-	37.69	0.49	0.49	[109]
Bal.	-	-	-	-	40.67	-	0.34	[102]

Si addition produces fine intermetallic particles, improving machinability and mechanical properties. Si also affects the stability of the  $\alpha/\beta/\gamma$  phases in brasses.

**Table A9.** Novel brass composition with an increased content in antimony (Sb), graphite, magnesium (Mg), manganese (Mn), carbon (C) and cerium (Ce) (alloying elements expressed in wt.%).

Novel Brass Compositions—Uncommon Alloying Element Additions (Sb, Graphite, Mg, Mn, C, Ce)														
Cu	Fe	Sn	Zn	Al	Sb	Bi	Graphite	Si	Mg	Mn	Cr	C	Ce	Ref.
Bal.	0.095	-	30.1	-	-	0.173	-	-	-	1.26	-	-	-	[77]
Bal.	0.063	-	29.1	-	-	0.2	-	-	-	3.48	-	-	-	[77]
Bal.	0.096	-	29.6	-	-	0.204	-	-	-	5.83	-	-	-	[77]
Bal.	-	-	35	-	0.0–2.34	-	-	-	0.0–1.79	-	-	-	-	[22]
Bal.	-	-	40	-	-	-	0–1.0	-	0.3–1.9	-	-	-	-	[68]
Bal.	-	-	40	-	-	-	-	-	1	-	-	-	-	[59]
Bal.	-	-	39.2	-	-	-	0.0–1.0	-	-	-	-	-	-	[1]
Bal.	4.78	-	38	-	-	-	-	-	-	-	-	0.22	-	[69]
Bal.	-	-	38.6	-	-	-	-	-	-	-	-	-	0.07	[74]
Bal.	-	0.5	41.6	0.5	0.4	-	-	1	-	-	-	-	-	[73]
Bal.	-	0.5	41	0.5	1	-	-	1	-	-	-	-	-	[73]
Bal.	-	0.5	40.6	0.5	1.4	-	-	1	-	-	-	-	-	[73]
Bal.	-	0.5	40	0.5	2	-	-	1	-	-	-	-	-	[73]
Bal.	0.22	0.59	40.86	-	-	-	-	-	-	-	0.34	-	-	[75]

Sb addition improves machinability by promoting the formation of  $\beta'$ . Produces intermetallic particles which compromise the mechanical properties but further improve machinability. Graphite addition acts similarly to Pb, thus increasing machinability and providing cutting tool lubrication. Mg addition improves machinability by promoting the formation of  $\beta'$ . Produces intermetallic particles which compromise the mechanical properties but further improve machinability. Mn addition promotes the formation of  $\beta'$  thus increasing the mechanical properties and machinability. C addition operates similarly to graphite, as in the relevant research [68] it was incorporated in the form of  $\text{Fe}_3\text{C}$  and underwent a graphitisation process. Ce addition reduces the flow stress of the brass.



## References

1. Imai, H.; Kosaka, Y.; Kojima, A.; Li, S.; Kondoh, K.; Umeda, J.; Atsumi, H. Characteristics and machinability of lead-free P/M Cu60–Zn40 brass alloys dispersed with graphite. *Powder Technol.* **2010**, *198*, 417–421. [\[CrossRef\]](#)
2. Chakrabarti, A.K.; Spretnak, J.W. The effect of solute (Zn) concentration on the plastic deformation properties of  $\alpha$  and  $\alpha + \beta$  Cu-Zn alloys. *Mater. Sci. Eng.* **1976**, *24*, 95–100. [\[CrossRef\]](#)
3. Panagopoulos, C.N.; Georgiou, E.P.; Simeonidis, K. Lubricated wear behavior of leaded  $\alpha + \beta$  brass. *Tribol. Int.* **2012**, *50*, 1–5. [\[CrossRef\]](#)
4. Achiței, D.C.; Minciună, M.G.; Vizureanu, P.; Sandu, A.V.; Cimpoeșu, R.; Istrate, B. Study on structure and properties of CuZnPb alloy. *IOP Conf. Ser. Mater. Sci. Eng.* **2019**, *133*, 012015. [\[CrossRef\]](#)
5. La Fontaine, A.; Keast, V.J. Compositional distributions in classical and lead-free brasses. *Mater. Charact.* **2006**, *57*, 424–429. [\[CrossRef\]](#)
6. Wolfenden, A.; Wright, P.K. Role of lead in free-machining brass. *Met. Technol.* **1979**, *6*, 297–302. [\[CrossRef\]](#)
7. Stoddart, C.T.H.; Lea, C.; Dench, W.A.; Green, P.; Pettit, H.R. Relationship between lead content of Cu-40Zn, machinability, and swarf surface composition determined by auger electron spectroscopy. *Met. Technol.* **1979**, *6*, 176–184. [\[CrossRef\]](#)
8. Pantazopoulos, G. Leaded brass rods C 38500 for automatic machining operations: A technical report. *J. Mater. Eng. Perform.* **2002**, *11*, 402–407. [\[CrossRef\]](#)
9. Leaded Brasses, Copper Development Association Inc. Available online: [https://www.copper.org/resources/properties/microstructure/lead\\_brasses.html](https://www.copper.org/resources/properties/microstructure/lead_brasses.html) (accessed on 17 January 2022).
10. Siu, K.W.; Kwok, J.C.M.; Ngan, A.H.W. Thermo-mechanical processing of brass components for potable-water usage increases risks of Pb leaching. *Water Res.* **2020**, *186*, 116414. [\[CrossRef\]](#)
11. Korshin, G.V.; Ferguson, J.F.; Lancaster, A.N. Influence of natural organic matter on the corrosion of leaded brass in potable water. *Corros. Sci.* **2000**, *42*, 53–66. [\[CrossRef\]](#)
12. Triantafyllidou, S.; Parks, J.; Edwards, M. Lead particles in potable water. *Am. Water Work. Assoc.* **2007**, *99*, 107–117. [\[CrossRef\]](#)
13. Tang, M.; Sinsheimer, P.; Sarver, E.; Parks, J.; Edwards, M. Evaluating “lead-free” brass performance in potable water. *Corrosion* **2019**, *75*, 865–875. [\[CrossRef\]](#)
14. Elfland, C.; Scardina, P.; Edwards, M. Lead-contaminated water from brass plumbing devices in new buildings. *Am. Water Work. Assoc.* **2010**, *102*, 66–76. [\[CrossRef\]](#)
15. Triantafyllidou, S.; Nguyen, C.K.; Zhang, Y.; Edwards, M.A. Lead (Pb) quantification in potable water samples: Implications for regulatory compliance and assessment of human exposure. *Environ. Monit. Assess.* **2021**, *185*, 1355–1365. [\[CrossRef\]](#)
16. Estelle, A.A. Drinking water lead regulations: Impact on the brass value chain. *Mater. Sci. Technol.* **2016**, *32*, 1763–1770. [\[CrossRef\]](#)
17. Li, S.; Kondoh, K.; Imai, H.; Atsumi, H. Fabrication and properties of lead-free machinable brass with Ti additive by powder metallurgy. *Powder Technol.* **2011**, *205*, 242–249. [\[CrossRef\]](#)
18. Available online: <https://www.epa.gov/sdwa/use-lead-free-pipes-fittings-fixtures-solder-and-flux-drinking-water> (accessed on 12 December 2021).
19. Schultheiss, F.; Windmark, C.; Sjöstrand, S.; Rasmusson, M.; Ståhl, J.E. Machinability and manufacturing cost in low-lead brass. *Int. J. Adv. Manuf. Technol.* **2018**, *99*, 2101–2110. [\[CrossRef\]](#)
20. Kuyucak, S.; Sahoo, M. A review of the machinability of copper-base alloys. *Can. Metall. Q.* **1996**, *35*, 1–15. [\[CrossRef\]](#)
21. Suksongkarm, P.; Rojananan, S.; Rojananan, S. Bismuth formation in lead-free Cu-Zn-Si yellow brass with various bismuth-tin alloy additions. *Mater. Trans.* **2018**, *59*, 1747–1752. [\[CrossRef\]](#)
22. Adineh, M.; Doostmohammadi, H. Microstructure, mechanical properties and machinability of Cu-Zn-Mg and Cu-Zn-Sb brass alloys. *Mater. Sci. Technol.* **2019**, *35*, 1504–1514. [\[CrossRef\]](#)
23. Atsumi, H.; Imai, H.; Li, S.; Kondoh, K.; Kosaka, Y.; Kojima, A. The effect of solid solutionizing Ti element on microstructural and mechanical properties of extruded Cu-40Zn-Ti ternary alloy. *Trans. JWRI* **2011**, *40*, 67–71.
24. Yang, C.; Ding, Z.; Tao, Q.C.; Liang, L.; Ding, Y.F.; Zhang, W.W.; Zhu, Q.L. High-strength and free-cutting silicon brasses designed via the zinc equivalent rule. *Mater. Sci. Eng. A* **2018**, *723*, 296–305. [\[CrossRef\]](#)
25. Toulfatzis, A.; Pantazopoulos, G.; David, C.; Sagris, S.; Paipetis, A. Final heat treatment as a possible solution for the improvement of machinability of Pb-free brass alloys. *Metals* **2018**, *8*, 575. [\[CrossRef\]](#)
26. Toulfatzis, A.I.; Pantazopoulos, G.A.; Paipetis, A.S. Microstructure and properties of lead-free brasses using post-processing heat treatment cycles. *Mater. Sci. Technol.* **2016**, *32*, 1771–1781. [\[CrossRef\]](#)
27. Pantazopoulos, G.; Vazdirvanidis, A. Characterization of the microstructural aspects of machinable  $\alpha$ - $\beta$  phase brass. *Microsc. Anal.* **2008**, *22*, 13–16.
28. Vaxevanidis, N.M.; Fountas, N.A.; Koutsomichalis, A.; Kechagias, J.D. Experimental investigation of machinability parameters in turning of CuZn39Pb3 brass alloy. *Procedia Struct. Integr.* **2018**, *10*, 333–341. [\[CrossRef\]](#)
29. Zoghypour, N.; Tascioglou, E.; Atay, G.; Kaynak, Y. Machining-induced surface integrity of holes drilled in lead-free brass alloy. *Procedia CIRP* **2020**, *87*, 148–152. [\[CrossRef\]](#)
30. Nobel, C.; Hofmann, U.; Klocke, F.; Veselovac, D.; Puls, H. Application of a new, severe-condition friction test method to understand the machining characteristics of Cu-Zn alloys using coated cutting tools. *Wear* **2015**, *344*, 58–68. [\[CrossRef\]](#)
31. Naik, D.B.; Dave, A.K. Multipass, multicriterion optimization in turning. *Int. J. Adv. Manuf. Technol.* **1998**, *14*, 544–548. [\[CrossRef\]](#)

32. Besseris, G.J. Non-linear nonparametric quality screening in low sampling testing. *Int. J. Qual. Reliab. Manag.* **2010**, *27*, 893–915. [[CrossRef](#)]
33. Amaral, L.; Quinta, R.; Silva, T.E.; Soares, R.M.B.; Castellanos, S.D.; De Jesus, A.M.P. Effect of lead on the machinability of brass alloys using polycrystalline diamond cutting tools. *J. Strain Anal.* **2018**, *53*, 602–615. [[CrossRef](#)]
34. Vaxevanidis, N.M.; Kechagias, J.D.; Fountas, N.A.; Manolakos, D.E. Evaluation of machinability in turning of engineering alloys by applying artificial neural networks. *Open Constr. Build. Technol. J.* **2014**, *8*, 389–399. [[CrossRef](#)]
35. Abbas, A.; Pimenov, D.; Erdakov, I.; Taha, M.; El Rayes, M.; Soliman, M. Artificial intelligence monitoring of hardening methods and cutting conditions and their effects on surface roughness, performance, and finish turning costs of solid-state recycled aluminum alloy 6061 chips. *Metals* **2018**, *8*, 394. [[CrossRef](#)]
36. Hrechuk, A.; Bushlya, V.; M'Saoubi, R.; Ståhl, J.-E. Quantitative analysis of chip segmentation in machining using an automated image processing method. *Procedia CIRP* **2019**, *82*, 314–319. [[CrossRef](#)]
37. Besseris, G.J. A methodology for product reliability enhancement via saturated-unreplicated fractional factorial designs. *Reliab. Eng. Syst. Saf.* **2010**, *95*, 742–749. [[CrossRef](#)]
38. Fountas, N.; Koutsomichalis, A.; Kechagias, J.D.; Vaxevanidis, N.M. Multi-response optimization of CuZn39Pb3 brass alloy turning by implementing Grey Wolf algorithm. *Frat. Ed Integrità Strutt.* **2019**, *50*, 584–594. [[CrossRef](#)]
39. Arvidsson, M.; Gremyr, I. Principles of robust design methodology. *Qual. Reliab. Eng. Int.* **2008**, *24*, 23–35. [[CrossRef](#)]
40. Manna, A.; Bhattacharyya, B. Taguchi and Gauss elimination method: A dual response approach for parametric optimization of CNC wire cut EDM of PRAISICMMC. *Int. J. Adv. Manuf. Technol.* **2006**, *28*, 67–75. [[CrossRef](#)]
41. Ilzarbe, L.; Álvarez, M.J.; Viles, E.; Tanco, M. Practical applications of design of experiments in the field of engineering: A bibliographical review. *Qual. Reliab. Eng. Int.* **2008**, *24*, 417–428. [[CrossRef](#)]
42. Viles, E.; Tanco, M.; Ilzarbe, L.; Alvarez, M.J. Planning experiments, the first real task in reaching a goal. *Qual. Eng.* **2009**, *21*, 44–51. [[CrossRef](#)]
43. Tanco, M.; Viles, E.; Ilzarbe, L.; Alvarez, M.J. Barriers faced by engineers when applying design of experiments. *TQM J.* **2009**, *21*, 565–575. [[CrossRef](#)]
44. Tanco, M.; Viles, E.; Ilzarbe, L.; Alvarez, M.J. Implementation of design of experiments projects in industry. *Appl. Stoch. Models Bus. Ind.* **2009**, *25*, 478–505. [[CrossRef](#)]
45. Pantazopoulos, G.; Vazdirvanidis, A. Failure analysis of a fractured leaded-brass (CuZn39Pb3) extruded hexagonal rod. *J. Fail. Anal. Prev.* **2008**, *8*, 218–222. [[CrossRef](#)]
46. Toulfatzis, A.I.; Besseris, G.J.; Pantazopoulos, G.A.; Stergiou, C. Characterization and comparative machinability investigation of extruded and drawn copper alloys using non-parametric multi-response optimization and orthogonal arrays. *Int. J. Adv. Manuf. Technol.* **2011**, *57*, 811–826. [[CrossRef](#)]
47. Mapelli, C.; Venturini, R. Dependence of the mechanical properties of an  $\alpha/\beta$  brass on the microstructural features induced by hot extrusion. *Scr. Mater.* **2006**, *54*, 1169–1173. [[CrossRef](#)]
48. Momeni, A.; Ebrahimi, G.R.; Faridi, H.R. Effect of chemical composition and processing variables on the hot flow behavior of leaded brass alloys. *Mater. Sci. Eng. A* **2015**, *626*, 1–8. [[CrossRef](#)]
49. Garcia, P.; Rivera, S.; Palacios, M.; Belzunce, J. Comparative study of the parameters influencing the machinability of leaded brasses. *Eng. Fail. Anal.* **2010**, *17*, 771–776. [[CrossRef](#)]
50. Toulfatzis, A.I.; Pantazopoulos, G.A.; David, C.N.; Sagris, D.S.; Paipetis, A.S. Machinability of eco-friendly lead-free brass alloys: Cutting-force and surface-roughness optimization. *Metals* **2018**, *8*, 250. [[CrossRef](#)]
51. Holler, K.; Reetz, B.; Müller, K.B.; Pyzalla, A.; Reimers, W. Microstructure and properties of hot extruded brass CuZn40Pb2. *Mater. Sci. Forum* **2003**, *426–432*, 3667–3672. [[CrossRef](#)]
52. Loginov, Y.N.; Ovchinnikov, S. Increase in the uniformity of structure and properties of extruded workpieces of alpha + beta lead brasses. *Metallurgist* **2015**, *8*, 342–347. [[CrossRef](#)]
53. Kunčická, L.; Jambor, M.; Weiser, A.; Dvořák, J. Structural factors inducing cracking of brass fittings. *Materials* **2021**, *14*, 3255. [[CrossRef](#)] [[PubMed](#)]
54. Kunčická, L.; Benč, M.; Andreyachshenko, V. Effect of residual stress on cracking of hot-die forged brass fittings. *IOP Conf. Ser. Mater. Sci. Eng.* **2021**, *1190*, 012031. [[CrossRef](#)]
55. Kunčická, L.; Kocich, R. Effects of temperature (in)homogeneity during hot stamping on deformation behavior, structure and properties of brass valves. *Adv. Res. Mater.* **2021**, 202101414. [[CrossRef](#)]
56. Chandra, T.; Jonas, J.J.; Taplin, D.M.R. Grain-boundary sliding and intergranular cavitation during superplastic deformation of  $\alpha/\beta$  brass. *J. Mater. Sci.* **1978**, *13*, 2380–2384. [[CrossRef](#)]
57. Hentati, N.; Makni, A.; Elleuch, R. Study of failure modes affecting a crimped nut related to forging process. *J. Fail. Anal. Prev.* **2012**, *12*, 130–138. [[CrossRef](#)]
58. Blaz, L.; Konior, Z.; Majda, T. Structural aspects of  $\alpha/\beta$  transformation in hot deformed CuZn-39Pb3 alloy. *J. Mater. Sci.* **2001**, *36*, 3629–3635. [[CrossRef](#)]
59. Pantazopoulos, G.A.; Toulfatzis, A.I. Fracture modes and mechanical characteristics of machinable brass rods. *Metallogr. Microstruct. Anal.* **2012**, *1*, 106–114. [[CrossRef](#)]
60. Adineh, M.; Doostmohammadi, H.; Raiszadeh, R. Effect of Si and Al on the microstructure, mechanical properties and machinability of 65Cu-35Zn brass. *Iran. J. Mater. Sci. Eng.* **2019**, *16*, 21–32.

61. Kashyap, B.P.; Verma, S.; Mandlik, P.; Kumar, N.; Toppo, S.P. Effect of test temperature on tensile properties of  $\alpha/\beta$  brass containing lead. *Mater. Sci. Technol.* **2006**, *22*, 363–367. [[CrossRef](#)]
62. Laporte, V.; Mortensen, A. Intermediate temperature embrittlement of copper alloys. *Int. Mater. Rev.* **2009**, *54*, 94–116. [[CrossRef](#)]
63. Wolley, D.J.; Fox, A.G. The embrittlement of leaded and unleaded  $\alpha+\beta$  (60-40) brasses in the temperature range 300 to 500 °C. *J. Mater. Sci. Lett.* **1988**, *7*, 763–765. [[CrossRef](#)]
64. Flegeau, G.; Taleb, L.; Hauet, A.; Vassal, C. Cyclic behavior of an industrial brass Cu Zn32. In *Key Engineering Materials*; Trans Tech Publications Ltd.: Bäch, Switzerland, 2013; Volume 535, pp. 189–192.
65. Johansson, J.; Persson, H.; Ståhl, J.-E.; Zhou, J.-E.; Bushlya, V.; Schultheiss, F. Machinability evaluation of low-lead brass alloys. *Procedia Manuf.* **2019**, *38*, 1723–1730. [[CrossRef](#)]
66. Atsumi, H.; Imai, H.; Li, S.; Kondoh, K.; Kousaka, Y.; Kojima, A. Fabrication and properties of high-strength extruded brass using elemental mixture of Cu-40% Zn alloy powder and Mg particle. *Mater. Chem. Phys.* **2012**, *135*, 554–562. [[CrossRef](#)]
67. Li, S.; Imai, H.; Atsumi, H.; Kondoh, K.; Kojima, A.; Kousaka, Y.; Yamamoto, K.; Takahashi, M. The effects of Ti and Sn alloying elements on precipitation strengthened Cu40Zn brass using powder metallurgy and hot extrusion. *Mater. Sci. Eng. A* **2012**, *535*, 22–31. [[CrossRef](#)]
68. Zhang, X.; Ma, C.; Li, S.; Pan, D.; Zhen, F. Interface design of lead-free free-cutting titanium reinforced graphite brass composites and its effect on mechanical properties and cutting performance. *Mater. Sci. Eng. A* **2020**, *774*, 138909. [[CrossRef](#)]
69. Zhuo, H.-O.; Tank, J.-C.; Xue, Y.-Y.; Ye, N. Preparation of lead-free free-cutting graphite brasses by graphitization of cementite. *Trans. Nonferrous Met. Soc. China* **2015**, *25*, 3252–3257. [[CrossRef](#)]
70. Alirezai, M.; Doostmohammadi, H. Microstructure evolution in cast and equilibrium heat-treated CuZn30-(Si) alloys. *Int. J. Cast Met. Res.* **2016**, *29*, 222–227. [[CrossRef](#)]
71. Yang, C.; Yang, Y.; Lin, G. Tailoring chip morphology by correlating the microstructure and dynamic yield strength in turning of lead-free silicon brasses. *J. Manuf. Processes* **2020**, *53*, 420–430. [[CrossRef](#)]
72. Yang, C.; Ye, W.; Yang, Y.; Wang, F.; Ding, Y.; Zhu, Q.; Zhang, W. Microstructural evolution and mechanical behavior of lead-free silicon brass manufactured by low-pressure die casting. *J. Mater. Eng. Perform.* **2018**, *27*, 5478–5488. [[CrossRef](#)]
73. Suksongkarm, D.; Rojananan, S.; Rojananan, S. Microstructure and hardness of Cu-Zn-Si-Al-Sn with antimony addition. *Adv. Mater. Res.* **2013**, *802*, 179–183. [[CrossRef](#)]
74. Chandra, T.; Jonas, J.J.; Taplin, D.M.R. The mechanical behavior of cerium-modified alpha-beta brass at high temperatures. *J. Mater. Sci.* **1976**, *11*, 1843–1848. [[CrossRef](#)]
75. Atsumi, H.; Imai, H.; Li, S.; Kondoh, K.; Kousaka, Y.; Kojima, A. High-strength, lead-free machinable  $\alpha-\beta$  duplex phase brass Cu-40Zn-Cr-Fe-Sn-Bi alloys. *Mater. Sci. Eng. A* **2011**, *529*, 275–281. [[CrossRef](#)]
76. Thomson, J.; Zavadil, R.; Sahoo, M. Development of a lead-free bearing material for aerospace applications. *Int. J. Met.* **2010**, *4*, 19–30. [[CrossRef](#)]
77. Basori, I.; Pratiwi, H.I.; Sofyan, B.T. Effects of manganese on the microstructures, mechanical properties and deformation characteristics of Cu-29Zn alloy. *Mater. Sci. Forum* **2017**, *917*, 212–217. [[CrossRef](#)]
78. Li, Z.Q.; WeiDong, W.; KaiZhou, L.; GengChun, C.; WeiPing, C. Study on microstructure and properties of brass containing Sb and Mg. *Sci. China Ser. E Technol. Sci.* **2009**, *52*, 2172–2174.
79. Toulfatzis, A.I.; Pantazopoulos, G.A.; Paipetis, A.S. Fracture behavior and characterization of lead-free brass alloys for machining applications. *J. Mater. Eng. Perform.* **2014**, *23*, 3193–3206. [[CrossRef](#)]
80. Toulfatzis, A.I.; Pantazopoulos, G.A.; Paipetis, A.S. Fracture mechanics properties and failure mechanisms of environmental-friendly brass alloys under impact, cyclic and monotonic loading conditions. *Eng. Fail. Anal.* **2018**, *90*, 497–517. [[CrossRef](#)]
81. Kozana, J.; Garbacz-Klempka, A.; Piękoś, M. Lead-free casting brasses. Investigations of the corrosion resistance and shaping of microstructure and properties. *Arch. Foundry Eng.* **2019**, *19*, 113–118.
82. Iecks, G.; Maiolo, L.M.A.; Bortolozzo, A.D.; Osório, W.R. Designing a microstructural array associated with hardness of dual-phase Cu-Zn alloy using investment casting. *Mater. Res.* **2018**, *21*, e20171059. [[CrossRef](#)]
83. Lobanov, M.L.; Danilov, S.V.; Pastukhov, V.I. Crystallographic peculiarities of  $\beta-\alpha$  transformation in brass induced by hot extrusion. *Solid State Phenom.* **2019**, *299*, 541–545. [[CrossRef](#)]
84. Dhinwal, S.S.; Shukla, A.J.; Biswas, S.; Chouhan, D.K. Evolution of microstructure and crystallographic texture in  $\alpha-\beta$  brass during equal channel angular pressing. *Mater. Characteris.* **2020**, *163*, 110270. [[CrossRef](#)]
85. Ibrahim, A.; Rizal, S.; Ali, N.; Huzni, S. The effect of chemical composition on grain size and formability of the free-lead Cu-30Zn alloy: A short review. *IOP Conf. Ser. Mater. Sci. Eng.* **2019**, *536*, 012019. [[CrossRef](#)]
86. Pantazopoulos, G. A review of defects and failures in brass rods and related components. *Pract. Fail. Anal.* **2003**, *3*, 14–22. [[CrossRef](#)]
87. Gupta, I.; Mishra, R.R.; Nagaraj, M.; Rajesha, S. An overview on modes of failure of brass components. *Int. J. Mech. Prod. Eng.* **2014**, *2*, 33–36.
88. Izumi, O.; Harada, Y. Hot Shortness of  $\alpha$ -Brass. *Trans. Jpn. Inst. Met.* **1970**, *11*, 292–299. [[CrossRef](#)]
89. Martinez-Hernandez, M.; Juarez-Hernandez, A.; González-Rivera, C.; Hernandez-Rodriguez, M.A.L. Bismuth segregation and crack formation on a free lead yellow brass tap. *Eng. Fail. Anal.* **2013**, *28*, 63–68. [[CrossRef](#)]
90. Hsieh, C.-C.; Wang, J.-S.; Wu, P.T.-Y.; Wu, W. Microstructural development of brass alloys with various Bi and Pb additions. *Met. Mater. Int.* **2013**, *19*, 1173–1179. [[CrossRef](#)]

91. Chunlei, G.; Dongfu, S.; Kaihong, Z.; Haiyan, W.; Nan, Z. Failure analysis of a lead-free brass tap used in potable water. *Eng. Fail. Anal.* **2016**, *59*, 377–383. [[CrossRef](#)]
92. Chunlei, G.; Nan, Z.; Yuehua, K.; Shuncheng, W.; Kaihong, Z. Failure analysis of lead-free brass valve bodies. *Eng. Fail. Anal.* **2019**, *100*, 536–543. [[CrossRef](#)]
93. Pantazopoulos, G.; Vazdirvanidis, A. Identification of corrosion and damage mechanisms by using Scanning Electron Microscopy and Energy Dispersive X-ray Microanalysis: Contribution to Failure Analysis Case Histories. *IOP Conf. Ser. Mater. Sci. Eng.* **2014**, *55*, 012015. [[CrossRef](#)]
94. Pantazopoulos, G.; Toulfatzis, A.I. Failure analysis of a machinable brass connector in a boiler unit installation. *Case Stud. Eng. Fail. Anal.* **2013**, *1*, 18–23. [[CrossRef](#)]
95. Lisenko, N.; Evans, C.D.; Yao, Y.L. Effect of brass composition and phases on stress corrosion mitigation by laser shock peening. *Manuf. Lett.* **2020**, *23*, 5–8. [[CrossRef](#)]
96. Choucri, J.; Balbo, A.; Zanutto, F.; Grassi, V.; Touhami, M.E.; Mansouri, I.; Monticelli, C. Corrosion behavior and susceptibility to stress corrosion cracking of leaded and lead-free brasses in simulated drinking water. *Materials* **2021**, *15*, 144. [[CrossRef](#)] [[PubMed](#)]
97. ISO 3685; Tool-Life Testing with Single-Point Turning Tools. International Organization for Standardization (ISO): Geneva, Switzerland, 1993.
98. Gane, N. The effect of lead on the friction and machining of brass. *Philos. Mag. A* **1981**, *43*, 545–566. [[CrossRef](#)]
99. Hassan, K.; Kumar, A.; Garg, M.P. Experimental investigation of material removal rate in CNC turning using Taguchi method. *Int. J. Eng. Res. Appl.* **2012**, *2*, 1581–1590.
100. Nobel, C.; Hofmann, U.; Klocke, F.; Veselovac, D. Experimental investigation of chip formation, flow, and breakage in free orthogonal cutting of copper-zinc alloys. *Int. J. Adv. Manuf. Technol.* **2016**, *84*, 1127–1140. [[CrossRef](#)]
101. Laakso, S.V.A.; Hokka, M.; Niemi, E.; Kuokkala, V.-T. Investigation of the effect of different cutting parameters on chip formation of low-lead brass with experiments and simulations. *Proc. Inst. Mech. Eng. Part B J. Eng. Manuf.* **2013**, *227*, 1620–1634. [[CrossRef](#)]
102. Doostmohammadi, H.; Moridshahi, H. Effect of Si on microstructure, ordering transformation and properties of the Cu<sub>60</sub>Zn<sub>40</sub> alloy. *J. Alloys Compd.* **2015**, *640*, 401–407. [[CrossRef](#)]
103. Rajabi, Z.; Doostmohammadi, H. Effect of addition of tin on the microstructure and machinability of  $\alpha$ -brass. *Mater. Sci. Technol.* **2018**, *34*, 1218–1227. [[CrossRef](#)]
104. Taha, M.A.; El-Mahallawy, N.A.; Hammouda, R.R.; Moussa, T.M.; Gheith, M.H. Machinability characteristics of lead free-silicon brass alloys as correlated with microstructure and mechanical properties. *Ain Shams Eng. J.* **2012**, *3*, 383–392. [[CrossRef](#)]
105. Suksongkarm, P.; Rojananan, S.; Rojananan, S. Using recycled bismuth-tin solder in novel machinable lead-free brass. *Mater. Trans.* **2017**, *58*, 1754–1760. [[CrossRef](#)]
106. Klocke, F.; Nobel, C.; Veselovac, D. Influence of tool coating, tool material, and cutting speed on the machinability of low-lead brass alloys in turning. *Mater. Manuf. Processes* **2016**, *31*, 1895–1903. [[CrossRef](#)]
107. Schultheiss, F.; Johansson, D.; Bushlya, V.; Zhou, J.; Nilsson, K.; Ståhl, J.E. Comparative study on the machinability of lead-free brass. *J. Clean. Prod.* **2017**, *149*, 366–377. [[CrossRef](#)]
108. Nobel, C.; Klocke, F.; Lung, D.; Wolf, S. Machinability enhancement of lead-free brass alloys. In Proceedings of the 6th CIRP International Conference on High Performance Cutting, Berkeley, CA, USA, 23–25 June 2014; pp. 95–100.
109. Vilarinho, C.; Davim, J.P.; Soares, D.; Castro, F.; Barbosa, J. Influence of the chemical composition on the machinability of brasses. *J. Mater. Processing Technol.* **2005**, *170*, 441–447. [[CrossRef](#)]
110. Tam, P.L.; Schultheiss, F.; Ståhl, J.-E.; Nyborg, L. Residual stress analysis of machined lead-free and lead-containing brasses. *Mater. Sci. Technol.* **2016**, *32*, 1789–1793. [[CrossRef](#)]
111. Gaitonde, V.N.; Karnik, S.R.; Davim, J.P. Selection of optimal MQL and cutting conditions for enhancing machinability in turning of brass. *J. Mater. Processing Technol.* **2008**, *204*, 459–464. [[CrossRef](#)]
112. Gaitonde, V.N.; Karnik, S.R.; Davim, J.P. Study on the influence of MQL and cutting conditions on machinability of brass using Artificial Neural Network. *Int. J. Mater. Prod. Technol.* **2010**, *3*, 155–172. [[CrossRef](#)]
113. Al-Zaharah, I.T. Suppressing vibrations of machining processes in both feed and radial directions using an optimal control strategy: The case of interrupted cutting. *J. Mater. Processing Technol.* **2006**, *172*, 305–310. [[CrossRef](#)]
114. Xiaoliang, J.; Altintas, Y. Chatter stability model of micro-milling with process damping. *J. Manuf. Sci. Eng.* **2013**, *135*, 031011.
115. Kundrak, J.; Szabo, G.; Markopoulos, A.P. Experimental and numerical investigation of the influence of cutting speed and feed rate on forces in turning of steel. *Mater. Sci. Forum* **2016**, *862*, 270–277. [[CrossRef](#)]
116. Monka, P.P.; Monkova, K.; Majstorovic, V.D.; Božić, Ž.; Andrej, A. Optimal cutting parameter specification of newly designed milling tools based on the frequency monitoring. *Int. J. Adv. Manuf. Technol.* **2020**, *115*, 777–794. [[CrossRef](#)]
117. Monka, P.; Monkova, K.; Modrak, V.; Hric, S.; Pastucha, P. Study of a tap failure at the internal threads machining. *Eng. Fail. Anal.* **2019**, *100*, 25–36. [[CrossRef](#)]



Article

# Multicomponent Fe-Based Bulk Metallic Glasses with Excellent Corrosion and Wear Resistances

Guan Zhang <sup>1,2</sup>, Wenlei Sun <sup>1,\*</sup>, Lei Xie <sup>3,4</sup>, Chengwu Zhang <sup>3,4</sup>, Jie Tan <sup>5</sup>, Xuan Peng <sup>2</sup>, Qiang Li <sup>4,\*</sup>, Xu Ma <sup>3,4</sup>, Dongmei Zhao <sup>6</sup> and Jiangtong Yu <sup>1</sup>

<sup>1</sup> School of Mechanical Engineering, Xinjiang University, Urumqi 830046, China; zhangguan0208@163.com (G.Z.); yujtong@163.com (J.Y.)

<sup>2</sup> Engineering Training Center, Xinjiang University, Urumqi 830046, China; xjdxpx@126.com

<sup>3</sup> Xinjiang Key Laboratory of Solid State Physics and Devices, Xinjiang University, Urumqi 830046, China; guanzxj@163.com (L.X.); zcw\_xju@163.com (C.Z.); mx2407383624@163.com (X.M.)

<sup>4</sup> School of Physics Science and Technology, Xinjiang University, Urumqi 830046, China

<sup>5</sup> Northwest Company of China Petroleum and Chemical Corporation, SINOPEC, Urumqi 830011, China; jie26@163.com

<sup>6</sup> Laboratory and Equipment Management Office, Xinjiang University, Urumqi 830046, China; zdm1925@163.com

\* Correspondence: sunwenxj@163.com (W.S.); qli@xju.edu.cn (Q.L.)

**Abstract:** In this study, new multicomponent Fe<sub>54</sub>M<sub>5</sub>Cr<sub>15</sub>Mo<sub>6</sub>Si<sub>2</sub>B<sub>4</sub>P<sub>10</sub>C<sub>4</sub> (M = Fe, Co, and Ni, denoted as Fe<sub>59</sub>, Fe<sub>54</sub>Co<sub>5</sub>, and Fe<sub>54</sub>Ni<sub>5</sub>, respectively) bulk metallic glasses (BMGs) with excellent corrosion and wear resistances were synthesized using the J-quenching technique and fluxing treatment. The synthesized Fe-based BMGs possessed a large glass-forming ability, and the maximum diameters of the Fe<sub>59</sub>, Fe<sub>54</sub>Co<sub>5</sub>, and Fe<sub>54</sub>Ni<sub>5</sub> glassy alloy rods reached 5.5, 4.5, and 4.0 mm, respectively. The Fe<sub>59</sub> BMG had a wide supercooled liquid region of 65 K. Potentiodynamic tests in 3.5 wt.% NaCl solution showed that the corrosion resistances of the synthesized Fe-based BMGs were relatively better than that of the 316L stainless steel. The Fe<sub>59</sub> BMG had the highest corrosion resistance, with the lowest self-corrosion current density in the order of 10<sup>-8</sup> A·cm<sup>-2</sup>. Wear tests showed that the synthesized Fe-based BMGs exhibited excellent wear resistances, and the wear rate of the Fe<sub>59</sub> BMG was as low as approximately 1.73 × 10<sup>-15</sup> m<sup>3</sup>·N<sup>-1</sup>·m<sup>-1</sup>. The rare-earth-element-free Fe-based BMGs, especially the Fe<sub>59</sub> BMG, have a low cost, large glass-forming ability, and excellent wear and corrosion resistance, which make them good candidates for wear-and corrosion-resistant coating materials.

**Keywords:** Fe-based bulk metallic glasses; glass forming ability; corrosion resistance; wear resistance

**Citation:** Zhang, G.; Sun, W.; Xie, L.; Zhang, C.; Tan, J.; Peng, X.; Li, Q.; Ma, X.; Zhao, D.; Yu, J. Multicomponent Fe-Based Bulk Metallic Glasses with Excellent Corrosion and Wear Resistances. *Metals* **2022**, *12*, 564. <https://doi.org/10.3390/met12040564>

Academic Editor: George A. Pantazopoulos

Received: 18 February 2022

Accepted: 24 March 2022

Published: 27 March 2022

**Publisher's Note:** MDPI stays neutral with regard to jurisdictional claims in published maps and institutional affiliations.



**Copyright:** © 2022 by the authors. Licensee MDPI, Basel, Switzerland. This article is an open access article distributed under the terms and conditions of the Creative Commons Attribution (CC BY) license (<https://creativecommons.org/licenses/by/4.0/>).

## 1. Introduction

Fe-based bulk metallic glasses (BMGs) have gained substantial attention in recent decades owing to their low cost and unique performance, such as high strength and hardness, excellent wear and corrosion resistance, and excellent soft magnetic properties [1–4]. The strength of Fe-based BMGs is generally higher than 2 GPa, which currently exceeds the strength of high-strength steel; in particular, the compressive fracture strength of a Fe<sub>33.5</sub>Co<sub>33.5</sub>Nb<sub>6</sub>B<sub>27</sub> BMG reaches 4.84 GPa [5]. Owing to their high strength, the microhardness of the Fe-based BMGs is larger than that of the Zr- and Cu-based BMGs, and their wear resistance is three orders of magnitude higher than that of the Zr- and Cu-based BMGs. Additionally, owing to their unique amorphous structure, Fe-based BMGs exhibit a chemically homogeneous single phase and high atomic reactivity, which results in the formation of an extremely uniform and stable passive film on the surface of the alloys; thus, Fe-based BMGs have higher corrosion resistances compared with their crystalline alloy counterparts. For example, Li et al. reported an Fe<sub>59</sub>Cr<sub>12</sub>Mo<sub>3.5</sub>Ni<sub>5</sub>P<sub>10</sub>C<sub>4</sub>B<sub>4</sub>Si<sub>2.5</sub> BMG with excellent corrosion resistance, with  $I_{\text{corr}}$  and  $E_{\text{corr}}$  values of 2.47 × 10<sup>-7</sup> A·cm<sup>-2</sup> and -0.22 V, respectively [6].

Owing to their low cost, ultra-high strength, and excellent wear and corrosion resistance, Fe-based BMGs have been considered good candidates as wear- and corrosion-resistant coating materials [7]. It has been extensively reported that alloying elements can significantly influence the corrosion and wear properties of Fe-based BMGs. Cr and Mo are the most effective elements for providing a high passivation ability for Fe-based BMGs [8,9]. Cr can form a dense and stable hydrated chromium oxyhydroxide passive film on the surface of alloys to prevent corrosion within the alloys [10]. Generally, the higher the Cr content, the better the corrosion resistance of Fe-based BMGs. However, when the Cr content is greater than 15 at.%, further increasing the Cr content does not significantly improve the corrosion resistance of the Fe-based BMGs but increases the material cost. The effect of Mo on the protective ability of the passivation layer is weaker than that of Cr. However, Mo can promote the enrichment of Cr in the passive film, thereby enhancing the corrosion and pitting resistances of Cr-containing Fe-based BMGs. However, the excess addition of Mo is detrimental to the corrosion resistance of Fe-based BMGs [11]. Recently, it was found that the substitution of Fe with a similar element, such as Ni or Co, can produce positive effects on the glass forming ability (GFA) and the mechanical and magnetic properties of Fe-based BMGs. For example, the substitution of 20 at.% Ni for Fe in Fe<sub>80</sub>P<sub>13</sub>C<sub>7</sub> BMG resulted in an increase in the critical diameter ( $D_c$ ) from 2.0 mm to 2.3 mm for full glass formation and a significant increase in room-temperature compressive plastic strain from 1.1% to 11.2% [12]. The room-temperature compressive plasticity of Fe<sub>80</sub>P<sub>13</sub>C<sub>7</sub> BMG improved from 1.1% to 3.0%, and the saturation magnetization increased from 1.45 T to 1.55 T due to the replacement of 10 at.% Fe with Co [13]. Based on the above considerations, new Fe<sub>54</sub>M<sub>5</sub>Cr<sub>15</sub>Mo<sub>6</sub>Si<sub>2</sub>B<sub>4</sub>P<sub>10</sub>C<sub>4</sub> (M = Fe, Co, and Ni) BMGs were successfully prepared in this study, and the corrosion and wear properties of the present Fe-based BMGs were systematically investigated.

## 2. Materials and Methods

Fe<sub>54</sub>M<sub>5</sub>Cr<sub>15</sub>Mo<sub>6</sub>Si<sub>2</sub>B<sub>4</sub>P<sub>10</sub>C<sub>4</sub> (M = Fe, Ni, and Co) alloy ingots were prepared by torch-melting a mixture of Fe<sub>3</sub>P pieces (99.5 mass% purity), Cr powder (99.9 mass% purity), Mo powder (99.9 mass% purity), Fe powder (99.9 mass% purity), Si powder (99.99 mass% purity), boron pieces (99.95 mass% purity), graphite powder (99.95 mass% purity), Co powder (99.9 mass% purity), and Ni powder (99.7 mass% purity) under a high-purity Ar atmosphere. All the as-prepared alloy ingots had a mass of 2 g. Subsequently, the ingots were purified through a fluxing treatment at an elevated temperature of approximately 1450 K for 2–3 h under a vacuum of ~50 Pa, in which a mixture of B<sub>2</sub>O<sub>3</sub> and CaO with a mass ratio of 3:1 was used as the fluxing agent. After the fluxing treatment, the alloys were subjected to the J-quenching technique [14–16]. Consequently, Fe<sub>54</sub>M<sub>5</sub>Cr<sub>15</sub>Mo<sub>6</sub>Si<sub>2</sub>B<sub>4</sub>P<sub>10</sub>C<sub>4</sub> (M = Fe, Ni, and Co) alloy rods with diameters ranging from 1.0–6.0 mm and lengths of several centimeters were prepared.

The amorphous nature of the specimens was examined using an X-ray diffractometer (XRD, Bruker D8 Discover, Bruker Inc., Karlsruhe, Germany) with Co K $\alpha$  radiation. The thermal behavior of the specimens was examined through differential scanning calorimetry (DSC, NETZSCH DSC 404F1, NETZSCH Inc., Selb, Germany) at a heating rate of 0.33 K/s under an Ar atmosphere. The corrosion behaviors of the specimens, as well as that of 316 stainless steel, which was used for comparison, were evaluated through electrochemical measurements (Zahner Zennium X, Zahner Inc., Kronach, Germany). This was conducted in a three-electrode cell using the glassy rod alloy specimens as the working electrode, a saturated calomel electrode as the reference electrode, and a metal platinum electrode as the counter electrode. The working face of the samples was polished to a mirror face using sandpaper, and the non-working parts were sealed with epoxy resin. The potentiodynamic polarization curves were measured in a 3.5% NaCl solution at room temperature with a potential sweep rate of 1 mV/s after immersing the specimens for approximately 30 min to stabilize the open-circuit potential. Electrochemical impedance spectroscopy (EIS) measurements were carried out in a frequency range of 10 kHz to

10 mHz, using a sinusoidal potential perturbation of  $\pm 10$  mV relative to the OCP. The fitting of EIS data was operated by using the software ZSimpWin (3.60, AMETEK Inc. Middleboro, MA, USA). The surface morphology of the specimens after immersion was observed using scanning electron microscopy (SEM, SU8010). The chemical states of the surface elements of the specimens after polarization were analyzed using X-ray photoelectron spectroscopy (XPS, ESCALAB 250Xi, Thermo Fisher Scientific Inc., Waltham, MA, USA) with a monochromatic Al  $K_{\alpha}$  X-ray source ( $h\nu = 1486.6$  eV). The binding energies were calibrated using carbon contamination with a C 1s peak value of 284.8 eV. The Vickers hardness (HV) of the specimens was measured at a load of 200 g and dwell time of 15 s using a microhardness test instrument (MT-401MVA, BangYi Co., Shanghai, China). Prior to testing, the specimens were polished to a mirror face using sandpaper and cleaned with alcohol, and the average of ten measurement values was taken as the final hardness value for each specimen. Tribological tests of the specimens were conducted under ambient conditions using a pin-on-disc tribometer (CSM, Graz, Austria) with a pin-on-disk contact geometry; a GCr15 (860HV) plate with a diameter of 60 mm was used as the counter body. A normal load of 7 N and a total sliding distance of 5000 m with a sliding speed of 1.8 m/s were adopted for all the tribological tests. The wear rate was calculated using Equation (1).

$$V = \frac{\Delta m}{PS\rho} = \frac{m_1 - m_2}{PS\rho} \quad (1)$$

where  $V$  is the wear rate,  $\Delta m$  is the wear mass loss,  $m_1$  and  $m_2$  are the masses of the sample before and after the test, respectively,  $S$  is the sliding distance of the sample,  $p$  is the load, and  $\rho$  is the density of the test sample, which was measured using density testing equipment (Micromeritics, AccuPyc-1340, Micromeritics Inc., Atlanta, GA, USA). The surface and subsurface morphologies of the worn tracks were observed using scanning electron microscopy (SEM, Hitachi s4800, Hitachi Inc., Tokyo, Japan). The topography and chemical composition of the worn surfaces were examined using energy-dispersive X-ray spectrometry (EDS HORIBA 7593-H, HORIBA Inc., Tokyo, Japan).

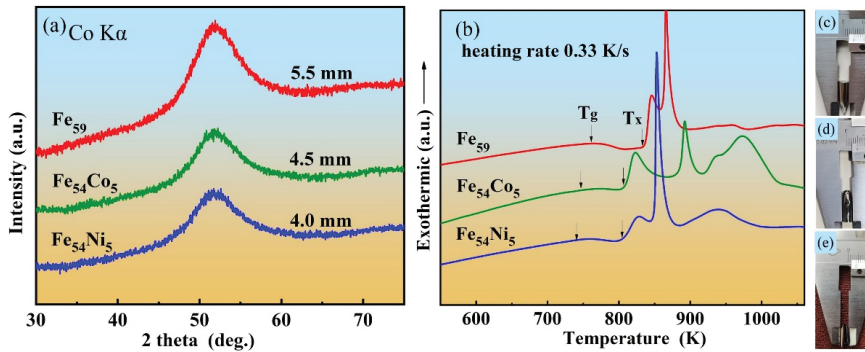
### 3. Results and Discussion

#### 3.1. Material Preparation and Glass Forming Ability (GFA)

The XRD (X-ray diffraction) patterns of the as-prepared  $\text{Fe}_{54}\text{M}_5\text{Cr}_{15}\text{Mo}_6\text{Si}_2\text{B}_4\text{P}_{10}\text{C}_4$  ( $M = \text{Fe}, \text{Ni}, \text{and Co}$ ) glassy alloy rods with critical diameters ( $D_{\text{max}}$ ) for glass formation are shown in Figure 1a. There was only a broad diffraction peak and no detectable sharp crystalline peaks in the XRD patterns of all the specimens, indicating the fully amorphous structure of the specimens [17]. Among the present Fe-based BMGs, the  $\text{Fe}_{59}$  alloy had the largest GFA with a  $D_{\text{max}}$  of 5.5 mm, and the substitution of Fe with 5 at.% Co or Ni degraded the GFA of  $\text{Fe}_{59}$  alloy; the  $D_{\text{max}}$  of  $\text{Fe}_{54}\text{Co}_5$  and  $\text{Fe}_{54}\text{Ni}_5$  alloys were 4.5 and 4.0 mm, respectively [17]. Figure 1b shows the DSC curves of  $\text{Fe}_{54}\text{M}_5\text{Cr}_{15}\text{Mo}_6\text{Si}_2\text{B}_4\text{P}_{10}\text{C}_4$  ( $M = \text{Fe}, \text{Ni}, \text{and Co}$ ) BMGs at a heating rate of 0.33 K/s. The DSC (Differential scanning calorimetry) curves of all specimens exhibited a distinct glass transition, followed by a supercooled liquid region and multistep crystallization peaks. The thermal parameters associated with the glass transition temperature ( $T_g$ ), crystallization temperature ( $T_x$ ), and supercooled liquid region ( $\Delta T_x = T_x - T_g$ ) are summarized in Table 1. It can be seen that the substitution of Co and Ni for Fe led to a decrease in the  $T_g$  and  $T_x$  of the Fe-based BMGs. The  $T_g$  of amorphous alloys mainly depends on the atomic bonding strength among the constituent elements, which can be evaluated through the mixing enthalpy between the constituent elements. It is suggested that the dominant short-range order unit for Fe-metalloid amorphous alloys can be characterized as solute-centered atomic clusters, in which the metallic atoms are located on the shell and the metalloid atoms are located in the center [18]. The mixing enthalpies between Fe and the metalloid elements Si, B, P, and C are  $-35$ ,  $-26$ ,  $-39.5$ , and  $-50$  kJ/mol, respectively; those between Co and the metalloid elements are  $-38$ ,  $-24$ ,  $-35.5$ , and  $-42$  kJ/mol, respectively; and those between Ni and the metalloid elements are  $-40$ ,  $-24$ ,  $-34.5$ , and  $-39$  kJ/mol, respectively [19]. Except



for Si, the mixing enthalpies between Fe and the metalloid elements were more negative than those between Co/Ni and the metalloid elements, which could be the reason for the decrease in the  $T_g$  and  $T_x$  of the  $Fe_{59}$ ,  $Fe_{54}Co_5$ , and  $Fe_{54}Ni_5$  alloys. It was also observed that the  $\Delta T_x$  of the  $Fe_{59}$ ,  $Fe_{54}Co_5$ , and  $Fe_{54}Ni_5$  BMGs decreased. Inoue suggested that a wider  $\Delta T_x$  reflects a better GFA [20], which may account for the compositional dependence of  $D_{max}$  of the Fe-based BMGs in this study. Additionally, it can be noted that the  $\Delta T_x$  of the  $Fe_{59}$  BMG reaches 65 K, indicating an extremely high thermal stability.



**Figure 1.** (a) XRD patterns and (b) DSC curves of as-prepared  $Fe_{54}M_5Cr_{15}Mo_6Si_2B_4P_{10}C_4$  ( $M = Fe, Ni, \text{ and } Co$ ) glassy alloy rods with the critical diameter ( $D_{max}$ ) for glass formation. Photos of (c)  $Fe_{59}$ , (d)  $Fe_{54}Co_5$ , and (e)  $Fe_{54}Ni_5$  glassy alloy rods with the  $D_{max}$  values.

**Table 1.** Summary of the critical diameters for glass formation ( $D_{max}$ ), thermal properties, and the GFA indicators of  $Fe_{54}M_5Cr_{15}Mo_6Si_2B_4P_{10}C_4$  ( $M = Fe, Ni, \text{ and } Co$ ) glassy alloy rods determined from the DSC curves at a heating rate of 0.33 K/s ( $T_g$ : glass transition temperature,  $T_x$ : onset crystallization temperature,  $\Delta T_x = T_x - T_g$ ).

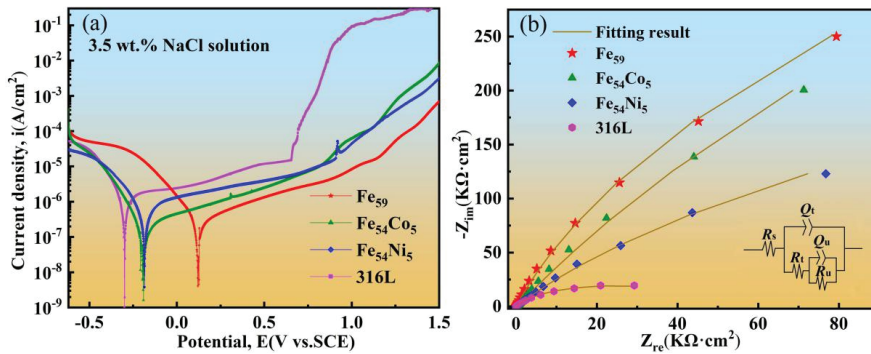
Alloys	$D_{max}$ (mm)	$T_g$ (K)	$T_x$ (K)	$\Delta T_x$ (K)
$Fe_{59}$	5.5	768	833	65
$Fe_{54}Co_5$	4.5	765	805	40
$Fe_{54}Ni_5$	4.0	762	800	38

### 3.2. Corrosion Resistance

To evaluate the corrosion resistance, electrochemical measurements of the Fe-based BMGs were performed in a 3.5 wt.% NaCl solution at room temperature. Figure 2 shows representative potentiodynamic polarization curves of the  $Fe_{59}$ ,  $Fe_{54}Co_5$ , and  $Fe_{54}Ni_5$  glassy alloy rods. The self-corrosion current density ( $I_{corr}$ ) and self-corrosion potential ( $E_{corr}$ ) obtained using the Tafel extrapolation method are listed in Table 2.

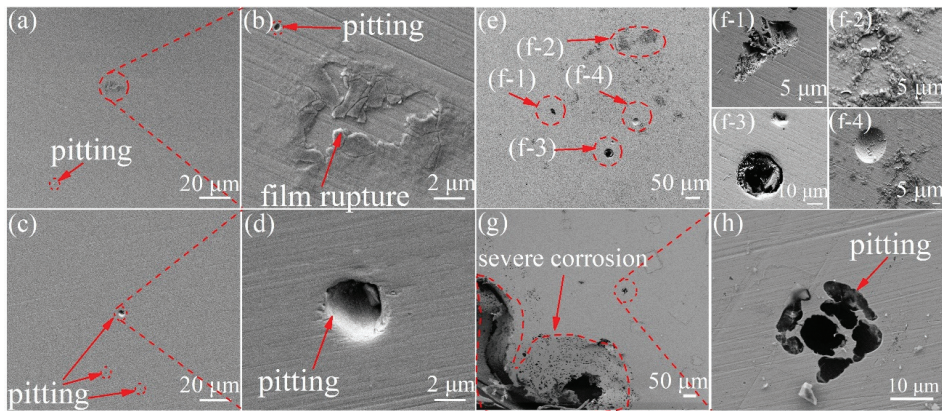
**Table 2.** Electrochemical parameters derived from potentiodynamic polarization curves and EIS analysis of the  $Fe_{54}M_5Cr_{15}Mo_6Si_2B_4P_{10}C_4$  ( $M = Fe, Co, \text{ and } Ni$ ) BMGs and 316L stainless steel ( $E_{corr}$ : self-corrosion potential,  $I_{corr}$ : self-corrosion current density,  $R_s$ : solution resistance,  $R_t$ : charge transfer resistance,  $R_u$ : charge transfer resistance,  $Q_t$ : non-ideal capacitance,  $Q_u$ : non-ideal capacitance).

Alloys	$E_{corr}$ (V)	$I_{corr}$ ( $\times 10^{-8}$ A·cm $^{-2}$ )	$R_s$ ( $\Omega$ ·cm $^2$ )	$R_t$ ( $\times 10^6$ $\Omega$ ·cm $^2$ )	$R_u$ ( $\times 10^6$ $\Omega$ ·cm $^2$ )	$Q_t$ ( $\times 10^{-5}$ $\mu$ F·cm $^2$ )	$Q_u$ ( $\times 10^{-5}$ $\mu$ F·cm $^2$ )
$Fe_{59}$	0.12	8.4	1.71	0.64	1.8	3.59	9.37
$Fe_{54}Co_5$	−0.19	8.6	1.67	0.76	1.68	3.16	4.12
$Fe_{54}Ni_5$	−0.18	38.3	0.85	3.06	0.82	2.87	2.99
316L	−0.29	98.5	1.16	0.0000013	0.049	2.79	5.28



**Figure 2.** (a) Potentiodynamic polarization curves in 3.5 wt.% NaCl solution at room temperature for  $\text{Fe}_{54}\text{M}_5\text{Cr}_{15}\text{Mo}_6\text{Si}_2\text{B}_4\text{P}_{10}\text{C}_4$  ( $M = \text{Fe, Ni, and Co}$ ) glassy alloy rods and 316L stainless steel; (b) Nyquist plots and the corresponding equivalent circuit (inset) for fitting the impedance spectra of  $\text{Fe}_{54}\text{M}_5\text{Cr}_{15}\text{Mo}_6\text{Si}_2\text{B}_4\text{P}_{10}\text{C}_4$  ( $M = \text{Fe, Co, and Ni}$ ) glassy alloy rods and 316L in 3.5 wt.% NaCl solution at room temperature.

Figure 2a shows the potentiodynamic polarization curves in 3.5 wt.% NaCl solution exposed to air at room temperature for the Fe-based glassy alloy rod specimens as well as the 316L stainless steel (316L) for comparison. The self-corrosion potential ( $E_{\text{corr}}$ ) and self-corrosion current density ( $I_{\text{corr}}$ ) of the specimens listed in Table 2 were obtained from the potentiodynamic polarization curves using the Tafel extrapolation method. Compared with the 316L, the Fe-based BMGs exhibited a more positive  $E_{\text{corr}}$ , lower  $I_{\text{corr}}$ , and a more stable and wider passive region, indicating a relatively higher corrosion resistance and superior passive film protection. Among the Fe-based BMGs used in this study, the Fe<sub>59</sub> BMG exhibited the highest corrosion resistance, with the lowest  $I_{\text{corr}}$  and  $I_{\text{pass}}$  in the order of 10<sup>-8</sup> and 10<sup>-7</sup> A/cm<sup>2</sup>, respectively. Further, the potentiodynamic polarization curve of the Fe<sub>59</sub> BMG had a smooth shape, as shown in Figure 2a, indicating that a stable passivation layer was formed on the surface and tiny pit corrosion occurred during the entire measurement period. However, few sharp peaks were found in the curves of the Fe<sub>54</sub>Co<sub>5</sub> and Fe<sub>54</sub>Ni<sub>5</sub> BMGs, as shown in Figure 2a, indicating that pit corrosion occurred during the measurement period; evidence of pit corrosion is shown in Figure 3. It is worth noting that the corrosion resistance of the Fe<sub>59</sub> BMG was better than that of most reported Fe-based BMGs, of which  $I_{\text{corr}}$  is usually in the order of 10<sup>-6</sup>–10<sup>-7</sup> A/cm<sup>2</sup>. For example, it has been reported that a  $\text{Fe}_{36}\text{Cr}_{23}\text{Mo}_{10}\text{W}_8\text{C}_{15}\text{B}_6\text{Y}_2$  BMG possesses good corrosion resistance with an  $I_{\text{corr}}$  of  $6.16 \times 10^{-7}$  A·cm<sup>-2</sup> and  $E_{\text{corr}}$  of  $-0.275$  V [1]. Compared with this Fe-based BMG, the Fe<sub>59</sub> BMG exhibited a lower  $I_{\text{corr}}$  but contained less Cr and Mo. This result may be related to the metalloid elements in the alloys, which can significantly influence the corrosion properties of Fe-based BMGs [4]. For example, Si can improve the passivation ability and corrosion resistance of Fe-based BMGs, which can be attributed to the formation of a dense and stable passive film rich in Si and Cr-oxides [21]. The  $\text{Fe}_{43}\text{Cr}_{16}\text{Mo}_{16}\text{C}_{10}\text{B}_5\text{P}_{10}$  BMGs exhibited a wide passive region, indicating a higher corrosion resistance compared to that of the P-free metallic glass [22].



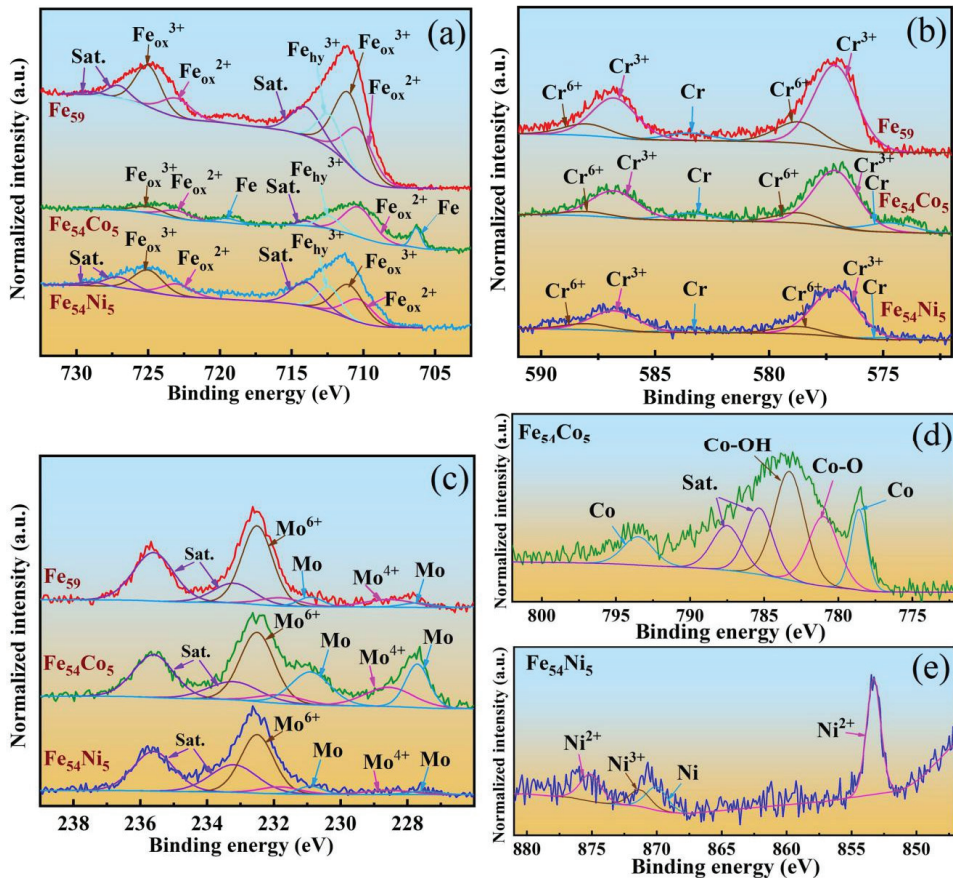
**Figure 3.** SEM micrographs of the electrochemical corroded surfaces of the Fe<sub>59</sub> BMG (a), Fe<sub>54</sub>Co<sub>5</sub> BMG (c), Fe<sub>54</sub>Ni<sub>5</sub> BMG (e), and 316L (g), respectively, and (b,d,f,h) are corresponding partial enlarged views.

Figure 2b shows the Nyquist plots of the Fe-based BMGs and 316L in 3.5 wt.% NaCl solution at room temperature. The Nyquist plots of all samples show a double capacitive loop, implying two time constants in the electrochemical measurements. The semicircle diameter in the Nyquist plots of the Fe<sub>59</sub>, Fe<sub>54</sub>Co<sub>5</sub>, and Fe<sub>54</sub>Ni<sub>5</sub> BMGs and 316L stainless steel decreased, implying that their corrosion resistances also decreased. An appropriate equivalent circuit for fitting the impedance spectra is shown in Figure 2b, where  $R_s$  is the solution resistance;  $R_t$  and  $R_u$  are the charge transfer resistances; and  $Q_t$  and  $Q_u$  represent the possibility of non-ideal capacitance. These fitting parameters are listed in Table 2. The  $R_t$  values of the Fe<sub>59</sub>, Fe<sub>54</sub>Co<sub>5</sub>, Fe<sub>54</sub>Ni<sub>5</sub> BMGs, and 316L stainless steel decreased. It is known that a larger  $R_t$  implies better corrosion resistance [23], and thus, the results of the EIS measurements agree well with those of the electrochemical measurements.

Figure 3 shows the SEM micrographs of the electrochemical corroded surfaces of the Fe-based BMGs and 316L specimens. There were a few pitting pits and a film rupture zone on the surface of the Fe<sub>59</sub> BMG specimen, as shown in Figure 3a,b, revealing the excellent corrosion resistance of the Fe<sub>59</sub> BMG. It can be seen in Figure 3c,d that there were pitting pits with diameters of approximately 4 μm and of a few nanometers on the surface of the Fe<sub>54</sub>Co<sub>5</sub> BMG specimen. Compared with the Fe<sub>59</sub> and Fe<sub>54</sub>Co<sub>5</sub> BMGs, there were more and larger pitting pits and more corrosion products on the surface of the Fe<sub>54</sub>Ni<sub>5</sub> BMG specimen, as shown in Figure 3e,f, which could be attributed to the sharp peaks in the potentiodynamic polarization curve of the Fe<sub>54</sub>Ni<sub>5</sub> BMG shown Figure 2a. The surface of the 316L specimen was completely damaged, covered with a thick layer of polarized product, and had huge pitting pits caused by a severe corrosion, as shown in Figure 3g,h. The observed electrochemical corroded surfaces of the specimens confirmed the results of the electrochemical and EIS measurements.

To better understand the effect of the elements on the corrosion mechanism of the Fe-based BMGs, an XPS (X-ray Photoelectron Spectroscopy) analysis was performed to characterize the chemical composition of the oxide films formed on the surfaces of the specimens after electrochemical measurement in 3.5 wt.% NaCl solution. Figure 4 shows the Fe 2p, Cr 2p, Mo 3d, Co 2p, and Ni 2p spectra of the Fe-based BMGs. The Fe 2p spectra of the specimens comprised the peaks of Fe 2p<sub>1/2</sub> and 2p<sub>3/2</sub> corresponding to the peaks of the metallic (Fe) and Fe<sup>2+</sup>, Fe<sub>hy</sub><sup>3+</sup>, and Fe<sub>ox</sub><sup>3+</sup> oxide (Fe<sup>ox</sup>) states of Fe [23–27]. The peak intensities of Fe<sup>m</sup> in the Fe<sub>54</sub>Co<sub>5</sub> and Fe<sub>54</sub>Ni<sub>5</sub> BMGs were relatively higher than that of the Fe<sub>59</sub> BMG. The Cr 2p peaks represented the metallic (Cr) and Cr<sup>3+</sup> and Cr<sup>6+</sup> oxide (Cr<sup>ox</sup>) states of Cr [26,28–30]. Cr<sup>6+</sup> dissolves in water and causes the corrosion current density to increase; however, it has a self-repairing ability and can promote the formation of denser

Cr<sub>2</sub>O<sub>3</sub> to prevent chloride ions from penetrating into the internal damage [31,32]. As shown in Figure 4b, the total area of the Cr 2p peaks in the Fe<sub>59</sub> BMG was the largest, suggesting a higher concentration of Cr on its surface than on the Fe<sub>54</sub>Co<sub>5</sub> and Fe<sub>54</sub>Ni<sub>5</sub> BMGs. The Mo 3d spectrum, consisting of the Mo 3d 3/2 and 3d 5/2 peaks, corresponded to the metallic Mo and Mo<sup>4+</sup> and Mo<sup>6+</sup> oxide states [24,27,29,30]. The Fe<sub>54</sub>Co<sub>5</sub> BMG had the highest intensity of the low-valence Mo<sup>4+</sup> peak on the surface, followed by the Fe<sub>59</sub> and Fe<sub>54</sub>Ni<sub>5</sub> BMGs. The Fe<sub>59</sub> BMG had the highest intensity of the high-valence Mo<sup>6+</sup> peak in the surface film, followed by the Fe<sub>54</sub>Co<sub>5</sub> and Fe<sub>54</sub>Ni<sub>5</sub> BMGs. Mo can promote the enrichment of Cr in the passive film and, consequently, enhance the corrosion resistance of amorphous alloys [33–35]. The Co 2p spectrum consisted of the metallic Co (Co<sup>m</sup>), Co<sub>hy</sub><sup>2+</sup>, and Co<sub>ox</sub><sup>2+</sup> peaks, as shown in Figure 4d. The Ni 2p spectrum consisted of the peaks corresponding to the metallic Ni (Ni), Ni<sup>2+</sup>, and Ni<sup>3+</sup>, as shown in Figure 4e. It is known that Co and Ni are more effective in providing a high passivation ability for alloys compared with Fe; however, the corrosion resistance of the Fe-based BMGs in this study decreased with the substitution of Co and Ni for Fe. This could be due to the small amount of crystallization in the Fe<sub>54</sub>Co<sub>5</sub> and Fe<sub>54</sub>Ni<sub>5</sub> BMGs owing to the lower GFA, which degraded their corrosion resistance.



**Figure 4.** XPS spectra of Fe 2p (a), Cr 2p (b), Mo 3d (c), Co 2p (d), and Ni 2p (e) in the passive films on the surface of the Fe<sub>54</sub>M<sub>5</sub>Cr<sub>15</sub>Mo<sub>6</sub>Si<sub>2</sub>B<sub>4</sub>P<sub>10</sub>C<sub>4</sub> (M = Fe, Co, and Ni) glassy alloy rod specimens after electrochemical measurements in a 3.5 wt.% NaCl solution.

The outstanding corrosion resistance of amorphous alloys is primarily influenced by the stability of a uniform passive film. Figure 4b,c show that the Cr<sup>ox</sup> and Mo<sup>ox</sup> fractions in

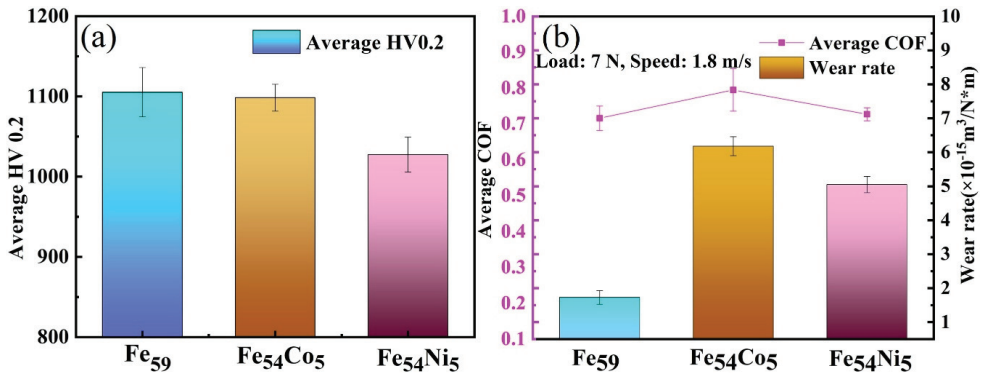
the Fe<sub>59</sub> and Fe<sub>54</sub>Co<sub>5</sub> BMGs in the surface film after the electrochemical test were apparently higher than those in the Fe<sub>54</sub>Ni<sub>5</sub> BMG. The enrichment of Cr<sup>ox</sup> and Mo<sup>ox</sup> was beneficial for the modification of the passive film quality of the BMGs and thus improved the corrosion resistance. The XPS results for the Fe<sub>59</sub>, Fe<sub>54</sub>Co<sub>5</sub>, and Fe<sub>54</sub>Ni<sub>5</sub> BMGs were consistent with the SEM morphology of the samples after the electrochemical test, as shown in Figure 3, in which the Fe<sub>54</sub>Ni<sub>5</sub> BMG exhibited a more severely corroded surface than the Fe<sub>59</sub> and Fe<sub>54</sub>Co<sub>5</sub> BMGs.

### 3.3. Microhardness and Wear Resistance

The measured microhardness values (HV0.2) of the Fe-based BMG specimens are listed in Table 3 and shown in Figure 5a. The Fe-based BMGs exhibited extremely high microhardnesses, exceeding 1000 HV0.2. The microhardness values of the Fe<sub>59</sub>, Fe<sub>54</sub>Co<sub>5</sub>, and Fe<sub>54</sub>Ni<sub>5</sub> BMGs decreased in turn. Similar to the  $T_g$  of amorphous alloys, the hardness of the alloys depends on the atomic bonding strength between the constituent elements; therefore, the microhardness has a similar change trend as the  $T_g$  of the synthesized Fe-based BMGs.

**Table 3.** Density, average microhardness, average COF, and wear rate of the Fe<sub>54</sub>M<sub>5</sub>Cr<sub>15</sub>Mo<sub>6</sub>Si<sub>2</sub>B<sub>4</sub>P<sub>10</sub>C<sub>4</sub> (M = Fe, Ni, and Co) BMGs.

Alloys	Density (g/cm <sup>3</sup> )	Average HV0.2	Average COF	Wear Rate (×10 <sup>-15</sup> m <sup>3</sup> /N·m)
Fe <sub>59</sub>	6.62 ± 0.02	1105 ± 31	0.716 ± 0.034	1.73 ± 0.20
Fe <sub>54</sub> Co <sub>5</sub>	6.83 ± 0.02	1098 ± 17	0.795 ± 0.059	6.18 ± 0.28
Fe <sub>54</sub> Ni <sub>5</sub>	6.79 ± 0.01	1024 ± 22	0.727 ± 0.018	5.05 ± 0.24

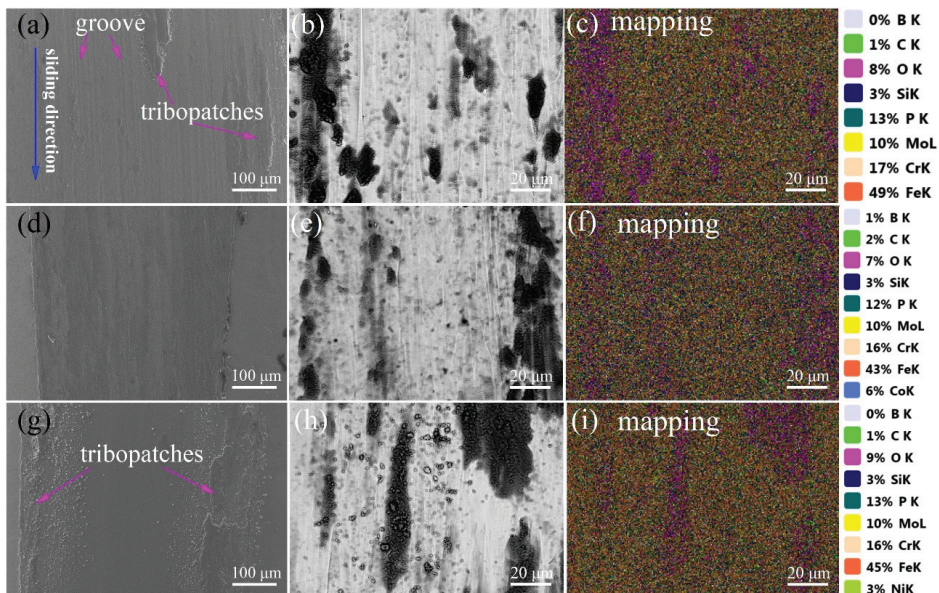


**Figure 5.** (a) Microhardness, (b) average coefficient of friction (COF), and wear rate of the Fe<sub>54</sub>M<sub>5</sub>Cr<sub>15</sub>Mo<sub>6</sub>Si<sub>2</sub>B<sub>4</sub>P<sub>10</sub>C<sub>4</sub> (M = Fe, Ni, and Co) BMGs.

Friction and wear tests of the Fe-based BMGs were performed using pin-on-disk experiments, which were run against a GCr15 plate with a diameter of 60 mm and a hardness of 860 HV under a constant normal load of 7 N, a rolling speed of 1.8 m/s, and a sliding distance of 5000 m. The obtained average steady-state coefficient of friction (COF) and the wear rate, which is calculated by Equation (1), of the Fe-based BMG specimens are listed in Table 3 and shown in Figure 5b. Among the Fe-based BMGs, the Fe<sub>59</sub> BMG had the smallest wear rate of  $1.73 \times 10^{-15} \text{ m}^3 \cdot \text{N}^{-1} \cdot \text{m}^{-1}$ , followed by the Fe<sub>54</sub>Ni<sub>5</sub> BMG with a wear rate of  $5.05 \times 10^{-15} \text{ m}^3 \cdot \text{N}^{-1} \cdot \text{m}^{-1}$ ; the Fe<sub>54</sub>Co<sub>5</sub> BMG had the largest wear rate of  $6.18 \times 10^{-15} \text{ m}^3 \cdot \text{N}^{-1} \cdot \text{m}^{-1}$ . Furthermore, the wear rate of the Fe<sub>59</sub> BMG was relatively lower than those of the Fe<sub>54</sub>Co<sub>5</sub> and Fe<sub>54</sub>Ni<sub>5</sub> BMGs. The COF values for the Fe<sub>59</sub>, Fe<sub>54</sub>Co<sub>5</sub>, and Fe<sub>54</sub>Ni<sub>5</sub> BMGs under dry friction conditions were 0.716, 0.795, and 0.727, respectively. It was clear that the wear rates of the Fe-based BMG specimens exhibited an obvious

positive association with their COF under dry sliding conditions [36]. It should also be noted that the wear rates of the  $\text{Fe}_{54}\text{Co}_5$  and  $\text{Fe}_{54}\text{Ni}_5$  BMGs were negatively correlated, but not inversely proportional, with the microhardness. This indicates that the wear resistance of the Fe-based BMGs cannot be simply determined by their hardness, as predicted by the Archard equation.

Figure 6 shows the SEM (Scanning electron microscope) images of the worn areas of the  $\text{Fe}_{59}$ ,  $\text{Fe}_{54}\text{Co}_5$ , and  $\text{Fe}_{54}\text{Ni}_5$  BMGs. An EDS mapping test was performed on typical regions of the worn surfaces; their chemical compositions are summarized in Figure 6c,f,i. The worn surfaces of  $\text{Fe}_{59}$  exhibited various ploughed grooves parallel to the sliding direction, with different widths and depths, which are typical features corresponding to the abrasive-wear mechanism. In addition, as shown in Figure 6a,b, the worn surface of the  $\text{Fe}_{59}$  BMG was covered with tribo-patches, in which a high fraction of oxygen was observed through EDS (Energy Disperse Spectroscopy) mapping analysis, as shown in Figure 6c. This result demonstrates the oxidation of the tribo-patches of the  $\text{Fe}_{59}$  BMG during the sliding process. The worn surface of  $\text{Fe}_{54}\text{Co}_5$ , as shown in Figure 6d,e, exhibited a smooth morphology covered with a uniform oxide film (Figure 6f), including some small tribo-patches, indicating an oxidation wear mechanism. As shown in Figure 6g,h, the worn morphology of the  $\text{Fe}_{54}\text{Ni}_5$  BMG exhibited much wear debris with grain-like wear particles, which resulted from a brittle failure characteristic, and many tribo-patches with diverse widths and lengths, indicating an adhesive wear mechanism.



**Figure 6.** SEM images of wear surface morphology and EDS mapping of the  $\text{Fe}_{59}$  (a–c),  $\text{Fe}_{54}\text{Co}_5$  (d–f), and  $\text{Fe}_{54}\text{Ni}_5$  (g–i) glassy alloy rod specimens.

#### 4. Conclusions

In this study, a new series of rare-earth-element-free  $\text{Fe}_{54}\text{M}_5\text{Cr}_{15}\text{Mo}_6\text{Si}_2\text{B}_4\text{P}_{10}\text{C}_4$  ( $\text{M} = \text{Fe}$ ,  $\text{Ni}$ , and  $\text{Co}$ ) BMGs were prepared, and the effects of Fe, Co, and Ni contents on the thermal stability, corrosion, and wear resistances of the Fe-based BMGs were investigated. The main results are as follows.

- (1)  $\text{Fe}_{54}\text{M}_5\text{Cr}_{15}\text{Mo}_6\text{Si}_2\text{B}_4\text{P}_{10}\text{C}_4$  ( $\text{M} = \text{Fe}$ ,  $\text{Ni}$  and  $\text{Co}$ ) bulk glassy alloy rods were successfully prepared using the J-quenching and fluxing techniques. The  $D_{\text{max}}$  of the  $\text{Fe}_{59}$ ,  $\text{Fe}_{54}\text{Co}_5$ , and  $\text{Fe}_{54}\text{Ni}_5$  alloys reached 5.5, 4.5, and 4.0 mm, respectively.

- (2) The Fe-based BMGs exhibited high thermal stability, and the  $\Delta T_x$  of the Fe<sub>59</sub> BMG reached 65 K. The  $T_g$ ,  $T_x$ , and  $\Delta T_x$  of the Fe-based BMGs decreased when Co and Ni substituted for Fe.
- (3) Electrochemical and EIS tests showed that, compared with 316L stainless steel, the Fe-based BMGs exhibited excellent corrosion resistance in a 3.5% NaCl solution with very low  $I_{corr}$  in the order of  $10^{-8}$ – $10^{-7}$  A/cm<sup>2</sup>. Among the Fe-based BMGs, the Fe<sub>59</sub> BMG exhibited the highest corrosion resistance with the highest positive  $E_{corr}$ , the lowest  $I_{corr}$ , and the most stable and widest passive region.
- (4) Friction and wear tests showed that the COF values of the Fe<sub>59</sub> (0.716), Fe<sub>54</sub>Co<sub>5</sub> (0.795), and Fe<sub>54</sub>Ni<sub>5</sub> (0.727) BMGs under the dry-friction condition had slight differences. Among the Fe-based BMGs, the Fe<sub>59</sub> BMG had the lowest wear rate of  $1.73 \times 10^{-15}$  m<sup>3</sup>·N<sup>-1</sup>·m<sup>-1</sup>, followed by the Fe<sub>54</sub>Ni<sub>5</sub> BMG with a wear rate of  $5.05 \times 10^{-15}$  m<sup>3</sup>·N<sup>-1</sup>·m<sup>-1</sup> and the Fe<sub>54</sub>Co<sub>5</sub> BMG with a wear rate of  $6.18 \times 10^{-15}$  m<sup>3</sup>·N<sup>-1</sup>·m<sup>-1</sup>. SEM observation of the wear surface morphology indicated that the wear mechanisms of the Fe<sub>59</sub>, Fe<sub>54</sub>Co<sub>5</sub>, and Fe<sub>54</sub>Ni<sub>5</sub> BMGs were abrasive and oxidation, oxidation, and adhesive and oxidation, respectively.
- (5) The rare-earth-element-free Fe-based BMGs, particularly the Fe<sub>59</sub> BMG, showed potential as a coating material, owing to its combined advantages (low cost, large GFA, and excellent wear and corrosion resistances).

**Author Contributions:** Conceptualization, G.Z., Q.L. and W.S.; methodology, G.Z. and J.T.; validation, G.Z., Q.L. and W.S.; formal analysis, G.Z.; investigation, G.Z. and L.X.; resources, Q.L. and D.Z.; data curation, Q.L.; writing—original draft preparation, G.Z.; writing—review and editing, G.Z., Q.L., W.S., C.Z., X.P., X.M. and J.Y.; visualization, G.Z.; project administration, Q.L. and W.S.; funding acquisition, G.Z., Q.L. and W.S. All authors have read and agreed to the published version of the manuscript.

**Funding:** This research was funded by the University Science Research Planning Project of Xinjiang Uygur Autonomous Region, grant number XJEDU2021Y008, the key University Science Research Planning Project of Xinjiang Uygur Autonomous Region, grant number XJEDU2021I003, the Tianshan Innovation Team Program of Xinjiang Uygur Autonomous Region, grant number 2020D14038, the Xinjiang Autonomous Region Key Laboratory Open Fund, grant number 2020520002 and the “Talent Projects” of Urumqi Key Training Object.

**Institutional Review Board Statement:** Not applicable.

**Informed Consent Statement:** Not applicable.

**Data Availability Statement:** Not applicable.

**Conflicts of Interest:** The authors declare no conflict of interest.

## References

1. Zhang, X.; Lai, L.; Xiao, S.; Zhang, H.; Zhang, F.; Li, N.; Guo, S. Effect of W on the Thermal Stability, Mechanical Properties and Corrosion Resistance of Fe-Based Bulk Metallic Glass. *Intermetallics* **2022**, *143*, 107485. [[CrossRef](#)]
2. Inoue, A.; Shen, B.L.; Chang, C.T. Super-High Strength of over 4000 MPa for Fe-Based Bulk Glassy Alloys in [(Fe<sub>1-x</sub>Co<sub>x</sub>)<sub>0.75</sub>B<sub>0.2</sub>Si<sub>0.05</sub>]<sub>96</sub>Nb<sub>4</sub> System. *Acta Mater* **2004**, *52*, 4093–4099. [[CrossRef](#)]
3. Madge, S.V. Toughness of Bulk Metallic Glasses. *Metals* **2015**, *5*, 1279–1305. [[CrossRef](#)]
4. Li, H.X.; Lu, Z.C.; Wang, S.L.; Wu, Y.; Lu, Z.P. Fe-Based Bulk Metallic Glasses Glass Formation, Fabrication, Properties and Applications. *Prog. Mater. Sci.* **2019**, *103*, 235–318. [[CrossRef](#)]
5. Zhao, C.; Dun, C.; Man, Q.; Shen, B. Enhancement of Plastic Deformation in FeCoNbB Bulk Metallic Glass with Superhigh Strength. *Intermetallics* **2013**, *32*, 408–412. [[CrossRef](#)]
6. Li, J.; Yang, L.; Ma, H.; Jiang, K.; Chang, C.; Wang, J.; Song, Z.; Wang, X.; Li, R. Improved Corrosion Resistance of Novel Fe-Based Amorphous Alloys. *Mater. Design* **2016**, *95*, 225–230. [[CrossRef](#)]
7. Ndumia, J.N.; Kang, M.; Gbenontin, B.V.; Lin, J.; Nyambura, S.M. A Review on the Wear, Corrosion and High-Temperature Resistant Properties of Wire Arc-Sprayed Fe-Based Coatings. *Nanomaterials* **2021**, *11*, 2527. [[CrossRef](#)]
8. Shi, M.; Pang, S.; Zhang, T. Towards Improved Integrated Properties in FeCrPCB Bulk Metallic Glasses by Cr Addition. *Intermetallics* **2015**, *61*, 16–20. [[CrossRef](#)]
9. Suryanarayana, C.; Inoue, A. Iron-Based Bulk Metallic Glasses. *Int. Mater. Rev.* **2013**, *58*, 131–166. [[CrossRef](#)]

10. Pang, S.J.; Zhang, T.; Asami, K.; Inoue, A. Bulk Glassy Fe–Cr–Mo–C–B Alloys with High Corrosion Resistance. *Corros. Sci.* **2002**, *44*, 1847–1856. [[CrossRef](#)]
11. Li, S.; Wei, Q.; Li, Q.; Jiang, B.; Chen, Y.; Sun, Y. Development of Fe-Based Bulk Metallic Glasses as Potential Biomaterials. *Mater. Sci. Eng. C* **2015**, *52*, 235–241. [[CrossRef](#)] [[PubMed](#)]
12. Ma, X.; Yang, X.; Li, Q.; Guo, S. Quaternary Magnetic FeNiPC Bulk Metallic Glasses with Large Plasticity. *J. Alloy Compd.* **2013**, *577*, 345–350. [[CrossRef](#)]
13. Xu, K.; Ling, H.; Li, Q.; Li, J.; Yao, K.; Guo, S. Effects of Co Substitution for Fe on the Glass Forming Ability and Properties of Fe<sub>80</sub>P<sub>13</sub>C<sub>7</sub> Bulk Metallic Glasses. *Intermetallics* **2014**, *51*, 53–58. [[CrossRef](#)]
14. Qiang, L. Formation of Bulk Ferromagnetic Nanostructured Fe<sub>40</sub>Ni<sub>40</sub>P<sub>14</sub>B<sub>6</sub> Alloys by Metastable Liquid Spinodal Decomposition. *Sci. China Ser. E-Tech. Sci.* **2009**, *52*, 1919–1922.
15. Shen, T.D.; Schwarz, R.B. Bulk Ferromagnetic Glasses in the Fe–Ni–P–B System. *Acta Mater.* **2001**, *49*, 837–847. [[CrossRef](#)]
16. Zhang, L.; Ma, X.; Li, Q.; Zhang, J.; Dong, Y.; Chang, C. Preparation and Properties of Fe<sub>80-x</sub>Ni<sub>x</sub>P<sub>14</sub>B<sub>6</sub> Bulk Metallic Glasses. *J. Alloy Compd.* **2014**, *608*, 79–84. [[CrossRef](#)]
17. Nishiyama, N.; Takenaka, K.; Miura, H.; Saidoh, N.; Zeng, Y.; Inoue, A. The World’s Biggest Glassy Alloy Ever Made. *Intermetallics* **2012**, *30*, 19–24. [[CrossRef](#)]
18. Cheng, Y.Q.; Ma, E. Atomic-Level Structure and Structure-Property Relationship in Metallic Glasses. *Prog. Mater. Sci.* **2011**, *56*, 379–473. [[CrossRef](#)]
19. Takeuchi, A.; Inoue, A. Classification of Bulk Metallic Glasses by Atomic Size Difference, Heat of Mixing and Period of Constituent Elements and Its Application to Characterization of the Main Alloying Element. *Mater Trans* **2005**, *46*, 2817–2829. [[CrossRef](#)]
20. Inoue, A. Stabilization of Metallic Supercooled Liquid and Bulk Amorphous Alloys. *Acta Mater.* **2000**, *48*, 279–306. [[CrossRef](#)]
21. Zheng, S.; Li, J.; Zhang, J.; Jiang, K.; Liu, X.; Chang, C.; Wang, X. Effect of Si Addition on the Electrochemical Corrosion and Passivation Behavior of Fe–Cr–Mo–C–B–Ni–P Metallic Glasses. *J. Non-Cryst Solids* **2018**, *493*, 33–40. [[CrossRef](#)]
22. Pang, S.J.; Zhang, T.; Asami, K.; Inoue, A. Synthesis of Fe–Cr–Mo–C–B–P Bulk Metallic Glasses with High Corrosion Resistance. *Acta Mater.* **2002**, *50*, 489–497. [[CrossRef](#)]
23. Yamashita, T.; Hayes, P. Analysis of XPS Spectra of Fe<sup>2+</sup> and Fe<sup>3+</sup> Ions in Oxide Materials. *Appl. Surf. Sci.* **2008**, *254*, 2441–2449. [[CrossRef](#)]
24. Si, J.; Wu, Y.; Wang, T.; Liu, Y.; Hui, X. Composition-Controlled Active–Passive Transition and Corrosion Behavior of Fe–Cr(Mo)–Zr–B Bulk Amorphous Steels. *Appl. Surf. Sci.* **2018**, *445*, 496–504. [[CrossRef](#)]
25. Hua, N.; Hong, X.; Liao, Z.; Zhang, L.; Ye, X.; Wang, Q.; Liaw, P.K. Corrosive Wear Behaviors and Mechanisms of a Biocompatible Fe-Based Bulk Metallic Glass. *J. Non-Cryst Solids* **2020**, *542*, 120088. [[CrossRef](#)]
26. Gan, Z.; Zhang, C.; Zhang, Z.-R.; Chen, Z.-J.; Liu, L. Crystallization-Dependent Transition of Corrosion Resistance of an Fe-Based Bulk Metallic Glass under Hydrostatic Pressures. *Corros. Sci.* **2021**, *179*, 109098. [[CrossRef](#)]
27. Li, Y.; Zhang, C.; Xing, W.; Guo, S.; Liu, L. Design of Fe-Based Bulk Metallic Glasses with Improved Wear Resistance. *ACS Appl. Mater. Inter.* **2018**, *10*, 43144–43155. [[CrossRef](#)]
28. Si, J.J.; Chen, X.H.; Cai, Y.H.; Wu, Y.D.; Wang, T.; Hui, X.H. Corrosion Behavior of Cr-Based Bulk Metallic Glasses in Hydrochloric Acid Solutions. *Corros. Sci.* **2016**, *107*, 123–132. [[CrossRef](#)]
29. Liang, D.; Wei, X.; Chang, C.; Li, J.; Wang, Y.; Wang, X.; Shen, J. Effects of W Addition on the Electrochemical Behaviour and Passive Film Properties of Fe-Based Amorphous Alloys in Acetic Acid Solution. *Acta Metall. Sin.-Engl.* **2018**, *31*, 1098–1108. [[CrossRef](#)]
30. Li, Y.; Wang, S.; Wang, X.; Yin, M.; Zhang, W. New FeNiCrMo(P, C, B) High-Entropy Bulk Metallic Glasses with Unusual Thermal Stability and Corrosion Resistance. *J. Mater. Sci. Technol.* **2020**, *43*, 32–39. [[CrossRef](#)]
31. Wang, Y.; Jiang, S.L.; Zheng, Y.G.; Ke, W.; Sun, W.H.; Wang, J.Q. Electrochemical Behaviour of Fe-Based Metallic Glasses in Acidic and Neutral Solutions. *Corros. Sci.* **2012**, *63*, 159–173. [[CrossRef](#)]
32. Xia, H.; Chen, Q.; Wang, C. Evaluating Corrosion Resistances of Fe-Based Amorphous Alloys by YCr/Mo Values. *J. Rare Earth* **2017**, *35*, 406–411. [[CrossRef](#)]
33. Tan, M.W.; Akiyama, E.; Habazaki, H.; Kawashima, A.; Asami, K.; Hashimoto, K. The Role of Chromium and Molybdenum in Passivation of Amorphous Fe–Cr–Mo–P–C Alloys in Deaerated 1 M HCl. *Corros. Sci.* **1996**, *38*, 2137–2151. [[CrossRef](#)]
34. Tan, M.-W.; Akiyama, E.; Kawashima, A.; Asami, K.; Hashimoto, K. The Effect of Air Exposure on the Corrosion Behavior of Amorphous Fe–8Cr–Mo–13P–7C Alloys in 1 M HCl. *Corros. Sci.* **1995**, *37*, 1289–1301. [[CrossRef](#)]
35. Souza, C.A.C.; Ribeiro, D.V.; Kiminami, C.S. Corrosion Resistance of Fe–Cr-Based Amorphous Alloys: An Overview. *J. Non-Cryst. Solids* **2016**, *442*, 56–66. [[CrossRef](#)]
36. Hua, N.; Zhang, X.; Liao, Z.; Hong, X.; Guo, Q.; Huang, Y.; Ye, X.; Chen, W.; Zhang, T.; Jin, X.; et al. Dry Wear Behavior and Mechanism of a Fe-Based Bulk Metallic Glass: Description by Hertzian Contact Calculation and Finite-Element Method Simulation. *J. Non-Cryst. Solids* **2020**, *543*, 120065. [[CrossRef](#)]





Article

# Electron Backscatter Diffraction (EBSD) Analysis of Machinable Lead-Free Brass Alloys: Connecting Texture with Fracture

Athanasios Vazdirvanidis, Andreas Rikos, Anagnostis I. Toulfatzis and George A. Pantazopoulos \*

ELKEME Hellenic Research Centre for Metals S.A., 61st km Athens—Lamia National Road, 32011 Oinofyta, Greece; avazdirvanidis@elkeme.vionet.gr (A.V.); arikos@elkeme.vionet.gr (A.R.); atoulfatzis@elkeme.vionet.gr (A.I.T.)

\* Correspondence: gpantaz@elkeme.vionet.gr; Tel.: +30-2262-60-4463

**Abstract:** The current paper is related to the study of the microstructure and texture of two machinable lead-free brass alloys, namely CuZn42 (CW510L) and CuZn38As (CW511L), which were evaluated in the as-drawn and post heat treated condition. Electron backscatter diffraction (EBSD) was employed for the examination of the brass rods' crystallographic properties in order to correlate the effect of post processing heat treatment on the evolution of phase structure and texture towards the interpretation of dynamic (impact) fracture properties. It is shown that  $\alpha$ - and  $\beta$ -phase volume fractions, mean grain size, and grain boundary misorientation are the most influential factors altering the fracture resistance of single- and dual-phase brass alloy rods. The role of grain boundary engineering, through the formation of coincidence site lattice (CSL) boundaries and their evolution during thermomechanical processing, is of major importance for the design of the mechanical behaviour of new eco-friendly machinable brass alloys.

**Keywords:** brass; machinability; coincidence site lattice; grain boundary; EBSD; lead-free brass

**Citation:** Vazdirvanidis, A.; Rikos, A.; Toulfatzis, A.I.; Pantazopoulos, G.A. Electron Backscatter Diffraction (EBSD) Analysis of Machinable Lead-Free Brass Alloys: Connecting Texture with Fracture. *Metals* **2022**, *12*, 569. <https://doi.org/10.3390/met12040569>

Academic Editor: Shi-Hoon Choi

Received: 1 March 2022

Accepted: 25 March 2022

Published: 28 March 2022

**Publisher's Note:** MDPI stays neutral with regard to jurisdictional claims in published maps and institutional affiliations.



**Copyright:** © 2022 by the authors. Licensee MDPI, Basel, Switzerland. This article is an open access article distributed under the terms and conditions of the Creative Commons Attribution (CC BY) license (<https://creativecommons.org/licenses/by/4.0/>).

## 1. Introduction and Literature Review

Brass alloys (Cu–Zn) are broadly used industrial metallic materials in domestic, mechanical, and electrical engineering as a result of their significant formability, corrosion and mechanical resistance, electrical conductivity, and, of course, high machinability [1–3]. Lead (Pb) is a basic alloying element of conventional brass due to its significant positive effect on machinability, resulting in high lubrication activity at the tool/workpiece interface and intense chip-fracturing, affecting the cutting tool service life and process [4–7]. However, the use of brass as a component in drinking water installations has increased the demands for the elimination of lead toxicity, inaugurating a new class of copper alloys, the eco-friendly or lead-free/low-lead brass alloys. A simple version of lead-free/low-lead machinable alloys include (almost) binary Cu–Zn systems, such as CuZn42 (CW510L) and CuZn38As (CW511L) (see [8–10]). New eco-friendly systems containing various (micro)alloying elements, such as Si, Ti, Bi, Sn, Mg, Sb, and Al aim, in their majority, to offer a significant advantage in chip breaking, replacing Pb with other intermetallic or second-phase particle constituents [11–17]. A recent review, summarizing the entire spectrum of such an extended family of copper alloys, highlighting the various technical approaches and machinability improvement strategies, outlines the necessity of the optimization of the manufacturing process towards the fabrication of eco-friendly components, satisfying the requirement of the relevant environmental and health and safety regulations [18].

Evidently, chip rupture constitutes a significant aspect of machinability performance and it is strongly related to the fracture properties of brass alloys under different loading conditions [7,19]. Therefore, the study of the fracture behaviour of leaded and lead-free/low-lead brasses constitutes a significant element, not only for the insightful understanding of the role of microstructure (e.g., lead particle size and distribution, phase structure, grain structure) on chip breaking, but also for the design and optimization of

the machinability performance, without compromising the mechanical properties of the fabricated components [20,21].

Failure and embrittlement mechanisms, such as intermediate temperature embrittlement (ITE) and transgranular-to-intergranular fracture, together with properties-processing relationships, have been extensively studied in brass alloys systems (see [22–26]). Among the most typical failure mechanisms, dezincification, stress corrosion cracking (SCC), and liquid metal embrittlement (LME) causing hot-shortness due to localized (intergranular) Pb fusion and grain boundary decohesion are revealed in characteristic case histories studied in the authors' Institute, and representative works are shown in [27–29].

## 2. Background Information and Research Objectives

The microstructure of common brass alloys typically consists of one (single-phase,  $\alpha$ -brasses) or two (dual-phase,  $\alpha + \beta$  brasses) phases, as is shown by the well-known binary Cu–Zn phase diagram [30]. The  $\alpha$ -phase is rich in copper, contains less than 37 wt.% zinc, and has a face-centred-cubic (fcc) crystal structure. Single,  $\alpha$ -phase alloys have moderate strength and excellent formability at room temperature due to their low stacking-fault energy (SFE < 10 mJ/m<sup>2</sup>) (see [31]). Therefore, they easily form twins and they can also form coincidence site lattice (CSL) boundaries.

At a higher zinc content, the  $\beta$ -phase is formed, which possesses a body-centred-cubic (bcc) crystal structure. The copper alloys which include a  $\beta$ -phase have excellent hot workability and machinability. The  $\beta$ -phase is also referred to as an intermetallic compound due to the almost 50–50 atomic stoichiometry of Cu and Zn. It is stable at 800 °C from 39 to 55 wt.% Zn and at 500 °C between 45 and 49 wt.% Zn [30].

Above the temperature of 470 °C, Cu and Zn atoms occupy random locations of the lattice, forming a disordered structure which is known as the  $\beta$ -phase, but below this critical temperature thermal vibrations are decreased and atoms take preferential sites, forming a long-range ordered structure known as the  $\beta'$ -phase. This is constituted by smaller regions of ordered structure called domains. Their boundaries are called antiphase boundaries (APBs) and they can be only observed with transmission electron microscopy (TEM). Quenching from the ordered  $\beta$ -phase region leads to fine domain size and increased hardness. The CuZn or  $\beta'$ -phase belongs to B2 super lattice materials, having a structure similar to that of FeAl [30,32].

Extrusion products with variable volume fractions of  $\alpha$ - and  $\beta$ -phases can be produced by altering extrusion temperature. Higher extrusion temperatures favour the formation of a  $\beta$ -phase and result in alloys with a lower yield strength if the  $\alpha$ -phase is considerably coarsened [25].

It has been shown that grain boundary engineering (GBE) can be performed in fcc metals of low stacking-fault energy (SFE) through thermo-mechanical processing (TMP) in order to improve their mechanical properties. The proposed mechanism is the formation of coincident site lattice (CSL) boundaries, through the development of annealing twin boundaries with low values of  $\Sigma$ , such as  $\Sigma 3$  boundaries, and its variants,  $\Sigma 9$  and  $\Sigma 27$ , which together with low-angle grain boundaries (LAGBs; considered to have 5–15 degrees of misorientation) are resistant to intergranular cracking in comparison to the more brittle behaviour shown by high-angle grain boundaries (HAGBs), which have misorientation values larger than 15 degrees [33].

It has been found that one reason for the more brittle behaviour of HAGBs could be their tendency to attract segregated elements, as opposed to LAGBs and the CSL boundaries. When a crack is formed, propagation is preferential through the network of HAGBs, while the fracture mode can be altered from intergranular to transgranular when the crack meets LAGBs and CSL junctions. The amount of CSL boundaries is also linearly increased with decreasing mean grain size, enabling the manufacturing of fracture-resistant alloy products [34].

In dual-phase brass alloys, the grain boundaries' "character" should be evaluated separately for the two distinct phases, since during deformation and post-processing

annealing, the  $\alpha$ - and  $\beta$ -phases show different tendencies in HAGBs formation, with the  $\alpha$ -phase exhibiting a high volume fraction of CSL boundaries, depending on the thermo-mechanical process scheme and the  $\beta$ -phase random values of HAGBs, which are considered of minor importance in GBE.

The current research is a follow-up work, aiming to shed light, using texture analysis, on the alteration of fracture mechanics and failure mechanisms of environmentally friendly brass alloys under different processing conditions, i.e., as-drawn and heat treated [35].

As presented in [35], apart from the benefits in machinability of CW510L (CuZn42) and CW511L (CuZn38As) alloys provided by heat treatment through the increase and stabilization of  $\beta$ -phase content, controversial results were obtained in impact toughness testing:

- The CuZn42 alloy shows an increasing tendency (from 47 to 52 J).
- The CuZn38As alloy shows a decreasing tendency (from 104 to 84 J)

The fracture surfaces of the respective Charpy specimens have also been studied in detail in [35]. The CuZn42 alloy sample in the as-received condition exhibited a typical, ductile fracture failure mechanism with multiple size dimples, while after the heat treatment it principally showed an intergranular fracture topography, with minute dimples on the grain facets. In the CuZn38As alloy sample, a fully ductile behaviour with multiple size dimples and large, deep voids was observed in the as-received condition as compared to the heat treated condition, where finer and shallower dimples were evident [35].

The present study is exclusively focused on electron backscatter diffraction (EBSD), in order to seek potential fracture–texture relationships that could justify the eminent evolution of fracture behaviour and crack propagation modes in the as-received and heat treated brass alloys. More specifically, further attention was placed on the salient interpretation of the observed “paradox” demonstrated by the CuZn42 sample, described as follows:

*“The CuZn42 alloy after heat treatment exhibited improved fracture toughness, even though (i) the fully  $\beta$ -phase microstructure, established by the heat treatment, is expected to induce to fracture toughness deterioration and (ii) the obtained impact fracture topography presents an almost complete intergranular pattern which microscopically implies to lower impact energy.”*

On the contrary, in the CuZn38As sample, the anticipated decrease in impact energy after the heat treatment was expected considering the attained phase transformations and the observed fracture mechanism demonstrated by the obtained fracture morphology which consists of smaller and shallower dimples.

To the best of the authors’ knowledge, there is no similar study concerning the investigation and interpretation of the fracture mechanisms of low-lead/lead-free brass alloys under various thermomechanical processing conditions (as-drawn and heat treated), using detailed texture and grain boundary analysis through electron backscatter diffraction (EBSD) analysis.

### 3. Materials and Methods

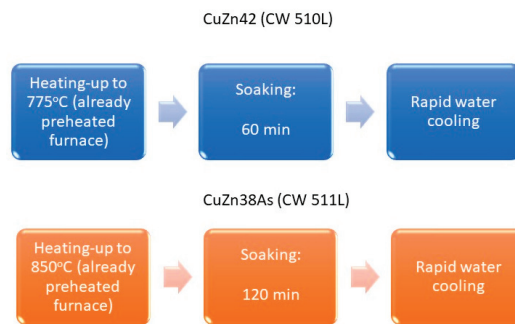
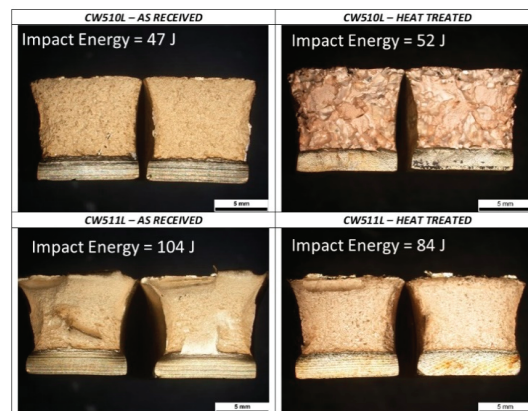
#### 3.1. Brass Alloy Samples

Two distinct lead-free brass alloys were employed for the present study, namely CuZn42 (CW510L) and CuZn38As (CW511L). The chemical composition of the studied alloy samples is shown in Table 1 (see also [35]).

The samples are originated from 35 mm diameter extruded and drawn rods of two types of lead-free brass alloys, namely CuZn42 (CW510L) and CuZn38As (CW511L). The CuZn42 alloy rod was heat treated at 775 °C for 60 min and the CuZn38As at 850 °C for 120 min and they were both water quenched for maximization of the  $\beta$ -phase percentage and suppression of  $\alpha$ -phase precipitation with the aim to improve machinability. A simple schematic showing the heat treatment processes for the different brass alloys is illustrated in Figure 1. The respective fracture surfaces after Charpy impact testing are shown in Figure 2.

**Table 1.** Chemical composition of the brass alloy rods under examination (analysis by optical emission spectroscopy, elemental contents are expressed in wt.%).

Alloy (Spec. Limits)	Cu	Sn	Pb	Fe	Ni	Al	Sb	As	Zn
CuZn42 (CW510L)	57.5	0.006	0.10	0.03	0.003	0.0002	0.003	0.001	42.4
EN 12164	57–59	0.30 max	0.20 max	0.30 max	0.30 max	0.050 max	-	-	Rem.
CuZn38As (CW511L)	62.05	0.004	0.09	0.02	0.001	0.0002	0.003	0.03	37.8
EN 12164	61.5–63.5	0.10 max	0.20 max	0.10 max	0.30 max	0.050 max	-	0.02–0.15	Rem.

**Figure 1.** Simple schematic diagram showing the performed heat treatment processes (blue blocks for CuZn42 and orange blocks for CuZn38As alloy samples). Heat treatment conditions—CuZn42: 775 °C for 60 min followed by water quenching; CuZn38As: 850 °C for 120 min followed by water quenching.**Figure 2.** Macroscopic fracture surfaces after impact fracture toughness tests (Charpy) before and after heat treatment of CW510L and CW511L brass alloys. The average values of the induced impact energies are referred too.

### 3.2. Electron Backscatter Diffraction (EBSD)

EBSD analysis was performed in suitably sectioned impact-tested samples using an EDAX Hikari XP camera (EDAX, Mahwah, NJ, USA) mounted on a JEOL IT-800 HL (JEOL Ltd., Tokyo, Japan) Scanning Electron Microscope (SEM), under 20 kV of accelerating voltage. A tilt of 70 degrees,  $4 \times 4$  binning, and various magnifications and step sizes, depending on the grain size of the samples, prior to and following the heat treatment, were applied to assist in microstructure (phase structure), texture, and grain boundary analysis towards the interpretation of the alterations of fracture mechanisms.

Visualization of the strains caused by the impact tests, near the fracture surfaces, and examination of their distribution on the  $\alpha$ - and  $\beta$ -phases, as well as the characterization and calculation of misorientation between adjacent grains, were performed. In the relative statistics, the  $15^\circ$  angle value was deployed as a distinction criterion of LAGBs from HAGBs.

Examination of the microstructure (phase structure) and fracture surface profile was performed in cross-sections parallel to the extrusion direction. The automatic collection and analysis of EBSD patterns was performed. Data mapping and information regarding the orientation, phase distribution, grain size, morphology, grain boundary, and local deformation of crystallographic regions was realized by using Orientation Image Mapping Software (OIM Analysis, version, EDAX, Mahwah, NJ, USA).

Coincident site lattice (CSL) boundaries are special character boundaries. These boundaries are classified in terms of  $\Sigma$ -values. The CSL boundaries are considered as special due to the fact that they possess a given fraction of atoms in the grain boundary plane which are coincident to both lattices which are separated by the grain boundary. The  $\Sigma$ -value denotes the fraction of atoms in coincidence. The detection of CSL boundaries is automatically performed by the OIM Analysis software.

The various EBSD settings used for the presented images/maps are summarized in Table 2.

**Table 2.** List of settings (scanned area, magnification, step size) used for the collection of the relevant EBSD patterns.

Figure	Scanned Area ( $\mu\text{m}^2$ )	Magnification	Step Size ( $\mu\text{m}$ )
Figure 3	707 × 693	100×	3
Figure 4	1780 × 2300	50×	7
Figure 5	400 × 500	150×	0.8
Figure 6	400 × 500	150×	2
Figure 7a,b	100 × 240	300×	1
Figure 7c	330 × 710	100×	2
Figure 8	140 × 150	370×	1
Figure 9	30 × 90	500×	0.3
Figure 10a	125 × 170	180×	0.4
Figure 10b	70 × 75	500×	0.3

Two representative EBSD scans per sample from the matrix in the as-drawn and heat treated conditions are shown concerning the phase structure examination. The following maps were acquired from each scan (the results are presented in Section 4.1):

- An inverse pole figure (IPF-Z) map and texture plot for representation of the prevailing orientations. This was achieved after a  $90^\circ$  rotation of the original EBSD data, in order to create an equivalent to the transverse section image. Transverse sections are typically studied for the analysis of extruded and drawn products.
- Phase mapping for calculation of the relative  $\alpha$ - and  $\beta$ -phase volume fractions.
- A grain boundary map for characterization of grain boundaries' "character" and misorientation values between neighbouring grains.

One additional scan per sample of the fracture surface profile after Charpy impact testing in the as-drawn and heat treated conditions was performed and the retrieved results were as follows (the results are presented in Section 4.2):

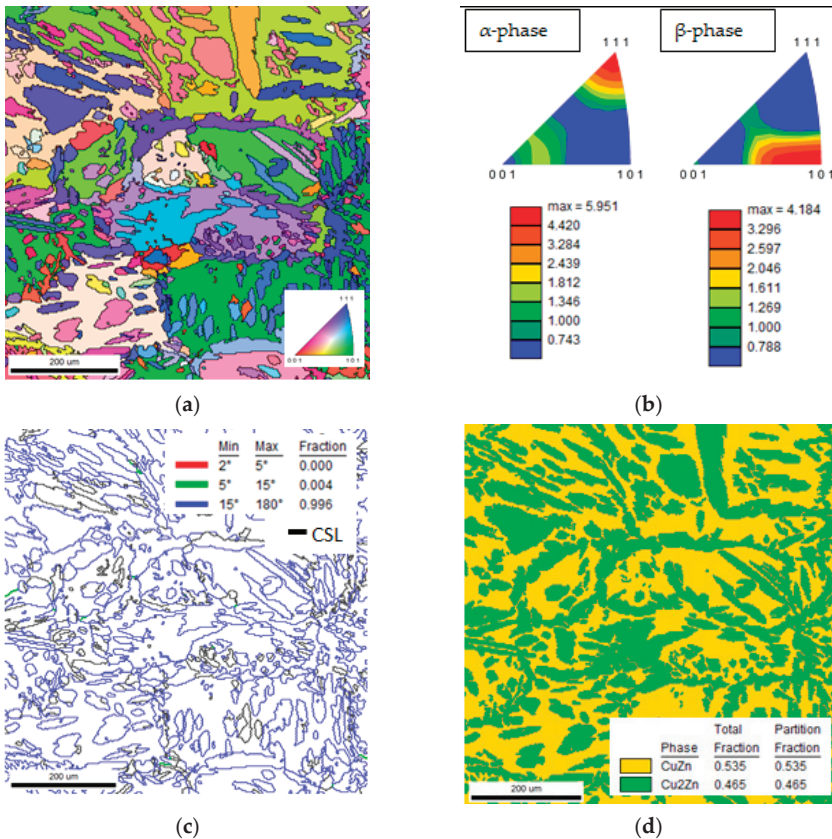
- Phase maps for the correlation of  $\alpha$ - and  $\beta$ -phases with surface fracture topography.
- Kernel average misorientation (KAM) maps for representation of the residual strains (deformation) underneath the fracture surface.

## 4. Results

### 4.1. Microstructure and Texture Characterization

#### 4.1.1. CuZn42—As-Drawn Condition

The texture and volume fraction percentages of the  $\alpha$ - and  $\beta$ -phases in CuZn42 were determined by EBSD (see Figure 3 and Table 3). A (111) fibre structure was exhibited by the  $\alpha$ -phase and a single (101) fibre with minor (335) preferred orientations structure was observed by the  $\beta$ -phase (see Figure 3a,b). The results showed a 46 vol.% fraction for the fcc ( $\alpha$ -phase) and a 54 vol.% fraction for the bcc ( $\beta$ -phase) (see Figure 3d).



**Figure 3.** CuZn42 alloy in the as-drawn condition. (a) Inverse pole figure (IPF-Z) map and (b) texture plots. (c) Misorientation and (d) phase maps. The  $\alpha$ -phase is precipitated in various morphologies from the  $\beta$ -grains. Note: CuZn ( $\beta$ -phase), Cu<sub>2</sub>Zn ( $\alpha$ -phase). Unit:  $\mu\text{m}$ .

The  $\alpha$ -phase appeared in various forms, mainly exhibiting an allotriomorphic morphology nucleated on the  $\beta$ -phase grain boundaries, but also as coarse intra-crystalline “islands”, typical of a slow cooling rate from a hot working temperature (Figure 3a). The mean grain size of both the  $\alpha$ -phase and  $\beta$ -phases was 25  $\mu\text{m}$ . A large fraction (20%) of the  $\alpha$ -phase grains exhibited thermal or annealing twins. The microstructure was characterized by the presence of almost exclusively high angle grain boundaries (see Figure 3c and Table 4). No sub-grains (2–5 degrees) were detected, while low angle boundaries (5–15 degrees) were almost null and were located exclusively on  $\alpha$ – $\alpha$  interface boundaries (see the green lines in Figure 3c). The high angle boundaries included 19% CSL boundaries, consisting of 10%  $\Sigma 3$  and the remaining 9% distributed to other CSL categories. All CSL

high angle boundaries were related to the  $\alpha$ -phase, while approximately half of them were located on  $\alpha$ - $\beta$  interphase boundaries, with the other half on  $\alpha$ - $\alpha$  boundaries.

**Table 3.** Results of EBSD scans, % phase volume fractions, mean grain size, % twinned grains, and mechanical testing data.

Alloy	Metallurgical Condition	Phases			Mean Grain Size ( $\mu\text{m}$ )		$\alpha$ -Phase Twinned Grains (%)	Charpy Test Results [35]	
		vol.% $\alpha$	vol.% $\beta$	$\alpha$	$\beta$	Impact Energy (J)		Fracture mode	
CuZn42 (CW510L)	As-drawn	46	54	25	25	20	47	Ductile, dimpled fracture	
	Heat treated	-	100	-	Macro (several thousand $\mu\text{m}$ , i.e., mm)	52	52	Intergranular (predominantly)	
CuZn38As (CW511L)	As-drawn	98	2	14	3	52	104	Ductile, dimpled fracture (also including large, deep voids)	
	Heat treated	86	14	23	6	21	84	Ductile, dimpled fracture (mostly shallow dimples)	

**Table 4.** Results of EBSD scans, distribution of grain boundaries' angles (%).

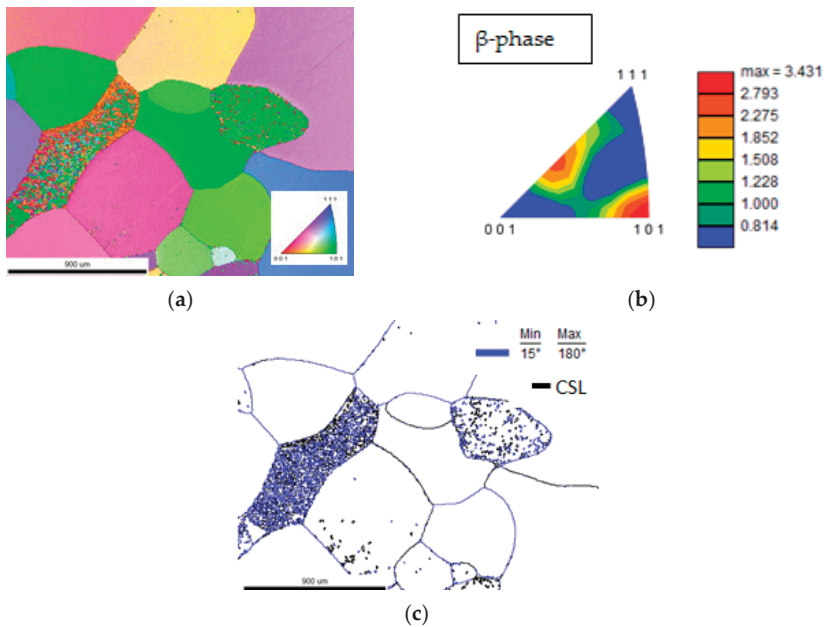
Alloy	Metallurgical Condition	Sub-Grain Boundaries (2–5°)	Low Angle (5–15°)	High Angle (>15°)			CSL			
				CSL	Rem.	$\Sigma 3$	$\Sigma 5$	$\Sigma 9$	$\Sigma 49$	Rem.
CuZn42 (CW510L)	As-drawn			19	81	10	2	2	3	2
	Heat treated			20	80	15				5 ( $\Sigma 7$ , $\Sigma 15$ , and $\Sigma 21$ )
CuZn38As (CW511L)	As-drawn	1	17	33	49	22	3			8
	Heat treated	22	7	21	50	8	1	2	8	2

#### 4.1.2. CuZn42—Heat Treated Condition

After the heat treatment, the microstructure consisted merely of macroscopic size (several thousand  $\mu\text{m}$ , i.e., mm)  $\beta$ -phase grains, while any  $\alpha$ -phase precipitation had been suppressed by the rapid water quenching (Figure 4 and Table 3). A double (101) and (113) fibre structure was exhibited by the single  $\beta$ -phase alloy (Figure 4b). Exclusively high angle boundaries were observed (Figure 4c). The  $\beta$ -phase exhibited poor quality in EBSD scans in most of the grains, which rendered difficulties in processing the respective maps. This could be attributed to (i) the disorder–order transformation which led to fine ordered domain size and multiple orientations within a single grain or (ii) due to the minute lattice parameters deviation between the  $\beta$ - and  $\beta'$ -phase, which could not be resolved by the EBSD technique [36]. Interestingly, the examination showed that approximately 20% of the grain boundaries were CSL, with the higher percentage being  $\Sigma 3$  and the remainder being  $\Sigma 7$ ,  $\Sigma 15$ , and  $\Sigma 21$  (Table 4). The coarse grain size is an indication of the exaggerated grain growth which took place during the heat treatment of the brass rod.

The quality of the  $\beta$ -phase regions in the EBSD maps in the as-drawn condition was higher than in the heat treated conditions, since any quenching effects resulting in fine domain sizes were avoided.





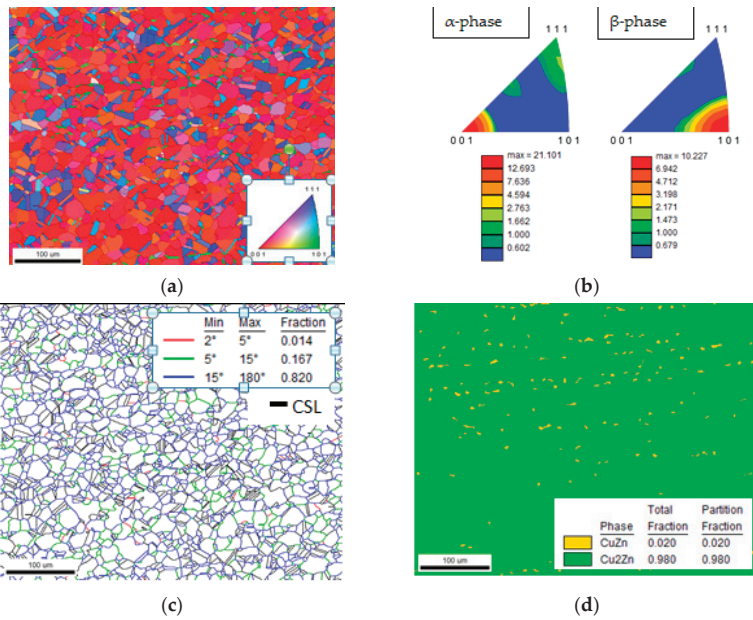
**Figure 4.** CuZn42 alloy in the heat treated condition. (a) Inverse pole figure (IPF-Z) map and (b) texture plot. (c) Misorientation map. The poor quality of the map was attributed to fine domain size within the macroscopic  $\beta$ -phase grains. Unit:  $\mu\text{m}$ .

#### 4.1.3. CuZn38As—As-Drawn Condition

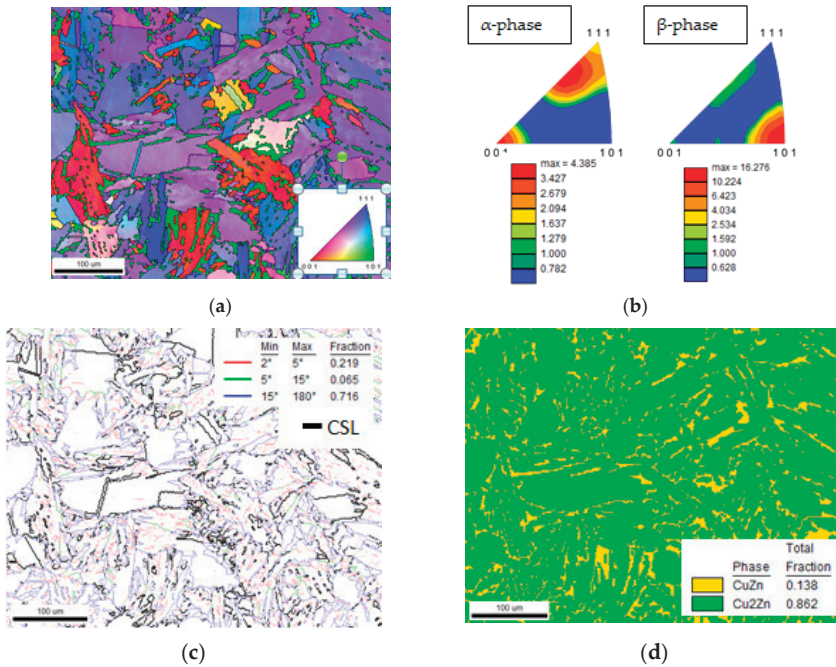
The texture and microstructure of CuZn38As in the as-drawn condition is shown in Figure 5 and the summary of the results are listed in Tables 3 and 4. The material was strongly textured with the (001) direction oriented parallel to the extrusion/drawing direction (Figure 5a,b). The microstructure consisted of partially recrystallized, equiaxed  $\alpha$ -phase grains with a 14  $\mu\text{m}$  mean grain size with a 98 vol.% fraction, while the  $\beta$ -phase was aligned parallel to the extrusion direction (longitudinal sections were performed). The volume fraction of the  $\beta$ -phase was 2% and its mean grain size was 3  $\mu\text{m}$  (Figure 5d). An approximate 52% of  $\alpha$ -phase grains exhibited thermal twins. A total of 1% of the grain boundaries constituted subgrain boundaries (2–5 degrees), 17% consisted of LAGBs, and the remaining 82% consisted of HAGBs (Figure 5c). The subgrain and LAGBs were detected within  $\alpha$ -phase regions and could be considered as an indication of a fully recovered and partially recrystallized microstructure. The CSL fraction constituted 33% of the total boundaries, which were mainly encountered in the  $\alpha$ -phase twins and on  $\alpha$ - $\beta$  interface boundaries in equal amounts. Approximately 22% of the total boundaries were  $\Sigma 3$ , 3% were  $\Sigma 5$ , and the remaining 8% was distributed to other categories (see Table 4).

#### 4.1.4. CuZn38As—Heat Treated Condition

The texture and microstructure of CuZn38As in the heat treated condition are shown in Figure 6 and the results are summarized in Tables 3 and 4. The  $\alpha$ -phase exhibited a (001) and (335) double fibre texture with equal amounts of both directions while the  $\beta$ -phase was strongly textured with prevailing (101) directions and minor (112) (see Figure 6a,b).



**Figure 5.** CuZn38As alloy in the as-drawn condition. (a) Inverse pole figure (IPF-Z) map and (b) texture plot. (c) Misorientation and (d) phase map. Note: CuZn ( $\beta$ -phase), Cu<sub>2</sub>Zn ( $\alpha$ -phase). Unit:  $\mu\text{m}$ .



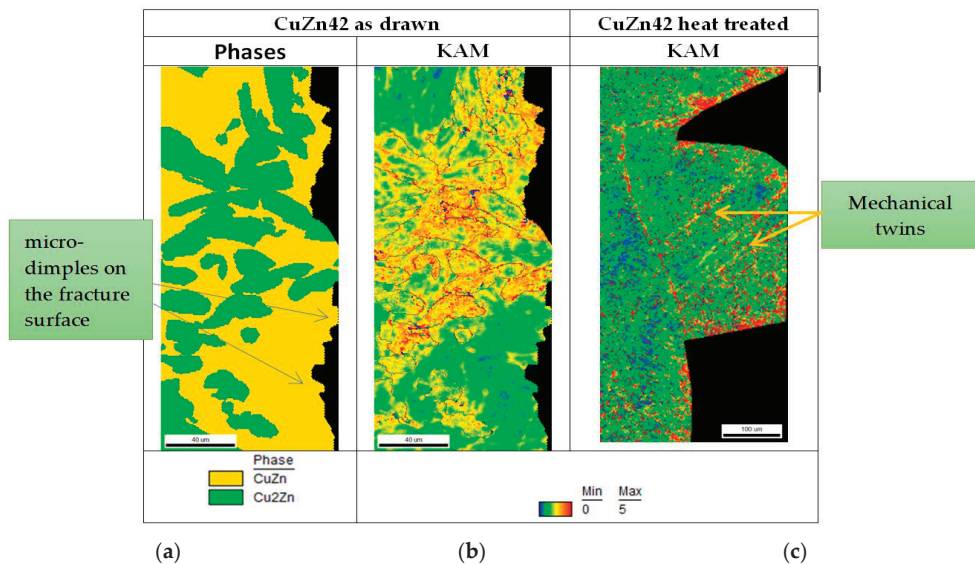
**Figure 6.** CuZn38As alloy in the heat treated condition. (a) Inverse pole figure (IPF-Z) map and (b) texture plot. (c) Misorientation and (d) phases map. Note: CuZn ( $\beta$ -phase), Cu<sub>2</sub>Zn ( $\alpha$ -phase). Unit:  $\mu\text{m}$ .

After the heat treatment, the  $\alpha$ -phase grains were coarsened, with a 23  $\mu\text{m}$  mean grain size, and the fraction of the twinned grains was reduced to 21% (see Figure 6 and Tables 3 and 4). The  $\beta$ -phase percentage was increased to 14% and the banding morphology was altered since a more uniform distribution of the  $\beta$ -phase was created. The  $\beta$ -phase mean grain size was 6  $\mu\text{m}$ , which was double the size of that prior to the heat treatment condition, and it exhibited a plate-like, elongated morphology (Figure 6d). The grain boundaries' character was also significantly altered by the heat treatment, i.e., 22% of the total boundaries were sub-grain boundaries, 7% were LAGBs, and the remaining 71% were HAGBs. Among them, 21% was characterized as CSL boundaries, with  $\Sigma 3$  and  $\Sigma 49$  occupying 8% of the total boundaries each,  $\Sigma 5$  and  $\Sigma 9$  occupying 3% in total, and the remainder being distributed to other categories (Table 4).

#### 4.2. Microstructure Characterization of the Impact Specimens' Fracture Surface Profile

##### 4.2.1. Sample CuZn42—As-Drawn and Heat Treated Conditions

The profile of the fracture surface of the impact test specimen in the as-drawn condition is shown in Figure 7a. The existence of micro-dimples was apparent as various size protrusions, not exceeding 2  $\mu\text{m}$ . These protrusions did not exhibit the same amount of misorientation values in the KAM map, the latter being dependent on the phase where they were formed. The higher values were found by dimples formed within  $\alpha$ -phase regions on the fracture surface or within the  $\beta$ -phase having a short distance from the  $\alpha$ -phase, at maximum up to 10  $\mu\text{m}$ . The  $\alpha$ -phase network presented high misorientation values in the KAM map at even higher distances from the fracture surface.

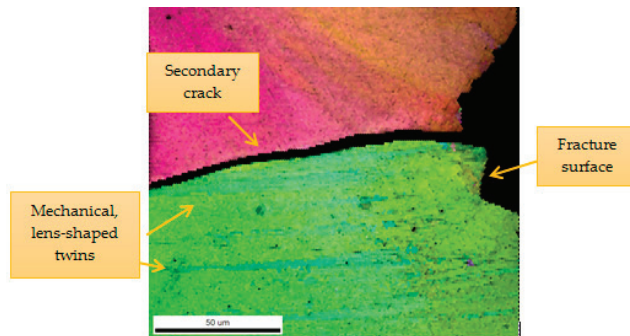


**Figure 7.** Phase and KAM maps of the fracture surface profile of Charpy impact tested CuZn42 alloy samples: (a) phase map, (b) KAM map in the as-drawn condition, and (c) KAM map in the heat treated condition. Unit:  $\mu\text{m}$ .

In Figure 7c, the fracture surface profile of the CuZn42 alloy sample after the heat treatment is shown. It is typical of the occurrence of a brittle, intergranular fracture, with the presence of mechanical twins formed during the impact test. Mechanical twins can be produced in bcc metals under conditions of shock loading in decreased temperatures [31]. The “noise” in the map did not allow a definite recognition of deformed and non-deformed areas, but other than the angle boundaries which were high angle and lead to local high

misorientation values, a uniform distribution of lattice rotations was observed, close and far from the fracture surface.

In Figure 8, lens-shaped twins are shown extending across the width of the grain (deformation twins do not extend to adjacent grains). This is the main existing deformation mechanism exhibited by the coarse, single  $\beta$ -phase brass alloy, since the crack tip created a limited plastic zone size compared to the grain size, hindering the activation of multiple sets of slip systems in adjacent grains, and dislocation emission was impeded by the existing microstructural barriers, causing dislocation pile-up to the activated slip systems and grain boundaries [37]. Twinning behaviour in bcc alloys is considered important in orientation changes that enable the activation of new slip systems in order to allow deformation by slip. In the intergranular crack, shown in Figure 8, on both the fracture surface and across the secondary crack, no appreciable deformation has occurred, leading to the hypothesis that mechanical twinning produced by the shock loading was the predominant deformation mechanism, explaining the reason for the uniform misorientation values for the same grain close and far from the fracture surface.

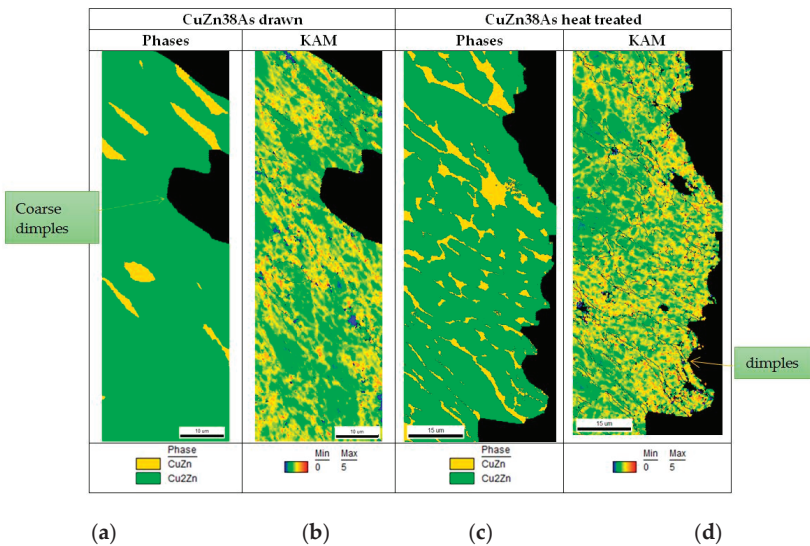


**Figure 8.** Mechanical twins developed on the fracture surface of  $\beta$ -phase grains after Charpy impact test; CuZn42 alloy sample in heat treated condition, section transverse to fracture surface. Combined image quality and IPF map. Unit:  $\mu\text{m}$ .

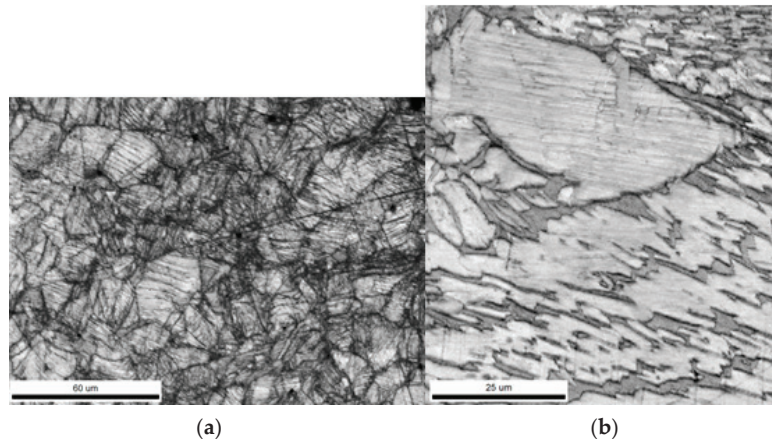
#### 4.2.2. CuZn38As—As-Drawn and Heat Treated Conditions

The fracture surface profile of the sample in the as-drawn condition is shown in Figure 9a,b. It manifested appreciable ductility and the coarse formation of dimples reaching a size of  $30\ \mu\text{m}$ , which is multiple times the size of the dimples of the CuZn42 alloy in the same metallurgical condition. The equiaxed  $\alpha$ -phase grains exhibited extensive strain markings close to the fracture surface as a contributing mechanism to the energy absorbance potential (Figure 10a). These constitute very fine deformation twins which are observed as a major deformation mechanism in low stacking-fault energy alloys such as the  $\alpha$ -brass ( $20\ \text{mJ}\cdot\text{m}^{-2}$ ) [38]. The fine grain size of the  $\alpha$ -phase grains contributed to improved ductility and the respective high energy values in the Charpy impact test ( $104\ \text{J}$ ).

In the heat treated condition, the fracture surface was also deformed, showing the presence of shallower dimples reaching a maximum size of  $17\ \mu\text{m}$ , since the more resistant to deformation  $\beta$ -phase did not allow the development of coarser dimples (Figure 9c,d). The  $\alpha$ -phase grain structure, which was coarser ( $23\ \mu\text{m}$ ) than in the as-drawn condition, negatively affected the material's deformation capacity during the impact test, leading to a lower energy absorption ( $84\ \text{J}$ ). Strain markings in the  $\alpha$ -phase were also developed close to the fracture surface and were more readily observed in the coarser  $\alpha$ -phase grains, especially in the heat treated condition (see Figure 10).



**Figure 9.** Phase and KAM maps of the fracture surface profile of Charpy impact tested CuZn38As alloy samples in the (a,b) as-drawn and (c,d) heat treated conditions. Unit:  $\mu\text{m}$ .



**Figure 10.** Strain markings close to the fracture surface of (a) CuZn38As as-drawn and (b) CuZn38As heat treated alloy sample. EBSD image quality map. Unit:  $\mu\text{m}$ .

## 5. Discussion

The presented results, concerning the fracture behaviour of brass alloys, can be summarized and classified in two main categories: single-phase alloys and dual-phase ( $\alpha + \beta$ ) alloys.

### 5.1. Single-Phase Alloys: CuZn42, Heat Treated and CuZn38As, As-Drawn Condition

The CuZn38As sample, in the as-drawn condition, possessed a higher amount of  $\alpha$ -phase (98 vol.%: it can be considered for simplicity purposes as a “single-phase” alloy) and a finer grain size, rendering a high deformation and energy absorbance capacity. Moreover, it contained the higher fraction of LAGBs and CSL boundaries (~50% in total), which promote ductile, transgranular fracture modes. The high extent of strain markings formation was an additional indication of a strained material with a high energy absorbance capacity.

The opposite condition was observed by the CuZn42 alloy sample in the heat treated condition, which showed a single  $\beta$ -phase structure and macroscopic grain size. These attributes favoured the development of mainly brittle intergranular cracking.

However, the average impact energy value for CuZn42 at the heat treated condition presented a slight increasing tendency (from 47 to 52 J; i.e., approximately 10%), compared with the same alloy at the as-drawn condition. The fact that CSL boundaries were detected (~20%) also led to the appearance of a minor transgranular crack propagation mode in the heat treated CuZn42 alloy. In addition, the occurrence of mechanical twinning constituted the dominant deformation mechanism of this sample with appreciable strain energy absorption during the shock loading. The incremental tendency of impact energy could potentially be explained by the following phenomena:

- The presence of a significant fraction of CSL boundaries  $\alpha$  (total of 20%, including a higher percentage of  $\Sigma 3$  boundaries up to 15%).
- The mechanical twinning of the bcc  $\beta$ -phase.

In addition, the higher impact energy can be also supported by the higher hardness of the heat treated CuZn42 (fully  $\beta$ -phase) as compared to the as-drawn one, i.e., approximately 140 HV vs. 130 HV [35].

Grain boundaries are mostly influential on dynamic and static mechanical properties behaviour and can act as preferred locations for crack initiation and propagation. HAGBs hinder dislocation motion as a result of their high degree of misorientation, leading to dislocation pile-up and localized stress concentration that can induce failure [39]. In contrast, the slip systems of neighbour grains at LAGBs possess a higher alignment which favours dislocation mobility and retain slip homogeneity across the grain boundaries. Conclusively, LAGBs resist intergranular fracture, which tends to propagate along HAGBs [39].

#### 5.2. Dual-Phase ( $\alpha + \beta$ ) Alloys: CuZn38As, Heat Treated Condition and CuZn42, As-Drawn Condition

Concerning the samples of CuZn42 in the as-drawn condition and CuZn38As in the heat treated condition, which constitute dual-phase alloys, the significant difference in energy absorbance capacity and dimple size, which are indicators of higher plasticity (for CuZn38As), seem to be related to the following factors (see also Tables 3 and 4):

1. The increasing volume fraction of the  $\alpha$ -phase (the CuZn42 alloy contains 46 vol.%  $\alpha$ -phase and the CuZn38As alloy contains 86 vol.%  $\alpha$ -phase) results in the amplification of impact energy from 47 and 84 J, respectively.
2. A decreasing  $\beta$ -phase mean grain size (25  $\mu\text{m}$  for CuZn42 and 6  $\mu\text{m}$  for CuZn38As) leads to a higher toughness (47 J and 84 J, respectively).
3. For the total amount of LAGBs plus CSL boundaries, a higher amount leads to a higher impact toughness (19% for CuZn42 as compared to 28% for CuZn38As), which promotes transgranular ductile fracture.
4. The existence of a subgrain structure (subgrain boundaries were mostly detected in CuZn38As under the heat treated condition, summed up to 22%).

## 6. Conclusions and Further Research

From the crystallographic examination of the single- and dual-phase brass rods, the following conclusions could be derived:

- There is a strong tendency for energy absorbance in Charpy impact tests to be related to the amount of the sum of subgrains, LAGBs, and CSL boundaries. It is characteristic that the CuZn38As alloy under as-drawn and heat treated conditions, possessing in total 50% of the above interfaces, had the largest energy absorbance values (>80 J).
- $\Sigma 3$  was the predominant type of CSL boundary occurring in all the studied metallurgical conditions: (i) extruded and drawn and (ii) heat treated in the single-phase region and quenched.
- Post processing heat treatment led to a single  $\beta$ -phase structure for CuZn42 alloy and a 12 vol.% increase for the  $\beta$ -phase in the CuZn38As alloy. The augmentation of the

$\beta$ -phase volume fraction inherits a negative effect on impact toughness for dual-phase brasses ( $\alpha + \beta$  brasses).

- The size of dimples and the prevalence of transgranular fracture mode in the Charpy impact test specimens' fracture surfaces are strongly related with the amount of the  $\alpha$ -phase volume fraction. Strain is also preferentially concentrated in  $\alpha$ -phase regions on the fracture surfaces compared with the more brittle  $\beta$ -phase. KAM maps are advantageous in revealing the phases–strains relationships near the fracture surfaces.
- In the absence of an  $\alpha$ -phase, as in the case of CuZn42-heat treated condition, the fraction of dimpled fractures is negligible. On the other hand, in samples of CuZn42 in the as-drawn condition, CuZn38As in the heat treated condition, and CuZn38As in the as-drawn condition, as the  $\alpha$ -phase volume fraction increases, the size of micro-dimples, viewed transverse to fracture surface sections, respectively increases.
- Interestingly enough, as it was obtained from the systematic impact energy results, the presence of a full  $\beta$ -phase microstructure could have a potential beneficial contribution to fracture toughness, due to the combination of higher hardness with the activation of the mechanical twinning process under shock loading conditions, while the limited size of the plastic zone ahead of the crack tip in combination with the coarse  $\beta$ -phase grains promotes intergranular crack propagation.
- The increase of mean grain size of  $\alpha$ - and  $\beta$ -phases offers a negative effect on strength and impact toughness in CuZn38As brass.
- The texture of the  $\alpha$ -phase in the as-received condition was different in the two different alloys, a single (111) in CuZn42 and (001) in CuZn38As, revealing a process and/or chemical composition relationship with the resulting texture. The dominant texture of the  $\beta$ -phase was (101) in both alloys and metallurgical conditions.

The fact that CSL boundaries were also observed in the single  $\beta$ -phase CuZn42 heat treated alloy, constituted mostly by  $\Sigma 3$  boundaries, offers a promising ground for further research since the investigation of the influence of texture on single  $\beta$ -phase properties will provide valuable knowledge towards the development of advanced copper alloys with superior mechanical behaviour and machinability.

**Author Contributions:** Conceptualization, A.V. and G.A.P.; primary materials testing and methodology, A.V., A.R. and A.I.T.; sample preparation, A.R.; writing—original draft preparation, A.V.; writing—review and editing, A.I.T. and G.A.P.; project supervision and management, G.A.P. All authors have read and agreed to the published version of the manuscript.

**Funding:** This research received no external funding.

**Institutional Review Board Statement:** Not applicable.

**Informed Consent Statement:** Not applicable.

**Data Availability Statement:** The data supporting the findings of this study are available upon request from the corresponding author.

**Acknowledgments:** The encouragement and support of ELKEME management is highly appreciated.

**Conflicts of Interest:** The authors declare no conflict of interest.

## References

1. Achiței, D.C.; Minciună, M.G.; Vizureanu, P.; Sandu, A.V.; Cimpoeșu, R.; Istrate, B. Study on structure and properties of CuZnPb alloy. *IOP Conf. Ser. Mater. Sci. Eng.* **2019**, *133*, 012015. [[CrossRef](#)]
2. Imai, H.; Kosaka, Y.; Kojima, A.; Li, S.; Kondoh, K.; Umeda, J.; Atsumi, H. Characteristics and machinability of lead-free P/M Cu60–Zn40 brass alloys dispersed with graphite. *Powder Technol.* **2010**, *198*, 417–421. [[CrossRef](#)]
3. La Fontaine, A.; Keast, V.J. Compositional distributions in classical and lead-free brasses. *Mater. Charact.* **2006**, *57*, 424–429. [[CrossRef](#)]
4. Wolfenden, A.; Wright, P.K. Role of lead in free-machining brass. *Met. Technol.* **1979**, *6*, 297–302. [[CrossRef](#)]
5. Stoddart, C.T.H.; Lea, C.; Dench, W.A.; Green, P.; Pettit, H.R. Relationship between lead content of Cu-40Zn, machinability, and swarf surface composition determined by auger electron spectroscopy. *Met. Technol.* **1979**, *6*, 176–184. [[CrossRef](#)]

6. Pantazopoulos, G. Leaded brass rods C 38500 for automatic machining operations: A technical report. *J. Mater. Eng. Perform.* **2002**, *11*, 402–407. [[CrossRef](#)]
7. Johansson, J.; Alm, P.; M'Saoubi, R.; Malmberg, P.; Ståhl, J.-E.; Bushlya, V. On the Function of Lead (Pb) in Machining Brass Alloys. *Res. Sq.* **2022**, Preprint. [[CrossRef](#)]
8. Toulfatzis, A.; Pantazopoulos, G.; David, C.; Sagris, S.; Paipetis, A. Final heat treatment as a possible solution for the improvement of machinability of Pb-free brass alloys. *Metals* **2018**, *8*, 575. [[CrossRef](#)]
9. Toulfatzis, A.I.; Pantazopoulos, G.A.; Paipetis, A.S. Microstructure and properties of lead-free brasses using post-processing heat treatment cycles. *Mater. Sci. Technol.* **2016**, *32*, 1771–1781. [[CrossRef](#)]
10. Toulfatzis, A.I.; Pantazopoulos, G.A.; David, C.N.; Sagris, D.S.; Paipetis, A.S. Machinability of eco-friendly lead-free brass alloys: Cutting-force and surface-roughness optimization. *Metals* **2018**, *8*, 250. [[CrossRef](#)]
11. Schultheiss, F.; Johansson, D.; Bushlya, V.; Zhou, J.; Nilsson, K.; Ståhl, J.E. Comparative study on the machinability of lead-free brass. *J. Clean. Prod.* **2017**, *149*, 366–377. [[CrossRef](#)]
12. Nobel, C.; Klocke, F.; Lung, D.; Wolf, S. Machinability enhancement of lead-free brass alloys. In Proceedings of the 6th CIRP International Conference on High Performance Cutting, Berkeley, CA, USA, 23–25 June 2014; pp. 95–100.
13. Atsumi, H.; Imai, H.; Li, S.; Kondoh, K.; Kousaka, Y.; Kojima, A. The effect of solid solutionizing Ti element on microstructural and mechanical properties of extruded Cu-40Zn-Ti ternary alloy. *Trans. JWRI* **2011**, *40*, 67–71.
14. Suksongkarm, P.; Rojananan, S.; Rojananan, S. Bismuth formation in lead-free Cu-Zn-Si yellow brass with various bismuth-tin alloy additions. *Mater. Trans.* **2018**, *59*, 1747–1752. [[CrossRef](#)]
15. Adineh, M.; Doostmohammadi, H. Microstructure, mechanical properties and machinability of Cu-Zn-Mg and Cu-Zn-Sb brass alloys. *Mater. Sci. Technol.* **2019**, *35*, 1504–1514. [[CrossRef](#)]
16. Vilarinho, C.; Davim, J.P.; Soares, D.; Castro, F.; Barbosa, J. Influence of the chemical composition on the machinability of brasses. *J. Mater. Processing Technol.* **2005**, *170*, 441–447. [[CrossRef](#)]
17. Rajabi, Z.; Doostmohammadi, H. Effect of addition of tin on the microstructure and machinability of  $\alpha$ -brass. *Mater. Sci. Technol.* **2018**, *34*, 1218–1227. [[CrossRef](#)]
18. Stavroulakis, P.; Toulfatzis, A.I.; Pantazopoulos, G.A.; Paipetis, A.S. Machinable leaded and eco-friendly brass alloys for high performance manufacturing processes: A critical review. *Metals* **2022**, *12*, 246. [[CrossRef](#)]
19. Toulfatzis, A.I.; Pantazopoulos, G.A.; Paipetis, A.S. Fracture behavior and characterization of lead-free brass alloys for machining applications. *J. Mater. Eng. Perform.* **2014**, *23*, 3193–3206. [[CrossRef](#)]
20. Toulfatzis, A.I.; Pantazopoulos, G.A.; Paipetis, A.S. Fracture Analysis of Eco-Friendly Brass Alloys: Comparison Study and Preliminary Assessment. In Proceedings of the 14th International Conference on Fracture (ICF 14), Rhodes, Greece, 18–23 June 2017.
21. Pantazopoulos, G.A.; Toulfatzis, A.I. Fracture modes and mechanical characteristics of machinable brass rods. *Metallurg. Microstruct. Anal.* **2012**, *1*, 106–114. [[CrossRef](#)]
22. Laporte, V.; Mortensen, A. Intermediate temperature embrittlement of copper alloys. *Int. Mater. Rev.* **2009**, *54*, 94–116. [[CrossRef](#)]
23. Wolley, D.J.; Fox, A.G. The embrittlement of leaded and unleaded  $\alpha$ - $\beta$  (60-40) brasses in the temperature range 300 to 500 °C. *J. Mater. Sci. Lett.* **1988**, *7*, 763–765. [[CrossRef](#)]
24. Felli, A.; Brotzu, A.; Pilone, P. Analysis of the fracture criticality of biphasic brass. *Proc. Struct. Integr.* **2016**, *2*, 2959–2965. [[CrossRef](#)]
25. Mapelli, C.; Venturini, R. Dependence of the mechanical properties of an  $\alpha/\beta$  brass on the microstructural features induced by hot extrusion. *Scr. Mater.* **2006**, *54*, 1169–1173. [[CrossRef](#)]
26. Pantazopoulos, G. A review of defects and failures in brass rods and related components. *Pract. Fail. Anal.* **2003**, *3*, 14–22. [[CrossRef](#)]
27. Pantazopoulos, G.; Vazdirvanidis, A. Identification of corrosion and damage mechanisms by using Scanning Electron Microscopy and Energy Dispersive X-ray Microanalysis: Contribution to Failure Analysis Case Histories. *IOP Conf. Ser. Mater. Sci. Eng.* **2014**, *55*, 012015. [[CrossRef](#)]
28. Pantazopoulos, G.; Toulfatzis, A.I. Failure analysis of a machinable brass connector in a boiler unit installation. *Case Stud. Eng. Fail. Anal.* **2013**, *1*, 18–23. [[CrossRef](#)]
29. Pantazopoulos, G.; Vazdirvanidis, A. Failure analysis of a fractured leaded-brass (CuZn39Pb3) extruded hexagonal rod. *J. Fail. Anal. Prev.* **2008**, *8*, 218–222. [[CrossRef](#)]
30. *Copper and Copper Alloys Specialty Handbook*; ASM International: Materials Park, OH, USA, 2001.
31. Dieter, G.E. *Mechanical Metallurgy*; McGraw-Hill Book Company: New York, NY, USA, 1988.
32. Voort, G.F.V. *ASM Handbook, Vol. 9*; ASM International: Materials Park, OH, USA, 2004.
33. Al-Fadhalah, K.J.; Aleem, R.M.; Nicky, T. Microstructure and texture development in thermomechanically processed leaded brass. *Metals* **2021**, *11*, 998. [[CrossRef](#)]
34. Watanabe, T. Structural effects on grain boundary segregation, hardening and fracture. *J. Phys. Colloques* **1985**, *46*, C4-555–C4-566. [[CrossRef](#)]
35. Toulfatzis, A.I.; Pantazopoulos, G.A.; Paipetis, A.S. Fracture mechanics properties and failure mechanisms of environmentally-friendly brass alloys under impact, cyclic and monotonic loading conditions. *Eng. Fail. Anal.* **2018**, *90*, 459–517. [[CrossRef](#)]
36. Regina, J. Ordered Structures. In *ASM Handbook, Volume 9: Metallography and Microstructures*; ASM International: Materials Park, OH, USA, 2004.



37. Janssen, M.; Zuidema, J.; Wanhill, R. *Fracture Mechanics*, 2nd ed.; SPON Press: Oxford, UK, 2004.
38. Humphrey, F.J.; Hatherly, M. *Recrystallization and Related Annealing Phenomena*; Elsevier: Amsterdam, The Netherlands, 2004.
39. Bond, D.; Zikry, M.A. Microstructural modeling of intergranular fracture in tricrystals with random low- and high-angle grain boundaries. *JOM* **2017**, *69*, 856–862. [[CrossRef](#)]

Article

# An Analytical Model for Stress and Curvature Prediction of a Strip Leveling Process

Shih-Kang Kuo<sup>1</sup>, Yi-Liang Ou<sup>1</sup> and Dung-An Wang<sup>2,3,\*</sup>

<sup>1</sup> Steel Research and Development Department, China Steel Corporation, Kaohsiung 81233, Taiwan; 150359@mail.csc.com.tw (S.-K.K.); 165688@mail.csc.com.tw (Y.-L.O.)

<sup>2</sup> Graduate Institute of Precision Engineering, National Chung Hsing University, 250 Kuo Kuang Rd., Taichung 40227, Taiwan

<sup>3</sup> Faculty of Mechanical Engineering, Industrial University of Ho Chi Minh City, 12 Nguyen Van Bao, Ward 4, Go Vap District, Ho Chi Minh City 800010, Vietnam

\* Correspondence: daw@dragon.nchu.edu.tw; Tel.: +886-4-22857207

**Abstract:** An analytical model of a steel strip under alternate bending/reverse bending during a roller leveling process is developed. A combined isotropic/kinematic hardening model is implemented through a combined hardening parameter. A formulation of the change of the effective stress as a function of the change of the effective strain under cyclic loading is combined with the developed analytical model to predict the stress distributions and residual curvature of a steel strip under roller leveling efficiently and accurately. Dissimilar to the commonly used assumption of one contact point between the stripe and the rolls, an effective radius modelling the wrap-around contact characteristics is proposed. An arc contact of the strip around a roll is described by the contact model. An oscillatory behavior of the residual curvature is observed when a range of roll intermesh setting is considered. The contact model added to the analytical model may enhance the accuracy in predicting the oscillatory behavior of the residual curvatures. A range of the roll intermesh setting can be suggested by the developed model to obtain a flat strip after roller leveling.

**Keywords:** roller leveling; steel strip; combined hardening; analytical model

**Citation:** Kuo, S.-K.; Ou, Y.-L.; Wang, D.-A. An Analytical Model for Stress and Curvature Prediction of a Strip Leveling Process. *Metals* **2022**, *12*, 757. <https://doi.org/10.3390/met12050757>

Academic Editors: George A. Pantazopoulos and Zhengyi Jiang

Received: 14 March 2022

Accepted: 24 April 2022

Published: 28 April 2022

**Publisher's Note:** MDPI stays neutral with regard to jurisdictional claims in published maps and institutional affiliations.



**Copyright:** © 2022 by the authors. Licensee MDPI, Basel, Switzerland. This article is an open access article distributed under the terms and conditions of the Creative Commons Attribution (CC BY) license (<https://creativecommons.org/licenses/by/4.0/>).

## 1. Introduction

Steel strips after rolling and annealing may possess defects such as wavy edges, center buckles, cambers, and twists. The flatness defects can be corrected by leveling in steel mills. Amor et al. [1] reported that shape defects of metal strips after rolling process or coiling operation can be removed by leveling in order to meet the quality requirement. Customers may cut the as-received flat stripes in order to achieve end functionalities. Unacceptable shape defects found after cutting the strips are serious issues of concern raised by the customers of steel mills. Li et al. [2] reported that these flatness/shape defects are mainly due to residual stresses generated from rolling, annealing, leveling, coiling, etc. Morris et al. [3] classified the shape defects into two categories—latent and manifest. Shape defects of the latent category appear flat prior to cutting operation, whereas manifest defects, such as wavy edges and center buckles, are visible in the coiled form. Conventionally, tension levelers are used upstream to remove manifest defects. Roller leveling with lower line tension and smaller rolls has been the essential step to flatten metal strips and attenuate the effects of inhomogeneous distribution of residual stress in strips. Roller leveling is a complex forming process involving multiple, alternate bending and reverse bending cycles. In order to achieve more effective leveling operation without resorting to on site trial and error approach, a lot of efforts have been devoted to the development of efficient, accurate simulation tools for roller leveling.

Finite element analyses and analytical modeling are two main approaches adopted to investigate the roller leveling process. Hira et al. [4] developed an analytical model for

calculation of curling and residual stress of a strip in longitudinal and width directions after tension leveling. Isotropic material hardening was considered in their model. Doege et al. [5] analyzed a levelling process using the Euler–Bernoulli beam theory and a combined isotropic and kinematic hardening model. Contact points between the strip and the rolls were computed iteratively assuming that only one contact point between the roll and the strip exists. They calculated the range of roll intermeshes for zero strip curvature at the exit roll for a seven-roll leveling system. Details of the verification of their analytical modeling were not described. Behrens et al. [6] developed an analytical model to find suitable settings of a leveler for flat strips. Contact points between the metal strip and the rolls were calculated by assuming that the curve of the strip was composed of arcs and common tangents between two rolls. Lengths of several segments dissected from the strip longitudinally were equalized with different plastic deformations to eliminate wave defects of the strip. Dratz et al. [7] also adopted this common tangent contact condition to develop their roller leveling model. Residual stress and curvature results of the strip after levelling were not reported. The common tangent assumption contradicts with the fact that the curvature between two rolls exhibits a nonlinear distribution. Liu et al. [8] developed an analytical model to analyze the residual stress and curvature of a plate subjected to roller leveling. Isotropic hardening was adopted in their model and a single contact between the plate and each roll was assumed. Chen et al. [9] developed an analytical model of a roller leveler for the strip with transverse and longitudinal wave defects. They divided the strip longitudinally in order to find a suitable bending amount of the rolls to attain equal length of each longitudinal section. Higo et al. [10] presented a theoretical model for a roller leveler based on Euler–Bernoulli beam theory and a single point contact model between a strip and each roll. They examined the influence of the exit roll intermesh on the residual curvature of the strip.

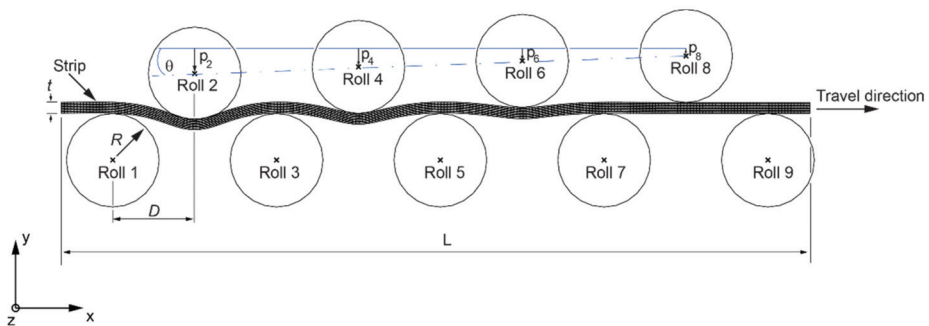
Morris et al. [11] built a finite element model to analyze the deformed shape and surface residual stress of a steel strip after a three-roll leveling process. They concluded that kinematic work-hardening can represent the loading condition experienced during tension levelling more closely than that of isotropic work-hardening by comparing model predictions of the deformed shapes with experiments. Schleinzer and Fischer [12] presented a finite element model for roller leveling of rails. Combined isotropic/kinematic hardening was assumed for the material. A friction coefficient of 0.2 was used between the rail and the rolls. Park and Hwang [13] conducted finite element analyses and experiments to examine the residual curvature and stress distribution of strips after roller leveling. They verified that the strips with various initial curvatures can attain residual curvatures with small deviation given an optimum entrance roll intermesh. Huh et al. [14] built a finite element model for a roller leveler in order to study the effects of process parameters on the curvature solution of roller leveling. They identified the parameters with significant effects on the residual curvature through a design of experiment approach. Roberts et al. [15] carried out a finite element study to compare modeled curvature distributions with experiments of a two-roll stretch-bending process. Their results showed that a reduction in the wrap-around contact length was caused by decreasing intermesh. Jin et al. [16] conducted a three-dimensional finite element analysis of a roller leveler. They presented residual stress distribution in the strip. Kim et al. [17] developed a finite element model for a roller leveling process. They implemented an implicit stress integration procedure in a constitutive material model which can capture the material yield behavior and the Bauschinger effect during reverse bending. Grüber et al. [18] employed a finite element analysis of roller levelling to determine several combinations of roll intermeshes to attain a flat strip after levelling. They identified that the roll intermesh of the center load triangle and the last load triangle of a seven-roll leveler is crucial to reach desired values of flatness and residual stress distribution.

Leveler operators have relied on parameter settings for strips with various yield strengths and through-gauges provided by leveler suppliers. Due to degradation of the leveler through years of usage, empirical methods were used to fine tune the settings for production. Although manifest defects appeared to be invisible after leveling, latent

defects may still exist and cause the end products to fail to satisfy customer requirements. Analytical solutions of residual stress and curvature of the roller leveling process are necessary to provide rapid parameter settings to aid in its operation. In this investigation, an analytical model for a nine-roll leveler is developed. The nine-roll cold leveler was installed at the plate mill plant of the Chinese Steel Company for leveling heavy gauge steel plates. One of the motivations of this investigation is to provide operational parameters for the leveler to improve the quality of steel plates. Solutions of stress distributions after each bending/reverse bending and residual curvature of the strip are obtained based on the Euler–Bernoulli beam theory within a two-dimensional geometric framework. The material hardening is implemented through a combined isotropic/kinematic hardening parameter. Finite element analyses are carried out to verify the accuracy of the developed model. Results of the stress distributions and residual curvature of a steel strip are compared with the results based on the analyses. Finally, a roll intermesh range to produce a flatness condition of the strip is presented.

## 2. Analytical Model

Figure 1 is a schematic of a nine-roll leveler. The strip has the thickness  $t$ , the length  $L$ , and the width  $W$ . The rolls have a radius of  $R$  and a roll spacing of  $D$ . A strip enters the entry roll from the left, undergoes alternate bending and reverse bending, then leaves the exit roll. Flatness defects can be removed by the plastic deformation under the leveler rolls. Partial reduction in the flatness defect is ensued by insufficient plastic deformation. The intermesh settings, usually in a linear, declining trend, provide for the gradual flattening of the shape defects as the strip travels through the leveler. The roll intermeshes  $p_2$ ,  $p_4$ ,  $p_6$ , and  $p_8$  are indicated in Figure 1. The value of the roll intermesh is positive when the gap between the top roll and the bottom roll is larger than the strip thickness. In this investigation, the amount of the roll intermesh is defined by the inclination angle  $\theta$  of the upper roll carriage and the roll intermesh at the next-to-last roll  $p_8$  as indicated in Figure 1. The bottom rolls are fixed, and the top rolls are moved downward to specified roll intermeshes. The width of the strip is assumed to be sufficiently large. Therefore, the strain in the width direction is neglected, and the plane strain condition is considered. Since the leveling process can be viewed as a series of three-point bending/reverse bending actions with groups of three rolls, the analytical model of the roller leveling process is conducted based on the framework of Euler–Bernoulli beam theory.



**Figure 1.** A schematic of a nine-roll leveler.

### 2.1. Material Model

In development of the analytical model, friction forces at the roll/strip interface, tension forces in the strip, and gravity are neglected. Figure 2 schematically shows a differential element of the strip. The strip has a thickness of  $t$  and a width of  $W$ . A Cartesian coordinate system is also shown in the figure.  $x$  represents the longitudinal direction, and  $y$  is along the thickness direction. The neutral axis is assumed to coincide with the mid-surface of the strip. The origin of the  $y$  coordinate is at the middle of the beam as

shown in the figure.  $\rho$  is the radius of the curvature of the differential element under the moment loading  $M$ . Longitudinal strain  $\varepsilon_x$  is expressed as

$$\varepsilon_x = -\kappa y \tag{1}$$

where  $\varepsilon_x$  and  $\kappa$  [1/m] are the longitudinal strain and the curvature, respectively. In the elastic regime, the longitudinal stress  $\sigma_x$  [N/m<sup>2</sup>] is related to the longitudinal strain  $\varepsilon_x$  by

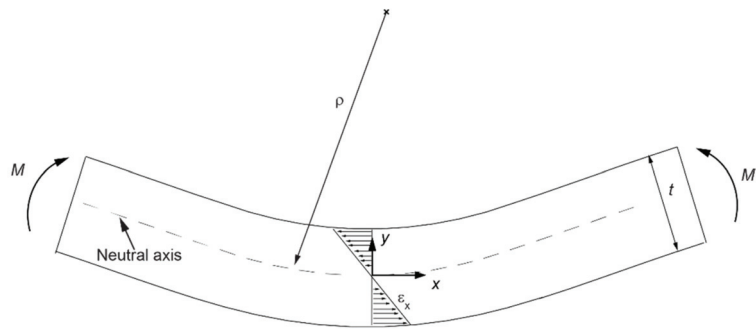
$$\sigma_x = E\varepsilon_x \tag{2}$$

where  $E$  [N/m<sup>2</sup>] is the Young’s modulus. The material hardening behavior is given by an exponential law

$$\bar{\sigma} = \sigma_s + Q_i \left( 1 - e^{-b_i \bar{\varepsilon}} \right) \tag{3}$$

where  $\bar{\sigma}$  [N/m<sup>2</sup>] and  $\bar{\varepsilon}$  are the effective stress and the effective plastic strain, respectively.  $\sigma_s$  [N/m<sup>2</sup>] is the initial yield stress.  $Q_i$  [N/m<sup>2</sup>] and  $b_i$  are the isotropic hardening parameters, where  $Q_i$  specifies the maximum change in the size of the yield surface, and  $b_i$  defines the rate at which the size of the yield surface changes as plastic straining develops. For uniaxial loadings as the strip bending case,  $\bar{\sigma}$  and  $\bar{\varepsilon}$  can be taken as  $\sigma_x$  and  $\varepsilon_x$ , respectively. Relatively large plastic deformation is considered for the roller levelling. This simplification of  $\bar{\varepsilon} \approx \varepsilon_x$  contributes to a very small fraction of error to the results. Values of  $(Q_1, b_1)$  and  $(Q_2, b_2)$  are obtained by fitting experimental stress–strain curve with Equation (3) for the first half cycle and the second half cycle of the loading, respectively. Therefore,  $Q_1$  and  $b_1$  are used to model the material hardening behavior in the first half loading cycle.  $Q_2$  and  $b_2$  are adopted for the subsequent loadings. The bending moment  $M$  [N·m] of the cross section of the strip is given as

$$M = -2W \int_0^{t/2} \sigma_x y dy \tag{4}$$



**Figure 2.** A schematic of a differential element of the strip.

The sign convention for the moment  $M$  and the curvature  $\kappa$  is related to the orientation of the coordinate axes.

During the first bend loading, the material of the strip exhibits isotropic hardening behavior. In the subsequent bend loadings, the material hardening of the strip is taken as a combined isotropic/kinematic type. Zhang et al. [19] formulated the change of the effective stress  $\Delta\bar{\sigma}$  [N/m<sup>2</sup>] as a function of the change of the effective strain  $\Delta\bar{\varepsilon}$  under cyclic bend loading as

$$|\Delta\bar{\sigma}| = \begin{cases} E|\Delta\bar{\varepsilon}| & , |\Delta\bar{\varepsilon}| < \frac{|\Delta\bar{\sigma}|_{\text{lim}}}{E} \\ \sigma_s + Q_i \left( 1 - e^{-b_i (|\Delta\bar{\varepsilon}| - \frac{|\Delta\bar{\sigma}|_{\text{lim}}}{E})} \right) & , |\Delta\bar{\varepsilon}| \geq \frac{|\Delta\bar{\sigma}|_{\text{lim}}}{E} \end{cases} \tag{5}$$

where  $|\Delta\bar{\sigma}_{lim}|$  [N/m<sup>2</sup>] is the elastic limit of the effective stress change at the stress reversal point and can be written as

$$|\Delta\bar{\sigma}_{lim}| = (1 + m)|\bar{\sigma}_r| + (1 - m)(2\sigma_s - |\bar{\sigma}_r|) \tag{6}$$

where  $|\bar{\sigma}_r|$  [N/m<sup>2</sup>] is the magnitude of the effective stress at the point of stress reversal.  $m$  is the combined hardening coefficient.  $m = 1$  and  $m = 0$  correspond to the isotropic hardening case and kinematic hardening case, respectively, and  $0 < m < 1$  is for the case of combined hardening. The value of  $m$  for each bending during the roller leveling is calibrated by matching the stress–strain curves based on the model of Equations (1)–(6) to the experimental measurements in the corresponding cycles over a strain range expected in the roller leveling process. Kotov et al. [20] experimentally demonstrated the validity of a kinematic hardening model of a steel strip under roller leveling.

2.2. Contact Model

Contact points between the strip and the rolls can be computed iteratively assuming that only one contact point between the roll and the strip exists [5,10]. Behrens et al. [6] and Dratz et al. [7] adopted the common tangent contact condition to develop their roller leveling model. The single point contact and common tangent contact assumptions render a simple means to model the contact between the strip and rolls. A line contact between the strip and each roll is assumed in the initial modeling work here. In the two-dimensional model considered in this investigation, the strip contacts with each roll tangentially as shown in Figure 3. The expanded radius of the roll  $R_e$  [m] is given as

$$R_e = R + \frac{t}{2} \tag{7}$$

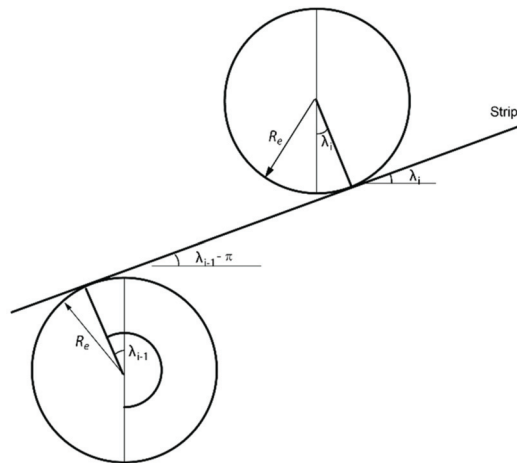


Figure 3. Tangential contact condition of the strip with the rolls.

The tangent of the contact angle  $\lambda_i$  [rad] is the gradient of the longitudinal axis of the strip

$$\tan\lambda_i = \left. \frac{dy}{dx} \right|_{x_i} \tag{8}$$

where  $y(x)$  is the deflected curve of the longitudinal axis of the strip,  $(x_i, y_i)$  is the  $i$ th contact point, and  $\lambda_i$  is the  $i$ th contact angle. The contact point  $(x_i, y_i)$  [m] is

$$\begin{aligned} x_i &= x_c + R_e \sin\lambda_i \\ y_i &= y_c - R_e \cos\lambda_i \end{aligned} \tag{9}$$

where  $(x_c, y_c)$  [m] is the coordinates of the center of the roll. Müller et al. [21] also used the expanded radius of the roll to calculate the contact point between a strip and a roll in a leveler.

A recursive scheme is adopted to calculate the curvature, bending moment, deflected curve of the strip, and the contact points. Initially, the location of the contact points and the curvature  $\kappa_i$  of the strip curve at the  $i$ th contact point are assumed. The bending moment  $M_i$  at the  $i$ th contact point is computed using Equations (1)–(6). Based on the assumption of a linear distribution of the moment between the contact points, the curvature of the deflected strip curve is estimated. Using the curvature distribution  $\kappa(x)$ , the deflected strip curve  $y$  [m] is calculated by

$$y(x) = \kappa(x)dx + C_1x + C_2 \quad (10)$$

where  $C_1$  and  $C_2$  are the integration constants, and can be determined by the known contact points. A Newton–Raphson algorithm is used to obtain converged solutions of the deflected strip curve, moment distribution, curvature distribution, and contact points that satisfy both the Euler–Bernoulli beam theory and the geometrical constraints. Guan et al. [22] adopted a similar curvature integration approach to find the contact points for a roller leveler. They verified their model by comparing the deflection curves calculated by their model with those from experiments.

### 2.3. Residual Curvature

The flatness of the strip after exiting the leveler is related to the residual curvature. The bending and reverse bending cycle is repeated until the material reaches the last roll in the leveler. The strip is free to rotate at the last roll where the bending moment applied to the strip can be considered as zero. The internal stress distribution of the cross section of the strip at the last roll should result in a zero-bending moment. This condition can be enforced by imposing an artificial bending moment of the same magnitude but opposite sign to the moment at the last roll before unloading. Assuming no reverse yielding during unloading, the residual curvature  $\kappa'$  [1/m] of the strip at the last roll can be expressed as

$$\kappa' = \kappa - \frac{M}{EI} \quad (11)$$

where  $\kappa$  and  $M$  are the curvature and moment, respectively, before unloading, and  $I$  is the second moment of inertia of the cross section of the strip. Hosford and Caddell [23] and Guan et al. [24] also adopted this approach to calculate the residual curvature for beam bending problems.

## 3. Finite Element Analysis

In order to examine the accuracy of the developed analytical model, a two-dimensional finite element analysis of a roller leveler is carried out. A quasi-static condition is assumed in the finite element analyses. Due to the sufficiently large width, the strain in the width direction can be neglected, and the plane strain condition is considered in the finite element analysis. Both the upper and lower rolls are modeled as rigid bodies. A strip and a nine-roll leveler are shown in Figure 1. A Cartesian coordinate system is also shown in the figure. The direction of the  $z$  axis is given by the right-hand rule. In this investigation, the strip is moved forward by a displacement boundary condition and the bottom rolls are assumed to be fixed in the  $x$  and  $y$  directions and free to rotate with respect to the  $z$  axis. The displacements in the  $-y$  direction of the upper rolls are specified to represent the amount of roll intermeshes, while their displacements in the  $x$  direction are constrained. As shown in Figure 1, a uniform displacement is applied in the  $+x$  direction to the right edge surface of the strip, and the displacement in the  $y$  direction for the right edge surface is constrained to represent the strip travel horizontally along the  $+x$  direction.

The commercial software, Abaqus (6.14, Dassault Systemes, Waltham, MA, USA), is adopted to compute the stress and deformation of the strip during the leveling process. Mises yield surface is used with the nonlinear isotropic/kinematic hardening model in Abaqus. The nonlinear kinematic hardening component is modeled through the back stress to describe the translation of the yield surface. The isotropic hardening component is modeled through the equivalent stress as a function of the equivalent plastic strain to define the size of the yield surface. The hardening law for the back stress  $\alpha$  [N/m<sup>2</sup>] is

$$\dot{\alpha} = \frac{C}{\sigma_t} (\sigma_x - \alpha) \dot{\epsilon}^{pl} - \gamma \alpha \dot{\epsilon}^{pl} \tag{12}$$

where  $C$  [N/m<sup>2</sup>] and  $\gamma$  are kinematic hardening parameters that are calibrated from symmetric strain, cyclic test data.  $\sigma_t$  and  $\dot{\epsilon}^{pl}$  are the current size of the yield surface and the plastic strain rate, respectively. Figure 4 schematically shows a stabilized cycle. The plastic strain  $\epsilon^{pl}$  is determined by

$$\epsilon^{pl} = \epsilon_x - \frac{\sigma_x}{E} - \epsilon_0 \tag{13}$$

where  $\epsilon_0$  is the strain value of the intercept of the left half of the stabilized cycle with the strain axis as shown in Figure 4. The value of  $\alpha$  [N/m<sup>2</sup>] is given as

$$\alpha = \sigma_x - \sigma_t \tag{14}$$

where  $\sigma_t = (\sigma_1 + \sigma_n)/2$  is the current size of the yield surface. The stresses  $\sigma_1$  and  $\sigma_n$  are marked in Figure 4. To solve the back stress hardening law of Equation (12) over this stabilized cycle, with the first data point of  $\sigma_x = \sigma_1$  and  $\epsilon^{pl} = 0$ , the expression of  $\alpha$  [N/m<sup>2</sup>] is

$$\alpha = \frac{C}{\gamma} (1 - e^{-\gamma \epsilon^{pl}}) + (\sigma_1 - \sigma_t) e^{-\gamma \epsilon^{pl}} \tag{15}$$

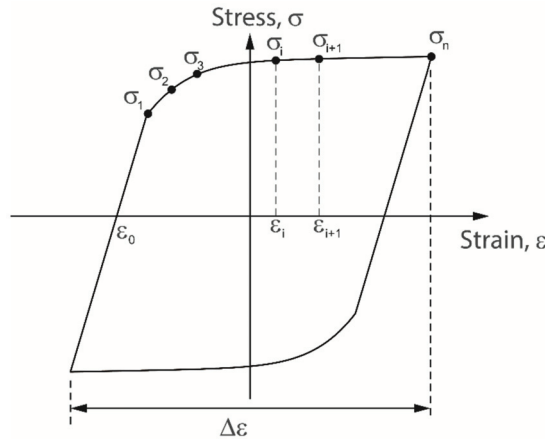


Figure 4. A schematic of a stabilized cycle.

Data pairs of  $(\alpha, \epsilon^{pl})$  extracted from the stabilized stress–strain curve are used to calibrate values of the kinematic hardening parameters  $C$  and  $\gamma$ .

The isotropic hardening model of the Abaqus is defined as

$$\sigma_t = \sigma_s + Q_\infty (1 - e^{-b\epsilon^{pl}}) \tag{16}$$



where  $\sigma_t$  [N/m<sup>2</sup>] and  $\sigma_s$  [N/m<sup>2</sup>] are the current size and the initial size of the yield surface, respectively, and  $\bar{\varepsilon}^{pl}$  is the equivalent plastic strain.  $Q_\infty$  [N/m<sup>2</sup>] and  $b_i$  are the isotropic hardening parameters of the finite element model. The isotropic hardening parameters are calibrated from the data of the current size of the yield surface  $\sigma_t$ -equivalent plastic strain  $\bar{\varepsilon}^{pl}$  relation based on a symmetric strain-controlled cyclic experiment with strain range  $\Delta\varepsilon$  as shown schematically in Figure 4. For the  $i$ th cycle, the current size of the yield surface  $\sigma_t$  [N/m<sup>2</sup>] is calculated by

$$\sigma_t = \sigma_i^p - \alpha_i \quad (17)$$

where  $\sigma_i^p$  [N/m<sup>2</sup>] and  $\alpha_i$  [N/m<sup>2</sup>] are the peak tensile stress and the back stress, respectively, in the  $i$ th cycle.  $\alpha_i$  [N/m<sup>2</sup>] is calculated by

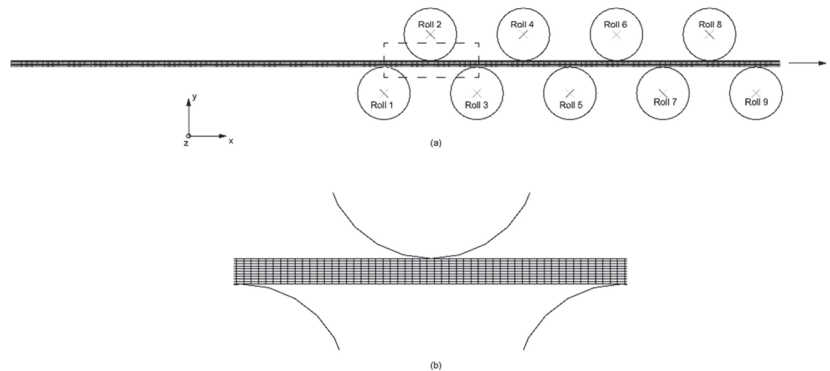
$$\alpha_i = \frac{\sigma_i^p + \sigma_i^n}{2} \quad (18)$$

where  $\sigma_i^n$  [N/m<sup>2</sup>] is the compressive stress with the same  $\varepsilon^{pl}$  value as the peak tensile stress  $\sigma_i^p$  in the  $i$ th cycle. Since the value of the back stress  $\alpha_i$  in each cycle at a particular strain level is nearly the same based on the model,  $\alpha_i$  is approximated by the values of  $\sigma_1^p$  and  $\sigma_1^n$ . The equivalent plastic strain  $\bar{\varepsilon}^{pl}$  corresponding to the  $i$ th cycle is

$$\bar{\varepsilon}^{pl} = \frac{4i - 3}{2} \Delta\varepsilon^{pl} \quad (19)$$

where  $\Delta\varepsilon^{pl}$  can be approximated by  $\Delta\varepsilon - 2\sigma_1^p/E$ .

Figure 5a is a mesh of the finite element model. Two-dimensional plane strain 4-noded CPE4R element is employed in the model. The total number of elements is 8188. Figure 5b is a close-up view of the mesh near a work roll. Ten elements are used in the thickness direction of the strip in order to obtain an accurate solution of the stress–strain distribution. The “analytical rigid surface” in Abaqus is used to model the rolls. Frictionless contact is assumed at the interface between the strip and the rolls.

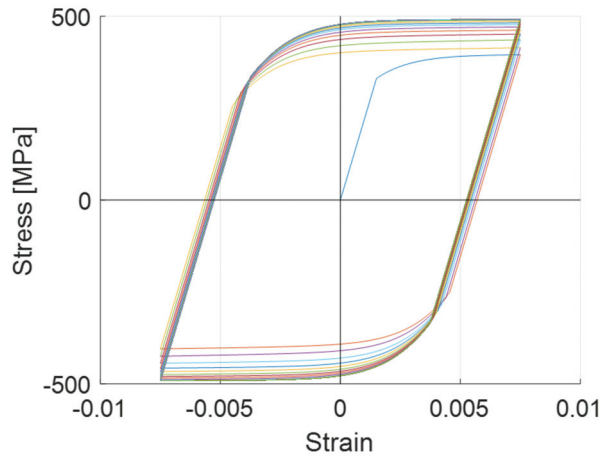


**Figure 5.** (a) A finite element model. (b) A close-up view of the mesh near a roll.

## 4. Analyses, Results, and Discussions

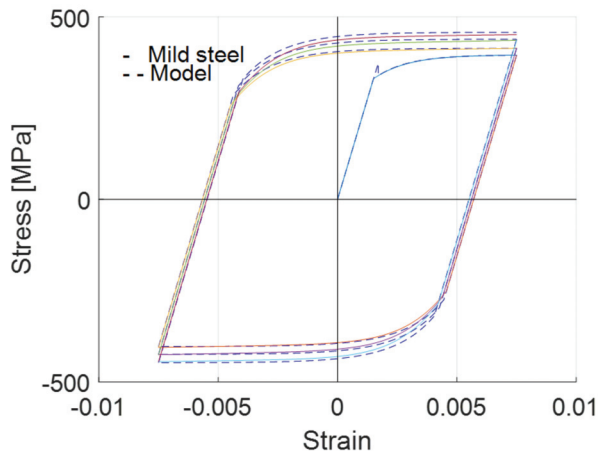
### 4.1. Analysis and Results of the Analytical Model

Figure 6 shows the stress–strain curves of a mild steel under a uniaxial, symmetric strain-controlled, cyclic test. The strain range  $\Delta\varepsilon$  is 0.015. Based on the first half of the stress–strain curve of the first cycle, the calibrated values of the Young’s modulus  $E$  and the initial yield stress  $\sigma_s$  are 219.8 GPa and 329.7 MPa, respectively, and  $Q_1$  and  $b_1$  have values of 66.3 MPa and 742.7, respectively. The values of  $Q_2$  and  $b_2$  are calibrated as 128.3 MPa and 604.7, respectively, based on the second half of the stress–strain curve of the first cycle.



**Figure 6.** Stress–strain curves of a uniaxial, symmetric strain-controlled, cyclic test.

By specifying the combined hardening coefficient  $m$ , computational stress–strain curves based on the analytical model of Equations (1)–(11) with the strain range  $\Delta\varepsilon$  of 0.0015 can be obtained. For a nine-roll roller leveler, the total number of bends equals seven. The values of the combined hardening coefficient  $m$  for the seven bends can be calibrated by comparing the computational stress–strain curves with the stress–strain curves of the mild steel shown in Figure 6 for the first seven bend loadings. Figure 7 shows the computational stress–strain curves and the stress–strain curves of Figure 6. The computational curves agree with those of the mild steel. The calibrated  $m$  values for the second to the seventh bending are 0.0784, 0.2, 0.3, 0.4, 0.45, and 0.5, respectively. The hardening behavior of the material for the first bending is taken as isotropic.



**Figure 7.** Stress–strain curves for calibration of the combined hardening coefficients.

Consider the case where the strip has the thickness  $t$  (=20 mm), the length  $L$  (=2480 mm), and the width  $W$  (=100 mm). The radius  $R$  of the rolls is 85 mm. The roll spacing  $D$  is 150 mm. The strip is taken as flat and free of residual stress. The upper roll carriage has an inclination angle  $\theta$  of  $0.1^\circ$  and the roll intermesh at the next to the last roll  $p_8$  ranges from  $-1.2$  mm to  $0.8$  mm. Note that the value of the roll intermesh is positive when the gap between the top

roll and the bottom roll is larger than the strip thickness. Therefore, a negative value of the intermesh means the work roll plunges into the strip.

With  $p_8 = -0.70$  mm and the upper roll carriage inclined at the angle  $\theta$  of  $0.1^\circ$ ,  $p_2$ ,  $p_4$ , and  $p_6$  have values of  $-2.32$  mm,  $-1.78$  mm, and  $-1.24$  mm, respectively. Sixty divisions are taken along the thickness direction of the strip for calculation of the stress and strain distributions. Figure 8 shows the deformed strip between roll 1 and roll 9 based on the analytical model. Figure 9a–c shows the distribution of the bending moment per unit width, the curvature, and the deformed center line of the strip, respectively, between roll 1 and roll 9. The contact points between the strip and the rolls are marked by circles in the figure. One hundred nodes are used between the contact points in the computations. Figure 9a shows the linear distribution of the bending moment between the contact points. At the entry roll and the exit roll, the values of the bending moment are zero. Figure 9b shows the curvature distribution. Values of the curvatures are nearly two orders smaller than the roll curvature  $1.176 \times 10^{-2} \text{ mm}^{-1}$ . The curvature of the strip at the exit roll has a value of  $3.054 \times 10^{-5} \text{ mm}^{-1}$ . The positive value of the curvature indicates that the strip is bent upward. Higo et al. [10] pointed out that the abrupt increase in magnitude of the curvature near all contact points except the final one is due to the nonlinear material hardening behavior. This is evidenced by the nonlinear sections of the moment–curvature curves during the leveling process plotted in Figure 10. The moment and the curvature are normalized by the maximum bending moment  $M_0$  and the maximum curvature  $C_0$  for which elastic conditions hold, respectively.

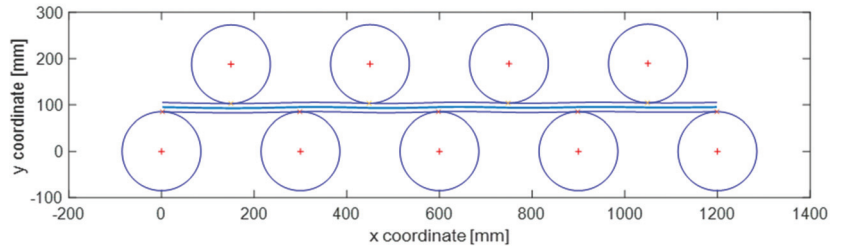


Figure 8. The deformed strip between roll 1 and roll 9.

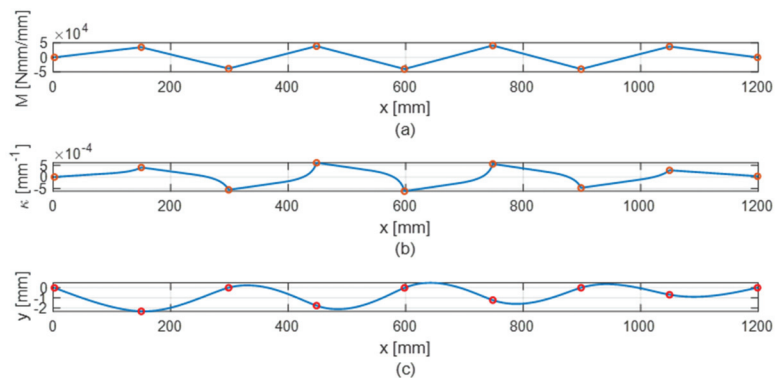
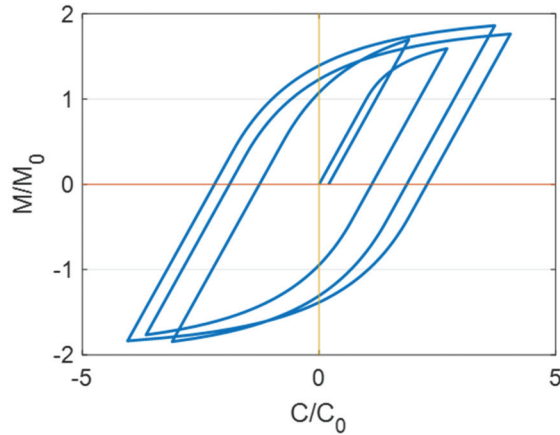


Figure 9. Distributions of (a) bending moment per unit width, (b) curvature, and (c) deformed center line of the strip between roll 1 and roll 9.



**Figure 10.** Normalized moment as a function of normalized curvature during leveling.

Figure 11a–c shows the stress distributions in the strip thickness direction when the strip travels through the leveler. The results computed by the analytical model are displayed by lines in the figure. Significant plastic deformations appear in the first three bends as seen in Figure 11a. The fractions of the plastic deformation are nearly 40%, 50%, and 60% for the first, the second, and the third bend, respectively. As the strip traverses through the fifth roll and the sixth roll, the region of plastic deformation stays at 60% as seen in Figure 11b. Figure 11c shows the stress distributions in the strip thickness direction at the eighth roll and the exit roll. The stress distribution at the exit roll can be taken as the residual stress distribution since the total moment applied to the strip at the exit roll is nearly zero. The stress at the  $i$ th roll is calculated based on a linear superposition assumption. The remnant stress of the cross section of the strip at the  $(i - 1)$ th roll and the loading stress at the  $i$ th roll are superimposed to obtain the stress distribution at the  $i$ th roll. Guan et al. [25] also adopted this stress inheritance law in their roller leveling model. Yonetani [26] reported that the stress of a microscopic segment at the cross section in a uniaxial stress state satisfies the linear superposition assumption. The uniaxial stress loading condition is also assumed in the model considered in this investigation.

#### 4.2. Analysis and Results of the Finite Element Model

Finite element analyses are carried out to verify the accuracy of the analytical model. The material properties for the mild steel used in the finite element analyses are listed in Table 1. The isotropic hardening parameters,  $Q_\infty$  and  $b$ , and the kinematic hardening parameters,  $C$  and  $\gamma$ , are calibrated from the uniaxial, symmetric strain-controlled, cyclic test with the strain range  $\Delta\varepsilon$  of 0.015 as shown in Figure 6. The calibration procedure is described in Section 3.

**Table 1.** Material properties employed in the finite element analyses.

Property	$E$ (Gpa)	$\sigma_s$ (MPa)	Poisson's Ratio	$C$ (Mpa)	$\gamma$	$Q_\infty$ (Mpa)	$b$
Value	219.8	329.7	0.3	44,600.6	673.1	96.9	12.7

The strip is taken as flat and free of residual stress in the beginning of the leveling process. Smith [27] reported that the initially flat condition is useful in the leveling analysis since the incoming flatness defects of a strip may vary from one location to another, and a strip generally has some initially flat area. Figure 12a shows the initial configuration of the finite element model. A Cartesian coordinate system is also shown in the figure. A displacement of 1200 mm in the  $+x$  direction is given to the right edge surface of the

strip. The displacement equals the distance from the center of roll 1 to the center of roll 9. Therefore, the cross-section A (marked in Figure 12a) travels from roll 1 at the beginning of the analysis to roll 9 at the end of the analysis. The  $y$ -displacement of the nodes at the right edge surface is constrained to represent the horizontal motion of the strip. Figure 12b shows the deformed shape of the mesh when the cross-section A reaches roll 9. Then, the constraints at the right edge surface of the strip are released for the strip to spring back. Figure 12c shows the deformed shape of the mesh after spring-back.

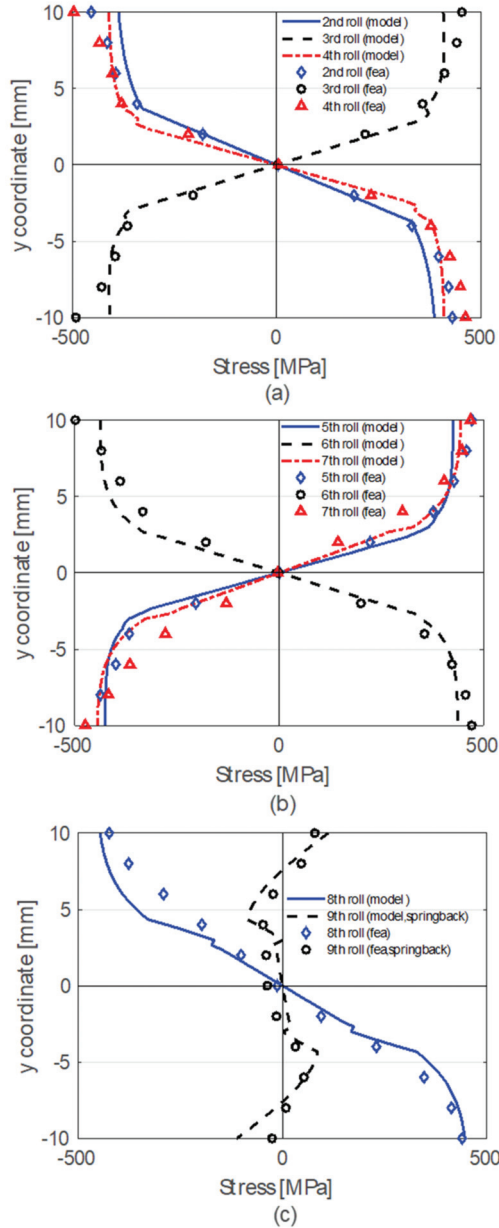
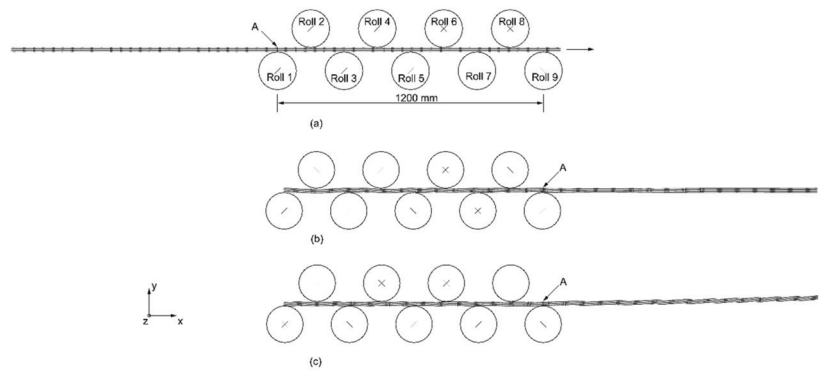


Figure 11. Stress distributions of the strip at (a) rolls 2, 3, and 4; (b) rolls 5, 6, and 7; (c) rolls 8 and 9.



**Figure 12.** (a) The initial configuration, (b) a deformed configuration before spring-back, and (c) a deformed configuration after spring-back of the finite element model.

The stress distributions of the cross-section A at rolls 2–4, rolls 5–7, and rolls 8–9 based on the finite element analyses are shown in Figure 11a–c, respectively. The results based on the finite element analyses (FEA) are plotted with the markers in the figure. As shown in the figure, the analytical results agree with the results of finite element analyses. The discrepancy can be attributed to different contact conditions between the analytical model and the finite element model. Multiple contact points between the strip and each roll are observed in the finite element model. However, a single contact point between the strip and each roll is assumed in the analytical model.

#### 4.3. Residual Curvature

Flatness is an important factor to evaluate the strip quality after roller leveling processes. The residual curvature of the strip at the exit roll can be used as a metric to evaluate the strip flatness after leveling. Figure 13 shows the residual curvatures  $\kappa'$  of the strip as a function of the averaged intermesh based on the analytical model and the finite element analyses. The averaged intermesh is the averaged value of the roll intermeshes,  $p_2$ ,  $p_4$ ,  $p_6$ , and  $p_8$ , where  $p_8$  ranges from  $-1.2$  mm to  $0.8$  mm. The residual curvature  $\kappa'$  is an indicator of the deviation of the strip from an initially flat surface at the entry roll. The curve with the dash-dot line and the markers represent the results based on the analytical model and the finite element analyses, respectively. The analytical predictions generally agree with the finite element analyses for the averaged intermeshes ranging from  $-1.71$  mm to  $0$ . As the averaged intermesh decreases from zero, the values of  $\kappa'$  decreases.  $\kappa'$  appears to exhibit an oscillatory behavior when the averaged intermesh is less than  $-0.11$  mm based on the analytical model. As the averaged intermesh decreases further, the amplitude of the oscillation of  $\kappa'$  grows. When the averaged intermesh is less than  $-1.41$  mm (analytical predictions),  $\kappa'$  has positive values of increasing magnitude. Five crossover points are observed at the averaged intermesh of  $-0.36$  mm,  $-0.61$  mm,  $-0.86$  mm,  $-1.11$  mm, and  $-1.41$  mm (analytical predictions). Smith [27] reported that the several crossover points with zero residual curvature underlie the reason why successful leveling can be achieved by the series roll leveling process in practice.

In the analytical model, a point contact is assumed between the strip and each roll, which means the strip does not wind around the work rolls. This contradicts with the fact that multi-point contact between the strip and the roll predicted in the finite element analyses. Morris et al. [3] reported that the wrap angle near the exit roll has a significant influence on the flatness of the strip. Wrap-around contact length between the strip and the roll may depend on the intermesh and roll spacing. In describing the arc of contact of the strip around a roll, an effective radius can be assumed to model the wrap-around contact characteristics. The concept of the effective radius is illustrated schematically in Figure 14. Figure 14a shows the original contact model, where the strip contacts with roll  $i$

tangentially.  $R_e$  is the expanded radius of the roll, which is defined by Equation (7).  $(x_i, y_i)$  is the  $i$ th contact point, and  $\lambda_i$  is the  $i$ th contact angle. Figure 14b shows that the strip makes contact elastically with roll  $i$  when subjected to an external force  $F_i$ . The circumferences of the deformed roll and the original roll are represented by the solid line and the dashed line, respectively, in Figure 14b.  $(x'_i, y'_i)$  is the  $i$ th contact point, and  $\lambda'_i$  is the  $i$ th contact angle for the Hertz contact model. A local deformation is ensued to cause a reduction in the local radius of roll  $i$ . The effective radius of the roll  $R_s$  is given as

$$R_s = R_e - sF_i \tag{20}$$

where  $s$  is the contact compliance of roll  $i$ . The external force  $F_i$  is computed from the moment distribution in the analytical model. Based on the Hertz contact model, the contact point  $(x'_i, y'_i)$  is

$$\begin{aligned} x'_i &= x_c + R_s \sin \lambda'_i \\ y'_i &= y_c - R_s \cos \lambda'_i \end{aligned} \tag{21}$$

where  $(x_c, y_c)$  is the coordinates of the center of the roll. As shown in Figure 14b, the deformed center line of the strip based on the analytical model with the Hertz contact compliance may be thought to have an arc segment bounded by the two virtual contact points,  $U$  and  $V$ , wrapped around the circumference of the original roll  $i$ , shown as a dashed circle in Figure 14b. When the contact angle  $\lambda'_i$  is very small which is the case in the roller leveler, the line segment and the arc segment bounded by the two end points  $U$  and  $V$  are approximately equal. The contact compliance of the rolls is taken as a fitting parameter in the analytical model with the Hertz contact compliance to fit the analytical predictions with the finite element computations. Yi et al. [28] considered the wrap angle on a roll during a roller leveling process by fitting an arc curve around a roll. A parameter determined by experiments is needed for curve fitting.

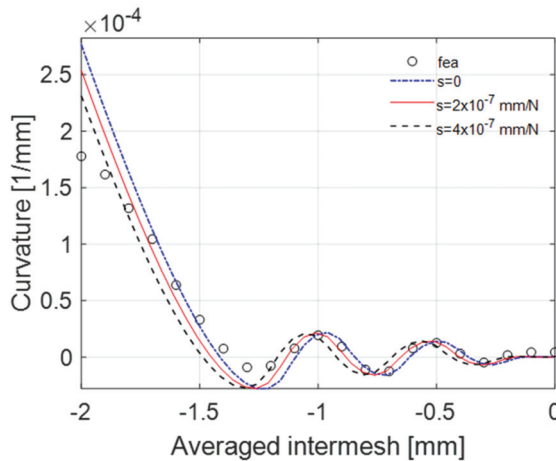
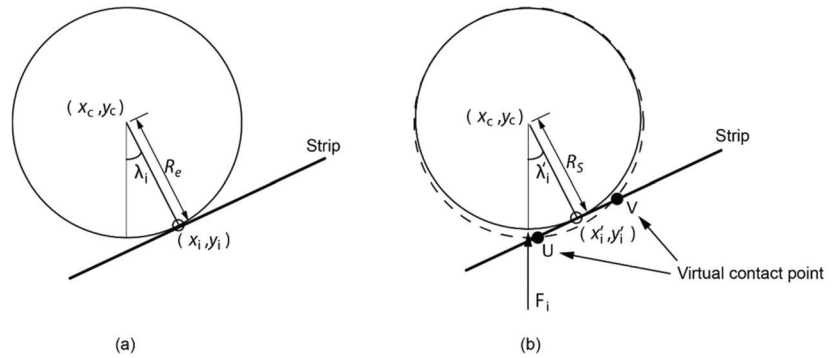


Figure 13. Residual curvature as a function of the averaged intermesh.

The residual curvatures  $\kappa'$  of the strip calculated by the analytical model with the Hertz contact compliance are plotted in Figure 13. The curves with the compliance  $s = 0$  and  $4 \times 10^{-7}$  mm/N appear to envelop the results based on the finite element analyses. The curve with the compliance  $s = 2 \times 10^{-7}$  mm/N may be able to predict the general trend of the results based on the finite element analyses for the averaged intermesh ranging from 0 mm to  $-2$  mm. The wrap-around contact condition between the strip and the rolls can be manifested by the analytical model with the Hertz contact compliance within an acceptable accuracy, compared with the results of the finite element analyses.



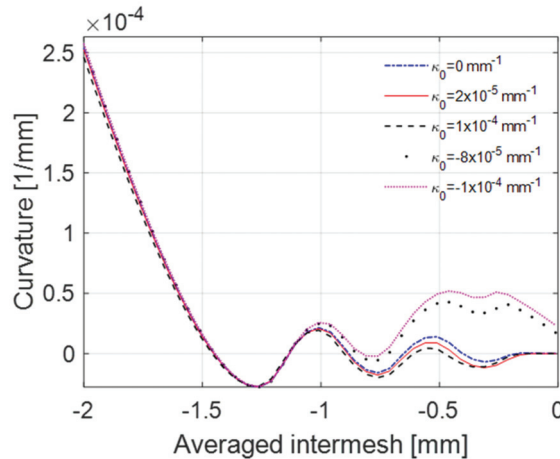
**Figure 14.** Illustration of (a) the original contact model; (b) the Hertz contact model.

A series of simulations was run to calculate the residual curvatures  $\kappa'$  of the strip with an initial curvature  $\kappa_0$  based on the analytical model with the Hertz contact compliance  $s = 2 \times 10^{-7}$  mm/N. The initial stress in the strip is neglected without losing generality of the residual curvature predictions. Mathieu et al. [29] considered initial flatness defects in their finite element analyses of a leveling process. They introduced the flatness defects in the strip which was free of stress. Figure 15 shows the residual curvature as a function of the averaged intermesh for the strip with the initial curvature  $\kappa_0$  varying between  $-1 \times 10^{-4}$  mm $^{-1}$  to  $1 \times 10^{-4}$  mm $^{-1}$ . As shown in Figure 15, at low levels of roll intermesh (averaged intermeshes greater than  $-0.1$ ), the residual curvatures  $\kappa'$  for the three cases of  $\kappa_0 = -1 \times 10^{-4}$  mm $^{-1}$ ,  $0$ , and  $1 \times 10^{-4}$  mm $^{-1}$  deviate from each other significantly. For the averaged intermesh in this level, the curve for the case of  $\kappa_0 = -1 \times 10^{-4}$  mm $^{-1}$  oscillates mostly in the positive-curvature region ( $\kappa' > 0$ ), in contrast to the cases of  $\kappa_0 = 0$  and  $1 \times 10^{-4}$  mm $^{-1}$ , which oscillate between the positive  $\kappa'$  region and the negative  $\kappa'$  region. The initially bowed-down defect for the strip with  $\kappa_0 = -1 \times 10^{-4}$  mm $^{-1}$  exits the leveler with the residual curvature in the same direction for the averaged intermesh greater than  $-0.71$ . As the extent of the averaged intermesh increases, the residual curvatures for the three cases of  $\kappa_0 = -1 \times 10^{-4}$  mm $^{-1}$ ,  $0$ , and  $1 \times 10^{-4}$  mm $^{-1}$  gradually converge to the same values. For the values of the averaged intermesh less than  $-1.1$ , the curves for the three cases appear identical, where two cross over points with the interpolated averaged intermesh values of  $-1.46$  and  $-1.13$  were found. For the values of the averaged intermesh less than  $-1.46$ , positive residual curvatures were produced. For the averaged intermesh values within the interval of  $-1.46$ ,  $-1.13$ , the minimum of the residual curvature is  $-0.27 \times 10^4$  mm $^{-1}$ . In this region of the leveler settings, the residual curvatures of the strip seem to be insensitive to its initial curvatures. This result can serve to the advantage of leveler operators to obtain nearly zero residual curvature for strips with various initial curvatures. Grüber et al. [18] also demonstrated robustness of the roll intermesh settings for a roller leveler regarding a change in the initial curvature. In this investigation, the plane strain condition is considered in the finite element analyses. The width-to-thickness ratio of the strip considered in the analyses is 5. Carvalho et al. [30] reported that, in order to develop near plain strain conditions, it is important to maintain a ratio of width-to-thickness greater than 5.

A combined isotropic/kinematic hardening is implemented to describe the material hardening of the strip in this investigation. Doege et al. [5] also adopted combined isotropic/kinematic hardening for their leveling model, where mathematical formulations of their hardening model were not presented. Detailed formulations of the hardening model are provided in this investigation. Doege et al. [5] presented analysis results of their model. Results of the stress distributions and residual curvature of a steel strip based on our analytical model are verified by the finite element analyses. Doege et al. [5] computed the contact points between the strip and the rolls by assuming only one contact point



between the strip and each roll. An effective radius modelling the wrap-around contact characteristics by the Hertz contact compliance is proposed to describe the arc of contact of the strip around a roll. A roll inter-mesh range to produce a flatness condition of the strip is presented based on the analytical model with the Hertz contact compliance.



**Figure 15.** Residual curvature as a function of the averaged intermesh for the strip with an initial curvature.

Indeed, the initial curvature considered in the model is the longitudinal wave defect of a strip. Behrens et al. [6] sectioned a strip longitudinally and showed that the length of all sections after leveling should be the same in order to remove a transverse wave defect. Therefore, bendable rolls, as practiced in the industry, can be applied into a leveler to cause various degree of plastic deformation in each longitudinal section to achieve equal length. Chen et al. [9] developed an analytical model of a roller leveler with consideration to the bending of the rollers to eliminate transverse wave defects. This approach can be implemented in the analytical model to extend its applicability. Park and Hwang [13] slit a strip longitudinally to calculate the initial curvature of each longitudinal section. Given proper roll intermesh settings, the longitudinal sections with various initial curvatures can reach similar values of residual curvature after leveling based on finite element analyses and experiments. The results shown in Figure 15 based on the developed model also provide evidence that the residual curvatures of the strips with different initial curvatures can converge to the same value given enough amount of roll intermesh.

Given the multiple forming processes and complex machine settings involved in the roller leveling, tradeoffs between a simple, efficient model and an elaborate, detailed model should be balanced. Baumgart et al. [31] described that the effects of parts of the leveler, such as support rolls, frames, posts, and adjustment screws, should also be considered in order to obtain a more accurate leveler model. Wang and Li [32] reported that stiffness of roll cassettes and leveler housing are important factors of the leveling process. In this study, a relatively simple analytical model was developed based on the assumptions of two-dimensional geometry, pure bending of the strip, and the uniaxial loading condition. Compared to previously reported models, the Hertz contact compliance implemented in the model relaxed the single point contact condition between the strip and the roll, and a relatively accurate prediction of the residual curvature can be attained. The model could serve as a guide in the development of strategies for effective adjustment of roller levelers.

## 5. Conclusions

An analytical model for analyzing the residual stress distribution and residual curvatures of a strip during roller leveling is developed. The model verified by the finite element analyses is based on a simplified, two-dimensional geometric framework. The combined

isotropic and kinematic material hardening model is implemented through a combined hardening parameter. The stress distributions after each bending/reverse bending and the residual curvature at the exit roll subjected to various leveler settings can be obtained by the developed model. The model was further enhanced by considering a Hertz contact model to eliminate the discrepancies between the model predictions and the finite element analyses. Based on the analytical model with the Hertz contact compliance, a range of the leveler settings can be determined to robustly obtain a strip with a nearly zero curvature at the exit roll.

Analytical models with combined isotropic/kinematic material hardening for roller leveling have been reported previously. A formulation of the change of the effective stress as a function of the change of the effective strain under cyclic bend loading is adopted in the developed analytical model with the combined hardening. The model is efficient and accurate in predicting the stress distributions and residual curvature of a steel strip. Unlike the assumption of a single contact point between the strip and the rolls, an effective radius modelling the wrap-around contact characteristics by the Hertz contact compliance is proposed in this investigation. An arc contact of the strip around a roll is described by the Hertz contact model. A roll intermesh range to produce a flatness condition of the strip can be obtained by the analytical model with the Hertz contact compliance.

**Author Contributions:** Conceptualization, S.-K.K. and D.-A.W.; methodology, D.-A.W.; software, Y.-L.O.; validation, D.-A.W.; formal analysis, D.-A.W.; resources, S.-K.K.; data curation, D.-A.W.; writing—original draft preparation, D.-A.W.; writing—review and editing, D.-A.W.; funding acquisition, S.-K.K. All authors have read and agreed to the published version of the manuscript.

**Funding:** This research was funded by China Steel Corporation, grant number 106T7D-RE18 and the Ministry of Science and Technology, Taiwan, grant number MOST 106-2221-E-005-038.

**Data Availability Statement:** Data presented in this article are available at request from the corresponding author.

**Acknowledgments:** The authors would like to express their appreciation to the National Center for High-Performance Computing (NCHC), Taiwan for their assistance.

**Conflicts of Interest:** The authors declare no conflict of interest.

## References

1. Amor, A.; Rachik, M.; Sfar, H. Combination of finite-element and semi-analytical models for sheet metal leveling simulation. *Key Eng. Mater.* **2011**, *473*, 182–189. [[CrossRef](#)]
2. Li, S.-Z.; Yin, Y.-D.; Xu, J.; Hou, J.-M.; Yoon, J. Numerical simulation of continuous tension leveling process of thin strip steel and its application. *J. Iron Steel Res. Int.* **2007**, *14*, 8–13. [[CrossRef](#)]
3. Morris, J.W.; Hardy, S.J.; Lees, A.W.; Thomas, J.T. Some fundamental considerations for the control of residual flatness in tension levelling. *J. Mater. Processing Technol.* **2002**, *120*, 385–396. [[CrossRef](#)]
4. Hira, T.; Abe, H.; Azuma, S. Analysis of sheet metal bending deformation behavior in processing lines and its effectiveness. *Kawasaki Steel Eng. Rep.* **1988**, *19*, 54–62.
5. Doege, E.; Menz, R.; Huinink, S. Analysis of the levelling process based upon an analytic forming model. *CIRP Ann. Manuf. Technol.* **2002**, *51*, 191–194. [[CrossRef](#)]
6. Behrens, B.-A.; El Nadi, T.; Krimm, R. Development of an analytical 3D-simulation model of the levelling process. *J. Mater. Processing Technol.* **2011**, *211*, 1060–1068. [[CrossRef](#)]
7. Dratz, B.; Nalewajk, V.; Bikard, J.; Chaste, Y. Testing and modelling the behavior of steel sheets for roll levelling applications. *Int. J. Mater. Form.* **2009**, *2*, 519. [[CrossRef](#)]
8. Liu, Z.; Wang, Y.; Yan, X. A new model for the plate leveling process based on curvature integration method. *Int. J. Mech. Sci.* **2012**, *54*, 213–224. [[CrossRef](#)]
9. Chen, W.-H.; Liu, J.; Cui, Z.-S.; Wang, Y.-J.; Wang, Y.-R. A 2.5-dimensional analytical model of cold leveling for plates with transverse wave defects. *J. Iron Steel Res. Int.* **2015**, *22*, 664–671. [[CrossRef](#)]
10. Higo, T.; Matsumoto, H.; Ogawa, S. Influence of delivery-side roll position of roller leveler to plate flatness. In Proceedings of the 2016 AISTech Conference, Pittsburgh, PA, USA, 16–19 May 2016; pp. 2129–2137.
11. Morris, J.W.; Hardy, S.J.; Lees, A.W.; Thomas, J.T. Formation of residual stresses owing to tension levelling of cold rolled strip. *Ironmak. Steelmak.* **2001**, *28*, 44–52. [[CrossRef](#)]

12. Schleinzer, G.; Fischer, F.D. Residual stress formation during the roller straightening of railway rails. *Int. J. Mech. Sci.* **2001**, *43*, 2281–2295. [[CrossRef](#)]
13. Park, K.-C.; Hwang, S.-M. Development of a finite element analysis program for roller leveling and application or removing blanking bow defects of thin steel sheet. *ISIJ Int.* **2002**, *42*, 990–999. [[CrossRef](#)]
14. Huh, H.; Heo, J.H.; Lee, H.W. Optimization of a roller levelling process for Al7001T9 pipes with finite element analysis and Taguchi method. *Int. J. Mach. Tools Manuf.* **2003**, *43*, 345–350. [[CrossRef](#)]
15. Roberts, I.; Wang, C.; Mynors, D.; Adams, P.; Lane, K.; Unwin, P. Numerical analysis of strip-roll conformity in tension levelling. In Proceedings of the 10th International Conference of Technology of Plasticity (ICTP 2011), Aachen, Germany, 25–30 September 2011; pp. 315–319.
16. Jin, H.-R.; Yi, Y.-L.; Han, X.-Y.; Liang, Y. Roller straightening process and FEM simulation for stainless steel clad plate. *Open Mech. Eng. J.* **2014**, *8*, 557–561.
17. Kim, J.; Park, K.-C.; Kim, D.-N. Investigating the fluting defect in v-bending due to the yield-point phenomenon and its reduction via roller-leveling process. *J. Mater. Processing Technol.* **2019**, *270*, 59–81. [[CrossRef](#)]
18. Grüber, M.; Kümmel, L.; Hirt, G. Control of residual stresses by roller leveling with regard to process stability and one-sided surface removal. *J. Mater. Processing Technol.* **2020**, *280*, 116600. [[CrossRef](#)]
19. Zhang, D.; Cui, Z.; Ruan, X.; Li, Y. An analytical model for predicting springback and side wall curl of sheet after U-bending. *Comput. Mater. Sci.* **2007**, *38*, 707–715. [[CrossRef](#)]
20. Kotov, K.A.; Bolobanova, N.L.; Nushtaev, D.V. Modeling the stress state of a steel strip with a roller leveling machine under cyclic alternating deformations. *Steel Transl.* **2020**, *50*, 750–755. [[CrossRef](#)]
21. Müller, U.; Krambeer, H.; Wolff, A.; Viella, A.E.; Richardson, A.D.; Perä, J.-O.; Luoto, P.; Weberm, W. *Optimisation of Final Plate Flatness by Set-Up Coordination for Subsequent Manufacturing Process (Final Plate Flatness)*; Final Report, EUR 25852 EN; Europe Commission: Brussels, Belgium, 2013.
22. Guan, B.; Zhang, C.; Zang, Y.; Wang, Y. Model for the whole roller leveling process of plates with random curvature distribution based on the curvature integration method. *Chin. J. Mech. Eng.* **2019**, *32*, 47. [[CrossRef](#)]
23. Hosford, W.F.; Caddell, R.M. *Metal Forming—Mechanics and Metallurgy*; Prentice Hall: Hoboken, NJ, USA, 1993.
24. Guan, B.; Zang, Y.; Wu, D.; Qin, Q. Study on mechanical behavior of thin-walled member during precision straightening process. *Sens. Transducers* **2014**, *179*, 36–42.
25. Guan, B.; Zang, Y.; Wu, D.; Qin, Q. Stress-inheriting behavior of H-beam during roller straightening process. *J. Mater. Processing Technol.* **2017**, *244*, 253–272. [[CrossRef](#)]
26. Yonetani, S. *The Engender Theory and Countermeasure of Residual Stress*; China Machine Press: Beijing, China, 1983.
27. Smith, R.P. The effect of the number of leveling rolls on the straightening process. *Iron Steel Technol.* **2007**, *4*, 57–68.
28. Yi, G.; Wang, Z.; Hu, Z. A novel modeling method in metal strip leveling based on a roll-strip unit. *Math. Probl. Eng.* **2020**, *2020*, 1486864. [[CrossRef](#)]
29. Mathieu, N.; Dimitriou, R.; Parrico, A.; Potier-Ferry, M.; Zahrouni, H. Flatness defects after bridle rolls: A numerical analysis of leveling. *Int. J. Mater. Form.* **2013**, *6*, 255–266. [[CrossRef](#)]
30. Carvalho, A.P.; Reis, L.M.; Pinheiro, R.P.R.P.; Pereira, P.H.R.; Langdon, T.G.; Figueiredo, R.B. Using Plane Strain Compression Test to Evaluate the Mechanical Behavior of Magnesium Processed by HPT. *Metals* **2022**, *12*, 125. [[CrossRef](#)]
31. Baumgart, M.; Steinboeck, A.; Kiefer, T.; Kugi, A. Modelling and experimental validation of the deflection of a leveler for hot heavy plates. *Math. Comput. Model. Dyn. Syst.* **2015**, *21*, 202–227. [[CrossRef](#)]
32. Wang, X.; Li, X. Research on force simulation of main leveler housing and roll cassettes in medium and heavy plate leveling. *J. Converg. Inf. Technol.* **2012**, *7*, 153–161.

# Research of Resistance of Selected Materials to Abrasive Wear to Increase the Ploughshare Lifetime

Monika Vargova <sup>1,\*</sup>, Miroslava Tavodova <sup>1</sup>, Katarina Monkova <sup>2,3,\*</sup> and Miroslav Dzupon <sup>4</sup>

<sup>1</sup> Faculty of Technology, Technical University in Zvolen, Studentska 26, 960 01 Zvolen, Slovakia; tavodova@tuzvo.sk

<sup>2</sup> Faculty of Manufacturing Technologies with a Seat in Presov, Technical University of Kosice, Sturova 31, 080 01 Presov, Slovakia

<sup>3</sup> Faculty of Technology, Tomas Bata University in Zlin, Vavreckova 275, 760 01 Zlin, Czech Republic

<sup>4</sup> Institute of Materials Research, Slovak Academy of Sciences, Watsonova 47, 040 01 Kosice, Slovakia; mdzupon@saske.sk

\* Correspondence: monika.vargova@tuzvo.sk (M.V.); katarina.monkova@tuke.sk (K.M.)

**Abstract:** Road maintenance and cleaning in winter are performed with ploughshares. Due to the fact that the layer of snow and ice that is removed from the road surface contains various hard impurities, ploughshares are exposed to high intensity abrasive wear. This article deals with the resistance to abrasive wear of originally used ploughshare materials and the materials that were designed as a suitable modification of the ploughshare to increase its service life. The chemical composition of materials used to manufacture ploughshare components is unknown. For this reason, they were analyzed with an ARL 4460 spectrometer, which was used to analyze the element content. The main part of the research was focused on the abrasion resistance test, which was performed according to the GOST 23.208-79 standard. Based on the chemical analysis, it was found that the basic body of the ploughshare was made of S355J2G3 steel, and the raking blade material was made of 37MnSi5 steel. The original material (steel S355J2G3) of the ploughshare body as a reference standard was compared to steel HARDOX 450. Furthermore, a sample made of the original material of the raking blade (steel 37MnSi5) was used as a reference standard, the properties of which were compared to the newly designed OK 84.58 and UTP 690 hardfacing materials. The parametric test method of statistical hypotheses was also used to process and evaluate the weight losses of the selected materials.

**Keywords:** abrasive wear; wear resistance; ploughshare; hardfacing materials; hypothesis testing

**Citation:** Vargova, M.; Tavodova, M.; Monkova, K.; Dzupon, M. Research of Resistance of Selected Materials to Abrasive Wear to Increase the Ploughshare Lifetime. *Metals* **2022**, *12*, 940. <https://doi.org/10.3390/met12060940>

Academic Editor: George A. Pantazopoulos

Received: 27 April 2022

Accepted: 26 May 2022

Published: 30 May 2022

**Publisher's Note:** MDPI stays neutral with regard to jurisdictional claims in published maps and institutional affiliations.



**Copyright:** © 2022 by the authors. Licensee MDPI, Basel, Switzerland. This article is an open access article distributed under the terms and conditions of the Creative Commons Attribution (CC BY) license (<https://creativecommons.org/licenses/by/4.0/>).

## 1. Introduction

Forest roads are important in terms of making forests accessible for heavy machinery and timber transportation. Therefore, it is necessary to maintain these roads both in summer and winter. It is necessary to remove a layer of snow or ice from the road surface in the winter time. Snow is removed from the road using a snow ploughshare. Since the removed layer of snow contains various hard impurities, the ploughshares are exposed to high—and especially abrasive—wear and their replacement is relatively economical. Therefore, it is necessary to look for ways to increase their service life and examine their resistance to abrasive wear.

Wear is one of the main factors affecting the performance and lifetime of the components of various mechanisms [1]. Abrasive wear is one of the dominant and common tribological wear processes [2–4] leading to expensive costs for repairing worn mechanisms and replacing spare parts [1]. This wear is characterized by a reduction in the volume of the material and a change in its shape, causing a decrease in work efficiency [5]. Wear caused by shocks and abrasion by hard abrasive particles is a major problem in many industries, especially in agriculture, forestry, mining, mineral processing, etc. [6,7].

Abrasive wear occurs when a hard rough surface slides across a softer surface; in this case, wear is defined as damage to a solid surface that generally involves the progressive loss of material and is due to relative motion between that surface and a contacting substance or substances.

The material from grooves is usually removed in the form of loose particles [8–10]. The material resistance against abrasive wear is higher with higher hardness [5,11].

This type of wear is caused by sharp particles that slide or flow over the metal surface at different speeds and pressures, grinding the material from the surface like small cutting tools. The harder the particles and the sharper their shapes, then the more intense the abrasion is. Typical cases of abrasive wear are encountered in earthworks, material transportation and agricultural equipment [12,13].

During abrasive wear, the material is removed from the surface when the stress in it reaches a critical value. This local fracture stress can be achieved by one or more abrasive particles coming into contact with the tool surface. Material that is not removed in this way can be deformed due to abrasion as well as impact [14,15].

One of the very effective measures to increase wear resistance is to protect functional surfaces with a suitable coating material [16]. Hardfacing is a commonly used method to improve the surface properties of agricultural tools, mining components and soil preparation equipment, among others [17]. The alloy is applied to the surface of the base material (usually on low-carbon or medium-carbon steels) by hardfacing in order to increase the hardness and wear resistance without a significant loss in the ductility and toughness of the base material [16,17].

Important factors that determine the resistance to abrasive wear include the hardness, size, shape and intensity of the particles; as well as the hardness, shape, size and number of hard phases and their distribution in the parent metal. Wear resistance increases with the increasing hardness of hard structural components (carbides, borides, etc.) and with their increasing share in the structure [9,12].

The main components of Fe-based alloys are chromium, molybdenum and boron, which make Fe-based alloys resistant to wear. Wang et al. studied the microstructure, hardness and wear resistance of Fe-based alloys by adding the elements ferrotitanium (Fe–Ti), ferromolybdenum (Fe–Mo), ferrovanadium (Fe–V) and graphite, which were applied by the arc welding process. The results showed that the hardness and resistance of the hardfacing metal layer increase with an increasing proportion of Fe–Ti, Fe–V, Fe–Mo and graphite. Their amounts must be controlled in the range of 8–10% graphite, 12–15% Fe–Ti, 10–12% Fe–V and 2–4% Fe–Mo. However, cracks begin to form in the layer of hardfacing metal if the amount of Fe–Mo is more than 5% [18,19].

Xu et al. studied the effect of the carbide type on the resistance to abrasive wear at different sizes and abrasive particle loads. The results showed that  $M_6C$  carbides showed higher resistance to wear by fine abrasive particles compared to  $M_2C$  [20].

During impact wear, the material is exposed to impact and high pressure, due to which it deforms or locally breaks—it can even crack. Due to the relatively high working speeds of ploughshare vehicles, it is necessary to protect the ploughshare from the effects of the impact of the ploughshare hitting with a solid obstacle, e.g., ice and abrasion by mineral particles, gravel and stones [9,12].

For this reason, it is necessary to pay attention to the possibilities of increasing the life of the blades and examine their resistance to abrasive wear, which was also the main goal of the authors' long-term research.

Based on the experience and study of already published outputs in the field, the authors tried to bring new solutions to the issue [16,21]. To the best of the authors' knowledge, no relevant studies have yet been published that compare the resistance of a selected combination of materials (37MnSi5, S355JG3 and HARDOX 450 steels, as well as OK 84.58 and UTP 690 hardfacing materials) to abrasive wear. The achieved results will be contributing and applicable not only to ploughshares, construction machines and forest manipulators, but can also be used in the mechanical engineering, civil and mining industries.

## 2. Materials and Methods

The ploughshare (Figure 1), the resistance of which to abrasive wear is the subject of our research, is a commonly used tool for modifying forest roads during wintertime. The ploughshare works in a heterogeneous environment, coming into contact with the road and thus with snow, stones, mineral particles, gravel, sand, etc. First, the raking blade comes into contact with the road. It is stressed by the impact of the first contact with the road and with corrosion and abrasion during the raking. In addition, the rest part of the ploughshare is also stressed because the accumulated snow, together with sand and gravel, creates a force on the ploughshare body from the point of pick-up until it is pushed to the side of the road. As a result, wear occurs due to abrasion and corrosion not only on the raking blade but on the entire working part of the ploughshare (weldment).



Figure 1. The arrow ploughshare [22].

The basic dimensions of the currently used steel raking blades and their geometry, symmetrically placed in the shape of an arrow on the front part of the tractors, are shown in Figure 2. The values of these basic dimensions, declared by the manufacturer [23], are listed in Table 1.

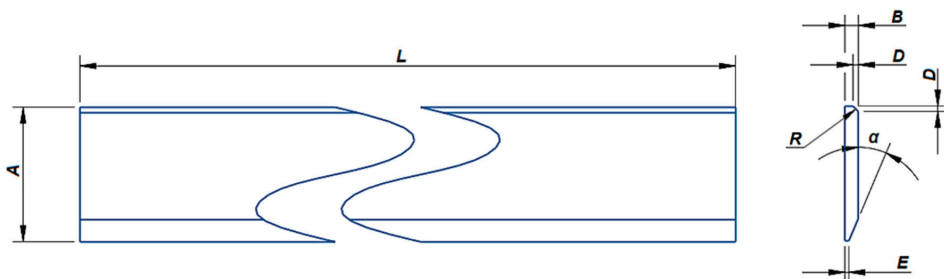


Figure 2. Basic dimension of steel raking blade.

Table 1. Basic dimension of steel raking blade [23].

A (mm)	B (mm)	$\alpha$ (°)	R/D (mm)	E (mm)	L (mm)
80–400	12–50	20.2–24	R3/5–12	3–28	6000–6300

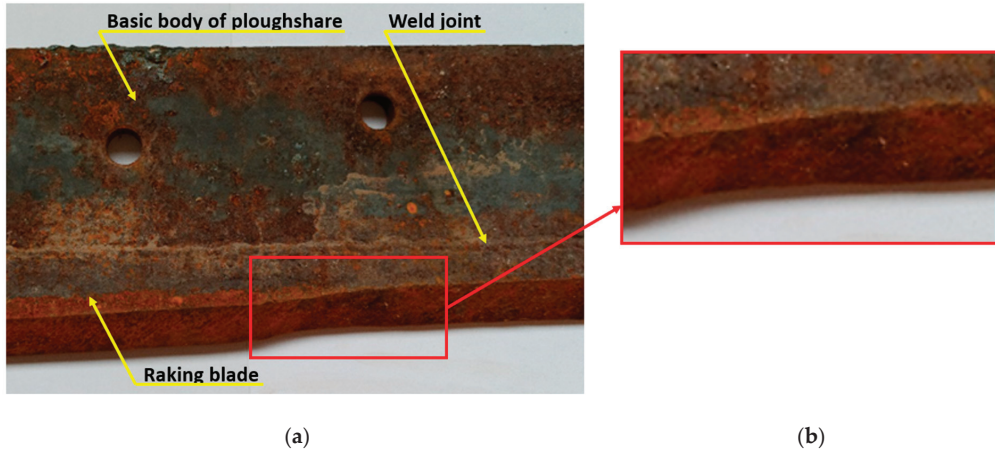
### 2.1. Materials of Research Samples

The raking blades of the ploughshares can be attached to the ploughshare body (to the base material of the ploughshare) in two ways:

- Threaded joint;
- Welded joint.

Due to the rapid wear of the ploughshare and the need for its frequent replacement, the operator of such ploughshares initiated research that would have increased their lifetime and ensured greater efficiency in the use of funds spent on their purchase and replacement.

For the ploughshare that was the subject of the research, the raking blade was attached by a weld, so it can be said that the ploughshare consisted of 3 main parts, namely the basic ploughshare body, the raking blade and the weld (Figure 3a). There is a detail of the raking blade which is that its significant damage due to the heterogeneity of the working environment is visible in Figure 3b.



**Figure 3.** Part of the discarded ploughshare: (a)—main parts of the ploughshare; and (b)—detail of a raking blade).

The chemical composition of materials used to manufacture ploughshare components is unknown. From this concern, their elemental analyses were carried out using ARL 4460 spectrometer. The results of the chemical analysis of the individual parts of the originally used ploughshare are shown in Table 2.

**Table 2.** Chemical composition of the individual parts of the original ploughshare.

Element	C	Mn	Si	Cr	Ni	Cu	Mo	P	S	Fe
Basic body of the ploughshare (wt.%)	0.2	1.4	0.3	0.04	0.055	0.16	<0.01	<0.005	<0.15	balance
Base weld metal (wt.%)	0.06	1.3	0.55	-	-	-	-	-	-	balance
Raking blade (wt.%)	0.33	1.24	1.36	-	-	0.04	0.178	0.017	<0.15	balance

Based on the performed chemical analysis, it is possible to state that:

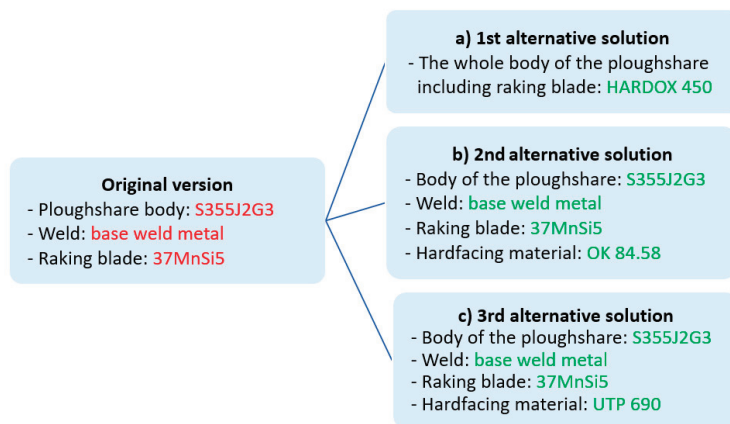
- The basic body of the ploughshare was made of S355J2G3 steel. It is the steel of the usual quality for low temperatures with guaranteed weldability. It is used in parts of equipment operating at temperatures up to  $-50\text{ }^{\circ}\text{C}$  made of sheet metal with a guaranteed value of notch toughness up to  $-50\text{ }^{\circ}\text{C}$ . The yield strength is  $R_m = 355\text{ MPa}$  and the ultimate tensile strength is  $Re = 470\text{--}610\text{ MPa}$  [24]. The chemical composition of the tested steel, according to the data from the material sheet, is shown in Table 3;
- The base weld metal—an electrode for general use, suitable for welding carbon and low-alloy steels—was used for welding the basic ploughshare body with a raking blade. The weld metal of the electrode is tough and resistant to cracking [14];
- The raking blade was made of 37MnSi5 material (Wr. Nr. 1.5122). It is manganese-silicon steel suitable for tempering. It is used on medium-stressed machine parts and particularly wear-resistant road vehicle parts, e.g., shafts, axles, connecting rods,

levers, bolts, etc. The ultimate tensile strength of 37MnSi5 steel is  $R_m = \max$ . The 760 MPa and hardness 217 HBW [25]. The chemical composition of the tested steel, according to the data from the material sheet, is shown in Table 3.

The ploughshare that was the subject of the research worked for 6–8 weeks. After this time, the raking blade of the ploughshare was worn and unusable. The frequent replacement of the raking blades caused economic and technical problems. Due to the fact that the currently used ploughshare was functionally usable only for a short time and did not meet the requirements for the lifetime of this type of product, it was necessary to design a new solution that improved the situation. Based on the authors' own research and practical experience, as well as on the results described in the professional and scientific literature presented in the Introduction, the following options are suggested to increase the lifetime of the ploughshare and thus increase its resistance to abrasive wear (Figure 4):

- (a) Change of ploughshare material for HARDOX 450 material;
- (b) Application of the OK 84.58 hardfacing material to the exposed surfaces of the functional parts of the ploughshare;
- (c) Application of the UTP 690 hardfacing material to exposed areas of functional parts of the ploughshare.

The first alternative solution was the idea of replacing the original ploughshare with one compact body made of HARDOX material, replacing all three parts of the ploughshare: the ploughshare body, the weld metal, and the raking blade. HARDOX steels are produced in several designs. HARDOX sheets are considered a worldwide standard in the field of abrasion-resistant steel due to their unique combination of hardness and toughness. The hardness of this steel ranges from 400 HBW to 600 HBW. It is available in the form of sheet metal in thicknesses from 0.7 mm to 160 mm but also in the form of tubes and rods [9,26]. HARDOX 450 material is an abrasion-resistant steel with excellent construction properties. The hardness of this steel is 450 HBW, and the yield strength is  $R_e = 1100\text{--}1300$  MPa. HARDOX 450 material is a well flexible material that has guaranteed weldability. It provides good abrasion resistance and thus a longer lifetime. It has better wear resistance [27], higher load capacity, and a longer lifetime compared to ordinary steel with the same hardness. It is used in various components and constructions that are subject to wear [9,27,28]. The chemical composition of HARDOX 450 material is shown in Table 3.

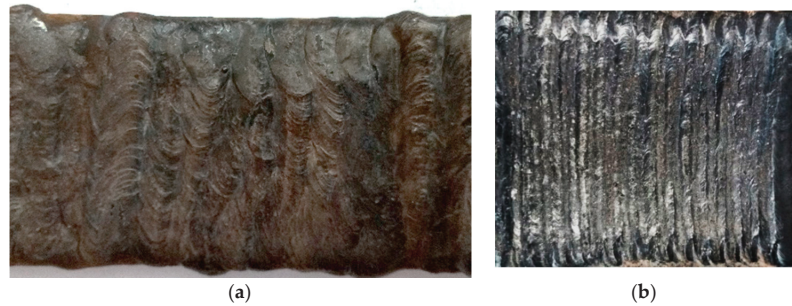


**Figure 4.** Suggested research solutions regarding the current state.

The second alternative solution was to apply a new layer in the form of a hardfacing material to the original 37MnSi5 steel of the raking blade part (see Figure 4). Such a sample with OK 84.58 hardfacing material (Figure 5a) was prepared in the company ŽOS Zvolen, a.s. in a single layer by certified welders. The electrode was dried for 2 h at 200 °C without



preheating the sample. The applied hardfacing voltage was  $U = 21.5$  V and the hardfacing current was  $I = 140$  A. The stated parameters were chosen according to the experience of experts from the company.



**Figure 5.** Sample with hardfacing materials; (a) OK 84.58; and (b) UTP 690.

The OK 84.58 electrode is a high-yield electrode for hardfacing functional surfaces resistant to wear under simultaneous shock stress with the required partial corrosion resistance, used, e.g., for parts of agricultural and forestry machines, mixers, transport equipment, etc. It forms a martensitic structure after hardfacing. It is possible to treat hardfacing materials by grinding [29,30]. The chemical composition of the OK 84.58 electrode is shown in Table 3.

The sample with hardfacing material UTP 690 (Figure 5b), prepared in the company ŽOS Zvolen, a.s. by certified welders, was used as the third alternative solution (see Figure 4). The hardfacing layer was applied to the original 37MnSi5 material of the raking blade part. The electrode was dried for 2 h at 300 °C with the preheating of the sample to 230 °C. The applied hardfacing voltage was  $U = 21.5$  V, and the hardfacing current was  $I = 105$  A. In this case, the parameters were also designed according to the experience of the experts from the company.

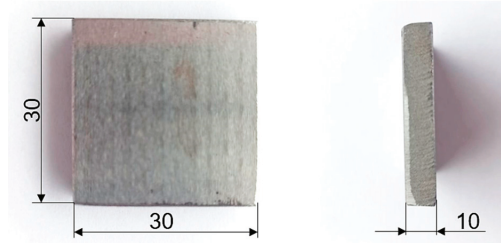
The UTP 690 electrode is used for the repair and production of cutting tools, especially for the restoration of cutting edges and work surfaces. The coating is highly resistant to friction, compression and impact even at elevated temperatures up to 550 °C [31]. Using this electrode, it is also possible to produce new tools by hardfacing on carbon and low-alloyed base steels [31]. This forms a martensitic structure after hardfacing [16]. The chemical composition of the UTP 690 electrode is shown in Table 3.

**Table 3.** Chemical composition of S355J2G3 [24], 37MnSi5 [25], HARDOX 450 [27] steels and OK 84.58 [29] and UTP 690 [31] hardfacing materials according to the datasheets.

Material	Element (wt.%)														
	C	Mn	Si	Cr	Ni	Cu	Cr+Ni+Cu	Ti	P	Mo	B	S	V	W	Fe
S355J2G3	max. 0.20	max. 1.40	max. 0.55	max. 0.30	max. 0.30	max. 0.30	max. 0.70	max. 0.20	max. 0.03	-	-	max. 0.03	-	-	balance
37MnSi5	0.33– 0.41	1.10– 1.40	1.10– 1.40	-	-	-	-	-	max. 0.035	-	-	max. 0.035	-	-	balance
HARDOX 450	max. 0.23	max. 1.60	max. 0.5	max. 1.20	max. 0.25	-	-	-	max. 0.025	max. 0.25	max. 0.005	max. 0.010	-	-	balance
OK 84.58	0.67	0.70	0.7	10.40	-	-	-	-	-	-	-	-	-	-	balance
UTP 690	0.90	0.50	0.80	4.50	-	-	-	-	-	-	-	-	1.20	2.00	balance

All samples, both standard (S355J2G3 and 37MnSi5) and reference ones (HARDOX, OK 84.58 and UTP 690), were prepared according to the GOST 23.208-79 standard by abrasive water jet cutting technology (AWJM), machined by milling and ground by a magnetic surface grinder for obtaining dimensions 30 mm × 30 mm × 10 mm and surface roughness

$R_a = 0.4 \mu\text{m}$  (Figure 6). OTTAWA  $\text{SiO}_2$  silica sand with a grain size of 0.1–0.3 mm was used as an abrasive material [31]. The hardness corresponds to the hardness value according to Vickers 500 HV and Rockwell 54 HRC.



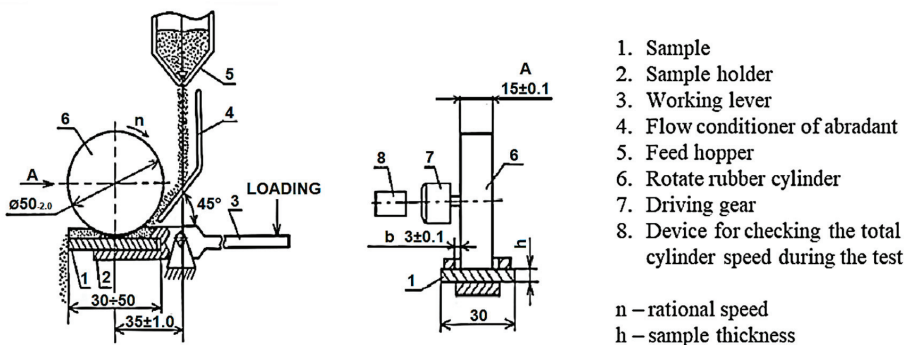
**Figure 6.** Sample for abrasion resistance test with marked dimensions.

## 2.2. Testing Methods

There are several methods for testing the wear resistance of materials. Based on the ploughshare operating environment, the method simulating its load in the laboratory conditions at the Technical Faculty of CULS in Prague was chosen. The abrasion resistance test was performed according to standard GOST 23.208-79—Ensuring wear resistance of products. The wear resistance testing of materials by friction against loosely fixed abrasive particles [32].

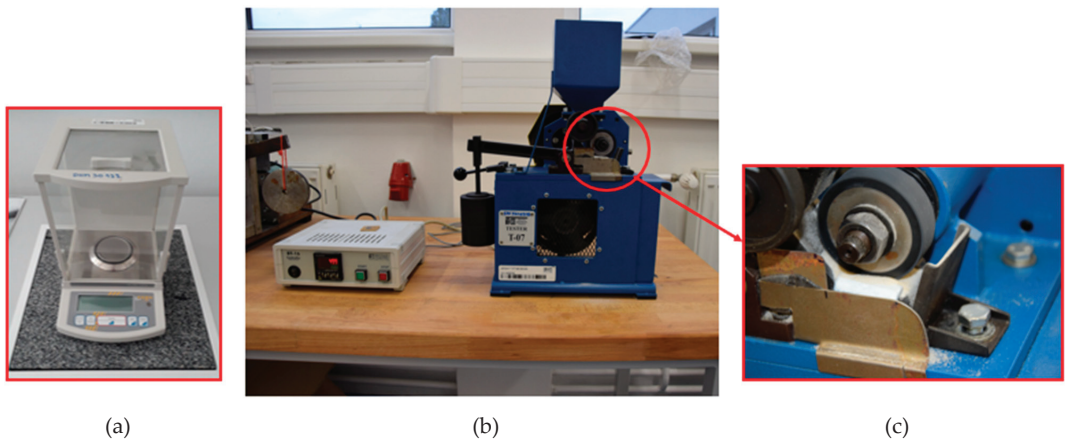
The principle of the method is to compare the loss of test material and the loss of standard material under the same test conditions. The abrasive material used is electrocorundum with a grain size of 100–250  $\mu\text{m}$  [33] and with a maximum relative mass moisture content of 0.15%. The standard further states that when assessing wear resistance under specific wear conditions, it is permitted to use abrasive material corresponding to the material used during operation but with a maximum grain size of 1.0 mm [32].

Each test sample (standard, test sample) is weighed before the test and placed in the test equipment. Subsequently, the abrasive supply is started, and the rubber disc is pressed against the test sample. A schematic diagram of test equipment for testing the abrasive resistance of materials with a sample ready for testing is shown in Figure 7.



**Figure 7.** Scheme of the test equipment with a test sample [32].

The test equipment Tester T-07, ITC PIB Institution of Technology Radom and the BT-16 Controller (Instytut Technologii Eksploatacji, Radom, PL) used in the presented research are shown in Figure 8b,c, together with the scales (Figure 8a). Three samples were used for each material. After each cycle, the sample was weighed three times on Kern ABS analytical scales with a maximum weight of 120 g and an accuracy of  $g = 1.5 \text{ mg}$ . The parameters of the test equipment and samples are shown in Table 4.



**Figure 8.** Abrasion resistance and weight measuring equipment (scales); (a)—scales; (b)—abrasion resistance equipment; (c)—detail of a driving gear with abrasive particles.

**Table 4.** Parameters of the test equipment.

Length of the Friction Path in One Cycle $R$ (m)	153.6
Diameter of rubber cylinder $D$ (mm)	48.9
Compression force $F$ (N)	15.48
Cylinder revolutions in one cycle (revolutions)	1000
Abrasive material	OTTAWA silica sand

The sample is taken and weighed again after passing the track. Weight loss was calculated as a mean value based on the measurements of each sample.

The hardness coefficient  $K_T$  (-) is calculated from Equation (1) [32] as follows:

$$K_T = \frac{H}{H_a} \quad (-) \quad (1)$$

where  $H$ —standard material hardness, which is the reference sample (HRC), and  $H_a$ —abrasive hardness (HRC).

The relative abrasion resistance is calculated from Equation (2) [12,32] as follows:

$$\Psi_h = \frac{W_{hE}}{W_{hPV}} \quad (-) \quad (2)$$

where  $W_{hE}$ —weight loss standard (g);  $W_{hPV}$ —a weight loss of the reference sample (g).

### 2.3. Evaluation Methods

TESCAN VEGA3 electron microscope (Tescan Orsay Holding, a. s., Brno, CZ) was used for microscopy. The samples were etched in a solution of  $\text{HNO}_3$  in ethyl alcohol—2% Nital and in etchant Cor (120 mL  $\text{CH}_3\text{COOH}$ , 20 mL  $\text{HCl}$ , 3 g picric acid, 144 mL  $\text{CH}_3\text{OH}$ ).

The parametric test method of statistical hypotheses was chosen to verify the established hypothesis of the weight loss of materials 37MnSi5, S355JG3, HARDOX 450 and OK 84.58 and UTP 690 hardfacing materials. STATISTICA 12 software (Version number 1.0-0, StatSoft, Inc., Tulsa, OK, USA) was used to test statistical hypotheses.

The significance level of the test is chosen to be  $\alpha = 0.05$ . It is necessary to test the equality of the variances before testing the difference between the two means. Additionally, therefore [34,35]:

$$H_0 : \sigma_1^2 = \sigma_2^2 \quad (3)$$

against

$$H_1 : \sigma_1^2 \neq \sigma_2^2 \quad (4)$$

where  $\sigma_1^2$ —variance of material weight loss values of standards S355J2G3, 37MnSi5;  $\sigma_2^2$ —variance of material weight loss values of reference samples HARDOX 450 material, OK 84.58 and UTP 690 hardfacing materials.

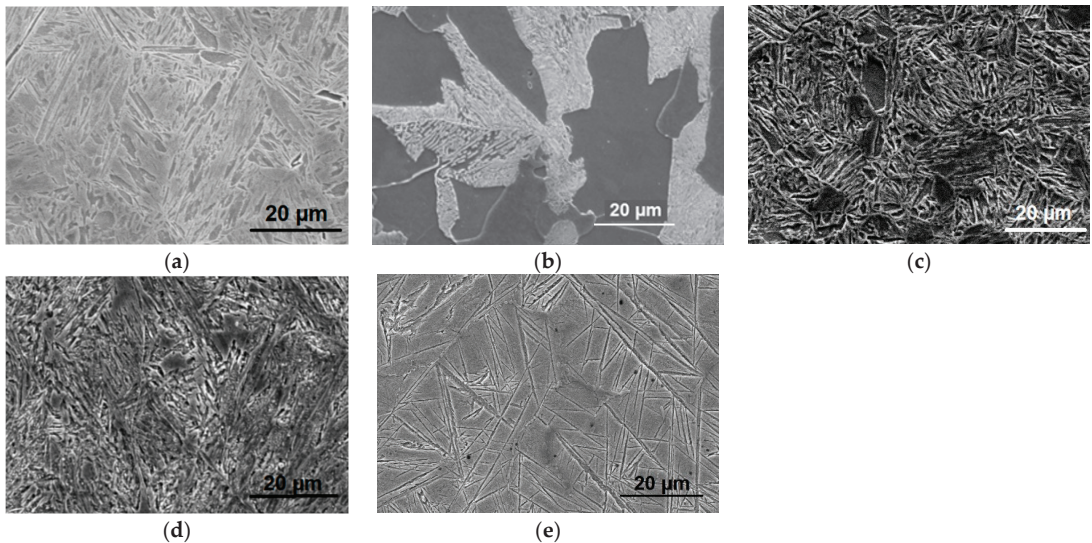
A test of the two means difference was then performed. The software calculates the appropriate p-level. In order to verify the hypothesis on the basis of the graph, that the average value of the weight losses of the standard material is greater or smaller than the material of the reference sample. In this case, the software-calculated p-level must be divided by 2, as the software works with two-way hypothesis testing.

If the value of the p-level is greater than  $\alpha$ , then  $H_0$  is not rejected, and thus the equality of the variances is confirmed. Conversely, if the p-level value is less than  $\alpha$ , then  $H_0$  is rejected in favor of  $H_1$ .

### 3. Results and Discussion

#### 3.1. Preliminary Research

Individual materials were analyzed in terms of microstructure during the initial phase of the research. Figure 9a shows the microstructure of the standard material of 37MnSi5. The samples were etched in a solution of HNO<sub>3</sub> in ethyl alcohol—2% Nital. The microstructure of the material was predominantly sorbite, referring to the fact that the raking blade was heat treated-hardened and then tempered at a high temperature.



**Figure 9.** Microstructure of the materials; (a) 37MnSi5; (b) S355J2G3; (c) HARDOX 450; (d) hardfacing material OK 84.58; (e) hardfacing material UTP 690.

Figure 9b shows the microstructure of the S355J2G3 material. A ferritic-pearlitic structure was observed, with a predominance of ferrite, corresponding to the type of microstructure of structural low carbon steels. We used 2% Nital as an etchant. This part of the ploughshare is not directly exposed to abrasion in contact with the road. It is a supporting part for the raking blade connected to the base material by a weld. However, with a larger amount of material to be cleaned, this part also comes into contact with the abrasive particles but with a lower degree of attack on its surface and is thus exposed to an abrasive load. The ferritic-pearlitic structure is characterized by a low degree of abrasive resistance.

This was the reason for the idea of replacing such a weldment with one unit made of abrasion-resistant material.

Figure 9c shows the microstructure of HARDOX 450 material. The sample was etched with Cor etchant (120 mL  $\text{CH}_3\text{COOH}$ , 20 mL HCl, 3 g picric acid, 144 mL  $\text{CH}_3\text{OH}$ ). The fine-grained structure corresponds to the state after heat treatment-hardening and tempering, which is stated and declared by the manufacturer in his technical sheet [27].

Figure 9d shows the microstructure of OK 84.58 hardfacing coating. The samples were also etched with Cor etchant. The microstructure corresponds to the chemical composition with a high Cr and medium C content. These elements create a precondition for the formation of carbides and intermediate phases, hardening the softer ferritic matrix. This increases the hardness and also partly the abrasion resistance while maintaining the good toughness of the material.

Figure 9e shows the microstructure of the UTP 690 hardfacing coating. Samples were also etched with Cor etchant. The microstructure of UTP 690 material is very similar to the microstructure of OK 84.58 material. The hardfacing material UTP 690, with its chemical composition represented by Cr and W, increases wear resistance and hardness. The elements V and W refine the grain, which also promotes the abrasion resistance of the material where V increases the toughness needed to balance the increased hardness with carbides C, Cr and W. Compared to OK 84.58 hardfacing material, we can observe a needle-like structure in the UTP 690 hardfacing material, which could better transfer the loads that act on it and is thus a premise for better resistance to abrasive wear.

Microstructural analyses confirmed that the choice of hardfacing materials, which due to their chemical composition, create different and more suitable structures than the analyzed structures of the original ploughshare materials, was correct. This creates the premise of better abrasion resistance and impact resistance on the ploughshare.

The hardness was measured after verifying the microstructure of the materials. Hardness is the ability of a metallic material to resist the ingress of a foreign body. Therefore, the hardness of the material is an important value providing information on the resistance of the material to abrasive wear. At the same time, hardness values are needed to calculate  $K_T$  hardness coefficients. The hardness of steel 37MnSi5, S355J2G3, HARDOX 450 and OK 84.58 and UTP 690 hardfacing materials was measured according to Vickers and Rockwell. Vickers hardness was measured according to the procedure stated in ISO 6507-1: 2018 [36] with a Vickers 432SVD hardness tester. The duration of the load was  $t = 15$  s, and the loading force was  $F = 98.07$  N. The Rockwell hardness was measured according to the procedure stated in ISO 6508-1: 2016 [37], with a UH250 hardness tester, and the loading force was  $F = 1471$  N. Vickers hardness was used because it is more sensitive to small differences in material hardness. Rockwell hardness was used to better compare harder hardfacing materials. The average values of measured hardnesses obtained from ten measurements are shown in Table 5.

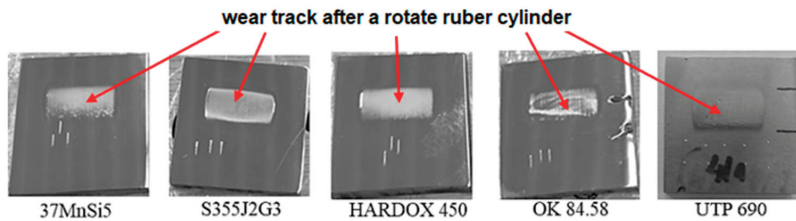
The measured hardness of 37MnSi5 steel (raking blade) was 538 HV0.5 and 50 HRC. The hardness of S355J2G3 steel (raking blade body) was 168 HV0.5 and 18 HRC. During its work, the ploughshare is stressed by abrasive wear not only on the raking blade but also on its supporting part. The idea of modifying the ploughshare within the meaning of changing the weldment into a solid piece of HARDOX 450 steel was based not only on removing the connecting part acting as a notch under stress, but also increasing the hardness of the new material compared to S355J2G3 material. The hardness of the HARDOX 450 material is higher compared to the S355J2G3 material, its value according to Vickers is 519HV0.5 and Rockwell is 45HRC. The aim of hardfacing additional materials to the raking blade was to increase the lifetime of the raking blade (37MnSi5) of the ploughshare. The OK 84.58 hardfacing material was the same hardness as the 37MnSi5 material, and its value was 546HV0.5 and 50 HRC. Significantly higher hardness compared to the 37MnSi5 material was achieved only by hardfacing material UTP 690, with which the hardness value was 677HV0.5 and 62 HRC. The results of the material hardness measurements predicted that the UTP 690 hardfacing material could be a suitable solution for ploughshare modification.

**Table 5.** Measured hardness values.

Hardness Type	37MnSi5	S355JG3	HARDOX 450	OK 84.58	UTP 690
Vickers hardness (HV 0.5)	538 ± 40	168 ± 20	519 ± 30	546 ± 40	677 ± 40
Rockwell hardness (HRC)	50 ± 2	18 ± 2	45 ± 2	50 ± 2	62 ± 2

### 3.2. Abrasive Wear Resistance Analysis

The abrasion resistance test was firstly performed on standard samples of 37MnSi5 and S355J2G3 materials. Subsequently, the test was also performed on reference samples made of HARDOX 450 steel and with OK 84.58 and UTP 690 hardfacing materials. In Figure 10, samples after an abrasive wear test with traces of a rubber disc are presented.

**Figure 10.** Samples after abrasive wear test.

For each material, three samples were used for the abrasion test. After each cycle, the sample was weighted three times on Kern ABS analytical scales, while the average values of the weight losses that were used for the next processing are shown in Table 6.

**Table 6.** Average weight losses of 37MnSi5, S355J2G3, HARDOX 450 steels and OK 84.58 and UTP 690 hardfacing materials.

Tracked Distance R (m)	Weight Loss (g)				
	37MnSi5	S355J2G3	HARDOX 450	OK 84.58	UTP 690
153.6	0.0062	0.0158	0.0133	0.0062	0.0022
307.2	0.0088	0.0223	0.0108	0.0075	0.0009
460.8	0.0067	0.0208	0.0091	0.0078	0.0013
614.4	0.0072	0.0145	0.0077	0.0062	0.001
768.0	0.0072	0.0126	0.0066	0.0078	0.0011
921.6	0.0043	0.0197	0.0069	0.0072	0.0010
1075.2	0.0042	0.0133	0.0081	0.0072	0.0008
1228.8	0.0098	0.0141	0.0076	0.0070	0.0009
1382.4	0.0053	0.0131	0.0067	0.0050	0.0012
1536.0	0.0056	0.0118	0.0068	0.0062	0.0012
1689.6	0.0061	0.0141	0.0072	0.0053	0.0038
Average weight loss $W_{hi}$	0.0064	0.0157	0.0082	0.0066	0.0014

Equation (1) [16] was used to calculate the hardness coefficients  $K_{TE}$  and  $K_{TV}$  of the standard materials 37MnSi5 and S355J2G3 and reference samples HARDOX 450, OK 84.58 and UTP 690 materials. The resulting values are shown in Table 7.

**Table 7.** Hardness coefficient values  $K_T$ .

Sample Material	37MnSi5	S355J2G3	HARDOX 450	OK 84.58	UTP 690
Hardness coefficient $K_T$	0.93	0.33	0.83	0.93	1.15

If this coefficient is higher than 1, it is assumed that the material and the hardfacing material can withstand abrasive particles. It is clear from the graph that the largest value of the  $K_T$  hardness coefficient was reached by the UTP 690 hardfacing material, namely 1.15. Other steels (37MnSi5, S355J2G3, HARDOX 450) and hardfacing material (OK 84.58) reached a value of  $K_T$  inferior to 1. The S355J2G3 material of the ploughshare body reached the lowest value of  $K_{TE2} = 0.33$  in comparison with all examined materials and the standard. Based on this result, it would also be appropriate to consider changing the base material to a HARDOX one.

The relative abrasion resistance  $\Psi_h$  was then calculated according to Equation (2) from the weight losses of  $W_h$ . The relative resistance to abrasive wear was also calculated for the S355J2G3 basic material of the ploughshare, as it is also exposed to abrasive wear during raking [8]. The resulting values are shown in Table 8.

**Table 8.** Relative abrasion resistance  $\Psi_h$ .

Sample Material	37MnSi5	S355J2G3	HARDOX 450	OK 84.58	UTP 690
Relative abrasion resistance $\Psi_h$	1	1	1.91	0.97	4.57

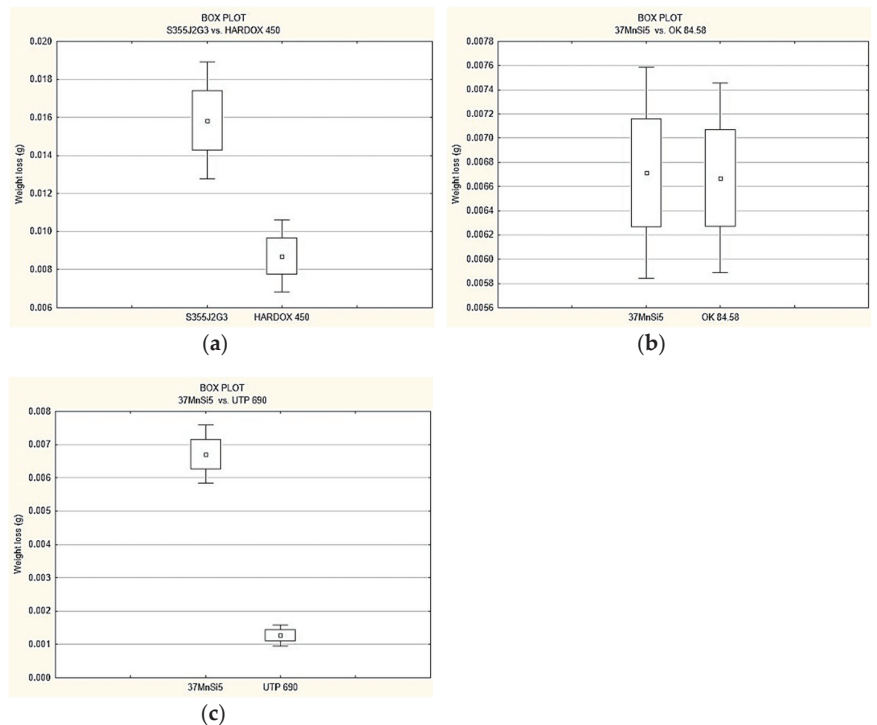
Materials 37MnSi5 and S355J2G3 have the value  $\Psi_h = 1$  because they are standard materials. The relative resistance to abrasive wear is the ratio of the weight loss of the standard material to the weight loss of the material, respectively, of the reference sample. If this coefficient is higher than 1, it is assumed that the material and the hardfacing material of the reference sample can withstand abrasive wear better than the material of the standard sample. Based on the test of resistance to abrasive wear, we can state that the sample from HARDOX 450 material achieved almost twice as good results as the standard sample from S355J2G3 steel.

As the abrasion resistance increases in direct proportion to the hardness of the material [5,9] by using higher grade HARDOX abrasion resistant steel with higher hardness, we can achieve even better abrasion resistance. With OK 84.58 hardfacing material, we achieved almost the same resistance to abrasive wear as the standard sample made of 37MnSi5 material. The highest value of  $\Psi_h$  was reached by the UTP 690 hardfacing material, up to 4.5 times higher than the 37MnSi5 standard material. Based on these results, we can state that UTP 690 hardfacing material could be the most suitable for modifying the ploughshare.

Figure 11 shows the box plots with 95% confidence intervals. In the first case (Figure 11a), the weight loss values of S355J2G3 and HARDOX 450 materials were compared. It can be stated from the graph that the average values of weight loss of S355J2G3 and HARDOX 450 materials are not the same. Based on these results, it can be assumed that HARDOX 450 material will have better resistance to abrasive wear.

In the second case (Figure 11b), the values of the weight loss of 37MnSi5 material and OK 84.58 hardfacing material were compared. Based on the graph, it can be stated that the average values of the weight loss of 37MnSi5 material and OK 84.58 hardfacing material are almost the same, and thus hardfacing with such a hardfacing material on the exposed parts of the ploughshare will not significantly increase the lifetime.

In the third case, the values of mass losses of the 37MnSi5 material and UTP 690 hardfacing material were compared (Figure 11c). A comparison of the graphs clearly shows that the average values of weight loss of 37MnSi5 material and UTP 690 hardfacing material that UTP 690 hardfacing material will have better resistance to abrasive wear.



**Figure 11.** Box charts: (a) weight loss of S355J2G3 and HARDOX 450 materials; (b) weight loss of 37MnSi5 material and OK 84.58 hardfacing material; and (c) weight loss of 37MnSi5 material and UTP 690 hardfacing material.

### 3.3. Discussion

(a) Change of the S355J2G3 material of the supporting part of the ploughshare for the HARDOX 450 material

Based on the results, we can state that HARDOX 450 material has significantly better results compared to the S355J2G3 material of the basic ploughshare body. The hardness of HARDOX 450 material was 45 HRC, and the hardness coefficient of  $K_{TV1}$  reached the value of 0.83. The hardness of the basic body S355J2G3 material was 18 HRC, and the hardness coefficient of  $K_{TE2}$  reached the value of 0.33. These two basic data provide us with the initial information that HARDOX 450 material will better resist the abrasive particles present during the work cycle than the S355J2G3 material of the basic ploughshare body. The relative abrasion resistance  $\Psi_{h1}$  reached the value of 1.91. Based on this datum, we can say that HARDOX 450 material achieved almost twice as good results as the standard sample No. 2 made of S355J2G3 steel. In this case, it would be appropriate to verify the suitability of the higher class HARDOX material, e.g., HARDOX 550, which has higher hardness.

(b) Hardfacing on the exposed part of the raking blade with the OK 84.58 hardfacing material

Based on the results, we can state that the OK 84.58 hardfacing material achieved almost the same results in comparison with the 37MnSi5 material of the raking blade. The hardness of the raking blade 37MnSi5 material was 50 HRC, and the hardness coefficient of  $K_{TE1}$  reached the value of 0.93. The hardness of the OK 84.58 hardfacing material was 50 HRC, and the hardness coefficient of  $K_{TV2}$  reached the value of 0.93. These two basic data provide us with the initial information that the OK 84.58 hardfacing material will be



worse as well as resist the abrasive particles present during the work cycle as a 37MnSi5 material. The relative resistance to abrasive wear  $\Psi_{h2}$  reached the value of 0.97. Based on this datum, we can say that the OK 84.58 hardfacing material achieved worse results by only 3% compared to the 37MnSi5 standard material of the raking blade. These elements create a precondition for the formation of carbides and intermedial phases hardening the softer ferritic matrix. This increases the hardness as well as partly the abrasion resistance while maintaining the good toughness of the material.

- (c) Hardfacing on the exposed part of the raking blade with the UTP 690 hardfacing material

Based on the results, it can be stated that UTP 690 hardfacing material achieved better results compared to the 37MnSi5 material of the raking blade. The hardness of the UTP 690 hardfacing material was 62 HRC, and the hardness coefficient  $K_{TV3}$  reached the value of 1.15. These two basic data provide us with initial information that the UTP 690 hardfacing material will better withstand the abrasive particles present during the working cycle. The relative resistance to abrasive wear  $\Psi_{h3}$  reached the value of 4.57. Based on this data, we can say that the UTP 690 hardfacing material achieved more than 4.5 times better results compared to the 37MnSi5 standard material of the raking blade. In this case, we can state that the UTP 690 hardfacing material could significantly affect the lifetime of the ploughshare. The hardfacing material of the UTP 690 coating with its chemical composition represented by Cr and W increases wear resistance and hardness. The elements V and W soften the grain promoting the abrasion resistance of the material, where V increases the toughness needed to balance the increased hardness with carbides C, Cr and W. Compared to the OK 84.58 hardfacing material to transfer the loads that act on it and is, therefore, an assumption for better resistance to abrasive wear.

Based on the results, we can state that the hardness of the material strongly correlates with the resistance to abrasive wear. The hardness of HARDOX 450 was almost 2.5 times higher than S355J2G3. The relative abrasion resistance was almost twice as high for HARDOX 450 as for S355J2G3. The hardness and relative abrasion resistance of the 37MnSi5 material and the OK 84.58 hardfacing material were almost the same. Compared to the 37MnSi5 material, the UTP 690 material achieved higher hardness and higher resistance to abrasive wear.

#### 4. Conclusions

Ploughshares are exposed to high wear, especially of the abrasive type, and their replacement is relatively economical. For this reason, it is necessary to look for ways to increase their lifetime and examine their resistance to abrasive wear.

When working with a ploughshare, it is not only the raking blade that wears rapidly but also its supporting part which the raking blade welded to. The article analyzes three ways to modify ploughshares. Based on the results, it is possible to state the following:

- (a) The HARDOX 450 material achieved significantly better results compared to the basic S355J2G3 material, not only in terms of hardness and hardness coefficient  $K_T$  but also in terms of relative resistance to abrasive wear, where the coefficient  $\Psi_{h1}$  for HARDOX 450 material achieved almost twice as good results compared to the standard sample from S355J2G steel;
- (b) The OK 84.58 hardfacing material achieved almost the same results compared to the 37MnSi5 original material of the raking blade and therefore does not significantly affect the lifetime of the raking blade on the ploughshares;
- (c) The UTP 690 hardfacing material achieved more than 4.5 times better results than the 37MnSi5 standard material of the raking blade, so it could significantly affect the lifetime of the ploughshare. Compared to the OK 84.58 hardfacing material, we can observe a needle-like structure in the UTP 690 hardfacing material, which could better transfer the loads that act on it, and thus it is an assumption for the better resistance to abrasive wear.

Based on the results, the manufacturer of ploughshares was recommended to use HARDOX 450 material as a basic material and UTP 690 coating material hardfacing on exposed parts of functional surfaces as a suitable means of increasing the lifetime of ploughshares.

In further research, it would be appropriate to also perform a test of resistance to abrasive wear for abrasion-resistant HARDOX sheet but of a higher class, i.e., with higher hardness, e.g., HARDOX 550 material, as well as for OK 84.58 hardfacing material which would be hardfaced in several layers. Then, the most suitable adjustments would be selected and tested under real operating conditions.

**Author Contributions:** Conceptualization, M.V., M.T. and K.M.; methodology, M.V. and M.T.; software, M.V., M.T. and K.M.; validation, M.V., M.T., K.M. and M.D.; formal analysis, M.V., investigation, M.V. and M.D.; resources, M.T. and M.V.; data curation, M.T., K.M. and M.D.; writing—original draft preparation, M.V., M.T. and K.M.; writing—review and editing, M.V. and K.M.; visualization, M.V. and K.M.; supervision, M.T.; project administration, M.T. and K.M.; funding acquisition, K.M. All authors have read and agreed to the published version of the manuscript.

**Funding:** This research was supported by the Ministry of Education, Science, Research, and Sport of the Slovak Republic through project APVV-19-0550.

**Institutional Review Board Statement:** Not applicable.

**Informed Consent Statement:** Not applicable.

**Data Availability Statement:** Not applicable.

**Acknowledgments:** The article was supported by the APVV-16-0194 “Research on Impact of Innovation in Production Processes on the Life of Tooling and Components of Forest Mechanisms”.

**Conflicts of Interest:** The authors declare no conflict of interest.

## References

- Jankauskas, V.; Katinas, E.; Pusvaškis, M.; Leišys, R. A Study of the Durability of Hardened Plough Point. *J. Frict. Wear* **2020**, *41*, 78–84. [\[CrossRef\]](#)
- Stawicki, T.; Kostencki, P.; Białobrzieszka, B. Roughness of Ploughshare Working Surface and Mechanisms of Wear during Operation in Various Soils. *Metals* **2018**, *8*, 1042. [\[CrossRef\]](#)
- Singh, J.; Chatha, S.S.; Sidhu, B.S. Abrasive wear behavior of newly developed weld overlaid tillage tools in laboratory and in actual field conditions. *J. Manuf. Process.* **2020**, *55*, 143–152. [\[CrossRef\]](#)
- Doluk, A.; Rudawska, A.; Stančeková, D.; Mrázik, J. Influence of surface treatment on the strength of adhesive joints. *Manuf. Technol.* **2021**, *21*, 585–591. [\[CrossRef\]](#)
- Müller, M.; Novák, P.; Chotěborský, R.; Hrabě, P. Reduction of Ploughshare Wear by Means of Carbide Overlay. *Manuf. Technol.* **2018**, *18*, 72–78. [\[CrossRef\]](#)
- Kováč, J.; Krilek, J.; Štefánek, M.; Kuvik, T. Analysis of the selected technical parameters of skidders. *MM Sci. J.* **2016**, *2016*, 1273–1276. [\[CrossRef\]](#)
- Zdravecká, E.; Tkáčová, J.; Ondáč, M. Effect of microstructure factors on abrasion resistance of high-strength steels. *Res. Agric. Eng.* **2014**, *60*, 115–120. [\[CrossRef\]](#)
- Javaheri, V.; Porter, D.; Kuokkala, V.T. Slurry erosion of steel—Review of tests, mechanisms and materials. *Wear* **2018**, *408*, 248–273. [\[CrossRef\]](#)
- Ľavodová, M.; Vargová, M.; Falat, L. Possibilities of modification of ploughshares used for winter maintenance of forest roads. *Manuf. Technol.* **2020**, *20*, 834–844. [\[CrossRef\]](#)
- Petru, J.; Zlámal, T.; Čep, R.; Stančeková, D.; Pagač, M.; Vortel, O. Mechanism of cutting insert wear and their influence on cutting ability of the tool during machining of special alloys. In Proceedings of the 3rd International Conference on Manufacturing Engineering and Technology for Manufacturing Growth (METMG 2015), Vancouver, BC, Canada, 1–2 August 2015. [\[CrossRef\]](#)
- Hnilica, R.; Kotus, M.; Jankovský, M.; Hnilicová, M.; Dado, M. Qualitative classification of mulchers. *Agron. Res.* **2017**, *15*, 1890–1896. [\[CrossRef\]](#)
- Balla, J. *Náuka o Materiáloch*; SPU: Nitra, Slovakia, 2003; pp. 48–54.
- Natsis, A.; Petropoulos, G.; Pandazaras, C. Influence of Local Soil Conditions on Mouldboard Ploughshare Abrasive Wear. *Tribol. Int.* **2008**, *1*, 151–157. [\[CrossRef\]](#)
- ESAB. Opravy a Údržba. Available online: <http://products.esab.com/ESABImages/prirucka%206%20vydani%202011.pdf> (accessed on 1 April 2022).

15. Chinha, A.R.; Valtonen, K.; Kuokkala, V.T.; Kundu, S.; Peet, M.J.; Bhadeshia, H.K.D.H. Role of fracture toughness in impact-abrasion wear. *Wear* **2019**, *428*, 430–437. [[CrossRef](#)] [[PubMed](#)]
16. Müller, M.; Hrabě, P. Overlay materials used for increasing lifetime of machine parts working under conditions of intensive abrasion. *Res. Agric. Eng.* **2013**, *59*, 16–22. [[CrossRef](#)]
17. Buchely, M.F.; Gutierrez, J.C.; Leon, L.M.; Toro, A. The effect of microstructure on abrasive wear of hardfacing alloys. *Wear* **2005**, *259*, 52–61. [[CrossRef](#)]
18. Wang, X.; Han, F.; Liu, X.; Qu, S.; Zou, Z. Microstructure and wear properties of the Fe–Ti–V–Mo–C hardfacing alloy. *Wear* **2008**, *265*, 583–589. [[CrossRef](#)]
19. Wang, X.H.; Han, F.; Liu, X.M.; Qu, S.Y.; Zou, Z.D. Effect of molybdenum on the microstructure and wear resistance of Fe-based hardfacing coatings. *Mater. Sci. Eng. A* **2008**, *489*, 193–200. [[CrossRef](#)]
20. Xu, L.; Wei, S.; Xiao, F.; Zhou, H.; Zhang, G.; Li, J. Effects of carbides on abrasive wear properties and failure behaviours of high speed steels with different alloy element content. *Wear* **2017**, *376*, 968–974. [[CrossRef](#)]
21. Konat, L.; Zemlik, M.; Jasiński, R.; Grygier, D. Austenite Grain Growth Analysis in a Welded Joint of High-Strength Martensitic Abrasion-Resistant Steel Hardox 450. *Materials* **2021**, *14*, 2850. [[CrossRef](#)] [[PubMed](#)]
22. Šípová Snežná Radlica. Available online: <http://www.agrowest.cz/produkty/agrometall-celni-snehove-radlice/sipova-radlice-pracovni-sirka-3000-mm> (accessed on 8 February 2022).
23. Zhrňovací Nôž. Available online: <https://detvaservis.sk/brity-na-radlice/ocelove-brity-s-jednostrannym-ukosom/> (accessed on 1 April 2022).
24. Steel S355J2G3. Lexikon kovov 2.7, Verlag Dashöfer, Praha, 4/2019. Available online: <https://www.dashofer.cz/> (accessed on 6 March 2022).
25. Steel 37MnSi5. Lexikon Kovov 2.7, Verlag Dashöfer, Praha, 4/2019. Available online: <https://www.dashofer.cz/> (accessed on 6 March 2022).
26. HARDOX. Available online: <https://www.gamaocel.cz/4861/hardox/> (accessed on 6 March 2022).
27. HARDOX Wear Plate. Available online: <https://www.ssab.com/products/brands/hardox> (accessed on 6 February 2022).
28. Ulewicz, R.; Mazur, M.; Bokuvka, O. Structure and Mechanical Properties Offline-grained Steels. *Transp. Eng.* **2013**, *41*, 111–115. [[CrossRef](#)]
29. OK 84.58. Available online: <https://www.esab-slovakia.sk/sk/sk/products/filler-metals/repair-and-maintenance/hardfacing-alloys/ok-weartrode-55-hd.cfm> (accessed on 7 February 2022).
30. Vargová, M.; Ťavodová, M. Proposal for modification of a snow ploughshare by hard surfacing to increase its service life. *Acta Fac. Tech. Sci. J. Fac. Technol. Zvolen* **2020**, *2*, 59–70.
31. UTP 690. Available online: [https://www.zvarcentrum.sk/obchod\\_homedir/data/2616/prilohy/UTP%20690.pdf](https://www.zvarcentrum.sk/obchod_homedir/data/2616/prilohy/UTP%20690.pdf) (accessed on 7 February 2022).
32. GOST 23.208-79 Ensuring of Wear Resistance of Products. Wear Resistance Testing of Materials by Friction against Loosely Fixed Abrasive Particles. Available online: <http://docs.cntd.ru/document/gost-23-208-79> (accessed on 10 February 2022).
33. GOST 3647-80 Abrasives. Grain Sizing. Graininess and Fractions. Test Methods. Available online: <https://docs.cntd.ru/document/1200016841> (accessed on 10 February 2022).
34. Schmidtová, J.; Vacek, V. *Applied Statistics*; Technical University in Zvolen: Zvolen, Slovakia, 2013; pp. 85–102.
35. Markechová, D.; Tirbáková, A.; Stehlíková, B. *Základy Štatistiky pre Pedagógov*; Fakulta Prírodných vied UKF: Nitra, Slovakia, 2011; pp. 115–154.
36. *ISO 6507-1:2018*; Metallic Materials—Vickers Hardness Test—Part 1: Test Method. International Organization for Standardization: London, UK, 2018.
37. *ISO 6508-1:2016*; Metallic Materials—Rockwell Hardness Test—Part 1: Test Method. International Organization for Standardization: London, UK, 2018.

Article

# Effect of Machining Conditions on Temperature and Vickers Microhardness of Chips during Planing

Peter Pavol Monka <sup>1,2</sup>, Katarina Monkova <sup>1,2,\*</sup>, Martin Vasina <sup>2,3</sup>, Milena Kubisova <sup>2</sup>, Martin Korol <sup>1</sup> and Adriana Sekerakova <sup>1</sup>

<sup>1</sup> Faculty of Manufacturing Technologies with the Seat in Presov, Technical University of Kosice, Sturova 31, 080 01 Presov, Slovakia

<sup>2</sup> Faculty of Technology, UTB Tomas Bata University in Zlin, Vavreckova 5669, 760 01 Zlin, Czech Republic

<sup>3</sup> Faculty of Mechanical Engineering, VŠB-Technical University of Ostrava, 17. Listopadu 15/2172, 708 33 Ostrava-Poruba, Czech Republic

\* Correspondence: katarina.monkova@tuke.sk; Tel.: +421-55-602-6370

**Abstract:** For the machining of long and narrow surfaces and when processing multiple pieces, planing technology is used, the productivity of which can be higher than that of milling, although it is relatively slow machining. The article aims to study the degree of influence of the geometry of the tool (the angle of cutting-edge inclination and the angle of the tool-orthogonal rake), as well as the cutting conditions (cutting depth and cutting speed) on the chip characteristics (temperature and microhardness) in orthogonal and oblique slow-rate machining of steel 1.0503 (EN C45). The experiments were carried out on specially prepared workpieces designed for immediate stopping of machining. The results of the experiments were statistically processed, and behavioural models were created for temperature and Vickers microhardness of chips for individual combinations of factors. The obtained dependencies revealed how the geometry of the cutting tool and the cutting conditions affect the temperature and microhardness in the cutting area and at the same time allowed the best conditions for both orthogonal and oblique machining to be set up.

**Keywords:** planing; chip; Vickers microhardness; temperature; cutting conditions

**Citation:** Monka, P.P.; Monkova, K.; Vasina, M.; Kubisova, M.; Korol, M.; Sekerakova, A. Effect of Machining Conditions on Temperature and Vickers Microhardness of Chips during Planing. *Metals* **2022**, *12*, 1605. <https://doi.org/10.3390/met12101605>

Academic Editor: Sergey Kononov

Received: 27 August 2022

Accepted: 21 September 2022

Published: 26 September 2022

**Publisher's Note:** MDPI stays neutral with regard to jurisdictional claims in published maps and institutional affiliations.



**Copyright:** © 2022 by the authors. Licensee MDPI, Basel, Switzerland. This article is an open access article distributed under the terms and conditions of the Creative Commons Attribution (CC BY) license (<https://creativecommons.org/licenses/by/4.0/>).

## 1. Introduction

Cutting operations with relatively low cutting velocity include planing and broaching technologies. Planing is a cutting process in which the formed chip is visible to the eye, whereas in broaching, the chip generation process is hidden and invisible to the naked eye. Therefore, it is possible to monitor the development of the temperature field in the area of chip generation during planing with a temperature measuring device by laser aiming and thus providing an approximate idea of the temperature generated not only during cutting but also during broaching [1,2].

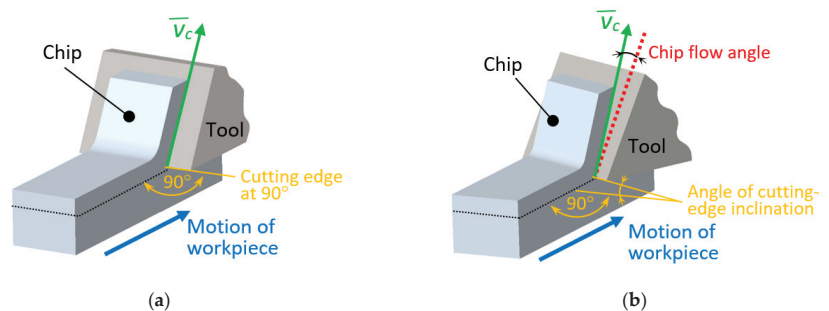
The planing process is one of the oldest among the so-called single-point machining processes, used in the production of long cuts. This type of machining technology uses a linear motion with a single-pointed cutting tool to create a flat surface. The cutting tool is clamped in the tilting head, which prevents damage to the cutting edge when returning the tool. Although the process seems to be easy, setting the cutting conditions is difficult [3–6].

During the planing, the workpiece moves linearly and is usually machined with one tool. Because the large, heavy workpiece and table are in motion at relatively low cutting speeds, planers come with several tool heads and multiple tools in one head [7]. In addition, many planers are constructed with tool heads to make cuts in both directions of table movement [8]. Nevertheless, as mentioned above, since only single-pointed tools and low cutting speeds are used, planing is classified as a low-productivity cutting process compared to other cutting methods. However, when machining long and narrow surfaces (such as guide rails, long grooves, etc.) and when cutting multiple pieces with a

planer, the efficiency of this type of workpiece processing can be much higher compared to milling [9,10]. The planing accuracy can reach IT9–IT8 and the surface roughness can be in the range of  $R_a$  is 3.2–1.6  $\mu\text{m}$  [11–13].

In spite of planing being considered an obsolete technology, for performing and observing experimental tests for machining at relatively low cutting speeds, planing appears to be a very attractive machining process [14]. At slow-rate machining, the chip-formation process can be observed in both cutting methods, orthogonal and oblique.

For orthogonal cutting (Figure 1a), it is characteristic that the cutting edge is perpendicular to the direction of movement of the tool and wider than the width of the cut. The shear force acts on a smaller area, so shear force per unit area is higher and the tool life is shorter than obtained in oblique cutting [15,16]. The forces that occur in this type of machining can be drawn in a plane, which is why it is also known as 2D machining [17]. If the angle between the cutting edge and the movement of the tool is not “right” ( $90^\circ$ ), it is an oblique cutting, which is also called 3D machining, because the cutting force is not planar, but spatial and is represented by 3 components [18]. All these facts affect the cutting conditions, tool life, durability as well as the quality of machined surface.



**Figure 1.** Principle of (a) orthogonal and (b) oblique machining.

In both types of machining, the chip resulting from the interaction of the tool with the workpiece plays a crucial role in determining the properties of the machined surface and tool life. Properties that reflect its behaviour in the shear plane (acceleration of shear deformation, shear stress and shear angle) can also be represented by temperature and microhardness [19,20].

Jain et al. [21] verified the degree of influence of shear strain accelerations on the microhardness of chips during machining under the same cutting conditions. The basis of the hypothesis was the fact that the acceleration of shear deformation controls machining parameters such as tool-chip interface temperature, shear angle, tool wear, etc., and the hypothesis was confirmed.

The process of chip development in high-speed machining of hardened steel was studied by Wang et al. [22]. Research has confirmed that the formation of chips, when cutting materials of different hardness, can be controlled by setting a suitable combination of technological parameters. The hardness of the material as well as the local temperature increases with increasing cutting speed. When the parameters are in equilibrium, the deformation is concentrated in the shear zone and adiabatic shear occurs.

The effect of cutting conditions on the microhardness of the material in the cutting area along with chip thickness was investigated by Alrabii and Zumot [23] in experimental tests. They reported that microhardness increases with increasing cutting parameters (depth of cut, speed and feed), but only to a certain extent. Above this level, an increase in cutting parameters causes a decrease in microhardness.

The influence of changes in the microstructure of AISI 1045 steel on diffusion wear during turning in a zone of chip formation as a function of variable cutting speed was investigated Pu et al. [24]. The results of the research showed that with the cutting speed increasing, the grain size of the various phases also increases.

Response surface methodology was used in the study of Senussi [25] to specify the root cause of an effect of the relationship between chip microhardness and input control variables influencing the response as a 2D or 3D hypersurface. He stated that the combined effect of cutting speed at its lower level, feed rate and cutting depth at their higher values could result in increasing the microhardness of the chip.

Various approaches have been used by many researchers to study the effect of cutting parameters on chip properties and behaviour. The issues of microhardness, temperature, geometry and chip shape within analytical and numerical models have been developed in several studies [26–30], however, the complexity of the chip generation process forced the authors to simplify the simulation conditions, which, however, affected the accuracy of the obtained results, which did not correspond to the real state.

It can be said that many studies were focused on the influence of cutting parameters on microhardness and temperature evaluation in the past, but mostly the object of their investigation was the machined material or the cutting tool. However, only a few studies have addressed the microhardness and temperature of the chips generated during machining, but no study has compared the degree of influence of both the tool geometry (angle of tool-cutting-edge inclination and angle of the tool-orthogonal rake) and the technological conditions (depth of cut, cutting speed) on the chip characteristics (temperature and microhardness) in orthogonal and oblique slow-rate machining of 1.0503 (EN C45) steel that is included in the presented research. Based on the measured data, behavioural models were created for the temperature and Vickers microhardness of chips at individual combinations of the factors. The experiments were carried out on specially prepared workpieces designed for immediate stopping of machining.

On the basis of the above, it can be said that the novelty of the research lies not only in its complexity and the combination of included research factors (from the type of machining and machined material, through the geometry of the tool to the technological conditions), which according to the authors' best knowledge have not yet been studied, but also in the newly proposed methodology for obtaining chips in an attempt to bring the observed chip samples as close as possible to the state in which they were created so that the texture of such a chip corresponds to the current cutting speed.

## 2. Materials and Methods

Planing technology, in which the workpiece performs the main movement, was selected for this study. In the experiments carried out as part of the presented research, a planing machine HJ8A type (KOVOSVIT inc., Holoubkov; Czech Republic) shown in Figure 2a was used. The process of planing of EN C45 steel is captured in Figure 2b. The machine is designed for the production of medium-heavy workpieces in piece and series production. The worktable has three levels of working and retraction speeds. The hydraulic drive is equipped with two gear pumps with separate electric motors, electromagnetic, hydraulic distribution and a combination of pump devices to change the speed levels of the table. The crossbar with support is vertically adjustable on the stand. The planer has two supports on the crossbar and one on the stands. Feeds and rapid feeds are controlled by the slide box at the end of the crossbar, either hydraulically or electrically. The table feed and the fast feeds of the crossbar, as well as the carriage, are controlled by the buttons from the hanging control box.

No cooling medium was used during machining, as the tool path was relatively short (about 200 mm), so there was no overheating of the tool and the material being processed.

Steel 1.0503 (EN C45), which is usually used in experiments as a standard [31], was chosen as the machined material within the experiments. It is a medium carbon-unalloyed structural steel that provides moderate tensile strength (in the range of 570–700 MPa), Brinell hardness of 170–210 and a good wear resistance. The material can be processed with hardening by means of quenching and tempering on focused and restricted areas. C45 can also be instigated with induction hardening up to the hardness level of HRC 55. This grade is in majority situations delivered in an unattended heat treatment state

i.e., normalized condition, although it can be furnished also in numerous heat treatment variations. Machinability of C45 is equivalent to that of mild steel for example CR1 grade; on the other hand weld ability is exhibited lower than that of mild steel [32]. Steel is suitable for producing shafts of turbochargers, pumps, traction machines, electric motors, more giant gears, screws, automobile crankshafts, connecting rods, steering levers, spring hinges or pins. The chemical composition of machined 1.0503 (EN C45) steel is in Table 1.



**Figure 2.** Experimental device (a) HJ8A planer, (b) experimental processing of a workpiece made of EN C45 steel.

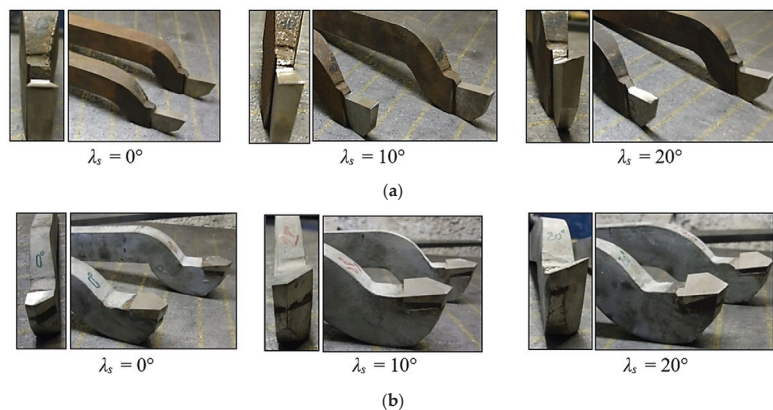
**Table 1.** Chemical composition of the 1.0503 (EN C45) steel [33].

Steel	C (%)	Mn (%)	Si (%)	Cr (%)	Ni (%)	Cu (%)	P (%)	S (%)
EN C45	0.42–0.50	0.50–0.80	0.17–0.37	max. 0.25	max. 0.30	max. 0.30	max. 0.040	max. 0.040

The values of the cutting parameters (cutting speed  $v_c$ , cutting depth  $a_p$ ) for experimental testing were chosen based on the requirements of technical practice, whereas the lowest cutting speed was given by the planer and corresponded to 60% of the machine's power. Values for cutting depth  $a_p$  were set based on machine limitations for maximum chip cross-section.

The planing necking tool type 32×20 ON 36550 HSS00 was used at orthogonal machining, whereas the straight roughing tool 32×20 ON 36500 HSS00 was employed at oblique machining. The brazed high-speed steel tips with three different values of the angle of cutting-edge inclination  $\lambda_s = 0^\circ$ ,  $10^\circ$  and  $20^\circ$  were applied within experimental testing [33].

The cutting tools used in the experiments are shown in Figure 3, and the next tools' characteristics are given in Table 2.



**Figure 3.** The cutting tools used at (a) orthogonal machining, (b) oblique machining.

**Table 2.** Values of tool angles [33].

Type of Tool Angle	Planing Necking Tool	Straight Roughing Tool
Tool-cutting-edge angle $\kappa_r$	0°	60°
Tool minor (end)-cutting-edge angle $\kappa_r'$	-	20°
Tool-included angle $\varepsilon_r$	-	100°
The angle of the tool-orthogonal rake $\gamma_o$	8°/12°/16°	3°/7°/11°
The angle of the tool-orthogonal clearance $\alpha_o$	15°/11°/7°	15°/11°/7°

The geometrical characteristics of the cutting tool were chosen in accordance with the machined material and the characteristics of the planing process. This method of machining requires the use of a more robust tool compared to turning. Increased robustness is required from the point of view of a significantly more dynamic way of first contact between the tool face and the workpiece [34]. The following requirements were also taken into account when choosing the tool geometry:

- Compliance with the condition of the tool's physical resistance to dynamic shocks when entering the cut;
- The range of variable values ensuring the statistical significance of the experiment;
- The difference in the characteristics of the chip formation process for orthogonal and oblique cutting.

According to the tool manufacturer's recommendations, the rake angle when planing type C45 steels is chosen in the range of 8°–14°, and the angle of tool-orthogonal clearance  $\alpha_o$  for this type of steel is chosen in the range of 7°–11° [35].

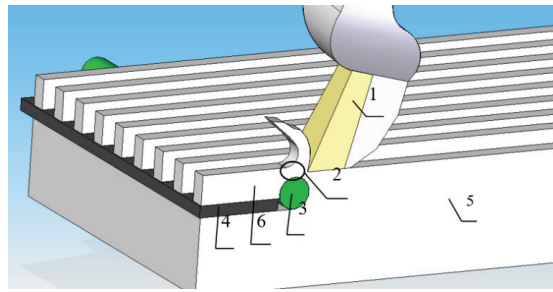
Considering all the demands and recommendations, the angle of tool-orthogonal clearance  $\alpha_o$ , adopted the strategy of using the smallest value (7°) in terms of production recommendations and the other two values are in a linear series with an increment of 4° for the tools within the presented experiments.

Similarly, in the research, the angles of the tool-orthogonal rake  $\gamma_o$  were set up so they reflected the requirement to ensure the lowest possible specific resistance, whereas the maximum value was related to the bending stiffness of the cutting wedge. Specifically, for the planing necking tool, an interval of three values graduated by 4° from the smallest recommended value (8°) was chosen for the angle of the tool-orthogonal rake  $\gamma_o$ . For the straight roughing tool, the manufacturer's recommended values of the angle of tool-orthogonal rake  $\gamma_o$  were reduced due to an effort to increase the strength properties of the tool tip and were used in gradations of 3°/7°/11°. For this tool, for the same reason of increasing the strength of the tip, the tool included angle  $\varepsilon_r$  in the value of 100° was used.

In order to observe changes in the chip formation zone, it was necessary to stop the machining process and break the contact of the tool with the workpiece. For this purpose, a methodology of immediate machining stop was developed based on the observation of chip behaviour during face milling, in which the end of the chip breaks off when leaving the cut. Observations have shown that the texture of such a chip corresponds to the actual speed at the moment of interruption of the cut. This know-how led the authors to use it in the presented research, and so they have developed a new methodology of obtaining chip roots based on the special modifications of the machined sample. The principle of the methodology is based on the designing of a specific workpiece (shown in Figure 4), and it is described below.

After milling the grooves of 10 mm × 10.5 mm into a semi-finished product with dimensions of 240 mm × 87.5 mm × 30 mm in the longitudinal direction, 11 protrusions with a rectangular cross-section of 10.5 mm × 2.5 mm were created, and each protrusion was used for a separate experiment.





**Figure 4.** The principle of the methodology to immediately break the contact of the tool and the workpiece for orthogonal cutting (1—cutting wedge of the tool, 2—the place of rupture of the sample, 3—a drilled hole reinforced with a metal rod due to the narrowing of the cross-section, 4—supporting plate preventing the deformation of the final sample, 5—workpiece, 6—the final sample used for observation after tearing away from the workpiece).

At the end of the sample, where the tool comes out of the grip, the protrusions were undercut, and a plate was inserted into the resulting gap, which had the task of preventing the deformation of the final sample. The most crucial role in the cutting interruption process was played by a transverse hole with a diameter of 8 mm, which was drilled in front of the reinforcing plate (from the point of view of the cutting direction) and which was subsequently also reinforced with a metal rod. When the tool passed over the hole, the cross-section narrowed, and the material was torn, and the end part of the protrusion was thrown sharply in the direction of the tool's movement at speed greater than the cutting speed. The separated end parts together with the resulting chip served as samples that captured the state of plastic deformation corresponding to the actual cutting speed.

An infrared thermometer UNI-T UT305C (Uni-trend Technology Co., Ltd., Dongguan City, Guangdong Province, China) was employed to measure the temperature of various surfaces by measuring the infrared radiation emitted from a focused surface and whose specifications were sufficient for the experiments carried out in this research. Its basic characteristics were: Temperature range  $-50\sim 1550$  °C; Accuracy  $\pm 1.8\%$ ; Repeatability  $\pm 0.5\%$ ; Resolution 0.1; Response time 250 ms (95% of reading); Emissivity 0.1~1.0 adjustable; Laser power <1 mW; Laser wavelength 630~670 nm; Spectral response 8~14  $\mu\text{m}$ .

Since the temperature measurement was performed only on a cutting length of 200 mm, it was assumed that the increase in temperature in the cutting area was directly proportional to the increase in the size of the cutting path of the tool.

The obtained samples were cast in technical dentacryl, which has good insulating properties, high mechanical strength and perfect thermal insulation. The cast samples were ground using water, which had a cooling effect and thus prevented the sample from being affected by heat. In Figure 5a, the ground and polished sample are shown. After polishing, the samples were etched with Nital, which is a 2% solution of nitric acid  $\text{HNO}_3$  in ethyl alcohol. After being etched on the surface, a sample structure of the material was observed with the Platinum USB digital microscope UM019 (Shenzhen Handsome Technology Co., Ltd., Shenzhen, China) with a magnification of 25–220 $\times$ . An example of an etched sample is shown in Figure 5b.

Microhardness was measured with a Micro-Vickers hardness tester CV-403DAT (Figure 6a) according to STN EN ISO 6507-1 standard. The measuring device involves a microscopic and a static method expressed on Vickers or Knoop scales, with magnifications of 200 $\times$  and 600 $\times$ . The microhardness measuring according to the Vickers method is determined by optical magnification by pressing a diamond regular quadrilateral needle with a peak wall angle of  $136^\circ$  into the tested material and then measuring the diagonals perpendicular to each other after relieving the load. The loading force acts in a perpendicular direction on the surface of the test specimen.



Figure 5. Investigated sample of a chip, (a) ground and polished, (b) etched, magnified 200 $\times$ .



Figure 6. (a) Micro-Vickers hardness tester CV-403DAT; (b) tested samples—imprint, magnification 600 $\times$ .

Hardness measurements were performed in the area of the shear angle at a load of 200 gf (gram-force) for a dwell of 10 s. An example of the tested sample with an imprint under 600 $\times$  magnifications is shown in Figure 6b.

### 3. Results and Discussion

The experiments were carried out within the so-called “planned experiment” that was designed at three levels (lower, basic, and upper). The temperatures were measured in a cutting zone for orthogonal and oblique machining, and the micro-hardness of the material was measured in the area where the shear angle was formed. Measured data were evaluated through the statistical method using a regression function. Outliers from each group of measurements were specified using Grubbs test criteria and were excluded from further statistical processing of the results. Regression coefficients were calculated by means of Matlab software, and their significance was examined according to Student’s test criterion. The adequacy of the regression function was evaluated according to the Fisher-Snedecor test criterion  $F < F_{0.05}(f_1, f_2)$ , where the degrees of freedom  $f_1 = Nq$  ( $N$  is a number of measures,  $q$  is a number of significant coefficients) and  $f_2 = N(m - 1)$ , where  $m$  is a number of assessed measurements within the Grubbs’ test [36–39].

The variables listed in Table 3 were considered within the experimental study, and the codes for individual variables’ specific values are referred in Table 4.

**Table 3.** The variables and the ranges of individual values [33].

Variables	Symbols	−1	−α	0	+α	+1	
Cutting speed (m·min <sup>−1</sup> )	$v_c$	$x_1$	6	8.25	10.5	12.75	15
Cutting depth (mm)	$a_p$	$x_2$	0.2	0.25	0.3	0.35	0.4
The angle of the tool-orthogonal rake— <i>orthogonal</i> cutting (°)	$\gamma_o$	$x_3$	8	10	12	14	16
The angle of the tool-orthogonal rake— <i>oblique</i> cutting (°)	$\gamma_o$	$(x_3)$	3	5	7	9	11
The angle of the tool-cutting-edge inclination (°)	$\lambda_s$	$x_4$	0	5	10	15	20

**Table 4.** The codes for specific values of individual variables.

Code	Specification of Variables
−1	$x_{\min}$
−α	$[(x_{\max} + x_{\min})/2] - [(x_{\max} - x_{\min})/2\alpha^2]$
0	$(x_{\max} + x_{\min})/2$
+α	$[(x_{\max} + x_{\min})/2] + [(x_{\max} - x_{\min})/2\alpha^2]$
+1	$x_{\max}$

Although the evaluation of tool wear was not the main goal of the research, it can be said that the dominant mechanism of tool wear during planing in the experiments was abrasive wear, which was manifested in the change of the geometry of the tool on the flank surface.

### 3.1. Temperature Evaluation

To evaluate the behaviour of the temperature and the influence of the monitored parameters on it, the regression dependencies for orthogonal machining of EN C45 steel were expressed by Equation (1), and for oblique machining by Equation (2), and the meaning of parameters  $x_1 \div x_4$  is explained in Tables 3 and 4 above. The calculated Fisher–Snedecor criterion [40] confirmed that the equations were functionally dependent and the coefficients of determination of the relations were  $R^2 = 0.90$  and  $0.91$ , respectively:

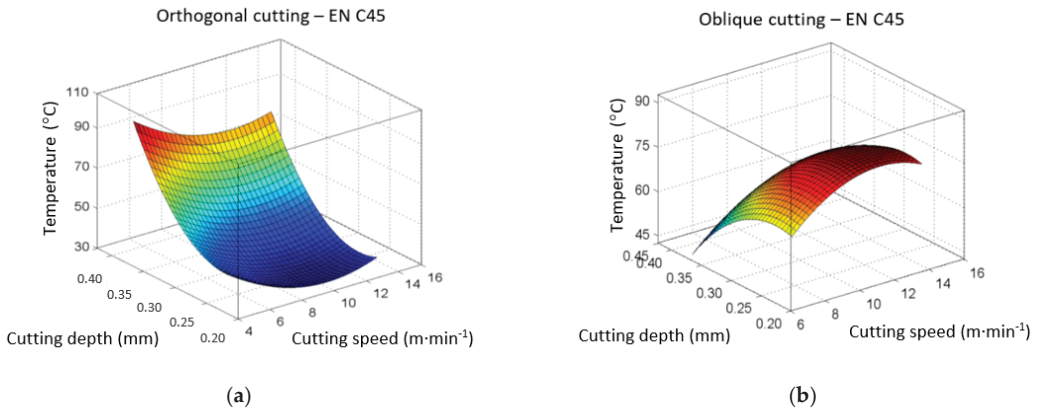
$$y = 3.4146 - 5.7289x_1 + 6.0652x_2 + 6.6299x_3 + 0.1732x_4 - 0.3957x_1x_2 + 0.3796x_1x_3 + 0.0634x_1x_4 - 0.3435x_2x_3 + 0.0202x_2x_4 + 0.0559x_3x_4 + 2.6854x_1^2 + 5.0529x_2^2 - 4.7508x_3^2 + 0.0934x_4^2 \quad (1)$$

$$y = -2.415 + 5.9456x_1 - 3.438x_2 + 0.5381x_3 + 0.1701x_4 - 0.0292x_1x_3 + 0.0163x_1x_4 + 0.2491x_2x_3 + 0.0355x_2x_4 - 0.0181x_3x_4 - 2.9253x_1^2 - 3.0763x_2^2 - 0.3104x_3^2 + 0.0592x_4^2 \quad (2)$$

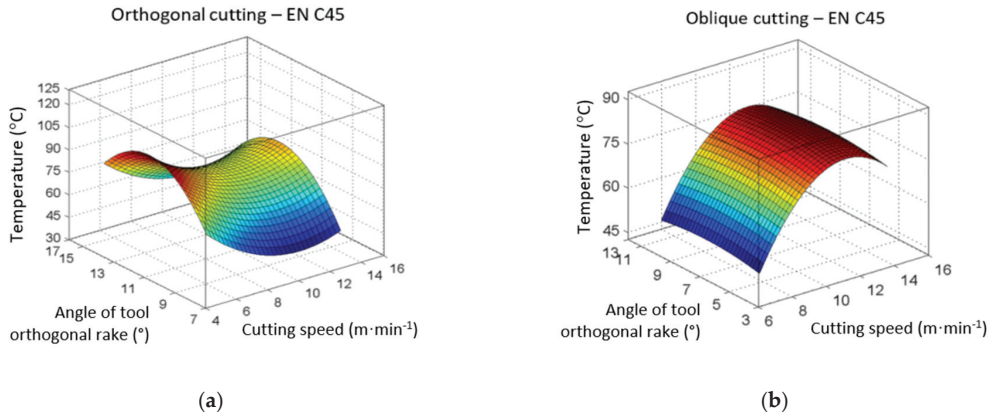
Using Equations (1) and (2), the temperature dependences on a combination of two parameters were plotted out of four monitored (depth of cut, cutting speed, face angle and inclination of the cutting edge of the tool) so that the behaviour of the temperature field could be evaluated.

When orthogonal cutting of carbon steel EN C45 in the interaction of cutting speed and cutting depth, the cutting depth had a more significant effect (Figure 7a). The cutting speed had a much milder effect, and the highest temperature values were achieved at the minimum cutting speed and the maximum values of the cutting depth. Conversely, in the oblique cutting of carbon steel (Figure 7b), the maximum temperatures were reached at the minimum cutting depth and the maximum cutting speed.

The influence of the angle of the tool-orthogonal rake and the cutting speed in orthogonal cutting is almost equally important/intense (Figure 8a), whereas in oblique cutting, the angle of orthogonal rake has an almost imperceptible effect compared to the impact of the cutting speed (Figure 8b). In both cases, the maximum temperature values were reached at the mean values of the angle of the tool-orthogonal rake, but as already mentioned, the temperature reacts in the opposite way to a change in cutting speed. The maximum temperature in orthogonal cutting is at the minimum cutting speed, and in oblique cutting, it is at the maximum cutting speed.



**Figure 7.** The graphs of the influence of cutting speed  $v_c$  and cutting depth  $a_p$  on temperature change  $T$ , (a) orthogonal cutting; (b) oblique cutting.

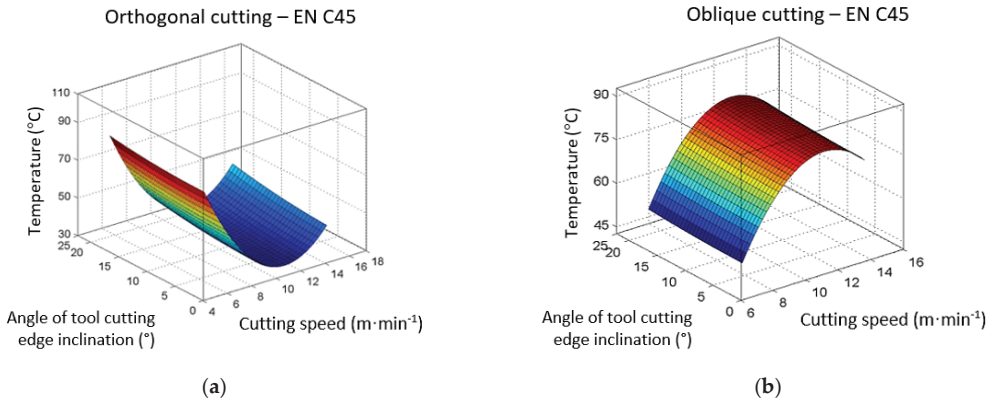


**Figure 8.** The graphs of the influence of cutting speed  $v_c$  and the angle of the tool-orthogonal rake  $\gamma_o$  on temperature change  $T$ , (a) orthogonal cutting; (b) oblique cutting.

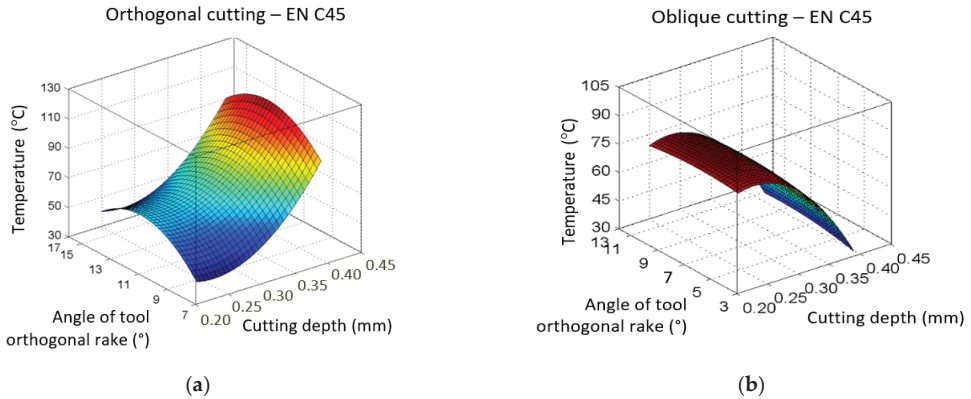
The influence of the angle of tool-cutting-edge inclination  $\lambda_s$  is almost undetectable; the more significant impact on temperature has the cutting speed (Figure 9).

The influence of the angle of the tool-orthogonal rake on the temperature is more evident in the orthogonal cutting of carbon steel (Figure 10a) than in oblique cutting (Figure 10b), and the maximum temperature values are reached at their mean values. The cutting depth has a more pronounced effect, and it is precisely in the opposite way. At orthogonal cutting, the maximum temperature values are reached at the maximum cutting depth values, and at oblique cutting, the maximum temperature is reached at the minimum cutting depth. In both types of cutting, the angle of tool-cutting-edge inclination  $\lambda_s$  has no noticeable effect on the change in cutting temperature compared to the cutting depth (Figure 11).

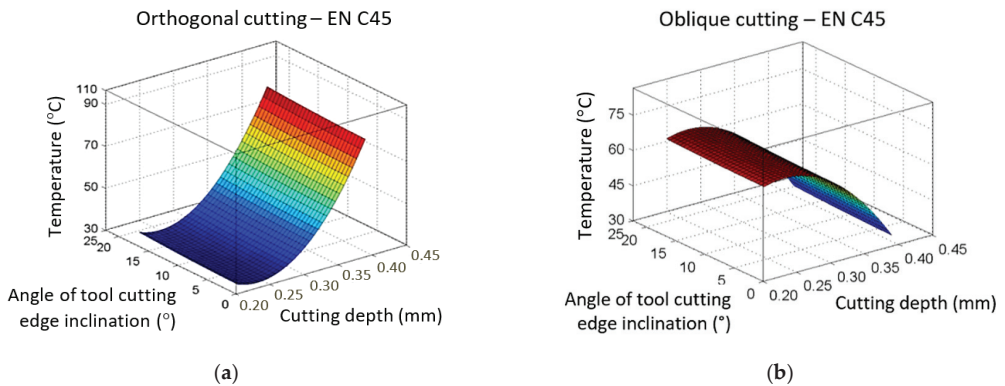
The angle of tool-cutting-edge inclination at the orthogonal cutting of carbon steel (Figure 12a) has an almost unnoticeable effect compared to the angle of the tool-orthogonal rake. However, it is different at oblique cutting (Figure 12b), where maximum temperature values are reached at the maximum angle of tool-cutting-edge inclination. The angle of the tool-orthogonal rake had a more prominent effect in orthogonal cutting, but the maximum temperature was reached at its mean values in both cutting methods.



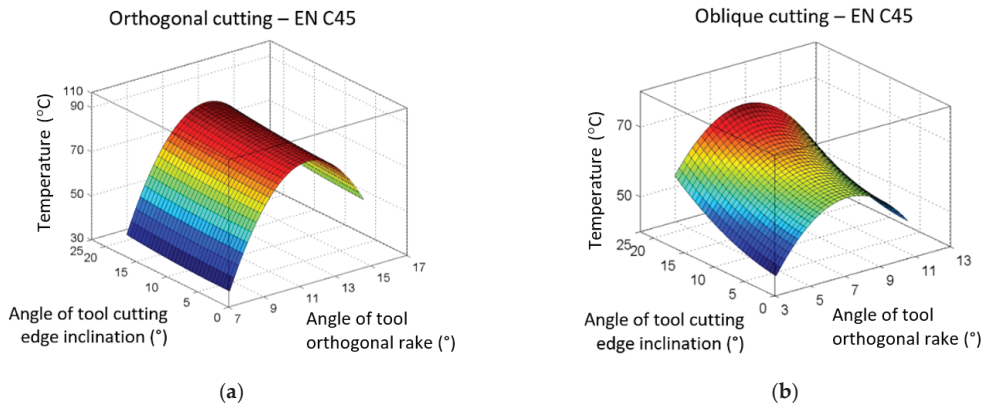
**Figure 9.** The graphs of the influence of cutting speed  $v_c$  and the angle of tool-cutting-edge inclination  $\lambda_s$  on temperature change  $T$ , (a) orthogonal cutting; (b) oblique cutting.



**Figure 10.** The graphs of the influence of the tool-orthogonal rake  $\gamma_o$  and cutting depth  $a_p$  on temperature change  $T$ , (a) orthogonal cutting; (b) oblique cutting.



**Figure 11.** The graphs of the influence of cutting depth  $a_p$  and the angle of tool-cutting-edge inclination  $\lambda_s$  on temperature change  $T$ , (a) orthogonal cutting; (b) oblique cutting.



**Figure 12.** The graphs of the influence of the tool-orthogonal rake  $\gamma_o$  and the angle of tool-cutting edge inclination  $\lambda_s$  on temperature change  $T$ , (a) orthogonal cutting; (b) oblique cutting.

On the basis of experiments aimed at determining the influence of the investigated factors on the temperature of the chip, it is possible to evaluate achieved results from three points of view:

- From the point of view of the cutting speed, the results of the research are characterized for orthogonal cutting by a slight decrease in the temperature of the chip as the cutting speed increases. From the point of view of theoretical and practical knowledge, such a trend occurs at very high cutting speeds, when the chip removal speed from the cutting site is significantly higher than the heat conduction speed in the machined material, which is used in high-speed machining. In oblique cutting, the maximum temperature of the chip is reached in roughly 2/3 of the range of cutting speeds, which decreases slightly with the further increase in the cutting speed values. However, according to theoretical knowledge, the trend should be rising. The deviation between the research results and the theoretical starting point is probably caused by the influence of the complexity of the experimental system, as well as the factors of the experimental conditions that are uncontrollable.
- From the point of view of the change in cutting depth, significantly opposite tendencies for orthogonal and oblique cutting occurred. With this phenomenon, it should be noted that the temperature gradient in the graphical interpretation of the results is about 45 °C for orthogonal cutting and about 15 °C for oblique cutting. The influence of the cutting depth on the cutting temperature in orthogonal cutting represents the current theoretical and practical knowledge very well—with increasing depth of cut, the degree of deformation of the machined material increases, which outwardly manifests as an increase in temperature in a geometric trend. In oblique cutting, this experiment showed a trend of a slight increase in chip temperature while reducing its thickness. This phenomenon is in contrast to the simplified theoretical model of cutting. This opposite trend in the behavior of the acquired dependence can be explained by the interaction of two factors causing a slight decrease in chip temperature when increasing its thickness (influence  $i$ ).
- From the perspective of the angle of the tool-orthogonal rake  $\gamma_o$ , the research results indicate for orthogonal cutting that the maximum chip temperature is reached in roughly half of the range of angles examined. This trend is most likely caused by the interaction of influences of both used methodologies of experimental measurement and data evaluation. In oblique cutting, the effect of the dependence of chip temperature on the angle of the tool-orthogonal rake  $\gamma_o$  is insignificant, which is in accordance with current knowledge.

- The influence of the angle of tool-cutting-edge inclination  $\lambda_s$  on chip temperature is almost undetectable in accordance with theoretical knowledge.

The influence of parameters on the maximum measured temperature during orthogonal and oblique EN C45 machining is clearly shown in Table 5.

**Table 5.** Effect of parameters on the maximum measured temperature during orthogonal and oblique machining EN C45.

Machining Type	Tool-Cutting-Edge Angle (°)	Cutting Parameters				Temperature
		$v_c$ (m·min <sup>-1</sup> )	$a_p$ (mm)	$\gamma$ (°)	$\lambda_s$ (°)	$T$ (°C)
orthogonal	$\kappa_r = 0$	6 <sup>1</sup>	0.4 <sup>2</sup>	12 <sup>3</sup>	- <sup>4</sup>	111.4
oblique	$\kappa_r = 60$	15 <sup>1</sup>	0.2 <sup>2</sup>	7 <sup>3</sup>	20 <sup>4</sup>	103.5

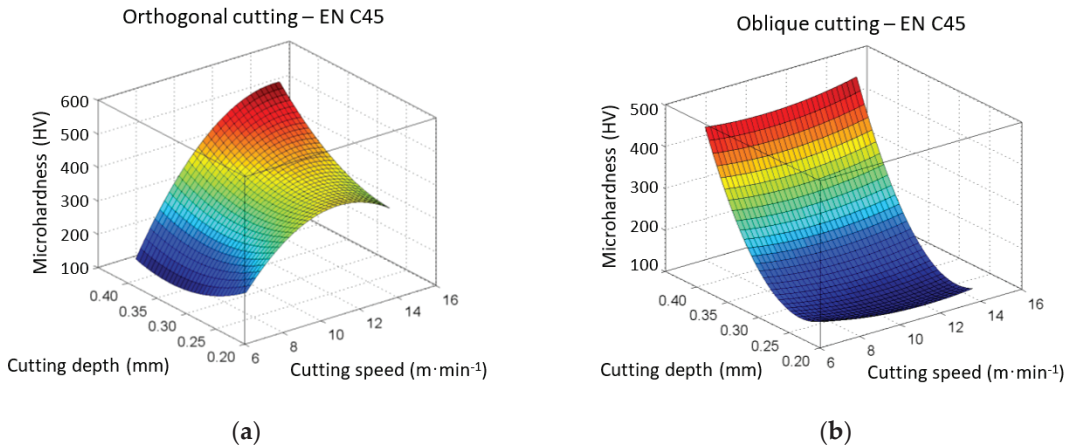
<sup>1</sup> significant influence; <sup>2</sup> the most significant influence; <sup>3</sup> little significant influence; <sup>4</sup> insignificant effect.

### 3.2. Vickers Microhardness Evaluation

Similar to the measured temperature results, as well as for the obtained HV microhardness values, regression analysis was used to determine the dependencies on the investigated parameters, which are expressed by Equations (3) and (4), for orthogonal and oblique cutting, respectively. The reliability of the relations is  $R^2 = 0.87$  and  $0.90$ , respectively. Plotted dependencies of microhardness on different combinations of two parameters are shown in Figures 13–18.

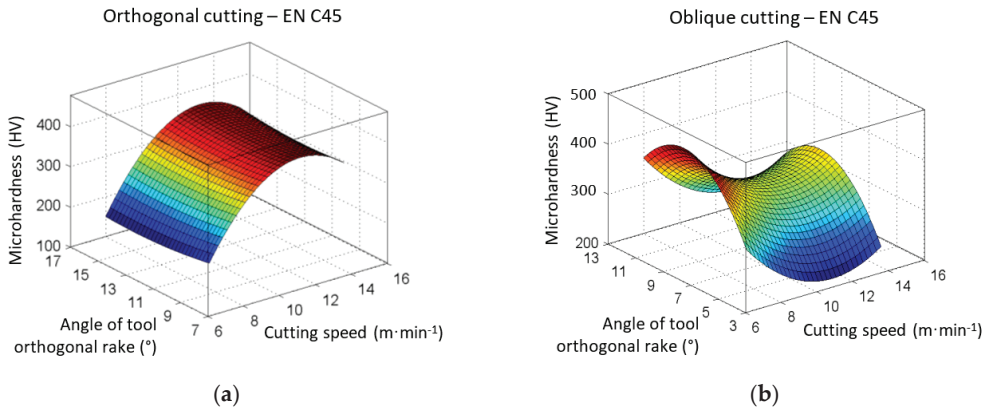
$$y = -0.0771 + 4.5677x_1 - 0.484x_2 - 0.2907x_3 - 0.1027x_4 + 1.2326x_1x_2 + 0.0893x_1x_3 + 0.0603x_1x_4 - 0.0892x_2x_4 + 0.0476x_3x_4 - 1.8966x_1^2 + 0.8444x_2^2 + 0.1503x_3^2 + 0.0208x_4^2 \quad (3)$$

$$y = -5.9254 - 2.2198x_1 + 12.092x_2 + 3.0554x_3 - 0.2568x_4 + 0.9296x_1x_2 - 0.0616x_1x_3 - 0.0356x_1x_4 - 0.6367x_2x_3 + 0.0233x_3x_4 + 1.4725x_1^2 + 11.3708x_2^2 - 2.1329x_3^2 - 0.096x_4^2 \quad (4)$$

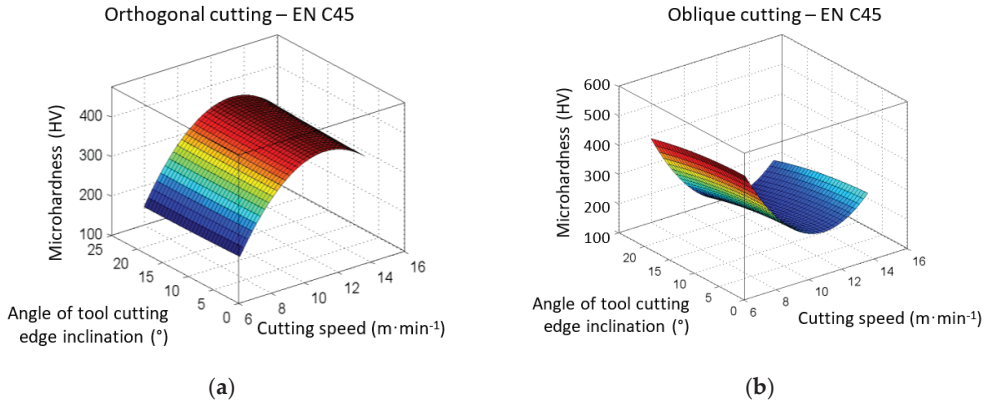


**Figure 13.** The graphs of the influence of cutting speed  $v_c$  and cutting depth  $a_p$  on change of microhardness according to Vickers HV, (a) orthogonal cutting; (b) oblique cutting.

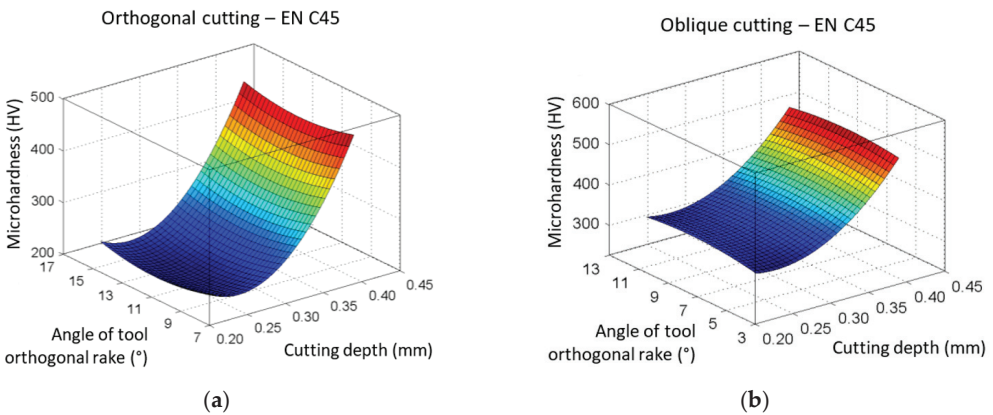
The microhardness in orthogonal machining (Figure 13a) is much more influenced by the cutting speed than the cutting depth. In oblique cutting, it is precisely the opposite (Figure 13b), and the cutting depth has a much more pronounced effect, and the greatest micro-hardness is achieved at its maximum values.



**Figure 14.** The graphs of the influence of cutting speed  $v_c$  and the angle of the tool-orthogonal rake  $\gamma_o$  on change of microhardness according to Vickers HV; (a) orthogonal cutting; (b) oblique cutting.

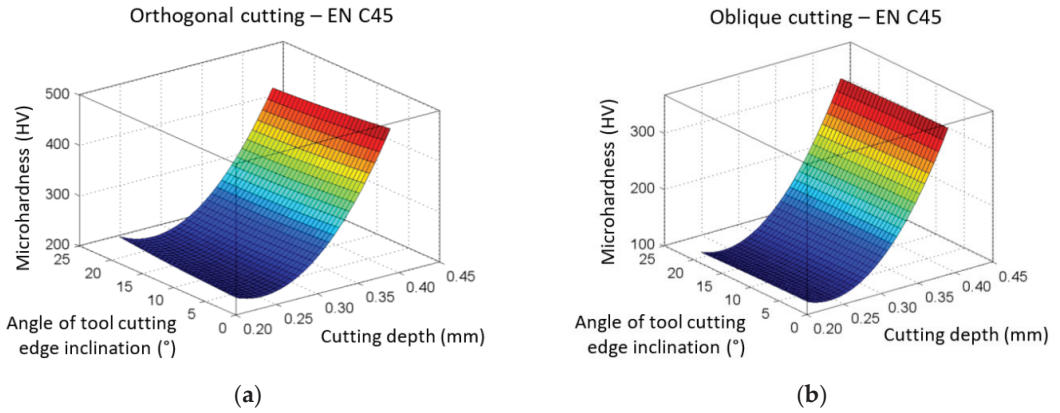


**Figure 15.** The graphs of the influence of cutting speed  $v_c$  and the angle of tool-cutting-edge inclination  $\lambda_s$  on change of microhardness according to Vickers HV; (a) orthogonal cutting; (b) oblique cutting.

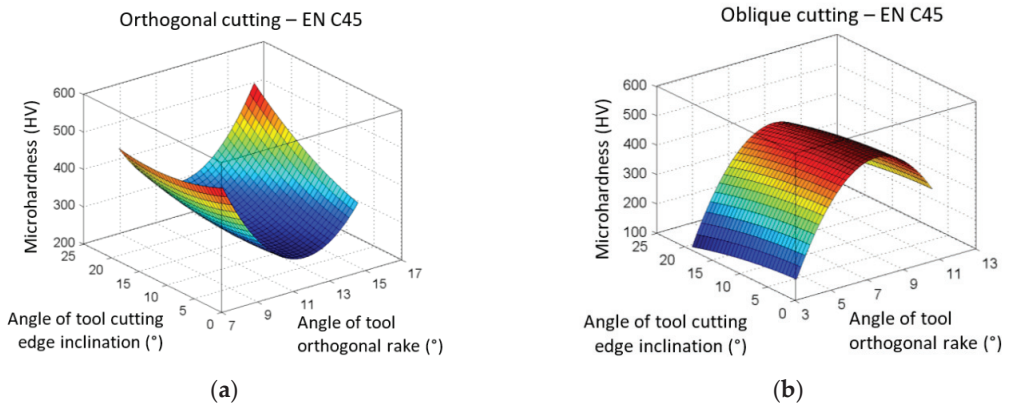


**Figure 16.** The graphs of the influence of the angle of the tool-orthogonal rake  $\gamma_o$  and cutting depth  $a_p$  on the change of microhardness according to Vickers HV; (a) orthogonal cutting; (b) oblique cutting.





**Figure 17.** The graphs of the influence of the cutting depth  $a_p$  and the angle of inclination of the main cutting edge  $\lambda_s$  on change of microhardness according to Vickers HV; (a) orthogonal machining; (b) oblique machining.



**Figure 18.** The graphs of the influence of the tool-orthogonal rake angle  $\gamma_o$  and the angle of inclination of the main cutting edge  $\lambda_s$  on change of microhardness according to Vickers HV; (a) orthogonal machining; (b) oblique machining.

The dependencies on Figure 14 show that the angle of the tool-orthogonal rake during orthogonal cutting (Figure 14a) affects the microhardness only imperceptibly compared to the effect of the cutting speed, whereas during oblique cutting (Figure 14b) the intensity due to the influence of the angle of the tool-orthogonal rake and the cutting speed is almost the same. In orthogonal machining, the maximum values of microhardness were achieved at the maximum rake of the cutting speed and marginal values of the angle of the tool-orthogonal rake. During oblique cutting, the maximum microhardness was achieved at the minimum cutting speed and medium values of the angle of the tool-orthogonal rake.

The angle of inclination of the main cutting edge in both carbon steel cutting methods (Figure 15) does not significantly affect the change in microhardness HV compared to the cutting speed.

The effect of the thickness of the cut layer in interaction with the face angle on the change of microhardness appears to be the same in orthogonal (Figure 16a) and in oblique cutting (Figure 16b). In this case, the influence of the face angle is interesting, where in orthogonal cutting the microhardness maxima are reached at its extreme values, in oblique cutting at its mean values.

The influence of the angle of inclination of the main cutting edge (Figure 17) is not noticeable in both cutting methods due to the influence of the thickness of the cut layer, which is very significant.

In the interaction of the tool-orthogonal rake angle and the angle of inclination of the main cutting edge (Figure 18), the angle of inclination has a non-significant effect on the microhardness change HV in both machining methods when compared to the effect of the angle of the tool-orthogonal rake.

The results of research aimed at determining the dependence of chip microhardness on selected factors of the cutting process pointed out that:

- The growing depth of the cut causes an increase in the rate of deformation in the primary deformation zone, which leads to an increase in strengthening and therefore of hardness. The increased rate of deformation, however, also tends to generate a significantly greater amount of heat, which reduces the manifestations of strengthening and thus microhardness. The experimentally obtained results are in accordance with theoretical knowledge for both orthogonal cutting and oblique cutting.
- From the point of view of the cutting speed, the values of the theoretical microhardness are achieved by a combination of two basic opposing phenomena—an increasing cutting speed participates in a higher strengthening of the removed material, but at the same time generates a greater amount of heat, which reduces the strengthening. Then, the mutual combination of these two opposing events with material and process properties participates in the final trend of microhardness dependence. For orthogonal cutting, the dependence shows a maximum in about 2/3 of the cutting speed range with a gradient of roughly 200 HV. In oblique cutting, the minimum microhardness of the chip with a gradient of approx. 125 HV is achieved in approximately 1/2 of the range of cutting speeds.
- From the perspective of the angle of the tool-orthogonal rake  $\gamma_o$ , the research results point to insignificant changes in microhardness with respect to this angle for orthogonal cutting. For oblique cutting, the trend of microhardness dependence on this angle shows a maximum in roughly half of the range of investigated values with a gradient of approximately 150 HV.
- The influence of the angle of tool-cutting-edge inclination  $\lambda_s$  on HV microhardness is almost undetectable in accordance with theoretical knowledge.

The overview of the influence of selected parameters on Vickers microhardness in the area of occurrence of the shear angle on samples made of carbon steel EN C45 is shown in Table 6.

**Table 6.** Effect of parameters on the maximum measured temperature during orthogonal and oblique machining EN C45.

Machining Type	Tool-Cutting-Edge Angle (°)	Cutting Parameters				Microhardness
		$v_c$ (m·min <sup>-1</sup> )	$a_p$ (mm)	$\gamma$ (°)	$\lambda_s$ (°)	(HV)
orthogonal	$\kappa_r = 0$	15 <sup>1</sup>	0.4 <sup>2</sup>	8/16 <sup>3</sup>	20 <sup>4</sup>	550.6
oblique	$\kappa_r = 60$	6 <sup>2</sup>	0.4 <sup>1</sup>	7 <sup>3</sup>	0 <sup>4</sup>	472.1

<sup>1</sup> the most significant influence; <sup>2</sup> significant influence; <sup>3</sup> little significant influence; <sup>4</sup> insignificant effect.

#### 4. Conclusions

Planing is one of the slow-speed machining types, and although it is a technology that is rarely used today, its effectiveness for specific types of workpieces can be much higher than that of milling. However, the phenomena taking place at slow-speed machining are similar to, for example, broaching, but in this case the chip remains between the teeth of the broaching mandrel and inside the workpiece, and therefore the process of chip formation cannot be observed or investigated (or only under very complicated conditions).

The presented research aimed to analyse the influence of selected parameters on the temperature during cutting operations performed at relatively low cutting speeds and

to compare the results at orthogonal and oblique machining. The new methodology for obtaining the chip root was designed so that the chip samples correspond as much as possible to the conditions of the ongoing event and to the current speed at the given moment of machining,

The experiment was designed by the orthogonal experimental composition plan of the investigation through the “star points”. The effect of four parameters (cutting speed  $v_c$ , the angle of inclination of the main cutting edge  $\lambda_s$ , the depth of cut  $a_p$  and the angle of the tool-orthogonal rake  $\gamma$ ) on temperature  $T$  ( $^{\circ}$ ) and Vickers microhardness HV was investigated in the area where the shear angle was formed.

Carbon steel EN C45, which is usually used in the experiments as a standard, was tested in two types of cutting, i.e., orthogonal cutting with a planing necking tool and oblique cutting with a straight roughing tool without cooling. Based on the measured values, the statistical regression dependencies were compiled, where various test criteria were used to verify the measured results, e.g., Grubbs criterion for detecting outlying measured results or gross errors, Cochran’s criterion for homogeneity of variance, Student’s test criterion for determining the significance of regression coefficients, Fisher-Snedecor test criterion for confirming the adequacy of the statistical model. Subsequently, graphical dependencies were constructed and evaluated.

Based on the dependencies of the temperature on the selected parameters on samples made of carbon steel EN C45 in the area of occurrence of the shear angle, it can be concluded:

- The most significant influence has the cutting depth in both orthogonal and oblique cutting, followed by the cutting speed, and the angle of the tool-orthogonal rake.
- The observations have shown that the influence of the angle of inclination of the main cutting edge is inconspicuous (or almost non-existent).
- The maximum temperature was reached at the maximum cutting depth at orthogonal cutting, in contrast to oblique cutting, in which the maximum temperature was measured at the minimum cutting depth. In both cases of cutting at the maximum temperature, the mean values of the angle of the tool-orthogonal rake played a role.

When evaluating the influence of selected parameters on Vickers microhardness, it can be stated:

- The significance of the parameters for the change of the shear angle was manifested differently. In orthogonal cutting, the highest microhardness was measured at the highest cutting speed. In this case, the highest values of the cutting depth and the angle of cutting-edge inclination were also acquired.
- During oblique cutting, the most significant influence on the change of microhardness HV had the cutting depth.

Information on the temperature development in the chip and microhardness values achieved under certain conditions indicate the suitability (or unsuitability) of choosing the selected combination of technological parameters, and together with the geometry of the tool, it is possible to subsequently increase/regulate the quality of the machined surface and the service life of the tool.

Although in the presented experimental research, the effort was to capture as much as possible the real state of the chip at the moment of separation from the machined surface and to prepare samples not only for measuring microhardness, but in the future also for observing microstructure changes, the authors realize that the machining process is so complex that obtaining samples that would perfectly reflect the state of chip formation at a given moment is almost impossible.

**Author Contributions:** Conceptualization, P.P.M. and A.S.; methodology, P.P.M. and K.M.; software, P.P.M. and M.K. (Martin Korol); validation, M.V. and M.K. (Milena Kubisova); investigation, P.P.M. and K.M.; resources, M.K. (Martin Korol) and K.M.; data curation, P.P.M. and M.K. (Milena Kubisova); writing—original draft preparation, K.M.; writing—review and editing, K.M.; visualization, M.V. and K.M.; supervision, P.P.M.; project administration, K.M.; funding acquisition, K.M. and P.P.M. All authors have read and agreed to the published version of the manuscript.

**Funding:** This research was funded by the grants APVV-19-0550, SK-CN-21-0046, KEGA 005TUKE-4/2021 and KEGA 032TUKE-4/2022.

**Institutional Review Board Statement:** Not applicable.

**Informed Consent Statement:** Not applicable.

**Data Availability Statement:** Not applicable.

**Acknowledgments:** The article was prepared thanks to support of the Ministry of Education of the Slovak Republic through the grants APVV-19-0550, SK-CN-21-0046, KEGA 005TUKE-4/2021 and KEGA 032TUKE-4/2022.

**Conflicts of Interest:** The authors declare no conflict of interest.

## References

- Varga, G.; Sovilj, B.; Jakubowicz, M.; Babič, M. Experimental Examination of Surface Roughness in Low-Environmental-Load Machining of External Cylindrical Workpieces. In *Advances in Manufacturing II*; Lecture Notes in Mechanical Engineering; Springer: Cham, Switzerland, 2019; Volume 2, pp. 307–321. [\[CrossRef\]](#)
- Prasetyo, L.; Tauviqirrahman, M. Study of chip formation feedrates of various steels in low-speed milling process. *IOP Conf. Ser. Mater. Sci. Eng.* **2017**, *202*, 012097. [\[CrossRef\]](#)
- Pastucha, P.; Majstorovic, V.; Kucera, M.; Beno, P.; Krile, S. Study of Cutting Tool Durability at a Short-Term Discontinuous Turning Test. In *Advances in Manufacturing Engineering and Materials*; Lecture Notes in Mechanical Engineering; Springer: Cham, Switzerland, 2019; pp. 493–501. [\[CrossRef\]](#)
- Karkalos, N.E.; Markopoulos, A.P.; Manolakos, D.E. Cutting Speed in Nano-Cutting as MD Modelling Parameter. *Int. J. Manuf. Mater. Mech. Eng.* **2016**, *6*, 1–13. [\[CrossRef\]](#)
- Toufatzis, A.I.; Pantazopoulos, G.A.; Besseris, G.J.; Paipetis, A.S. Machinability evaluation and screening of leaded and lead-free brasses using a non-linear robust multifactorial profiler. *Int. J. Adv. Manuf. Technol.* **2016**, *86*, 3241–3254. [\[CrossRef\]](#)
- Neslušán, M.; Mrkvica, I.; Čep, R.; Kozak, D.; Konderla, R. Deformations after heat treatment and their influence on cutting process. *Teh. Vjesn.* **2011**, *18*, 601–608.
- Tomczewski, L. The application of planing tools during turning. *Adv. Sci. Technol. Res. J.* **2015**, *9*, 83–86. [\[CrossRef\]](#)
- Chukarin, A.; Meskhi, B.; Shoniya, D. Theoretical analysis on regularities of the process of noise generation of planing, slotting and planing-milling machines. *Akustika* **2021**, *41*, 173–177. [\[CrossRef\]](#)
- Zetek, M.; Zetkova, I. Increasing of the Cutting Tool Efficiency from Tool Steel by Using Fluidization Method. *Procedia Eng.* **2015**, *100*, 912–917. [\[CrossRef\]](#)
- Kundrák, J.; Markopoulos, A.P.; Karkalos, N.E.; Makkai, T. The Examination of Cutting Force as Function of Depth of Cut in Cases with Constant and Changing Chip Cross Section. In *Advances in Manufacturing II, Volume 4—Mechanical Engineering*; Springer: Cham, Switzerland, 2019; pp. 405–415.
- Saglam, H.; Yaldiz, S.; Unsacar, F. The effect of tool geometry and cutting speed on main cutting force and tool tip temperature. *Mater. Des.* **2007**, *28*, 101–111. [\[CrossRef\]](#)
- Jurko, J.; Panda, A.; Behun, M. Prediction of a new form of the cutting tool according to achieve the desired surface quality. *Appl. Mech. Mater.* **2013**, *268–270*, 473–476. [\[CrossRef\]](#)
- Filippov, V.; Filippova, E.O. Determination of Cutting Forces in Oblique Cutting. *Appl. Mech. Mater.* **2015**, *756*, 659–664. [\[CrossRef\]](#)
- Bagci, E. 3-D numerical analysis of orthogonal cutting process via mesh-free method. *Int. J. Phys. Sci.* **2011**, *6*, 1267–1282.
- Filice, L.; Micari, F.; Rizzuti, S.; Umbrello, D. A critical analysis on the friction modeling in orthogonal machining. *Int. J. Mach. Tools Manuf.* **2007**, *47*, 709–714. [\[CrossRef\]](#)
- Aydin, M.; Koklu, U. A study of ball-end milling forces by finite element model with Lagrangian boundary of orthogonal cutting operation. *J. Fac. Eng. Archit. Gazi Univ.* **2018**, *33*, 507–516.
- Seah, K.H.W.; Rahman, M.; Li, X.P.; Zhang, X.D. A three-dimensional model of chip flow, chip curl and chip breaking for oblique cutting. *Int. J. Mach. Tools Manuf.* **1996**, *36*, 1385–1400. [\[CrossRef\]](#)
- Saglam, H.; Unsacar, F.; Yaldiz, S. Investigation of the effect of rake angle and approaching angle on main cutting force and tool tip temperature. *Int. J. Mach. Tools Manuf.* **2006**, *46*, 132–141. [\[CrossRef\]](#)
- Dewangan, S.; Chattopadhyaya, S.; Hloch, S. Wear Assessment of Conical Pick used in Coal Cutting Operation. *Rock Mech. Rock Eng.* **2015**, *48*, 2129–2139. [\[CrossRef\]](#)
- Vukelic, G.; Vizentin, G.; Ivosevic, S.; Bozic, Z. Analysis of prolonged marine exposure on properties of AH36 steel. *Eng. Fail. Anal.* **2022**, *135*, 106132. [\[CrossRef\]](#)
- Jain, V.K.; Kumar, S.; Lal, G.K. Effects of Machining Parameters on the Microhardness of Chips. *J. Eng. Ind.* **1989**, *111*, 220. [\[CrossRef\]](#)
- Wang, C.; Xie, Y.; Zheng, L.; Qin, Z.; Tang, D.; Song, Y. Research on the Chip Formation Mechanism during the high-speed milling of hardened steel. *Int. J. Mach. Tools Manuf.* **2014**, *79*, 31–48. [\[CrossRef\]](#)

23. Alrabii, S.A.; Zumot, L.Y. Chip Thickness and Microhardness Prediction Models during Turning of Medium Carbon Steel. *J. Appl. Math.* **2007**, *2017*, 051905. [[CrossRef](#)]
24. Pu, C.L.; Zhu, G.; Yang, S.B.; Yue, E.B.; Subramanian, S.V. Effect of Dynamic Recrystallization at Tool-Chip Interface on Accelerating Tool Wear During High-Speed Cutting of AISI1045 Steel. *Int. J. Mach. Tools Manuf.* **2016**, *100*, 72–80. [[CrossRef](#)]
25. Senussi, G.H. Interaction Effect of Feed Rate and Cutting Speed in CNC-Turning on Chip Micro-Hardness of 304-Austenitic Stainless Steel. *World Acad. Sci. Eng. Technol.* **2007**, *28*, 121–126.
26. Mabrouki, T.; Courbon, C.; Zhang, Y.; Rech, J.; Nélias, D.; Asad, M.; Hamdi, H.; Belhadi, S.; Salvatore, F. Some insights on the modelling of chip formation and its morphology during metal cutting operations. *C. R. Mécanique* **2016**, *344*, 335–350. [[CrossRef](#)]
27. Umer, U.; Qudeiri, J.A.; Ashfaq, M.; Al-Ahmari, A. Chip morphology predictions while machining hardened tool steel using finite element and smoothed particles hydrodynamics methods. *J. Zhejiang Univ. Sci. A* **2016**, *17*, 873–885. [[CrossRef](#)]
28. Adekunle, A.S.; Adedayo, S.M.; Ohijeagbon, I.O.; Olusegun, H.D. Chip morphology and behaviour of tool temperature during turning of AISI 301 using different biodegradable oils. *J. Prod. Eng.* **2015**, *18*, 18–22.
29. Bai, W.; Sun, R.; Roy, A.; Silberschmidt, V.V. Improved analytical prediction of chip formation in ortho-gonal cutting of titanium alloy Ti6Al4V. *Int. J. Mech. Sci.* **2017**, *133*, 357–367. [[CrossRef](#)]
30. Karmiris-Obratański, P.; Papazoglou, E.L.; Leszczyńska-Madej, B.; Karkalos, N.E.; Markopoulos, A.P. An Optimization Study on the Surface Texture and Machining Parameters of 60CrMoV18–5 Steel by EDM. *Materials* **2022**, *15*, 3559. [[CrossRef](#)]
31. Saez-de-Buruaga, M.; Soler, D.; Aristimuño, P.X.; Esnaola, J.A.; Arrazola, P.J. Determining tool/chip temperatures from thermography measurements in metal cutting. *Appl. Therm. Eng.* **2018**, *145*, 305–314. [[CrossRef](#)]
32. Krašnik, M.; Čep, R.; Kouřil, K.; Baloš, S.; Antić, A.; Milutinović, M. Characterization of Microstructural Damage and Failure Mechanisms in C45E Structural Steel under Compressive Load. *Crystals* **2022**, *12*, 426. [[CrossRef](#)]
33. Monkova, K.; Monka, P.P.; Sekerakova, A.; Tkac, J.; Bednarik, M.; Kovac, J.; Jahnatek, A. Research on Chip Shear Angle and Built-Up Edge of Slow-Rate Machining EN C45 and EN 16MnCr5 Steels. *Metals* **2019**, *9*, 956. [[CrossRef](#)]
34. Abdallah, F.; Abdelwahab, S.A.; Aly, W.I.; Ahmed, I. Influence of cutting factor on the cutting tool temperature and surface roughness of steel C45 during Turning process. *Int. J. Eng. Res. Technol.* **2019**, *7*, 1065–1072.
35. Puneeth Kumar, N.; Srikantappa, A.S. Temperature and Tool Wear Analysis on Machining of Two Different Composition of C45 Steel. *Int. J. Eng. Res. Technol.* **2022**, *11*, 208–211.
36. D’Amato, R.; Amato, G.; Ruggiero, A. Adaptive Noise Cancellation-Based Tracking Control for a Flexible Rotor in Lubricated Journal Bearings. In Proceedings of the 23rd International Conference on Mechatronics Technology (ICMT), Fisciano, Italy, 23–26 October 2019.
37. Obeng, D.P.; Morrell, S.; Napier-Munn, T.J. Application of central composite rotatable design to modeling the effect of some operating variables on the performance of the three-product cyclone. *Int. J. Miner. Process.* **2005**, *76*, 181–192. [[CrossRef](#)]
38. Davim, J.P.; Silvia, J.; Baptista, A.M. Experimental cutting model of metal matrix composites (MMCs). *J. Mater. Process. Technol.* **2007**, *183*, 358–362. [[CrossRef](#)]
39. Arioli, M.; Gratton, S. Linear regression models, least-squares problems, normal equations, and stopping criteria for the conjugate gradient method. *Comput. Phys. Commun.* **2012**, *183*, 2322–2336. [[CrossRef](#)]
40. Paris, A.S.; Tarcolea, C.; Croitoru, S.M.; Majstorović, V.D. Statistical Study of Parameters in the Process of Orthogonal Cutting Surface Hardness. In Proceedings of the 4th International Conference on the Industry 4.0 Model for Advanced Manufacturing, Industry 4.0 and Internet of Things for Manufacturing (AMP), Belgrade, Serbia, 3–6 June 2019; pp. 68–77.

Article

# Tribological Behaviors of Inconel 718–Tungsten Carbide Friction Pair with Sulfur Additive Lubrication

Ye Yang <sup>1,\*</sup>, Hao Luan <sup>1</sup>, Songshan Guo <sup>1</sup>, Fengbin Liu <sup>1</sup>, Yuanjing Dai <sup>2</sup>, Chenhui Zhang <sup>3</sup>, Duzhou Zhang <sup>4</sup> and Gang Zhou <sup>4</sup><sup>1</sup> School of Mechanical and Material Engineering, North China University of Technology, Beijing 100144, China<sup>2</sup> Tianjin Research Institute for Advanced Equipment, Tsinghua University, Tianjin 300308, China<sup>3</sup> State Key Laboratory of Tribology, Tsinghua University, Beijing 100084, China<sup>4</sup> Beijing Key Laboratory of Long-Life Technology of Precise Rotation and Transmission Mechanisms, Beijing Institute of Control Engineering, Beijing 100094, China

\* Correspondence: yangye@ncut.edu.cn

**Abstract:** This work investigated the lubricating and anti-wear properties of several sulfur additives for a nickel-based superalloy–tungsten carbide friction pair. Compared with PAO40 without any active chemical compounds, the three kinds of sulfur additives could decrease the friction coefficient from 0.2 to 0.1 and the wear volume by 90%. Sulfurized fatty acid ester had the best performance under high temperature and heavy load with COF below 0.1 and the smallest wear volume. Furthermore, the lubricating mechanism was investigated by XPS. The physical adsorptive film and the tribochemical film together enhanced the friction-reducing and anti-wear performances of the lubricants. This effective lubricant for Inconel 718 can be applied to the machining of nickel-based alloy.

**Keywords:** Inconel 718; sulfur additives; boundary lubrication; wear mechanism

**Citation:** Yang, Y.; Luan, H.; Guo, S.; Liu, F.; Dai, Y.; Zhang, C.; Zhang, D.; Zhou, G. Tribological Behaviors of Inconel 718–Tungsten Carbide Friction Pair with Sulfur Additive Lubrication. *Metals* **2022**, *12*, 1841. <https://doi.org/10.3390/met12111841>

Academic Editor: George A. Pantazopoulos

Received: 7 October 2022

Accepted: 24 October 2022

Published: 28 October 2022

**Publisher's Note:** MDPI stays neutral with regard to jurisdictional claims in published maps and institutional affiliations.



**Copyright:** © 2022 by the authors. Licensee MDPI, Basel, Switzerland. This article is an open access article distributed under the terms and conditions of the Creative Commons Attribution (CC BY) license (<https://creativecommons.org/licenses/by/4.0/>).

## 1. Introduction

Nickel-based superalloys such as Inconel 718 are widely used in aerospace, gas turbine, nuclear, and automotive industries because of their excellent high-temperature mechanical strength and corrosion resistance [1]. At the same time, nickel-based superalloys are recognized as difficult-to-machine materials. These metals exhibit serious problems during machining such as high cutting force, rapid tool wear, short tool life, and poor surface quality of the machined surface due to the physical, chemical, and thermal properties of metals [2–5]. Tungsten carbide tools are the first choice for their good thermal conductivity, high strength, and poor affinity with nickel [6]. It is of great importance to understand the relationship between nickel-based alloy and carbide material, especially the tribological behaviors, to reduce tool wear and improve tool life. The use of suitable cutting fluids can effectively improve the machining conditions of nickel-based superalloys [7–9]. The cutting fluid acts as a lubricant to reduce friction and as a coolant to cool the temperature at the cutting zone. The lubricating ability of a cutting fluid greatly influences the quality of the machined surface, as well as the tool life [10,11].

The chemical additives in the cutting fluid can act with the metal surface at high temperature and pressure; thus, a lubricant film is formed to reduce friction between the rake face and chips, the flank face, and machined surfaces. Sulfur additives are well known for their extreme-pressure performance and anti-wear characteristics [12–14]. The sulfur compounds, under extreme-pressure conditions, undergo chemical decomposition causing sulfur release (rupture of the R–S bond) and their reaction with the metallic surface that promotes the formation of an inorganic iron sulfide layer [12,15]. Most of the cutting fluids are designed for ferrous metals [11,16–18]. However, there is a matching problem between the additives and the workpiece materials [19,20]. Whether these additives have

the same reaction with nickel-based superalloys is not clear. Few scholars have studied the lubricants for nickel-based alloy–tungsten carbide contacts. Moreover, metal working fluid which consists of several chemically active additives has a very complex chemical composition. The individual actions of each component are not easily identifiable. However, it is necessary for new metals such as nickel-based superalloys whose characteristics are very different from traditional ferrous metals. Therefore, it is important to separate contributions from different types of additives to the lubrication so as to select the most efficient lubricant molecules and optimize the components of the cutting fluid. This work focuses on the lubricating effect of different sulfur additives for the nickel-based superalloy (Inconel 718)–tungsten carbide (YG8) tribopair, and the lubricating mechanism is further investigated.

## 2. Experimental Details

Inconel 718 is the most widely used superalloy. YG8 (WC-Co) tungsten carbide is the optimal tool material for nickel-based superalloy machining. The specimen used in this paper was bought from Hengshihui company, Jiangsu, China. Table 1 shows the chemical composition of Inconel 718 superalloy. The main component is Ni (60.01 wt.%) followed by Cr (17.28 wt.%) and Fe (15.58 wt.%). The Table 2 displays the mechanical parameters of Inconel 718.

**Table 1.** Chemical compositions of Inconel 718 superalloy (wt.%).

Ni	C	O	Al	Ti	Cr	Mo	Nb	Fe
60.01	2.31	0.62	0.29	0.51	17.28	1.25	2.15	15.58

**Table 2.** The mechanical parameters of Inconel 718.

Young's Modulus (GPa at 20 °C)	Poisson's Ratio	Hardness (HRC)	Yield Strength (MPa)
199.9	0.3	26.4	1035

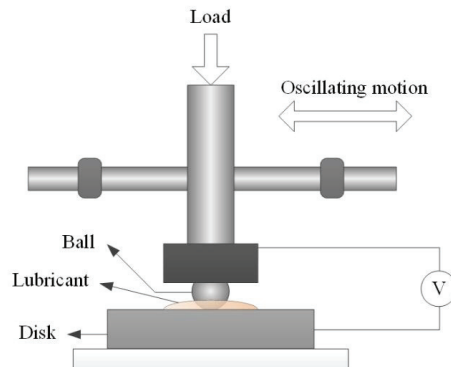
The commercial sulfur additives were bought from Symarin company, Shanghai, China. Each additive contained a different amount of sulfur in the molecule (by weight), and the sulfur bonding mechanism was different in each additive. According to the manufacturer's data, the sulfur content of sulfurized olefin was as much as 40%, more than that of sulfurized fatty acid ester (17%) and sulfurized lard (10%). The kinematic viscosity of sulfurized olefin was much smaller than that of the other two kinds of additives for the smallest molecular weight. Table 3 shows the available information about the lubricants. Furthermore, PAO40, the viscosity of which is 396 mm<sup>2</sup>/s, was used as pure oil without any active elements for comparison.

**Table 3.** The basic parameters of sulfur additives.

Name	Sulfur Content	Kinematic Viscosity mm <sup>2</sup> /s (at 40 °C)	Appearance	Flash Point (°C)
Sulfurized olefin	40%	45	pale yellow	150
Sulfurized fatty acid ester	17%	582	tan	210
Sulfurized lard	10%	900–1300	dark brown	>160

The frictional tests were carried out utilizing a ball-on-disc apparatus SRV-IV (Optimol, Munich, Germany) under different lubricating conditions. The schematic diagram of the tester is displayed in Figure 1. The discs were Inconel 718 with a hardness of HRC 35. All of the specimens were polished before frictional tests by an automatic polishing/grinding machine, and a surface roughness (Sa) less than 40 nm was obtained. The counter specimen

was tungsten carbide YG8 ball with a diameter of 10 mm and surface roughness ( $S_a$ ) of 25 nm. The hardness of the carbide ball was 89HRA. The samples were ultrasonically cleaned using acetone and ethanol and then ultrapure water successively, each for 10 min, before tests. The upper ball slid reciprocally against the stationary disc with an amplitude of 2 mm and frequency of 20 Hz for 5 min. Before the frictional test, plenty of lubricant was dropped onto the surface of the disc, and the ball returned to yield a normal load of 100 N.



**Figure 1.** The schematic diagram of SRV-IV tribo-tester.

After the frictional tests, the morphology of rubbing surfaces was observed using a LEXT<sup>TM</sup>OLS5100 laser scanning confocal microscope (Olympus, Tokyo, Japan), and wear volume is calculated. Each test was repeated three times, and the average values were used. The relative errors were on the order of  $\pm 5\%$ . A Quanta200 scanning electron microscope (SEM) (FEI, Hillsboro, OR, USA) combined with energy dispersion spectrometry (EDS) (FEI, Hillsboro, OR, USA) was used for the surface analysis of the investigated materials. The chemical compositions of the worn surfaces were characterized using a PHI Quantera SXM X-ray photoelectron spectrometer (ULVAC-PHI, Chigasaki, Japan).

### 3. Results and Discussions

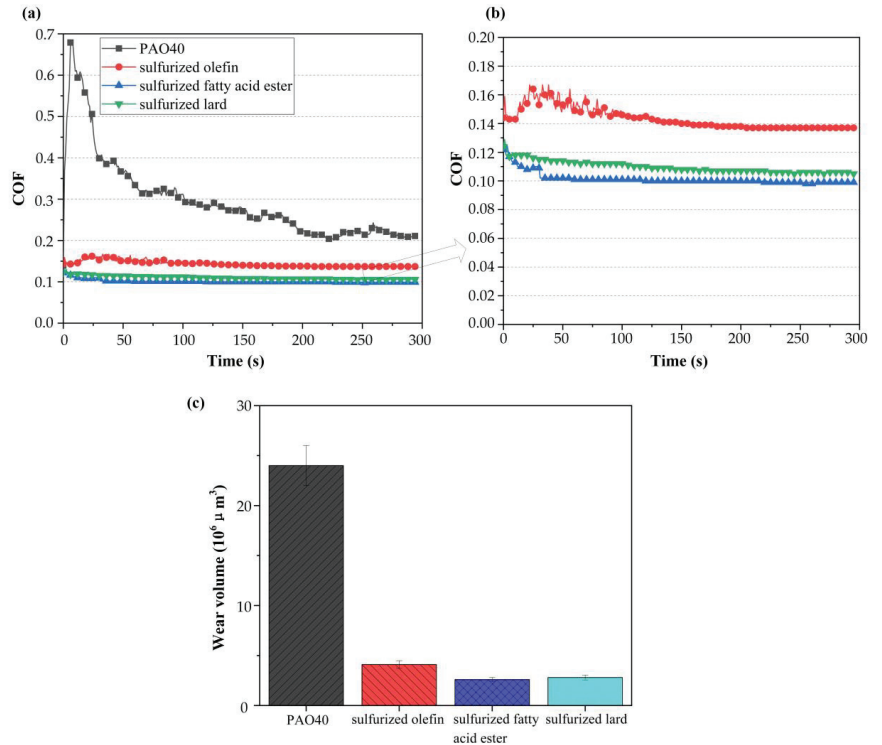
#### 3.1. Friction and Wear Properties Lubricated with Sulfur Additives

The curves of the friction coefficient and wear volume of the lower samples lubricated by the four kinds of lubricants are shown in Figure 2. For PAO40, the friction coefficient increased to 0.7 rapidly in the running-in period. Then, it decreased gradually and stabilized at about 0.2 after 200 s. When using sulfurized olefin as lubricant, the initial friction coefficient fluctuated to 0.17, before remaining stable at about 0.14 after 100 s. For sulfurized fatty acid ester and sulfurized lard, the friction coefficients remained stable at 0.1 and 0.11, respectively, until the end of the experiment. Compared with PAO40, the three kinds of sulfur-containing additives could reduce the friction coefficient significantly for the nickel-based superalloy. The friction coefficient of sulfurized fatty acid ester was the smallest, while that of sulfurized olefin was 27% larger.

Considering that tungsten carbide is much harder than nickel-based superalloys, wear occurs on the surface of the disc apparently while no wear is observed on the ball. After the frictional tests, the remaining solution and debris on the wear track are washed away by water and alcohol. From Figure 2b, it can be seen that the wear volume of the disc lubricated by PAO40 was  $2.4 \times 10^7 \mu\text{m}^3$ , about ten times that lubricated by the sulfur additives. Thus, basic oil without any active chemical elements failed to lubricate nickel-based superalloy under boundary lubrication. Compared with PAO40, the sulfur additives showed good lubricating and anti-wear performance for the Inconel 718–tungsten carbide friction pair. It is easy to generate inorganic protective films in the tribochemical reaction for an excellent anti-wear effect. For sulfurized fatty acid ester and sulfurized lard, the wear volumes were  $2.6 \times 10^6 \mu\text{m}^3$  and  $2.8 \times 10^6 \mu\text{m}^3$ , respectively. With sulfurized olefin lubrication, the wear volume was  $4.1 \times 10^6 \mu\text{m}^3$ . The relatively big wear volume is related to the long running-in



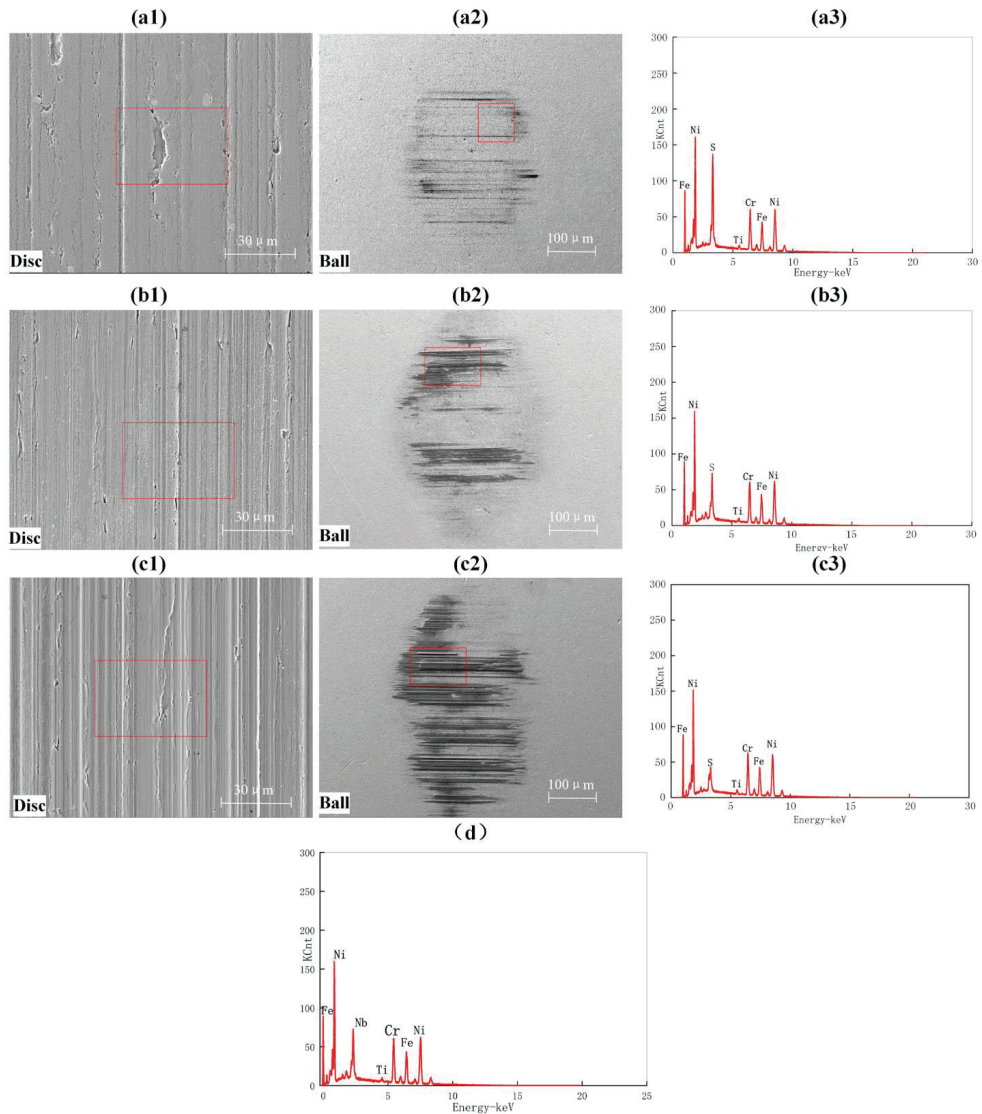
period during the friction test. A lubricating film was formed, but it was not stable enough to prevent direct contact between Inconel 718 and tungsten carbide completely during the running-in period. It can be concluded that sulfurized fatty acid had the best lubrication for Inconel 718 with the smallest COF and wear volume.



**Figure 2.** (a) Friction coefficients with (b) enlarged view, and (c) wear volume of the discs lubricated by different lubricants ( $F = 100 \text{ N}$ ,  $f = 20 \text{ Hz}$ ,  $L = 2 \text{ mm}$ ).

The micro-morphology of the friction pairs was obtained by SEM as shown in Figure 3. It can be seen that there were furrows on the surface of the superalloy discs and irregular block materials on the surface of the balls lubricated by the three kinds of additives. From Figure 3(a1), delaminated scars and abrasive particles can be seen on the surface of the disc lubricated by sulfurized olefin. There were obvious furrows on the worn surface lubricated by sulfurized lard (Figure 3(c1)). Furthermore, large dark blocky materials were detected on the ball surface (Figure 3(c2)). The worn surface was compared to the smoothest with no adhesive scar when lubricated by sulfurized fatty acid ester (Figure 3(b1)). However, there were still patches on the surface of the ball (Figure 3(b2)). To ascertain the ingredients of the materials on the surface (the red frame in Figure 3), EDS analysis was conducted. The results show that the nickel-based superalloy on the ball surface was transferred from the discs and adhered to the balls (Figure 3d). The materials on the balls were the same; thus, the EDS result is listed once. The main wear mechanism of the superalloy was significant adhesion, delamination, and ploughing. From the EDS results of the worn surface of the discs, the sulfur element was detected, which did not belong to the alloy. This demonstrates that sulfides formed on the metal surface during the friction process. However, the sulfur contents on the surface of the discs lubricated by the additives were different, seen from Table 4. The sulfur content of the worn surface lubricated by sulfurized olefin was the highest (12.37%), while the adhesion on the ball was relatively mild. It should be considered that the active sulfur content of sulfurized olefin was also the highest. The sulfur content

of the worn surface lubricated by sulfurized lard was the lowest (1.34%) with the most adhesive blocky material on the ball. For the sulfurized fatty acid ester, the adhesion on the ball was significantly decreased compared with the sulfurized lard. This indicates that the sulfide generated on the metal surface during the friction process played an important role in reducing the adhesion of nickel-based superalloy to tungsten carbide ball during friction. Sulfurized fatty acid ester contains active sulfur that can react with the metal surface at a lower temperature; hence, the surface quality of the disc and the adhesion of the ball were better than those lubricated by sulfurized lard. Meanwhile, the sulfurized fatty acid ester molecule has a long carbon chain which helps to separate the two surfaces; thus, direct contact was avoided compared with sulfurized olefin.



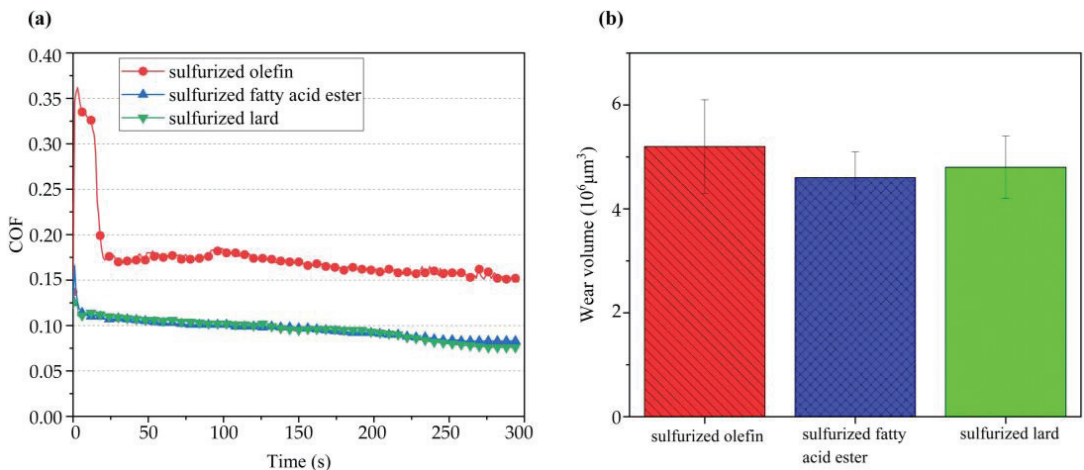
**Figure 3.** SEM morphology of the tracks on Inconel 718 and tungsten carbide ball lubricated by (a1,a2) sulfurized olefin, (b1,b2) sulfurized fatty acid ester, and (c1,c2) sulfurized lard; (a3,b3,c3) EDS spectrum of the red box in (a1,b1,c1); (d) EDS spectrum of the red box in (a2).

**Table 4.** The elements content of the above EDS analysis.

Element (wt.%)	Ni	Fe	Cr	S	C	Al	Si	Ti	Nb
(a3)	45.23	18.2	16.8	12.37	6.09	0.36	0.16	0.96	–
(b3)	43.71	17.67	16.75	2.71	6.75	0.37	0.97	0.87	10.19
(c3)	46.44	18.93	18.36	1.34	4.54	0.52	0.14	1.35	8.38
Element (wt.%)	Ni	Fe	Cr	Nb	Ti	C	W	O	–
(d)	33.92	16.54	16.01	8.54	1.13	7.31	9.04	1.5	–

### 3.2. Temperature Effect

Temperature is very important for the chemical reaction of additives with tribo-surface. The influence of temperature on the friction and wear behavior of Inconel 718 sliding against WC-Co under the lubrication of sulfur additives was investigated. The experimental temperature was increased to 150 °C with the other experimental parameters the same as those in Section 3.1. Figure 4a shows the friction coefficient curve at 150 °C. For sulfurized olefin, the fluctuation of the friction coefficient was reduced at the beginning of the test compared with that at 30 °C. Furthermore, the friction coefficient stabilized at about 0.18 after 20 s. For sulfurized fatty acid ester and sulfurized lard, the friction coefficient remained at 0.1 from the beginning to the end of the test without running-in time at 150 °C. This indicates that the lubricant film formed rapidly and remained more stable under high temperature as expected. The wear volumes of the Inconel 718 discs are shown in Figure 4b. Compared with that at 30 °C, the wear volume of the discs with different sulfur lubricants did not change much. The wear volume lubricated by sulfurized fatty acid ester was slightly smaller compared to the other two kinds of additives. It can be seen that the sulfur lubricants had very good temperature stability for nickel-based superalloys.



**Figure 4.** (a) Friction coefficients and (b) wear volume when lubricated by sulfur additives at 150 °C ( $F = 100$  N,  $f = 20$  Hz,  $L = 2$  mm).

The morphology of the lower disc and the upper tungsten carbide ball after frictional tests at 150 °C was observed by SEM, and the pictures are shown in Figure 5. Compared with 30 °C, the furrows on the surface of the discs decreased, especially for sulfurized fatty acid ester and sulfurized lard (Figure 5(b1,c1)). This indicates that high temperature promoted the formation of a lubricant film, thus increasing the surface quality of the nickel-based superalloy. With respect to the surface of the balls, the adhesive materials

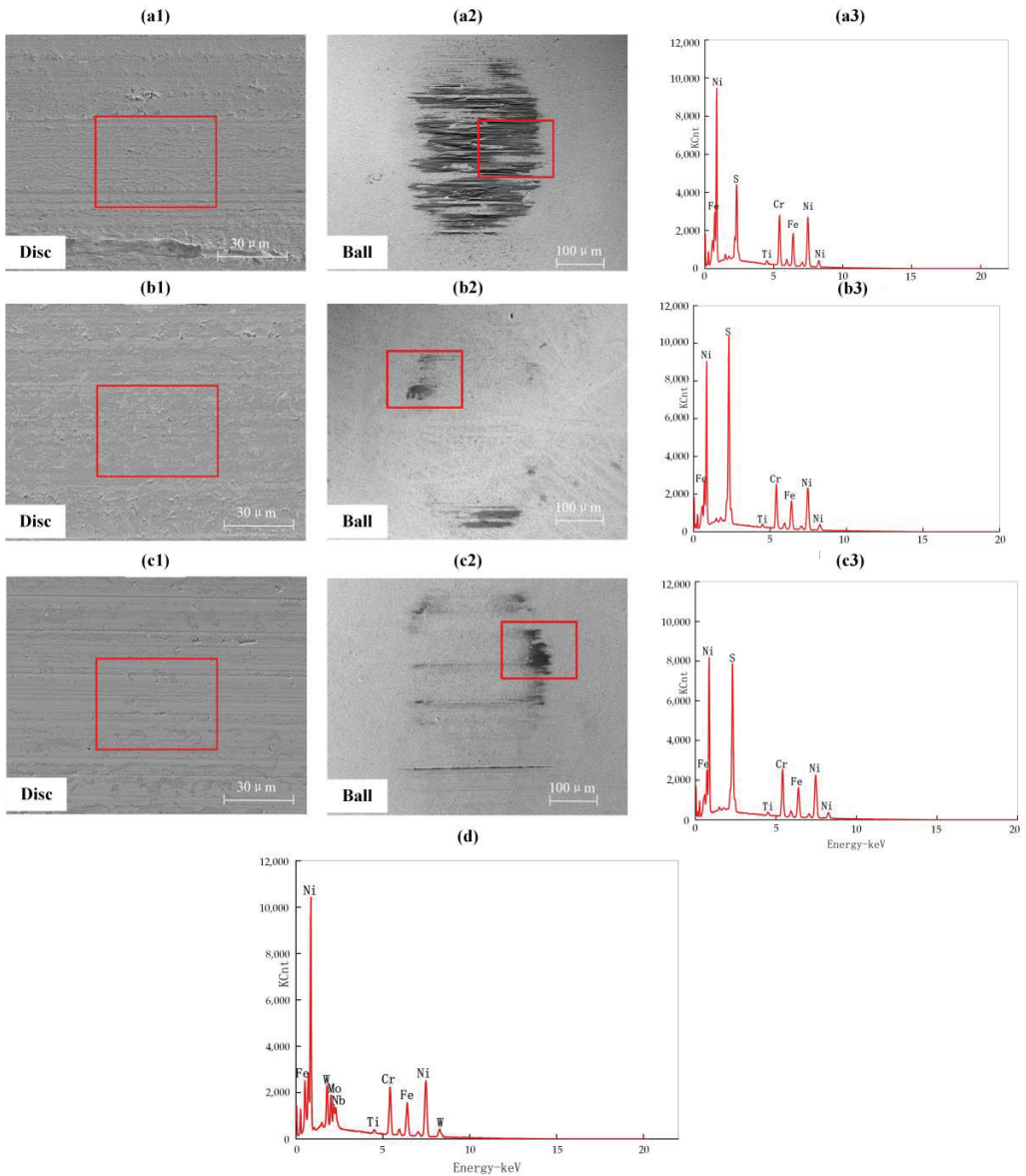
were also decreased when lubricated by sulfurized fatty acid ester and sulfurized lard (Figure 5(b2,c2)). However, the block material on the surface of the ball lubricated by sulfurized olefin increased significantly, indicating that adhesion was aggravated, as seen in Figure 5(a2). EDS analysis was performed on the wear scar of the nickel-based superalloy and the adhesion area on the tungsten carbide (the red box in Figure 5). The dark materials on the balls were the same; thus, the EDS results are listed once (Figure 5d). A nickel-based superalloy was transferred from the disc and adhered to the ball. It can be speculated that, under high temperature, the main wear mechanism of the superalloy was adhesion. The elements content of the EDS analysis is listed in Table 5. From the EDS spectrum of the surface lubricated by sulfurized fatty acid ester (Figure 5(b3)), it can be seen that the peak of sulfur in the wear scar increased significantly and the sulfur content increased from 2.71% (30 °C) to 16.33% (150 °C). The sulfide acted as an effective lubricant film, which significantly decreased the adhesion on tungsten carbide balls and the ploughing on nickel-based superalloy discs. For sulfurized lard, the sulfur content increased from 1.34% (30 °C) to 5.43% (Figure 5(c3)), and the surface quality of the frictional pairs improved. As for sulfurized olefin, the sulfur peak did not change very much, and the content of sulfur was 11.63%. This indicates that high temperature did not promote the tribochemical reaction of sulfurized olefin with nickel-based superalloy. Considering that the flash point of sulfurized olefin is 150 °C, when the experimental temperature increased to 150 °C, the sulfurized olefin began to volatilize continuously, and the material left in the friction area was unstable. This led to the aggravation of adhesion at 150 °C lubricated by sulfurized olefin. The flash points of the other two sulfur lubricants were both higher than 150 °C, and the molecules remained stable with temperature increasing. Moreover, the tribochemical reaction was promoted, leading to better surface quality and less adhesion.

**Table 5.** The elements content of the above EDS analysis.

Element (wt.%)	Ni	Fe	S	C	Ti	Cr	Nb	–
(a3)	41.8	16.12	11.63	6.22	0.72	16.26	3.68	–
(b3)	43.71	17.67	16.33	6.45	0.71	15.4	10.19	–
(c3)	47.56	17.7	5.43	4.35	0.81	17.27	4.16	–
Element (wt.%)	Ni	Fe	Nb	Cr	Ti	C	W	O
(d)	45.29	14.14	3.73	13.7	0.7	6.22	10	3.51

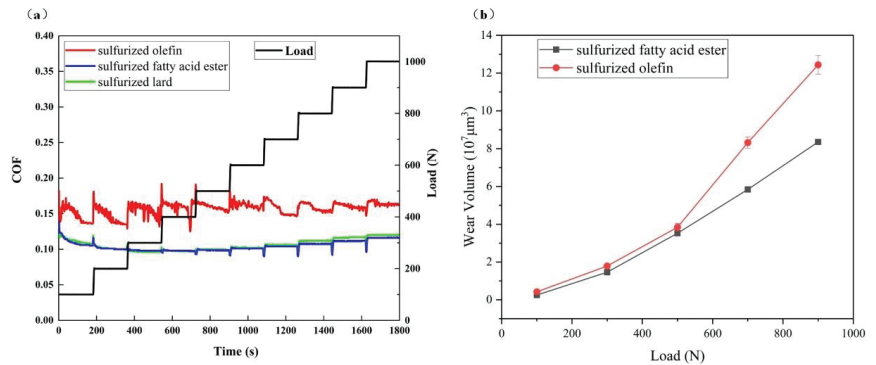
### 3.3. Load Capacity

The extreme-pressure performance of the lubricants is also an important index used to measure the lubricating property. To illustrate the performance under extreme pressure, the load slope test results of the three kinds of sulfur additives are shown in Figure 6a. The test load increased from 100 N to 1000 N in steps of 100 N. The friction coefficient of sulfurized olefin fluctuated significantly with each load increase. For sulfurized fatty acid ester and sulfurized lard, the friction coefficients remained stable at about 0.1 before the load increased to 600 N. When the load was more than 600 N, the friction coefficients had a little fluctuation. Thus, the load-bearing capacity of sulfurized fatty acid ester and sulfurized lard was better than that of sulfurized olefin.



**Figure 5.** SEM morphology of the tracks on Inconel 718 and tungsten carbide ball lubricated under 150 °C lubricated by (a1,a2) sulfurized olefin, (b1,b2) sulfurized fatty acid ester, and (c1,c2) sulfurized lard; (a3,b3,c3) EDS spectrum of the red box in (a1,b1,c1); (d) EDS spectrum of the red box in (a2).

The wear volumes of sulfurized fatty acid ester and sulfurized lard on nickel-based superalloy under different loads were further tested. The experimental load was set to 300 N, 500 N, 700 N, and 900 N, and the results are shown in Figure 6b. When sulfurized fatty acid ester lubricated the nickel-based superalloy, the wear volume increased steadily with the increase in load. As for sulfurized lard, the wear volume had a larger increase compared to sulfurized fatty acid when the load increased to 700 N. The big wear volume was consistent with the large friction coefficient, indicating unstable lubricant condition.



**Figure 6.** (a) Friction coefficient vs. time during a load slope test from 100 N to 1000 N and (b) wear volume under different loads ( $f = 20$  Hz,  $L = 2$  mm,  $t = 25$  °C).

### 3.4. Exploration of the Adsorption Characteristics

XPS is a practical method to clarify the chemical states of elements within the adsorption film on the surface of tribopair. To further explain the lubrication mechanism of sulfur additives for nickel-based superalloy, the worn surfaces were tested by XPS. Figures 7 and 8 show the spectra of the several elements lubricated by sulfurized fatty acid ester and sulfurized olefin. It can be observed that the peak shapes and binding energies of the corresponding elements were similar. Therefore, the tribochemical reaction processes were the same when sulfurized fatty acid ester and sulfurized lard were used as lubricants for the nickel-based superalloy. Figure 7a shows typical XPS survey scans inside and outside the wear track over a binding energy at the range of 0–1400 eV with the lubrication of sulfurized fatty acid ester. The values were shifted 400,000 upward from the second line to show a clear contrast. The peak intensities of Ni2p and Fe2p inside the wear track are lower than those outside the wear track. Furthermore, a sulfur peak at 168 eV appeared at the position inside the wear track, while no sulfur was detected outside the track. This demonstrates that sulfide compounds remained after the frictional test when lubricated by sulfurized fatty acid ester. Ni2p inside the wear track was apparently lower than the substrate, which further demonstrates that some film existed on the wear track. To further investigate the way in which the sulfide compounds acted with nickel-based superalloy, detailed high-resolution XPS scans of Ni2p, Fe2p, S2p, and O1s were recorded, and the results are shown in Figure 7b–e. The peak at 852.8 eV is Ni–S, and the peak at 855.2 eV is Ni–SO<sub>4</sub> (Figure 7b). The peaks at 710.11 eV and 723.4 eV correspond to Fe–S and FeSO<sub>4</sub>, respectively (Figure 7c) [11]. The S2p spectrum is shown in Figure 7d. The peak at 161 eV–162 eV corresponds to Fe–S, the peak at 162.8 eV corresponds to Ni–S, and the peak at 169.7 eV is the metal sulfate [21]. The O1s spectrum is shown in Figure 7e. The peak at 531.7 eV corresponds to S–O in –SO<sub>4</sub>, and the peak at 530.2 is metallic oxide. Combining the Ni2p, S2p, and O1s data, it can be inferred that NiSO<sub>4</sub> may have existed on the surface of the wear track. Compared with the S2p spectra on the surface lubricated by sulfurized fatty acid ester, the peak intensities of Ni2p and Fe2p inside the wear track were higher when lubricated by sulfurized olefin (Figure 8a). Moreover, the peak of metal sulfates was much lower than that lubricated by sulfurized fatty acid ester (Figure 8c). It can be speculated that the tribochemical reaction film on Inconel 718 surface lubricated by sulfurized olefin was thinner than that lubricated by sulfurized fatty acid ester, leading to a higher COF and bigger wear volume.

According to the XPS results, the lubricating mechanism of the sulfur additives for Inconel 718–tungsten carbide contact can be summarized. In the frictional process, the molecules adsorb on the metal surface to form a physical adsorption protective film. The active element S reacts with the metal matrix Inconel 718. A tribochemical protective film composed of high-toughness inorganic salts such as nickel sulfide and nickel sulfate is

formed, playing a role in lubrication. The physical adsorptive film and the tribochemical film together enhance the friction-reducing and anti-wear performances of the lubricants.

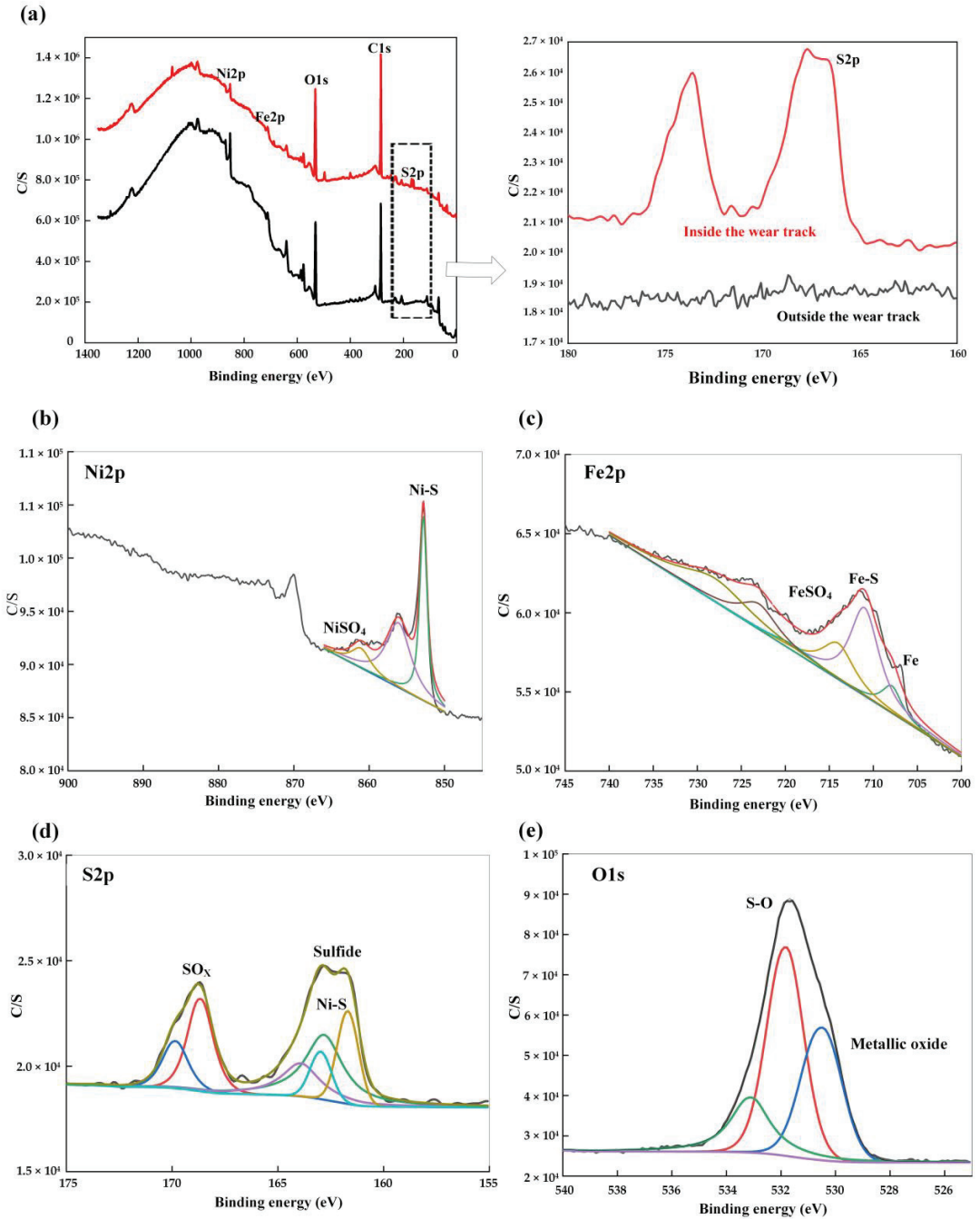
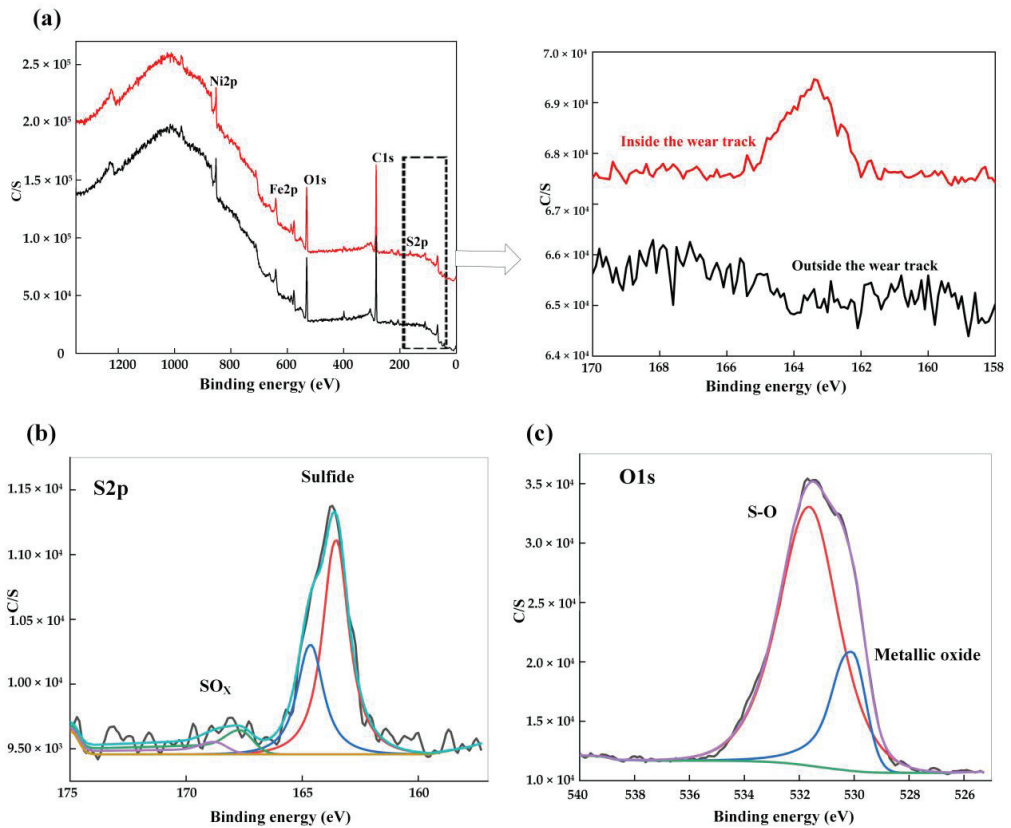


Figure 7. (a) XPS survey scans of Inconel 718 surface after tribological test: (b) Ni2p, (c) Fe2p, (d) S2p, and (e) O1s inside the wear track lubricated by sulfurized fatty acid ester.

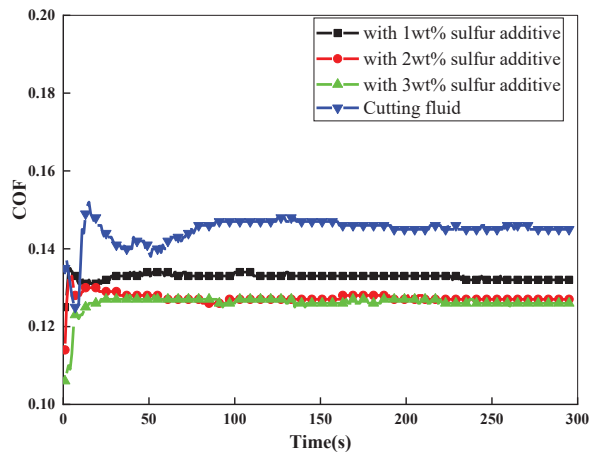


**Figure 8.** (a) XPS survey scans of Inconel 718 surface after tribological test, (b) S2p, and (c) O1s inside the wear track lubricated by sulfurized olefin.

### 3.5. The Improvement of the Cutting Fluid

The experimental results show that, for the nickel-based superalloy–tungsten carbide friction pair, sulfurized fatty acid ester had the best lubricating and anti-wear performance among the three kinds of extreme-pressure agents. The effect of sulfurized fatty acid ester on the lubricating performance of some kind of cutting fluid without sulfur-containing additives was tested. The cutting fluid was diluted to 5 wt.% with different content of sulfur additives. The frictional experiments were completed, and the friction coefficients are shown in Figure 9. The results show that the friction coefficient dropped to 0.133 with the concentration of sulfurized fatty acid ester at 1 wt.%. When the concentration of sulfurized fatty acid ester increased to 2%, the friction coefficient further dropped to 0.127. The ester concentration was further increased to 3%, and the friction coefficient did not continue to decrease and remained stable at 0.127. It can be seen that 2 wt.% sulfurized fatty acid ester could successfully decrease the friction coefficient of the cutting fluid.





**Figure 9.** The COF of some cutting fluids with different contents of sulfurized fatty acid ester ( $F = 100\text{ N}$ ,  $f = 20\text{ Hz}$ ,  $L = 2\text{ mm}$ ,  $t = 25\text{ }^{\circ}\text{C}$ ).

#### 4. Conclusions

In the present work, the tribological performance of three kinds of sulfur additives for the Inconel 718–tungsten carbide friction pair was investigated. The friction experiment results showed that sulfurized fatty acid ester possessed excellent antifriction (COF 0.1) and anti-wear performance (wear volume 90% smaller than that lubricated by PAO 40), particularly at the high temperature of  $150\text{ }^{\circ}\text{C}$  and at heavy load. The lubrication mechanism of the sulfur additives for the Inconel 718–tungsten carbide friction pair was investigated using XPS. The physical adsorptive film and the tribochemical film together enhanced the friction-reducing and anti-wear performance of the lubricants. This effective lubricant for Inconel 718 can be applied to the machining of nickel-based superalloy.

**Author Contributions:** Conceptualization, Y.Y. and C.Z.; methodology, Y.Y. and Y.D.; validation, F.L.; formal analysis, F.L.; investigation, H.L., S.G. and Y.Y.; resources, C.Z., Y.Y. and G.Z.; data curation, H.L. and S.G.; writing—original draft preparation, H.L.; writing—review and editing, Y.Y.; visualization, Y.Y.; supervision, F.L.; project administration, F.L. and D.Z.; funding acquisition, C.Z., Y.Y. and G.Z. All authors have read and agreed to the published version of the manuscript.

**Funding:** This research was funded by National Key Research and Development Program of China grant number 2018YFB2002204 and National Natural Science Foundation of China grant number 52005010 and U1837602.

**Data Availability Statement:** The data presented in this study are available on request from the corresponding author.

**Conflicts of Interest:** The authors declare no conflict of interest.

#### References

- Mohsan, A.U.; Liu, Z.; Padhy, G.K. A review on the progress towards improvement in surface integrity of Inconel 718 under high pressure and flood cooling conditions. *Int. J. Adv. Manuf. Technol.* **2017**, *91*, 107–125. [[CrossRef](#)]
- Devillez, A.; Schneider, F.; Dominiak, S.; Dudzinski, D.; Larrouquere, D. Cutting forces and wear in dry machining of Inconel 718 with coated carbide tools. *Wear* **2007**, *262*, 931–942. [[CrossRef](#)]
- Ezugwu, E.O. Key improvements in the machining of difficult-to-cut aerospace superalloys. *Int. J. Mach. Tools Manuf.* **2005**, *45*, 1353–1367. [[CrossRef](#)]
- Pusavec, F.; Deshpande, A.; Yang, S.; M'Saoubi, R.; Kopac, J.; Dillon, O.W., Jr.; Jawahir, I.S. Sustainable machining of high temperature Nickel alloy–Inconel 718: Part 1—Predictive performance models. *J. Clean. Prod.* **2014**, *81*, 255–269. [[CrossRef](#)]
- Pusavec, F.; Deshpande, A.; Yang, S.; M'Saoubi, R.; Kopac, J.; Dillon, O.W., Jr.; Jawahir, I.S. Sustainable machining of high temperature Nickel alloy–Inconel 718: Part 2—Chip breakability and optimization. *J. Clean. Prod.* **2015**, *87*, 941–952. [[CrossRef](#)]

6. Pervaiz, S.; Rashid, A.; Deiab, I.; Nicolescu, M. Influence of tool materials on machinability of titanium and nickel-based alloys: A review. *Mater. Manuf. Process.* **2014**, *29*, 219–252. [[CrossRef](#)]
7. Debnath, S.; Reddy, M.M.; Yi, Q.S. Environmental friendly cutting fluids and cooling techniques in machining: A review. *J. Clean. Prod.* **2014**, *83*, 33–47. [[CrossRef](#)]
8. Busch, K.; Hochmuth, C.; Pause, B.; Stoll, A.; Wertheim, R. Investigation of cooling and lubrication strategies for machining high-temperature alloys. *Procedia CIRP* **2016**, *41*, 835–840. [[CrossRef](#)]
9. Eskandari, B.; Bhowmick, S.; Alpas, A.T. Flooded drilling of Inconel 718 using graphene incorporating cutting fluid. *Int. J. Adv. Manuf. Technol.* **2021**, *112*, 1–14. [[CrossRef](#)]
10. Brinksmeier, E.; Meyer, D.; Huesmann-Cordes, A.G.; Herrmann, C. Metalworking fluids-mechanisms and performance. *CIRP Ann.-Manuf. Technol.* **2015**, *64*, 605–628. [[CrossRef](#)]
11. Bierla, A.; Fromentin, G.; Minfray, C.; Martin, J.M.; Le Mogne, T.; Genet, N. Mechanical and physico-chemical study of sulfur additives effect in milling of high strength steel. *Wear* **2012**, *286–287*, 116–123. [[CrossRef](#)]
12. Li, Y.R.; Pereira, G.; Lachenwitzer, A.; Kasrai, M.; Norton, P.R. X-ray Absorption spectroscopy and morphology study on antiwear films derived from ZDDP under different sliding frequencies. *Tribol. Lett.* **2007**, *27*, 245–253. [[CrossRef](#)]
13. Li, Y.R.; Pereira, G.; Kasrai, M.; Norton, P.R. Studies on ZDDP anti-wwear films formed under different conditions by XANES spectroscopy, atomic force microscopy and <sup>31</sup>P NMR. *Tribol. Lett.* **2007**, *28*, 319–328. [[CrossRef](#)]
14. Najman, M.N.; Kasrai, M.; Bancroft, G.M. X-ray Absorption spectroscopy and atomic force microscopy of films generated from organosulfur extreme-pressure (EP) oil additives. *Tribol. Lett.* **2003**, *14*, 225–235. [[CrossRef](#)]
15. Alves, S.M.; Oliveira, J.F.; Klocke, F.; Maier, B. Effects of sulfur additive EP in ester coolants during friction with CBN. *Tribol. Trans.* **2008**, *51*, 278–284. [[CrossRef](#)]
16. Chan, C.H.; Tang, S.W.; Mohd, N.K.; Lim, W.H.; Yeong, S.K.; Idris, Z. Tribological behavior of biolubricant base stocks and additives. *Renew. Sustain. Energy Rev.* **2018**, *93*, 145–157. [[CrossRef](#)]
17. Yu, Q.; Zhang, C.; Dong, R.; Shi, Y.; Wang, Y.; Bai, Y.; Zhang, J.; Cai, M.; Zhou, F. Novel N, P-containing oil-soluble ionic liquids with excellent tribological and anti-corrosion performance. *Tribol. Int.* **2019**, *132*, 118–129. [[CrossRef](#)]
18. Pettersson, A.; Elisabet, K.; Minami, I. Additives for environmentally adapted lubricants-friction and wear protection. *Tribol. Online* **2008**, *3*, 163–167. [[CrossRef](#)]
19. Jayal, A.D.; Balaji, A.K. Effects of cutting fluid application on tool wear in machining: Interactions with tool-coatings and tool surface features. *Wear* **2009**, *267*, 1723–1730. [[CrossRef](#)]
20. Xavier, M.A.; Adithan, M. Determining the influence of cutting fluids on tool wear and surface roughness during turning of AISI 304 austenitic stainless steel. *J. Mater. Process. Technol.* **2009**, *209*, 900–909. [[CrossRef](#)]
21. Guo, B.; Li, Y.; Zheng, J.; Li, F.; Li, X.; Du, X.; Yuan, L. Tribological properties of a halogen-free ionic liquid for Inconel 690–tungsten carbide contact. *Tribol. Int.* **2021**, *163*, 107153. [[CrossRef](#)]



Article

# Assessment of the Effect of Thermal-Assisted Machining on the Machinability of SKD11 Alloy Steel

Thi-Bich Mac<sup>1</sup>, The-Thanh Luyen<sup>1</sup> and Duc-Toan Nguyen<sup>2,\*</sup><sup>1</sup> Faculty of Mechanical Engineering, Hungyen University of Technology and Education, Hungyen 100000, Vietnam<sup>2</sup> School of Mechanical Engineering, Hanoi University of Science and Technology, 1A-Dai Co Viet Street, Hai Ba Trung District, Hanoi City 100000, Vietnam

\* Correspondence: toan.nguyenduc@hust.edu.vn; Tel.: +84-43-869-2007

**Abstract:** This study aimed to investigate the effects of Thermal-Assisted Machining (TAM) on SKD11 alloy steel using titanium-coated hard-alloy insert cutting tools. The microstructure, material hardness, chip color, cutting force, chip shrinkage coefficient, roughness, and vibration during TAM were evaluated under uniform cutting conditions. The machining process was monitored using advanced equipment. The results indicated that thermal-assisted processing up to 400 °C did not alter the microstructure and hardness of the SKD11 alloy steel. However, a significant variation in chip color was observed, indicating improved heat transfer through TAM. The cutting force, vibration amplitude of the workpiece, and surface roughness all decreased with increasing TAM. Conversely, the chip shrinkage coefficient of the machined chips tended to increase due to the high temperatures.

**Keywords:** SKD11 alloy steel; machinability; thermal-assisted machining (TAM)

## 1. Introduction

The cutting mode and tool geometry parameters play a critical role in machining techniques, especially when working with materials that are challenging to machine due to their high hardness. These parameters affect various output parameters of the machining process, such as cutting force, cutting heat, cutting tool wear, cutting process vibration, surface roughness, and chip geometry. To improve productivity, part quality, and cost-effectiveness, researchers are constantly seeking new technological solutions to support the machining process, including the use of smooth cold techniques, new cutting tool materials, vibration-assisted cutting, and thermal-assisted machining. Difficult-to-machine materials, characterized by high hardness, good wear resistance, and little change in mechanical properties at high temperatures, are widely used in various industries, such as mechanical, automotive, aerospace, aviation, defense, medical, and electrical-electronics-automation. Surveys have shown that over 30% of milling, turning, and drilling operations are performed on such materials [1].

Thermal-assisted machining (TAM) is a machining process that involves heating the workpiece before machining it using traditional or CNC machines. This technique has been extensively used in industrial production since its introduction in 1945 [1,2]. Compared to traditional machining methods, TAM offers several advantages, such as increased tool life, reduced cutting force, decreased tool wear, and improved surface quality, resulting in enhanced productivity [3–5]. TAM is suitable for both cutting processes (e.g., turning, milling, drilling) and deformation processes (e.g., forging, stamping, drawing). Several heating methods can be employed for TAM, including electrical current heating, laser beam heating (LAM), plasma heating (PEM), furnace heating (FAM), and induction heating (IAM). While each method has its own benefits and drawbacks, induction heating (IAM) is particularly effective due to its high heating capacity, ease of use, and affordability, making it a great choice for metalworking operations [6].

**Citation:** Mac, T.-B.; Luyen, T.-T.; Nguyen, D.-T. Assessment of the Effect of Thermal-Assisted Machining on the Machinability of SKD11 Alloy Steel. *Metals* **2023**, *13*, 699. <https://doi.org/10.3390/met13040699>

Academic Editors: George A. Pantazopoulos and Badis Haddag

Received: 17 February 2023

Revised: 27 March 2023

Accepted: 31 March 2023

Published: 3 April 2023



**Copyright:** © 2023 by the authors. Licensee MDPI, Basel, Switzerland. This article is an open access article distributed under the terms and conditions of the Creative Commons Attribution (CC BY) license (<https://creativecommons.org/licenses/by/4.0/>).

Many studies have suggested eco-friendly dry and minimum quantity lubrication or optimization to improve machining productivity, increase tool life, and enhance product quality [7–9]. However, for challenging-to-machine materials, like those commonly used in heavy-duty industries such as automotive, marine, and aviation, advanced machining methods such as diamond grinding or discharge machining are often used but limited by low material removal rates, expensive tools, and rapid wear [2]. Among these materials, SKD11 Tool Steel is frequently utilized in mold and automotive sectors due to its hardness, strength, and ductility [10]. Although traditional techniques like diamond grinding or discharge machining are limited by high costs and specialized technologies, TAM has been introduced as an innovative solution to the challenges of machining SKD11. Studies have indicated that machining with TAM can reduce cutting forces by up to 40%, increase tool life, enhance surface roughness by up to 50%, and increase material removal rate when compared to machining at room temperature [11–13].

Recent research has shown that using thermal-assisted machining (TAM) can offer several advantages, including improved tool life, enhanced productivity, and better working conditions between the tool and workpiece [14–16]. Studies have revealed that workpiece temperature is directly proportional to tool life and inversely proportional to cutting speed. Induction heating has been investigated for milling titanium alloy Ti-6Al-4V, with heat treatment significantly improving tool life and material removal rate, by up to 169.4% at a temperature of 650 °C. However, heating above 640 °C may negatively impact the workpiece's mechanical properties, reducing machining efficiency [5,17]. Studies have also shown that cutting and shear forces are inversely proportional to temperature, with a 13% reduction in cutting force observed when machining at 500 °C compared to room temperature. A novel approach to machining Inconel 718 was presented by Wang et al. [18], which combines traditional turning, cryogenic enhanced machining, and plasma heating. Cold working techniques can reduce the heat generated during cutting, enhancing the cutting tool's longevity. The implementation of this method has been shown to result in a substantial enhancement of the machining process, with the surface gloss of the machined material increased by a factor of 2.5, the required machining force decreased by half, and the cutting tool's lifespan prolonged by a factor of 1.7 compared to traditional machining at room temperature.

Efficiently machining hard alloys has long been a challenge, but thermally assisted machining (TAM) offers a promising solution. TAM involves cutting the material and then softening it with an external heat source, which has been shown to reduce the hardness and tensile strength of the workpiece material, thereby improving machinability [19]. Research indicates that TAM is linked to higher material removal rates, better control of machining time, and improved surface finishes. TAM is particularly advantageous for machining bio-implant titanium alloys, which require high precision. Hard steels can also be successfully machined using TAM, resulting in lower cutting forces, increased tool life, and higher material removal rates [20–24]. TAM can reduce cutting force amplitudes and chip morphology changes, resulting in less vibration and better surface integrity. However, machining certain hardenable steels, such as 1090 steel, can lead to increased cutting forces due to phase transformation hardening when the laser-preheated part enters the cutting zone. Softening the workpiece by reaching surface temperatures of 300–400 °C for an uncut chip thickness of 0.05 mm, on the other hand, can reduce the magnitude and amplitude variation of cutting forces, and limit the evolution of tool wear [25]. TAM also induces a change in chip morphology from sawtooth to continuous, improving the surface finish. While TAM can lead to higher cutting forces in some hardenable steels, it can also enhance surface integrity [26].

TAM techniques have been extensively researched and used in production. However, little is known about the use of magnetic induction heating for mold steel, particularly when milling difficult materials like SKD11 steel, which is commonly used in industry. This study aims to evaluate the influence of TAM on milling SKD11 steel and its effect on the material's machinability by analyzing cutting force, vibration amplitude of the workpiece, and surface

roughness. This analysis provides a basis for selecting appropriate TAM process parameters. A significant challenge when using electromagnetic induction heating in machining is its application to large parts with varying sizes or complex shapes. This study proposes a potential technological solution for processing difficult materials using electromagnetic induction heating. The results demonstrate that the heating process effectively reduces cutting force, cutting heat, and vibration during cutting, while improving the surface quality of the workpieces. The findings of this study have practical implications and are applicable to the manufacturing industry.

## 2. Experimental Setup

The ease or difficulty of processing a material is known as its machinability, which can be evaluated using parameters such as tool life, MRR, cutting force, cutting process vibration, and surface gloss of the machined material. The machinability of a material is greatly affected by its microstructure, which can be further influenced by the cutting mode. Therefore, it is essential to assess the machinability of materials during heating processing and compare it to conventional machining to determine the impact of heating on the machinability of SKD11 steel materials.

### 2.1. Schematic of Experimental System

This study establishes an experimental research model that is based on the research objectives and the available experimental equipment, as depicted in Figure 2.

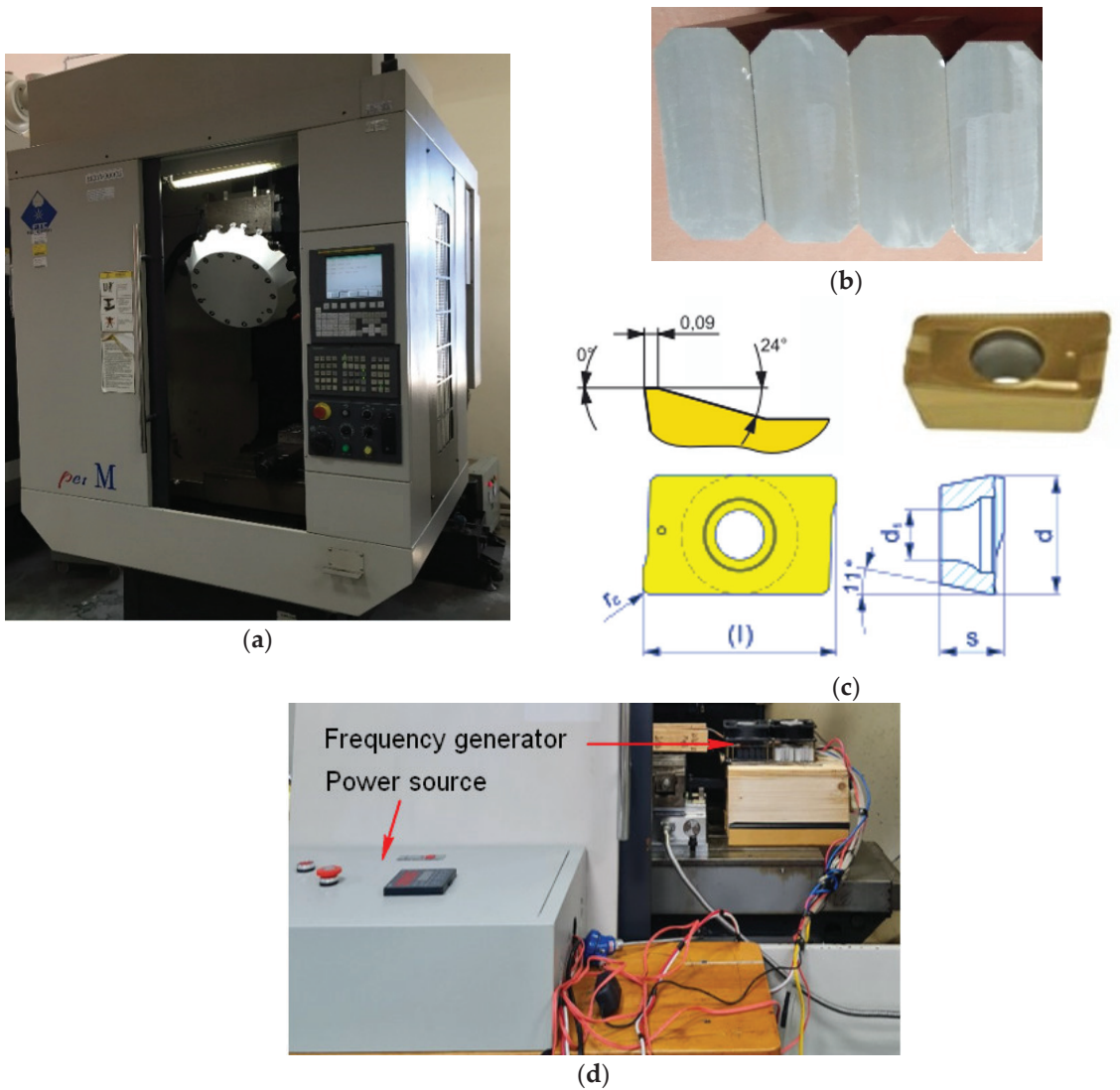
### 2.2. Materials and Testing Equipment

SKD11 steel is a frequently used alloy steel in mold processing, as defined by JIS-G4404. This steel is notable for its hardness, strength, and ductility, and can maintain its hardness even at high temperatures for an extended period, making it suitable for use in the production of molds for extrusion, plastic injection, pressure, and components that require specific performance characteristics. Table 1 presents a breakdown of the SKD11 steel components, expressed as a weight percentage (wt%).

**Table 1.** The chemical composition of SKD11 steel (wt%) [27].

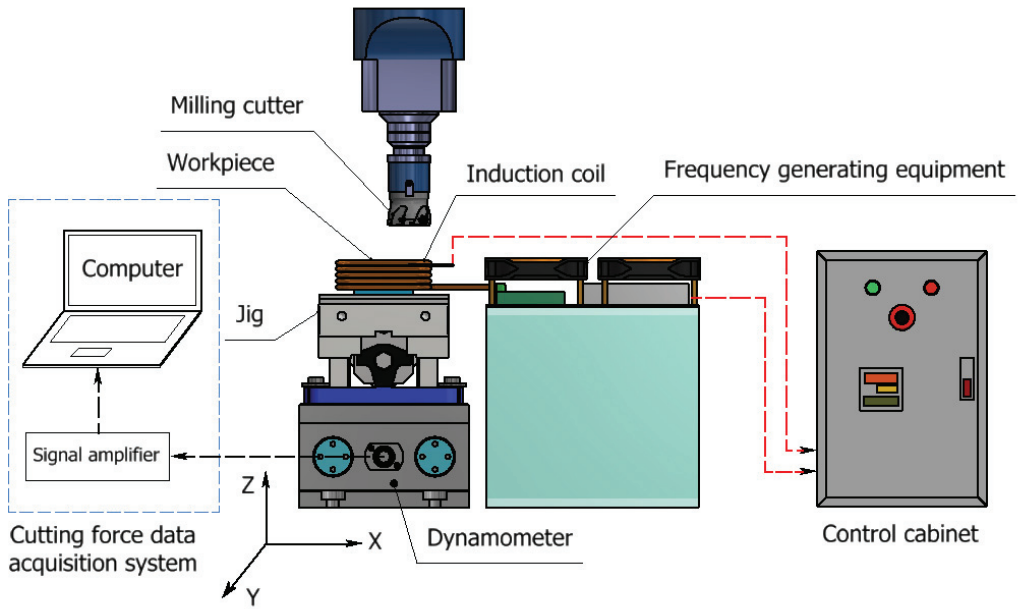
C	Cr	Mo	Si	Mn	Ni	V
1.4–1.6	11–13	0.7–1.2	≤0.6	≤0.6	-	0.15–0.3

In this study, a machining experiment was conducted on SKD11 steel test specimens using a Taiwanese MC500 milling machine. The billet was rough-worked and had dimensions of  $70 \times 31 \times 80 \text{ mm}^3$ , and a chamfer of  $7 \text{ mm} \times 7 \text{ mm}$  was applied for uniform contact with the induction coil. For the milling process, a 40 mm face milling cutter was used, equipped with a titanium-coated hard alloy insert manufactured by PRAMET, a tool manufacturer from the Czech Republic. Specifically, the APKT 1604PDR–GM hard alloy piece was utilized, with cutting edge parameters such as the rake angle, clearance angle, and cutting-edge radius set at  $24^\circ$ ,  $11^\circ$ , and 0.8 mm, respectively. Other geometric parameters, including  $l = 16 \text{ mm}$ ,  $d = 9.44 \text{ mm}$ ,  $s = 5.67 \text{ mm}$ , and  $d_1 = 4.6 \text{ mm}$ , were also specified. No coolant was applied during the machining process. One significant challenge in this research was the application of electromagnetic induction heating in machining, as depicted in Figure 1d.

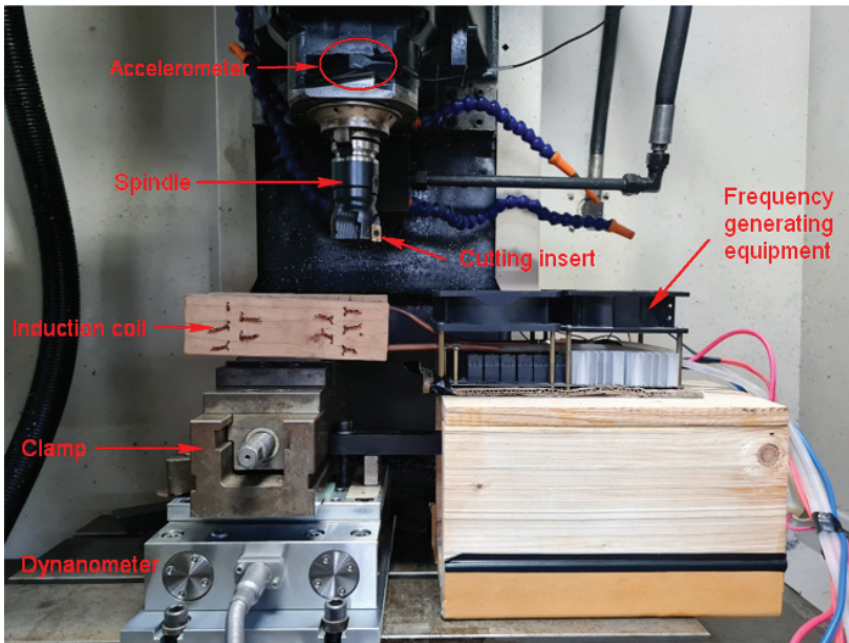


**Figure 1.** Components of the experimental system. (a) MC500 Milling Machine, (b) Sample Workpieces, (c) Hard Alloy Insert, and (d) Power Source-Frequency Generator.

The study utilized the Axiovert 25 CA optical microscope (Figure 3a) to examine the microstructure of the material after heating at different temperatures and compare it with the original sample. This microscope, specifically designed for materials research, is used in conjunction with Image-Pro Plus image analysis software to analyze the material phase. The study also employed the Brinell hardness tester (Figure 3b) to test the initial and post-heating samples for hardness.



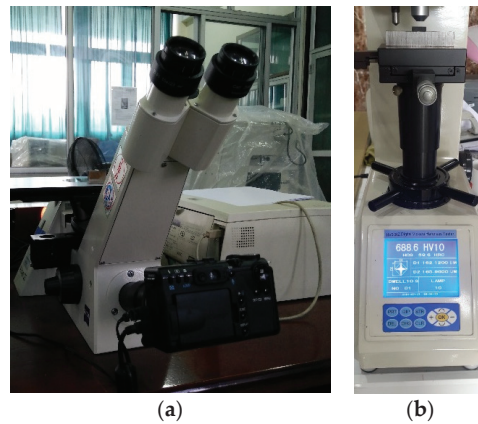
(a)



(b)

**Figure 2.** Schematic of Experimental System. Schematic diagram (a) and experiment photograph in working zone (b).





**Figure 3.** Equipment used in the tests: (a) Axiovert 25 CA Optical Microscope, (b) Brinell Hardness Tester.

### 3. SKD11 Steel Material Machinability Results

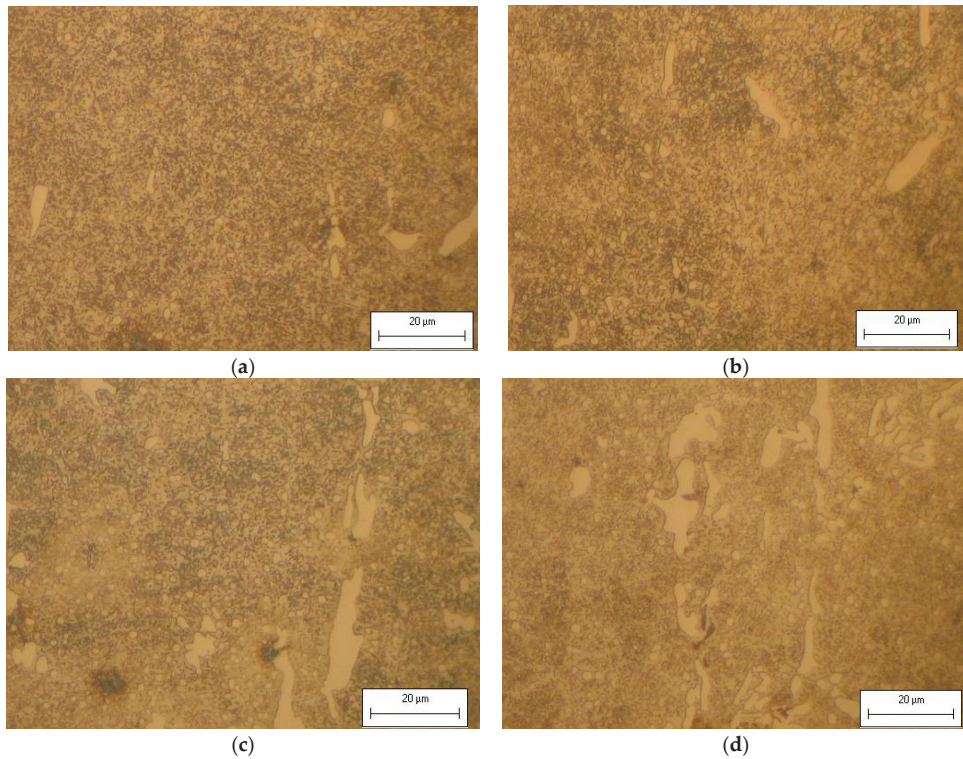
#### 3.1. Effect of TAM on Microstructure of SKD11 Steel

To conduct an accurate examination of the microscopic structure of materials, proper sample preparation is crucial. The process of preparing metal samples involves multiple stages, including cutting, grinding, polishing, and impregnation. Specimens are initially machined following established standards to achieve a size that can be impregnated. Figure 4 displays the experimental samples and their cross-sections for SEM examination.

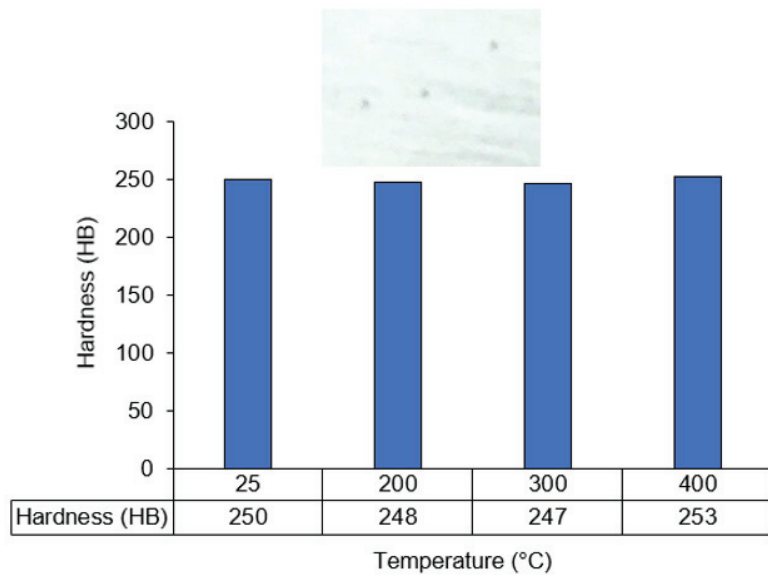
Figure 4 illustrates the microstructural analysis of SKD11 alloy steel samples before and after thermal-assisted machining (TAM) at different temperatures, using optical microscopy. Figure 4a presents an image of the microstructure of the original material sample, while Figure 4b–d show images of the microstructure after TAM at different temperatures. The analysis reveals that the microstructure of the samples after TAM at room temperature and 400 °C is similar to that of the original material. Specifically, the microstructure of the four samples includes white plates and bright round particles of chromium Cr<sub>7</sub>C<sub>3</sub> carbides, spherical dark dots of Cementite, and a light background of Pearlite. These observations suggest that the microstructure of the specimen remains unchanged even when the temperature is increased to 400 °C, which is below the phase transition temperature of 700 °C for the SKD11 alloy steel [28].

#### 3.2. Effect of TAM on Hardness

To evaluate the impact of elevated temperatures on workpiece hardness after heating, the workpiece was exposed to the designated temperature and allowed to cool naturally via exposure to ambient air. Surface hardness measurements necessitated meticulous sample preparation, including cutting, grinding, polishing, and impregnation. In order to prevent the influence of cutting heat, wire cutters were employed during sample cutting. The grinding process aimed to minimize undulation caused by the varying hardness of structural elements, while polishing removed any coarse grinding marks and scratches. Finally, deformations from the cutting, grinding, and polishing stages were either eliminated or leveled to a size sufficient for removal with an impregnating agent. Three hardness measurements were taken on each sample using a Brinell hardness tester at distinct locations, as illustrated in Figure 5. The results, presented in Figure 5, showed that increasing temperatures resulted in decreased specimen hardness to 2–3 HB at 200 °C and 300 °C. However, at 400 °C the sample demonstrated increased hardness compared to the other temperatures, although this increase was not significant within the chosen experimental temperature range.



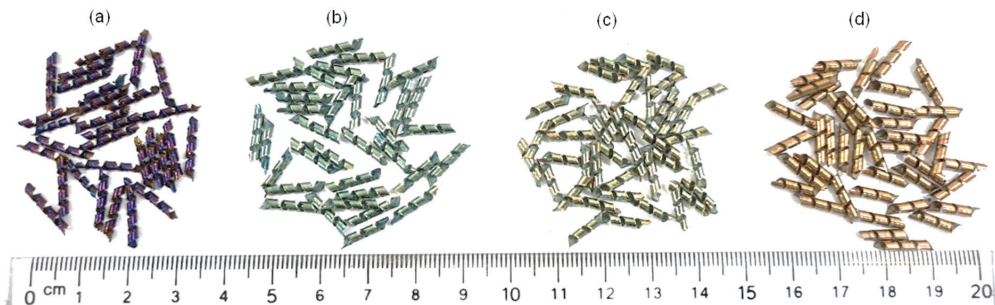
**Figure 4.** Microstructure of Material Samples at Different Temperatures: (a) Room Temperature, (b) 200 °C, (c) 300 °C, and (d) 400 °C.



**Figure 5.** Workpiece hardness after heating at different temperatures and natural air-cooling.

### 3.3. Effect of TAM on Chip Color

The geometry and morphology of chips play a crucial role in assessing the machinability of materials. Chip geometry affects cutting force, cutting heat, and tool wear, while chip morphology provides valuable insights for milling tool design. Therefore, when analyzing the impact of heating on the machinability of SKD11, examining chip formation is crucial. Figure 6 shows chip images obtained during the milling of SKD11 steel under different cutting modes and heating conditions. Figure 6a–d display chip formations during machining at various temperatures. The formation of wire chips is due to the workpiece material's ductile properties. The chip color varies significantly, with the normal machining chip appearing purple-black in color due to excessive cutting heat generated during machining at room temperature (Figure 6a). In contrast, chips appear bright white (Figure 6b) and yellow (Figure 6c) when machined at 200 °C and 300 °C, respectively. The chip appears darker yellow when machined at 400 °C (Figure 6d). This variation can be attributed to the uniform transfer of heat between the cutting tool, workpiece, and chip during heating processing. The high temperature reduces the material's tensile strength, mechanical strength, and yield stress, while increasing its deformation, improving heat transfer conditions, and decreasing the bonding force between metal molecules [19,20]. As a result, chip removal becomes easier, cutting heat is reduced, and chips appear light-colored during hot machining. The results suggest that temperatures between 200–300 °C preserve the chip color compared to the original substrate material.



**Figure 6.** Chip Formation at Different Temperatures: (a) Room Temperature, (b) 200 °C, (c) 300 °C and (d) 400 °C.

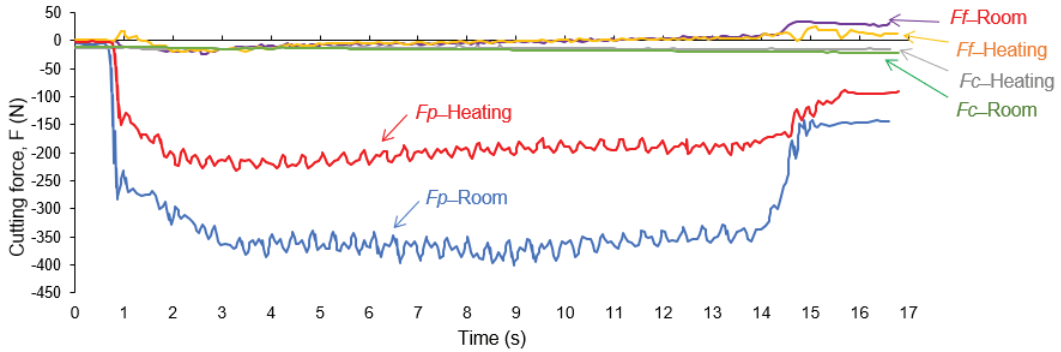
### 3.4. Effect of TAM on Cutting Force

An experimental study was conducted to investigate the effect of elevated temperature on cutting forces ( $F$ ) during milling with identical cutting parameters at room temperature and elevated temperature. The cutting force is a dynamic phenomenon and changes throughout the machining cycle [29]. Figure 7 displays the cutting force transformation with respect to tool distance during milling at room temperature (25 °C) and elevated temperature (200 °C). The cutting parameters used were a cutting speed of 235 m/min, feed rate of 305 mm/min, and cutting depth of 1.5 mm. The average cutting force ( $F$ ) was calculated from the component cutting forces ( $F_f$ ,  $F_p$ ,  $F_c$ ) using Equation (1). Table 2 shows the component cutting force values and the average cutting force under conventional machining and elevated temperature conditions. The results indicate that the  $F_p$  component cutting force (direct force) has the largest value, while the radial force ( $F_f$ ) and axial force ( $F_c$ ) have relatively smaller values. The average cutting force reduction at elevated temperature compared to conventional machining is 37.5%, as determined by Equation (2).

$$F = \sqrt{F_f^2 + F_p^2 + F_c^2} \quad (1)$$

$$\Delta F(\%) = \frac{F_T - F_R}{F_R} \times 100\% \quad (2)$$

where  $F_T$  represents the cutting force during heating and  $F_R$  represents the cutting force when machining at room temperature ( $T = 25\text{ }^\circ\text{C}$ ).



**Figure 7.** Cutting force during machining at room temperature and at elevated temperature ( $200\text{ }^\circ\text{C}$ ).

**Table 2.** Average cutting force at room and elevated temperature.

Temperature	$F_f$ (N)	$F_p$ (N)	$F_c$ (N)	$F$ (N)
Room	4.317	360.031	9.028	360.170
$200\text{ }^\circ\text{C}$	8.958	214.583	9.071	214.962

The experimental results (shown in Figure 8) indicate a significant reduction in cutting force ( $F$ ) during machining at  $200\text{ }^\circ\text{C}$  compared to conventional machining. As the heating temperature increased to  $300\text{--}400\text{ }^\circ\text{C}$ , the cutting force decreased at a slower rate. The maximum reduction in cutting force ( $\Delta F$ ) was 65.1% during milling at  $400\text{ }^\circ\text{C}$ . This reduction can be attributed to the weakening of the strength and bonding between metal molecules due to the heating process, making the cutting process easier. Moreover, in the second strain region, the compressive stress was found to decrease during heating, which led to a decrease in cutting force.

### 3.5. Effect of TAM on Surface Roughness ( $R_a$ )

The surface quality of a workpiece is critical and influenced by various factors, including the machining method, cutting tool geometry, and machining environment. Surface roughness, in particular, is essential in determining the workability and performance of the final product. This study used the average deviation criterion  $R_a$  to evaluate surface roughness. According to ISO standards,  $R_a$  is the arithmetic average of the absolute values of the profile over the reference length range ( $L = 250\text{ }\mu\text{m}$ ) for machined surfaces with a smoothness level of 8–11. The research investigated the effect of elevated temperatures on  $R_a$  during Thermal Assisted Machining (TAM) while maintaining the same cutting parameters, including speed, feed rate, and cutting depth, under various temperature conditions. The method of surface roughness measurement is shown in Figure 9a, where the measuring head moves perpendicularly to the machining trace, and each sample is measured at three locations (1, 2, 3) to ensure reliability, within the reference length range of  $250\text{ }\mu\text{m}$ , as shown in Figure 9b,c. Results indicated that heating the workpiece before machining significantly reduced surface roughness compared to conventional machining.

This is because the thermal softening of the material results in increased smoothness and stability during the cutting process.

$$\Delta Ra(\%) = \frac{Ra_R - Ra_T}{Ra_R} \times 100\% \tag{3}$$

where  $Ra_R$  and  $Ra_T$  represent the surface quality (Ra) at room and high temperature, respectively.

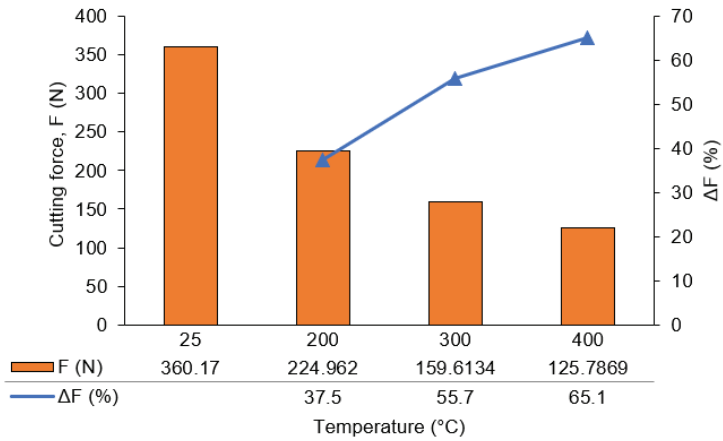


Figure 8. The mean cutting forces and the corresponding reductions observed during machining at various temperatures.

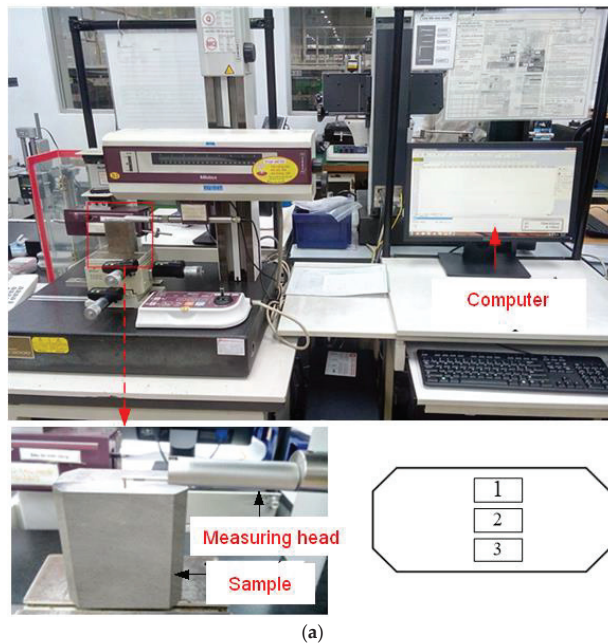
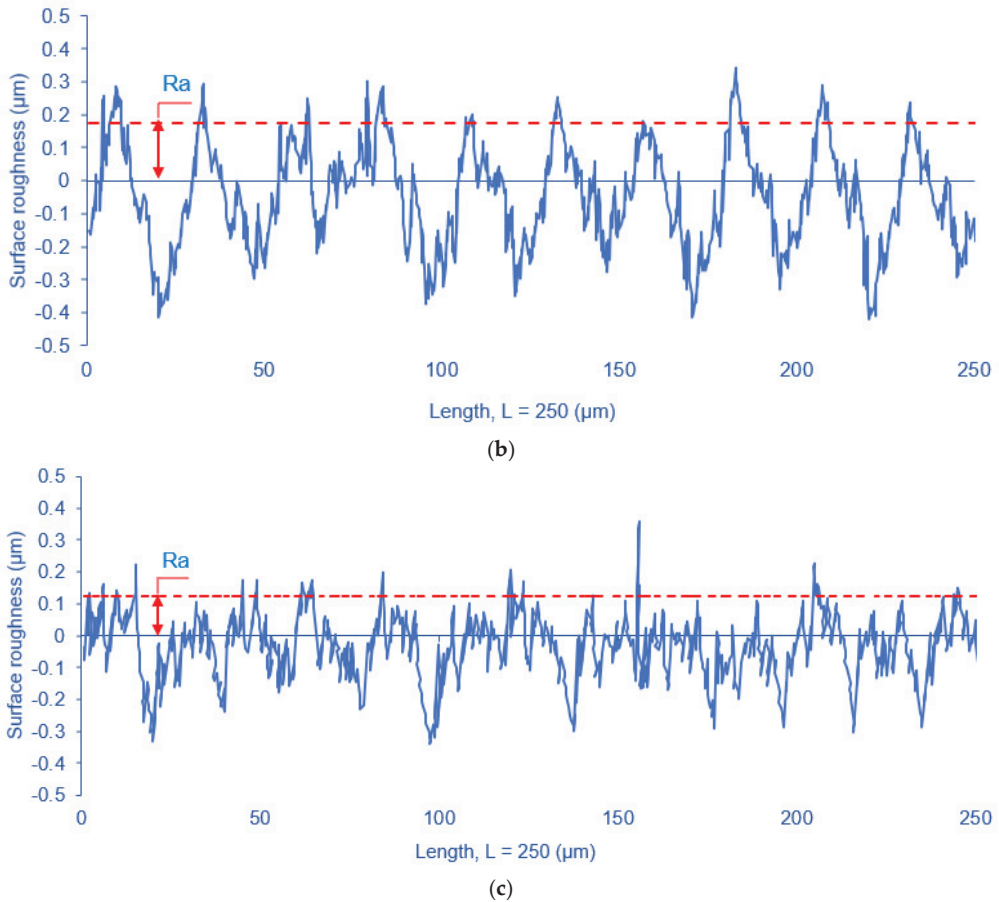


Figure 9. Cont.



**Figure 9.** Measurement of Surface Roughness with Equipment and Method (a) and Comparison of Surface Roughness Profiles for Machining at Room Temperature (b) and 200 °C (c).

In Figure 10, the average Ra values for machining at various temperatures are plotted. The decrease in Ra was calculated using Equation (3). The results indicate that there is an inverse relationship between Ra and workpiece temperature. The greatest reduction in roughness, 47.1%, was observed at 400 °C.

### 3.6. Effect of TAM on Cutting Vibration

To investigate the impact of temperature-assisted machining (TAM) on vibration, experiments were conducted using the same cutting parameters of  $V$ ,  $f$ , and  $t$  at 235 m/min, 305 mm/min, and 1.5 mm, respectively, but at various temperature conditions. The vibration amplitudes in directions of (X, Y) as ( $A_X$  and  $A_Y$ ) were summed to obtain the  $A_{XY}$  using Equation (4).

$$A_{XY} = \sqrt{A_X^2 + A_Y^2} \quad (4)$$

Figure 11 displays the vibration amplitudes at room temperature (a) and at 200 °C (b) in directions of (X, Y). The analysis of the no-load and individual vibration data did not indicate any resonance. The results showed that TAM reduced the vibration amplitude compared to conventional machining. The reduction in cutting vibration amplitude ( $\Delta A_{XY}$ )

during TAM, as compared to milling at room temperature, is calculated using Equation (5).

$$\Delta A_{XY}(\%) = \frac{A_{XY-R} - A_{XY-T}}{A_{XY-R}} \times 100\% \tag{5}$$

where  $A_{XY-R}$ ,  $A_{XY-T}$  represent the vibration amplitudes in directions of (X, Y) during machining at room and high temperature, respectively.

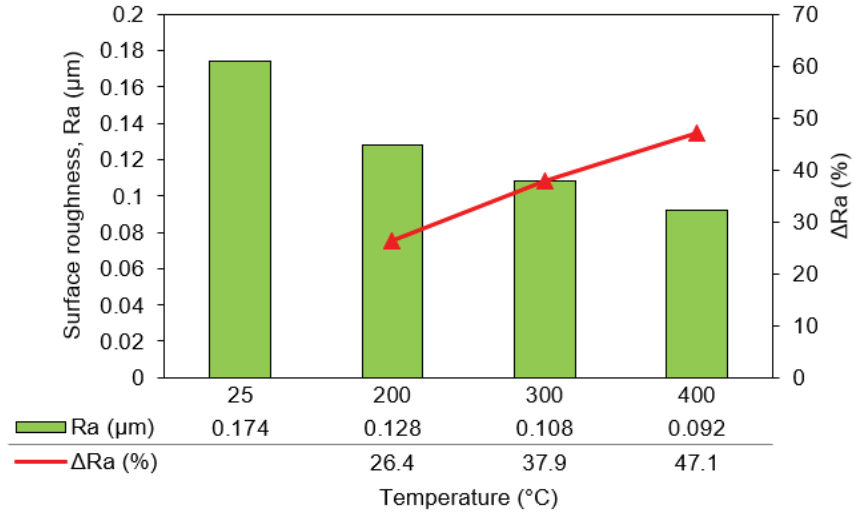


Figure 10. Surface Roughness and Reduction at Elevated Machining Temperatures.

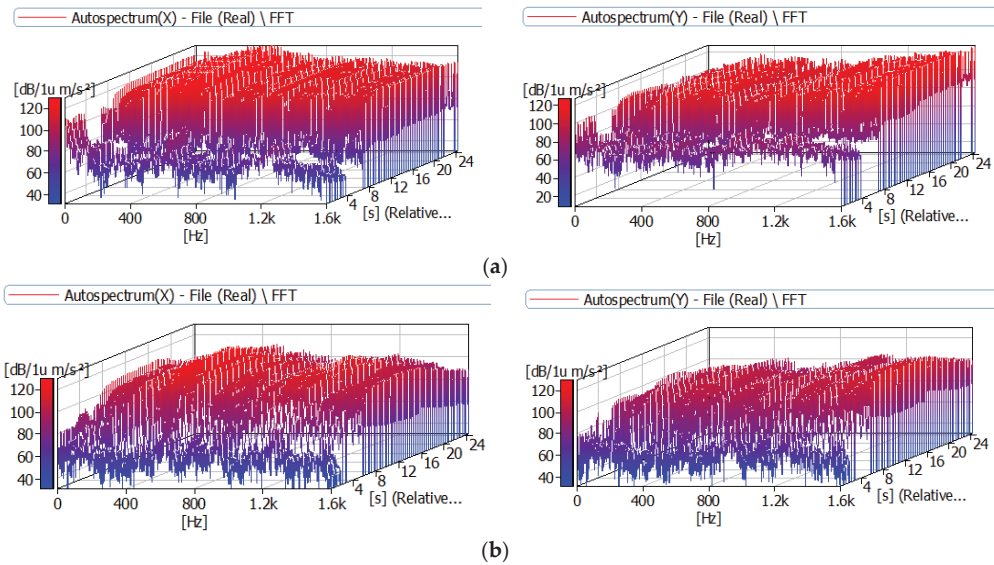
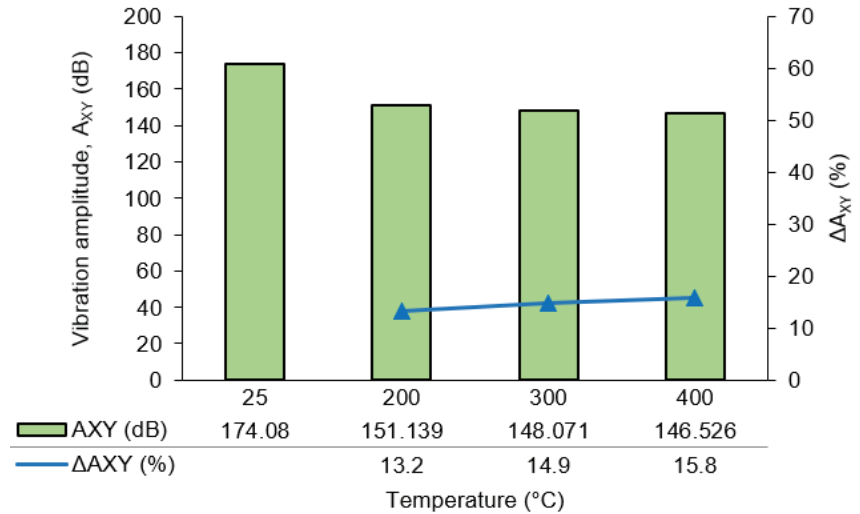


Figure 11. The vibration results at room (a) and heating at 200 °C (b) in the X and Y directions.

Figure 12 illustrates the vibration amplitude and reduction in vibration amplitude during SKD11 steel machining at various temperatures, as compared to milling at room temperature. The results indicated that  $A_{XY}$  decreased by 13.2% at 200 °C, 14.9% at

300 °C, and 15.8% at 400 °C. These findings indicate increased stability during SKD11 steel processing when conducted at higher temperatures, due to the reduction in metallic bond strength resulting in an easier cutting process. However, the reduction in vibration amplitude did not exhibit a significant change when high temperature was used to facilitate the cutting process.



**Figure 12.** Vibration amplitude and vibration amplitude reduction during machining at various temperature conditions.

### 3.7. Effect of TAM on Chip Shrinkage Coefficient ( $K$ )

$K$  is a vital parameter used to assess the plastic strain of a material during machining, and it has a significant influence on the dimensional accuracy of the machined surface. Several factors affect  $K$ , including the mechanical properties of the workpiece material, cutting tool geometry, cutting mode, and other cutting conditions. This study aims to analyze the impact of elevated temperatures on  $K$  and compare it to conventional machining under the same cutting mode. The objective is to assess the material's softening and formability at high-temperature conditions. The chip shrinkage coefficient, computed using Equation (6), is utilized to determine  $K$ .

$$K = \frac{1000 \cdot Q}{\rho \cdot L_f \cdot f \cdot t} \quad (6)$$

where  $Q$  and  $\rho$  represent the mass of chip (g) and the material density ( $\text{g}/\text{cm}^3$ ), respectively,  $L_f$  is the chip cutting length (mm), and  $f$  and  $t$  are the feed rate (mm/rev) and cutting depth (mm), respectively.

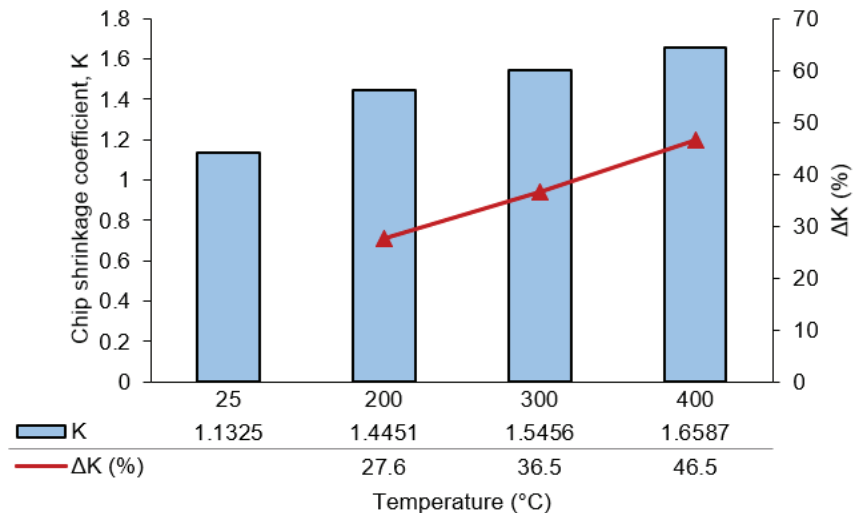
Figure 13 displays the chip shrinkage coefficient at different temperatures for the machining process conducted at cutting parameters of  $V = 235 \text{ m}/\text{min}$ ,  $f = 305 \text{ mm}/\text{min}$ , and  $t = 1.5 \text{ mm}$ . The results demonstrate that the chip shrinkage coefficient increases with heating compared to conventional machining at room temperature. The increase in  $K$ , denoted as  $\Delta K$ , is calculated using Formula (7). The chip shrinkage coefficient experiences a 27.6% increase when the workpiece is heated to 200 °C, and the maximum increase in  $K$  of 46.5% is observed at a temperature of 400 °C. This trend suggests that an increase in temperature enhances the cutting process by improving the chip shrinkage coefficient. The observed phenomenon can be attributed to the material softening under high temperatures,



resulting in weakened atomic bonds and increased metal deformation, leading to a higher chip shrinkage coefficient.

$$\Delta K(\%) = \frac{K_T - K_R}{K_R} \times 100\% \quad (7)$$

where  $K_T$  and  $K_R$  represent the chip shrinkage coefficient during heating and at room temperature ( $T = 25\text{ }^\circ\text{C}$ ), respectively.



**Figure 13.** Chip shrinkage coefficient and chip shrinkage increase during machining at various temperatures.

#### 4. Conclusions

The aim of this study was to investigate and compare the effectiveness of using electromagnetic induction heating versus conventional methods for machining SKD11 steel, a material that is difficult to cut. The study analyzed various output parameters, including chip geometry, chip shrinkage coefficient, vibration amplitude, surface roughness, and cutting force. Experimental results indicated that the TAM process did not alter the material's microscopic structure in the temperature range of 200 °C to 400 °C, and the machined workpiece, cooled in air, maintained its original hardness. Additionally, the chip geometry changed and cutting force significantly decreased, with a maximum reduction of 65.1%. The  $K$  value increased by 31.7%, while surface roughness decreased notably, with a maximum reduction of 47.1% at 400 °C. Lower vibration amplitude also indicated a more stable machining process compared to traditional methods. These findings demonstrate the potential of this method to enhance machining performance and contribute to the development of high-precision and high-efficiency machining processes for difficult-to-cut materials.

**Author Contributions:** Conceptualization, D.-T.N.; Data curation, T.-B.M.; Formal analysis, D.-T.N.; Funding acquisition, T.-T.L.; Investigation, T.-T.L.; Methodology, D.-T.N.; Project administration, T.-B.M.; Resources, T.-B.M.; Software, T.-T.L.; Supervision, D.-T.N.; Validation, D.-T.N.; Visualization, D.-T.N.; Writing—original draft, T.-B.M.; Writing—review & editing, D.-T.N., T.-B.M. All authors have read and agreed to the published version of the manuscript.

**Funding:** This work was supported by Vietnam Ministry of Education and Training (MOET) under grant number B2022-BKA-08.

**Acknowledgments:** This work was supported by the Vietnam Ministry of Education and Training (MOET) under grant number B2022-BKA-08.

**Conflicts of Interest:** The authors declare no conflict of interest.

## References

- Irving, A.D.; Clarence, L.M.; Russell, F.H. *High Temperature Machining Methods*; Armed Services Technical Information Agency, Arlington Hall Station: Arlington, VA, USA, 1963.
- Rajput, M. CFD Modelling of Hot Machining Operation. Ph.D. Thesis, National Institute of Technology Rourkela, Rourkela, Orissa, India, 2010.
- Makwana, R.; Prajapati, H. Experimental Investigation on Effect of Machining Parameters on Surface Roughness in Thermally Assisted Turning of mild steel. In Proceedings of the International Conference on Multidisciplinary Research & Practice, Ahmedabad, India, 30 November 2014; Volume 1, pp. 488–489.
- Harpreet, E.M.G.S.; Sharma, E. Analysis of Surface Roughness and Material Removal Rate in Dry and Thermal Assisted Machining of EN8 Steel. *Int. J. Eng. Sci. Res. Technol.* **2015**, *4*, 577–583.
- Baili, M.; Wagner, V.; Dessein, G.; Sallaberry, J.; Lallement, D. An Experimental Investigation of Hot Machining with Induction to Improve Ti-5553 Machinability. *Appl. Mech. Mater.* **2011**, *62*, 67–76. [[CrossRef](#)]
- Rahim, E.A.; Warap, N.; Mohid, Z. Thermal-assisted machining of nickel-based alloy. In *Superalloys*; IntechOpen: London, UK, 2015; pp. 3–29.
- Pimenov, D.Y.; Mia, M.; Gupta, M.K.; Machado, R.A.; Pintaude, G.; Unune, D.R.; Khanna, N.; Khan, A.M.; Tomaz, I.; Wojciechowski, S.; et al. Resource saving by optimization and machining environments for sustainable manufacturing: A review and future prospects. *Renew. Sustain. Energy Rev.* **2022**, *166*, 112660. [[CrossRef](#)]
- Barewar, S.D.; Kotwani, A.; Chougule, S.S.; Unune, D.R. Investigating a novel Ag/ZnO based hybrid nanofluid for sustainable machining of inconel 718 under nanofluid based minimum quantity lubrication. *J. Manuf. Process.* **2021**, *66*, 313–324. [[CrossRef](#)]
- Unune, D.R.; Mali, H.S. Current status and applications of hybrid micro-machining processes: A review. *Proc. Inst. Mech. Eng. Part B J. Eng. Manuf.* **2014**, *229*, 1681–1693. [[CrossRef](#)]
- Xavierarockiaraj, S.; Kuppan, P. Investigation of cutting forces, surface roughness and tool wear during Laser assisted machining of SKD11 Tool steel. *Procedia Eng.* **2014**, *97*, 1657–1666. [[CrossRef](#)]
- Thi-Bich, M.; Van-Chien, D.; Tien-Long, B.; Duc-Toan, N. Cutting Force Model for Thermal-Assisted Machining of Tool Steel Based on the Taguchi Method. *Metals* **2018**, *8*, 992. [[CrossRef](#)]
- Mac, T.-B.; Banh, T.-L.; Nguyen, D.-T. Study on cutting force and chip shrinkage coefficient during thermal-Assisted machining by induction heating of SKD11 steel. *J. Korean Soc. Precis. Eng.* **2019**, *36*, 803–811. [[CrossRef](#)]
- Mac, T.-B.; Luyen, T.-T.; Nguyen, D.-T. A Study for Improved Prediction of the Cutting Force and Chip Shrinkage Coefficient during the SKD11 Alloy Steel Milling. *Machines* **2022**, *2022*, 229. [[CrossRef](#)]
- Thanh-Huan, N.; Duc-Toan, N. Experimental Researches of Turning Hardened 9CrSi Alloy Tool Steel with Laser-Assisted Machining. *Arab. J. Sci. Eng.* **2021**, *46*, 11725–11738. [[CrossRef](#)]
- Dong, T.P.; Toan, N.D. A study on the investigation of the microstructure of SKD61 steel after selected quenching and tempering processes. *Mod. Phys. Lett. B* **2023**, 2340022. [[CrossRef](#)]
- Ginta, T.L.; Amin, A.K.M.N. Thermally-Assisted End Milling of Titanium Alloy Ti-6Al-4V Using Induction Heating. *Int. J. Mach. Mach. Mater.* **2013**, *14*, 194–212. [[CrossRef](#)]
- Wang, Y.; Ding, C.; Tang, F.; Zheng, D.; Li, L.; Xie, S. Modeling and simulation of the high-speed milling of hardened steel SKD11 (62 HRC) based on SHPB technology. *Int. J. Mach. Tools Manuf.* **2016**, *108*, 13–26. [[CrossRef](#)]
- Wang, Z.Y.; Rajurkar, K.P.; Fan, J.; Lei, S.; Shin, Y.C.; Petrescu, G. Hybrid machining of Inconel 718. *Int. J. Mach. Tools Manuf.* **2003**, *43*, 1391–1396. [[CrossRef](#)]
- Dong, T.; Toan, N.; Dung, N. Influence of heat treatment process on the hardness and material structure of SKD61 tool steel. *Mod. Phys. Lett. B* **2023**, 2340014. [[CrossRef](#)]
- Mruthunjaya, M.; Yogesha, K.B. A review on conventional and thermal assisted machining of titanium based alloy. *Mater. Today Proc.* **2021**, *46*, 8466–8472. [[CrossRef](#)]
- Sun, S.; Brandt, M.; Dargusch, M.S. Thermally enhanced machining of hard-to-Machine materials—A review. *Int. J. Mach. Tools Manuf.* **2010**, *50*, 663–680. [[CrossRef](#)]
- Maitya, K.; Swain, P. An experimental investigation of hot-machining to predict tool life. *J. Mater. Process. Technol.* **2008**, *198*, 344–349. [[CrossRef](#)]
- Germain, G.; Lebrun, J.-L.; Robert, P.; Santo, P.; Poitou, A. Experimental and numerical approaches of laser assisted turning. *Int. J. Form. Process.* **2005**, *8*, 347–361.
- Jeon, Y.; Pfefferkorn, F. Effect of laser preheating the workpiece on micro end milling of metals. *J. Manuf. Sci. Eng. Trans. ASME* **2008**, *130*, 1–9. [[CrossRef](#)]
- Dumitrescu, P.; Koshy, P.; Stenekes, J.; Elbestawi, M. High-power diode laser assisted hard turning of AISI D2 tool steel. *Int. J. Mach. Tools. Manuf.* **2006**, *46*, 2009–2016. [[CrossRef](#)]
- Kannatey-Asibu, E. *Principles of Laser Materials Processing*; John Wiley & Sons, Inc.: Hoboken, NJ, USA, 2009.
- Wang, C.; Xie, Y.; Zheng, L.; Qin, Z.; Tang, D.; Song, Y. Research on the Chip Formation Mechanism during the high-speed milling of hardened steel. *Int. J. Mach. Tools Manuf.* **2014**, *79*, 31–48. [[CrossRef](#)]
- Rudnev, V.; Love30less, D.; Cook, R.; Black, M. *Handbook of Induction Heating*; Marcel Dekker: New York, NY, USA, 2003.

29. Thi-Hoa, P.; Thi-Bich, M.; Van-Canh, T.; Tien-Long, B.; Duc-Toan, N. A study on the cutting force and chip shrinkage coefficient in high-speed milling of A6061 aluminum alloy. *Int. J. Adv. Manuf. Technol.* **2017**, *98*, 177–188. [[CrossRef](#)]

**Disclaimer/Publisher’s Note:** The statements, opinions and data contained in all publications are solely those of the individual author(s) and contributor(s) and not of MDPI and/or the editor(s). MDPI and/or the editor(s) disclaim responsibility for any injury to people or property resulting from any ideas, methods, instructions or products referred to in the content.

Article

# Effect of Wear on Vibration Amplitude and Chip Shape Characteristics during Machining of Eco-Friendly and Leaded Brass Alloys

Peter Pavol Monka<sup>1,2</sup>, Katarina Monkova<sup>1,2,\*</sup>, George A. Pantazopoulos<sup>3,\*</sup> and Anagnostis I. Toulfatzis<sup>3</sup>

<sup>1</sup> Faculty of Manufacturing Technologies, Technical University in Kosice, Sturova 31, 080 01 Presov, Slovakia; peter.pavol.monka@tuke.sk

<sup>2</sup> Faculty of Technology, Tomas Bata University in Zlin, Nam. T.G. Masaryka 275, 760 01 Zlin, Czech Republic

<sup>3</sup> ELKEME Hellenic Research Centre for Metals S.A., 61st km Athens—Lamia National Road, 32011 Oinofyta, Greece; atoulfatzis@elkeme.vionet.gr

\* Correspondence: katarina.monkova@tuke.sk (K.M.); gpantaz@elkeme.vionet.gr (G.A.P.)

**Abstract:** The dynamic stability of the machining set and the entire cutting process, together with the appropriate form of chips generated during machining under the given conditions, are the basic prerequisites for autonomous machining in accordance with the Industry 4.0 trend. The research, based on a newly designed method, aims to study the frequency response of the machining system to different values of tool wear and cutting speed, which cause the worsening of the machined parts' quality and the instability of the whole cutting process. The new idea is based on the inverse principle, in which the wear with various values of VB was artificially prepared in advance before machining. Consequently, the effect of artificial wear and cutting speed on vibration and chip shape characteristics were studied. Three types of brass alloys were used within the experiments as the machined materials. Measured data were statistically processed and the desired dependencies were plotted. Chips were collected for each combination of machining conditions, while the article presents a database of the obtained chip shapes at individual cutting speeds so that they can be compared and classified. The results showed that brass alloys CW510L and CW614N exhibit an average of three times lower vibration damping compared to the CW724R alloy, while relatively good chip formation was noted in the evaluated machining conditions even without the use of a chip breaker. The problematic chip shape occurred only in some cases at the machining of CW510L and CW724R, which cannot be generalized.

**Keywords:** artificial wear; vibration response; brass alloys; machining process; chip form

**Citation:** Monka, P.P.; Monkova, K.; Pantazopoulos, G.A.; Toulfatzis, A.I. Effect of Wear on Vibration Amplitude and Chip Shape Characteristics during Machining of Eco-Friendly and Leaded Brass Alloys. *Metals* **2023**, *13*, 828. <https://doi.org/10.3390/met13050828>

Academic Editor: Yadir Torres Hernández

Received: 31 March 2023

Revised: 18 April 2023

Accepted: 20 April 2023

Published: 23 April 2023



**Copyright:** © 2023 by the authors. Licensee MDPI, Basel, Switzerland. This article is an open access article distributed under the terms and conditions of the Creative Commons Attribution (CC BY) license (<https://creativecommons.org/licenses/by/4.0/>).

## 1. Introduction

Material removal has been a significant set of operations in production since the beginning of the Industrial Revolution. Its importance is highlighted by the significant contribution of machining to the development of the industry by enabling the development of new, more precise and efficient technological solutions. This field includes concentrated knowledge in a wide range of expertise—physical laws, chemistry, mathematics, material sciences, technical sciences, economic disciplines, environmental research, and many others.

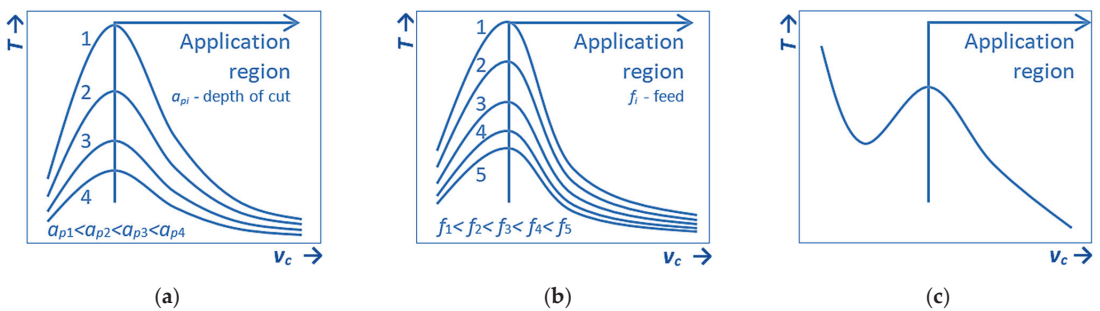
Cutting off the material rate (measured by the machined volume over time) and durability of the cutting tool (represented by the duration of its work) are considered the most important results of the cutting process [1–3].

The results of the cutting process are directly influenced by machining environment variation, while the most important factors are [1]: Cutting tool; Workpiece; Machine Tool; Technological Process; and Technological Settings.

Following the rules of economic efficiency, ecological reform demands, societal regulations, and high demands for constant refinement of production (micro and nano dimensions), the complexities of the above factors unite in a significant way. Therefore, the

integrity of modern machining systems requires a very precise and demanding design and formulation with optimization for the given production conditions [4,5].

In the finally determined production system (given mainly by the product, machine tool, cutting tool, and process), only cutting factors can be used for the optimization of efficiency and productivity (durability of cutting tool and material removal rate). Generally, the basic cutting factors are depth of cut, feed, and cutting speed. However, the depth of cut can be a factor related to machining efficiency that increases only in the case of small series and piece production if it is not possible to provide material with dimensions and shapes close to the manufactured product. In that case, it is an operation with an inefficient use of input material, and such a production method would need to be optimized for the application of more economical technologies. Therefore, it is not assumed that this factor will be used for optimization. The general effect of depth of cut  $a_p$  on durability  $T$  is shown in Figure 1a [1,6].

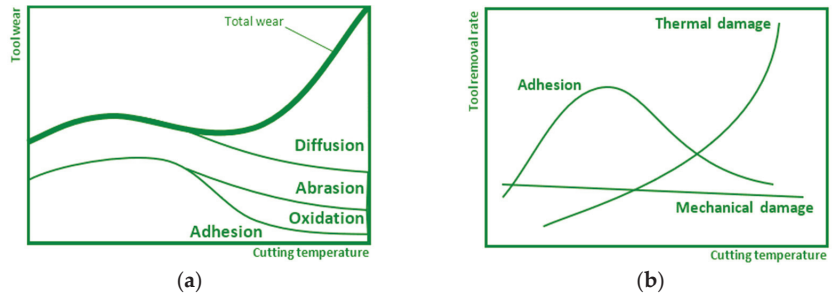


**Figure 1.** Influence of cutting parameters on tool life: (a)  $a_p$ —depth of cut, (b)  $f$ —feed, (c)  $v_c$ —cutting speed.

Feed rate linearly affects productivity. However, its speed is limited by the required quality parameters of the final surfaces, and therefore the value of this speed cannot be increased without special solutions, e.g., smoothing geometry of the cutting tool, etc. The general effect of feed  $f$  on durability  $T$  is shown in Figure 1b [1].

Cutting speed affects machining productivity in a linear relationship, but tool life, expressed by cutting ability, is degraded exponentially. The relationship between these two physical regularities of the cutting tool is determined by the kinematics of the machine tool and the events (both physical and chemical) in contact between the tool and the machined material. The general effect of cutting speed  $v_c$  on durability  $T$  is documented in Figure 1c. This dependence shows the region appropriate for the good relationship of cutting speed and durability of the tool [1,7,8].

The next important parameter that enters the machining process is temperature. The general regularities of the influence of the temperature reached at the point of the cut on the nonlinearity of the course of the investigated factors are shown in Figure 2. The temperature mainly depends on the type of machined material, the rate of deformation in shear volume, the friction conditions on the front and back plane of the tool, and the cooling characteristics of the process. All these physical factors are also influenced by variations in other factors of the machining environment, as mentioned above.

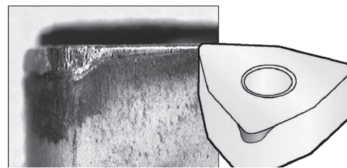


**Figure 2.** Regularities of the (a) cutting tool degradation and (b) removal rate—depending on the temperature at the point of the cut.

The dependence of the achieved wear limit on the cutting speed is also a very important regulator of machining. The wear limit is the maximum value of admissible degradation of the cutting edge, at which the admissible quality characteristic of the work-piece surface by machining can still be achieved [9,10]. In the given conditions, wear of the flank or face on the cutting tool depends not only on the type of machined material but also on the proportion between feed and cutting speed. The dimensions of worn parts of the tool are usually specified by [11]:

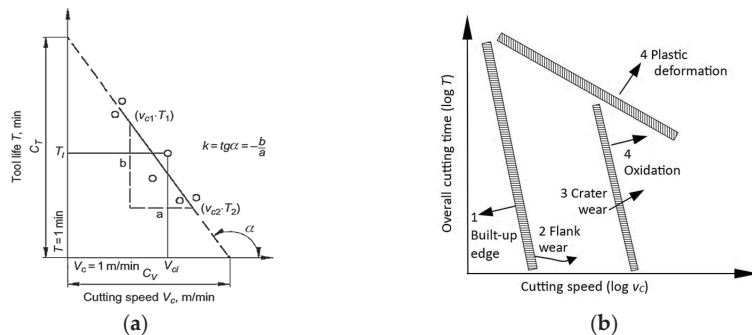
- VB—width of the wear area on the flank;
- KT—depth of wear groove on the face;
- KVs—wear of the tool corner by wear.

An effective machining process requires controlling and checking the tool’s wear propagation. The best way of the wear propagation is uniform flank wear of the cutting insert as shown in Figure 3.



**Figure 3.** Optimal wear of the cutting tool—uniform flank wear.

Tool wear is closely related to tool durability since it directly affects the tool’s durability and life. Figure 4 presents the dependence of the decrease in durability on the cutting speed for the determined wear limit and the area of degradation effects as a function of the overall cutting time  $T$  on the cutting speed  $v_c$  in logarithmic coordinates [12,13].



**Figure 4.** (a) Taylor tool-life curve, (log-log scale); (b) The wear and failure criteria for carbide inserts.

Following the above it can be said that the joint action of a group of factors in the production system (tools and tool materials, tool geometry, tool coating, and procedural media), as well as groups of process factors (cutting speed, depth of cut, and feed) creates the resulting heat generation and degradation indices of the tool. The intensity of abrasion appears to be a relationship between a combination of processed material and cutting tool, and in terms of the dependence of the tool wear on the achieved cutting temperature, it shows quasi-static characteristics. The adhesion intensity slowly increases as the cutting temperature increases and gradually decreases when the temperature of the diffusion and oxidation processes is reached. The oxidation intensity begins to develop after critical cutting temperatures and its magnitude stabilizes when the maximum saturation is reached. The intensity of the diffusion processes is imperceptible at low cutting temperatures and increases very progressively when the critical cutting temperature is reached.

Several studies have already dealt with machining process monitoring in which the influence of cutting conditions on the machining set and system stability was investigated. Dimla [14] identified that time domain features were deemed to be more sensitive to cutting conditions than tool wear, whereas frequency-based features correlated well with the tool wear and measured wear values correlated well with certain resonant peak frequencies. Chuangwen [15] obtained results for 022Cr17Ni12Mo2 stainless steel where the root-mean-square value of vibration acceleration signals increased with wear progression in general. Bouhalais [16] confirmed a good match between high-frequency vibration components' energy values and tool wear monitoring. Sridhar [17] found ten times larger vibration amplitudes of a worn drill compared to a sharp one. Babu [18] found that the correlation of experimentally measured tool wear with tool acceleration is practically feasible for real-time flank wear prediction at any time. Antic [19] noted that most research studies on the development of tool wear monitoring systems focus on the type of machining and the machining process to which they are applicable. The types and types of input signals, methods and techniques of signal processing and feature extraction are not primarily considered. This approach limits the scope of the investigation. Data processing of the instrument monitoring system proposed by Anticom includes these steps: signal acquisition and processing; data classification by grouping into an input function; and definition of tool wear status [19].

The study of the effect of conditions on the machining process and the durability of the tool can generally be carried out by tests categorized into two groups: short-term and long-term tests. Short-term durability tests are more commonly used in practice because of shorter time and less amount of processed material, but also for efficiency and economy. This testing is employed usually as the first step in checking the material of a workpiece or as a quick comparison of the durability of the examined cutting tools with a standardized etalon [20]. The principle of the short-term test, in which the material is removed by facing, consists in machining a workpiece with a relatively large diameter ( $D_{max}$  is about 300 mm). The material is removed in the radial direction, i.e., from a pre-drilled coaxial hole in the center of the workpiece towards the edge of the disc. This means that the cutting speed gradually increases, and, at a specific  $D_n$  diameter, the cutting speed reaches the maximum  $v_n$  value at which the ability to cut the material is lost. Pastucha et al. [21] have proposed a prospective variant to a short-term test, which is based on discontinuous cutting thus leading to higher intensity of tool wear to make this method more effective. In this method, the workpiece is radially placed on a large-diameter disk, while the cutting tool removes the material from the workpiece in circular segments.

However, the short-term tests described above also have their weaknesses. Except for certain short-term tests where the cutting speed is not constant, making it difficult to evaluate the effect of cutting speed on tool wear, such types of tests are not applicable when the workpieces with a larger diameter are for various reasons unavailable, or the turning machine does not allow workpieces with such a large diameter to be clamped.

These disadvantages were taken into account in the present study, and in order to eliminate them, the authors proposed a new methodology for investigating the appearance

of tool wear that can be considered a novelty and a contribution of the authors to the scientific field. Since the dynamic stability of the machining set and the entire cutting process, together with the appropriate form of chips generated during machining under the given conditions, are the basic prerequisites for autonomous machining in accordance with the Industry 4.0 trend, it is, therefore, important to deal with this issue.

Manufacturing within Industry 4.0 is planned and programmed to perform tasks with minimal human intervention, with autonomous manufacturing equipment varying greatly in size and function, from drone inventory scanning to autonomous mobile robots for pick and place operations. Equipped with cutting-edge software, artificial intelligence, sensors and machine vision, the devices are capable of performing demanding and delicate tasks. They should be able to recognize, analyze, and act on the information they receive from their surroundings. It is very important to ensure that the manufacturing machines work smoothly and that the impact of external conditions causing problems was eliminated where possible. A number of such problems can be caused by inappropriate chip shaping. Too short chips cause intermittent machining, which leads to micro-cracks on the cutting edge and shortens the tool life. In terms of life, long chips are slightly more favorable. Long, smooth-shaped chips show less micro-vibration when machining, which contributes to improving the quality of the machined surface. For the cutting process itself, however, long chips are also not suitable. Long chips can cause the cutting tool to become tangled and lose its ability to cut. They may damage the machine tool, workpiece, and cutting tool, and induce dangerous working conditions for operators. They can also cause problems with jamming in the conveyor and outages in operation. Thus, inappropriate chip problems can cause the cutting process not to be autonomous and will therefore not be suitable for inclusion in the automated process.

Based on these trends in the automation of production processes and their requirements, the present research focused on knowing the frequency response of the system for various tool wear values, resulting in deterioration of the quality of the processed parts and unsteadiness of the whole cutting operation. Understanding and knowledge of the behavior trend of vibration characteristics allow not only setting the most suitable technological conditions for machining the given material and thus increasing the tool life but also comparing the durability of the tool when machining selected brass alloys. The new idea is based on the inverse principle, at which the wear with various values of VB was artificially prepared before machining. Consequently, the effect of artificial wear and cutting speed on vibration and chip shape characteristics were studied. The combination of the studied parameters and the designed methodology that removes the disadvantages of the traditional short-term tests is unique, so this approach can be considered a novelty and the authors' contribution to the research area.

## 2. Materials and Methods

### 2.1. Machined Materials

Two types of eco-friendly (CW510L and CW724R) and one conventional standard (CW614N) brass alloy were selected as the material to be machined in this study.

Brass alloys are generally characterized by high thermal and electrical properties and conductivity as well as excellent antibacterial properties. Therefore, they are widely used in various industries such as electrical and electronic, automotive, and sanitary. Due to a large number of cutting operations in the production of brass components, various alloying elements improving machinability are usually added to brass. The most important element in this context is lead, which improves machinability due to excellent chip breaking, low tool wear and high usable cutting parameters. These aspects can be explained by two basic phenomena. First, the solubility of lead in brass is very low, and consequently, lead segregation occurs throughout the microstructure, especially at the grain boundaries. This will significantly reduce shear strength, resulting in very good chip breaking. Second, lead exhibits a low melting point  $T_m = 327.5$  °C. During cutting, lead decreases the chip



ductility while a thin, semi-liquid lead film reduces friction and thus cutting forces and tool wear [22–25].

However, since Pb is currently a strongly regulated substance due to environmental and medical concerns, its substitution is of primary importance. Stavroulakis [26] and his team have proposed four directions for further applied research to optimize the design and processing of alloys without lead so as to overcome the characteristics and functionality of conventional lead brass, which meet the requirements of environmental protection, human health and sustainable development.

Brass alloy CW614N is the standard leaded alloy for free cutting purposes, while CW510L and CW724R are lead-free brasses with good machinability, belonging to the group of so-called eco-friendly brass alloys since, for both environmental and health reasons, the reduction of lead in brass parts has great importance [27,28]. The basic characteristics of the brass alloys used in the study are given in Table 1 [29–31] and chemical compositions are given in Table 2 [32,33].

**Table 1.** Basic characteristics of machined brass alloys data from [29–31].

Characteristic	Unit	CW510L (Material 1)	CW614N (Material 2)	CW724R (Material 3)
Tensile strength $R_m$	(MPa)	478–484 [25] 220–500 [28] *	456 [25] 360–500 [28] *	654 [25] 500–670 [28] *
Yield strength $R_{p0.2}$	(MPa)	310–315 [25]	324 [25]	400 [25]
Hardness	HB	134–157 [25]	154 [25]	210 [25]
		90–160 [28] *	90–160 [10] *	130–220 [28] *
Elongation to break A	(%)	25–29 [25]	26 [25]	21 [25]
		5–20 [28] *	5–20 [28] *	10–15 [28] *
Thermal conductivity $\lambda$	(W/mK)	113–139 [25]	123 [25]	35 [25]
		139 [28]	113 [28]	35 [28]

\* Depending on the method of production.

**Table 2.** Indicative chemical compositions of machined brass alloys (wt%) data from [32,33].

	Cu	Zn	Pb	Si	As	P
CW510L (Material 1)	57.38	42	0.07	-	-	-
CW614N (Material 2)	57.61	39	3.32	-	-	-
CW724R (Material 3)	75.86	21	0.02	3.4	-	0.05

The presence of lead (Pb) in conventional leaded brasses (typical composition range ~2.5–3.5 wt%) favors machinability and machining operations, since it results in chip fracturing, enhances lubrication and reduces cutting force minimizing tool wear, see for instance [23,26,32]. It can therefore be said that when replacing the original (leaded) brass with environmentally friendly brass alloys, the conditions of machining deteriorate (due to a decreasing amount of lead), which can virtually directly reduce the productivity of the machining process by reducing technological factors (especially cutting speed and feed) to ensure the required qualitative factors (surface roughness, dimensions) and the efficiency of the process (durability of the cutting tool).

The workpiece was provided in the form of rods with a diameter of 35 mm and a length of 400 mm (Figure 5a). The bar was clamped with a maximum overhang of 200 mm to maintain the required rigidity and before measurements, it was finely machined to a diameter of 34.6 mm. The machined bar after experimental testing is shown in Figure 5b.

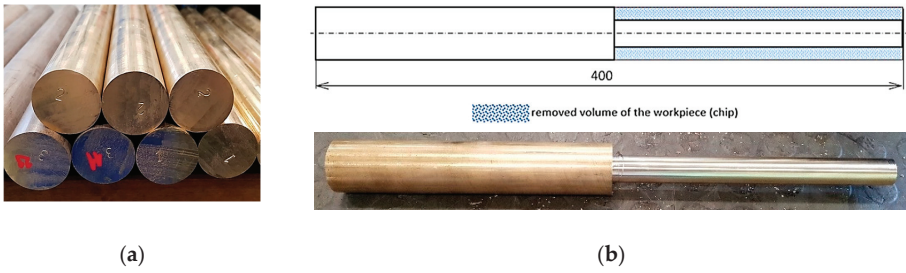


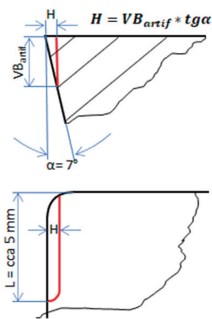
Figure 5. Workpiece (a) rods provided by the supplier; (b) machined part.

2.2. Machining Process Using the Newly Designed Artificial Wear Methodology

A newly designed methodology was used for the machining of brass alloys based on artificial wear to find out the response of the cutting tool and the whole system to machining under given conditions. The approach was selected because of the existing settings, which were mainly connected to the small diameter of the supplied bars. A diameter of 35 mm is not suitable for long-term testing as it does not enable reaching the desired cutting speed, and when the diameter of the workpiece is becoming smaller, the stiffness of the bar reduces very quickly [33–35].

A total of 80 pieces of cutting inserts were specially modified by the experienced supplier, while the artificial tool wear  $VB_{artif}$  was created only on the major flank of the tool. A tool wear  $VB$  was chosen as the most important factor affecting the quality of the machined surface and the dimensional accuracy of the machined component. The values of artificial wear within the experiments were selected in a geometric series so that they could capture critical values and which are reflected in vibrations. From the point of view of the machined surface,  $VB = 0.4$  mm wear is considered critical during finishing. In the experiment, this range was doubled to better understand the behavior of the machining system and its responses to machining with a worn tool.

At every new test, a cutting tip with a new cutting wedge was used, so one cutting insert was active for four experiments (with different corners). The geometry of created artificial wear  $VB_{artif}$ , as well as the values of the  $VB_{artif}$  (mm) and grinding depth  $H$  (mm) for the individual cutting inserts, are shown in Figure 6a, while prepared cutting inserts are shown in Figure 6b.



Cutting insert designation	$VB_{artif}$ (mm)	$H$ (mm)
T01...T10	0.000	0.000
T11...T20	0.050	0.006
T21...T30	0.080	0.010
T31...T40	0.128	0.016
T41...T50	0.205	0.025
T51...T60	0.328	0.040
T61...T70	0.524	0.064
T71...T80	0.839	0.103



Figure 6. (a) Geometrical and dimensional characteristics of artificial wear; (b) Cutting inserts with prepared artificial wear.

Durability evaluation, with a constant cutting depth  $a_p = 1$  mm, constant feed  $f = 0.06$  mm, and cutting speeds  $v_c = 100, 150, 225,$  and  $337.5$  m/min, was realized according to the relation of diameters to the artificial wears listed in Table 3.

**Table 3.** Relation of artificial wear and the workpiece diameters used in machining.

Range of the Workpiece Diameters (mm)	$VB_{\text{artif}}$ (mm)
34.6–32.6	0.84
32.6–30.6	0.52
30.6–28.6	0.33
28.6–26.6	0.21
26.6–24.6	0.13
24.6–22.6	0.08
22.6–20.6	0.05
20.6–18.6	0.00

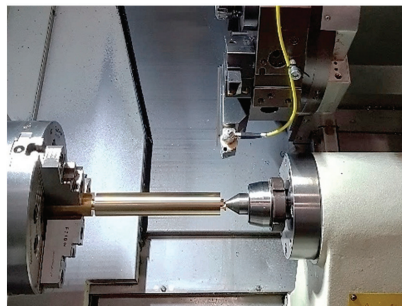
As is seen from Table 3, the tool with the highest wear (0.84 mm) was used for turning the workpiece with the largest diameter (34.6 mm) and the tool with a sharp wedge was used for machining the smallest considered diameter (20.6 mm) to ensure the best possible degree of stability.

ISO 3685 recommendations were used for the maximum extent of geometric and dimensional characteristics of the cutting tool, including working conditions as the basis for settings, given that a similar standard for turning brass alloys with single-point turning tools is not available. The cutting tool consists of a cutting insert (type SCGW 12T304 K10) and a tool holder (type SSBCR 2525 M 12-M-A); the basic characteristics are shown in Table 4. On every machined surface, a new corner of a cutting insert was used.

**Table 4.** Geometrical and dimensional characteristics of the cutting tool.

Geometrical and Dimensional Characteristic	Value
Cutting insert	
Rake angle $\gamma$	$0^\circ$
Clearance angle $\alpha$	$7^\circ$
Cutting edge inclination angle $\lambda_s$	$0^\circ$
Tool cutting edge angle $\kappa_r$	$75^\circ$
Tool included angle $\varepsilon_r$	$90^\circ$
Corner radius $r_\epsilon$	0.4 mm
Tool holder	
Tool cross-section	$25 \times 25$ mm
Insert shape	Square
Insert size	12.7 mm
Insert thickness	3.18 mm

The universal CNC turning machine DMG MORI ecoTurn 450 was used for experiments. A three-jaw chuck and a rotational tailstock were used for the workpiece clamping and supporting as shown in Figure 7.

**Figure 7.** Positions of the individual items of the machining set.

### 2.3. Measurement and Evaluation of Vibration Intensity

A very important accompanying factor of machining is the generation of vibrations. Machining vibrations are forced and self-excited in general. For the safety of the process and the quality of its outputs, it is necessary to monitor self-excited vibrations [36,37].

The self-excitation mechanism in the chip generation during cutting contributes significantly to the characteristic vibrational spectrum of the entire process. Chipping can cause the edge fracture of the machining tool, impairing cutting-edge sharpness and leading to tool blunting. This type of tool failure increased cutting forces, resulting therefore in further degradation of the machining performance (longer chips, higher fluctuations and chattering, part distortion), causing serious defects in the machined surface quality [38–40]. The friction on surfaces between the tool and machined material generated a dynamically discontinuous process. Tool wear significantly affects these friction-induced nonlinear vibrations and can be observed through the vibration characteristics of new and worn cutting tools. The evolution of the vibration characteristics can be used for the tool wear progress monitoring, too [41–43].

The advantage of installing a system for collecting and evaluating the vibration characteristics of the machining system for monitoring the tool wear process is that it only minimally interferes with the construction of the machine tool and the cutting tool, the monitoring takes place in real time, and this system can also be used to identify the condition of the machine tool.

The assessment of experiments focused on the vibration response analysis was performed in the complex system (Machine tool—Cutting tool—Fixture—Workpiece), therefore the vibration characteristics of the process were examined over a wide range of frequencies (0–25 kHz).

The acceleration sensor Wilcoxon Research WR-712F-M4 was fixed on the bottom of the tool holder, on the opposite side as a cutting insert was attached. The location of the sensor was selected as close as possible to the cutting edge and at the same time in such a way that it was protected from being attacked by chips. A National Instruments PXI-4462 measurement card and LabView software were used to collect and analyze vibration data [44].

An example of a vibro-diagnostics signal in the time domain obtained for one minute of a running machining process is shown in Figure 8. Signals obtained by all measurements were analyzed by the Fast Fourier Transformation (FFT) method. Figure 9 shows the same signal as in Figure 8 but is processed using Fast Fourier Transform (FFT) to observe the measured amplitudes in the frequency domain.

The frequencies at which the peaks occurred are the so-called natural frequencies (indicated in Figure 9 with red crosses). These correspond to the resonant frequencies of the individual elements of the complex machining set, which can seriously influence the overall oscillating properties of the system.

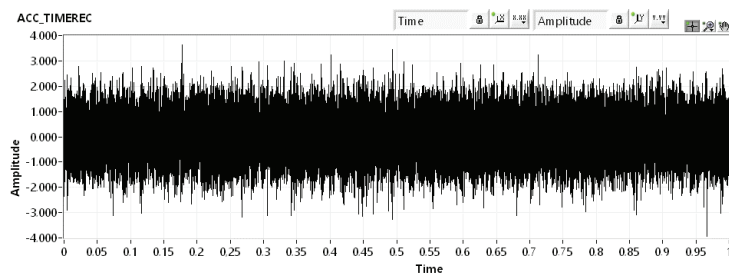


Figure 8. Example of signal collected for the evaluation process (time domain).

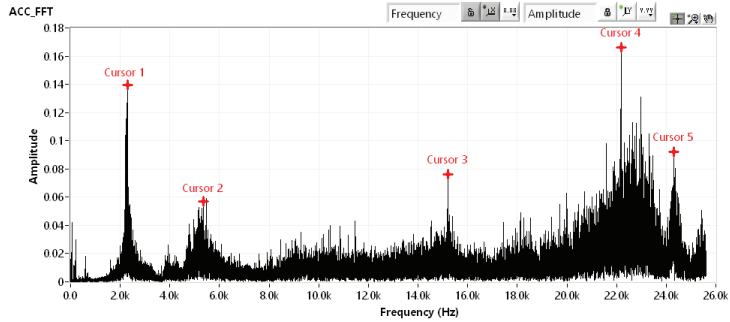


Figure 9. Example of the signal in the frequency domain processed using Fast Fourier Transformation.

To specify the effect of individual “components” of the machining set on the frequency characteristics and their rigidity, a numerical modal analysis of individual components of the set was performed using the software Ansys 2022 R2. Figure 10 shows a modal analysis of a cutting tool with  $VB_{artif} = 0.05$  mm. (Note: The numerical analysis is not the goal of the presented research, so the authors do not go into detail with the boundary conditions).

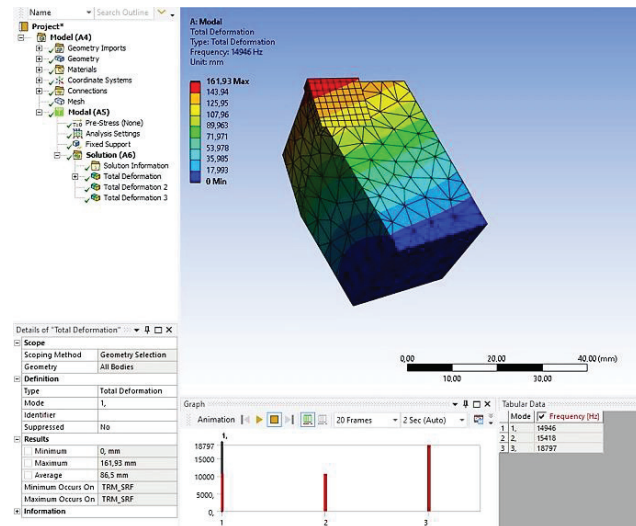


Figure 10. Numerical modal analysis of the cutting tool.

Based on the results, it was specified that, e.g., the peak highlighted in Figure 9 as the “Cursor 3” corresponds to the cutting tool, since the first natural frequency of the cutting tool identified by numerical analysis is close to 15,000 Hz (i.e., it was precisely 14,946 Hz for the presented numerical model consisting of the cutting insert and the tool holder, the back planar surface of which was fixed).

A mean value of amplitude as an output of measurement of accelerations was taken into account to evaluate the vibration intensity at the given conditions (specified by the alternate combination of cutting speed and tool wear, and constant parameters cutting depth  $a_p = 1$  mm, constant feed  $f = 0.06$  mm).

The measured data were statistically processed using multiple linear regression methodology in this sequence of steps [45,46]:

- Exclusion of outliers through the Grubbs test;
- Computing the regression coefficients  $b_i$  for a linear model with independent variables  $VB_{artif}$  and  $v_c$  and their mutual interaction;

- Diagnosis of outliers using residuals;
- Determination of significance of linear regression relationships;
- Generation of graphical representation of statistically processed data.

An example of the datasheet with processed statistical evaluation of measured data realized in MATLAB software is shown in Figure 11.

Vibrations characteristic (Acceleration)						
<b>Material 1 (CW510L)</b>						
<b>Coefficients of the regression function</b>						
$b_0 = 2.4948$	$b_1 = 2.3929$	$b_2 = 0.0071$	$b_3 = -0.0027$			
$t_0 = 4.7922$ <input checked="" type="checkbox"/>	$t_1 = 1.7463$ <input checked="" type="checkbox"/>	$t_2 = 3.0269$ <input checked="" type="checkbox"/>	$t_3 = 0.4373$ <input checked="" type="checkbox"/>			
Statistical significance of regression coefficients evaluated by Student t-criterion $t_i > t_{0.05} = 2.02$						
<b>Regression function</b>						
$A = 2.4948 + 2.3929.VB_{artif} + 0.0071.v_c - 0.0027.VB_{artif} \cdot v_c$ <input checked="" type="checkbox"/>						
Adequacy of the regression function approximation evaluated by Fisher-Snedocor test criterion $F = 8.681 > \text{tabulated value } F_{0.05} = 1.841$						
Multi-factor Analysis of Variance Purpose (ANOVA):						
'Source'	'SS'	'df'	'MS'	'F'	'Prob>F'	
'Columns'	860240	2	430120	157.2681	5.1776e-25	
'Rows'	86411	31	2787.5	1.0192	0.4619	
'Error'	169570	62	2734.9		[]	
'Total'	1116200	95			[]	
<b>Material 2 (CW614N)</b>						
<b>Coefficients of the regression function</b>						
$b_0 = 2.6552$	$b_1 = 4.4460$	$b_2 = -0.0028$	$b_3 = -0.0163$			
$t_0 = 1.0599$ <input checked="" type="checkbox"/>	$t_1 = 4.4043$ <input checked="" type="checkbox"/>	$t_2 = 0.2478$ <input checked="" type="checkbox"/>	$t_3 = 0.5488$ <input checked="" type="checkbox"/>			
Statistical significance of regression coefficients evaluated by Student t-criterion $t_i > t_{0.05} = 2.02$						
<b>Regression function</b>						
$A = 2.6552 + 4.4460.VB_{artif} - 0.0028.v_c - 0.0163.VB_{artif} \cdot v_c$ <input checked="" type="checkbox"/>						
Adequacy of the regression function approximation evaluated by Fisher-Snedocor test criterion $F = 15.616 > \text{tabulated value } F_{0.05} = 1.841$						
Multi-factor Analysis of Variance Purpose (ANOVA):						
'Source'	'SS'	'df'	'MS'	'F'	'Prob>F'	
'Columns'	865190	2	432590	153.8746	9.0996e-25	
'Rows'	82515	31	2661.8	0.9468	0.5555	
'Error'	174300	62	2811.3		[]	
'Total'	1122000	95			[]	
<b>Material 3 (CW724R)</b>						
<b>Coefficients of the regression function</b>						
$b_0 = 21.9040$	$b_1 = -9.6844$	$b_2 = -0.0569$	$b_3 = 0.2663$			
$t_0 = 8.3031$ <input checked="" type="checkbox"/>	$t_1 = 1.3947$ <input checked="" type="checkbox"/>	$t_2 = 4.7870$ <input checked="" type="checkbox"/>	$t_3 = 1.1539$ <input checked="" type="checkbox"/>			
Statistical significance of regression coefficients evaluated by Student t-criterion $t_i > t_{0.05} = 2.02$						
<b>Regression function</b>						
$A = 21.9040 - 9.6844.VB_{artif} - 0.0569.v_c + 0.2663.VB_{artif} \cdot v_c$ <input checked="" type="checkbox"/>						
Adequacy of the regression function approximation evaluated by Fisher-Snedocor test criterion $F = 11.295 > \text{tabulated value } F_{0.05} = 1.841$						
Multi-factor Analysis of Variance Purpose (ANOVA):						
'Source'	'SS'	'df'	'MS'	'F'	'Prob>F'	
'Columns'	838940	2	419470	144.9515	4.2173e-24	
'Rows'	77627	31	2504.1	0.8653	0.6642	
'Error'	179420	62	2893.9		[]	
'Total'	1096000	95			[]	

Figure 11. The example of a datasheet with statistical evaluation of measured data.

#### 2.4. Chip Form Evaluation

The form of the chip created in the cutting process is an essential feature of the process evaluation. The chip form influences mainly [47,48]:

- The quality of the process—e.g., long-length chips can attack finished surfaces;
- The stability of the process—e.g., long-length chips do not leave the machine, fill the working space of the machine, and can be wound on a tool or workpiece, and they harm the cutting process itself;

- The environmental effect of the production—e.g., small, broken chips are far easier to handle, store, transport and recycle.

A very good system of chip form evaluation is given in ISO 3685. The standard classifies the chip form from the following points of view [49]:

1. The first aspect of chip classification consists of the basic characteristics of the chip form:
  - (a) Shape characteristic (represented by the first number in the classification, e.g., 1—Ribbon, 6—Arc, 7—Elementary);
  - (b) Chip form extended characteristics (represented by the second number in the classification, e.g., 1—Long, or 2—Short, etc.);
2. The second aspect is the direction of chip movement (represented by the third number within the classification; these can be numbers from 1 to 4, e.g., 1—from the workpiece in the feed direction; etc.).
3. The third aspect is the area on which the chip breaks (represented by the third number within the classification; there can be used numbers from 5 to 8; e.g., 7—broken against the workpiece surface).

Following the above chip form evaluation characteristics, it is possible to state the criteria for the chip form suitability, while several priorities are considered in the criteria statement:

- Secure required quality characteristics of machined surface;
- Safety automatic chip removal from the machine tool working area;
- Efficient chip handling, storage and removal, etc.

The chip form suitability classification scale can be tailored to specific requirements, e.g., Good/Acceptable/Unacceptable, etc.

In order to simplify the above-mentioned chip form evaluation approach by using a binary scale for basic and extended chip form characteristics, for the sake of clarity and a better summary of the characteristics of the created chip, the authors chose to divide the chip form in the final statement into two basic groups:

- Favorable
- Unfavorable.

No chip breaker was used for the cutting tool used for evaluation.

### 3. Results and Discussion

#### 3.1. The Influence of Tool Wear and Cutting Speed on the Intensity of Tool Vibrations

During the vibration measurements, many data were recorded that needed to be processed. Therefore, they had to be studied using several practices and methods related to the phenomena of wear with respect to the chosen scope of cutting speed [50]. The most important analysis focused on increasing the credibility of durability assessment was the determination of the “general intensity of the vibration intensity of the system”. Specification of “intensity” had to take into account the vibro-diagnostic changes of the experimental system to determine the needed machining factors, since any change in spindle rotation (due to the required cutting speeds) considerably affects the frequency range that is interconnected with the tool wear rate and manifested in the machining characteristics [51].

Data recorded during measurements for individual brass alloys are shown in Figure 12.

At first sight, it is clear from the dependencies in Figure 12 that the vibration intensity of the tool is different for each of the three tested materials. The mean value of the vibration intensity under the given conditions was further considered when generating the dependence of the amplitude on wear and cutting speed. A graphical representation of statistically processed data (mesh color surface) is shown in Figure 13.

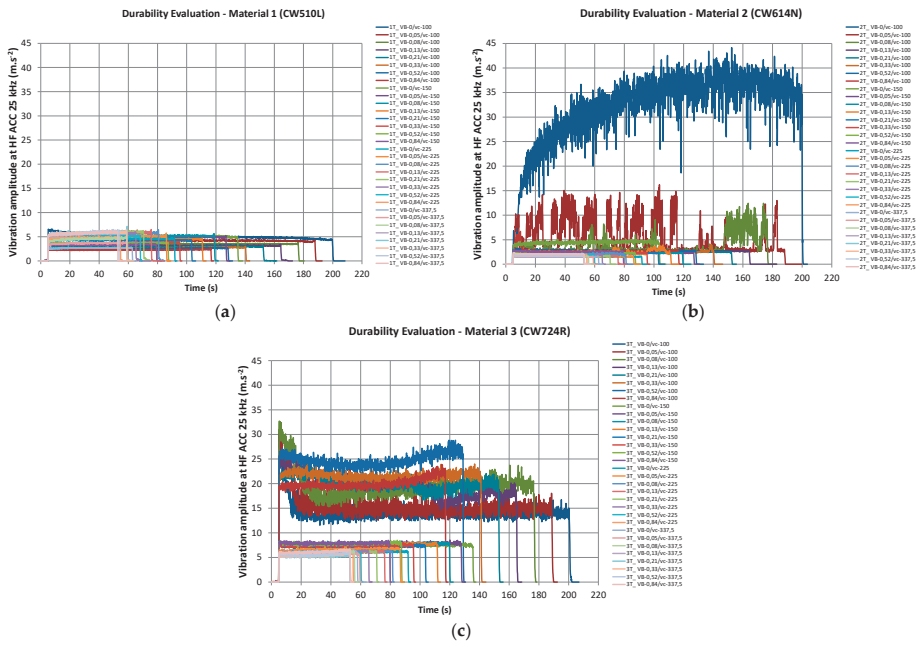


Figure 12. Measured vibrations in a time domain for individual materials; (a) CW510L; (b) CW614N; (c) CW724R.

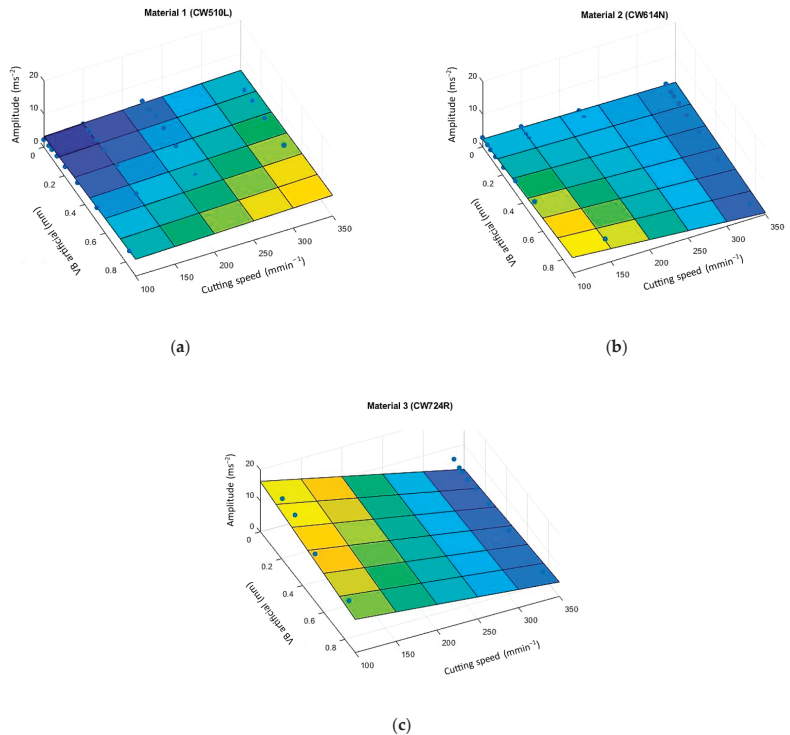


Figure 13. Graphical interpretation of vibration relationship on cutting speed and artificial tool wear for individual materials; (a) CW510L; (b) CW614N; (c) CW724R.



The results of the vibration amplitude divided the materials into two groups:

- I. Material 1 (CW510L) and Material 2 (CW614N) show relatively low sensitivity for generating vibrations through tool wear;
- II. Material 3 (CW724R) shows the higher vibration intensity generated by tool wear at lower cutting speeds.

To analyze the behavior of vibrating responses of the machining tool during the turning of individual brass alloys, the following statements can be made.

When machining CW510L brass alloy, the vibration amplitude value increased with wear and the cutting speed increased. This logically expected fact may be attributed to the heterogeneous structure of the material, made of a mixture of alpha and beta phases of the alloy, and the resulting very good value ductility, which is about twice as high as the remaining two compared materials.

From the strength characteristics ( $R_m/R_{p0.2}$ ) point of view, this material is at the lowest amplitude values of the materials studied, which certainly contributes to a more suitable force ratio in the chip root and the creation of the lowest cutting resistance. In this case, mechanical properties are very well correlated with the lowest hardness values of all compared materials and the resulting effect on the nature of chip formation and vibration generation. Excellent thermal conductivity is certainly included in the comprehensive action of the external manifestations during machining—which is comparable to the thermal conductivity of the CW614N material but is three times better compared to the CW724R. This gives a prerequisite for better heat distribution to the chips and machined material.

Monitoring of the vibrations during the machining of the CW614N alloy showed that the value of the vibration amplitude increased uniformly with increasing wear on the tool flank area, but decreased with increasing cutting speed. This was probably caused by the duplex microstructure of the material containing insoluble lead particles, which take over the function of reducing the friction of the contact surfaces of the tool and at the same time serve in the place of the cutting plane of the chip as non-cohesive particles, ensuring very good conditions for breaking the chip. The CW614N alloy showed half the ductility value compared to the CW510L material, which indicated its lower plasticity and lower ability to dampen vibrations. From the point of view of strength characteristics ( $R_m/R_{p0.2}$ ), the CW614N alloy is at the middle values of the studied materials, which also indicates the middle values of the strength ratios at the root of the chip and the degree of cutting resistance. Even in this case, the mechanical properties were well correlated with the average hardness values of the compared materials and the resulting effect on the character of chip formation and vibration generation. Excellent thermal conductivity, which is comparable to the material CW510L but is three times better compared to the material CW724R, certainly entered into the complex action of external manifestations during machining. This gives the assumption of a better distribution of heat to the chip and the machined material.

From the dependence of vibration intensity of the CW724R brass alloy on the wear and cutting speed it can be seen that the value of the amplitude decreased uniformly with increasing wear on the back surface of the tool and with increasing cutting speed. This resulted from the material's complex heterogeneous structure in which, compared to other materials, the content of silicon is high. The influence of silicon is manifested mainly by increasing the strength characteristics of brasses, which causes this material to have the highest. In the case of machining, the influence of silicon in the structure is also significant, with considerable grinding action on the tool flank surfaces, and increasing the width of the worn surface as a resulting effect of increasing the damping properties of this frictional contact. The lowest thermal conductivity of the compared materials probably caused a significant increase in temperature in the cutting plane of the chip, thus a substantial increase in local plasticity, and considerably different vibrational manifestations of the machining system.

3.2. Evaluation of Chip Form

Waste material from machining (chips, residues) was collected separately for each evaluated group of materials so that it could be recycled and thus ensure a higher degree of environmental protection and non-contamination.

Results of chip evaluation within durability tests are summarized in Figure 14.

		Material 1 (CW510L)				Material 2 (CW614N)				Material 3 (CW724R)				
		$v_c$ (m.min <sup>-1</sup> )				$v_c$ (m.min <sup>-1</sup> )				$v_c$ (m.min <sup>-1</sup> )				
		100	150	225	337	100	150	225	337	100	150	225	337	
VB <sub>artificial</sub> (mm)	0.00	2.2 / 6.2	2.2	2.2	2.2	7	2.2 / 6.2	6.2	6.2	6.2	6.2	4.2 / 6.2	6.2	1.2
	0.05	2.2 / 6.2	2.2	2.2	2.2	7	6.2	6.2	6.2	6.2	6.2	6.2	6.2	5.2
	0.08	2.2 / 6.2	2.2	2.2	2.2	7	6.2	6.2	6.2	6.2	6.2	6.2	2.2 / 2.3	
	0.01	6.2 / 1.1	2.2	2.2 / 1.1	2.2	7	6.2	6.2	6.2	6.2	6.2	6.2	6.2	6.2
	0.21	1.3	2.2	2.2 / 1.1		7	6.2	6.2	6.2	6.2	6.2	6.2	6.2	2.3
	0.33	6.2	2.2	2.2 / 1.1	2.2	7	6.2	6.2	6.2	6.2	6.2	6.2	6.2	2.3
	0.52	2.2 / 6.2	2.2	2.2	2.2	7	6.2	6.2	6.2	6.2	6.2	6.2	6.2	1.3
	0.84	2.2 / 6.2	2.2	2.2	2.2	7	7	6.2	6.2	6.2	6.2	6.2	6.2	1.3
		<div style="display: flex; justify-content: space-around; align-items: center;"> <div style="width: 20px; height: 10px; background-color: yellow; border: 1px solid black;"></div> Unfavourable chip form                     <div style="width: 20px; height: 10px; background-color: lightgreen; border: 1px solid black;"></div> Favourable chip form                 </div>												

Figure 14. Evaluation of chip form produced during experimental verification.

It can be stated that the machined brass alloys have shown relatively good chip formation. The problematic chip form occurred only in some cases of Material 1 (CW510L) and Material 3 (CW724R) that is marked in Figure 14 in yellow with the statement “Unfavourable chip form”.

For each combination of machining conditions (given by the type of brass alloy, cutting speed and artificial wear), a representative sample of the removed material was documented in the form of a chip, which was registered and stored in the authors’ internal database. Figures 15–18 document the comparison of the resulting forms of chips arising at individual cutting speeds.

From the practical point of view, based on the results related to the chip form originating at the machining of selected brass alloys, it can be said that there are good production conditions in terms of chip shape since it was affected very little by the type of alloy. Undesirable areas of unsuitable chip forms can be easily adjusted by changing the cutting conditions (cutting speed and feed) or—the best practical solution—by using a cutting tool with a chip breaker.

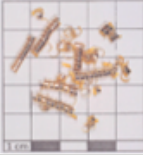

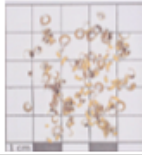
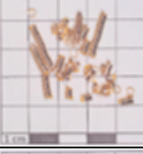


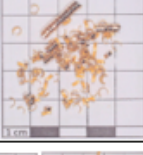

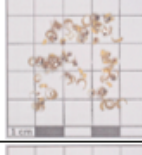



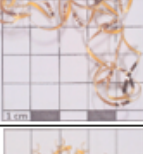

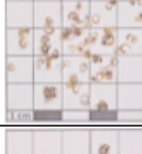
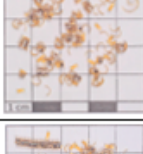


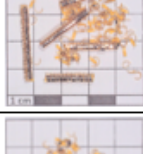


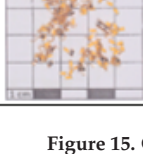
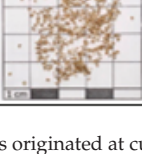

Artificial wear (mm)		Cutting speed ( $\text{mmin}^{-1}$ )											
		100											
		Material 1 – CW510L			Material 2 – CW614N			Material 3 – CW724R					
0.00		Chip form: 2.2 & 6.2		Chip form: 7		Chip form: 6.2	0.05		Chip form: 2.2 & 6.2		Chip form: 7		Chip form: 6.2
0.08		Chip form: 2.2 & 6.2		Chip form: 7		Chip form: 6.2	0.13	 0'5"      3'16"	Chip form: firstly 6.2, later 1.1		Chip form: 7		Chip form: 6.2
0.21		Chip form: 1.3		Chip form: 7		Chip form: 6.2	0.33		Chip form: 6.2		Chip form: 7		Chip form: 6.2
0.52		Chip form: 2.2 & 6.2		Chip form: 7		Chip form: 6.2	0.84		Chip form: 2.2 & 6.2		Chip form: 7		Chip form: 6.2

Figure 15. Comparison of chips originated at cutting speed 100 m/min.

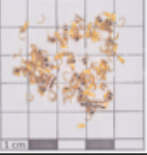

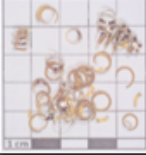
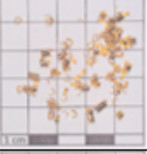
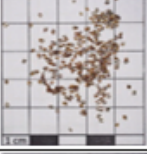
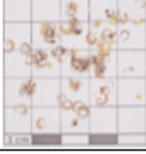
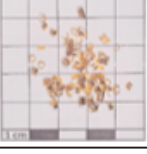

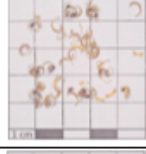


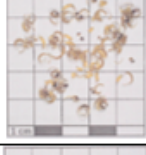
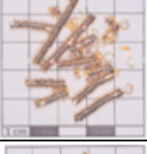

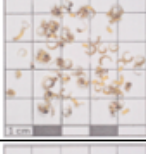
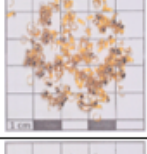

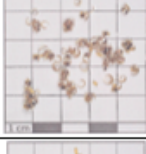
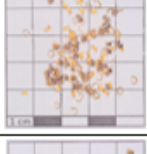
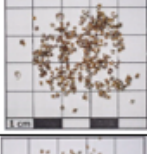

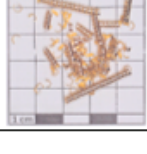


Artificial wear (mm)		Cutting speed (mmin <sup>-1</sup> )											
		150											
		Material 1 – CW510L			Material 2 – CW614N			Material 3 – CW724R					
0.00		Chip form: 2.2		Chip form: 2.2 & 6.2		Chip form: 4.2 & 6.2	0.05		Chip form: 2.2		Chip form: 6.2		Chip form: 6.2
0.08		Chip form: 2.2		Chip form: 6.2		Chip form: 6.2	0.13		Chip form: 2.2		Chip form: 6.2		Chip form: 6.2
0.21		Chip form: 2.2		Chip form: 6.2		Chip form: 6.2	0.33		Chip form: 2.2		Chip form: 6.2		Chip form: 6.2
0.52		Chip form: 2.2		Chip form: 6.2		Chip form: 6.2	0.84		Chip form: 2.2		Chip form: 7		Chip form: 6.2

Figure 16. Comparison of chips originated at cutting speed 150 m/min.

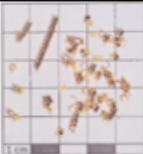


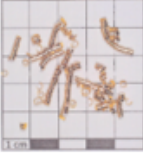

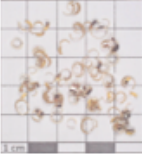
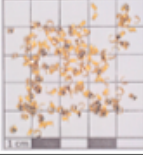

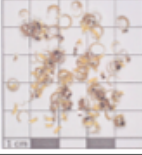
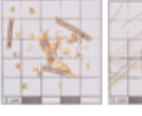
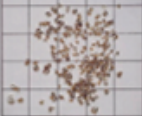
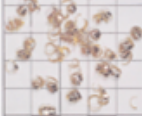
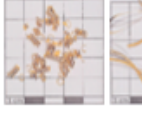


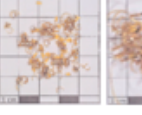


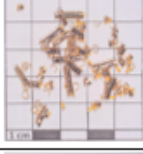
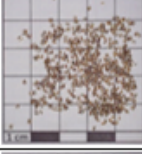
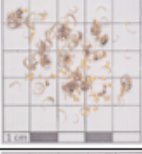
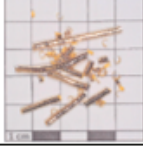

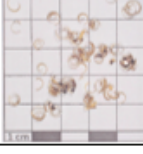
Artificial wear (mm)		Cutting speed ( $\text{mmin}^{-1}$ )											
		225											
		Material 1 – CW510L			Material 2 – CW614N			Material 3 – CW724R					
0.00		Chip form: 2.2		Chip form: 6.2		Chip form: 6.2	0.05		Chip form: 2.2		Chip form: 6.2		Chip form: 6.2
0.08		Chip form: 2.2		Chip form: 6.2		Chip form: 6.2	0.13		Chip form: firstly 2.2 later 1.1		Chip form: 6.2		Chip form: 6.2
0.21		Chip form: firstly 2.2 later 1.1		Chip form: 6.2		Chip form: 6.2	0.33		Chip form: firstly 2.2 later 1.1		Chip form: 6.2		Chip form: 6.2
0.52		Chip form: 2.2		Chip form: 6.2		Chip form: 6.2	0.84		Chip form: 2.2		Chip form: 6.2		Chip form: 6.2

Figure 17. Comparison of chips originated at cutting speed 225 m/min.



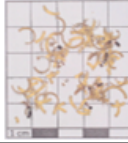


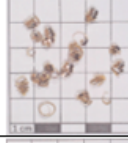






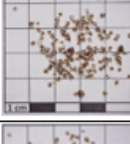




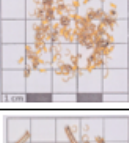
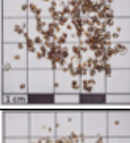

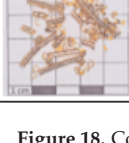

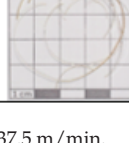
		Cutting speed ( $\text{mmin}^{-1}$ )		
		337		
		Material 1 – CW510L	Material 2 – CW614N	Material 3 – CW724R
Artificial wear (mm)	0.00	 Chip form: 2.2	 Chip form: 6.2	 Chip form: 1.2
	0.05	 Chip form: 2.2	 Chip form: 6.2	 Chip form: 5.2
	0.08	 Chip form: 2.2	 Chip form: 6.2	 Chip form: 2.2 & 2.3
	0.13	 Chip form: 2.2	 Chip form: 6.2	 Chip form: 6.2
	0.21	not collected	 Chip form: 6.2	 Chip form: 2.3
	0.33	 Chip form: 2.2	 Chip form: 6.2	 Chip form: 2.3
	0.52	 Chip form: 2.2	 Chip form: 6.2	 Chip form: 1.3
	0.84	 Chip form: 2.2	 Chip form: 6.2	 Chip form: 1.3

Figure 18. Comparison of chips originated at cutting speed 337.5 m/min.

#### 4. Conclusions

Machining is a complex process involving many variables and parameters. In many cases, the theoretically derived dependencies of the basic factors of the cutting process optimization cannot be directly applied in specific production settings, because the boundary conditions (properties of the processed material, product characteristics, machine tool characteristics, process conditions, etc.) in real practice significantly change the expected results. It follows that for each individual system (machine tool, cutting tool, and product),

lengthy experimental verification and evaluation would be necessary, which is not possible in practice due to the required high productivity and production efficiency.

A huge disadvantage of the classic approach when creating optimization models is that, despite very precise preparation and processing of experimental results, it is not possible to exclude the occurrence of random events that will significantly shorten the life of some cutting tools and thus cause complications in production. Therefore, in real production conditions, monitoring the response of the system to real stimuli appears to be the most suitable way of monitoring the actual state of the cutting tool, to which the presented research contributes to a large extent.

The primary objective of this research was to determine the level of vibration intensity of machining in response to a particular tool wear while turning brass alloys, and thus determine the level (borderline) at which the process is stable in the newly proposed methodology with an inverse approach that is based on artificially generated tool wear (prepared in advance in advance on the major flank). A supplementary part of the research was the study of chip formation when machining brass alloys in the given machining conditions, as this is directly connected to the wear of the tool. Specifically, the research results can be summarized as follows:

- The collection and processing of the experimentally obtained data were carried out using the standard steps of the multiple linear regression methodology to evaluate the dependence parameters (vibration characteristic and chip shape characteristic) on the experimental factors (cutting speed and artificial wear  $VB_{\text{artif}}$ ).
- Based on the measured data, the statistical dependences of the acceleration amplitude (A) as a vibration characteristic on the experimental factors ( $v_c$ ,  $VB_{\text{artif}}$ ) were determined—all at the required level of statistical reliability.
- CW510L and CW614N brass alloys were found to exhibit an average of three times lower vibration damping compared to CW724R alloy.
- The CW724R brass alloy showed significantly steeper dependences of vibration generation in terms of changes in cutting speed and  $VB_{\text{artif}}$  wear compared to the other two materials.
- Differences in susceptibility to the generation of vibration manifestations are probably caused by the structure of the evaluated materials.
- The evaluated material production conditions significantly affect the vibro-diagnostic characteristics of the machining process, while for CW510L the slope of the dependence of the amplitude on the cutting speed is opposite to that for the other two materials (with increasing speed, the amplitude grew).

Regarding the evaluation of chip shape properties, it can be concluded:

- The experiments showed relatively good chip formation in the evaluated machining conditions even without the use of a chip breaker.
- The problematic chip shape occurred only in some cases with material 1 (CW510L) and material 3 (CW724R), which cannot be generally determined.
- From the point of view of suitable chip formation, the production conditions were very little affected by the type of alloy.
- Undesirable areas of inappropriate chip shape can be easily adjusted in practical applications by changing the feed, cutting speed, or—the best practical solution—by using a cutting tool with a chip stiffener optimized for the given process.

In the near future, the authors would like to continue the research with the measurement of cutting forces for the same or for a reduced experimental design.

**Author Contributions:** Conceptualization, P.P.M., K.M., G.A.P. and A.I.T.; methodology, P.P.M. and K.M.; software, P.P.M. and K.M.; validation, P.P.M., K.M. and G.A.P.; formal analysis, A.I.T.; investigation, P.P.M. and K.M.; resources, P.P.M., K.M. and A.I.T.; data curation, K.M., P.P.M. and A.I.T.; writing—original draft preparation, K.M.; writing—review and editing, P.P.M. and G.A.P.; visualization, K.M., P.P.M. and G.A.P.; supervision, P.P.M. and G.A.P.; project administration, K.M.

and G.A.P.; funding acquisition, K.M., P.P.M. and G.A.P. All authors have read and agreed to the published version of the manuscript.

**Funding:** This research was funded by the Ministry of Education, Science, Research and Sport of the Slovak Republic by grants APVV-19-0550, KEGA 005TUKE-4/2021, KEGA 032TUKE-4/2022, and SK-CN-21-0046 as well as by ELKEME S.A.

**Data Availability Statement:** Not applicable.

**Acknowledgments:** The support and encouragement of ELKEME S.A. management and ELVAL-HALCOR Brass Rods and Tubes Plant are greatly appreciated. The article was prepared thanks to the support of the Ministry of Education, Science, Research and Sport of the Slovak Republic through the grants APVV-19-0550, KEGA 005TUKE-4/2021, KEGA 032TUKE-4/2022 and SK-CN-21-0046.

**Conflicts of Interest:** The authors declare no conflict of interest.

## References

- Grzesik, W. *Advanced Machining Processes of Metallic Materials—Theory, Modelling and Applications*; Elsevier: Amsterdam, The Netherlands, 2017; ISBN 978-0-444-63711-6.
- Trent, E.M.; Wright, P.K. *Metal Cutting: Theory and Application*; Butterworth Heinemann: Auckland, New Zealand, 2000; ISBN 0-7506-7069-X.
- Jurko, J.; Panda, A.; Behun, M. Prediction of a new form of the cutting tool according to achieve the desired surface quality. *Appl. Mech. Mater.* **2013**, *268–270*, 473–476. [[CrossRef](#)]
- Suh, C.S.; Liu, M.-K. *Control of Cutting Vibration and Machining Instability: A Time-Frequency Approach for Precision, Micro and Nano Machining*; John Wiley & Sons: Chichester, UK, 2013; ISBN 978-1-118-37182-4.
- Kuyucak, S.; Sahoo, M. A review of the machinability of copper-base alloys. *Can. Metall. Q.* **1996**, *35*, 1–15. [[CrossRef](#)]
- Jerzy, J.; Kuric, I.; Grozav, S.; Ceclan, V. Diagnostics of CNC machine tool with R-Test system. *Acad. J. Manuf. Eng.* **2014**, *12*, 56–60.
- Pitel, J.; Matiszkova, D.; Marasova, D. A new approach to evaluation of the material cutting using the artificial neural networks. *TEM J.* **2019**, *8*, 325–332.
- Markopoulos, A.P.; Pressas, I.S.; Papanioniou, I.G.; Karkalos, N.E.; Davim, J.P. Machining and machining modeling of metal matrix composites—A review. In *Modern Manufacturing Engineering*; Springer: Cham, Switzerland, 2015; pp. 99–141.
- Twardowski, P.; Legutko, S.; Krolczyk, G.M.; Hloch, S. Investigation of wear and tool life of coated carbide and cubic boron nitride cutting tools in high speed milling. *Adv. Mech. Eng.* **2015**, *7*, 1687814015590216. [[CrossRef](#)]
- Petru, J.; Schiffler, J.; Zlamal, T.; Cep, R.; Kratochvil, J.; Stancekova, D. Wear progress of exchangeable cutting inserts during Ti (6) Al (4) V alloy machining. In Proceedings of the 24th International Conference on Metallurgy and Materials, Brno, Czech Republic, 3–5 June 2015; pp. 1147–1155.
- Stavropoulos, P.; Papacharalampopoulos, A.; Vasiliadis, E.; Chryssolouris, G. Tool wear predictability estimation in milling based on multi-sensorial data. *Int. J. Adv. Manuf. Technol.* **2016**, *82*, 509–521. [[CrossRef](#)]
- Zetek, M.; Zetkova, I. Increasing of the cutting tool efficiency from tool steel by using fluidization method. *Procedia Eng.* **2015**, *100*, 912–917. [[CrossRef](#)]
- Bakša, T.; Kroupa, T.; Hanzl, P.; Zetek, M. Durability of cutting tools during machining of very hard and solid materials. *Procedia Eng.* **2015**, *100*, 1414–1423. [[CrossRef](#)]
- Dimla, D.E. The Correlation of Vibration Signal Features to Cutting Tool Wear in a Metal Turning Operation. *Int. J. Adv. Manuf. Technol.* **2002**, *19*, 705–713. [[CrossRef](#)]
- Xu, C.; Jianming, D.; Yuzhen, C.; Huaiyuan, L.; Zhicheng, S.; Jing, X. The relationships between cutting parameters, tool wear, cutting force and vibration. *Adv. Mech. Eng.* **2018**, *10*, 1687814017750434. [[CrossRef](#)]
- Bouhalais, M.L.; Nouioua, M. The analysis of tool vibration signals by spectral kurtosis and ICEEMDAN modes energy for insert wear monitoring in turning operation. *Int. J. Adv. Manuf. Technol.* **2021**, *115*, 2989–3001. [[CrossRef](#)]
- Sridhar, A.V.; Prasad, B.S.; Mouli, K.V. Evaluation of tool performance and wear through vibration signature analysis in drilling of IS3048 steel. *J. Eng. Appl. Sci.* **2021**, *68*, 27. [[CrossRef](#)]
- Babu, M.S.; Rao, T.B. Real-time cutting tool condition assessment and stochastic tool life predictive models for tool reliability estimation by in-process cutting tool vibration monitoring. *Int. J. Interact. Des. Manuf.* **2022**, 1–17. [[CrossRef](#)]
- Antić, A.; Šimunović, G.; Šarić, T.; Milošević, M.; Ficko, M. A model of tool wear monitoring system for turning. *Tech. Gaz.* **2013**, *20*, 247–254.
- Childs, T.; Maekawa, K.; Obikawa, T. *Metal Machining: Theory and Applications*; Butterworth-Heinemann: London, UK, 2000; ISBN 0-340-69159-X.
- Pastucha, P.; Majstorovic, V.; Kučera, M.; Beno, P.; Krile, S. Study of Cutting Tool Durability at a Short-Term Discontinuous Turning Test. In Proceedings of the International Conference on Manufacturing Engineering and Materials (ICMEM 2018), Novy Smokovec, Slovakia, 18–22 June 2018; pp. 493–501. [[CrossRef](#)]
- Toufatzis, A.I.; Pantazopoulos, G.A.; David, C.N.; Sagris, D.S.; Paipetis, A.S. Machinability of eco-friendly lead-free brass alloys: Cutting-force and surface-roughness optimization. *Metals* **2018**, *8*, 250. [[CrossRef](#)]



23. Pantazopoulos, G. Leaded brass rods C38500 for automatic machining operations. *J. Mater. Eng. Perform.* **2002**, *11*, 402–407. [[CrossRef](#)]
24. Gane, N. The effect of lead on the friction and machining of brass. *Philos. Mag.* **1981**, *43*, 545–566. [[CrossRef](#)]
25. Nobel, C.; Klocke, F.; Lung, D.; Wolf, S. Machinability Enhancement of Lead-free Brass Alloys. *Procedia CIRP* **2014**, *14*, 95–100. [[CrossRef](#)]
26. Stavroulakis, P.; Toulfatzis, A.I.; Pantazopoulos, G.A.; Paipetis, A.S. Machinable Leaded and Eco-Friendly Brass Alloys for High Performance Manufacturing Processes: A Critical Review. *Metals* **2022**, *12*, 246. [[CrossRef](#)]
27. Toulfatzis, A.; Pantazopoulos, G.; Paipetis, A. Fracture behavior and characterization of lead-free brass alloys for machining applications. *J. Mater. Eng. Perform.* **2014**, *23*, 3193–3206. [[CrossRef](#)]
28. Johansson, J.; Alm, P.; M'Saoubi, R.; Malmberg, P.; Ståhl, J.-E.; Bushlya, V. On the Function of Lead (Pb) in Machining Brass Alloys. *Res. Sq.* **2022**, *120*, 7263–7275. [[CrossRef](#)]
29. Company Sarbak Materials Data Sheets. Available online: [www.sarbak.com.tr](http://www.sarbak.com.tr) (accessed on 19 June 2022).
30. *EN 1982*; Copper and Copper Alloys—Ingots and Castings. CEN: Brussels, Belgium, 2017.
31. *EN 12164*; Copper and Copper Alloys—Rod for Free Machining Purposes. CEN: Brussels, Belgium, 2016.
32. Pantazopoulos, G.; Vazdirvanidis, A. Characterization of the microstructural aspects of machinable? *Phase brass. Microsc. Anal.* **2008**, *22*, 13–16.
33. Toulfatzis, A.I.; Pantazopoulos, G.A.; Paipetis, A.S. Fracture mechanics properties and failure mechanisms of environmental-friendly brass alloys under impact, cyclic and monotonic loading conditions. *Eng. Fail. Anal.* **2018**, *90*, 497–517. [[CrossRef](#)]
34. Garcia, P.; Rivera, S.; Palacios, M.; Belzunce, J. Comparative study of the parameters influencing the machinability of leaded brasses. *Eng. Fail. Anal.* **2010**, *17*, 771–776. [[CrossRef](#)]
35. Filippov, A.V.; Filippova, E.O. Determination of cutting forces in oblique cutting. *Appl. Mech. Mater.* **2015**, *756*, 659–664. [[CrossRef](#)]
36. Altintas, Y. Manufacturing automation: Metal cutting mechanics, machine tool vibrations, and CNC design. *Appl. Mech. Rev.* **2012**, *54*, B84.
37. Vazdirvanidis, A.; Rikos, A.; Toulfatzis, A.I.; Pantazopoulos, G.A. Electron Backscatter Diffraction (EBSD) Analysis of Machinable Lead-Free Brass Alloys: Connecting Texture with Fracture. *Metals* **2022**, *12*, 569. [[CrossRef](#)]
38. Hagarová, M.; Peterka, P.; Mantič, M.; Vojtko, M.; Baranová, G.; Matvija, M. Failure analysis of leaded brass bolt. *Eng. Fail. Anal.* **2023**, *143*, 106899. [[CrossRef](#)]
39. Toulfatzis, A.I.; Besseris, G.J.; Pantazopoulos, G.A.; Stergiou, C. Characterization and comparative machinability investigation of extruded and drawn copper alloys using non-parametric multi-response optimization and orthogonal arrays. *Int. J. Adv. Manuf. Technol.* **2011**, *57*, 811–826. [[CrossRef](#)]
40. Yaqoob, K.; Hashmi, F.; Hassan Tanvir, W. Failure Analysis of Cartridge Brass Shell. *Eng. Fail. Anal.* **2022**, *138*, 106325. [[CrossRef](#)]
41. Baron, P.; Dobransky, J.; Pollak, M.; Kocisko, M.; Cmorej, T. The parameter correlation of acoustic emission and high-frequency vibrations in the assessment process of the operating state of the technical system. *Acta Mech. Autom.* **2016**, *10*, 112–116. [[CrossRef](#)]
42. Filippov, A.V.; Nikonov, A.Y.; Rubtsov, V.E.; Dmitriev, A.I.; Tarasov, S.Y. Vibration and acoustic emission monitoring the stability of peakless tool turning: Experiment and modeling. *J. Mater. Process. Technol.* **2017**, *246*, 224–234. [[CrossRef](#)]
43. Chen, J.; Feng, J.; Wang, F.; Peng, Q.; Lan, G.; Zhao, L.; Wu, L. Cracking Analysis of a Brass Clamp Mounted on the Main Transformer in the Power Grid System. *Energies* **2023**, *16*, 3460. [[CrossRef](#)]
44. Monka, P.P.; Monkova, K.; Pantazopoulos, G.; Toulfatzis, A.I. Effect of Wear on the Vibrating Behaviour of the Tool at Turning CW724R Alloy. In Proceedings of the 13th International Conference on Mechanical and Aerospace Engineering (ICMAE), Bratislava, Slovakia, 20–22 July 2022; pp. 51–55. [[CrossRef](#)]
45. Panda, A.; Dobránsky, J.; Jančík, M.; Pandova, I.; Kačalová, M. Advantages and effectiveness of the powder metallurgy in manufacturing technologies. *Metalurgija* **2018**, *57*, 353–356.
46. Obeng, D.P.; Morrell, S.; Napier-Munn, T.J. Application of central composite rotatable design to modeling the effect of some operating variables on the performance of the three-product cyclone. *Int. J. Miner. Process.* **2005**, *76*, 181–192. [[CrossRef](#)]
47. Malotova, S.; Cep, R.; Cepova, L.; Petru, J.; Stancekova, D.; Kyncl, L.; Hatala, M. Roughness Evaluation of the Machined Surface at Interrupted Cutting Process. *Manuf. Technol.* **2016**, *16*, 168–173. [[CrossRef](#)]
48. Kouadri, S.; Necib, K.; Atlati, S.; Haddag, B.; Nouari, M. Quantification of the chip segmentation in metal machining: Application to machining the aeronautical aluminum alloy AA2024-T351 with cemented carbide tools WC-Co. *Int. J. Mach. Tools Manuf.* **2013**, *64*, 102–113. [[CrossRef](#)]
49. *ISO 3685: 1993(E)*; International Standard, Tool Testing with Single Point Turning Tools. ISO: Geneva, Switzerland, 1993.
50. Sahaoui, Z.; Mehdi, K.; Jaber, M.B. Analytical and experimental stability analysis of AU4G1 thin-walled tubular workpieces in turning process. *Proc. Inst. Mech. Eng. Part B J. Eng. Manuf.* **2020**, *234*, 1007–1018. [[CrossRef](#)]
51. Glaa, N.; Mehdi, K.; Moussaoui, K.; Zitoune, R. Numerical and experimental study of the drilling of multi-stacks made of titanium alloy Ti-6Al-4V: Interface and burr behaviour. *Int. J. Adv. Manuf. Technol.* **2020**, *107*, 1153–1162. [[CrossRef](#)]

**Disclaimer/Publisher's Note:** The statements, opinions and data contained in all publications are solely those of the individual author(s) and contributor(s) and not of MDPI and/or the editor(s). MDPI and/or the editor(s) disclaim responsibility for any injury to people or property resulting from any ideas, methods, instructions or products referred to in the content.

Article

# Inverse Thermal Analysis as a Tool for Optimizing Concentrated Solar Energy Elaboration of Wear Resistant Surface Layers

Anna D. Zervaki <sup>1</sup>, Samuel G. Lambrakos <sup>2</sup>, Athanasios G. Mourlas <sup>3</sup>, Ioannis G. Papantoniou <sup>4,5</sup>, José Rodríguez <sup>6</sup> and Pandora P. Psyllaki <sup>3,\*</sup>

<sup>1</sup> Shipbuilding Technology Laboratory, School of Naval Architecture and Marine Engineering, National Technical University of Athens, 9 Heroon Polytechniou Ave., 157 73 Athens, Greece

<sup>2</sup> U.S. Naval Research Laboratory, Washington, DC 20375, USA

<sup>3</sup> Surface Engineering Laboratory, Department of Mechanical Engineering, University of West Attica, 250 Thivon & P. Ralli Str., Ancient Olive Grove Campus, 122 41 Egaleo, Greece

<sup>4</sup> Laboratory of Manufacturing Technology, School of Mechanical Engineering, National Technical University of Athens, Heroon Polytechniou 9, 157 80 Athens, Greece

<sup>5</sup> Department of Naval Architecture, School of Engineering, University of West Attica, Ag. Spyridonos Str., Egaleo Park Campus, 122 43 Egaleo, Greece

<sup>6</sup> CIEMAT-Plataforma Solar de Almería, Aptdo, 22, 04200 Tabernas, Spain

\* Correspondence: psyllaki@uniwa.gr; Tel.: +30-210-5381292

**Abstract:** Concentrated Solar Energy (CSE) processing is considered a promising renewable energy source technique for elaborating thick, wear-resistant claddings onto metallic surfaces of large dimensions that are expected to operate in heavy duty applications, such as excavator shovels, mineral crushers, etc. However, the prediction of surface processing effects on the microstructure and the properties of the main construction base metal are of crucial importance, as they are commonly required in all surface modification techniques. Thus, the present study is focused on the inverse thermal analysis and parametric modeling of heat deposition associated with CSE surface processing of metals. In this preliminary attempt, experimental findings that concern the elaboration of TiC- and chromium carbide-reinforced clads onto common steel base metals were used to quantify the evaluation of the temperature histories within the volume of workpieces undergoing solar heating, where direct temperature measurements contain uncertainties and/or are not even possible. Results of prototype inverse thermal analyses of heat transfer in processed layer-substrate systems are presented, demonstrating the general aspects of a parametric model for thermal analysis and simulation.

**Keywords:** inverse thermal analysis; parametric modeling; concentrated solar energy processing; cladding; wear-resistant surface layers

**Citation:** Zervaki, A.D.; Lambrakos, S.G.; Mourlas, A.G.; Papantoniou, I.G.; Rodríguez, J.; Psyllaki, P.P. Inverse Thermal Analysis as a Tool for Optimizing Concentrated Solar Energy Elaboration of Wear Resistant Surface Layers. *Metals* **2023**, *13*, 942. <https://doi.org/10.3390/met13050942>

Academic Editor: Robert B. Heimann

Received: 30 March 2023

Revised: 9 May 2023

Accepted: 10 May 2023

Published: 12 May 2023



**Copyright:** © 2023 by the authors. Licensee MDPI, Basel, Switzerland. This article is an open access article distributed under the terms and conditions of the Creative Commons Attribution (CC BY) license (<https://creativecommons.org/licenses/by/4.0/>).

## 1. Introduction

Concentrated Solar Energy (CSE), that is, the production of medium- to high-temperature heat by means of movable mirrors that track the sun and concentrate its radiation on a focal point/area has been proposed, among others, as a “green” technique for implementing surface modifications of metallic substrates [1], leading to surface layers of superior performance during operation via surface hardening [2,3], gas nitrating [4], cladding [5–8] and surface alloying [7,9]. Almost twenty-five years ago, Flamant et al. [3] introduced solar processing to perform such high temperature material treatments, documenting on technical and economic data, when comparing concentrated solar beams to other nonconventional ones, namely laser and plasma. Although the capital cost of such solar systems is higher than those of laser and plasma sources, the higher overall energy efficiency and the feasibility of treating surfaces of much larger dimensions are attractive, important features for considering concentrated solar energy for applications in the specific field of surface modification of solids. Despite its

main disadvantage related to the sun availability [10], CSE remains a promising alternative to conventional heat sources [11] for specific applications, such as cladding of large dimension metallic surfaces.

The feasibility of CSE treatment in the field of materials science and metallurgy has been proven for various processes and several materials. However, the heat effects during the whole processing history of the treated material are still a matter of concern for the relevant scientific community, since the metallurgical transformations take place not only during solar exposure, but they last during cooling from above or near melting to ambient temperature, controlling in this way the microstructure and the properties of both the directly solar-treated layer, as well as those of the underlying material.

In the case of solar cladding process of AISI 316 stainless steel over AISI 1026 common steel [12], the satisfactory agreement between experimental observations and numerical simulation results carved out a solid base for further optimization of the solar cladding parameters. More precisely, stainless steel powder was pre-deposited on the base metal surface and the system was solar irradiated, whilst the temperature evolution of the base metal was recorded in real-time by the aid of K-type thermocouples welded at three different locations on the opposite side of the irradiated surface. These results, together with the thermophysical properties of the material system, were used to develop and validate a finite element model (FEM) that could reliably predict the level and extent of the thermal fields that occurred during solar processing. Microscopic observations revealed, mainly, the dendritic structure of the obtained clads and verified further the good agreement to the numerical thermal model's predictions.

In order to improve the homogeneity inside the test chamber for materials processing [13], a numerical thermal model was developed, taking as main assumptions that heat transfer occurs via: (i) conduction through the receiver plate; (ii) radiation between the up-plate and the down-plate; (iii) natural convection between the plates and the surrounding medium. For the validation of the numerical model, two materials of vastly different physical properties -thermal conductivity, specific heat capacity and emissivity- were used as receivers (up-plates) under three set-up configurations and the temperature evolution was recorded in real-time by the aid of a set of five K-type thermocouples placed at specific locations of the tested materials system. The combined evaluation of the numerical simulation and experimental results revealed that the thermal fields developed during solar irradiation are controlled by the thermal properties of both the down-plate and the surrounding medium; thus, the optimization of a required solar processing is strongly dependent on the proper selection of the set-up configuration and not exclusively on the solar irradiation parameters.

In the case where solar processing incorporates melting of the irradiated materials, as in welding [14], the thermal fields developed under the constraints imposed by the particular experimental configuration and solar exposure parameters determine also the microstructure obtained during materials re-solidification, as well as that of the heat affected zone (H.A.Z.). In the case of solar sintering of  $\text{Al}_2\text{O}_3$ -based ceramics [15], high levels of densification of the green bodies were achieved, which cannot be obtained by conventional sintering in electric furnaces without applying pressure. The relevant dense microstructure obtained was attributed to the high heating rates and short sintering duration during solar treatment that restrained grain growth, whilst the use of a  $95\text{N}_2:5\text{H}_2$  mixture as surrounding medium was found to result in pores elimination. Similar observations were reported in the case of solar sintering of Ni-Zn ferrites [16]; compared to sintering in conventional electric furnace, the solar-based technique led to ferrites of higher densification that influenced both their mechanical and magnetic properties.

Solar sintering of bulk carbide-reinforced metallic-matrix composites [17] was achieved by pre-mixing vanadium carbide and AISI M2 high speed steel powders, and successive solar exposure using (a) Fresnel lens and (b) solar furnace, for various reinforcing particles percentages and treatment parameters. The experimental results revealed the high

microstructural quality of the treated material and are significantly encouraging for performing further such metallurgical processes via concentrated solar energy.

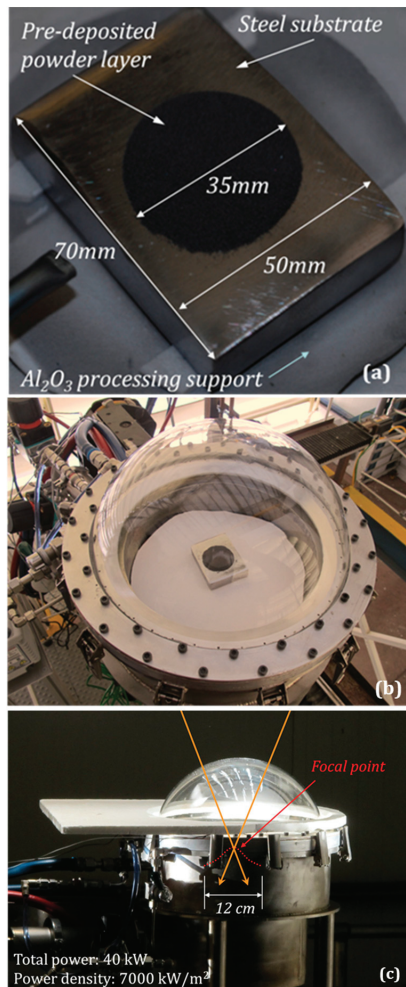
Finally, the particular thermal cycles during solar processing, that is, high heating rate and controlled dwell time at a temperature level, as well as the thermal field implied in the receiver's volume allowed foaming of Al-Si precursors and led to stable porous metallic structures, overcoming the common drawback of pore collapse when thermal treatment takes place in electric furnaces [18].

Inverse analysis of volumetric heat-deposition processes [19–24], for example, welding [25,26], poses a specific problem, which follows from the unique characteristics and relative complexity of such processes. These processes are typically characterized by regions of volumetric heat deposition having complex shapes and heat-source-workpiece interactions. Modeling and inverse analysis of thermal processes within these regions of volumetric deposition, for example, inverse thermal analysis, remains an open problem, distinct from other problems of inverse analysis. Heat-deposition fields, for example, temperature fields, associated with these processes are a function of the nature of the energy source interaction (or coupling) with the ambient medium. The general characteristics of interactions between sources and ambient media, especially for the case of energy-deposition processes such as welding, motivates a relatively well-defined posing of the problem for inverse analysis of deposition processes. This posing establishes the need for parametric models of deposition processes whose formulations are optimal for inverse analysis of complex source-ambient-medium interactions. For example, inverse thermal analysis of welding processes still remains an open problem, because of the complexity of energy-source-workpiece coupling related to the wide range of different welding processes [27].

The present study continues upon experimental research previously published by members of the authors' team [7,8], where the feasibility of using CSE technology for the elaboration of wear-resistant surface layers has been proven. Nevertheless, the evaluation of the temperature field within the workpiece is the crucial factor that controls the microstructure obtained in both the solar-treated surface layers and the underlying metal and, thus, their mechanical properties that finally affect the machinability of the so-treated workpiece using conventional tools, as well as the in-service performance of the surface-treated mechanical components. For this purpose, the particular work—part of which has been presented at the Advances in Welding & Additive Manufacturing Research Conference [28]—is targeted to the inverse thermal analysis and parametric modeling of heat deposition associated with the specific heat-deposition taking place during CSE surface processing, in order to describe temperature histories within the volume of the solar-treated workpieces, where direct temperature measurements contain uncertainties and/or are not even possible.

## 2. Materials and Methods

The inverse thermal analysis developed is based on microscopic observations of two CSE-treated materials systems, namely TiC and Cr<sub>3</sub>C<sub>2</sub> powders pre-deposited onto similar carbon steel substrates, at the installations of Plataforma Solar de Almería, PSA (Spain), in particular at the horizontal solar furnace SF40 [29]. As mentioned above [7,8], the general aspects of the surface solar processing have been described in detail in previous works. Carbon steel (DIN 17100 St 37-2) specimens with dimensions 50 × 70 × 15 mm were used as base metals on the polished surface on which the carbide powders were deposited, under preparation conditions such that no interactions between the powder and the substrate material could take place. More precisely, 3.37 g of TiC powder with a particle size distribution −149 + 74 μm and 5.71 g Cr<sub>3</sub>C<sub>2</sub> powder with a particle size distribution of −106 + 45 μm had been manually deposited in the form of disks (∅35, thickness: 1.5 mm), prior to solar processing (Figure 1a). The so-prepared specimens were placed at the center of the processing chamber (Figure 1b), onto a thermal insulating Al<sub>2</sub>O<sub>3</sub> support and exposed to concentrated solar energy (Figure 1c) under continuous flow of Ar inert gas.

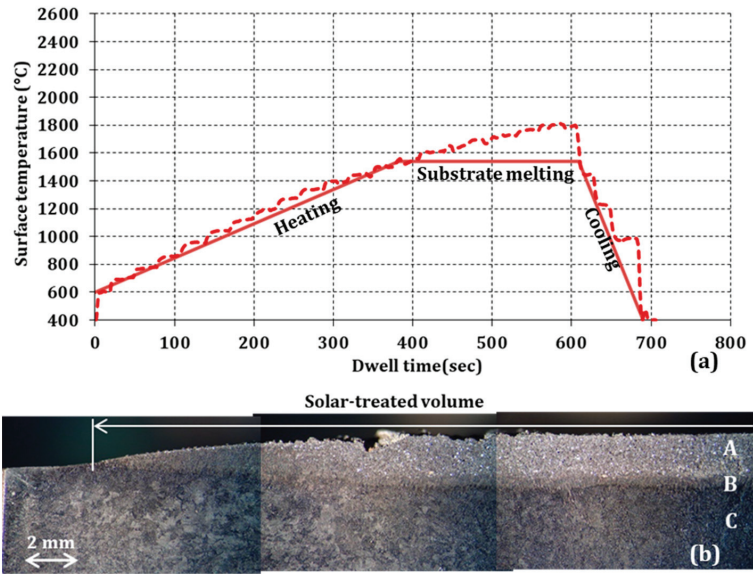


**Figure 1.** Experimental details for the CSE processing aiming to surface cladding: (a) material system to be solar-treated; (b) positioning of the prepared specimen in the processing chamber; (c) experimental arrangement for solar processing.

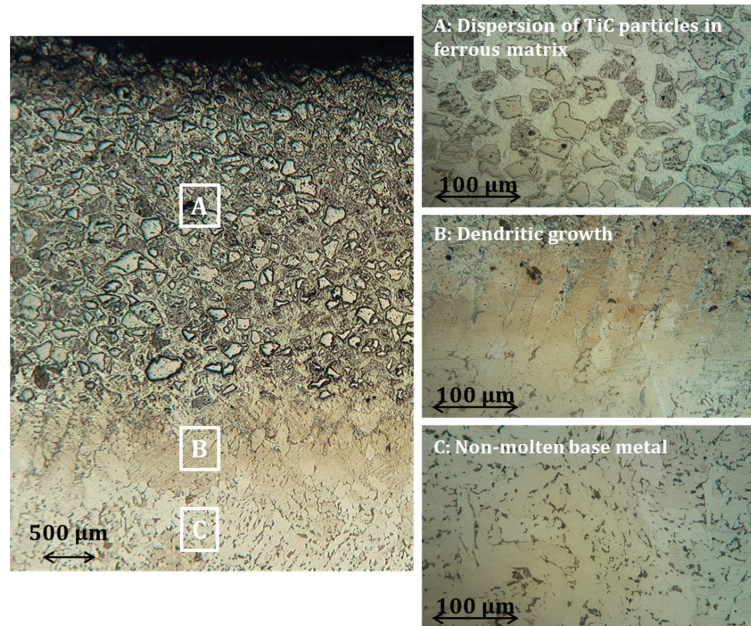
For both material systems, the microscopic observations provide quantitative results on both the extent and geometry of the surface layer that has been led to melting, and the underlying Heat Affected Zone (H.A.Z.), as well as on the metallurgical reactions taking place in the melt and its microstructure obtained during solidification.

### 3. Experimental Findings and Physical Model

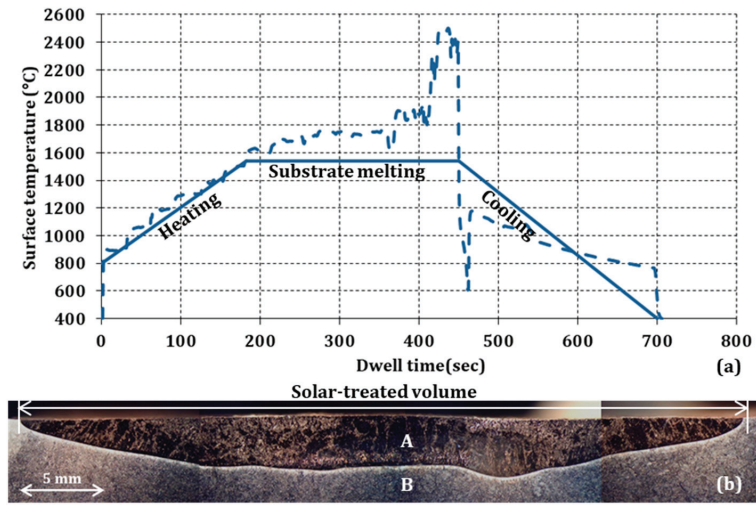
The two material systems considered for prototyping solar-heating analysis in this study exhibited extremely different behavior [7]. In the case of TiC powder (Figure 2), the ceramic particles were dispersed in the liquid metallic matrix, without any metallurgical reaction with it, leading to a “clear” surface composite layer after cooling to ambient temperature (Figure 3). On the contrary, after sufficient solar exposure (Figure 4) the Cr<sub>3</sub>C<sub>2</sub> particles were totally incorporated in the molten pool and diluted in it, leading to a new surface alloy rich in Cr rather than to a surface composite layer (Figure 5).



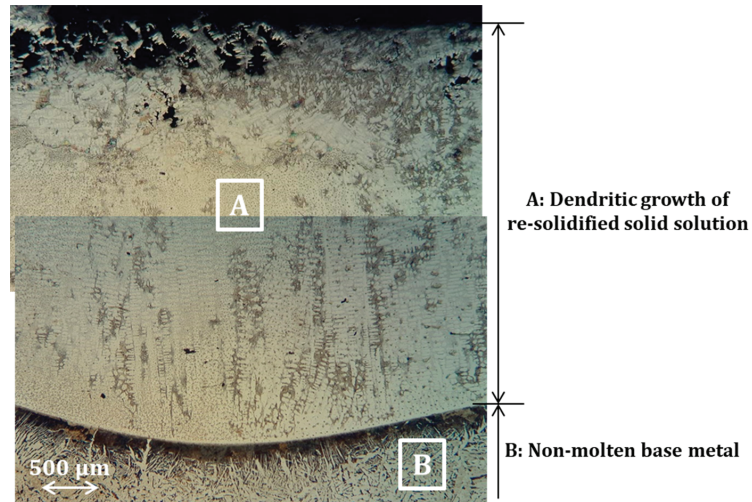
**Figure 2.** Solar processing of TiC/carbon steel system: (a) successive stages during solar processing (dashed line: experimental measurements, reproduced from [7], license number: 5545980711788); (b) half area of the solar-treated specimen obtained (stereoscope cross-section).



**Figure 3.** Optical micrograph of the solar-treated TiC/carbon steel system cross-section, where areas of different microstructure can be clearly identified (middle of the CSE-affected area). Areas marked as A, B and C on the left image, are presented in higher magnification at the right column.



**Figure 4.** Solar processing of  $\text{Cr}_3\text{C}_2$ /carbon steel system: (a) successive stages during solar processing (dashed line: experimental measurements, reproduced from [7], license number: 5545980711788); (b) overall cross section of the solar-treated specimen obtained (stereoscope cross-section).



**Figure 5.** Optical micrograph of the solar-treated  $\text{Cr}_3\text{C}_2$ /carbon steel system cross-section, where areas of different microstructure can be identified (middle of the CSE-affected area).

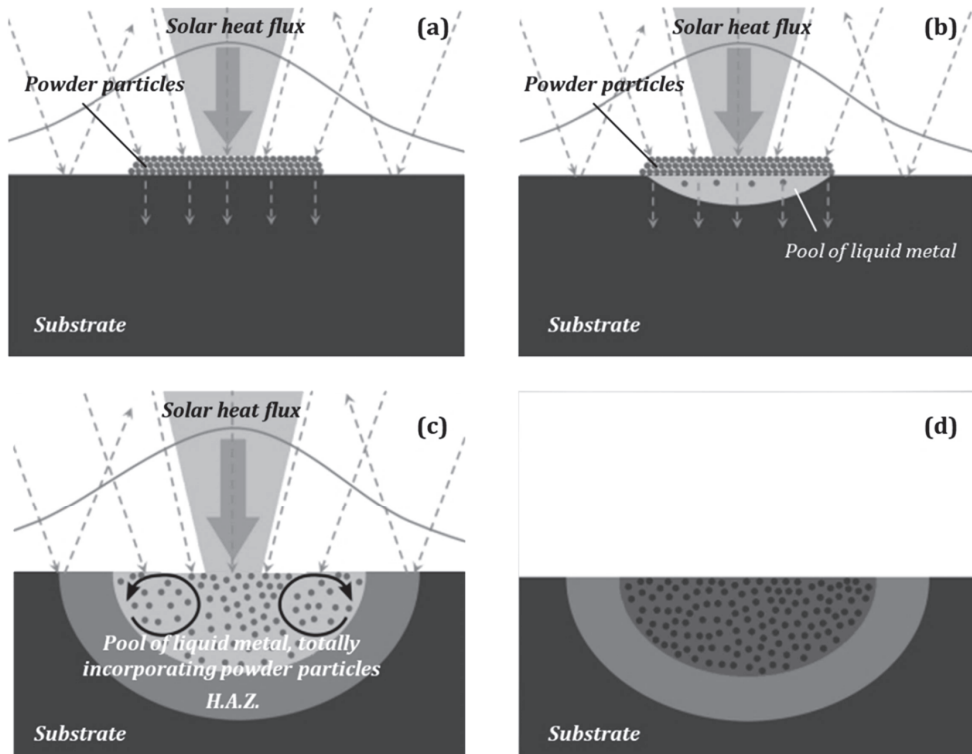
During solar treatment, the surface temperatures of irradiated specimens were monitored in real-time via an optical pyrometer. It should be noted that with respect to inverse thermal analysis, it is assumed that the measured temperatures are estimates, owing to uncertainties due to liquid-surface movement during process-evolution and ambient vapor in the sealed testing bell-jar chamber.

Based on the above experimental findings, a generic physical model describing phenomena that take place during successive stages can be proposed (Figure 6):

- During heating at surface temperature below the melting temperature of the substrate ( $T_{\text{max}}$ : 1540 °C), the concentrated solar energy is absorbed only by the area covered by

the black-colored ceramic particles, while it is reflected by the noncovered polished surface of the base metal (Figure 6a).

- During heating at surface temperature above the melting temperature of the substrate, the solar energy absorbed results in progressive melting of the underlying metal and immersion of the pre-deposited powder in the melting pool (Figure 6b).
- Lasting the solar exposure of the workpiece, the depth of the melting pool increases and the circulation currents in the ferrous melt lead to the homogeneous distribution of the carbide particles in the liquid metal (Figure 6c). Depending on the nature of the incorporated carbides, they either remain non-attached (TiC case), or are diluted in the molten steel ( $\text{Cr}_3\text{C}_2$  case).
- During cooling to ambient temperature, the solidification of the melts follows the thermodynamic path imposed by their chemical composition, whilst solid state metallurgical transformations complete the final microstructure of the obtained solar-treated surface, as well as that of the heat-affected area, H.A.Z., (Figure 6d). In both material systems, the areas of dendritic growth (Figures 3 and 5)—at the bottom of the re-solidified pool, in contact to the nonmolten base metal—are indicative of the solidification starting points and the heat dissipation directions.



**Figure 6.** Simplified schematic representation of the successive stages that can be distinguished during surface solar processing: (a) absorption of concentrated solar energy by the area covered by the black-colored powder particles; (b) heat transfer to the metallic substrate and surface liquidation of the volume wherein temperature exceeded its characteristic melting value; (c) immersion and dispersion of the pre-deposited particles in the molten metallic pool; (d) re-solidified surface volume, consisting of dispersion (case of TiC powder) or total dilution (case of  $\text{Cr}_3\text{C}_2$  powder) of the ceramic particles within the substrate metallic matrix and cooled to ambient temperature.



This physical model (Figure 6) is applied to describe thermal phenomena taking place during the particular solar processing. As depicted, the heat transfer associated with this process is time-dependent and rather complex, as it is governed by the:

- nature of coupling between the surface-heating source and the workpiece that consists of a powder layer onto a metallic substrate. This coupling is not purely diffusive, but in principle, is a combination of Beer—Lambert-type volumetric energy deposition and advection-diffusion of heat;
- thermal contact properties at the pre-deposited powder layer-metallic substrate interface,
- complexity of the metallurgical transformations taking place between the powder layer and substrate materials;
- changes in volume and shape of the molten region that are produced by the dispersion of the powder particles in the solar-affected region of the substrate materials.

It should be noted that the schematic description presented in Figure 6 does not include the process phases of dilatation of the metallic substrate during liquidation of the metal and shrinkage of the composite volume, which is the sum of layer and substrate material volumes during re-solidification and cooling to ambient temperature.

#### 4. Inverse Thermal Analysis

The posing of the associated inverse thermal analysis problem can be derived from the above experimental observations, the surface temperature measurements and the generic physical model described. Given the known qualitative characteristics of the solar-heating process, thermal properties of the constitute materials, shapes and geometries of the powder-layer-substrate system at onset of heating and the re-solidified region after termination of process, and estimates of surface temperature as a function of time, the first step is to construct a parametric model structured for input of this information for prediction of temperature histories within the volume of processed workpieces. Then, the inverse problem is solved accordingly, constrained by the resulting molten volume of mixed material at the surface and estimated surface-temperature history, for the purpose of controlling treatment depth as a function of irradiation time. In principle, treatment depth would be defined by metallurgical transformations taking place within the volume of mixed material during processing. Temperature histories calculated by inverse thermal analysis would be used as input to transformation models and associated software for prediction of metallurgical transformations [26]. The inverse problem, as defined by the solar-heating process, consists of two separate parts, namely estimation of time-dependent temperature fields during heating and cooling, each one associated with the respective stage of the process. As revealed in what follows, more detailed information tends to be available for inverse thermal analysis during the cooling phase, owing to its accessibility by convenient measurement and post-process metallographic analysis.

Presented in this section is a parametric model for inverse thermal analysis of heat transfer through a thin layer of surface material, and a volume of an underlying substrate material, which is characteristic of the process considered here. This model, which uses the heat-kernel solution of the heat-conduction equation as ansatz [27], is given by:

$$T(x, t) = C(t)G(x, x_k, t) \quad (1)$$

and

$$T(x = x_k, t) = T_{Surface}(t) \quad (2)$$

for  $t < t_h$ , the heating period, and for  $t > t_h$ , the cooling period,

$$T(x, t) = C(t_h)G(x, x_k, t) \quad (3)$$

where:

$$G(x, x_k, t) = \frac{1}{\sqrt{4\pi\kappa_u t}} \exp\left[-\frac{(x-x_k)^2}{4\kappa_u t}\right] + \frac{W_0}{\sqrt{4\pi\kappa_u t}} \exp\left[-\frac{(x_{imag})^2}{4\kappa_u t}\right] \quad (4)$$

for  $x \geq x_l$ :

$$G(x, x_k, t) = \frac{W_1}{\sqrt{\pi\kappa_d t}} \exp\left[-\frac{1}{4t} \left(\frac{x-x_l}{\sqrt{\kappa_d}} + \frac{x_l-x_k}{\sqrt{\kappa_u}}\right)^2\right] \quad (5)$$

and for  $x \geq x_s$ :

$$G(x, x_k, t) = \frac{W_1}{\sqrt{\pi\kappa_d t}} \exp\left[-\frac{1}{4t} \left(\frac{x-x_s}{\sqrt{\kappa_s}} + \frac{x_s-x_l}{\sqrt{\kappa_d}} + \frac{x_l-x_k}{\sqrt{\kappa_u}}\right)^2\right] \quad (6)$$

where the weight coefficients  $W_0$  and  $W_1$  are given by:

$$W_0 = \frac{k_u \sqrt{\kappa_d} - k_d \sqrt{\kappa_u}}{k_u \sqrt{\kappa_d} + k_d \sqrt{\kappa_u}} \quad (7)$$

and

$$W_1 = \frac{2k_u \kappa_d}{\sqrt{\kappa_u} (k_u \sqrt{\kappa_d} + k_d \sqrt{\kappa_u})} \quad (8)$$

The distance within the layered material from the surface (at  $x_k$ ) is  $(x - x_k)$ , and the location of the interface between the thin-layer and the substrate is  $(x_s - x_k)$ . The quantities  $k_u, \kappa_u$  are the estimated thermal conductivity and diffusivity of the thin-layer, and  $k_s$  is the thermal diffusivity of substrate materials, respectively. The quantities  $x_l, k_d$  and  $\kappa_d$  are adjustable phenomenological parameters for modeling thermal coupling of layer to substrate at their interface. Accordingly, the distance parameter  $x_l$  is not associated with an actual physical location within the layer system. For  $x < x_l$ ,  $x_{imag} = x + x_k - 2x_l$ , which is also a phenomenological parameter, is not associated with the image-distance of a physical location. Similarly, although  $k_d$  and  $\kappa_d$  are formally conductivity and diffusivity, respectively, they do not represent bulk material properties, relevant schema is presented in Figure 7. The function  $C(t)$  is specified by the boundary and initial conditions defined by Equations (2) and (3), respectively. Specifically, the model assigns two conditions during heating, namely the measured surface temperature and the time period of heating, and one after termination of heating, the time period of cooling. Equations (4)–(8) are the heat-kernel solution to the heat-conduction equation for a one-dimensional system consisting of a layer of a material of finite thickness, on a substrate of essentially infinite extent, where the layer and substrate materials have different thermal properties [25], and there exists complex coupling between the surface-heating source and workpiece, that can be a combination of:

- Beer—Lambert-type volumetric energy-deposition and advection diffusion of heat;
- differentiation of the thermal properties of the surface layer-substrate at the contact interface;
- nonuniform mixing of layer and substrate materials;
- temporal changes of the volume and the exact shape of the molten pool.

This complex coupling is modeled via the adjustable phenomenological parameters  $x_l, \kappa_d$  and  $k_d$ , whilst for the TiC/steel system, the estimated thermal properties and model parameters are:  $k_u = 5.64 \text{ W}/(\text{kg } ^\circ\text{C})$ ,  $\kappa_u = 1.306 \times 10^{-6} \text{ m}^2/\text{s}$  [30],  $\kappa_s = 1.483 \times 10^{-5} \text{ m}^2/\text{s}$  and  $x_s = 1.5 \text{ mm}$ , and those for the  $\text{Cr}_3\text{C}_2/\text{steel}$  system are:  $k_u = 15 \text{ W}/(\text{kg } ^\circ\text{C})$ ,  $\kappa_u = 1.612 \times 10^{-5} \text{ m}^2/\text{s}$  [31–34],  $\kappa_s = 1.483 \times 10^{-5} \text{ m}^2/\text{s}$  and  $x_s = 3.0 \text{ mm}$ . For the analyses whose results are shown in Figures 8–13, the quantity  $g$  is an adjustable coefficient for assigning values to the phenomenological parameters  $k_d$  and  $k_d$ , which is completed by scaling of measured thermal properties of material layers.

The results of inverse thermal analyses for the solar processing of the TiC/common steel system are presented in Figures 8–10, whilst those of the Cr<sub>3</sub>C<sub>2</sub>/common steel system are presented in Figures 11–13. In all cases, the values of the adjustable phenomenological parameters  $x_l$ ,  $k_d$  and  $\kappa_d$  are provided in the figure captions.

Shown in Figure 8 are different volumetric temperature distributions at completion of surface heating of the TiC/common steel system, which is on a timescale that is small relative to that of heat conduction in the layered material (see inset of Figure 9b). As indicated in Figure 8, the shapes of these temperature distributions are a function of the phenomenological parameters  $x_l$ ,  $k_d$  and  $\kappa_d$ . Referring to Figure 8, the temperature distributions for  $x_l = (70/100)1.5$  mm and  $x_l = (10/100)1.5$  mm correspond, respectively, to total and partial volumetric energy deposition.

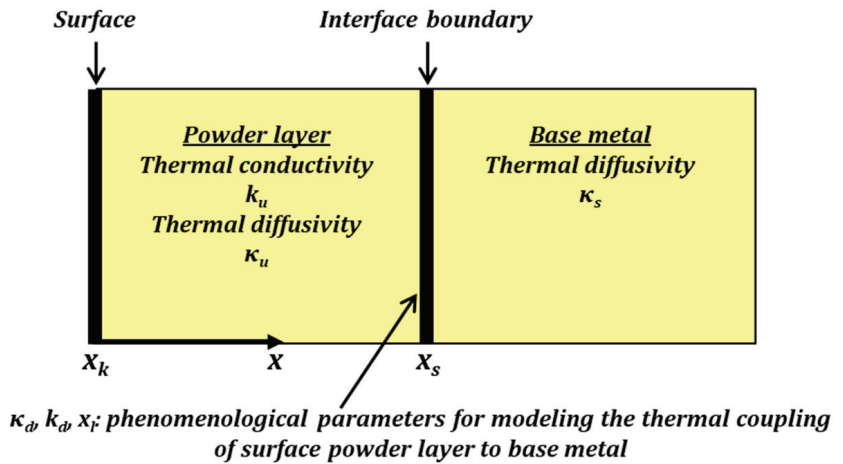


Figure 7. 2D-Schematic representation of regions of the layered-system, and associated material properties and phenomenological parameters for the 1D model defined by Equations (1)–(7).

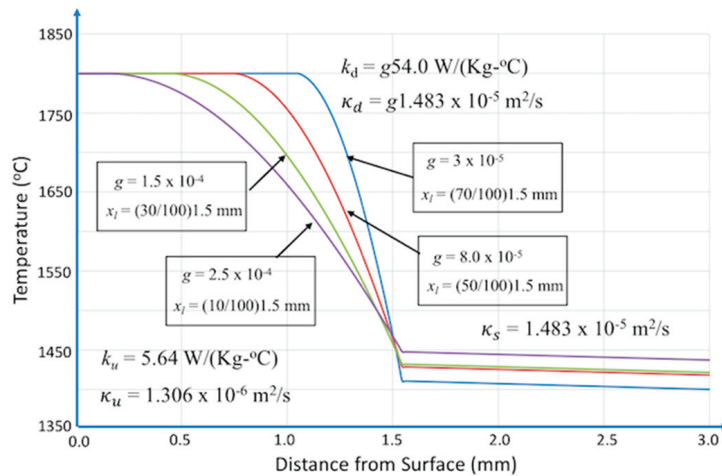
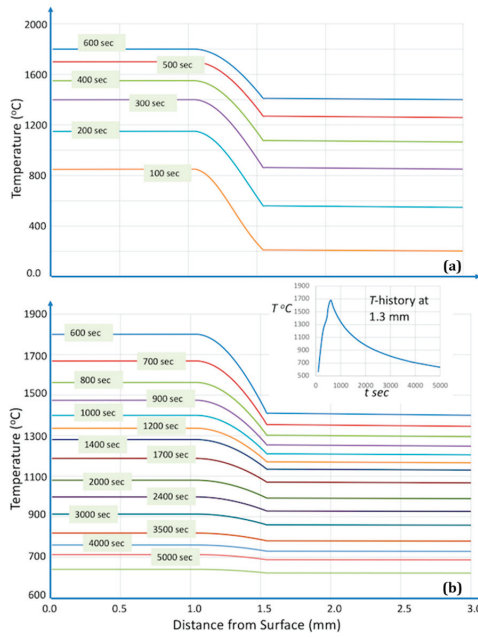
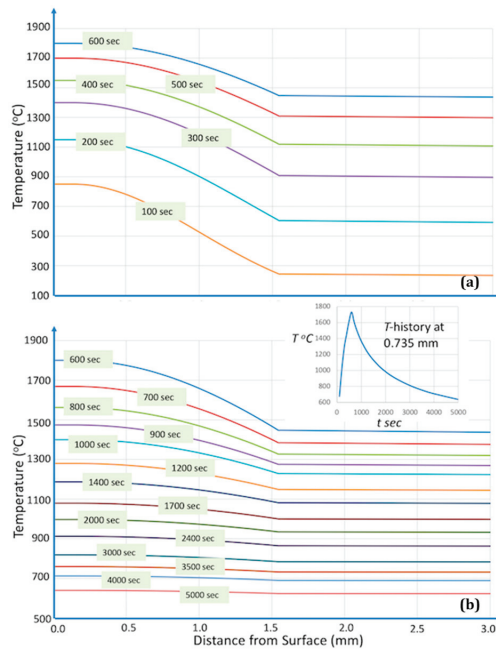


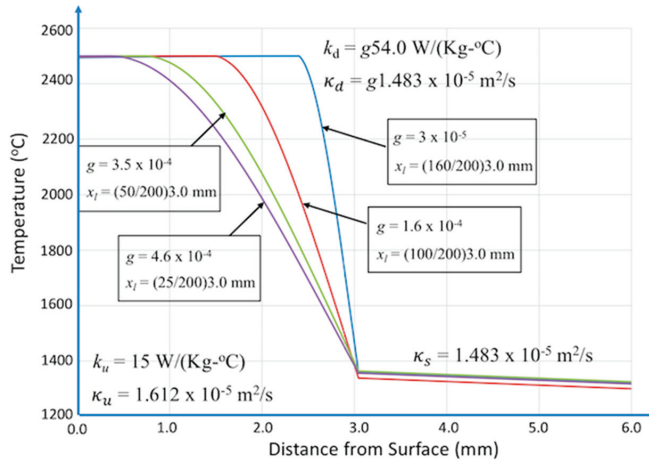
Figure 8. Temperature field at end of heating period as a function of adjustable phenomenological parameters  $x_l$ ,  $k_d$  and  $\kappa_d$  (system TiC/common steel).



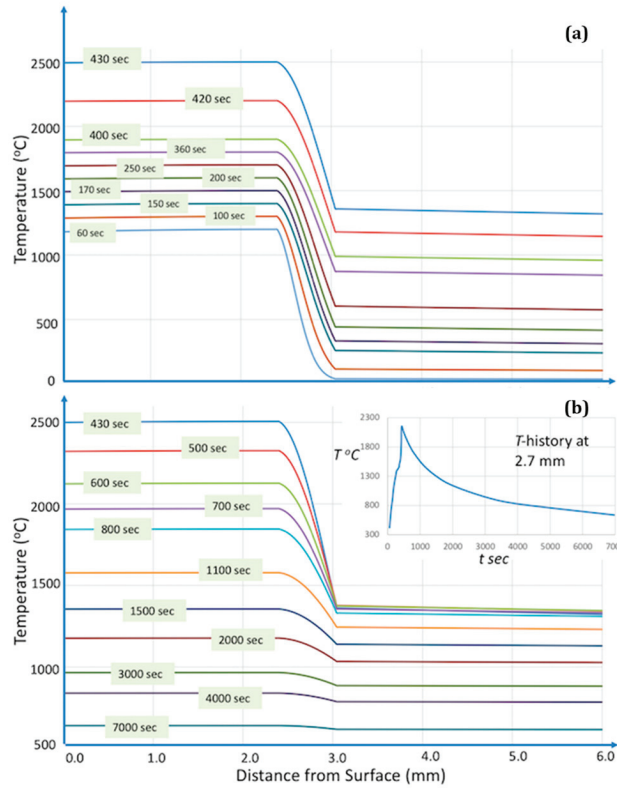
**Figure 9.** Simulations for the system TiC/common steel at  $x_l = (70/100) 1.5$  mm: (a) heating period; (b) cooling period [ $k_d = g54.0$  W/(kg. °C),  $\kappa_d = g1.483 \times 10^{-5}$  m<sup>2</sup>/s, where  $g = 3 \times 10^{-5}$ ].



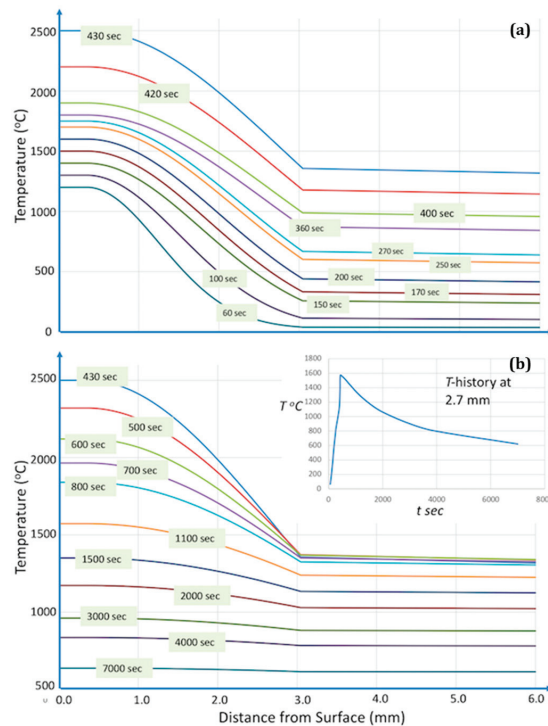
**Figure 10.** Simulations for the system TiC/common steel at  $x_l = (10/100) 1.5$  mm: (a) heating period; (b) cooling period [ $k_d = g54.0$  W/(kg. °C),  $\kappa_d = g1.483 \times 10^{-5}$  m<sup>2</sup>/s, where  $g = 2.5 \times 10^{-4}$ ].



**Figure 11.** Temperature field at end of heating period as a function of adjustable phenomenological parameters  $x_l$ ,  $k_d$  and  $\kappa_d$  (system  $\text{Cr}_3\text{C}_2$ /common steel).



**Figure 12.** Simulations for the system  $\text{Cr}_3\text{C}_2$ /common steel at  $x_l = (160/200) 3.0 \text{ mm}$ : (a) heating period; (b) cooling period [ $k_d = g54.0 \text{ W}/(\text{kg} \cdot ^\circ\text{C})$ ,  $\kappa_d = g1.483 \times 10^{-5} \text{ m}^2/\text{s}$ , where  $g = 3 \times 10^{-5}$ ].



**Figure 13.** Simulations for the system  $\text{Cr}_3\text{C}_2$ /common steel at  $x_l = (25/200)3.0$  mm: (a) heating period; (b) cooling period [ $k_d = g54.0$  W/(kg $^\circ\text{C}$ ),  $\kappa_d = g4.6 \times 10^{-4}$  m $^2$ /s, where  $g = 3 \times 10^{-5}$ ].

Shown in Figures 9 and 10 are heating and cooling periods for the TiC/common steel system, corresponding, respectively, to total and partial energy deposition during surface heating. Comparison of temperature histories shown in Figures 9 and 10 indicates a relative insensitivity of temperature histories in terms of trend during cooling to the range of volumetric energy deposition from partial to total. This result is significant in that estimating the temperature distribution at completion of surface heating, because the complexity of the solar heating process, consisting of multiple coupled physical processes, poses a more difficult problem than estimating the temperature history in the layered system, which is based on heat conduction alone. In particular, of significance is that the temperature distribution at completion of surface heating provides a boundary condition, in terms of the heat conduction equation [27], for prediction of temperature histories in the layer system. There is a direct correlation between maximum temperature at layer-substrate interface and the extent of energy deposition at the surface (see insets of Figures 9 and 10).

From a practical point of view, the feasibility of a quantitative analysis of temperature fields developed during solar processing could be used as a useful tool for the prediction of the microstructure of the solar-treated surface layers (e.g., top layer reinforced by a dispersion of TiC particles, dendritic growth at the bottom melt pool area in contact with the unmolten metal), the extent and the microstructure of the underlying heat affected zone, as well as the solid state modifications of the base metal microstructure (e.g., stress relief, grains growth).

The analysis whose results are shown in Figures 11–13, for the  $\text{Cr}_3\text{C}_2$ /common steel system, follows the same procedure as above for the TiC/common steel system. Shown in Figure 11 are different volumetric temperature distributions at completion of surface heating of the  $\text{Cr}_3\text{C}_2$ /common steel system, ranging from partial to total volumetric energy deposition. Referring to Figure 11, the temperature distributions for  $x_l = (160/200) 3.0$  mm

and  $x_1 = (25/200)$  3.0 mm correspond, respectively, to total and partial volumetric energy deposition. Shown in Figures 12 and 13 are heating and cooling periods for the  $\text{Cr}_3\text{C}_2$ /common steel system, corresponding, respectively, to total and partial energy deposition during surface heating. As for the previous analysis, comparison of temperature histories shown in Figures 12 and 13 indicates a relative insensitivity of temperature histories with respect to trend during cooling to the range of volumetric energy deposition from partial to total, and direct correlation between maximum temperature at layer-substrate interface and the extent of energy deposition at the surface (see insets of Figures 12 and 13).

From a practical point of view, the verification of the quantitative description potency in the case of  $\text{Cr}_3\text{C}_2$  powder that is totally dissolved in the liquid ferrous matrix constitutes strong evidence for the development of a generic model, valid for the quantitative description of solar surface processing of other pre-deposited carbide powder/base metal systems, whatever the metallurgical reactions could be. Thus, such an inverse thermal analysis could be applied as a prediction tool for optimising the solar processing parameters, in order to control the microstructure and, consequently, the mechanical properties and in-service performance of solar-treated material systems.

Overall, the energy deposition process is multiscale with respect to heat transfer, owing to a region of rapid heating (top, directly irradiated layer) being coupled to one of purely diffusive heat transfer (underlying workpiece volume), thus posing a specific problem for inverse thermal analysis, as discussed above (see Figures 6 and 7). The model, Equations (1)–(8), and simulations using this model, whose results are shown in Figures 8–13, examines the nature of the coupling between two regions where heat transfer occurs on different timescales, and is controlled by characteristics of their interface coupling. The timescale and rate for heat transfer at the top layer can be estimated by in-situ surface-temperature measurements and ex-situ optical microscopy observations of the volume of the workpiece, while rate for heat transfer within the workpiece is predictable given the thermal diffusivity and observed microstructural changes within the workpiece, see Figures 2–5. The unknown characteristic of the layered system, to be estimated by inverse thermal analysis, is the coupling between these regions.

What is known a priori concerning the thermal physics of interfaces between two materials having different thermal properties is represented formally by the model Equations (1)–(8). Considered in this model is that even for the ideal case, where thermal contact resistance is not present, differences in thermal diffusivity are sufficient to induce reflected thermal transport during time-dependent heat transfer across an interface [27]. For the nonideal case, which should be assumed for the process considered here, contact resistance at the interface will contribute to reflected heat transfer within the top layer. The characteristics of contact resistance with respect to reflected heat transfer is by nature extremely complex, having multi-variable dependence, and thus modelled using phenomenological parameters. The results of simulations show that a range of reasonable estimated interface-coupling strengths, defined by phenomenological adjustable parameters (see Figures 8 and 11), can be determined by inverse thermal analysis, given the measured boundary constraints imposed by the top-layer and workpiece regions. With respect to process control, these simulations show that characteristics of the interface coupling are a significant controlling factor for heat transfer, as demonstrated by comparison of Figures 9 and 12 to Figures 10 and 13, respectively, and thus may suggest methods of process control in the future. Overall, the solar heating process is defined by rate of solar-energy coupling to the top layer, and subsequently, coupling of this energy to the workpiece, which is a function of interface heat-transport characteristics.

Recently, such an inverse analysis approach has been successfully adopted for the evaluation of the solidification path of stainless steel melts [35] and microstructure modifications of Inconel 718 [36], both taking place during additive manufacturing via Selective Laser Melting.

## 5. Conclusions

The purpose of this study was to describe a generic parametric model for the estimation of temperature histories within bi-material workpieces subjected to surface treatment applying Concentrated Solar Energy. During solar processing, details on the exact amount of the volumetric energy deposition within the workpiece are difficult to be determined. Thus, reverse thermal analysis constitutes a powerful tool for describing quantitatively the temporal and spatial temperature evolution, based on post-processing metallographic observations of the microstructures obtained.

In summary, the CSE surface treatment of two carbide powder/common steel systems resulted in reinforced surface clads that have been previously proven to exhibit acceptable machinability using conventional cutting tools and superior in-service wear resistance. The present first attempt revealed the potential of applying reverse thermal analysis and parametric modeling for the prediction of the temperature history within the CSE-affected area and to correlate, by extension, the solar-layers performance to the solar processing parameters.

**Author Contributions:** Conceptualization, P.P.P.; thermal analysis, S.G.L. and A.D.Z.; experimental validation, A.G.M., I.G.P. and J.R.; metallographic observation, I.G.P.; solar processing, A.G.M. and J.R.; initial manuscript preparation, S.G.L. and A.D.Z.; final manuscript preparation and editing, P.P.P. All authors have read and agreed to the published version of the manuscript.

**Funding:** The experimental work received partial funding from EU-DG RTDs Programme “Solar Facilities for the European Research Area—Second Phase –SFERA II” (projects: CarbiSol P1404300058, P1503060136 and P1602050194). The work of S.G.L. was supported by a Naval Research Laboratory (NRL) internal energy-deposition processes modeling core program.

**Institutional Review Board Statement:** Not applicable.

**Informed Consent Statement:** Not applicable.

**Data Availability Statement:** Data presented in this article are available at request from the corresponding author.

**Conflicts of Interest:** The authors declare no conflict of interest.

## References

1. Pitts, J.R.; Tracy, E.; Shinton, Y.; Fields, C.L. Applications of solar energy to surface modification processes. *Crit. Rev. Surf. Chem.* **1993**, *2*, 247–269.
2. Rodríguez, G.P.; de Damborenea, J.J.; Vázquez, A.J. Surface hardening of steel in a solar furnace. *Surf. Coat. Technol.* **1997**, *92*, 165–170. [[CrossRef](#)]
3. Flamant, G.; Ferriere, A.; Laplaze, D.; Monty, C. Solar processing of materials: Opportunities and new frontiers. *Sol. Energy* **1999**, *66*, 117–132. [[CrossRef](#)]
4. Rodríguez, G.P.; Herranz, G.; Romero, A. Solar gas nitriding of Ti6Al4V alloy. *Appl. Surf. Sci.* **2013**, *283*, 445–452. [[CrossRef](#)]
5. Pantelis, D.I.; Psyllaki, P.; Sarafoglou, C. Surface alloying on cast iron using concentrated solar energy. *Fonderie Fondateur Aujourd'hui* **2002**, *211*, 23–33.
6. Mourlas, A.; Psyllaki, P.; Pantelis, D. Anti-wear TiC-based surface layers using concentrated solar energy. *Key Eng. Mater.* **2016**, *674*, 296–301. [[CrossRef](#)]
7. Mourlas, A.; Pavlidou, E.; Vourlias, G.; Rodríguez, J.; Psyllaki, P. Concentrated solar energy for in-situ elaboration of wear-resistant composite layers. Part I: TiC and chromium carbide surface enrichment of common steels. *Surf. Coat. Technol.* **2019**, *377*, 124882. [[CrossRef](#)]
8. Mourlas, A.; Pavlidou, E.; Vourlias, G.; Rodríguez, J.; Psyllaki, P. Concentrated solar energy for in-situ elaboration of wear-resistant composite layers. Part II: Tungsten carbide surface enrichment of common steels. *Surf. Coat. Technol.* **2019**, *375*, 739–751. [[CrossRef](#)]
9. Pantelis, D.I.; Griniari, A.; Sarafoglou, C. Surface alloying of pre-deposited molybdenum-based powder on 304L stainless steel using concentrated solar energy. *Sol. Energy Mat. Sol. Cells* **2005**, *89*, 1–11. [[CrossRef](#)]
10. Fernández-González, D.; Ruiz-Bustanza, I.; González-Gasca, C.; Piñuela-Noval, J.; Mochón-Castaños, J.; Sancho-Gorostiaga, J.; Verdeja, L.F. Concentrated solar energy applications in materials science and metallurgy. *Sol. Energy* **2018**, *170*, 520–540. [[CrossRef](#)]
11. International Energy Agency. Renewable Energy for Industry: From Green Energy to Green Materials and Fuels. 2017. Available online: <https://www.iea.org/publications/freepublications/publication/> (accessed on 25 March 2023).



12. Sánchez Bautista, C.; Rodríguez, G.P.; Ferriere, A. Numerical modelling of the solar cladding process. *Surf. Coat. Technol.* **2008**, *202*, 1594–1605. [[CrossRef](#)]
13. Li, B.; Oliveira, F.A.C.; Rodríguez, J.; Fernandes, J.C.; Rosa, L.G. Numerical and experimental study on improving temperature uniformity of solar furnaces for materials processing. *Sol. Energy* **2015**, *115*, 95–108. [[CrossRef](#)]
14. Romero, A.; García, I.; Arenas, M.A.; López, V.; Vázquez, A. High melting point materials welding by concentrated solar energy. *Sol. Energy* **2013**, *95*, 131–143. [[CrossRef](#)]
15. Román, R.; Cañadas, I.; Rodríguez, J.; Hernández, M.T.; González, M. Solar sintering of alumina ceramics: Microstructural development. *Sol. Energy* **2008**, *82*, 893–902. [[CrossRef](#)]
16. Gutiérrez-López, J.; Levenfeld, B.; Várez, A.; Pastor, J.Y.; Cañadas, I.; Rodríguez, J. Study of the densification, mechanical and magnetic properties of Ni-Zn ferrites sintered in a solar furnace. *Ceram. Int.* **2015**, *41*, 6534–6541. [[CrossRef](#)]
17. Herranz, G.; Romero, A.; DeCastro, V.; Rodríguez, G.P. Processing of AISI M2 high speed steel Reinforced with vanadium carbide by solar sintering. *Mater. Des.* **2014**, *54*, 934–946. [[CrossRef](#)]
18. Cambronero, L.E.G.; Cañadas, I.; Martínez, D.; Ruiz-Román, J.M. Foaming of aluminium-silicon alloy using concentrated solar energy. *Sol. Energy* **2010**, *84*, 879–889. [[CrossRef](#)]
19. Ozisik, M.N.; Orlande, H.R.B. *Inverse Heat Transfer, Fundamentals and Applications*; Taylor & Francis: New York, NY, USA, 2000.
20. Kurpisz, K.; Nowak, A.J. *Inverse Thermal Problems—Computational Engineering*; WIT Press: Boston, MA, USA, 1995.
21. Alifanov, O.M. *Inverse Heat Transfer Problems*; Springer: Berlin/Heidelberg, Germany, 1994.
22. Beck, J.V.; Blackwell, B.; St. Clair, C.R., Jr. *Inverse Heat Conduction: Ill-Posed Problems*; John Wiley & Sons Inc.: New York, NY, USA, 1985.
23. Beck, J.V. Inverse Problems in Heat Transfer with Application to Solidification and Welding. In Proceedings of the 5th Conference on Modeling of Casting, Welding and Advanced Solidification Processes, Davos, Switzerland, 16–21 September 1990.
24. Beck, J.V. Inverse Problems in Heat Transfer. In *Mathematics of Heat Transfer*; Topholme, G.E., Wood, A.S., Eds.; Oxford University Press: New York, NY, USA, 1998; pp. 13–24.
25. Lambrakos, S.G. Parametric Modeling of welding processes using numerical-analytical basis functions and equivalent source distributions. *J. Mater. Eng. Perform.* **2016**, *25*, 1360–1375. [[CrossRef](#)]
26. Prosgolitis, C.G.; Lambrakos, S.G.; Zervaki, A. Phase-Field Modeling of Nugget Zone for a AZ31-Mg-Alloy Friction Stir Weld. *J. Mater. Eng. Perform.* **2018**, *27*, 5102–5113. [[CrossRef](#)]
27. Carslaw, H.S.; Jaeger, J.C. *Conduction of Heat in Solids*, 2nd ed.; Oxford University Press: New York, NY, USA, 1986; p. 374.
28. Zervaki, A.D.; Mourlas, A.G.; Psyllaki, P.P.; Lambrakos, S.G. Parametric Model of Concentrated Solar Energy Surface Processing. In Proceedings of the Advances in Welding & Additive Manufacturing Research Conference 2022, Miami, FL, USA, 13–16 June 2022.
29. Rodríguez, J.; Cañadas, I.; Zarza, E. New PSA high concentration solar furnace SF40. *AIP Conf. Proc.* **2016**, *1734*, 070028.
30. Shackelford, J.F.; Han, Y.-H.; Kim, S.; Kwon, S.-H. *CRC Materials Science and Engineering Handbook*, 4th ed.; Taylor & Francis: Boca Raton, FL, USA, 2015; pp. 50, 263, 279.
31. Pankratz, L.B. *Thermodynamic Properties of Carbides, Nitrides, and Other Selected Substances*; US Department of the Interior, Bureau of Mines: Washington, DC, USA, 1994; 696, p. 223.
32. Desorbo, W. Heat Capacity of Chromium Carbide ( $\text{Cr}_3\text{C}_2$ ) from 13 to 300 °K. *J. Am. Chem. Soc.* **1953**, *75*, 1825–1827. [[CrossRef](#)]
33. Oriani, R.A.; Murphy, W.K. The Heat Capacity of Chromium Carbide ( $\text{Cr}_3\text{C}_2$ ). *J. Am. Chem. Soc.* **1954**, *76*, 343–345. [[CrossRef](#)]
34. Kelley, K.K.; Boericke, F.S.; Moore, G.E.; Huffman, E.H.; Bangert, W.M. *Thermodynamic Properties of the Carbides of Chromium*; US Department of the Interior, Bureau of Mines: Washington, DC, USA, 1944; 662, pp. 7–15.
35. Abolhasani, D.; Hossein Seyedkashi, S.M.; Kang, N.; Kim, Y.J.; Woo, Y.Y.; Moon, Y.H. Analysis of Melt-Pool Behaviors during Selective Laser Melting of AISI 304 Stainless-Steel Composites. *Metals* **2019**, *9*, 876. [[CrossRef](#)]
36. Tabaie, S.; Rézaï-Aria, F.; Jahazi, M. Microstructure Evolution of Selective Laser Melted Inconel 718: Influence of High Heating Rates. *Metals* **2020**, *10*, 587. [[CrossRef](#)]

**Disclaimer/Publisher’s Note:** The statements, opinions and data contained in all publications are solely those of the individual author(s) and contributor(s) and not of MDPI and/or the editor(s). MDPI and/or the editor(s) disclaim responsibility for any injury to people or property resulting from any ideas, methods, instructions or products referred to in the content.

## Article

# Evaluating Surface Quality of Inconel 617 by Employing Deep Cryogenically Treated Electrodes in Surfactant-Added Dielectrics of Transformer Oil

Kashif Ishfaq <sup>1</sup>, Muhammad Sana <sup>1</sup>, Muhammad Arif Mahmood <sup>2,\*</sup>, Saqib Anwar <sup>3</sup> and Muhammad Umair Waseem <sup>1</sup>

<sup>1</sup> Department of Industrial and Manufacturing Engineering, University of Engineering and Technology, Lahore 54890, Pakistan

<sup>2</sup> Intelligent Systems Center, Missouri University of Science and Technology, Rolla, MO 65409, USA

<sup>3</sup> Industrial Engineering Department, College of Engineering, King Saud University, P.O. Box 800, Riyadh 11421, Saudi Arabia

\* Correspondence: mmahmood@mst.edu; Tel.: +1-573-341-4908

**Abstract:** Over the past few decades, better surface quality has remained of great interest to researchers. It deteriorates the fatigue life of the workpiece. The criticality arises when a material of greater strength is selected to work in high-temperature areas such as nickel (Ni)-based superalloys, categorically Inconel 617. Conventional machining operations are not the best choice for the machining of this alloy because of its low density and greater strength. Therefore, electric discharge machining (EDM) is generally engaged. Still, there is a great necessity to make a more reliable surface using EDM, which performs better even in harsh working areas. Therefore, this study examined the potential of deep-cryogenically treated electrodes under the modified dielectrics of transformer oil in the said context, which has not been discussed so far. A set of 30 experiments was performed, designed using the full factorial technique. Deep-cryogenically treated electrodes provided better surface quality in comparison to the non-treated electrodes. Amongst the deep-cryogenically treated electrodes, brass performed outstandingly and provided the lowest value of surface roughness (SR), 6.65  $\mu\text{m}$ , in the modified dielectric of transformer oil with Span 80. The surface finish of deep-cryogenically treated brass is 28.72% better compared to the average value of the overall deep-cryogenically treated electrodes. The lowest value of SR (8.35  $\mu\text{m}$ ) was gained by engaging a non-cryogenically treated Cu electrode with a T-20-transformer oil-modified dielectric. The said value of SR is 17.7% better than the highest value of SR achieved in the case of S-80-transformer oil with a non-cryogenically treated Cu electrode.

**Keywords:** surface quality; cryogenic treatment; transformer oil; Inconel 617; surfactant

**Citation:** Ishfaq, K.; Sana, M.; Mahmood, M.A.; Anwar, S.; Waseem, M.U. Evaluating Surface Quality of Inconel 617 by Employing Deep Cryogenically Treated Electrodes in Surfactant-Added Dielectrics of Transformer Oil. *Metals* **2023**, *13*, 1092. <https://doi.org/10.3390/met13061092>

Academic Editor: George A. Pantazopoulos

Received: 8 May 2023

Revised: 2 June 2023

Accepted: 4 June 2023

Published: 9 June 2023



**Copyright:** © 2023 by the authors. Licensee MDPI, Basel, Switzerland. This article is an open access article distributed under the terms and conditions of the Creative Commons Attribution (CC BY) license (<https://creativecommons.org/licenses/by/4.0/>).

## 1. Introduction

Surface quality is an essential aspect of all machining processes, i.e., traditional, and nontraditional. The better surface quality of difficult-to-machine alloys increased the fatigue life of work in harsh cutting areas [1]. The material removal phenomena cause overlapping craters in nontraditional machining operations, resulting in a rougher surface [2]. There is a functional relationship between the roughness and the performance/functional properties of the machined surface. The roughness of a machined surface has an important role in determining the interaction between the surface and its functional environment. A rough surface usually demonstrates a high wear rate and higher coefficient of friction than a smooth surface. It influences the mechanical and chemical properties of the machined component [3]. An increase in surface roughness (SR) upsurges the stress concentration factor, leading to a decrease in fatigue strength [4]. Moreover, a high roughness value promotes grain slip and crack initiation at the surface of the material [5]. The corrosion

rate is also affected by a variation in this parameter. It has been reported that the corrosion rate significantly improves as the arithmetic mean roughness ( $R_a$ )—one of the measures of surface roughness—is increased [6].

During the spark-off time, eroded material resolidified on the workpiece's surface, forming a recast layer that increased the material's SR. The SR parameter 'Ra' is termed as the arithmetic average of the irregularities produced on the surface of the machined specimen after the machining process. The recast layer showed different characteristics compared to the original material. Properties such as brittleness and hardness of the material after the recast layer are changed from the previous material [7]. Therefore, the recast layer in the non-conventional machining process must be avoided so that the fatigue life of work can be increased. Hard-to-cut Ni-based superalloys such as Inconel 617 are widely used in aerospace, gas turbines, super boilers, aircraft, and combustion cans [8]. Ni-based superalloys are employed in the above fields due to their high stability under vigorous cutting, strength, and low density [9]. Considering its unique properties, the increased strength, low thermal conductivity, and rapid strain hardening make Inconel 617 difficult to machine using typical methods such as milling, drilling, and lathe [10]. A non-traditional setup was built to process the Ni-alloy for this purpose. Electric discharge machining (EDM), wire-EDM, electric discharge drilling, and milling are examples of nonconventional processes [11,12]. Because of its new qualities, the EDM die sinker was chosen over all other choices. One of the great benefits of EDM is that it can be used for machining with a thin tool, resulting in precise geometric perfection as well as an excellent surface quality that cannot be achieved using other traditional machining procedures such as grinding [13]. As illustrated, regardless of mechanical properties, EDM can process difficult-to-cut materials such as Inconel 617 [14,15].

EDM, or spark erosion, is preferred over older methods because it can precisely build complicated morphologies, dies, and molds regardless of material type [16,17]. Researchers say EDM can cut strong metals, alloys, and composites without respect to metallurgical properties [18]. EDM uses repeated electric sparks between the workpiece–electrode gap to melt and vaporize the material. Discharges create a plasma channel in the gap by ionizing the dielectric fluid surrounding the electrode [12,19]. The tool's surface is opposite the object's needed shape [20,21]. EDM requires dielectric fluid [22,23]. It cools the material during pulse off-time and flushes debris/chips from the machined surface [24]. EDM uses several dielectrics based on need. Dielectric fluids include mineral oils, hydrocarbons, mineral seal oils, water-based dielectrics, water with and without additives, gaseous dielectrics, and powder-added dielectrics. Dielectrics differ in material removal rate (MRR), surface quality, wear ratios, and accuracy [25,26]. In EDM, kerosene oil is commonly utilized as a traditional dielectric liquid. However, its high flammability, minimum cutting rates, and poor performance as a result of material removal rate, tool wear rate, and surface polish make it unsuitable for operating Inconel 617 using EDM [27]. As a result, researchers have shifted their focus away from kerosene and onto another hydrocarbon-based dielectrics, i.e., transformer oil, with a higher flash point, fire point, lower viscosity, and higher thermal conductivity. Furthermore, transformer oil produces better results than kerosene oil, but the MRR, tool wear rate (TWR), and SR obtained using it as EDM oil are insignificant [28]. To overcome the said flaws, certain additives have been added to increase the dielectric properties and the machine reactions.

To address the restrictions of poor surface quality, an electrically conductive metal powder, such as alumina, copper, and silicon, is added to the dielectric fluid, reducing its insulating property [29]. These conductive microparticles/nanoparticles operate as a bridge when an appropriate voltage is supplied across the tool and workpiece material. Because these powder particles are scattered, they form chains in several locations beneath the sparking area, increasing the spark gap [30]. Fast sparking occurs when the number of sparks per unit time increases, causing the workpiece material to be removed quickly [29,31]. By expanding the plasma channel, added powder enhances spark density. As a result, regular sparking occurs on the material. This uniform sparking contributes to the workpiece's

smooth surface finish [32]. However, the introduction of micro/nano-powder to the dielectric medium experienced a serious difficulty of agglomeration, which curtailed sparking through the dielectric medium and hence limited EDM performance [33,34]. The creation of agglomeration during EDM reduces sparking, thereby affecting output results. Surfactants lower dielectric medium surface tension and facilitate additive mixing and mobility [35]. Surfactants are hydrophilic and lipophilic surface-active substances [36]. Emulsifiers, which are classified as a subgroup of the substance class known as surfactants, are also employed in dielectrics to increase surface smoothness [37].

Poor surface finish during material EDM is the key concern. Surfactants and metallic particles in dielectric media as well as electrodes treatment are used to solve the problem. Deep-cryogenically treated (CT) electrodes during EDM have solved this problem in previous investigations. Cryogenic treatment of electrodes increased wear characteristics by eliminating poor surface finish [38]. Ozdemir [39] performed shallow CT high Cr-Fe and low carbon cast steel at  $-84\text{ }^{\circ}\text{C}$  and discovered improved wear characteristics. Shallow cryogenic treatment improved microstructure, the study found. Senthilkumar and Rajendran [40] found that cryogenic treatment on En 19 steel increased its wear characteristics by 114% after shallow cold working and 214% after deep cold working. Jamadar and Kavade [32] measured the SR of AISI D3 steel using a copper electrode in EDM and aluminum powder particles in IPOL oil as a dielectric. At low peak current, higher pulse on time, and six grams per liter of aluminum powder in the dielectric medium, the SR of the steel improved significantly. Jafarian [20] used Inconel 718 alloy as base material and EDM against a square copper electrode in kerosene oil as a dielectric. By increasing the pulse on time from 120 to 240  $\mu\text{s}$ , the machined specimen's SR improved significantly, according to the author. Kumar et al. [30] examined Inconel 718 alloy workpiece and copper electrode EDM output responses. Stirrers suspended aluminum powder in EDM oil. Suspended aluminum powder increased the specimen's SR. The right current input parameter improved MRR and TWR output responses.

Kolli and Kumar [18] used the Taguchi design of the experiment to determine how the surfactant and graphite powder dispersed in dielectric medium-affected titanium alloy EDM against the copper electrode. The authors found that using the least surfactant, graphite powder, and discharge current resulted in the best surface finish. Abdul Razak et al. [41] investigated surfactant(s) addition during EDM of reaction-bonded silicon carbide against a copper electrode using EDM oil as the dielectric medium. MRR, SR, and TWR were better with the surfactant Span 20 than Span 80. Adding 0.4 weight % to the dielectric medium during EDM improved the surface finish. Li et al. [42] evaluated the machining proficiency of EDM by taking Inconel 718 alloy as the workpiece and two different electrodes, namely simple copper and a modified electrode, i.e., Cu-SiC, during the machining operation. The authors concluded that the modified electrode provided high surface quality compared to the simple one when the machined specimen was testified. The supremacy of EDM was examined by Wu et al. [43] by using SKD61 steel as the workpiece material and copper as the electrode, and in addition, surfactant was added to enhance the conductivity of the dielectric medium. The authors found that due to the addition of the surfactant in the dielectric medium, the output response, i.e., MRR, increased by 40%, but when the optimal settings were engaged, the said response was enhanced by 80%. The authors also claimed that the SR did not significantly deteriorate when MRR was of greater value. Kumar et al. [38] used the cryogenic treatment on different electrodes to determine tool life and study its effects on electrode materials. The cryogenic treatment on the electrodes increased tool life by 92% and improved tribological characteristics (wear and friction coefficient), hardness, and toughness. AbdulKareem et al. [44] examined the effect of cryogenic treatment on a copper electrode during EDM of titanium alloy. By cryogenically treating the copper electrode, the electrical and thermal conductivities increased, improving output responses.

Srivastava and Pandey [45] examined how cryogenic treatment affected a copper electrode against high-speed steel during EDM of M2-grade steel. The authors found that

cryogenic treatment on the copper electrode lowered EWR by 20% and improved surface quality by 27% compared to standard machining. Ram et al. [46] examined the influence of cryogenic treatment on a graphite electrode during the EDM of EN31 as the base material. The authors found that the CT graphite electrode enhanced the surface finish of EN31 when the machined specimen was testified, and statistical data approaches were engaged. Jaffer-son and Hariharan [47] investigated the wear properties of different electrode materials, i.e., tungsten, brass, and copper, against the workpiece material AISI304 during EDM. The authors found that a CT tungsten electrode provided better microhardness, less TWR, and better electrical conductivity compared to other electrodes.

Bartkowiak et al. [48] explored the surface topography of steel using graphite electrodes during the EDM process and by utilizing motif and multiscale analyses. The authors found that with the change in the machining parameters the surface topography, i.e., craters, changed. Along with that, the authors also claimed that the discharge energy was the most influential effect, which results in the production of large amounts of craters. Gogolewski [49] used spherical objects to assess the surface morphology of Ti alloy-based powder prepared using additive technology. The surface morphology was measured using a multiscale approach. The author claimed that the findings aid in the advancement of cutting-edge diagnostic systems that can examine surface topography swiftly and thoroughly across several phases of data collection and processing.

Based on the research discussed above, the effectiveness of surfactant-based dielectrics using deep cryogenically treated (CT) electrodes is still to be determined. Additionally, the surfactant(s) capacity for Inconel 617 EDM utilizing CT electrodes has not been thoroughly discovered using transformer oil. The SR of a Ni-based superalloy using CT and non-deep cryogenically treated (NT) electrodes in various dielectrics examined in this work will be a great contribution to impeding the recast layer and obtaining a better surface finish during the EDM process. The experiment used CT and NT electrodes with distinct dielectrics with the addition of surfactants in transformer oil. Energy-dispersive X-ray spectroscopy (EDS) analysis was also explored to investigate the deposition of materials on the workpiece surface after EDM. The optimal dielectric and electrode are recommended and tested for this project.

## 2. Materials and Methods

Using five tailored dielectric mediums, deep cryogenically treated (CT) and non-deep cryogenically treated (NT) electrodes were tested against a Ni-based superalloy during machining. Surface roughness (SR) was used to evaluate the most important process yield. Optical microscopy was used to determine Inconel 617's composition. SR was measured in terms of arithmetic mean ( $R_a$ ), which is a commonly used roughness parameter. The selection of this parameter was based on the rationale that it provides the mean value of surface asperities distributed about the mean line within the defined evaluation length. So, this parameter shows a holistic picture of the surface's quality. For each of the machined cavities, roughness measurements were made at five different points. Considering that the roughness values are closely related (standard deviation is small), an average of these five points was used for further analysis. Table 1 lists the chemical composition of the selected workpiece material and details the parameters kept constant in this study. These parameters were kept constant, as the focus of the current research is to evaluate the impact of nontreated and cryogenically treated electrodes on surface quality in EDM of Inconel-617 (IN617) under surfactant-based transformer oil dielectrics. Preliminary trials were carried out to determine the values of these parameters. Those parametric levels were identified for final experimentation, which ensures the availability of complete machining expression on the workpiece surface. Minimum chance of arcing was another important consideration that was kept in mind while finalizing the parametric values. A rectangular workpiece with dimensions 60 mm × 60 mm × 5 mm was used for experimental investigation.

**Table 1.** Chemical attributes of nickel-based superalloy and constant factor [50].

Element	%Wt.	Element	%Wt.	Constant Factors (Units)	Values
Ni	44.5	B	0.006	Surfactant concentration (vol %)	6
Cr	20.0–24.0	S	0.015	Spark voltage (volts)	4
Co	10.0–15.0	Cu	0.5	Current (amperes)	10
Mo	8.0–10.0	Ti	0.6	Pulse off time (μsec)	26
Fe	3.0	Mn	1.0	Pulse on time (μsec)	100
Al	0.8–1.5	Si	1.0	-	-
C	0.05–0.15	-	-	-	-

This investigation used 9 mm diameter copper, brass, and graphite electrodes. Electrode materials' efficiency was tested before and after cryogenic treatment. The electrodes were inserted in the nitrogen container and exposed to liquid nitrogen at  $-185\text{ }^{\circ}\text{C}$  to cryogenically operate. Electrodes were held at this temperature for around 24 h to finish the cryogenic process. Five dielectrics—transformer oil, Span 20+ transformer oil, Span 80+ transformer oil, Tween 20+ transformer oil, and Tween 80+ transformer oil—were tested against three electrodes. Table 2 shows the surfactants' main traits.

**Table 2.** Chemical and physical properties of surfactants [27,51,52].

Properties	Chemical Formula	Molecular Weight (g/mol)	Density (g/cm <sup>3</sup> at 25 °C)	Flashpoint (°C)	Hydrophilic-Lipophilic Balance (HLB) Value
T-80	C <sub>64</sub> H <sub>124</sub> O <sub>26</sub>	1309	1.08	148	15
T-20	C <sub>58</sub> H <sub>114</sub> O <sub>26</sub>	1227.54	1.095	>110	16.7
S-80	C <sub>24</sub> H <sub>44</sub> O <sub>6</sub>	428.60	1.068	186.2	4.6
S-20	C <sub>18</sub> H <sub>34</sub> O <sub>6</sub>	346.46	1.032	>110	8.6

Introductory tests determined how parametric settings affected the process. The technique was developed during the first experiments and used for final experimentation to match the workpiece's complete machining impression. These traits also reduce tool and workpiece burns. Table 3 lists the machine settings based on the experiments, Table 4 compiles the properties of electrodes [1,53] and Table 5 shows the properties of transformer oil dielectric. Determining transformer oil dielectric surfactant concentration was crucial. Preliminary experiments against the given selection criterion determined the final choice; however, a literature introduction guideline was used. Early results suggest a surfactant concentration of 6% for the criteria. A motorized stirrer tank was designed to mix surfactant and transformer oil. The stirrer mechanism mixed dielectric and surfactant during the experiment. Figure 1 shows an EDM machine (model: RJ230) used in this experiment, while Figure 2 exhibits the cross-sectional views of the electrodes.

**Table 3.** Input parameters levels.

Input Variable	Level 1	Level 2	Level 3	Level 4	Level 5
Treatment type	NT	CT	-	-	-
Electrode type	Copper	Brass	Graphite	-	-
Type of dielectric	Pure transformer oil	S-20—transformer oil	S-80—transformer oil	T-20—transformer oil	T-80—transformer oil

**Table 4.** Physical and electrical properties of the electrodes [1,53].

Properties	Copper	Brass	Graphite
Density (g/mm <sup>3</sup> )	$8.904 \times 10^{-3}$	$8.55 \times 10^{-3}$	$1.77 \times 10^{-3}$
Electrical resistivity ( $\Omega \cdot m$ )	$1.96 \times 10^{-8}$	$4.7 \times 10^{-7}$	$60 \times 10^{-5}$
Melting point ( $^{\circ}C$ )	1083	990	3350
Specific heat capacity (J/g $^{\circ}C$ )	0.835	0.380	7.1
Electrical conductivity (S/m)	$59 \times 10^6$	$16 \times 10^6$	$0.3 \times 10^6$

**Table 5.** Properties of transformer oil and physical attributes of superalloy [8,54].

Properties	Values	Properties	Values
Breakdown voltage (kV)	56.8	Density (kg/m <sup>3</sup> )	8360
Flash point ( $^{\circ}C$ )	>140	Melting range ( $^{\circ}C$ )	1332–1380
Pour point ( $^{\circ}C$ )	−40	Specific heat (J/kg C)	419
Viscosity (Pa-s)	$7.9 \times 10^{-3}$	Electrical resistivity ( $\mu \Omega m$ )	1.22
Density (kg/dm <sup>3</sup> ) at 20 $^{\circ}C$	0.81	-	-

The investigation was carried out using a full factorial experimental approach. Table 3 summarizes the input parameters with levels. Each test was machined 0.3 mm and 30 experiments were conducted. The first fifteen experiments used NT electrodes, and the last fifteen used CT electrodes. Once the experiment had been conducted satisfactorily, the output parameter was evaluated. The SR of the machined specimen was measured using a surface roughness tester (Surtronic-128) manufactured by Taylor Hobson, as shown in Figure 3. Before taking measurements, the instrument was calibrated using a standard specimen provided by the manufacturer. Afterward, the machined specimen was placed below the stylus probe of the equipment. It was ensured that the surface of the machined specimen was parallel to the stylus. A cutoff length of 0.8 mm and an evaluation length of 4 mm were used in this study to measure the roughness value. ISO-4287 roughness standard was used for measurements. As in the current scenario, the designed diameter of the machined cavity is 9 mm; therefore, the aforementioned cutoff length and evaluation length were used, which is the closest match as per the ISO standard for surface roughness measurement. The collected data were then analyzed using bar charts. Three-dimensional surface profilometry graphs can be seen in the Section 3 to determine surface attributes. Considering Inconel 617 EDM's physical phenomena, results are described. The best electrode material and most efficient dielectric were provided for the desired response characteristics.

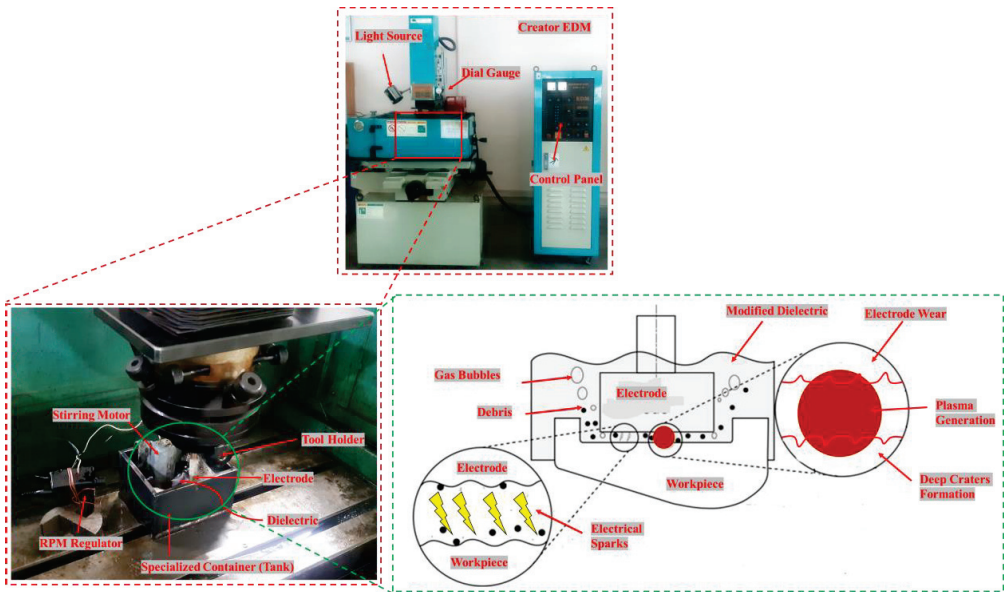


Figure 1. Experimental setup of electric discharge machining.

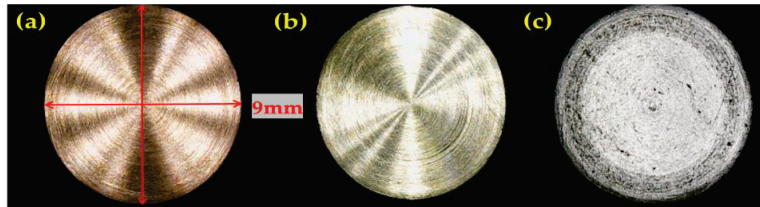


Figure 2. Profile of used deep-cryogenically treated (a) copper, (b) brass, and (c) graphite electrodes.

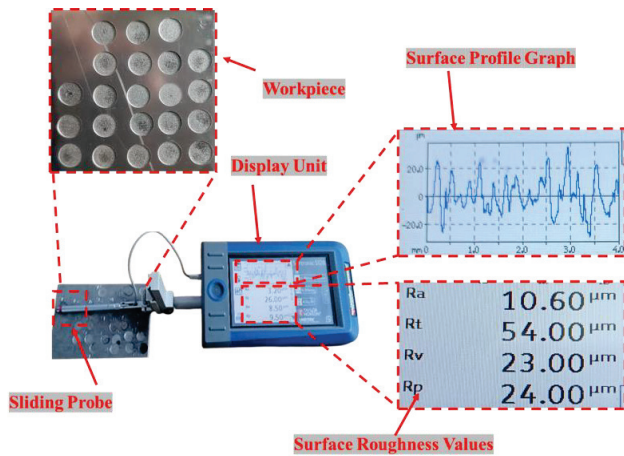
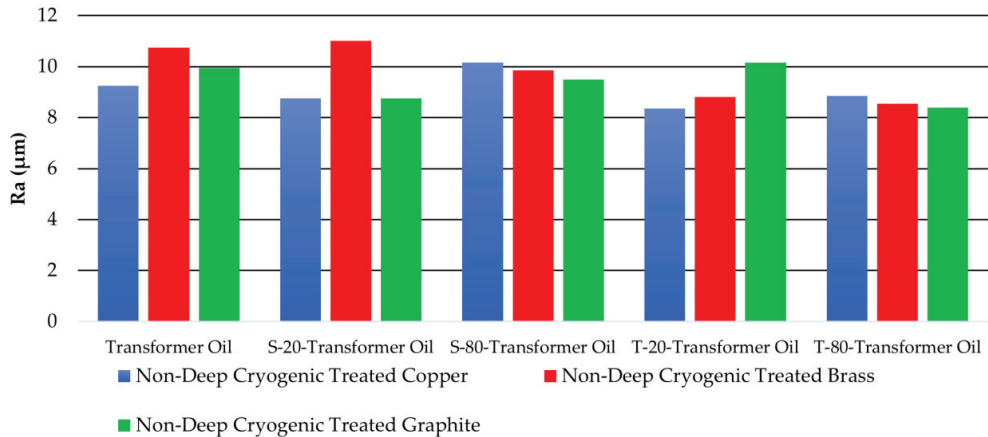


Figure 3. Surface roughness meter.



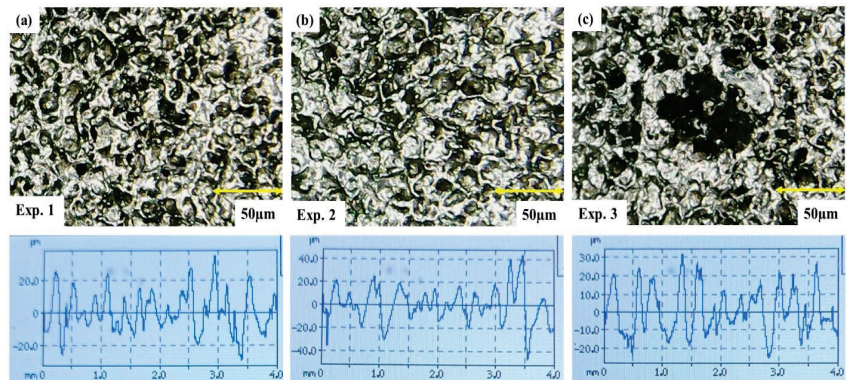
### 3. Results and Discussion

The machining performance of EDM of Inconel 617 in terms of surface roughness (SR) is evaluated using deep-cryogenically treated (CT) and non-deep cryogenically treated (NT) electrodes under different types of modified dielectric media to determine the effect of machining on the Ni-based superalloy. The results pertaining to SR, along with results due to NT electrodes, are presented in the form of bar charts, as shown in Figure 4.



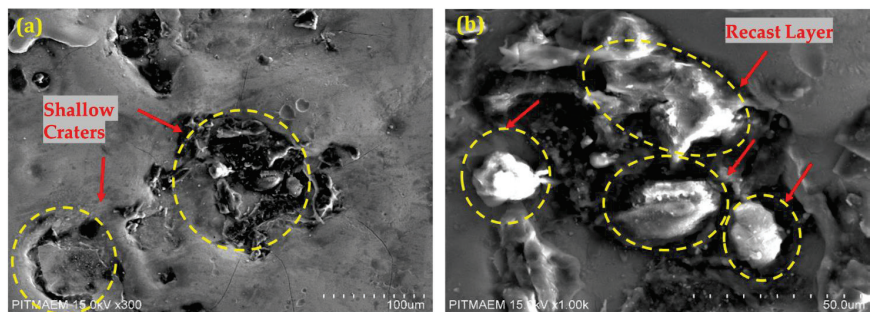
**Figure 4.** Surface roughness comparison of distinct non-deep cryogenic-treated electrodes.

EDM was used to study the effect of regime change—dielectric medium and electrode material in terms of surface roughness (SR)—on Inconel 617’s surface. In pure transformer oil, non-deep cryogenically treated (NT) Copper (Cu)-electrodes have the lowest SR, 9.25  $\mu\text{m}$ . The high flash point (140  $^{\circ}\text{C}$ ) of transformer oil and the high breakdown voltage (56.8 kV) of the dielectric utilized in this investigation explain the low SR in pure transformer oil due to the NT Cu-electrode. The transformer oil’s high flash point prevents erratic sparking and lowers the machined specimen’s SR. Figure 5a shows EDM-formed shallow craters on an Ni-based superalloy. Additionally, the Taylor Hobson roughness meter graph showed the machined profile’s low SR. The machining capability of EDM was investigated using an NT graphite electrode in pure transformer oil. It was found that the NT graphite electrode ranked second in achieving the minimum SR (9.95  $\mu\text{m}$ ) during the cutting phenomenon of Ni-based superalloy. The reason for the second-highest SR is due to the high pulse on time (100  $\mu\text{s}$ ), which leads to the generation of irregular and nonuniform sparking. This irregular sparking produced deep craters on the surface of Inconel 617 during EDM. The microscopic image shown in Figure 5c illustrates the high SR and depicts the deep crater formed on the machined profile. The graph attached below the microscopic image in Figure 5c demonstrates the peak values, which are an indication of high SR. In pure transformer oil, the NT brass electrode had the highest SR, 10.75  $\mu\text{m}$ . Pure transformer oil had the greatest SR value because brass has the lowest melting point (990  $^{\circ}\text{C}$ ) of the electrodes utilized in this investigation. The spark density melts and solidifies Ni-based superalloy due to its low melting point. The phenomenon increased the SR of the specimen due to the brass electrode, and the microscopic image shown in Figure 5b indicates the presence of shallow and wide craters.

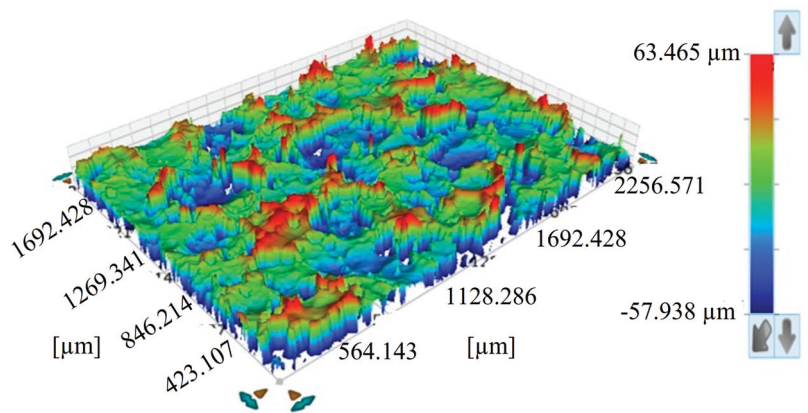


**Figure 5.** Microscopic surface roughness of non-deep cryogenically treated (a) copper, (b) brass, and (c) graphite electrodes in transformer oil.

S-20, a span representative, was studied for EDM using several NT electrodes. When non-deep cryogenically treated (NT) copper (Cu) and graphite electrodes are machined against Inconel 617 in S-20–transformer oil, they offer the same lowest value of surface roughness (SR) 8.75  $\mu\text{m}$ , which is 5.4% and 12.1% lower than in pure transformer oil. S-20 disperses dielectric molecules, which directly did not agglomerate the degraded particles of the Ni-based superalloy, reducing the SR of NT Cu and graphite electrodes. The Cu and graphite electrode and S-20 in transformer oil after EDM provide Inconel 617 with a low SR. The SEM analysis is shown in Figure 6a, representing shallow craters that illustrate better surface finish. EDM was used to measure SR using an NT brass in S-20–transformer oil-modified dielectric. The NT brass provided the maximum SR, i.e., 11.0  $\mu\text{m}$ , compared to other electrodes, and an increment of 2.2% was found using S-20–transformer oil relative to pure transformer oil. The reason for the increment in the SR is due to the NT brass electrode employed possessing the low electrical conductivity of brass ( $16 \times 10^6$  S/m). Due to the low electrical conductivity and low melting temperature (990  $^{\circ}\text{C}$ ) of the brass, eroded material melted and resolidified on the machined profile of the said superalloy. To justify this, the specimen machined by the NT brass electrode was testified using SEM. The SEM image shown in Figure 6b depicts the presence of the recast layer on the surface of Inconel 617. This recast layer is the primary reason for the increment in SR of the nickel (Ni)-based superalloy even after the addition of surfactant. Figure 7 shows a 3D surface profilometry of superalloy in S-20–transformer oil with NT brass, showing heightened peaks and valleys and a higher average Ra.



**Figure 6.** SEM of nickel-based superalloy using non-deep cryogenically treated (a) copper, and (b) brass electrodes.

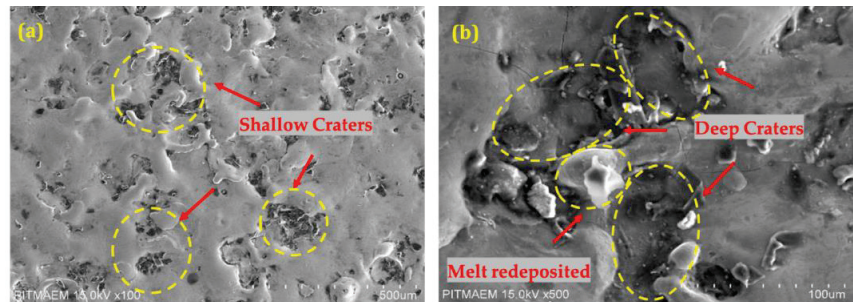


**Figure 7.** Three-dimensional profilometry in S-20–transformer oil using non-deep cryogenically treated brass.

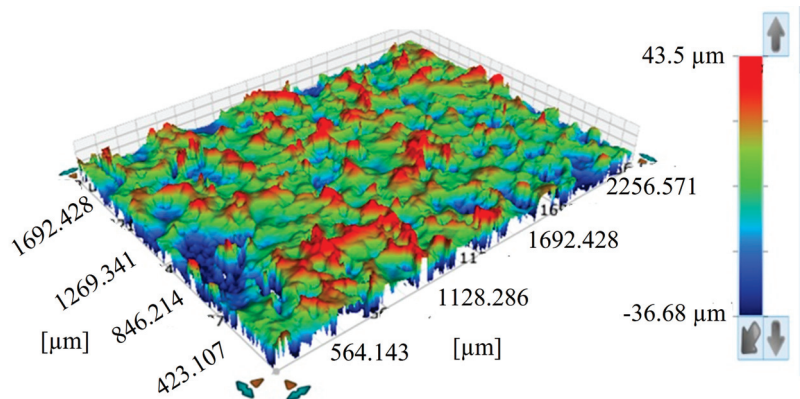
During Inconel 617 machining using S-80–transformer oil, the non-deep cryogenically treated (NT) graphite electrode had the lowest surface roughness (SR),  $9.5 \mu\text{m}$ . The rough surface in S-80–transformer oil was 9.7% more uneven than the profile acquired in S-20–transformer oil. NT graphite’s porousness and lower electrical conductivity ( $0.3 \times 10^6 \text{ S/m}$ ) explain why S-80’s modified dielectric SR was higher than S-20’s. Graphite’s characteristics caused erratic sparking. Thus, irregular and nonuniform sparking at a high pulse on time ( $100 \mu\text{s}$ ) melts more material, but in pulse off time, this eroded material resolidifies on the surface of Ni-based superalloy, resulting in poor surface quality. NT brass electrodes were used to study EDM machining efficiency. The S-80–transformer oil-modified dielectric had the second-lowest SR ( $9.85 \mu\text{m}$ ). Compared to S-20–transformer oil, S-80–transformer oil had 10.5% more designed surface. The reason for the greater surface finish in S-80 is linked with its high flash point ( $186.2 \text{ }^\circ\text{C}$ ) and that of the dielectric medium ( $140 \text{ }^\circ\text{C}$ ); because of the high flash points, the burning phenomenon did not take place and provided a greater surface finish in the modified dielectric of S-80 surfactant. The NT copper (Cu) electrode produced the highest SR ( $10.15 \mu\text{m}$ ) in Inconel 617 machining using the S-80–transformer oil dielectric. S-80–transformer oil’s SR was 13.8% higher than that of S-20–transformer oil due to the NT Cu electrode’s rougher surface. Cu’s high electrical conductivity ( $59 \times 10^6 \text{ S/m}$ ) caused the NT Cu electrode’s high SR. The S-80’s poor surface quality was caused by the NT Cu electrode’s increased electrical conductivity eroding more material from Inconel 617.

The representative of tweens, T-20, with varied NT electrodes machining nickel (Ni)-based superalloy, was used to determine EDM’s proficiency. Figure 4 shows that the NT Cu electrode had the lowest SR ( $8.35 \mu\text{m}$ ) in the T-20–transformer oil-modified dielectric, 13.8% better than S-80. T-20 had the highest HLB (16.7), which lowered SR and improved value compared to S-80 surfactant-based modified dielectric. Therefore, the higher the HLB was, the lower the tension of the dielectric was, which resulted in the impeding of the phenomenon of eroded debris agglomeration. SEM was performed on the machined profile of Ni-based superalloy gained after engaging with the NT Cu and T-20 surfactant, as shown in Figure 8a. The SEM image of the machined specimen shown in Figure 8. depicts the shallow craters formed, which is an indication of good surface finish. Figure 9 shows a 3D surface profilometry in T-20–transformer oil dielectric with NT Cu, showing short-heightened peaks and troughs. The NT brass electrode had the second-lowest SR ( $8.8 \mu\text{m}$ ) in T-20–transformer oil during Inconel 617 machining. Compared to the machined surface in S-80–transformer oil, a refined machined surface was achieved in T-20–transformer oil, which was a 10.7% improved surface compared to the machined surface gained in the case of S-80 with the same electrode. The reason for the low SR is due to the NT brass electrode being linked with the said findings in the case of the NT Cu electrode and T-20

surfactant. The machining performance of EDM due to use of an NT graphite electrode was investigated against the work part and in the presence of the T-20–transformer oil dielectric medium. The NT graphite provided the highest SR ( $10.15\ \mu\text{m}$ ), which was 6.4% higher than the value achieved using S-80–transformer oil. The porous nature of NT graphite is the primary reason for the highest SR even with the highest HLB of the T-20. This porosity of the graphite electrode causes an agglomeration phenomenon that leads to the poor surface finish in the modified dielectric of T-20. Moreover, the SEM image shown in Figure 8b depicts the melts redeposited and deep craters that increased the SR of the base material.



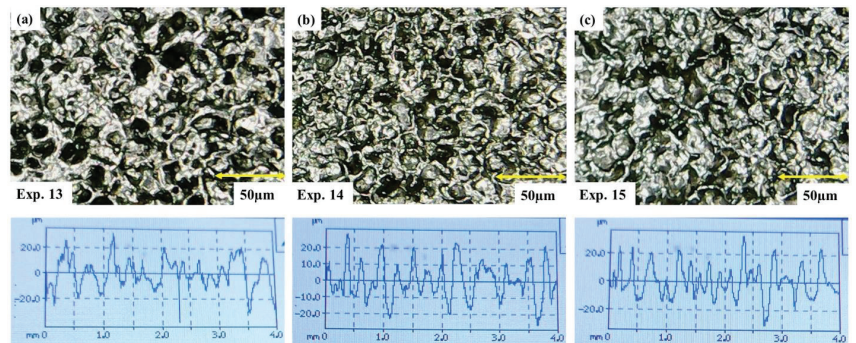
**Figure 8.** SEM images of nickel-based superalloy using non-deep cryogenically treated (a) copper, and (b) graphite electrodes in T-20 transformer oil.



**Figure 9.** Three-dimensional profilometry in T-20–transformer oil using non-deep cryogenically treated copper.

The non-deep cryogenically treated (NT) graphite electrode had the lowest surface roughness (SR) ( $8.4\ \mu\text{m}$ ) with Inconel 617 and T-80–transformer oil-modified dielectric metal. T-80–transformer oil with NT Graphite had 17.2% lower machining performance than S-80. Graphite had the greatest melting point ( $3350\ ^\circ\text{C}$ ) of all electrodes, which lowered SR in T-80–transformer oil-modified dielectric. This high melting point prevented electrode melting and vaporization, resulting in a high surface finish. Figure 10c shows small, shallow craters on the machined specimen, indicating a higher surface quality. In T-80–transformer oil, the NT brass had the second highest SR,  $8.55\ \mu\text{m}$ . The T-80–transformer oil with NT brass yielded 2.8% less than the T-20–transformer oil dielectric medium. The fact that greater surface finish was achieved due to NT brass electrode is due to brass having lower electrical conductivity ( $16 \times 10^6\ \text{S/m}$ ), and this lower electrical conductivity incorporated with the second highest HLB value (15) of T-80 to flush away the eroded material during the pulse-off time. In this way, solidification of worn debris is avoided, which helps in achieving a better surface finish. Figure 10b shows a microscopic view of the

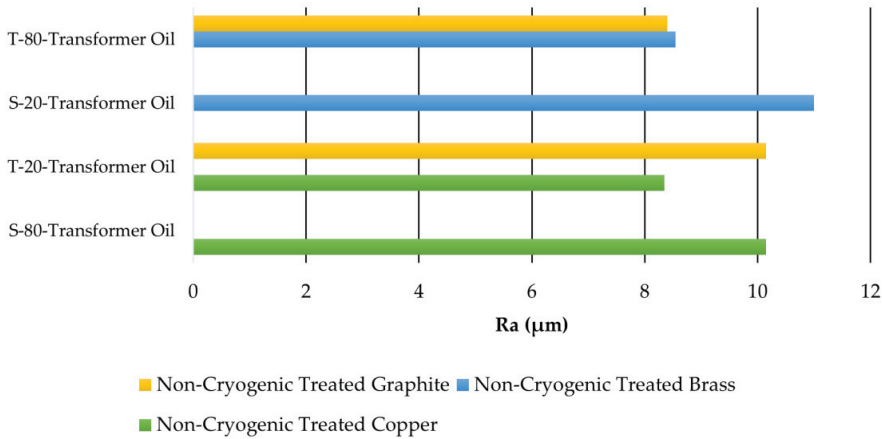
nickel (Ni)-based superalloy's machined profile with shallow craters. The potentiality of EDM was tested in the presence of T-80–transformer oil dielectric medium and NT copper (Cu). SR, 8.85  $\mu\text{m}$ , was 5.60% larger than that achieved during machining using NT Cu and T-20–transformer oil. The NT Cu electrode had high SR because Cu has high electrical conductivity ( $59 \times 10^6 \text{ S/m}$ ) compared to other electrodes tested in this investigation. Cu sparks irregularly and erodes material due to its strong electrical conductivity. Figure 10a shows deep and small superalloy craters.



**Figure 10.** Microscopic surface roughness of non-deep cryogenically treated (a) copper, (b) brass, and (c) graphite electrodes in T-80–transformer oil.

The following is the overall summary of non-deep cryogenically treated (NT) electrode performance during the EDM of nickel (Ni)-based superalloy. The NT copper (Cu) electrode provided the lowest surface roughness (SR) (8.35  $\mu\text{m}$ ) in the T-20–transformer oil-modified dielectric medium. The machined surface obtained in the presence of modified dielectric medium (T-20–transformer oil) was 9.7% more improved and refined than the machined profile achieved without the use of surfactant. The NT graphite electrode was observed as ranking second in achieving the lowest SR (8.4  $\mu\text{m}$ ) in the presence of T-80–transformer oil during the machining of hard-to-cut superalloy. An enhancement of 15.6% in the machined profile was observed when the Inconel 617 was cut in the presence of modified dielectric (T-80–transformer oil). The NT brass electrode achieved the lowest SR (8.55  $\mu\text{m}$ ) in the same modified dielectric, i.e., T-80–transformer oil. It was found that if T-80–transformer oil dielectric is used, then an improvement of 20.5% can be achieved in the machined surface other than if the pure transformer oil dielectric is considered. The graph shown in Figure 11, elaborates on the proficiency of NT electrodes in achieving the maximum and minimum values of SR in different modified dielectrics.

The machining ability of EDM of Inconel 617 in terms of surface roughness (SR) was investigated using deep cryogenically treated (CT) electrodes under different types of modified dielectric media. The results pertaining to SR, along with results due to CT electrodes are presented in the form of a bar chart, shown in Figure 12.



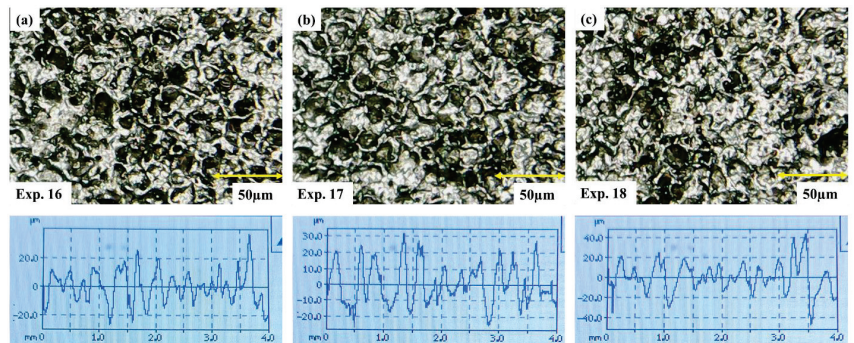
**Figure 11.** Comparison of different non-deep cryogenically treated electrodes in various modified dielectrics for maximum and minimum average surface roughness ( $R_a$ ).



**Figure 12.** Surface roughness comparison of distinct deep cryogenically treated electrodes.

Different deep cryogenically treated (CT) electrodes and modified dielectrics were used to investigate Inconel 617 surface roughness (SR) in EDM. Figure 12 shows that the CT copper (Cu) electrode had the lowest SR of 8.3  $\mu\text{m}$  in pure transformer oil compared to other cryogenic electrodes. The SR value was 10.3% better than the NT Cu electrode with the same dielectric medium. Cryogenic treatment refines the grain structure, preventing erratic sparking and lowering SR, resulting in higher surface quality in pure transformer oil. In pure transformer oil CT, copper achieved less SR, i.e., a better surface finish than the non-deep cryogenically treated (NT) electrode. This is quite understandable considering the phenomenon of crater size. Craters were larger and deeper on the surface machined using the NT Cu electrode as compared to CT electrodes, as shown in Figure 13a. It is well known that smaller crater dimensions result in a better surface finish [55]. Yildiz et al. [56] also reported that the use of CT electrodes results in lower SR compared to NT electrodes. The proficiency of EDM was evaluated using a CT brass electrode against work part 617 in pure transformer oil. It was found that the CT brass stood second in achieving the lowest SR (10.05  $\mu\text{m}$ ) in the pure transformer oil. The machined surface achieved in the case of CT brass and pure transformer oil dielectric showed a 6.5% improved machined

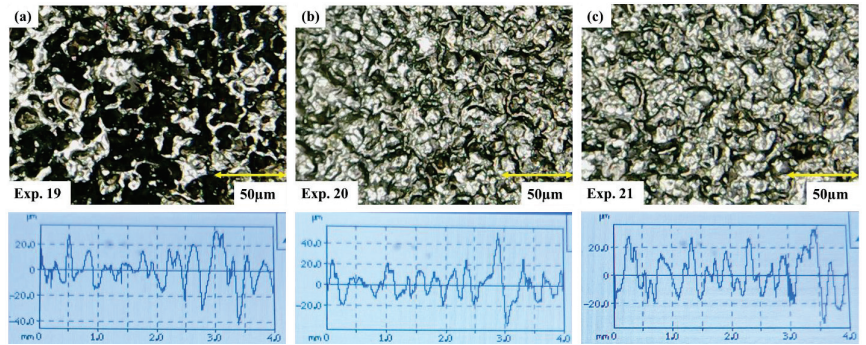
surface compared to the NT brass electrode. The surface asperities achieved due to the NT brass electrode were rougher and more crowded than the surface achieved in the case of the CT brass electrode. Figure 13b depicts those asperities as more random and wider in the NT scenario than the profiles achieved after the cryogenic treatment on the brass electrode. CT graphite achieved the highest SR ( $10.65 \mu\text{m}$ ) in pure transformer oil compared to other CT electrodes. The reason for the high SR value due to the CT graphite electrode is that the low electrical conductivity ( $0.3 \times 10^6 \text{ S/m}$ ) is assisted by cryogenic treatment. Moreover, the porous nature of the graphite electrode also improved due to said treatment, and these two properties were enhanced and incorporated to uplift the outcome response. The microscopic image shown in Figure 13c illustrates that even the CT graphite electrode achieved a higher SR compared to the NT graphite electrode, but the burn marks were reduced, which were produced by irregular sparking due to cryogenic treatment on the graphite electrode.



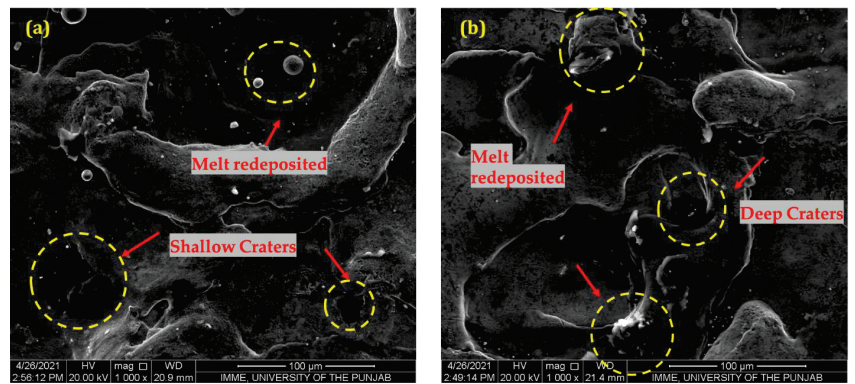
**Figure 13.** Microscopic surface roughness of deep cryogenically treated (a) copper, (b) brass, and (c) graphite electrodes in transformer oil.

S-20 with transformer oil as dielectric and various deep cryogenically treated (CT) electrodes against an Inconel 617 work part were used to measure EDM potentiality. In the modified dielectric, S-20–transformer oil, the CT copper (Cu) electrode had the lowest surface roughness (SR),  $9.1 \mu\text{m}$ . SR was 8.8% greater than CT Cu–pure transformer oil. Cryogenic treatment helps Cu’s electrical conductivity ( $59 \times 10^6 \text{ S/m}$ ) increase the SR value. Due to the assistance of cryogenic treatment in conductivity, higher spark density was produced during the pulse on time, and greater melting and vaporization occurred, which led to a poor surface finish. The microscopic image shown in Figure 14a describes the smaller but shallow crater formation on the surface of a Ni-based superalloy, which is an indication of poor surface finish. SEM of the specimen, machined using a CT Cu electrode in S-20–transformer oil dielectric, was performed, as shown in Figure 15a. The SEM image also shows a little melt redeposited on the surface of the Inconel 617, which is an indication of a greater surface finish. Figure 12 depicts that the CT brass electrode achieved the second lowest SR with a value of  $9.65 \mu\text{m}$  in the presence of S-20–transformer oil and, compared to the values with pure transformer oil in CT brass and S-20–transformer oil in non-deep cryogenically treated (NT) brass, improvements of 4.0% and 12.3% in SR value were observed using the same electrode. The reason for achieving a better surface finish is due to the CT brass electrode linked with the addition of S-20 in transformer oil. The surfactant addition in the dielectric medium lowers the surface tension of the dielectric, which incorporates flushing away the debris from the workpiece material. Due to this recast layer, a better surface finish is achieved. Figure 14b depicts the more refined surface of the specimen due to S-20 addition, and the cryogenic treatment on the electrode. The performance of EDM was evaluated using CT graphite against the machining of the said work part in S-20–transformer oil. CT graphite electrode achieved the highest SR value in S-20–transformer oil, and there was an increase in the value of SR by 1.40% compared

to the value gained in pure transformer oil. The reason for the increment in the SR due to the CT graphite electrode is that the porous nature of graphite is improved by the treatment and the conductivity of graphite is therefore assisted by the said treatment. These characteristics are responsible for providing a poor surface finish. The microscopic image shown in Figure 14c, describes the poor surface finish achieved in S-20–transformer oil due to the CT graphite electrode. Taylor Hobson’s SR graph also depicts higher average surface roughness ( $R_a$ ) peaks, which is an indication of poor surface finish. The SEM shown in Figure 15b illustrates the high deposition of melts redeposited that increased the SR of the specimen. Figure 16 shows a 3D surface profilometry of Inconel 617 in S-20–transformer oil dielectric with CT graphite, showing heightened peaks and valleys and a higher average  $R_a$  value.

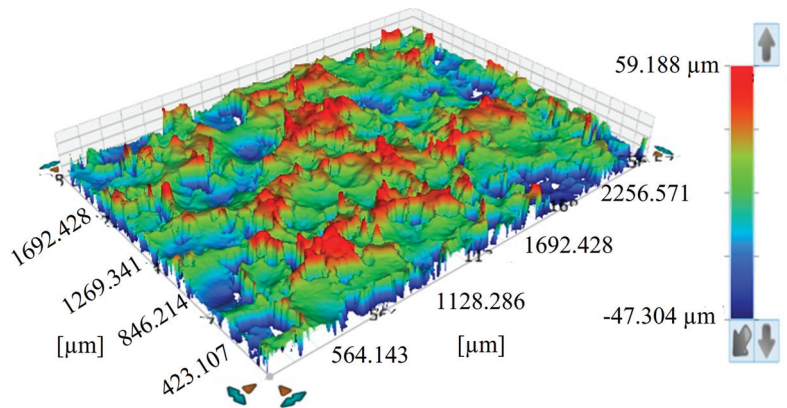


**Figure 14.** Microscopic surface roughness of deep cryogenically treated (a) copper, (b) brass, and (c) graphite electrodes in S-20–transformer oil.



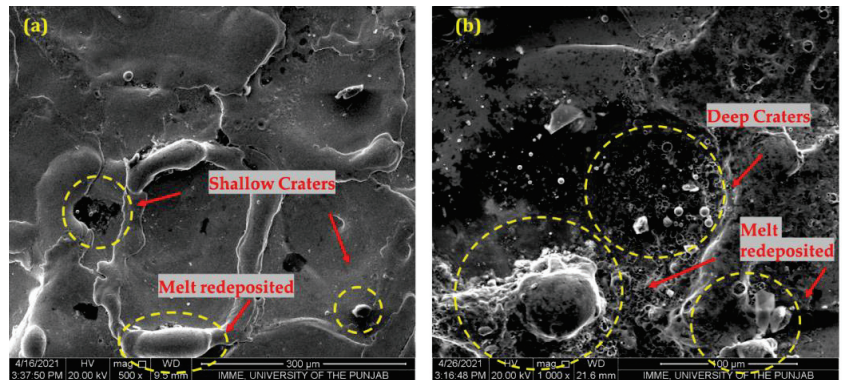
**Figure 15.** SEM images of nickel-based superalloy in S-20–transformer oil after the EDM using deep cryogenically treated electrodes (a) copper, and (b) graphite electrodes.



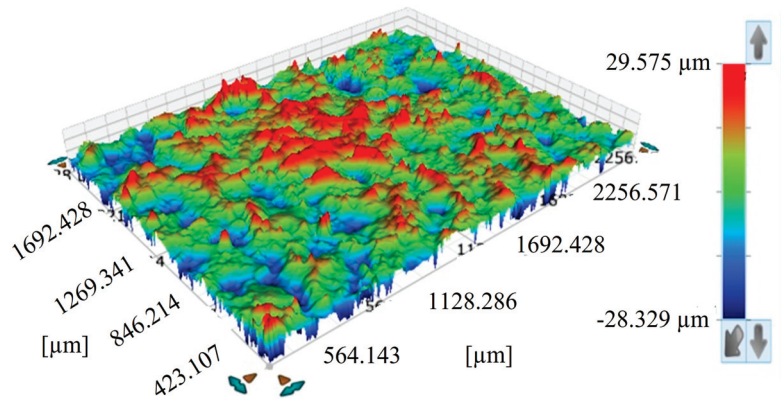


**Figure 16.** Three-dimensional profilometry in S-20–transformer oil using deep cryogenically treated graphite.

It was revealed that the deep cryogenically treated (CT) brass electrode stood first in achieving the lowest surface roughness (SR) value, and the minimum value of SR was  $6.65 \mu\text{m}$  compared to other CT electrodes in the S-80–transformer oil. The reduction in SR value was 31.1% and 32.5% compared to the value obtained using the S-20–transformer oil in CT brass and S-80–transformer oil in non-deep cryogenically treated (NT) brass, respectively. The reason for the improvement in the surface finish is linked to the high flash point of S-80 ( $186.2 \text{ }^\circ\text{C}$ ) and the high flash point of the transformer oil ( $144 \text{ }^\circ\text{C}$ ). The high flash point of the dielectric and surfactant impedes the flammability of the dielectric during the pulse on time, and the surfactant's addition curtails the surface tension of the dielectric. These two characteristics of the dielectric and the surfactant incorporated uplifting the surface finish of the CT brass electrode in the modified dielectric of S-80–transformer oil during the EDM of Inconel 617. SEM was performed on the nickel (Ni)-based superalloy after EDM due to the CT brass electrode in the modified dielectric T-80–transformer oil, as shown in Figure 17a. The SEM result pertains that shallow craters were formed on the surface of the machined specimen, which is an indication of an excellent surface finish. Figure 18 shows a 3D surface profilometry in S-80–transformer oil with CT brass, showing minor peaks and valleys. The CT copper (Cu) electrode, with the second lowest SR ( $9.85 \mu\text{m}$ ), determined the EDM performance. S-80–transformer oil had 7.60% more SR than S-20. Cryogenic treatment helps Cu's electrical conductivity ( $59 \times 10^6 \text{ S/m}$ ) increase the SR value. Due to the assistance of cryogenic treatment in conductivity, greater spark density was produced during the pulse on time, and greater melting and vaporization occurred, which led to a poor surface finish. The SEM image shown in Figure 17b depicts a high volume of melts redeposited, which increased the SR and the basic reason for the high SR of the machined specimen. The supremacy of EDM was evaluated using a CT graphite electrode and workpiece, i.e., Inconel 617 in the presence of S-80–transformer oil dielectric. It was found that the CT graphite electrode ranked third in maximum SR ( $10.60 \mu\text{m}$ ), and this value was 1.90% less than the value achieved in the S-20–transformer oil-modified dielectric medium. The reason for the reduction in SR in the presence of S-80–transformer oil-modified dielectric is that graphite has the highest melting point ( $3350 \text{ }^\circ\text{C}$ ) compared to other electrodes. This high melting point impeded the high melting and vaporization of the electrode due to which a high surface finish was achieved. Moreover, the high breakdown voltage of transformer oil ( $56.8 \text{ kV}$ ) was the other reason for the reduction in SR in the S-80–transformer oil.



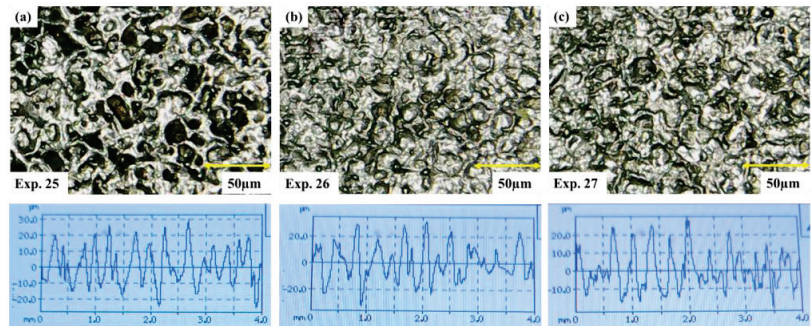
**Figure 17.** SEM images of nickel-based superalloy in S-80-transformer oil after the EDM using deep cryogenically treated (a) brass, and (b) copper electrodes.



**Figure 18.** Three-dimensional profilometry in S-80-transformer oil using deep cryogenically treated brass.

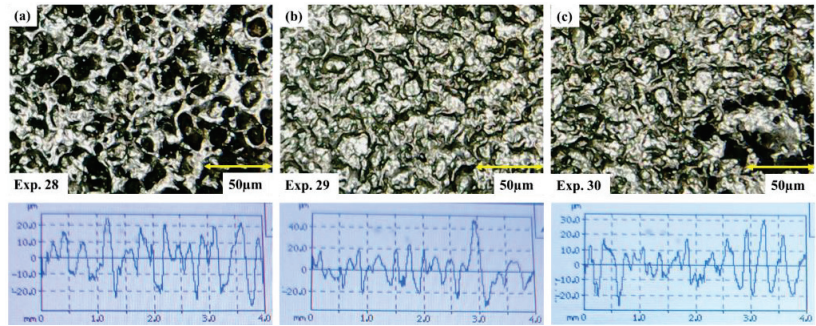
Machining proficiency of EDM was determined in tweens, i.e., T-20 with different types of deep cryogenically treated (CT) electrodes against the machining of nickel (Ni)-based superalloy. From Figure 12, the CT graphite electrode stood first in achieving the lowest surface roughness (SR) ( $8.1 \mu\text{m}$ ) in the presence of T-20-transformer oil-modified dielectric, a 23.6% improved surface compared to the surface gained in S-80-Transformer oil. There are possibly two reasons for the improvement in surface finish due to the CT graphite in the presence of T-20-transformer oil. The first and foremost reason for the reduction in SR of the Ni-based superalloy is linked with the highest HLB (16.2) of T-20. The high HLB value of the surfactant resulted in a reduction in surface tension of the dielectric, and this reduction in surface tension yielded a better mix of surfactant with the dielectric and greater flushing of the eroded debris from the workpiece. The second reason for the improvement in the surface finish was employed with the enhancement in the porosity of the graphite electrode. These two properties integrated to uplift the surface finish of the Ni-based superalloy. The microscopic image shown in Figure 19c describes the very small number of shallow craters present on the machined surface of the Inconel 617, which is in favor of a greater surface finish. The CT Cu electrode stood second in achieving the minimal value of SR ( $9.0 \mu\text{m}$ ) in the presence of T-20-transformer oil during the machining of Inconel 617. Compared to the machined surface in S-80-transformer oil, an 8.62% refined and better-machined surface was achieved in T-20-transformer oil. The reason for the better surface finish in the CT Cu electrode is that cryogenic treatment enhanced the grain structure due to which a uniform

sparking falls on the workpiece irrespective of the nonuniform sparking, which occurred in the noncryogenic treatment. This phenomenon helps in achieving a better surface finish due to cryogenic treatment in the modified dielectric medium. The microscopic image shown in Figure 19a illustrates the small and shallow crater formation on the surface of the said specimen. The machining performance of EDM due to the CT brass electrode was investigated against the work part and in the presence of T-20–transformer oil dielectric medium. The CT brass electrode achieved the highest value of SR ( $9.90\ \mu\text{m}$ ), which was 32.8% higher than the value achieved in S-80–transformer oil. The reason for the higher SR due to the CT brass electrode is elaborated in earlier findings, and Figure 19b shows the random, rougher surface obtained in the T-20–transformer oil scenario.



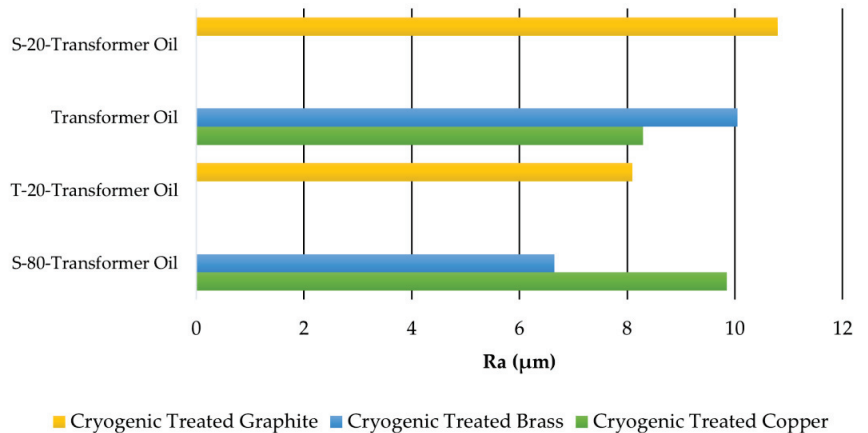
**Figure 19.** Microscopic surface roughness of deep cryogenically treated (a) copper, (b) brass, and (c) graphite electrodes in T-20–transformer oil.

With a deep cryogenically treated (CT) graphite electrode and T-80–transformer fluid, EDM outperformed Inconel 617 machining. CT graphite electrodes in T-80–transformer oil had the lowest surface roughness (SR) value of  $8.40\ \mu\text{m}$ . T-20–transformer oil had 3.6% less SR. The reason for the increment in the SR value is linked with the second highest value of HLB (15) of T-80. The lower the HLB, the higher the surface tension and vice versa. T-20 has the highest HLB, so it achieved the lowest SR due to the CT graphite electrode. T-80 has a slightly lower HLB than T-20, so it achieved a slightly higher SR compared to T-20. Figure 20c shows a rougher surface than T-20–transformer oil. The CT copper (Cu) electrode had the second-lowest SR ( $9.40\ \mu\text{m}$ ) in T-80–transformer oil. Inconel 617 machined against the CT Cu electrode increased SR by 4.3% compared to T-20–transformer oil. Cryogenic treatment helps Cu's electrical conductivity ( $59 \times 10^6\ \text{S/m}$ ) increase the SR value. Due to the assistance of cryogenic treatment in conductivity, higher spark density was produced during the pulse on time, and greater melting and vaporization occurred, which led to a poor surface finish. Figure 20a describes the smaller but deeper crater formation on the surface of nickel (Ni)-based superalloy, which is an indication of poor surface finish. The potentiality of EDM was observed in T-80–transformer oil using a CT brass electrode, which ranked third in achieved the lowest SR with a value of  $9.9\ \mu\text{m}$ . T-20–transformer oil lowered the SR by 3.5%. High HLB (15) and transformer oil flash point ( $144\ ^\circ\text{C}$ ) improve surface finish. The pulse on time dielectric's high flash point and surfactant reduces surface tension. These two said characteristics of the dielectric and the surfactant facilitated uplifting the surface finish of the CT brass electrode in the modified dielectric of T-80–transformer oil during the EDM of Inconel 617. The microscopic image shown in Figure 20b depicts the wider and shallow craters present on the machined specimen.



**Figure 20.** Microscopic surface roughness of deep cryogenically treated (a) copper, (b) brass, and (c) graphite electrodes in T-80-transformer oil.

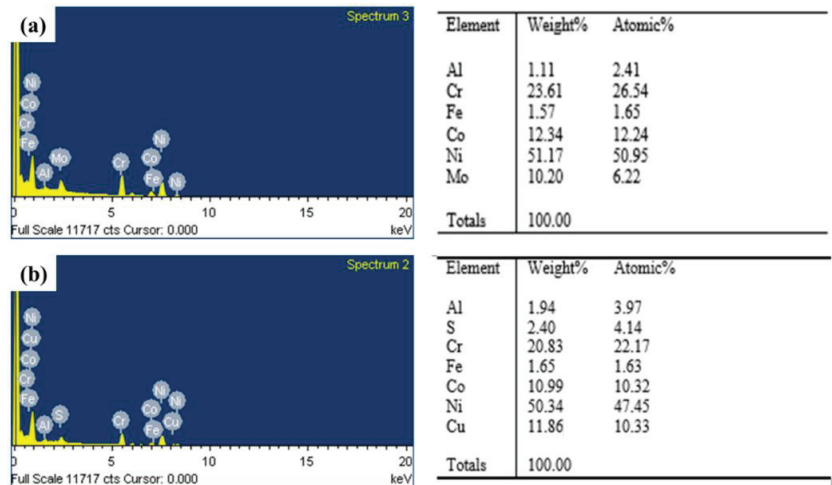
The deep cryogenically treated (CT) electrode’s surface roughness (SR) results can be interpreted as follows: The CT brass electrode achieved the lowest value of SR, i.e., 6.65 µm in the S-80-transformer oil, against the machining of Inconel 617. This achieved value of SR in the modified dielectric was a 33.8% improvement over the SR gained in pure transformer oil dielectric. The second lowest value of SR (8.3 µm) was found against the CT copper (Cu) electrode and in the presence of pure transformer oil during the cutting of Ni-based superalloy. The surface achieved in pure transformer oil using a CT Cu electrode had a 10.3% more polished surface than the machined surface achieved in pure transformer oil using a non-deep cryogenically treated (NT) Cu electrode. The CT graphite electrode was last in achieving the lowest SR (8.4 µm) value in the T-80-transformer oil. The said value achieved a more polished surface, i.e., 21.1%, than the machined surface did in pure transformer oil. The graph shown in Figure 21 elaborates on the proficiency of CT electrodes in achieving the maximum and minimum values of SR in different modified dielectrics.



**Figure 21.** Comparison of different deep cryogenically treated electrodes in various modified dielectrics for maximum and minimum average surface roughness ( $R_a$ ).

Energy-dispersive X-ray spectroscopy (EDS) analysis of the work part was performed to investigate the overall presence of the various metals in the base alloy. By the continuous dispersion of the dielectric fluid in the customized tank, the debris is flushed away from the workpiece material. During the discharge gap, deposition of the eroded material on the machined specimen occurs due to the incomplete flushing of debris from the workpiece material. Thereof, a little amount of the material is solidified on the surface of the work part from an electrode to the base material that is emersed in the dielectric medium. The

EDS examination provided a detailed composition of the Inconel 617 before and after the experimentation. Figure 22a,b depicts the EDS examination in terms of improved chemical composition, quality, and quantity as well as the investigation of the recast layer of electrode material on the surface of the Ni-based superalloy. When any surfactant is added to the dielectric medium, and EDM is performed using the CT Cu electrode, then some of the debris moves from electrode material to base material.



**Figure 22.** Energy-dispersive X-ray spectroscopy analysis of nickel-based superalloy (a) before EDM, and (b) after EDM.

Figure 22a shows the EDS analysis of the Inconel 617 before EDM was performed against the CT Cu electrode. The EDS examination discloses that before the machining, Ni, Cr, and Mo were the major peaks of the other metals of the Inconel 617. However, when the CT Cu electrode was engaged for the machining of Inconel 617, debris of the Cu from the electrode to the workpiece material were observed. This is because, during the pulse on time, high spark density is generated, which melts and vaporizes the minimum quantity of the electrode material, and this eroded material solidifies on the surface of the base material. Then, EDS analysis was performed after the EDM, and Figure 22b shows that Cu was the peak constituent of the base material after Ni.

Statistical analysis for the evaluation of average surface roughness ( $R_a$ ) was performed and is shown in Figure 23. A residual plot indicates the fitness of the data either using regression or analysis of variance. Studying the residual plots allows to see if the regular least-squares assumptions were met. From the normal probability plot, there is a close relationship between the observed data points of the response measure and the predicted line, i.e., a linear relationship exists, which is the indication of less error in the observed magnitudes of the response measure (surface roughness, SR). However, versus fits also presents less randomness in values of magnitudes. Moreover, the histogram favors less negative residual data.

If a comparison is developed between the current research findings and other research conducted by various researchers, then it can be concluded that the surface finish achieved by this study is 23.57% better than the highest magnitude of SR achieved using EDM of die steel by Jamadar and Kavade [32]. Now, if the comparison is made between the highest value of SR achieved in this study using the CT electrode, then it can be found that the surface finish is still better by about 30.56% than the highest SR gained using EDM of Inconel 718 by Jafarian [20].

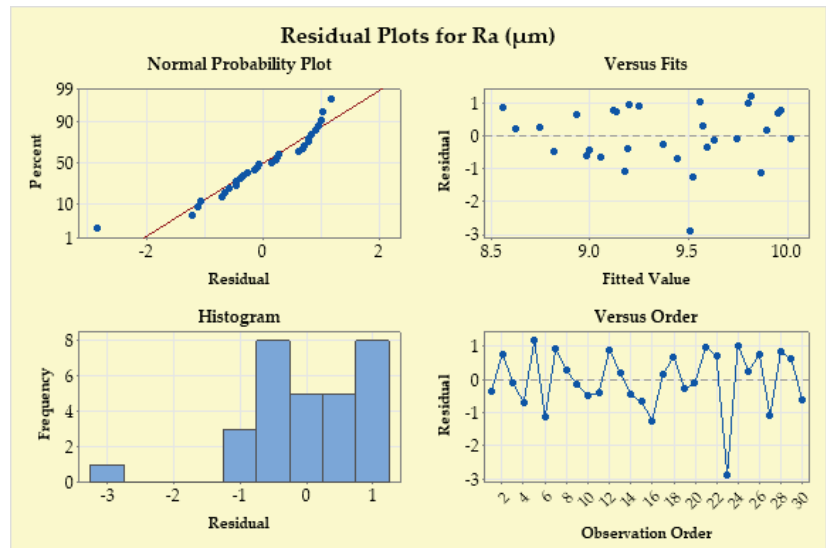


Figure 23. Statistical analysis of surface roughness.

#### 4. Conclusions

The machining proficiency of electric discharge machining (EDM) of nickel (Ni)-based superalloy in terms of surface roughness was examined using various types of modified dielectrics of transformer oil along with different kinds of non-deep cryogenically treated (NT) and deep cryogenically treated (CT) electrodes. The results were explained with the help of process physics, the possible primary reasons, and Energy-dispersive X-ray spectroscopy (EDS) analysis of the workpiece material. After studying the comprehensive investigation of the effect of NT and CT electrodes under various modified dielectrics of transformer oil, the following conclusions can be made:

- Brass excelled among CT electrodes, delivering the lowest surface roughness (SR) ( $6.65 \mu\text{m}$ ) in the modified dielectric of transformer oil (S-80). CT brass provides a surface polish that is 28.72% higher than the average value provided by all CT electrodes.
- Across a range of changed dielectric media, CT electrodes outperformed compared to NT electrodes in terms of machining performance, with an average of 1.2% higher surface polish.
- The performance of CT electrodes was also examined using span and tween in transformer oil. It was found that tweens had 4.1% better surface polish or less SR than spans.
- CT copper (Cu) electrode in pure transformer oil achieves the lowest SR ( $8.3 \mu\text{m}$ ), which is a 10.3% better-machined surface compared to pure transformer oil in the NT case. Similarly, average surface roughness ( $R_a$ ) of  $8.1 \mu\text{m}$  was achieved by using a CT graphite electrode in T-20–transformer oil, which was a 23.9% improved surface finish compared to the value obtained in pure transformer oil.
- In this investigation modified dielectrics, employed against NT electrodes in T-80–transformer oil, yielded the lowest values of SR.  $R_a$  magnitudes obtained in T-80–transformer oil during the EDM were lower by 4.32% for NT Cu, 20.5% for NT brass, and 15.6% for NT graphite compared to pure transformer oil.
- NT Cu electrode and T-20–transformer oil dielectric yielded the lowest SR ( $8.35 \mu\text{m}$ ). The greatest SR for S-80–transformer oil with NT Cu electrode was 17.7% higher than the T-20 value.
- In CT electrodes, span-based modified dielectrics performed 4.13% worse than tween-based ones. Tweens perform better because their high flash points reduce flammability.

- Similarly, the proficiency of tween-based modified dielectrics of transformer oil in NT electrodes was witnessed as superior by 8.41% compared to the span-added dielectrics.
- NT Cu, graphite, and brass were machined to the lowest SR of 8.35  $\mu\text{m}$ , 8.40  $\mu\text{m}$ , and 8.55  $\mu\text{m}$  in T-20-, T-80-, and T-80-modified dielectrics, respectively. SR values were 9.72%, 15.6%, and 20.5% higher than pure transformer oil.
- If a comparison is made between the current research findings with the other research conducted by various researchers, then it can be concluded that the surface finish achieved in this study is 23.57% better than the highest magnitude of SR achieved by EDM of die steel. Now, if the comparison is made between the highest value of SR achieved in this study using a CT electrode, then it is found that the surface finish is still better by about 30.56% than the highest of SR gained by EDM of Inconel 718.

In this work, EDM of Inconel 617 was carried out using five dielectric media under three different types of NT and CT electrodes. This work can be extended considering the influence of added powder and machining responses for further improvement of the process. Evaluation of a blend of dielectrics instead of single dielectrics is another valuable possible future direction. Furthermore, a comparative assessment using a multiscale approach is another area that can be explored. The measurement and analysis of other roughness-related parameters such as  $R_z$ ,  $R_p$ ,  $R_{SM}$ , etc., will be comprehensively explored in future investigations.

**Author Contributions:** Conceptualization, K.I., M.S. and M.U.W.; methodology, K.I., M.S. and M.U.W.; validation, K.I., M.S. and M.U.W.; formal analysis, K.I., M.S. and M.U.W.; investigation, K.I., M.S., S.A. and M.U.W.; resources, K.I., M.S., M.A.M., S.A. and M.U.W.; data curation, K.I., M.S., M.A.M., S.A. and M.U.W.; writing—original draft preparation, K.I., M.S., M.A.M., S.A. and M.U.W.; writing—review and editing, K.I., M.S., M.A.M., S.A. and M.U.W.; supervision, K.I., M.A.M. and S.A.; project administration, K.I., M.A.M. and S.A.; funding acquisition, K.I., M.A.M. and S.A. All authors have read and agreed to the published version of the manuscript.

**Data Availability Statement:** Not applicable.

**Acknowledgments:** The authors appreciate the support from Researchers Supporting Project number (RSPD2023R702), King Saud University, Riyadh, Saudi Arabia.

**Conflicts of Interest:** The authors declare no conflict of interest.

## References

1. Khan, A.R.; Rahman, M.; Kadrigama, K. An experimental investigation on surface finish in die-sinking EDM of Ti-5Al-2.5Sn. *Int. J. Adv. Manuf. Technol.* **2015**, *77*, 1727–1740. [[CrossRef](#)]
2. Abbas, N.M.; Solomon, D.G.; Bahari, F. A review on current research trends in electrical discharge machining (EDM). *Int. J. Mach. Tools Manuf.* **2007**, *47*, 1214–1228. [[CrossRef](#)]
3. Lee, G.M.; Lee, J.U.; Park, S.H. Effects of surface roughness on bending properties of rolled AZ31 alloy. *J. Magnes. Alloy.* **2022**, *11*, 1224–1235. [[CrossRef](#)]
4. Arola, D.; Williams, C.L. Estimating the fatigue stress concentration factor of machined surfaces. *Int. J. Fatigue* **2002**, *24*, 923–930. [[CrossRef](#)]
5. Zhao, B.; Song, J.; Xie, L.; Hu, Z.; Chen, J. Surface roughness effect on fatigue strength of aluminum alloy using revised stress field intensity approach. *Sci. Rep.* **2021**, *11*, 19279. [[CrossRef](#)] [[PubMed](#)]
6. Ye, H.; Sun, X.; Liu, Y.; Rao, X.-X.; Gu, Q. Effect of ultrasonic surface rolling process on mechanical properties and corrosion resistance of AZ31B Mg alloy. *Surf. Coat. Technol.* **2019**, *372*, 288–298. [[CrossRef](#)]
7. Azam, M.; Jahanzaib, M.; Abbasi, J.A.; Abbas, M.; Wasim, A.; Hussain, S. Parametric analysis of recast layer formation in wire-cut EDM of HSLA steel. *Int. J. Adv. Manuf. Technol.* **2016**, *87*, 713–722. [[CrossRef](#)]
8. Ishfaq, K.; Waseem, M.U.; Sana, M. Investigating cryogenically treated electrodes' performance under modified dielectric(s) for EDM of Inconel(617). *Mater. Manuf. Process.* **2022**, *37*, 1902–1911. [[CrossRef](#)]
9. Li, W.; Guo, Y.B. A Two-Parameter Method to Monitor and Characterize Tool Wear in End Milling Inconel 718. In Proceedings of the ASME 2012 International Manufacturing Science and Engineering Conference, Notre Dame, IN, USA, 4 June 2012; pp. 799–804.
10. Guo, Y.B.; Li, W.; Jawahir, I.S. Surface integrity characterization and prediction in machining of hardened and difficult-to-machine alloys: A state-of-art research review and analysis. *Mach. Sci. Technol.* **2009**, *13*, 437–470. [[CrossRef](#)]

11. Voigt, O.; Peuker, U.A. Suitability of Eroded Particles from Die-Sink Electro Discharge Machining for Additive Manufacturing—Review, Characterization and Processing. *Metals* **2022**, *12*, 1447. [[CrossRef](#)]
12. Abu Qudeiri, J.E.; Zaiout, A.; Mourad, A.-H.I.; Abidi, M.H.; Elkaseer, A. Principles and Characteristics of Different EDM Processes in Machining Tool and Die Steels. *Appl. Sci.* **2020**, *10*, 2082. [[CrossRef](#)]
13. Shastri, R.K.; Mohanty, C.P.; Dash, S.; Gopal, K.M.P.; Annamalai, A.R.; Jen, C.-P. Reviewing Performance Measures of the Die-Sinking Electrical Discharge Machining Process: Challenges and Future Scopes. *Nanomaterials* **2022**, *12*, 384. [[CrossRef](#)] [[PubMed](#)]
14. Alhodaib, A.; Shandilya, P.; Rouniyar, A.K.; Bisaria, H. Experimental Investigation on Silicon Powder Mixed-EDM of Nimonic-90 Superalloy. *Metals* **2021**, *11*, 1673. [[CrossRef](#)]
15. Masuzawa, T. State of the Art of Micromachining. *CIRP Ann.* **2000**, *49*, 473–488. [[CrossRef](#)]
16. Singh, S.; Maheshwari, S.; Pandey, P.C. Some investigations into the electric discharge machining of hardened tool steel using different electrode materials. *J. Mater. Process. Technol.* **2004**, *149*, 272–277. [[CrossRef](#)]
17. Gangil, M.; Pradhan, M.K. Modeling and optimization of electrical discharge machining process using RSM: A review. *Mater. Today Proc.* **2017**, *4*, 1752–1761. [[CrossRef](#)]
18. Kolli, M.; Kumar, A. Effect of dielectric fluid with surfactant and graphite powder on Electrical Discharge Machining of titanium alloy using Taguchi method. *Eng. Sci. Technol. Int. J.* **2015**, *18*, 524–535. [[CrossRef](#)]
19. Razak, M.A.; Abdul-Rani, A.M.; Nanimina, A.M. Improving EDM Efficiency with Silicon Carbide Powder-Mixed Dielectric Fluid. *Int. J. Mater. Mech. Manuf.* **2015**, *3*, 40–43. [[CrossRef](#)]
20. Jafarian, F. Electro discharge machining of Inconel 718 alloy and process optimization. *Mater. Manuf. Process.* **2020**, *35*, 95–103. [[CrossRef](#)]
21. Tiwary, A.P.; Pradhan, B.B.; Bhattacharyya, B. Application of multi-criteria decision making methods for selection of micro-EDM process parameters. *Adv. Manuf.* **2014**, *2*, 251–258. [[CrossRef](#)]
22. Saodaen, R.; Janmanee, P.; Rodchanarowan, A. Characteristics of Ternary Metal (Cu-Ni-TiN) Electrodes Used in an Electrical Discharge Machining Process. *Metals* **2021**, *11*, 694. [[CrossRef](#)]
23. Singh, K.; Agarwal, A.K.; Yadav, R. Effect of Dielectric Fluids Used on EDM Performance: A Review. *Int. J. Emerg. Technol. Eng. Res.* **2017**, *5*, 7.
24. Bhattacharyya, B.; Doloi, B. Machining Processes Utilizing Thermal Energy. In *Modern Machining Technology*; Elsevier: Amsterdam, The Netherlands, 2020; pp. 161–363. ISBN 978-0-12-812894-7.
25. Kumar, D.; Kumar, K.; Payal, D.H.S. A State-of-the-Art Review on Dielectric Fluid in Electric Discharge Machining: Uses and Its Effects. *Int. Res. J. Eng. Technol.* **2017**, *4*, 6.
26. Joshi, A.Y.; Joshi, A.Y. A systematic review on powder mixed electrical discharge machining. *Heliyon* **2019**, *5*, e02963. [[CrossRef](#)]
27. Razak, M.R.A.; Liew, P.J.; Hussein, N.I.S.; Ahsan, Q.; Yan, J. Effect of Surfactants and Additives on Electrical Discharge Machining of Reaction Bonded Silicon Carbide. *ARPN J. Eng. Appl. Sci.* **2017**, *12*, 4334–4339.
28. Tanteh, D.N.; Al, S.Y.; Ssekasiko, D. *Properties of Transformer Oil that Affect Efficiency*; Department of Electrical Engineering, Blekinge Institute of Technology: Karlskrona, Sweden, 2014.
29. Zhao, W.; Meng, Q.; Wang, Z. The application of research on powder mixed EDM in rough machining. *J. Mater. Process. Technol.* **2002**, *129*, 30–33. [[CrossRef](#)]
30. Kumar, A.; Maheshwari, S.; Sharma, C.; Beri, N. Analysis of Machining Characteristics in Additive Mixed Electric Discharge Machining of Nickel-Based Super Alloy Inconel 718. *Mater. Manuf. Process.* **2011**, *26*, 1011–1018. [[CrossRef](#)]
31. Kumar, A.; Maheshwari, S.; Sharma, C.; Beri, N. Research Developments in Additives Mixed Electrical Discharge Machining (AEDM): A State of Art Review. *Mater. Manuf. Process.* **2010**, *25*, 1166–1180. [[CrossRef](#)]
32. Jamadar, M.U.M.; Kavade, M.V. Effect of aluminium powder mixed edm on machining characteristics of die steel (AISI D3). *IJMPE* **2014**, *2*, 120–123.
33. Dewan, P.R.; Kundu, P.K.; Phipon, R. Powder Mixed Electric Discharge Machining—A Review. In Proceedings of the AIP Conference Proceedings 2273, Seoul, Republic of Korea, 20 January 2020; Volume 2, p. 050075.
34. Amin, A.; Abdul-Rani, A.M.; Rana, M.; Hastuty, S.; Danish, M.; Rubaiee, S.; bin Mahfouz, A. Evaluation of modified 316L surface properties through HAP suspended EDM process for biomedical application. *Surf. Interfaces* **2022**, *28*, 101600. [[CrossRef](#)]
35. Qazi, M.J.; Schlegel, S.J.; Backus, E.H.; Bonn, M.; Bonn, D.; Shahidzadeh, N. Dynamic Surface Tension of Surfactants in the Presence of High Salt Concentrations. *Langmuir* **2020**, *36*, 7956–7964. [[CrossRef](#)] [[PubMed](#)]
36. Dave, N.; Joshi, T. A Concise Review on Surfactants and Its Significance. *Int. J. Appl. Chem.* **2017**, *13*, 663–672. [[CrossRef](#)]
37. Bart, J.C.J.; Gucciardi, E.; Cavallaro, S. Formulating Lubricating Oils. In *Biolubricants*; Elsevier: Amsterdam, The Netherlands, 2013; pp. 351–395. ISBN 978-0-85709-263-2.
38. Kumar, S.; Khedkar, N.K.; Jagtap, B.; Singh, T.P. The Effects of Cryogenic Treatment on Cutting Tools. *IOP Conf. Series Mater. Sci. Eng.* **2017**, *225*, 012104. [[CrossRef](#)]
39. Özdemir, Z. Shallow Cryogenic Treatment (SCT) Effects on the Mechanical Properties of High Cr Cast Iron: Low-Carbon Cast Steel Bimetallic Casting. *Int. J. Met.* **2021**, *15*, 952–961. [[CrossRef](#)]
40. Senthilkumar, D.; Rajendran, I. Influence of Shallow and Deep Cryogenic Treatment on Tribological Behavior of En 19 Steel. *J. Iron Steel Res. Int.* **2011**, *18*, 53–59. [[CrossRef](#)]



41. Razak, M.R.A.; Liew, P.J.; Hussein, N.I.S.; Ahsan, Q. Effect of Surfactant on EDM of Low Conductivity Reaction-Bonded Silicon Carbide. *Key Eng. Mater.* **2016**, *701*, 107–111. [[CrossRef](#)]
42. Li, L.; Li, Z.Y.; Wei, X.T.; Cheng, X. Machining Characteristics of Inconel 718 by Sinking-EDM and Wire-EDM. *Mater. Manuf. Process.* **2015**, *30*, 968–973. [[CrossRef](#)]
43. Wu, K.L.; Yan, B.H.; Lee, J.-W.; Ding, C.G. Study on the characteristics of electrical discharge machining using dielectric with surfactant. *J. Mater. Process. Technol.* **2009**, *209*, 3783–3789. [[CrossRef](#)]
44. Abdulkareem, S.; Khan, A.A.; Konneh, M. Reducing electrode wear ratio using cryogenic cooling during electrical discharge machining. *Int. J. Adv. Manuf. Technol.* **2009**, *45*, 1146–1151. [[CrossRef](#)]
45. Srivastava, V.; Pandey, P.M. Performance Evaluation of Electrical Discharge Machining (EDM) Process Using Cryogenically Cooled Electrode. *Mater. Manuf. Process.* **2012**, *27*, 683–688. [[CrossRef](#)]
46. Ram, N.R.; Rao, K.V.; Kanth, C.L.; Sri, M.N.S. Parametric Analysis on the Effect of Cryogenic Treatment on the Work Piece Material of EDM Process. *Int. J. Eng. Resea. Technol.* **2014**, *3*, 8.
47. Jafferson, J.M.; Hariharan, P. Machining Performance of Cryogenically Treated Electrodes in Microelectric Discharge Machining: A Comparative Experimental Study. *Mater. Manuf. Process.* **2013**, *28*, 397–402. [[CrossRef](#)]
48. Bartkowiak, T.; Mendak, M.; Mrozek, K.; Wieczorowski, M. Analysis of Surface Microgeometry Created by Electric Discharge Machining. *Materials* **2020**, *13*, 3830. [[CrossRef](#)] [[PubMed](#)]
49. Gogolewski, D. Multiscale Data Treatment in Additive Manufacturing. *Materials* **2023**, *16*, 3168. [[CrossRef](#)]
50. Ishfaq, K.; Sana, M.; Waseem, M.U.; Anwar, S.; Alfaify, A.Y.; Zia, A.W. Surface quality investigation in surfactant-based EDM of Inconel 617 using deep cryogenically treated electrodes. *Int. J. Adv. Manuf. Technol.* **2023**. [[CrossRef](#)]
51. Reddy, V.V.; Kumar, A.; Valli, P.M.; Reddy, C.S. Influence of surfactant and graphite powder concentration on electrical discharge machining of PH17-4 stainless steel. *J. Braz. Soc. Mech. Sci. Eng.* **2015**, *37*, 641–655. [[CrossRef](#)]
52. Kassem, M.G.; Ahmed, A.-M.M.; Abdel-Rahman, H.H.; Moustafa, A.H. Use of Span 80 and Tween 80 for blending gasoline and alcohol in spark ignition engines. *Energy Rep.* **2019**, *5*, 221–230. [[CrossRef](#)]
53. Khan, A.A. Electrode wear and material removal rate during EDM of aluminum and mild steel using copper and brass electrodes. *Int. J. Adv. Manuf. Technol.* **2008**, *39*, 482–487. [[CrossRef](#)]
54. Tola, O.J.; Zungeru, A.M.; Usifo, F.; Garba, A.J. Experimental Study of the Characteristics of Transformer Oil and Some Selected Vegetable Oils. *Int. J. Eng. Res. Afr.* **2016**, *23*, 13–23. [[CrossRef](#)]
55. Cetin, A.; Cakir, G.; Aslantas, K.; Ucak, N.; Cicek, A. Performance of cryogenically treated Cu and CuCrZr electrodes in an EDM process. *Met. Mater.* **2018**, *55*, 431–440. [[CrossRef](#)]
56. Yildiz, Y.; Sundaram, M.M.; Rajurkar, K.P.; Nalbant, M. The Effects of Cold and Cryogenic Treatments on the Machinability of Beryllium-Copper Alloy in Electro Discharge Machining. In Proceedings of the 44th CIRP Conference on Manufacturing Systems, Madison, WI, USA, 31 May–3 June 2011.

**Disclaimer/Publisher’s Note:** The statements, opinions and data contained in all publications are solely those of the individual author(s) and contributor(s) and not of MDPI and/or the editor(s). MDPI and/or the editor(s) disclaim responsibility for any injury to people or property resulting from any ideas, methods, instructions or products referred to in the content.

MDPI  
St. Alban-Anlage 66  
4052 Basel  
Switzerland  
Tel. +41 61 683 77 34  
Fax +41 61 302 89 18  
[www.mdpi.com](http://www.mdpi.com)

*Metals* Editorial Office  
E-mail: [metals@mdpi.com](mailto:metals@mdpi.com)  
[www.mdpi.com/journal/metals](http://www.mdpi.com/journal/metals)







Academic Open  
Access Publishing

[www.mdpi.com](http://www.mdpi.com)

ISBN 978-3-0365-8281-8